Synthesis, Characterisation and Properties of Lithium Pyrophosphate Materials for Lithium Battery Applications

Kuang-Che Hsiao

Submitted for the Degree of Doctor of Philosophy

Supervisor: Prof. Anthony R. West

Department of Materials Science and Engineering

The University of Sheffield

October 2010 – June 2014

For Mum and Dad

Declaration

This thesis is submitted in consideration for the award of Doctor of Philosophy.

It is believed to be completely original, except where due references have been made.

Kuang-Che Hsiao

June 2014.

Acknowledgements

I would like to express my sincere thanks to my supervisor, Prof Anthony R. West, for all his valuable guidance and science wisdom to make this PhD thesis possible. I am truly grateful for his time, patience, encouragement and consideration throughout my PhD study. In addition, I want to thank Prof Derek C. Sinclair for sharing his abundant knowledge of e.g. impedance spectroscopy and defect chemistry, and precious advice in this thesis. I also thank Prof Peter R. Slater for his helpful comments and ideas in my viva. Thanks to E-Futures DTC, EPSRC, for financial support and specifically, Dr Neil J. Lowrie for his assistance in all my research projects.

I express special thanks to Dr Nahum Masó, Dr Nik Reeves-McLaren, Prof Alejandro Varez, Dr Yao-Chang (Ian) Chen and Dr Jordi Jacas Biendicho for their generosity in sharing their knowledge and insights with me for the Rietveld refinement and impedance work. I thank Dr Paul A. Bingham for Mössbauer measurement.

I would like to thank my colleagues from CCL group in the Department of Materials Science and Engineering for their experimental support in lab, interesting discussions and interaction in study: Andrew Mould, Rouzbeh Jarkaneh, Zhilun (Jack) Lu, Linhao (Leo) Li, Dr Denis Cumming, Bo Dong, John McCallum, Griffin Patterson, Abtsam Alagdl, Adil Alshoaibi, Gordon Brown, Fayaz Hussain, Greg Lewin, Simon Nicholls, Yen-Ju (Patrick) Wu and also other colleagues that have already left the department: Dr Chaou Choak Tan, Dr Yang Liu, Dr Yu Hu, Dr Liubin Ben, Dr Yi-Lin (Winson) Tsai. Many thanks to Dr Yi-Sheng Lee, Phei Yi Tan, Jeff Su, Dr Ruth Sayers and Wen Zhao for their warm friendship in life.

I would also like to thank my lovely sister, Dan Pan, who was my strongest supporter and lucky star during my study in Sheffield.

I want to thank my family members, grandmother, sister and brother as well as all my uncles/aunts and cousins for their life support and encouragement in my study. I am eternally grateful to Ya-Hui Chang for her lovely friendship and support during all these years and all the great moments we have spent together in Taiwan, USA and UK.

Most of all, I thank my parents, Mrs Hsiu-Chu Hung and Mr Chin-Chih Hsiao, for their understanding, patience, memory and unselfish love to make this all possible.

Abstract

Lithium transition metal pyrophosphates, $Li_2MP_2O_7$ (M=Fe, Mn, Co), have been successfully synthesised by a conventional solid-state method following a two-step process. XRD patterns show three isostructural analogues, $Li_2FeP_2O_7$, $Li_2MnP_2O_7$ and $Li_2CoP_2O_7$, and the solid solution, $Li_2Fe_{1/3}Mn_{1/3}Co_{1/3}P_2O_7$, synthesised at 700°C for 12 h in N_2, are single phase with monoclinic symmetry and space group $P2_1/c$. AC impedance results show the total conductivity of these four compositions at room temperature are $\sim10^{-10}$ Scm^{-1} for M=Fe, and $\sim10^{-11}$ Scm^{-1} for M=Mn, Co and $Fe_{1/3}Mn_{1/3}Co_{1/3}$. A detailed impedance investigation as a function of temperature, *dc*-bias, and atmosphere was carried out to evaluate the conduction mechanism and activation energy. Specifically, for M=Fe conduction is predominantly electronic. For Mn and Co, however, conduction is primarily ionic. $Li_2Fe_{1/3}Mn_{1/3}Co_{1/3}P_2O_7$ is a mixed conductor but with less electronic conduction. The materials were tested as possible cathodes in lithium batteries. $Li_2FeP_2O_7$ demonstrates better electrochemical properties, such as a stable voltage platform (~3.6 V), higher discharge capacity, high-rate performance and good cycle life attributed to its smaller particle size and higher electronic conductivity than those of $Li_2MnP_2O_7$, $Li_2CoP_2O_7$ and $Li_2Fe_{1/3}Mn_{1/3}Co_{1/3}P_2O_7$.

Attempted modification of the electrical properties of $Li_2FeP_2O_7$ by aliovalent doping (Al^{3+}, Zr^{4+}, Nb^{5+}) was studied, in particular with a view to increasing the level of lithium ion conductivity. Different doping mechanisms were considered; XRD results showed that Al and Zr do not substitute into the $Li_2FeP_2O_7$ structure but up to 5% Nb^{5+} can be substituted into $Li_2FeP_2O_7$, synthesised at 700°C in N_2, to form solid solutions, $Li_{1.85}Nb_{0.05}Fe_{0.95}P_2O_7$ and $Li_{1.95}Nb_{0.05}Fe_{0.9}P_2O_7$. Lattice parameters and unit volume are not changed in Nb-doped compounds and EDS mapping showed that the Nb dopants are not present uniformly in $Li_{1.85}Nb_{0.05}Fe_{0.95}P_2O_7$ and $Li_{1.95}Nb_{0.05}Fe_{0.9}P_2O_7$ and therefore, do not form a homogeneous solid solution. Impedance results show the doping of niobium enhances the bulk conductivity of material by a factor of 2~3 in air.

The anion doping of $Li_2FeP_2O_7$ was investigated by partial substitution of oxygen by nitrogen to create either interstitial Li^+ ions (mechanism 1: $Li_{2+x}FeP_2O_{7-x}N_x$) or holes (mechanism 2: $Li_2FeP_2O_{7-y}N_y$) for charge compensation. Electrical results show that mechanism 1 has little effect; the total conductivity and activation energy of

compositions x=0.05 and 0.1 have no big differences compared with that of x=0. For mechanism 2, composition y=0.05 has an increased electronic conductivity with a lower activation energy of 0.32(2) eV which is nearly half the value of 0.62(1) eV for undoped $Li_2FeP_2O_7$. This is attributed to the presence of Fe^{3+} ions (~1.2 %) in $Li_2FeP_2O_{6.95}N_{0.05}$ analysed by Mössbauer spectra and which therefore, give rise to electronic conduction associated with mixed valence Fe. A nitrogen content of y=0.0167 was obtained for y=0.05, which was confirmed by Mössbauer results of nitrogen incorporation into the sample. An improved synthesis method carried out in an Ar-filled glove box was developed for the targeted composition, $Li_2FeP_2O_{6.95}N_{0.05}$ (I-LFPN005); this sample had an electronic conductivity increased by a further three orders of magnitude to ~10^{-5} Scm^{-1} in N_2 and a lower activation energy of ~0.16 eV.

A range of lithium zinc pyrophosphate, $Li_{4x}Zn_{2-2x}P_2O_7$ ($0.2 \leq x \leq 0.75$) compositions were synthesised to investigate phase formation in the $Zn_2P_2O_7$–$Li_4P_2O_7$ binary system. Two single-phase, $LiZn_{1.5}P_2O_7$ (x=0.25) and $Li_{2.4}Zn_{0.8}P_2O_7$ (x=0.6), materials were successfully obtained at 600°C for 24 h in air to confirm results in the literature. A new phase, $Li_{1.33}Zn_{1.33}P_2O_7$ (x=0.33), was found and indexed as monoclinic with possible space group $P2_1/a$. A two phase mixture of $Li_{1.33}Zn_{1.33}P_2O_7$ and $Li_{2.4}Zn_{0.8}P_2O_7$ was observed in the composition $Li_2ZnP_2O_7$ (x=0.5) in contrast to literature reports. Three solid solution regions: x=0.2 to 0.25, 0.33 to 0.4 and 0.575 to 0.625 were found. The crystal structure determination of $Li_{2.4}Zn_{0.8}P_2O_7$ using neutron diffraction data showed that revision of the reported structure was necessary. In particular, revised M1 and M2 site occupancies in the distorted $M1O_4$ tetrahedra and $M2O_5$ trigonal-pyramids were necessary with Li:Zn ratios of 0.82:0.18 and 0.38:0.62. A systematic study of the electrical properties with composition x was carried out using impedance spectroscopy; in general, the conductivity increased with increasing x. The sample x=0.6 has the highest ionic conductivity, which is attributed to 2D Li^+ migration channels in the structure, and reaches a maximum of ~10^{-2} Scm^{-1} at 350°C equal to that reported for other Li^+ ion solid electrolytes such as $Li_{3.4}P_{0.6}Si_{0.4}O_4$ and $Li_{2.4}Zn_{0.8}SiO_4$.

Content

CHAPTER III

CHAPTER IV

CHAPTER I

Introduction & Literature Review

In order to decrease the global warming effect produced from CO_2 gas and to abate the energy crisis of fossil fuels, it is necessary to develop hybrid electric vehicles (HEVs) and electric vehicles (EVs) which are energy storage devices characterised by high energy density, acceptable charge/discharge rates, safety, and long cycle life [1-4]. The next-generation lithium-ion batteries should be used not only to power 3C portable products but also to meet global demands for advanced energy storage systems in terms of grid stabilization, renewable energy source integration (solar and wind power), transportation, and military applications. The key research factors concerning electrode materials for lithium-ion batteries focus on the need to increase energy and power density as well as developing a low-cost manufacturing process. High performance and nonflammable electrolyte also should be developed to improve thermal stability and cycling life of battery.

Since Sony's introduction of insertion compounds as electrodes in 1990, the early discovery and commercialization of cathode materials have been devoted to oxide-based electrodes such as $LiCoO_2$, $LiMn_2O_4$, $LiNiO_2$ and $LiNi_{1/3}Mn_{1/3}Co_{1/3}O_2$ [5-7]. Although organic liquid electrolytes are widely utilized due to their high ionic conductivities, wide operating temperature window, high performance and nonflammability, solid electrolytes should be developed to improve thermal stability and cycling life of batteries [8]. The practical application of solid electrolytes is currently limited because of their low ionic conductivities $\lesssim 10^{-2}$ Scm^{-1} at 50–80 °C and low chemical and electrochemical stabilities [9]. A room temperature conductivity of at least $\sim 10^{-3}$ Scm^{-1} is needed for an electrolyte to work well in battery systems [10].

In 1997, Goodenough's research on olivine-structured $LiFePO_4$ caused a paradigm shift from oxides to polyanionic compounds [11-13]. $LiFePO_4$ can reversibly deintercalate one lithium ion per iron atom (theoretical capacity: 170 mAh/g), at about 3.4 V vs. Li^+/Li. $LiFePO_4$ seems to be the best candidate for energy storage in hybrid and electric vehicles due to its thermal stability and low toxicity. However, in comparison with other cathode materials, $LiFePO_4$ suffers from the problem of low working voltage and poor capacity at

high rate mainly because of its low electronic conductivity and Li ion diffusivity. These shortcomings need to be overcome before its realization for practical uses. To store more energy density, new potential phosphate materials are needed in which the redox reaction exceeds one electron per transition metal.

1.1 Lithium Ion Batteries

A battery is an electrochemical energy storage system that can convert chemical energy into electricity. It consists of several electrochemical cells that are connected in parallel and/or in series to provide the required capacity and voltage, respectively. Each cell has a negative (the anode: **–**) and a positive electrode (the cathode: **+**), as the sources of chemical redox reactions separated by the non-aqueous electrolyte. The electrolyte possesses dissociated salts, which provides an ion transport path between the two electrodes. The electrolyte does not take part in the reaction except for conveying the electro-active lithium ions during discharge from a high (chemical) energy state in the anode to a low (chemical) energy state in the cathode while the electrons pass through the external circuit with a release of (electric) energy. If this process is reversible, in other words, the chemical energy can be restored by supplying electric power, the device which undertakes this process is called a rechargeable battery, as illustrated in the **Fig. 1-1**. Typical electrochemical reactions in a C/electrolyte/$LiCoO_2$ cell on charge are presented by following reaction, Equations 1.1–1.3:

- Anode: $xLi^+ + xe^- + C_6 \xrightarrow{charge} Li_xC_6$ (1.1)
- Cathode: $LiCoO_2 \xrightarrow{charge} Li_{1-x}CoO_2 + xLi^+ + xe^-$ (1.2)
- Overall reaction: $LiCoO_2 + 6C \xrightarrow{charge} Li_xC_6 + Li_{1-x}CoO_2$ (1.3)

Compared with mature battery technologies, e.g. Lead-acid, Ni-Cd, and Ni-MH, the lithium-ion battery is the dominant rechargeable battery technology because of its higher energy density up to 200 Wh/kg and design flexibility (lighter weight and smaller size), as shown in **Fig. 1-2**. In addition, the Li-ion battery possesses a relatively low self-discharge, no memory effect and is environmentally friendly.

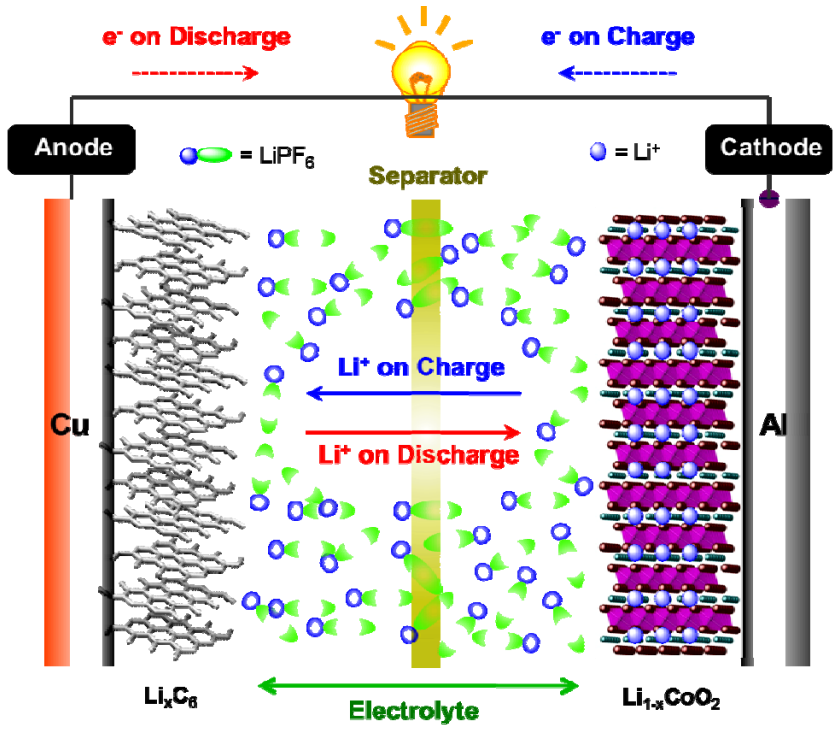

Figure 1-1 Schematic illustration of the lithium ion batteries (graphite/electrolyte/$LiCoO_2$) [14].

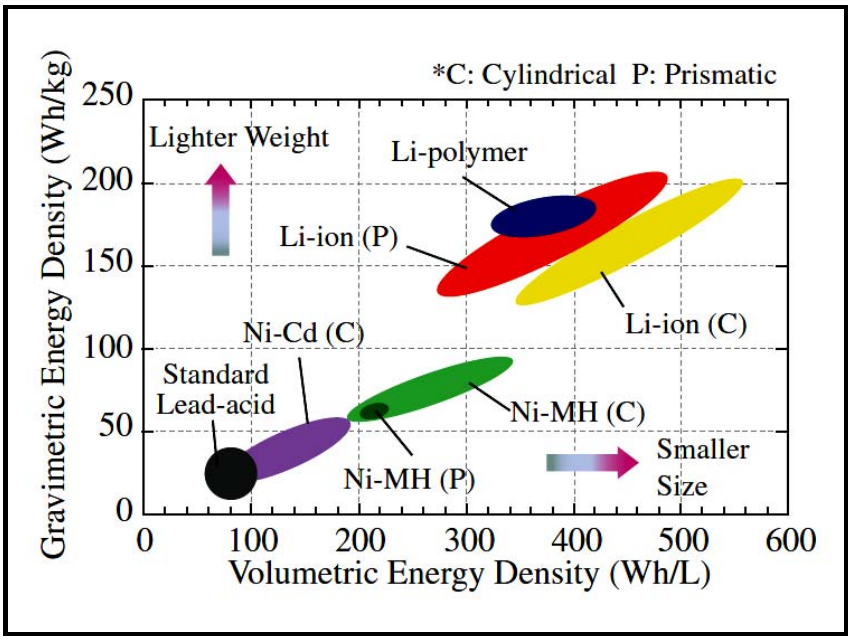

Figure 1-2 Graphic description of the volumetric and gravimetric energy density for different battery technologies [15].

A typical thermodynamic Equation (1.4) for the cell potential of an electrochemical cell is given as

$$\Delta G = -nFE \tag{1.4}$$

where n is the number of transferred electrons, F is Faraday's constant (96485.33 C/mole) and E is the cell voltage (V). The open-circuit voltage (V_{OC}) of a Lithium-ion cell can be described by Equation 1.5:

$$V_{OC} = \frac{-[\mu_{Li(Cathode)} - \mu_{Li(Anode)}]}{nF} \tag{1.5}$$

where μ_C and μ_A are the cathode and anode electrochemical potentials.

This voltage is the difference between μ_C and μ_A and is limited by the 'window' of the electrolyte which is the energy gap, E_g, between the lowest unoccupied and highest occupied molecular orbital (LUMO and HOMO) of a liquid electrolyte [16], illustrated in **Fig. 1-3**. A cathode with a μ_C below the HOMO oxidizes the electrolyte and therefore, a passivating SEI layer forms which blocks further electron transfer from the electrolyte HOMO to the cathode. A μ_A above the LUMO reduces the electrolyte unless a SEI creates a barrier to electron transfer from the anode to electrolyte LUMO [4]. Note that solid electrolyte interface (SEI) is a surface film that generally forms between an electrode and electrolyte. It is an internal resistor that limits power output and generates heat build-up in a standard Li-ion battery.

The challenges of developing Li-ion batteries for electric vehicles are to 1) design cathode and anode with their μ_C and μ_A values well-matched to the electrolyte window, such that each allows a large reversible capacity with a fast charge and discharge cycle; 2) investigate a nonaqueous electrolyte with high ionic conductivity ($\sigma_{Li} > 10^{-2}$ Scm^{-1}) over a wide operating temperature range, -40°C < T < 60°C [4].

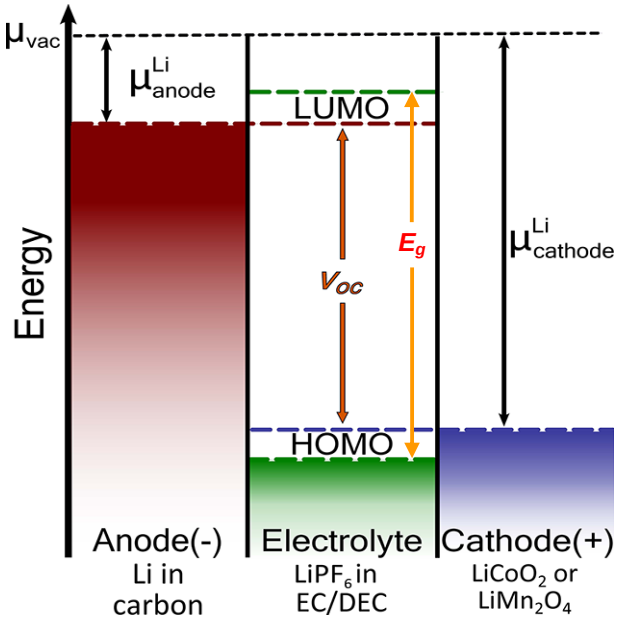

Figure 1-3 Schematic illustration of the energy levels in the Li-ion battery. LUMO: the lowest unoccupied molecular orbital; HOMO: the highest occupied molecular orbital; V_{OC}: open-circuit voltage; μ: chemical potential [17].

1.2 Design of Electrode Materials

In order to develop better electrode materials and electrolytes, there are many aspects that remain to be improved in the field of lithium ion batteries, such as control of the particle size, structure and morphology. Two crucial approaches have made it possible to improve the poorly-conductive nature of many electrode materials for practical application in batteries, as shown in **Fig. 1-4**. One is to reduce the particle size of the electrode from bulk to submicro- or nano-scale, which gives a shorter transport path of Li ions and therefore, an increased ionic conductivity. The other is to coat conductive carbon on the surface of the electrode to form a core-shell structure, which may dramatically increase the electronic conductivity [15].

The energy density of a battery is the product of its capacity and potential, as expressed by Equation 1.6 [16]:

$$energy = \int_0^{\Delta t} IV(t)dt = \int_0^{Q} V(q)dq \qquad (1.6)$$

where V is the working voltage (V) and Q is the discharge capacity ($Ah \cdot kg^{-1}$ or $Ah \cdot L^{-1}$) transferred by the discharge current $I_{dis} = dq / dt$. Therefore, the gravimetric or volumetric energy density ($Wh \cdot kg^{-1}$ or $Wh \cdot L^{-1}$) in a rechargeable cell depends on the voltage and specific capacity of electrode materials.

Fig. 1-5 illustrates the voltage vs. capacity of the cathode and anode materials currently used and potential candidates for the next-generation lithium ion battery. In terms of cathode material systems, they mainly consists of layered cathodes: lithium cobalt oxide ($LiCoO_2$, ~3.8 V), lithium-cobalt-nickel (manganese) oxide ($LiCoNi(Mn)O_2$, ~ 3.6–3.7 V), composite oxides ($Li_2MnO_3 \bullet (1-x)LiMO_2$, ~ 2.0–4.8 V); spinel structures: lithium manganese oxide ($LiMn_2O_4$, ~4.0 V), lithium nickel manganese oxide ($LiNi_{0.5}Mn_{1.5}O_4$, ~4.7 V); olivine structures: lithium iron phosphate ($LiFePO_4$, ~3.4 V); lithium iron manganese phosphate ($LiFe_xMn_{1-x}PO_4$, ~3.7 V); 3D metal fluoride (MF_3, ~ 2.0–3.5 V). To achieve higher energy density for Li-ion batteries, it is necessary to develop new cathode materials with increased capacity and/or higher voltage.

Anode materials mainly include commercial graphite, hard carbon and MesoCarbon MicroBeads (MCMB). The traditional anode in lithium ion battery possesses a specific capacity ca. 310~360 mAh/g, which has almost reached the maximum theoretical value (372 mAh/g). However, with the increasing challenges of battery technology, for high energy density, quick charge, low cost and high safety, for 3C portable product and electric vehicle applications, traditional carbon materials have been unable to meet these demands. Therefore, it is necessary to develop fast charge/discharge anode materials based on titanium (Ti) systems: titanium dioxide (TiO_2, ~1.8 V), lithium titanate ($Li_4Ti_5O_{12}$ (LTO), ~1.5 V); high-capacity silicon/carbon (Si-C, ~0.4 V) and tin/carbon (Sn-C, ~0.2 V) composite materials for the next-generation high energy and power density Li-ion batteries.

Fig. 1-6 summarizes the capabilities for lithium-ion battery R&D in Sheffield including new potential materials synthesis (cathode, anode and solid electrolyte), advanced characterization techniques, and electrochemical testing of battery materials [20].

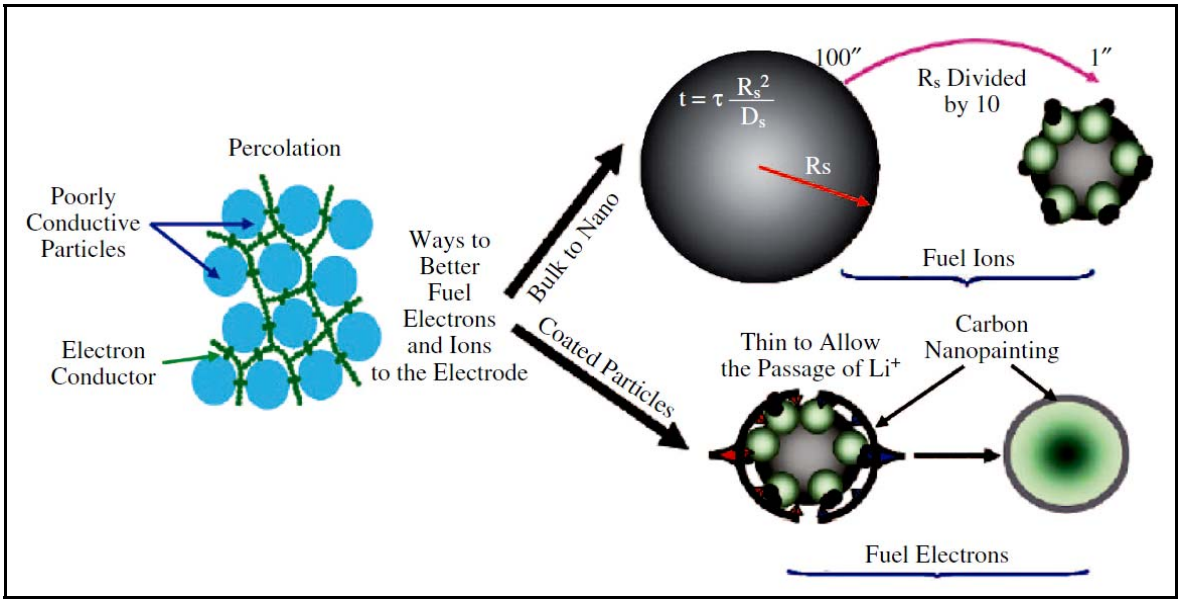

Figure 1-4 Schematic of two important improvements to poorly-conductive electrode materials by downsizing the particle size and carbon nanocoating [18].

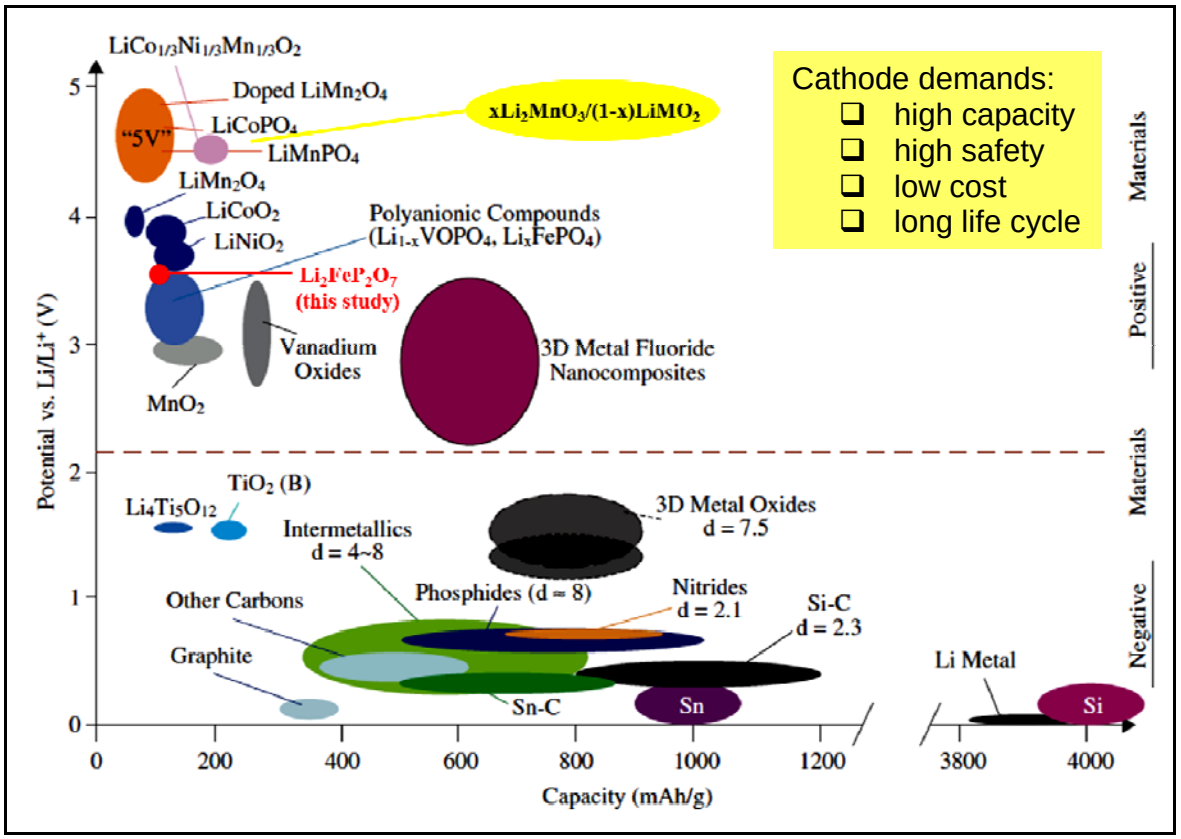

Figure 1-5 Voltage versus capacity for cathode and anode materials presently used and potential considerations for next-generation Li-ion batteries [19].

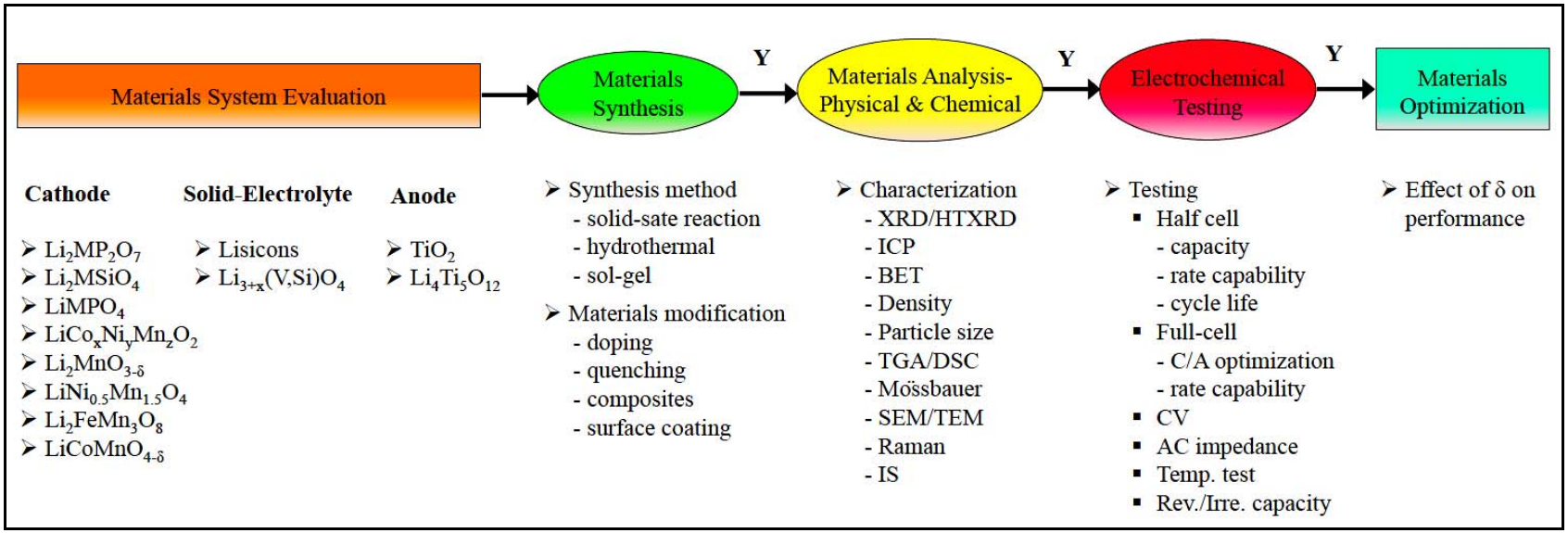

Figure 1-6 Development of battery materials in Sheffield [20].

1.3 Polyanionic Cathode Materials

Polyanionic compounds, containing transition metals and different polyanionic units $(XO_4)^{n-}$ or $(X_mO_{3m+1})^{n-}$ (X = P, S, Si), have received much recent attention as potential cathode materials for next-generation Li-ion batteries [21-22]. The olivine phosphate, $LiFePO_4$ has been the most successful so far due to its remarkable electrochemical performance and thermal stability. However, in order to increase energy density, further advances in polyanioic cathodes are needed in which either the operating voltage is enhanced and/or the redox reaction exceeds one electron per transition metal. A historical diagram including different Fe-based polyanionic electrode materials is shown in **Fig. 1-7**; a brief description of their crystal structures and electrochemical properties for one- and two-lithium metal polyanionic cathodes is given in the next section.

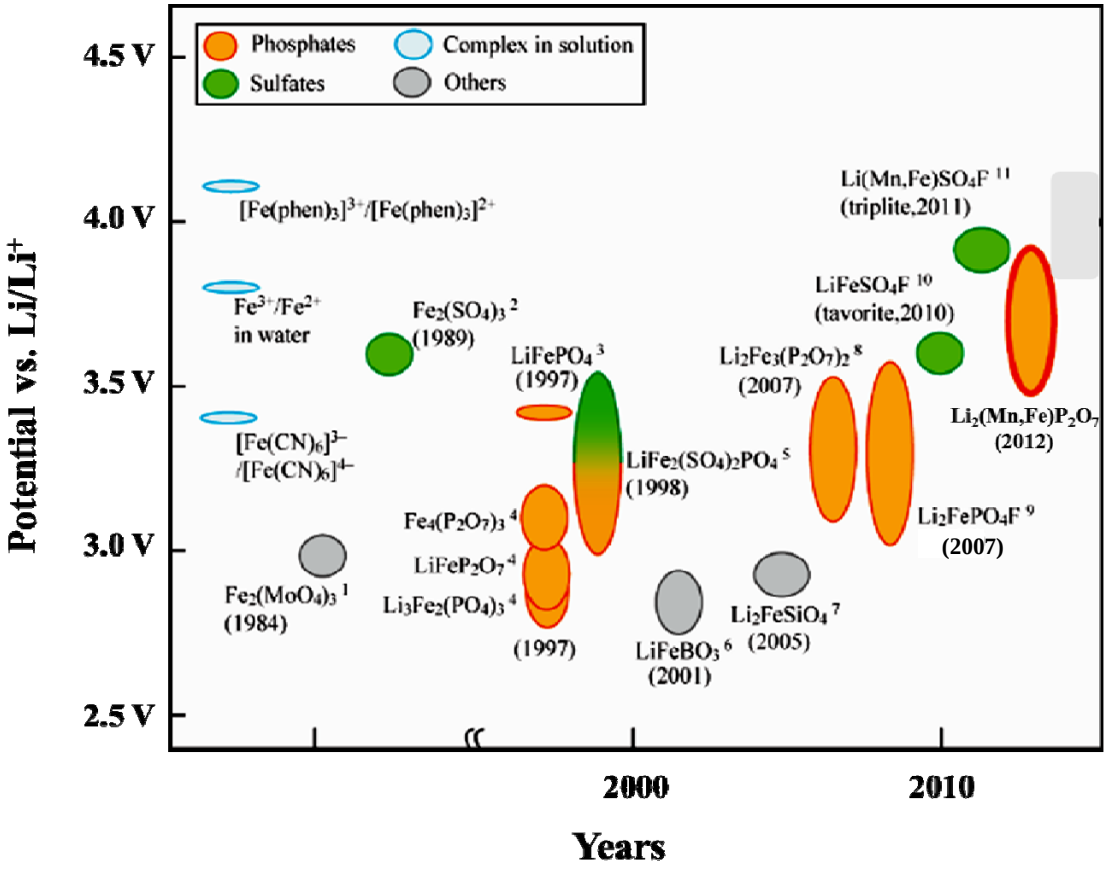

Figure 1-7 Historical overview of the iron oxyanionic cathodes (phosphates, sulphates, complexes and others) with the potential of Fe^{2+}/Fe^{3+} redox couple [23].

1.3.1 One-Lithium Polyanionic Cathodes

(i) $LiFePO_4$

Lithium iron phosphate ($LiFePO_4$) has been a very attractive cathode material because of its low cost, good cycle life and safety. The olivine structure of $LiFePO_4$ has an orthorhombic structure (P*nma*) wherein phosphorous (P) occupies tetrahedral sites, the transition metal iron (Fe) occupies octahedral sites and Li forms one-dimensional chains along the *b*-axis, as illustrated in **Fig. 1-8**. $LiFePO_4$ can reversibly insert and extract one lithium ion per iron atom (theoretical capacity = 170 mAh/g), at ~3.4 V vs. Li^+/Li (which makes it much more stable in the electrolytes commercially used in Li-ion batteries).

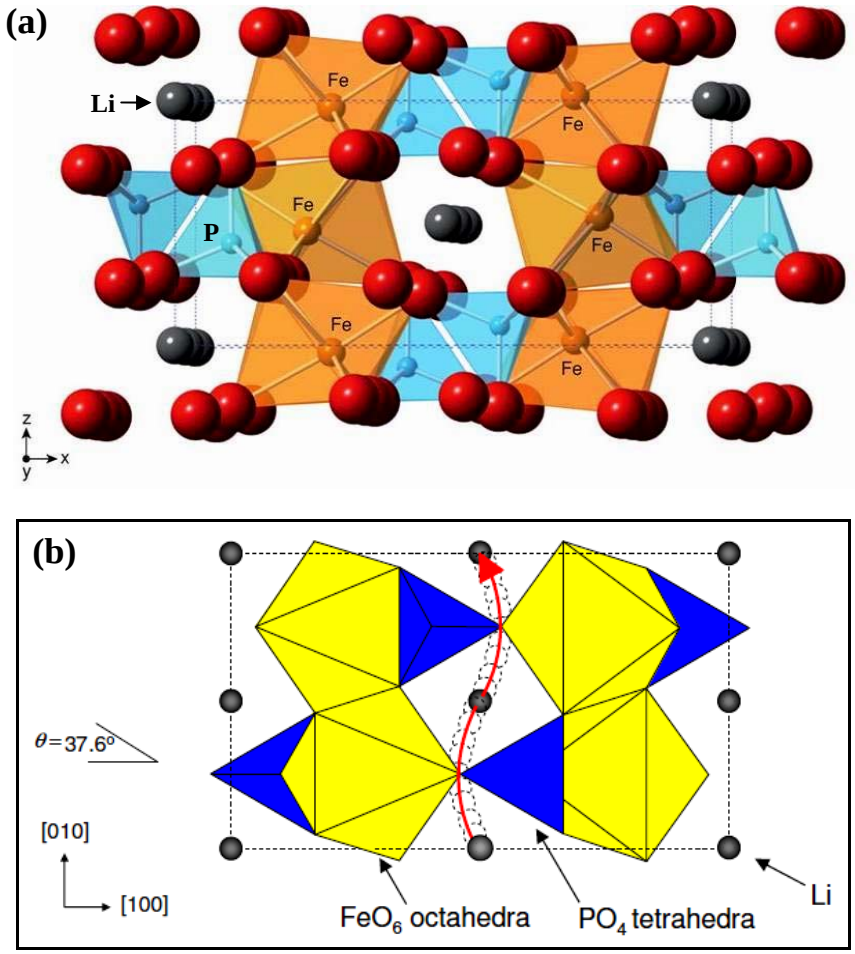

Figure 1-8 Schematic representation of the (a) $LiFePO_4$ olivine structure projected to *b*-axis [24], and (b) Li migration path in the [010] direction [25].

$LiFePO_4$ seems to be the best candidate for energy storage in hybrid and electric vehicles due to its thermal stability and low toxicity. However, in contrast to other cathode materials, e.g. $LiCoO_2$, $Li[Ni_{1-x-y}Mn_xCo_y]O_2$ and $LiMn_2O_4$, the main inherent shortcomings of $LiFePO_4$ are its low electronic conductivity ($\sigma \sim 10^{-9}$ Scm^{-1}) and low Li ion diffusivity ($D_{Li} \sim 10^{-14}$ cm^2s^{-1}), which result in relatively low working voltage and poor capacity at high rate discharge [26], see **Table 1-1**. These shortcomings need to be overcome before its realization for commercial application. It has been reported that the electronic and ionic conductivities of $LiFePO_4$ were increased by cation doping [27-28], carbon coating [29] and particle size reduction [30] and therefore, the high-rate discharge properties and high temperature stability of $LiFePO_4$ can be improved.

Table 1-1 Characterization of different cathode materials for lithium-ion batteries.

Materials	**$LiCoO_2$**	**$LiNiO_2$**	**$Li[NiCo]O_2$**	**$Li[NiMn]O_2$**	**$Li[NiMnCo]O_2$**	**$LiMn_2O_4$**	**$LiFePO_4$**
Structure	layer	layer	layer	layer	layer	spinel	olivine
Average working voltage (V) @ 0.2C	3.85	3.55	3.7	3.9	3.8	4.05	3.4
Energy density (mAh/g) @ 0.2C; 2.8–4.2V	145	200	180	155	170	110	145
Power density (W/Kg) @ 1C	456	621	602	546	570	436	452
Conductivity (S/cm)	$\sim 10^{-3}$	$\sim 10^{-4}$	4×10^{-4}	6×10^{-5}	1.4×10^{-4}	2×10^{-5}	$\sim 10^{-9}$
Li ion diffusivity (cm^2/s)	5×10^{-9}	2×10^{-7}	$10^{-9}\sim10^{-8}$	3×10^{-10}	…	1.2×10^{-11}	10^{-14}
Safety	O	×	~	O	OO	OO	OO
Cycle life @ 55°C	≈	×	~	~	≈	~	~
Cost	×	O	O	OO	O	OO	OO

(ii) $LiFe_{1.5}P_2O_7$

In 2007, Ramana *et al.* reported a new lithium iron pyrophosphate, $LiFe_{1.5}P_2O_7$, synthesised via a wet-chemical method using $Li(COOCH_3)\cdot 2H_2O$, $Fe(COOCH_3)\cdot 2H_2O$ and H_3PO_4 as reactants and reacted at 500~600 °C for 24 h in Ar/H_2 gas [31]. This compound had a thortveitite-like monoclinic structure with $P2_1/c$ symmetry, in which phosphorous P (purple) occupies tetrahedral sites, the transition metal Fe (brown) occupies octahedral sites and lithium (green) forms one-dimensional chains along the *a*-axis, as shown in **Fig. 1-9(a)**. The crystal structure of $LiFe_{1.5}P_2O_7$ is built up through the interconnection of the edge-sharing FeO_6 octahedra and P_2O_7 groups to form a three-dimensional framework.

Fig. 1-9(b) presents the first charge-discharge curve of $LiFe_{1.5}P_2O_7$ in the potential range 2.5–4.2 V at a constant charge/discharge rate of $C/20$ at 25°C; it shows a reversible capacity ~95 mAh/g, reaching 94% of the capacity of one-electron theoretical value of 101 mAh/g. Two distinguishable voltage plateaus were clearly observed by cyclic voltammetry measurement (insert), which correspond to the two sets of redox couples located at 3.56 and 3.22 V. The Fe^{2+}/Fe^{3+} redox potential of $LiFe_{1.5}P_2O_7$ was much higher than that of $LiFeP_2O_7$ (2.9 V) [32].

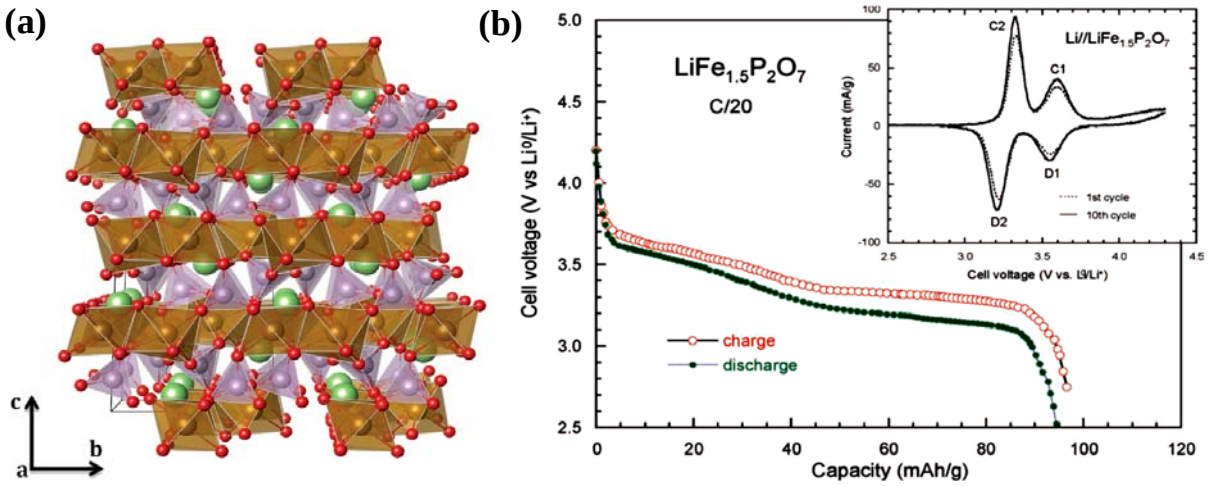

Figure 1-9 (a) 3D crystal structure of $LiFe_{1.5}P_2O_7$ along the *a*-axis, where FeO_6 octahedra and P_2O_7 diphosphate units are shown in brown and purple [23]; (b) charge- discharge curves of the $LiFe_{1.5}P_2O_7$ cell tested at $C/20$ for the 1st cycle and (inset) its cyclic voltammogram (CV) at 0.1 mV/s sweep rate between 2.5–4.3 V [31].

(iii) $LiFeSO_4F$

In 2010, Tarascon *et al.* reported a novel iron fluorosulfate ($LiFeSO_4F$) as cathode synthesized via a low-temperature ionothermal method to replace traditional ceramic solid-state calcination [33]. Specifically, 1-ethyl-3-methylimidazolium bis-(trifluoromethanesulfonyl) imide (EMI-TFSI) was chosen as the reacting medium to synthesise $LiFeSO_4F$, and $FeSO_4{\cdot}7H_2O$ and LiF as the Fe- and Li-based precursors, respectively. This material has a theoretical capacity 151 mAh/g in which the redox reaction is one electron per transition metal.

Fig. 1-10(a) illustrates $LiFeSO_4F$ has a Tavorite-type structure (space group P-1), with lattice constants: a = 5.1747(3) Å, b = 5.4943(3) Å, c = 7.2224(3) Å, α = 106.522(3)°, β = 107.210(3)°, γ = 97.791(3)° and V = 182.559(16) Å^3, with three-dimensional channels for Li-ions to migrate. In the triclinic cell of $LiFeSO_4F$, for two independent iron (Fe) atoms, one (Fe1) is located at the origin of the unit cell (0, 0, 0) and the other (Fe2) in the middle of the c-axis (0, 0, 1/2), which are interconnected through a SO_4 tetrahedra [33], **Fig. 1-10(b)**.

In terms of electrochemical performance of $LiFeSO_4F$, it had a slightly higher voltage ~3.6 V than $LiFePO_4$ (3.4 V) and delivered a first discharge capacity of 130~140 mAh/g (≈ 85% of the theoretical value) cycled between 2.5 and 4.2 V at $C/10$ rate without any carbon coating on the surface of $LiFeSO_4F$ particles. After being subjected to the 1st cycle, $LiFeSO_4F$ still demonstrates a good capacity retention of ~125 mAh/g at $C/10$ charge/discharge rate after 50 cycles, **Fig. 1-11**.

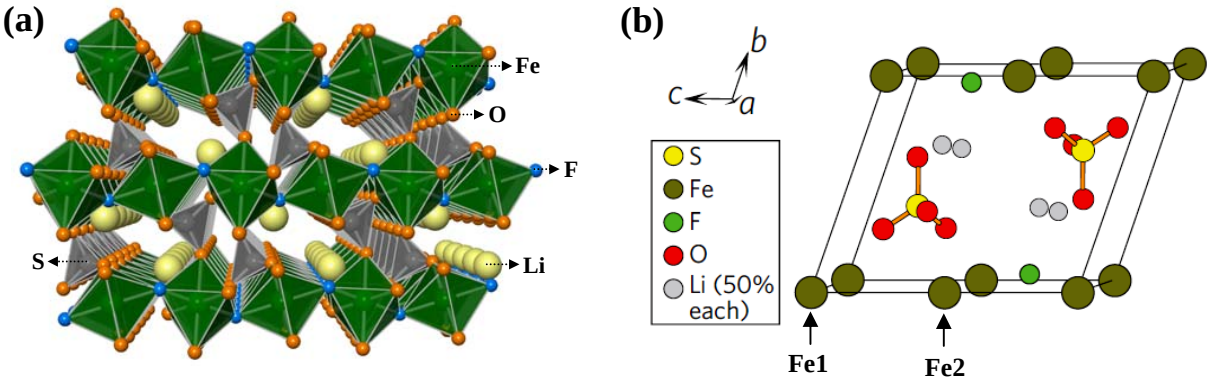

Figure 1-10 Schematic of $LiFeSO_4F$ Tavorite-type structure [17, 33].

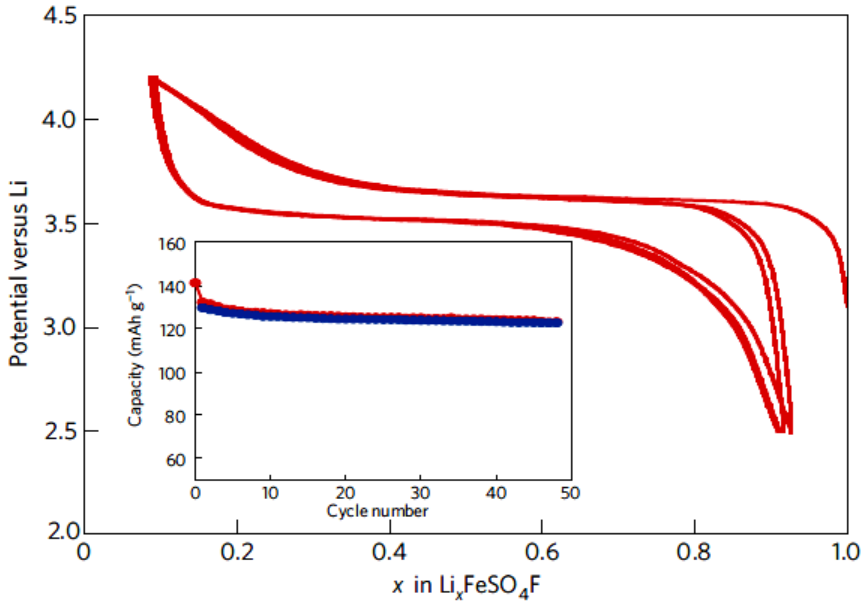

Figure 1-11 Charge/discharge galvanostatic curves and cycling performance for $LiFeSO_4F$ cell at *C*/10 (cut-off voltages: 2.5–4.2 V) [33].

1.3.2 Two-Lithium Polyanionic Cathodes

(i) Li_2FeSiO_4

In 2005, Nytén *et al.* first reported the lithium iron silicate, Li_2FeSiO_4, prepared by solid-state reaction using Li_2SiO_3 and $FeC_2O_4{\cdot}2H_2O$ reactants. This compound was initially indexed as an orthorhombic unit cell with space group P$mn2_1$ which is isostructural with Li_3PO_4 [34]. Electrochemical results showed the first discharge capacity was 165 mAh/g (99% of the one electron theoretical capacity of 165.5 mAh/g) and stabilised to ~140 mAh/g after a few cycles. In particular, an irreversible phase transition and structural ordering on Li/Fe sites were observed after the first charge/discharge process [34-36]. Subsequently, more research to gain insight into the nature of Li_2FeSiO_4 was widely carried out in the last decade, such as crystal structure determination on the products of different preparation temperatures [37-39], symmetry change to low temperature phase [40], and voltage and structure change in the various Li_2FeSiO_4 polymorphs by theoretical calculations [41]. In addition, clarification of the crystal structure and phase transformation mechanism upon charging and discharging is also significant to the design of Li_2FeSiO_4 materials.

Recently, Masese *et al.* investigated the structural changes of Li_2FeSiO_4 during charge and discharge process at different *C*-rates by synchrotron X-Ray diffraction [42]. It was found at lower rate $C/50$, that the original monoclinic Li_2FeSiO_4 structure ($P2_1/n$) transforms to a thermodynamically stable orthorhombic $LiFeSiO_4$ structure (P*nma*) with half of the Li/Fe antisite mixing after 1st charging process, **Fig. 1-12 (a, c)**. However, at higher rate $C/10$, the structure appears to be unchanged with little cationic mixing, **Fig. 1-12 (a, b)**. When given enough time to relax, the unstable monoclinic $LiFeSiO_4$ ($P2_1/n$) should undergo reconstructive phase transformation to the stable orthorhombic phase.

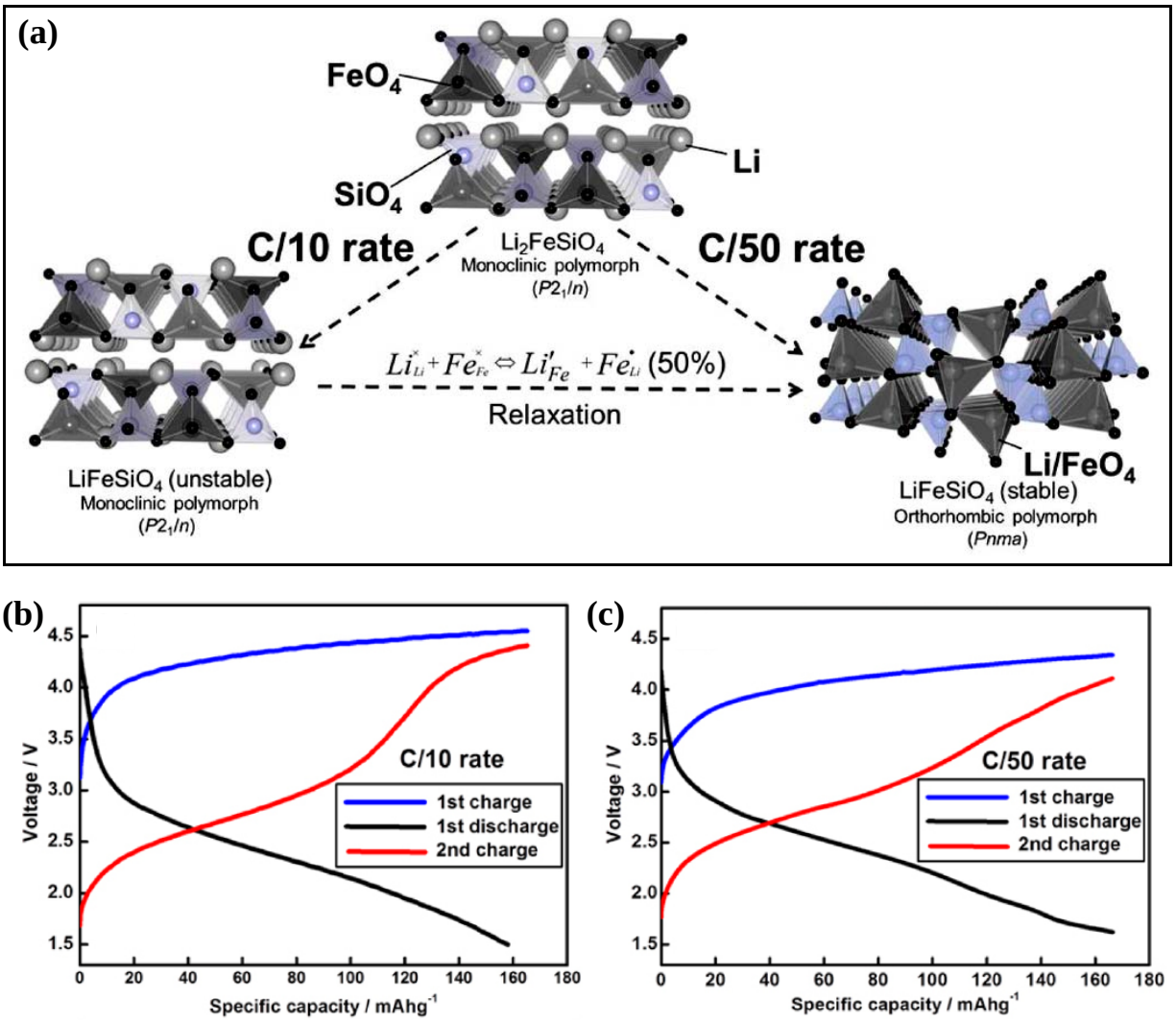

Figure 1-12 Schematic illustration of the phase transition occurred in the Li_2FeSiO_4–$LiFeSiO_4$ system upon cycling at $C/10$ and $C/50$ (a) and its corresponding charge and discharge curves at (b) $C/10$ and (c) $C/50$ [42].

(ii) $Li_2MnP_2O_7$

A novel manganese pyrophosphate, $Li_2MnP_2O_7$, has been first reported by Adam *et al.* in 2008 [43]. $Li_2MnP_2O_7$ has monoclinic symmetry (space group: $P2_1/a$), with lattice constants: a = 9.9158(6) Å, b = 9.8289(6) Å, c = 11.1800(7) Å, β = 102.466(5)°, Z = 8, and V = 1063.9(1) (Å^3), with channels running along the [100] direction for two lithium ions to be possibly mobile and removable, as illustrated in **Fig. 1-13(a)**. Monoclinic $Li_2MnP_2O_7$ has a 3D framework built of MnO_5 trigonal bipyramids (Mn1) sharing edges with MnO_6 octahedra (Mn2), **(b)**, which are interconnected through P_2O_7 groups, **(c)**. $Li_2MnP_2O_7$ was regarded as an ordered pyrophosphate and its structure possesses four different Li cation sites, Li1-4, with full occupancy, to form $[Li_2O_5]\infty$ and $[Li_2O_6]\infty$ layers.

In 2010, Zhou *et al.* reported the synthesis and detailed structural and electrochemical characterisation of $Li_2Mn_{1-y}Fe_yP_2O_7$ solid solution synthesised via a wet method (e.g. mixing stoichiometric precursors in aqueous solutions) followed by heat treatment [44]. Specifically, for the Mn-only phase, its electrochemical properties are very poor including low capacity of less than 5 mAh/g, high polarization, and no voltage plateaus observed during charge or discharge. This may be attributed to larger (> 5 μm) and inhomogeneous particle size. Similar results are obtained in $Li_{2-x}(Fe_{1-y}Mn_y)P_2O_7$ synthesised using the solid-state method by Yamada's group [45]. They also claimed the reasons for inactive Mn species are probably due to its lower electronic conductivity, Jahn-Teller distortion caused by Mn^{3+}, and a lack of isolated minority spin electron below the Fermi level [45].

Subsequently, Tamaru *et al.* showed that $Li_2MnP_2O_7$ can deliver ~60 mAh/g at the highest Mn^{3+}/Mn^{2+} redox potential of 4.45 V using a constant charge/discharge rate of C/50 [46], **Fig. 1-14**. One possible explanation for the improved electrochemical performance of $Li_2MnP_2O_7$ is that they added conductive Super-P into the active materials before electrode fabrication; as a result, smaller particle size (3~5 μm) resulted from inhibited grain-growth by carbon black and/or an increased electronic conductivity may have occurred. However, no conductivity measurements were reported for $Li_2MnP_2O_7$ in Ref. 44–46 to indicate whether this material is primarily an electronic or ionic conductor.

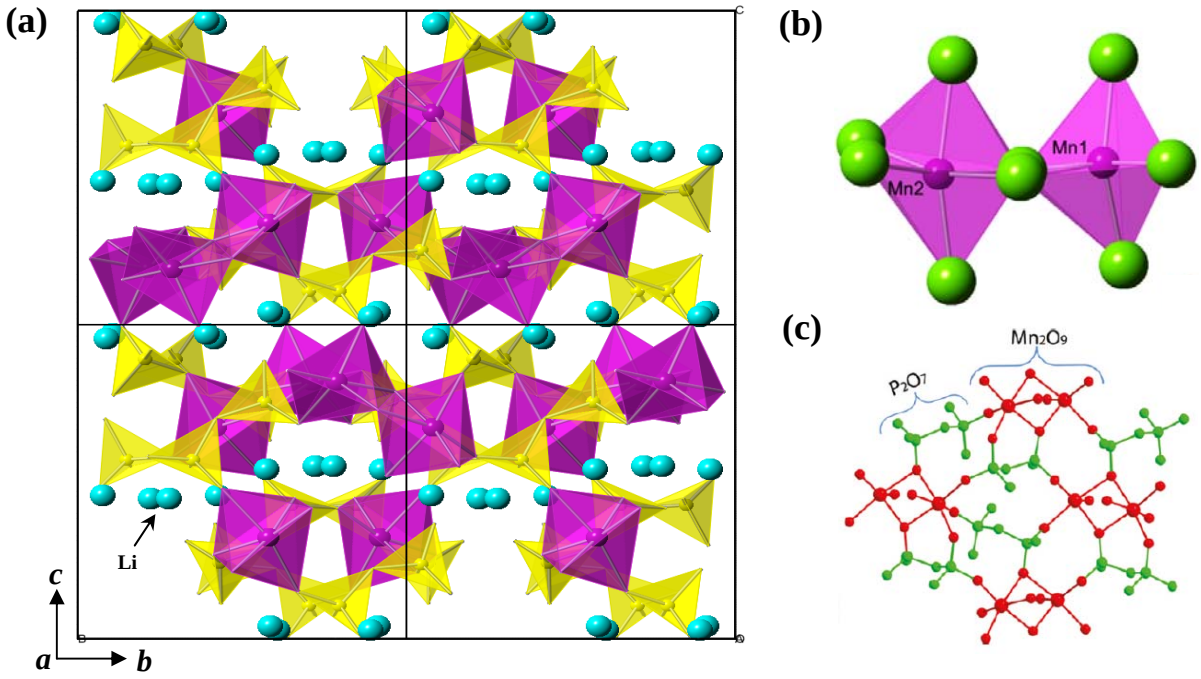

Figure 1-13 (a) 3D crystal structure of $Li_2MnP_2O_7$ along the *a*-axis, (b) local atomic coordination, and (c) connection between Mn_2O_9 with P_2O_7 groups in *ab* plane [44].

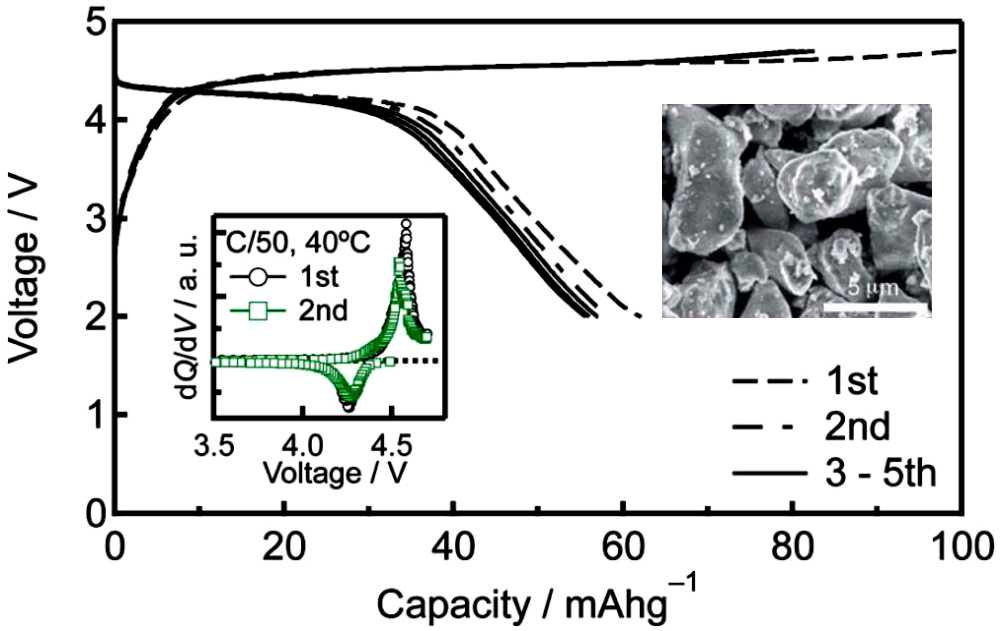

Figure 1-14 Charge-discharge curve of $Li_2MnP_2O_7$ for five cycles in the voltage range 2–4.7 V at *C*/50 (at 40°C) [46]. (Inset) SEM image and CV profile with two cycles.

(iii) $Li_2FeP_2O_7$

In 2010, Nishimura *et al.* first demonstrated a novel lithium iron pyrophosphate, $Li_2FeP_2O_7$, as cathode material for lithium ion batteries [47]. The $Li_2FeP_2O_7$ has a monoclinic structure ($P2_1/c$), in which FeO_5 trigonal bipyramids share edges with FeO_6 octahedra; these pairs are interconnected through P_2O_7 groups to form a 3D framework, **Fig. 1-15(a)**. $Li_2MnP_2O_7$ has two distinct Mn sites: fully occupied MnO_6 octahedra and MnO_5 bipyramids. In the case of $Li_2FeP_2O_7$, Fe1 sites in distorted FeO_6 are full, however, Fe2 and Fe3 sites in FeO_5 distorted bipyramids are partially occupied, see **(b)**; Fe3 partially moves into the LiO_5 bipyramidal sites, which shares an edge with Fe1 and Fe2 sites. Two sets of lithium ion sites may form quasi-two dimensional chains along the *a*-axis, which provide a mobile and removal path for Li diffusion, **(c)**. In short, $Li_2FeP_2O_7$ is a disordered pyrophosphate with Li-Fe anti-site defects attributed to similar ionic radii of Li^+ (0.76 Å-LiO_6) and Fe^{2+} (0.78 Å-FeO_6) [47].

$Li_2FeP_2O_7$ can reversibly insert and extract one lithium ion per iron atom (one electron theoretical capacity: 110 mAh/g) at about 3.5 V vs. Li^+/Li. The chemical composition $Li_{2-x}MP_2O_7$, however, involves a two electron reaction possibility between M^{2+} and M^{4+} ($0 < x < 2$), where the theoretical capacity would reach up to 220 mAh/g. New Fe-based lithium pyrophosphate compounds, therefore, may provide a new platform for related lithium battery electrode research and could be potential competitors to commercial olivine $LiFePO_4$. **Table 1-2** summarizes the comparison of properties of $Li_2FeP_2O_7$ and $LiFePO_4$ cathode materials.

In comparison to other cathode materials in **Fig. 1-5**, $Li_2FeP_2O_7$ also suffers from the problems of relatively low working voltage, limited capacity (one lithium per redox center), and poor capacity at high rate mainly because of its low electronic conductivity ($\sim 10^{-9}$ Scm^{-1}, 25°C in air) which was first presented in our work [14]. High-rate discharge properties and high temperature stability of $Li_2FeP_2O_7$ could be further improved by coating conductive carbon into the $Li_2FeP_2O_7$ material.

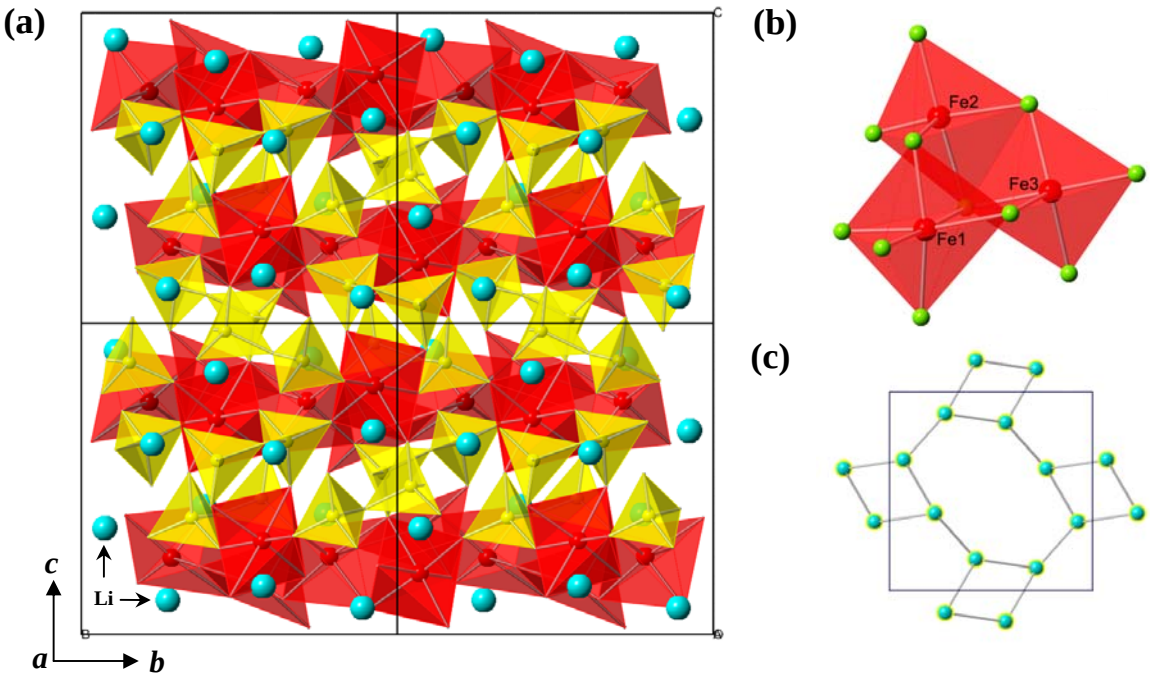

Figure 1-15 (a) 3D structure of $Li_2FeP_2O_7$ along the *a*-axis, (b) local atomic coordination, and (c) possible two dimensional Li diffusion path.

Table 1-2 Characterization of $Li_2FeP_2O_7$ and $LiFePO_4$ cathode materials.

Materials	**$Li_2FeP_2O_7$**	**$LiFePO_4$**
Average working voltage (V)	3.5	3.4
Density (g/cm^3)	3.141	3.5
Symmetry	monoclinic $P2_1/c$	orthorhombic $Pnma$
Theoretical specific capacity (mAh/g)	220	170
Practical capacity (mAh/g) @ $C/20$	85–110	140–150
Energy density (kWh/L) @ $C/20$	1.21	1.8
Conductivity (S/cm) @ 25°C in air	$\sim 10^{-9}$	$\sim 10^{-9}$
Cost	O	OO

1.4 Solid Electrolytes

The Li^+ conducting oxide materials can be used for application in the all-solid-state lithium batteries [48]. Lithium superionic conductors used as solid electrolyte in high density lithium batteries exhibit a higher conductivity and lower activation energy for Li^+ migration contributed from their rigid framework structure to form a mobile sublattice [49]. Since the 1970s, these materials based on $LiO_{1/2}$–$AO_{m/2}$–$BO_{n/2}$ system have been studied and are so-called *LISICONs* with a general formula $Li_{8-c}A_aB_bO_4$ ($c = ma + nb$), whereas the m and n are the valences of A and B cations, respectively [50-51]. The prime *LISICON* composition, $Li_{3.5}Zn_{0.25}GeO_4$, was discovered to possess an ionic conductivity of $\sim 2\times10^{-1}$ Scm^{-1} at 400°C with an activation energy of 0.24 eV between 250~400 °C [52]. Soon it opened up a wide range of crystalline lithium-ion conducting materials. **Fig. 1-16** shows an Arrhenius plot of the ionic conductivity of the $Li_{3.5}Zn_{0.25}GeO_4$ in comparison to those of other electrolytes; in particular, the new $Li_{10}GeP_2S_{12}$ exhibits the highest lithium ionic conductivity $\sim10^{-2}$ Scm^{-1} at 27°C in all solid- and liquid-electrolytes and in addition, even at temperatures below -30°C, the conductivity is still higher than the organic electrolyte, $LiPF_6$ in EC/PC, which may enable practical batteries to operate at low temperatures [9].

Except for the original solid solution $Li_{2+2x}Zn_{1-x}GeO_4$ system [52-53], another interesting system was focused on Li_4XO_4 and Li_3YO_4 based *LISICONs* (X=Si, Ge, Ti ; Y=P, As, V, Cr) with a general formula of $Li_{3+x}Y_{1-x}X_xO_4$ [50]. For example, in the binary system Li_4SiO_4–Li_3PO_4, i.e. $Li_{3+x}P_{1-x}Si_xO_4$, intermediate compositions, prepared by solid state techniques in air, have a conductivity at 25°C of $\sim10^{-6}$ Scm^{-1}, which is twelve orders of magnitude higher than that of $\sim10^{-18}$ Scm^{-1} for pure γ-Li_3PO_4 [54-55]. The reason for the enhanced conductivity is attributed to the partial occupation of interstitial sites by Li^+ ions [54]. The ionic conductivity in different families of polyanionic oxide systems, specifically, based on Li zinc pyrophosphate (P_2O_7), have yet to be studied and are considered to be of potential interest. Pyrophosphate compounds may offer a connected three-dimensional $(P_2O_7)^{-4}$–framework with possible multiple sites for Li ions conduction.

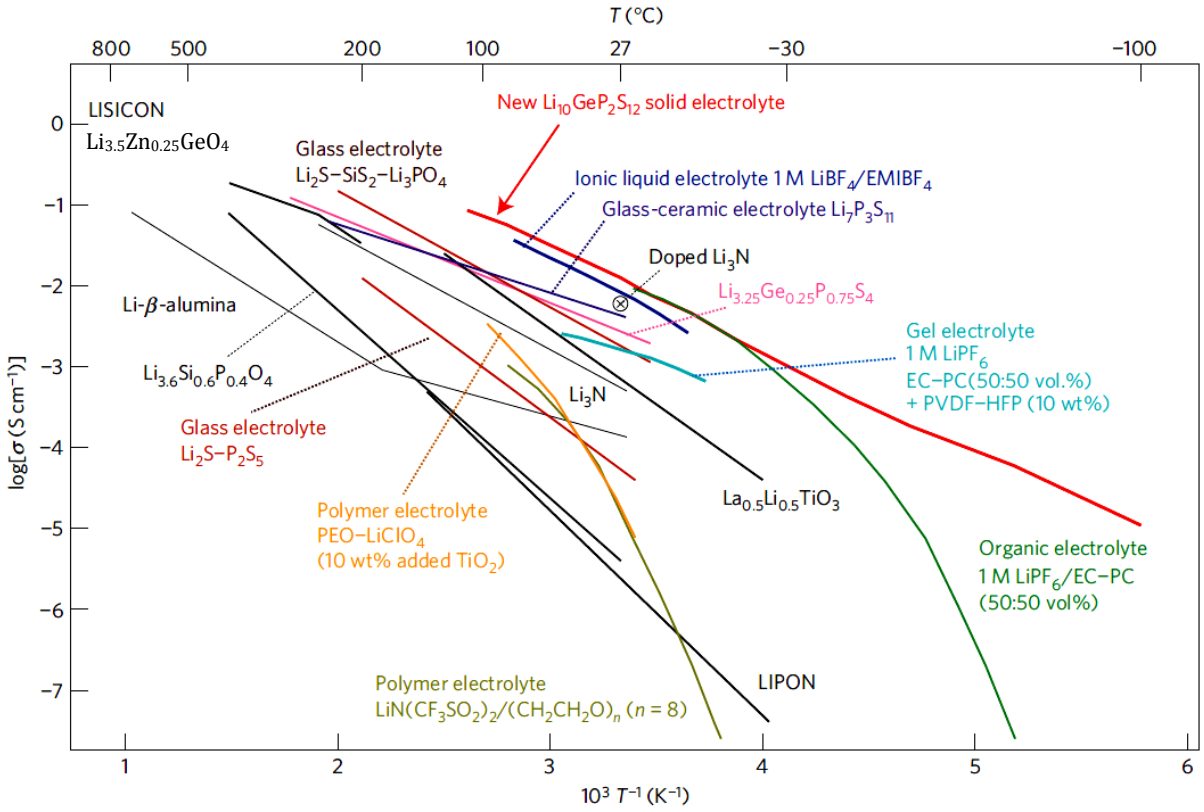

Figure 1-16 Arrhenius plots of the ionic conductivity for the lithium solid electrolytes, organic liquid electrolyte, polymer electrolytes, ionic liquid electrolytes and gel electrolytes [9].

1.5 Electrical Properties

Electrical conduction occurs by the long range migration of either electrons or ions and it is one of the main challenges to further improve electrode materials for Li-ion batteries. To maximize battery performance, it is required for electrical and ionic conductivities to be optimized in cathode materials as they can dictate the overall cell properties, such as capacity and cycle life [56-57]. Herein, a brief review of the fundamentals of electronic and ionic conduction theory are included.

1.5.1 Electronic Conductivity

Electronic conductivity occurs to varying extents and by different mechanism in various materials including metals, superconductors and semiconductors. Typical

conductivities are given in **Table 1-3**; in general, the conductivity of most semiconductors and insulators increases with increasing temperature except metals. Metallic materials with band gap ≈ 0 have very high electronic conductivity, and electron transport dominates their conduction mechanism.

Table 1-3 Typical values of electronic conductivity [49].

Material	σ (Scm^{-1})
Metals	10^{-1} – 10^{5}
Semiconductors	10^{-5} – 10^{2}
Insulators	< 10^{-12}

The conductivity, σ, is shown by Equation 1.7 [49]:

$$\sigma = n \cdot e \cdot \mu \tag{1.7}$$

where n is the number, e the charge and μ the mobility of the charge carriers. For all electronic conductors, e is constant and independent of temperature. The mobility term is similar in most materials. However, for metals and good semiconductors, it usually decreases slightly with increasing temperature because of collisions between the moving electrons and phonons. **Fig. 1-17** shows the conductivity of metals, semiconductors and insulators as a function a temperature. For metals, n is large and essentially constant with temperature. The only variable factor in σ is μ and therefore, conductivity decreases as μ gradually decreases with temperature.

In semiconductors, the number of mobile electrons is small and may be increased by enhancing the temperature to trigger more electrons from the valence band to the conduction band, or doping with impurities creating electrons or holes. The number of the charge carriers, n, is given by Equation 1.8 [49]:

$$n = n_0 \, exp(-E / k_B T) \tag{1.8}$$

where

n_0 : constant units of conductivity (the total number of electrons)

E : activation energy (eV)

k_B : Boltzmann's constant (1.38054×10^{-23} JK^{-1})

T : temperature (K)

For intrinsic semiconductors and insulators, n, and therefore, σ, usually increases exponentially with temperature, **Fig. 1-17**. Extra mobile carriers can be generated through the addition of dopants, specifically at low temperatures in the extrinsic region, wherein the concentration of extra carriers is much greater than the thermally-generated intrinsic concentration. As a result, the carrier concentration is independent of temperature for extrinsic semiconductors. For insulators, σ is sensitive to both temperature and dopants, however, σ is very small because n is small and E is large.

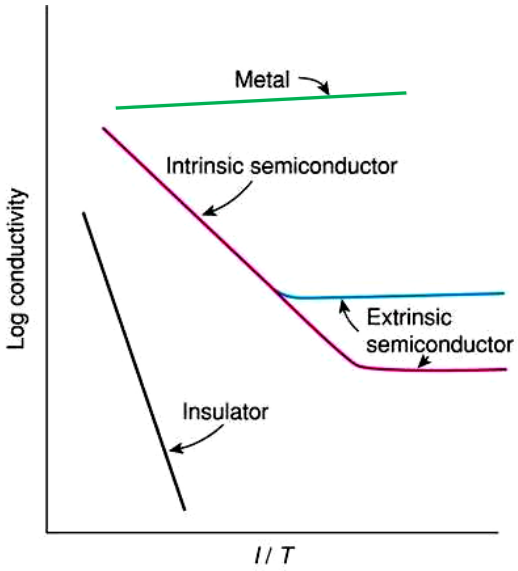

Figure 1-17 Conductivity of metals, semiconductors and insulators [58].

The layered intercalation compound $LiCoO_2$ possesses a primarily electronic conductivity $\sim10^{-3}$ at room temperature, which exhibits a semiconducting behavior. The mobile electrons are localized on individual atoms but they can hop to adjacent atoms

when given sufficient energy. The high concentration and considerable mobility of the electron carriers make $LiCoO_2$ a good electronic conductor [59], which is enough for fast charge transfer in order to achieve high-rate performance for lithium-ion batteries. In 1997, West *et al.* reported Mg-doped $LiCoO_2$, e.g. $LiMg_{0.05}Co_{0.95}O_2$, had an enhanced conductivity of ~0.5 Scm^{-1} at 25°C, which was over two orders of magnitude higher than undoped $LiCoO_2$. This is due to the generation of holes, i.e., Co^{4+} ions and therefore, a mixed $Co^{3+/4+}$ attributed to higher electronic conductivity [60].

1.5.2 Ionic Conductivity

Ionic conductivity occurs in materials widely named as solid electrolytes, fast ion conductors and superionic conductors. Typical values of ionic conductivity are shown in **Table 1-4**; in general, the conductivity of most ionic solids increases with temperature. Ionic conductivity has two main characteristics as follows [49]:

(i) These materials have a rigid framework wherein a set of ions form a mobile sublattice.
(ii) Two structural requirements to achieve high ionic conductivity are 1) there must be available empty sites for ions to hop into, and 2) the energy barrier for ions to hop between sites should be small.

Table 1-4 Typical values of ionic conductivity [49].

Material	σ (Scm^{-1})
Ionic crystals	$< 10^{-18} – 10^{-14}$
Solid electrolytes	$10^{-3} – 10^{1}$
Strong (liquid) electrolyte	$10^{-3} – 10^{1}$

Ionic conduction can occur in cases that either some sites are vacant and then adjacent ions can jump into the vacancies, leaving their original sites vacant, e.g. NaCl **(a)**, or there are some ions located in interstitial sites which can jump into adjacent interstitial sites, e.g. AgCl **(b)**, as shown in **Fig. 1-18**. At higher temperatures, ionic conduction is easier because not only ions do have greater thermal energy and can vibrate more strongly but

also defect concentrations are increased. For example, the conductivity of NaCl increases up to ~10^{-3} Scm^{-1} at 800°C, which is much higher than that of 10^{-12} Scm^{-1} at room temperature [49].

Ionic conduction also can occur by ions hopping or diffusing from site to site through a crystal structure with open channels or layers. For example, sodium *β*-alumina ($Na_2O{\cdot}nAl_2O_3$), exhibits a high ionic conductivity ~10^{-2} Scm^{-1} at 25°C with a low activation energy of 0.16(1) eV. This is due to the high mobility of Na^+ ions along *a*- and *b*-axes in the 3D framework, e.g. $NaAl_{11}O_{17}$, as illustrated in **Fig. 1-19**.

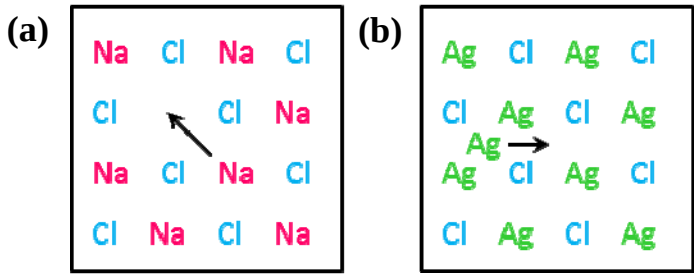

Figure 1-18 Conduction mechanism of (a) vacancy, e.g. Na^+ ions, in NaCl and (b) interstitials, e.g. Ag^+ ions in AgCl.

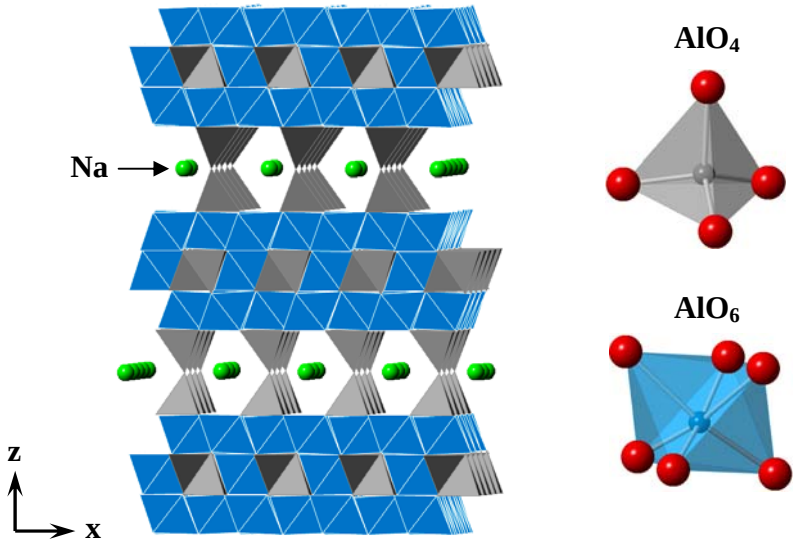

Figure 1-19 Sodium Beta Alumina ($NaAl_{11}O_{17}$): 3D arrangement of AlO_4 tetrahedra (grey) and AlO_6 octahedra (blue) with Na^+ ions in the conduction planes [61].

Ionic conductivity, σ_i, for any material can be evaluated using Eq. 1.7. For an ionic conductor, it is difficult to obtain individual estimates of n and μ by Eq. 1.7. However, the concentration of the mobile species, c_i, can vary by many orders of magnitude in ionic materials. For hopping semiconductors and ionic conductors, mobility is an activated process and therefore increases greatly with temperature.

An important strategy to increase the value of c_i is by means of doping with aliovalent ions, in particular to create vacancies or interstitial ions on the basis of charge balance. If the vacancies or interstitials are able to migrate, an increased conductivity can be expected. **Fig. 1-20** shows four fundamental ionic mechanisms by aliovalent doping of cations to achieve charge balance [62-63]. An example of each is included. Substituting with higher valence cations creates either cation vacancies (1) or anion interstitials (2); substituting with lower valence cations leads to the creation of either cation interstitials (3) or anion vacancies (4).

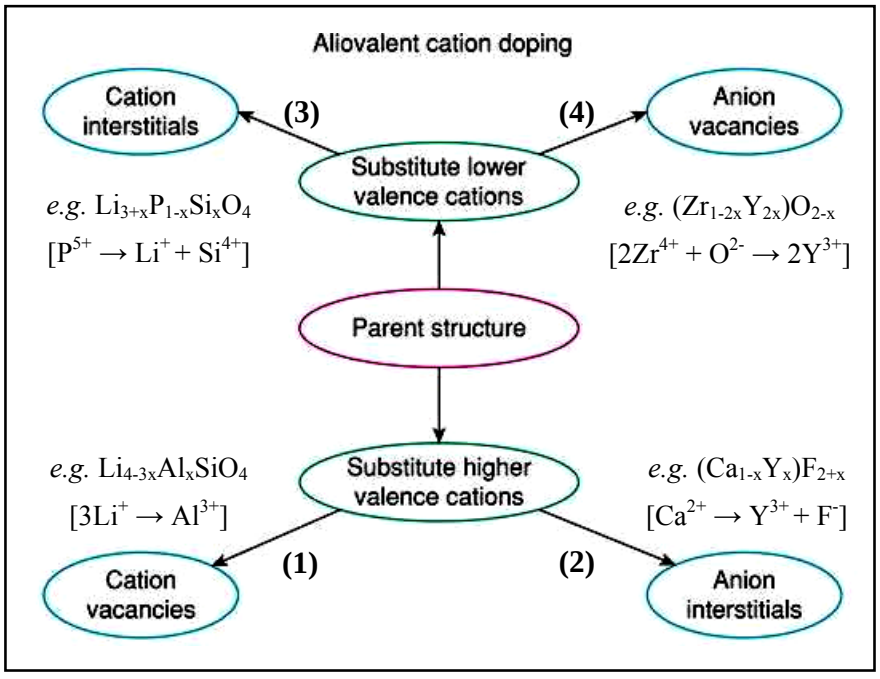

Figure 1-20 Solid solution mechanism by doping with aliovalent ions for ionic compensation [63].

It is possible to optimize the ionic conductivity through the product of the fraction of occupied mobile species, c_i, and fraction of empty mobile-ion sites, $(1-c_i)$ [62]. This important parameter, $c_i \cdot (1-c_i)$, may reach a maximum when the concentration of filled and empty sites is equal, based on random walk theory. A typical example to illustrate this effect is $Li_{4-3x}Al_xSiO_4$ solid solutions reported by West *et al.* [64], **Fig. 1-21**. Single phase solid solutions form with x in the range 0 to 0.5. When x=0 ($n_c \rightarrow 1$), i.e. Li_4SiO_4, the conductivity is low as all the Li^+ sites are full and there are few vacancies, i.e. $(1-c_i)$ is small. As x increases, one particular set of Li^+ sites in the crystal structure starts to empty and is completely empty at x=0.5 ($n_c \rightarrow 0$), i.e. $Li_{2.5}Al_{0.5}SiO_4$. Therefore, the conductivity is again low as ¼ of Li^+ sites are vacant and there are few mobile carriers, i.e. c_i is small. A broad conductivity maximum occurs around x=0.25 ($n_c \rightarrow 0.5$), at which the amounts of vacant sites and mobile ions are near equal, i.e. $c_i \sim (1-c_i)$.

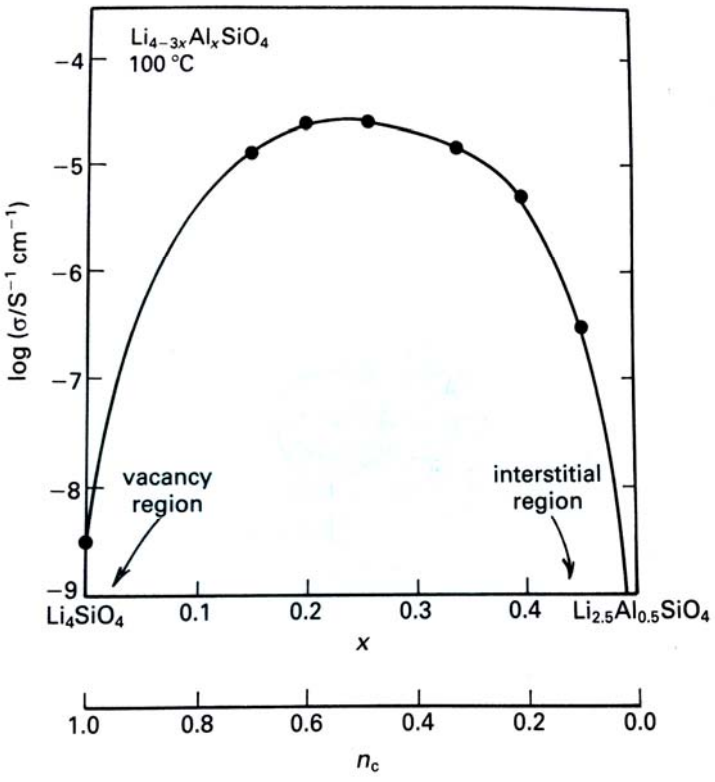

Figure 1-21 Conductivity of $Li_{4-3x}Al_xSiO_4$ solid solutions in which the fraction of occupied mobile ion sites, n_c, varies from 1 (at x=0) to 0 (at x=0.5) [62].

The temperature dependence of ionic conductivity (σ_i) is usually given by the Arrhenius Equation 1.9 [49]:

$$\sigma_i = A\, exp\left(\frac{-E_a}{RT}\right) \tag{1.9}$$

where A is the pre-exponential factor, which consists of many constants including the vibration frequency of the potentially mobile ions, R the gas constant, T the temperature in Kelvin, and E_a the activation energy which is the major factor controlling the ionic mobility (μ). Ea represents the ease of ion hopping and is directly associated with the crystal structure and in particular, with the openness of the conduction pathways [62].

1.5.3 Mixed Electronic/Ionic Conductivity

For mixed conductors, both electronic (σ_e) and ionic (σ_i) conduction occur simultaneously. They are used as electrodes for various applications in electrochemical cells. The electrical properties of mixed conductors cover three aspects [49]. First, the mixed valence of one of the atoms present is required for the electronic component. Second, for the ionic conduction component, the structural, compositional and doping characteristics are similar to ionic conductors. That is, an open framework structure with the mobile ion sites is necessary. Third, in mixed conductors, it is questionable whether the electronic and ionic conduction parts appear independently of each other or whether they influence each other.

For lithium cathode materials, electronic conductivity is related directly to mixed valence of transition metal ions in the structure, e.g. a mixture of Fe^{2+} and Fe^{3+} in $Li_{1-x}FePO_4$. Efforts to optimize the electronic and/or ionic conductivity of $LiFePO_4$ via doping have not yet been rewarding [26]. So far only conducting carbon coatings and scaling down particle size make a great contribution to higher conductivity of $LiFePO_4$ for cathode applications.

For an oxide ion conductor, the transition between ionic conduction and mixed conduction can often be induced in the same material by changing the partial pressure of O_2 in the atmosphere [49]. The ionic transport number, t_i, is given by Equation 1.10 [65]:

$$t_i = \frac{\sigma_i}{\sigma_i + \sigma_e} \tag{1.10}$$

A useful parameter to characterise the ease of reduction in oxide ion conductors is by means of the oxygen partial pressure ($P^*_{O_2}$), at which t_i =1/2 since

$$t_i = \frac{1}{2} = \left[1 + \left(P_{O_2} / P^*_{O_2}\right)\right]^{-1} \tag{1.11}$$

The dependence of ionic and electronic conductivity as a function of P_{O_2} is presented schematically in **Fig. 1-22**. Herein, $P^*_{O_2}(red)$ and $P^*_{O_2}(ox)$ indicate the transition from oxide ion conduction to *n*- and *p*-type conduction, respectively.

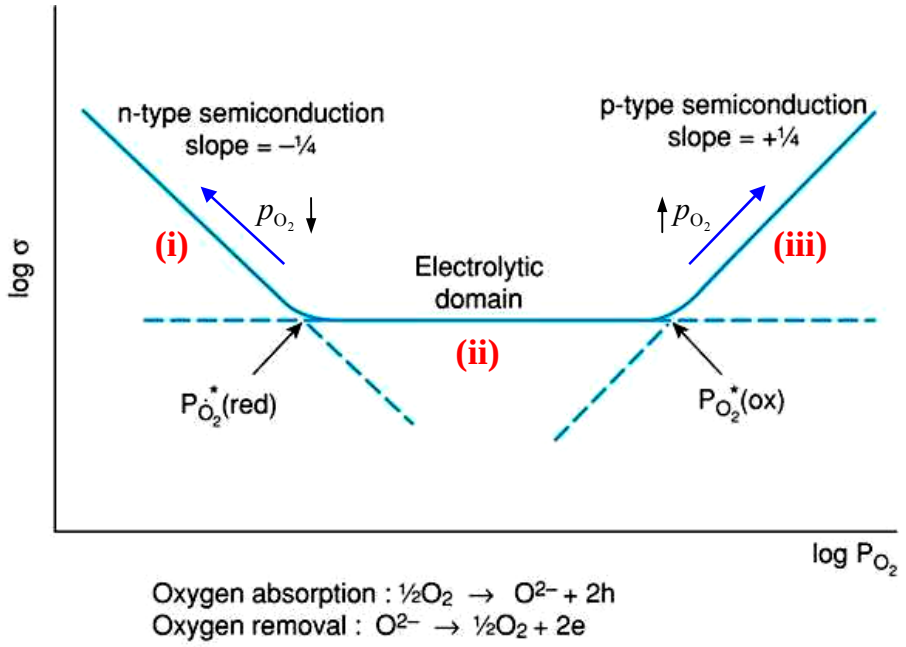

Figure 1-22 Variation of ionic and electronic conductivity domains as a function of oxygen partial pressure [65].

The schematic reactions of *n*-type and *p*-type semiconduction are represented in Kroger–Vink notation by Equations 1.12 and 1.13 [65]:

n-type: $O_O^{\times} \xrightarrow{p_{O_2}\downarrow} \frac{1}{2}O_2 + V_O^{\bullet\bullet} + 2e^-$ (1.12)

p-type: $\frac{1}{2}O_2 + V_O^{\bullet\bullet} \xrightarrow{p_{O_2}\uparrow} O_O^{\times} + 2h^{\bullet}$ (1.13)

In oxygen desorption region, the concentration of electrons is greater than that of oxygen vacancies and/or holes , and the equilibrium constant (K_d) is expressed by Equation 1.14:

$$K_d = \frac{[e^-]^2[V_O^{\bullet\bullet}][P_{O_2}]^{1/2}}{[O_O^{\times}]} \quad (1.14)$$

Since the concentration of lattice oxygens is unity and the concentration of oxygen vacancies is high due to a significant level of dopant concentration, the relationship between electron concentration and oxygen partial pressure can be given by Equation 1.15:

$$[e^-] \propto P_{O_2}^{-1/4} \quad (1.15)$$

At high temperature and low P_{O_2}, most oxides can lose small amounts of oxygen and become *n*-type semiconductors. The conductivity (σ_n) increases with a slope of –1/4 and the material is an *n*-type conductor **(i)**. At higher P_{O_2} (t_i=1), most electrolytes have an "electrolytic domain" where the conductivity is independent of P_{O_2} **(ii)**. At very high P_{O_2}, *p*-type electronic conduction may occur as the oxygen vacancies are filled **(iii)**. In this region, the sample absorbs oxygen either at the sample surface or by diffusion into vacant anion sites. Holes can be created by this process, which become the dominant charge carriers and therefore, the conductivity (σ_p) increases with a slope of +1/4.

1.6 Impedance Spectroscopy (IS)

Impedance spectroscopy is a powerful technique to study the electrical properties of ceramic materials, such as bulk, grain boundary and surface effects [66]. It is also suited to look at interfacial phenomena and discriminate between electronic and ionic conduction. In general, IS can be operated to extract resistance and capacitance data as a function of temperature, time, bias and/or oxygen partial pressure. Impedance measurements are

made over a wide range of frequency, 10^{-3} to 10^{7} Hz, and achieved by applying an alternating voltage across the sample and measuring the output current.

Different regions of the sample are characterised by a combination of resistance (R) and capacitance (C), and their responses can be modelled using an equivalent circuit, such as a "parallel RC element", as shown in **Fig. 1-23**. This element has a characteristic relaxation time or time constant, τ, which is given by the product of R and C, Equation 1.14 [66]:

$$\tau = RC \tag{1.14}$$

The time constant has unit in seconds and to separate the RC elements, Eqn. 1.14 is used in the frequency domain, Equation 1.15 [66]:

$$\omega_{max} RC = 1 \tag{1.15}$$

where ω_{max} is the angular frequency (rad·s^{-1}) at the frequency of maximum loss in the impedance spectrum, $\omega_{max} = 2\pi f$ and f is the applied frequency (Hz). Therefore, the different RC elements could be identified and assigned to their appropriate contributions in a sample.

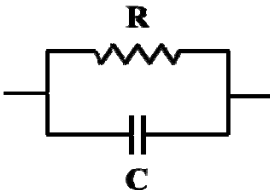

Figure 1-23 Single parallel *RC* element.

The typical electrical microstructure of a polycrystalline sample can be described via a 'brickwork' model [66], **Fig. 1-24**. As a current passes through a material, it may pass through the different structural regions, i.e. bulk (grains) and grain boundary. The model in **Fig. 1-24** represents a ceramic containing, ideally, cube-shaped grains of dimensions l_1, separated from each other by a grain boundary of thickness l_2, and sample-electrode interface of thickness l_3. The sample mainly stores charge and can be modelled electrically as a capacitor, which is formed when two conducting plates are separated by a non-conducting medium, called the dielectric. The value of the capacitance is dependent on the

size of the plates, the distance between the plates and the properties of the dielectric. The relationship is given by Equation 1.16 [66]:

$$C = \varepsilon' e_0 \frac{A}{l} \tag{1.16}$$

where C = capacitance of the element

ε' = sample permittivity

e_0 = permittivity of free space (8.854×10^{-14} Fcm^{-1})

A = area of parallel plate capacitor

l = plate separation

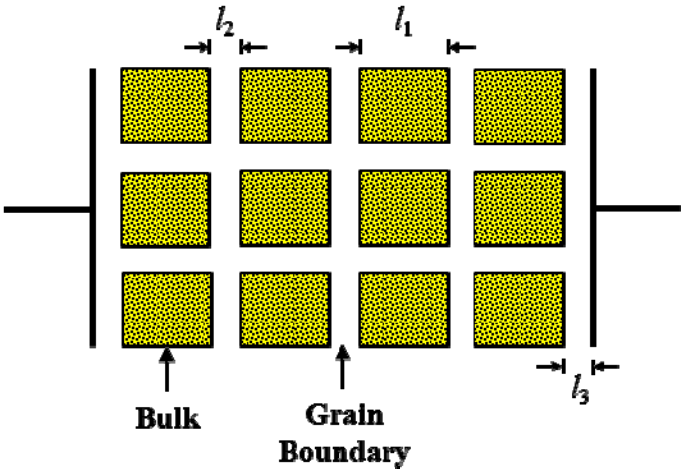

Figure 1-24 Brickwork model of grain and grain boundary regions in a ceramic placed between metal electrodes [66].

The magnitudes of the various C values are used to identify the regions in a ceramic response. For materials with a unit cell constant (l/A = 1 cm^{-1}) and a typical permittivity of ~10, a capacitance value of ~1×10^{-12} Fcm^{-1} is attributed to the bulk response. **Table 1-5** lists the capacitance values for different structural elements and their possible interpretation; a wide variety of ceramic microstructures occur in practice and the grain boundary has values in the range 10^{-8} to 10^{-11} Fcm^{-1} [66]. From the inverse relation

between capacitance and thickness given by Eqn. 1.16, the value of C depends primarily on l assuming a fixed cross-sectional area, A, Equation 1.17:

$$\frac{C_{\mathrm{b}}}{C_{\mathrm{gb}}} = \frac{l_2}{l_1} \tag{1.17}$$

Grain boundary regions can also store charge. These are thin layers and therefore have a higher capacitance than the bulk (Brickwork layer model, BLM). In general, grain boundary regions are 10^{-2}–10^{-4} and sample-electrode interface < 10^{-7} of the overall cell length; therefore, the thin layers have a high C value, i.e. $C_{\mathrm{b}} \ll C_{\mathrm{gb}} \ll C_{\mathrm{el}}$.

Table 1-5 General capacitance values and their interpretation [66].

Capacitance / Fcm^{-1}	Element Responsible
10^{-12}	Bulk
10^{-11}	Minor, second phase
10^{-11} – 10^{-8}	Grain boundary
10^{-10} – 10^{-9}	Bulk ferroelectric
10^{-9} – 10^{-7}	Surface layer
10^{-7} – 10^{-5}	Sample-electrode interface
10^{-4}	Electrochemical reactions

Higher capacitances occur in materials with well-sintered and narrow intergranular regions. In contrast, lower capacitances are usually observed in poorly-sintered or porous pellets that consist of constriction resistances or narrow contacting 'necks' between two grains [66]. **Fig. 1-25** shows a schematic constriction effect between two grains **(a)** and a model equivalent circuit is represented in **(b)**. Herein, the capacitances of the two regions are C_1 and C_2; C_1 corresponds to the grain region and C_2 to a combination of the capacitance of the constriction region, C_{c}, and the capacitance of the air gap, C_{a}, i.e. $C_2 = C_{\mathrm{c}} + C_{\mathrm{a}}$. The

Maxwell relaxation times of the grain region, τ_1, and constriction region, τ_2, are given using $\tau_1=R_1C_1$ and $\tau_2=R_1C_1$; τ_2 can be derived by Equation 1.18 [67]:

$$\tau_2 = \tau_1 + \frac{\tau_1}{\varepsilon'} \cdot \frac{A_g}{A_c} \tag{1.18}$$

where

R_1 and R_2: resistance of the grain and constriction region

A_g and A_c: cross-section area of the grain and constriction region

l_g and l_c: length of the grain and constriction region.

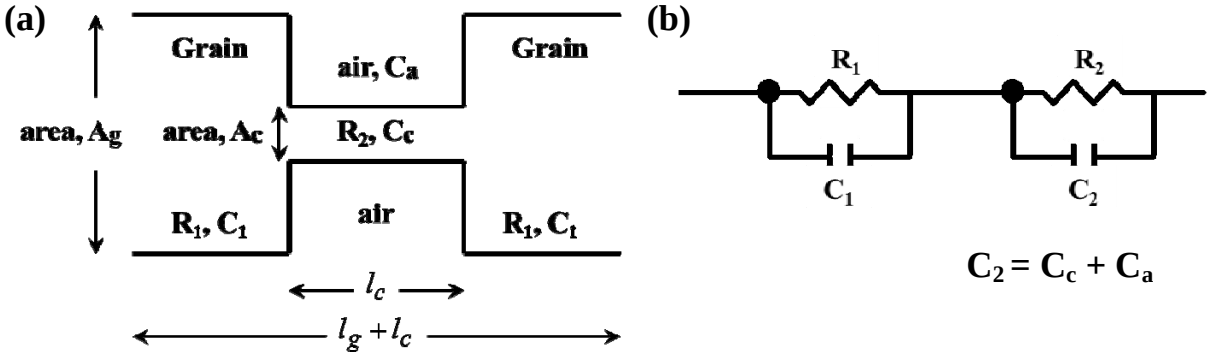

Figure 1-25 (a) Schematic diagram of an intergranular constriction resistance and (b) the equivalent electrical representation [67].

Data obtained from *ac* impedance can be analysed using four different complex formalisms: impedance Z^*, admittance, Y^*, permittivity ε^* and electric modulus M^* [68]. The interrelations between the four complex formalisms are summarized in **Table 1-6**. Each of them is represented by complex notation consisting of real and imaginary components, e.g. Z^* and Y^* in Equations 1.19 and 1.20, where j = $\sqrt{-1}$.

$$Z^* = Z' - jZ'' \tag{1.19}$$

$$Y^* = Y' + jY'' \tag{1.20}$$

Table 1.6 Interrelations between the four basic immittance functions [69].

Functions	Z^*	Y^*	ε^*	M^*
Z^*	Z^*	$\frac{1}{Y^*}$	$\frac{1}{\varepsilon^* j\omega C_0}$	$\frac{M^*}{j\omega C_0}$
Y^*	$\frac{1}{Z^*}$	Y^*	$\varepsilon^* j\omega C_0$	$\frac{j\omega C_0}{M^*}$
ε^*	$\frac{1}{Z^* j\omega C_0}$	$\frac{Y^*}{j\omega C_0}$	ε^*	$\frac{1}{M^*}$
M^*	$Z^* j\omega C_0$	$\frac{j\omega C_0}{Y^*}$	$\frac{1}{\varepsilon^*}$	M^*
C_0: vacuum capacitance of the cell; ω: angular frequency				

An equivalent circuit with two parallel RC elements in series is widely used to represent bulk and grain boundary phenomena in polycrystalline materials, **Fig. 1-26(a)**; the overall resistance may be a combination of the bulk crystal resistance, R_b, and the grain boundary resistance, R_{gb}; individual capacitances are C_b and C_{gb} [70].

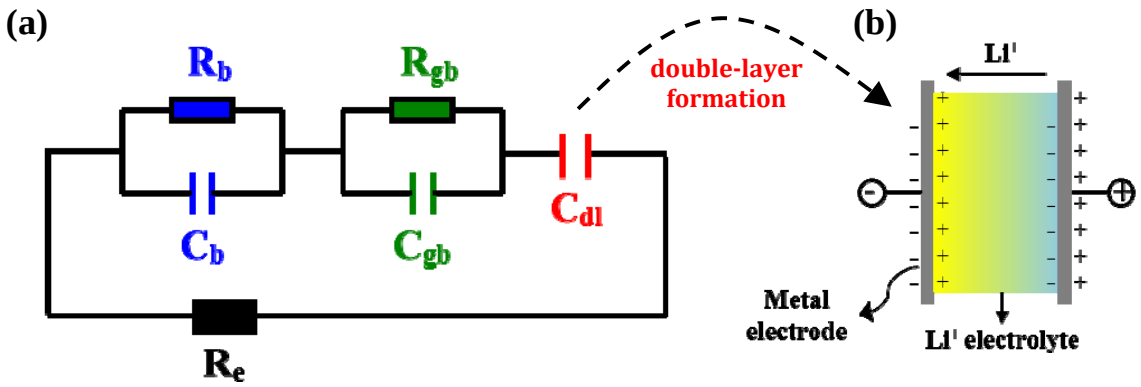

Figure 1-26 Equivalent circuit for a polycrystalline solid electrolyte [70].
R_b and C_b: bulk crystals; R_{gb} and C_{gb}: grain boundaries; R_e: electronic resistance; C_{dl}: electrode double-layer capacitance.

In general, the interface between a metal electrode and a solid electrolyte can store a charge without discharge or chemical reaction at the electrode-electrolyte interface. For

ionic conducting materials, there are two types of metal contacts, blocking and non-blocking [71]. Gold and platinum metals are usually employed as the blocking electrodes. In the case of Li^+ conductors, electrons are blocked at the metal surface in direct contact with oppositely charged Li^+ ions and therefore, an electrical double layer is produced, **Fig. 1-26(b)**. Due to the presence of the electrical double layer a "blocking" electrode behaves like a capacitor, i.e. double-layer capacitances, C_{dl}, with a typical magnitude of 1×10^{-6} Fcm^{-1}, in series with the sample resistance, see **(a)**. If the solid electrolyte possesses an electronic conductivity together with an ionic conductivity, the equivalent circuit can be modified to add a separate electronic resistance, R_e, in parallel with the other elements. In this case, the inverse of the total resistance, R_T^{-1}, is equal to the sum of inverse electronic, R_e^{-1}, and ionic resistances, $(R_b + R_{gb})^{-1}$, using Equation 1.21. When $R_e \gg (R_b+R_{gb})$, R_e^{-1} can be effectively ignored.

$$\frac{1}{R_T} = \frac{1}{R_e} + \frac{1}{(R_b + R_{gb})} \qquad (1.21)$$

Fig. 1-27 summarises the equivalent circuit from **Fig. 1-26** in the complex Z^* plane for a solid electrolyte with blocking electrodes over a wide frequency range. R_b and R_{gb} values are determined from the intercepts on the real Z'-axis; C_b and C_{gb} values can be calculated from the Z'' maximum of each semicircle, using the relations, $\omega_{b(max)}R_bC_b = 1$ and $\omega_{gb(max)}R_{gb}C_{gb} = 1$. The occurrence of an ideally vertical spike at low frequencies indicates the presence of a large series capacitance in the circuit that identifies the electrodes as probably blocking. Therefore, the electronic conduction within the solid electrolyte is small or can be ignored in comparison to the magnitude of the ionic conductivity. On the other hand, an inclined spike with angle $\sim45^o$ may be observed at low frequencies due to the diffusion of mobile species into or out of the electrode materials, referred to as Warburg-type behaviour [71].

The information available from the simulated Z^* plot, **Fig. 1-28**, can be further analysed by combined spectroscopic plots of the imaginary components of impedance, Z'' and electric modulus, M'', **Fig. 1-29**. The peaks in Z'' and M'' are described by means of Equations 1.22 and1.23 [71]:

$$Z'' = R_b\left[\frac{\omega R_b C_b}{1+(\omega R_b C_b)^2}\right] + R_{gb}\left[\frac{\omega R_{gb} C_{gb}}{1+(\omega R_{gb} C_{gb})^2}\right] \quad (1.22)$$

$$M'' = \frac{C_0}{C_b}\left[\frac{\omega R_b C_b}{1+(\omega R_b C_b)^2}\right] + \frac{C_0}{C_{gb}}\left[\frac{\omega R_{gb} C_{gb}}{1+(\omega R_{gb} C_{gb})^2}\right] \quad (1.23)$$

where ε_0 is the permittivity of free space and the term in square brackets, $(\omega RC/1+(\omega RC)^2)$, indicates a mathematical representation of a Debye peak. In this case, if the bulk and grain boundary regions have very different time constants, it is possible to distinguish their electrical contributions. At the Debye peak maxima in **Fig. 1-29**, $\omega_{max}RC = 1$ and the values of Z''_{max} and M''_{max} are $R_{gb}/2$ and $\varepsilon_0/2C_b$; therefore, values of R_{gb} and C_b can be calculated. Z" spectra are dominated by the largest R value (i.e. R_{gb}); M" spectra are dominated by the smallest capacitance values (i.e. C_b) [71]. For inhomogeneous ceramics, non-ideal Debye peaks are probably obtained, in which the full width at half maximum (FWHM) > 1.14 decades on a log f scale. R and C values calculated from -Z" or M" peaks, may show a deviation in comparison those directly calculated from Z* plots.

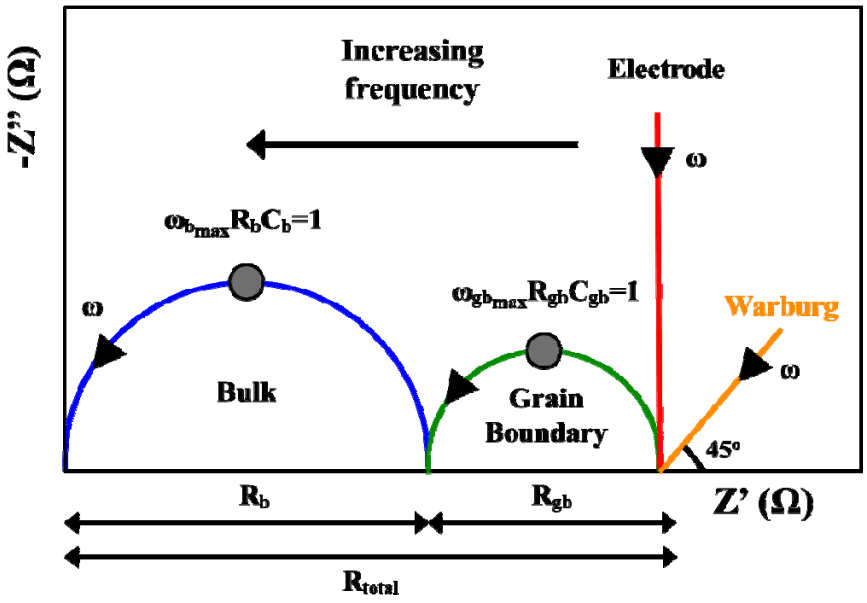

Figure 1-27 Semi-circles exhibiting bulk (blue) and grain boundary (green) response, ionic conduction with blocking electrodes (red), and infinite, Warburg-type ionic diffusion (orange) in a complex Z* plot.

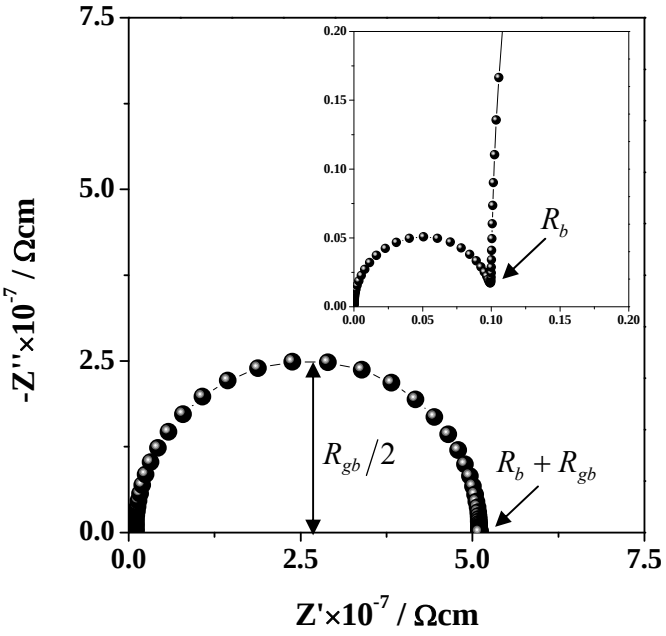

Figure 1-28 Simulated Z* plot for the BLM; R_b = 1 MΩcm, C_b = 15 pFcm^{-1}, R_{gb} =200 MΩcm, C_{gb}=2 nFcm^{-1}.

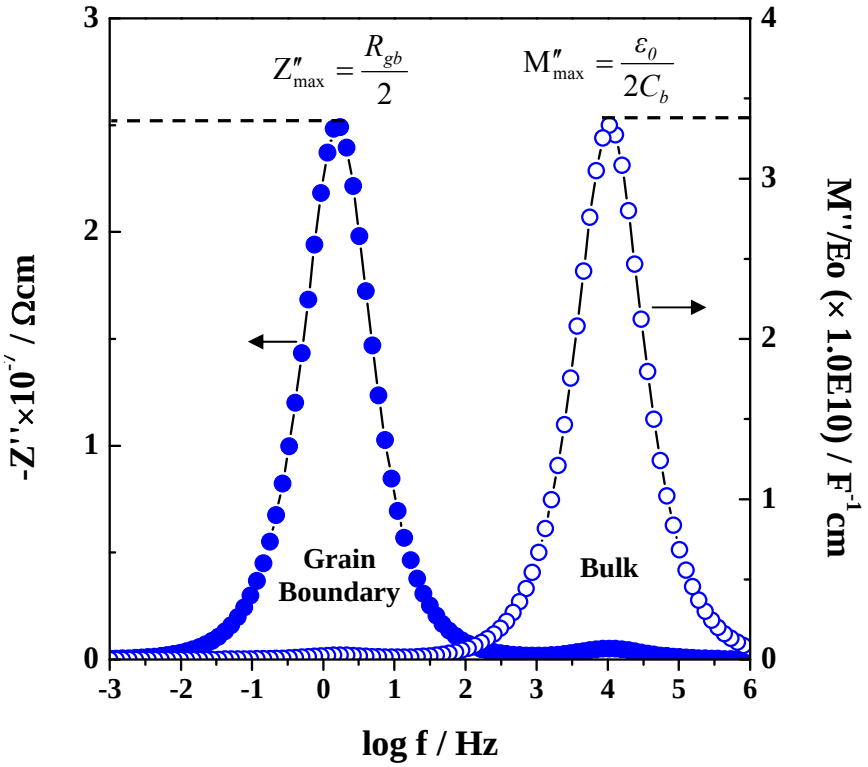

Figure 1-29 Simulated Z" and M" spectra for the BLM; R_b = 1 MΩcm, C_b = 15 pFcm^{-1}, R_{gb} = 200 MΩcm, C_{gb} = 2 nFcm^{-1}.

1.7 Aims of this Thesis

The overall aim of this thesis is to develop and test new pyrophosphate materials of general formula $Li_2MP_2O_7$ for possible lithium battery applications and to develop further the *ac* impedance technique for characterising lithium ion conductivity.

There are recent reports in the literature on the potential usefulness of the M=Fe, Mn analogue pyrophosphate phases as lithium battery cathodes. For example, $Li_2FeP_2O_7$ has potential as a new, two-lithium cathode material which could offer nearly double the specific capacity compared to existing cathode materials. Although two-lithium cycling has still not been demonstrated, this system has received most attention and future study is anticipated. In Chapter III, a) a survey of compound formation in this family of materials with variable M is reported; b) electrical properties are measured, specifically, to determine the σ_{e^-} and/or σ_{Li^+} in $Li_2MP_2O_7$ cathodes.

The supervalent dopants (e.g. Al^{3+}, Zr^{4+} and Nb^{5+}) have been reported to substitute either on the M1 or M2 sites in the $LiFePO_4$ structure with appropriate charge compensation, resulting in improved electrical and electrochemical properties [27]. However, experimental work of similar ideas to the poorly-conductive, two-lithium polyanionic cathodes are less studied in the literature. In Chapter IV, attempted modification of the electrical properties of $Li_2FeP_2O_7$ by aliovalent doping is described, in particular with a view to increasing the level of lithium ion conductivity.

The effect of using anionic substitution, e.g. N and F, for O on the electrical and electrochemical properties of polyanionic compounds has not been reported in experimental work. In Chapter V, N-doping of $Li_2FeP_2O_7$ is reported for the first time, leading to an increase in its ionic or electronic conductivity, and further improvement in the electrochemical properties.

In Chapter VI, different lithium zinc pyrophosphate ($Li_{4x}Zn_{2-2x}P_2O_7$) compositions were synthesised to confirm several phases reported in the $Zn_2P_2O_7$–$Li_4P_2O_7$ binary system. One new phase $Li_{1.33}Zn_{1.33}P_2O_7$ is reported. The crystal structure of $Li_{2.4}Zn_{0.8}P_2O_7$ (x=0.6) was restudied by neutron diffraction to compare with that obtained by XRD. A systematic study of the electrical properties with various *x* values was carried out using impedance

spectroscopy. Based on these results, a basic understanding of structure-composition-property relations for $Li_{4x}Zn_{2-2x}P_2O_7$ materials may be developed.

1.8 References

1. B. Scrosati, "Challenge of portable power", *Nature* **1995**, *373*, pp. 557–558.
2. R.F. Nelson, "Power requirements for batteries in hybrid electric vehicles", *J. Power Sources* **2000**, *91*, pp. 2–26.
3. C. Jiang, E. Hosono and H. Zhou, "Nanomaterials for lithium ion batteries", *Nanotoday* **2006**, *1 (4)*, pp. 28–33.
4. J.B. Goodenough and Y. Kim, "Challenge for Rechargeable Li Batteries", *Chem. Mater*. **2010**, *22 (3)*, pp. 587–603.
5. K. Mizushima, P.C. Jones, P.J. Wiseman and J.B. Goodenough, "Li_xCoO_2 ($0 < x < -1$): A new cathode material for batteries of high energy density", *Mater. Res. Bull.* **1980**, *15(6)*, pp. 783–799.
6. M.G. Thomas, W.I. David, J.B. Goodenough and P. Groves, "Synthesis and structural characterization of the normal spinel $Li[Ni_2]O_4$", *Mater. Res. Bull.* **1985**, *20*, pp. 1137–1146.
7. J. M. Tarascon, W. R. McKinnon, F. Coowar, T. N. Bowmer, G. Amatucci and D. Guyomard, "Synthesis Conditions and Oxygen Stoichiometry Effects on Li Insertion into the Spinel $LiMn_2O_4$", *J. Electrochem. Soc.* **1994**, *141*, pp. 1421–1431.
8. M. Park, X. Zhang, M. Chung, G.B. Less and A.M. Sastry, "A review of conduction phenomena in Li-ion batteries", *J. of Power Sources* **2010**, *195*, pp. 7904–7929.
9. N. Kamaya, K. Homma, Y. Yamakawa, M. Hirayama, R. Kanno, M. Yonemura, T. Kamiyama, Y. Kato, S. Hama, K. Kawamoto and A. Mitsui, "A lithium superionic conductor", *Nat. Mater.* **2011**, *10*, pp. 682–686.
10. R.J. Brodd, W. Huang and J.R. Akridge, *Macromolecular Symposia* **2000**, *159*, pp. 229–245.
11. A. K. Padhi, K. S. Nanjundaswamy and J. B. Goodenough, "Phospho-olivines as Positive-Electrode Materials for Rechargeable Lithium Batteries", *J. Electrochem. Soc.* **1997**, *144*, pp. 1188–1194.
12. A. K. Padhi, K. S. Nanjundaswamy, C. Masquelier and J. B. Goodenough, "Mapping of Transition Metal Redox Energies in Phosphates with NASICON Structure by Lithium Intercalation", *J. Electrochem. Soc.* **1997**, *144*, pp. 2581–2586.

13. A. Yamada, S. C. Chung and K. Hinokuma, "Optimized $LiFePO_4$ for Lithium Battery Cathodes", *J. Electrochem. Soc.* **2001**, *148*, pp. A224–229.

14. K.C. Hsiao, "New Potential Materials for Electrochemical Energy Storage", Imperial College London EFL CDT Seminars, 13th May **2011** (Oral Presentation)

15. (a) K.C. Hsiao, "Research Progress of Novel Cathode Materials for Next-generation Power Lithium Battery" *Industrial Materials Magazine 303*, TAIWAN, Mar. **2012**, pp. 160; (b) SANYO battery comparison, **2007** brochure.

16. J.B. Goodenough and K.S. Park, "The Li-Ion Rechargeable Battery: A Perspective", *J. Am. Chem. Soc.* **2013**, *135* (4), pp. 1167–1176.

17. B.C. Melot and J.M. Tarascon, "Design and Preparation of Materials for Advanced Electrochemical Storage", *Acc. Chem. Res.* **2013**, *46* (5), pp. 1226–1238.

18. J.M. Tarascon, N. Recham, M. Armand, J.N. Chotard, P. Barpanda, W. Walker and L. Dupont, "Hunting for Better Li-Based Electrode Materials via Low Temperature Inorganic Synthesis", *Chem. Mater.* **2010**, *22* (3), pp. 724–739.

19. (a) K.C. Hsiao, "Research Progress of Novel Cathode Materials for Next-generation Power Lithium Battery" *Industrial Materials Magazine 303*, TAIWAN, Mar. **2012**, pp. 163; (b) J.M. Tarascon and M. Armand, "Issues and challenges facing rechargeable lithium batteries", *Nature* **2001**, *414*, pp. 359–367.

20. K.C. Hsiao, "Sheffield's Capabilities in Battery Research," Battery Manufacturing 2013, University of Warwick, 24th Oct. **2013** (Poster Presentation).

21. Z. Gonga and Y. Yang, "Recent advances in the research of polyanion-type cathode materials for Li-ion batteries", *Energy Environ. Sci.* **2011**, *4*, pp. 3223–3242.

22. C. Masquelier and L. Croguennec, "Polyanionic (Phosphates, Silicates, Sulfates) Frameworks as Electrode Materials for Rechargeable Li (or Na) Batteries", *Chem. Rev.* **2013**, *113*, pp. 6552–6591.

23. P. Barpanda, S. Nishimura and A. Yamada, "High-Voltage Pyrophosphate Cathodes", *Adv. Energy Mater.* **2012**, *2*, pp. 841–859.

24. A.R. West, *Solid State Chemistry and its Application*, 2nd Edition, Student Edition, Wiley, New York, **2014**, pp. 71.

25. M. S. Islam, D. J. Driscoll, C. A. J. Fisher and P. R. Slater, "Atomic-Scale Investigation of Defects, Dopants, and Lithium Transport in the $LiFePO_4$ Olivine-Type Battery Material", *Chem. Mater.* **2005**, *17*, pp. 5085–5092.

26. M. Park, X. Zhang, M. Chung, G.B. Less and A.M. Sastry, "A review of conduction phenomena in Li-ion batteries", *J. of Power Sources* **2010**, *195*, 7904–7929.

27. S.Y. Chung, J.T. Bloking and Y.M. Chiang, "Electronically conductive phosphor-olivines as lithium storage electrodes", *Nat. Mater.* **2002**, *1*, pp. 123–128.

28. A. Yamada, Y. Takei, H. Koizumi, N. Sonoyama, R. Kanno, K. Itoh, M. Yonemura, T. Kamiyama, "Electrochemical, Magnetic, and Structural Investigation of the $Li_x(Mn_yFe_{1-y})PO_4$ Olivine Phases" *Chem. Mater.* **2006**, *18*, pp. 804–813.

29. S.W. Oh, S.-T. Myung, S.-M. Oh, K.H. Oh, K. Amine, B. Scrosati and Y.-K. Sun, "Double Carbon Coating of $LiFePO_4$ as High Rate Electrode for Rechargeable Lithium Batteries", *Adv. Mater.* **2010**, *22*, pp. 4842–4845.

30. A. Yamada, S.C. Chung and K. Hinokuma, "Optimized $LiFePO_4$ for Lithium Battery Cathodes", *J. Electrochem. Soc.* **2001**, *148*, pp. A224–229.

31. C. V. Ramana, A. Ait-Salah, S. Utsunomiya, A. Mauger, F. Gendron and C. M. Julien, "Novel Lithium Iron Pyrophosphate ($LiFe_{1.5}P_2O_7$) as a Positive Electrode for Li-Ion Batteries", *Chem. Mater.* **2007**, *19*, pp. 5319–5324.

32. A.K. Padhi , K.S. Nanjundaswamy , C. Masquelier , S. Okada and J.B. Goodenough, "Effect of Structure on the Fe^{3+}/Fe^{2+} Redox Couple in Iron Phosphates", *J. Electrochem. Soc.* **1997**, *14*, pp. 1609–1613.

33. N. Recham, J.N. Chotard, L. Dupont, C. Delacourt, W. Walker, M. Armand and J.M. Tarascon, "A 3.6 V lithium-based fluorosulphate insertion positive electrode for lithium-ion batteries", *Nat. Mater.* **2010**, *9*, pp. 68–74.

34. A. Nytén, A. Abouimrane, M. Armand, T. Gustafsson and J.O. Thomas, "Electrochemical performance of Li_2FeSiO_4 as a new Li-battery cathode material", *Electrochem. Commun.* **2005**, *7*, pp. 156–160.

35. P. Larsson, R. Ahuja, A.Nytén and J.O. Thomas, "An ab initio study of the Li-ion battery cathode material Li_2FeSiO_4", *Electrochem. Commun.* **2006**, *8*, pp. 797–800.

36. A. Nytén, S. Kamali, L. Häggström, T. Gustafsson and J.O. Thomas, "The lithium extraction/insertion mechanism in Li_2FeSiO_4", *J. Mater. Chem.* **2006**, *16*, pp. 2266–2272.

37. C. Sirisopanaporn, A. Boulineau, D. Hanzel, R. Dominko, B. Budic, A.R. Armstrong, P.G. Bruce and C. Masquelier, "Crystal Structure of a New Polymorph of Li_2FeSiO_4", Inorg. Chem. **2010**, *49*, pp. 7446–7451.

38. A. Boulineau, C. Sirisopanaporn, R. Dominko, A.R. Armstrong, P.G. Bruce and C. Masquelier, "Polymorphism and structural defects in Li_2FeSiO_4", *Dalton Trans.* **2010**, *39*, pp. 6310–6316.

39. C. Sirisopanaporn, C. Masquelier, P.G. Bruce, A.R. Armstrong and R. Dominko, "Dependence of Li_2FeSiO_4 Electrochemistry on Structure", *J. Am. Chem. Soc.* **2011**, *133* (5), pp. 1263–1265.

40. N. Yabuuchi, Y. Yamakawa, K. Yoshii and S. Komaba, "Low-temperature phase of Li_2FeSiO_4: crystal structure and a preliminary study of electrochemical behavior", *Dalton Trans.* **2011**, *40*, pp. 1846–1848.

41. C. Eames, A.R. Armstrong, P.G. Bruce and M.S. Islam, "Insights into Changes in Voltage and Structure of Li_2FeSiO_4 Polymorphs for Lithium-Ion Batteries", *Chem. Mater.* **2012**, *24*, pp. 2155–2161.

42. T. Masese, Y. Orikasa, C. Tassel, J. Kim, T. Minato, H. Arai, T. Mori, K. Yamamoto, Y. Kobayashi, H. Kageyama, Z. Ogumi and Y. Uchimoto, "Relationship between Phase Transition Involving Cationic Exchange and Charge–Discharge Rate in Li_2FeSiO_4", *Chem. Mater.* **2014**, *26*, pp. 1380–1384.

43. L. Adam, A. Guesdon and B. Raveau, "A new lithium manganese phosphate with an original tunnel structure in the $A_2MP_2O_7$ family ", *J. Solid State Chem.* **2008**, *181* (11), pp. 3110–3115.

44. Hui Zhou, Shailesh Upreti, Natasha A. Chernova, Geoffroy Hautier, Gerbrand Ceder and M. Stanley Whittingham, "Iron and Manganese Pyrophosphates as Cathodes for Lithium-Ion Batteries", *Chem. Mater.* **2011**, *23* (2), pp. 293–300.

45. Naoya Furuta, Shin-ichi Nishimura, Prabeer Barpanda and Atsuo Yamada, "Fe^{3+}/Fe^{2+} Redox Couple Approaching 4 V in $Li_{2-x}(Fe_{1-y}Mn_y)P_2O_7$ Pyrophosphate Cathodes", *Chem. Mater.* **2012**, *24* (6), pp. 1055–1061.

46. Mao Tamaru, Prabeer Barpanda, Yuki Yamada, Shin-ichi Nishimura and Atsuo Yamada, "Observation of the highest Mn^{3+}/Mn^{2+} redox potential of 4.45 V in a $Li_2MnP_2O_7$ pyrophosphate ", *J. Mater. Chem.* **2012**, *22*, pp. 24526–24529.

47. Shin-ichi Nishimura, Megumi Nakamura, Ryuichi Natsui and Atsuo Yamada, "New Lithium Iron Pyrophosphate as 3.5 V Class Cathode Material for Lithium Ion Battery", *J. Am. Chem. Soc.* **2010**, *132*, pp. 13596–13597.

48. Gin-ya Adachi, Nobuhito Imanaka and Hiromichi Aono, "Fast Li^+ Conducting Ceramic Electrolytes", *Adv. Mater.* **1996**, *8*(2), pp.127–135.

49. A.R. West, *Basic Solid State Chemistry*, 2nd Edition, Wiley, New York, **2000**, pp. 293–372.

50. A.D. Robertson, A.R. West, A.G. Ritchie, "Review of crystalline lithium-ion conductors suitable for high temperature battery applications", *Solid State Ionics* **1997**, *104*, pp. 1–11.

51. K. Fujimura, A. Seko, Y. Koyama, A. Kuwabara, I. Kishida, K. Shitara, C.A.J. Fisher, H. Moriwake and I. Tanaka, "Accelerated Materials Design of Lithium Superionic Conductors Based on First-Principles Calculations and Machine Learning Algorithms", *Adv. Energy Mater.* **2013**, *3*, pp. 980–985.

52. H. Y-P. Hong, "Crystal Structure and Ionic Conductivity of $Li_{14}Zn(GeO_4)_4$ and Other New Li^+ Superionic Conductors", *Mat. Res. Bul.* **1978**, *13*, pp. 117–124.

53. P.G. Bruce and A.R. West "Phase diagram of the LISICON solid electrolyte system, Li_4GeO_4-Zn_2GeO_4", *Mat. Res. Bull.* **1980**, *15*, pp. 379–385.

54. A. Khorassani, G. Izquierdo and A.R. West, "The Solid electrolyte system, Li_3PO_4-Li_4SiO_4", *Mat. Res. Bull.* **1981**, *16*, pp. 1561–1567.

55. B. Wang, B.C. Chakoumakos, B.C. Sales, B.S. Kwak and J.B. Bates, "Synthesis, Crystal Structure, and Ionic Conductivity of a Polycrystalline Lithium Phosphorus Oxynitride with the Li_3PO_4 structure", *J. Solid State Chem*. **1995**, *115*, pp. 313–323.

56. C. Wang and J. Hong, "Ionic/Electronic Conducting Characteristics of $LiFePO_4$ Cathode Materials", *Electrochem. Solid State Lett.* **2007**, *10*(3), A65–A69.

57. J. Ma, C. Wang and S. Wroblewski, "Kinetic characteristics of mixed conductive electrodes for lithium ion batteries", *J. of Power Sources* **2007**, *164*, 849–856.

58. A.R. West, *Solid State Chemistry and its Application*, 2nd Edition, Student Edition, Wiley, New York, **2014**, pp. 383.

59. J. Molenda, A. Stokłosa and T. Bąk, "Modification in the electronic structure of cobalt bronze Li_xCoO_2 and the resulting electrochemical properties", *Solid State Ionics* **1989**, *36*, 53–58.

60. A.R. West, *Solid State Chemistry and its Application*, 2nd Edition, Student Edition, Wiley, New York, **2014**, pp. 406.

61. H. Tukamoto and A.R. West, "Electronic Conductivity of $LiCoO_2$ and Its Enhancement by Magnesium Doping", *J. Electrochem. Soc.* **1997**, *44*, pp. 3164–3168.

62. P.G. Bruce, *Solid State Electrochemistry*, Cambridge University Press **1995**; A.R. West, "Crystalline solid electrolytes I: General considerations and the major materials", pp. 7–42.

63. A.R. West, *Solid State Chemistry and its Application*, 2nd Edition, Student Edition, Wiley, New York, **2014**, pp. 100.

64. A. Garcia, G. Torres-Treviño and A.R. West, "New lithium ion conductors based on the $LiAlO_2$ structure", *Solid State Ionics* **1990**, *40/41*, pp. 13–17.

65. A.R. West, *Solid State Chemistry and its Application*, 2nd Edition, Student Edition, Wiley, New York, **2014**, pp. 414–418.

66. J.T.S. Irvine, D.C. Sinclair and A.R. West, "Electroceramics: Characterization by Impedance Spectroscopy", *Adv. Mater.* **1990**, *2*, pp. 132–138.

67. P.G. Bruce and A.R. West, "The A-C Conductivity of Polycrystalline LISICON, $Li_{2+2x}Zn_{1-x}GeO_4$, and a Model for Intergranular Constriction Resistances", *J. Electrochem. Soc.* **1983**, *130*, pp. 662–669.

68. D.C. Sinclair, F.D. Morrison and A.R. West, "Applications of combined impedance and electric modulus spectroscopy to characterise electroceramics", *Internat. Ceram.* **2000**, *2*, pp. 33–37.

69. J.R. Macdonald, *Impedance Spectroscopy*, John Wiley & Sons, **1987**, pp. 7.

70. A.R. West, *Solid State Chemistry and its Application*, John Wiley & Sons Ltd., **1984**, pp. 482–489.

71. D.C. Sinclair, "Characterisation of Electro-materials using ac Impedance Spectroscopy", Bol. Soc. Esp. Cerám. Vidrio **1995**, *34* [2], pp. 55–65.

CHAPTER II

Experimental Procedure

The experimental flow chart is presented schematically in **Fig. 2-1** and each operating step is described in detail in the following sections.

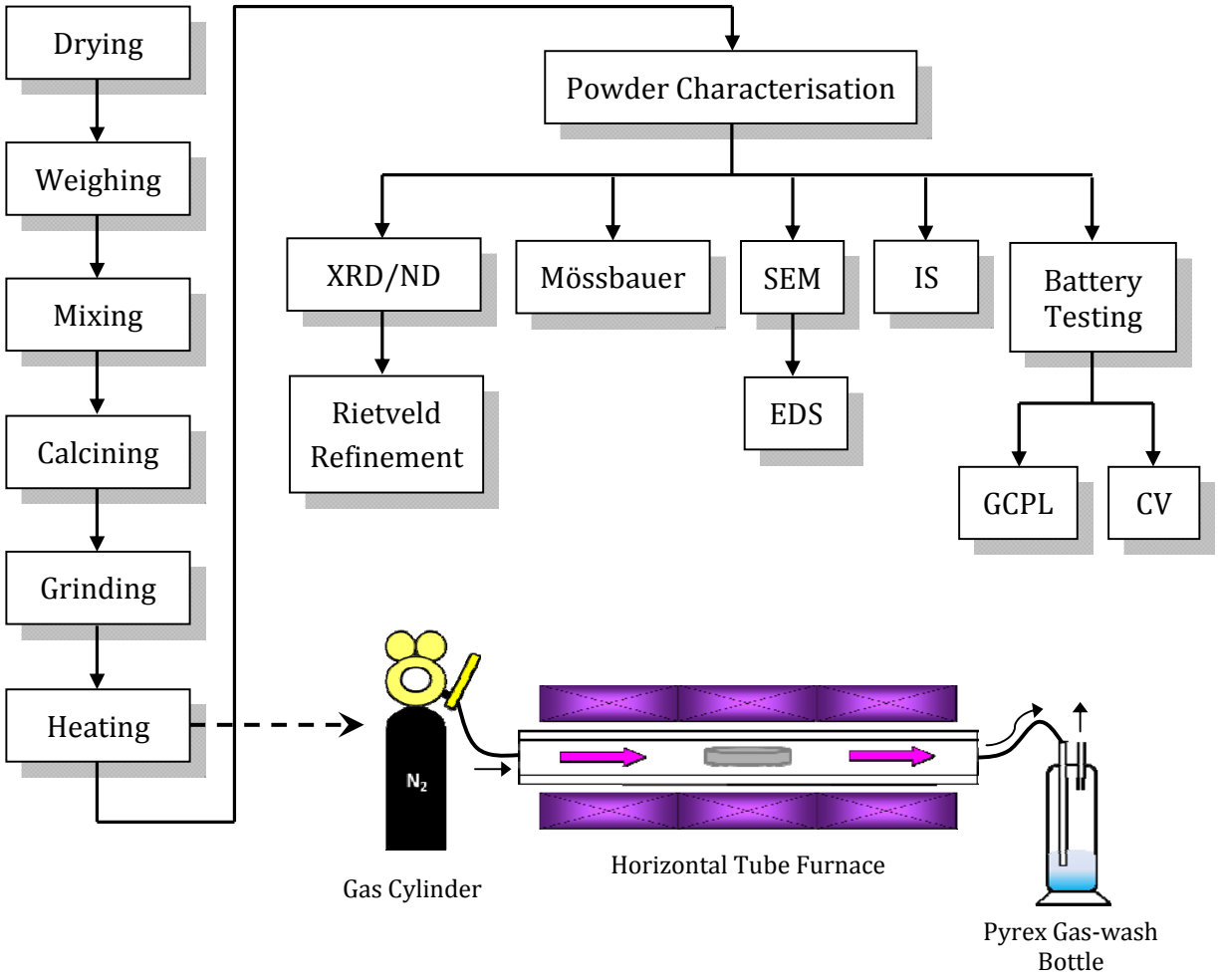

Figure 2-1 The experimental flow chart.

2.1 Solid-State Synthesis

Materials in this thesis were prepared by the mixed oxide solid-state method. All reagents were dried at appropriate temperatures before weighing, **Table 2-1**. ~5 g batches were prepared with stoichiometric amounts of reagents. The precursors were ground for ~30 min in an agate mortar with acetone, pressed into pellets and decomposed at 350°C for 6 hours (heating rate, 2.5 °C/min) to drive off H_2O and CO_2 under air or N_2 atmosphere. The calcined powders were reground, pressed into pellets and then heated at 600~800 °C for 12–24 hours (heating rate, 5 °C/min) in air or N_2. A horizontal tube furnace used for material synthesis in chapters III-V is illustrated in **Fig. 2-1**. Prior to each heating, the tube containing samples in the middle, constant temperature hot zone was purged by N_2 for 3 hours at a constant pressure of ~1.5 bar to ensure an oxygen-free atmosphere. The output connection was attached to a pyrex gas-wash bottle with water inside; the rate of the gas flow was monitored through an observation of two-bubbles per second to maintain a constant pressure during reaction.

Table 2-1 Drying temperatures and purity of all reagents.

Reagent	Drying Temperature (°C)	Source and Purity
Li_2CO_3	180	Aldrich, 99%
$FeC_2O_4 \cdot 2H_2O$	Not Applicable	Aldrich, 99%
$MnCO_3$	180	Aldrich, ≥99.9%
CoO	180	Aldrich, 99%
$Al(OC_2H_5)_3$	Not Applicable	Aldrich, 97%
ZrO_2	600	Aldrich, 99%
Nb_2O_5	700	Aldrich, 99.9%
$MgC_2O_4 \cdot 2H_2O$	Not Applicable	Alfa Aesar, 98.5%
CuO	600	Aldrich, 99%
ZnO	600	Sigma-Aldrich, 99.9%
$(NH_4)H_2PO_4$	Not Applicable	Fluka, ≥99%
Li_3N	Not Applicable	Aldrich, 99.9%

2.2 X-ray diffraction (XRD)

The phase composition of the produced powders was determined using X-ray diffraction (XRD, SIEMENS D5000, operated at 40 kV and 30 mA with Co or Cu K_α radiation at room temperature). Powder samples for XRD of about 0.5 g were prepared with double-sided adhesive plastic tape on an aluminium substrate. The scanning step size and counting time for each step were set at 0.05° and 5.5 seconds, respectively in the 2θ range 10–100°. The phase identification used *WinX*^{POW} or *Steve*$^{+}$ XRD software packages.

Lattice parameters were determined using a high-resolution STOE STADI P X-ray diffractometer (STOE & Cie GmbH, Germany) with Mo or Cu $K_{\alpha1}$ radiation in transmission mode using a position sensitive detector (PSD), as shown in **Fig. 2-2** [1]. The scanning step size and counting time were set at 0.2° and 200 seconds in the 2θ range 5–35° and 5–80° for Mo and Cu PSD, respectively. Peak calibration was carried out using Si powders as an external standard. A typical procedure is described elsewhere [2]. Diffraction data collected with different XRD instruments are summarised in **Table 2-2**.

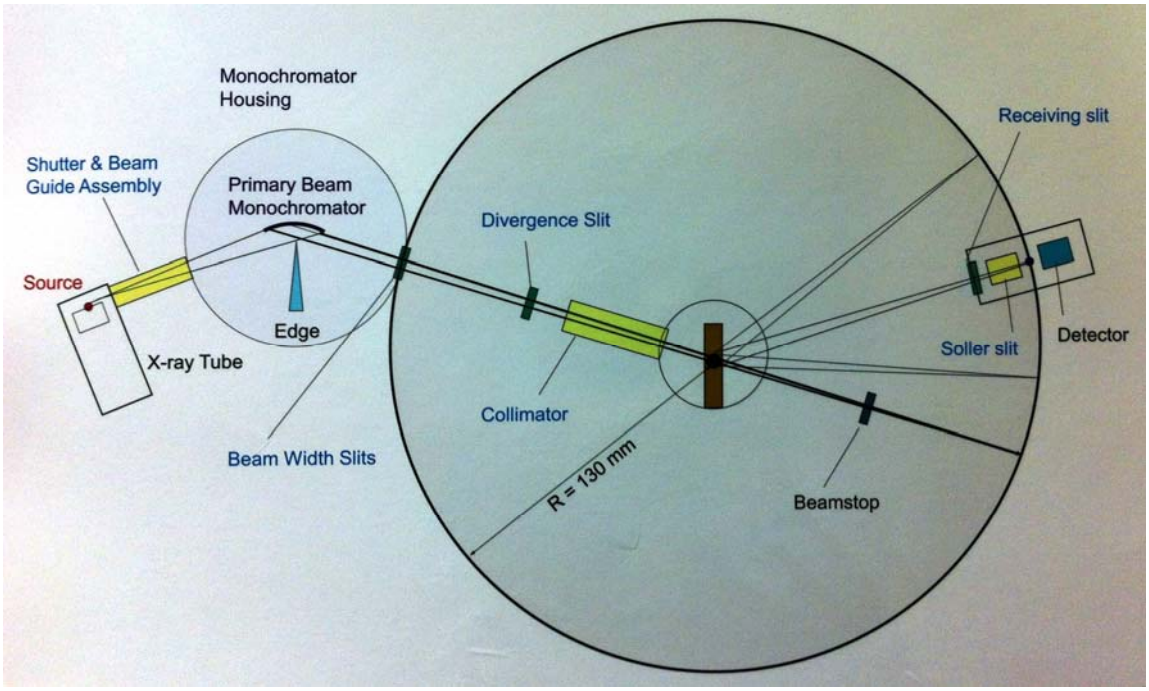

Figure 2-2 STOE STADI P powder diffractometer with PSD [1].

Table 2.2 XRD instruments used to collect data in this thesis.

Instrument	Type	Samples analysed	Purpose
Siemens D5000	Co Kᾱ radiation (1.78896 Å)	(III) $Li_2MP_2O_7$ (M=Mn, Fe, Co) (IV) Doped-$Li_2FeP_2O_7$ (V) N-doped $Li_2FeP_2O_7$ (VI) $Li_{4x}Zn_{2-2x}P_2O_7$	Phase analysis
	Cu Kᾱ radiation (1.54178 Å)	(VI) $Li_{4x}Zn_{2-2x}P_2O_7$	Phase analysis
STOE STADI P Diffractometer	Mo $K\alpha_1$ radiation (0.7093 Å)	(III) $Li_2MP_2O_7$ (M=Mn, Fe, Co) (IV) Doped-$Li_2FeP_2O_7$ (V) N-doped $Li_2FeP_2O_7$	Lattice parameter
	Cu $K\alpha_1$ radiation (1.5406 Å)	(VI) $Li_{4x}Zn_{2-2x}P_2O_7$	Lattice parameter
Siemens D5000 (Glancing Angle)	Cu Kᾱ radiation (1.54178 Å)	(V) N-doped $Li_2FeP_2O_7$: pellet by one-step synthesis	Phase analysis

The measured density of a sintered pellet was calculated by measuring its mass, M_g (g) and geometrical volume, V_g (g/cm^3), and therefore, a relative density was obtained using the following Equations 2.1 [3] and 2.2:

$$D_{theoretical} = \frac{FW \times Z \times 1.66}{V} \quad (2.1)$$

$$D_{relative} = \frac{D_{measured}}{D_{theoretical}} = \left[\left(\frac{M_g}{V_g} \right) / D_{theoretical} \right] \times 100 \quad (2.2)$$

where

$D_{theoretical}$: theoretical density (g/cm^3)

$D_{measured}$: measured density (g/cm^3)

FW: formula weight (g/mol)

Z: number of formula units per unit cell

V: volume of the unit cell (Å^3)

The average crystal size was evaluated through broadening of the XRD peaks using Scherrer's formula [4] as follows:

$$d_{XRD} = \frac{0.94 \cdot \lambda}{B \cdot \cos\theta_B} \tag{2.3}$$

Where d_{XRD} is the crystal size, λ is the X-ray wavelength (1.54186 Å), B is the peak width in radians at FWHM after correcting for instrumental broadening and θ_B is the Bragg angle. The instrumental peak broadening (B_i) which is caused by slit width, sample size, sample penetration, imperfect focusing and non-monochromaticity of the beam (α_1 and α_2 for example) was calibrated [4]. Gaussian shape for the peak is assumed and therefore, the integral breadth from the sample (B_s) is calculated by

$$B_s^2 = B_m^2 - B_i^2$$

where B_m is the measured FWHM of the XRD peaks .

2.3 Neutron Powder Diffraction (ND)

Neutron powder diffraction (ND) is an expensive but excellent technique to study the crystallography of polycrystalline samples in cases where XRD is not adequate [5]. Specifically, ND is much more sensitive to light elements such as Li, H and O to precisely locate their atomic coordinates and site occupancies in crystal structure determination. Neutrons interact with the atomic nuclei of elements, rather than the extranuclear electrons, and that is responsible for the scattering. This means that there is no simple intensity dependence of neutron scattering on atomic number. In terms of XRD, the scattering length of an atom is proportional to the square of the atomic number and this

makes light atoms diffract X-rays weakly. Neutron scattering lengths of the relevant elements in chapter VI are given in **Table 2-3**; the scattering length of neutrons does not increase with atomic number (Z) and in particular, oxygen has a relatively long scattering length [6]. Light elements, e.g. Li and O, make only a small contribution to peak intensities in XRD patterns, but make a significant contribution to ND intensities; this helps in determining accurate atomic positions, thermal parameters, and site occupancies of the elements in the structure.

Table 2-3 Neutron scattering lengths (b_c) for different elements [6].

Element(s)	Atomic Number (Z)	bc (fm)
Li	3	-1.90(3)
O	8	5.805(4)
P	15	5.13(1)
Zn	30	5.680(5)

Structural characterisation of $Li_{2.4}Zn_{0.8}P_2O_7$ powder was carried out by Rietveld refinement [7] of ND data obtained at room temperature. ND data were collected from the D2B diffractometer (λ=1.59432 Å) at the Institut Laue-Langevin (ILL), Grenoble, France. The wavelength was selected using a Ge monochromator. ~5 g samples were placed in a sealed cylindrical vanadium can (5-8 mm diameter; 80-100 mm length). Data collection times were ~2 h in the 2θ range of 10–150° with a step size of 0.05°. ND measurements were carried out by Dr Nahum Masó.

D2B, Institut Laue-Langevin, Grenoble, France

The D2B diffractometer has a constant wavelength with variable θ, and is generally similar to a transmission geometry XRD instrument setup in Debye-Scherrer mode. A large monochromator with take-off angle of 135° results in narrow peaks at high scattering angle, as shown in **Fig. 2-3**.

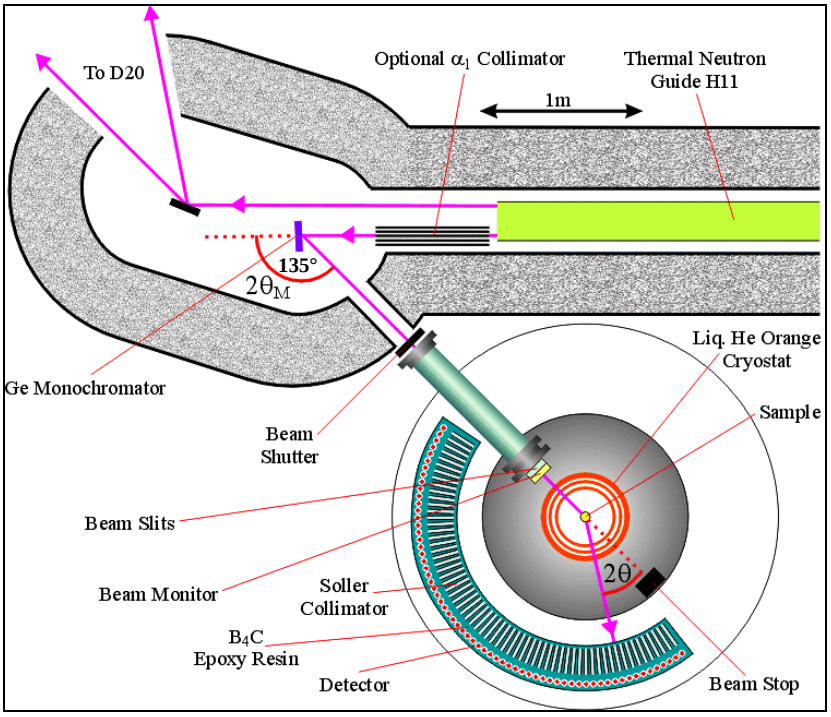

Figure 2-3 Schematic layout of the diffractometer D2B [8].

2.4 Rietveld Refinement

The Rietveld method is a computational technique for structural analysis. It was developed by Hugo M. Rietveld in ~1969, and has been widely used with powder diffraction data for crystal structure refinement [7]. A least squares approach is applied to obtain the best-fit between the calculated diffraction profile of a model structure and the measured diffraction profile [9]. The quantity minimised in the refinement is the residual, S_y,

$$S_y = \sum_i w_i \left[y_i(obs) - y_i(calc) \right]^2 \tag{2.4}$$

where

$w_i = 1/y_i$ = weighting factor at step i

y_i(obs) = observed intensity at the i th step

y_i(calc) = calculated intensity at the i th step

The best fit is achieved when the calculated diffraction patterns are best matched to the observed ones. Several R-values have been developed to estimate whether the refinement is proceeding satisfactorily and when the refinement is sufficiently close to completion, equations 2.5–2.8 [9].

R-pattern (R_p)
$$R_p = \frac{\sum_i |y_i(obs) - y_i(calc)|}{\sum_i y_i(obs)} \quad (2.5)$$

R-weighted pattern (R_{wp})
$$R_{wp} = \left[\frac{\sum_i w_i [y_i(obs) - y_i(calc)]^2}{\sum_i w_i [y_i(obs)]^2} \right]^{1/2} \quad (2.6)$$

R-expected (R_{exp})
$$R_{exp} = \left[\frac{(N-P)}{\sum_i w_i [y_i(obs)]^2} \right]^{1/2} \quad (2.7)$$

Goodness-of-fit (χ^2)
$$\chi^2 = \left[\frac{R_{wp}}{R_{\exp}} \right]^2 \quad (2.8)$$

where

$y_i(obs)$ = observed intensity at data point, i^{th}

$y_i(calc)$ = calculated intensity at data point, i^{th}

w_i = weighting factor=$1/\sigma_i^2$; σ_i is the standard deviation of $y_i(obs)$

N = number of data points

P = number of least-squares variables

R_p indicates the difference between the observed and calculated patterns (Eq. 2.5). R_{wp} is similar to R_p but is more accurate because it not only takes account of general fitting, but takes the standard deviations of the background and peak intensities into consideration

(Eq. 2.6). R_{exp} reflects the quality of the experimental data (Eq. 2.7). The '*goodness-of-fit*' indicator, χ^2, is used to evaluate the overall quality of refinement results; if the model fits all data exactly, R_{wp} should be equal to R_{exp} and therefore, the ideal value of χ^2 would be 1 (Eq. 2.8). The statistical measures start off large but decrease as the fit is improved during refinement. In general, a reasonable fit should have *R*-values and χ^2 between 1 and 10; when *R*-values are larger than 20%, the structural model is probably only partial correct.

Apart from the numerical indicators, it is also important to study the graphical difference plots for each histogram to ensure the fit to the experimental data is adequate.

Rietveld refinements in this thesis were carried out using *FullProf* software [10]. The usual refinable parameters are as follows [11]:

i. Scattering Factor:

   This parameter is to ensure that the observed and calculated peak intensities are on the same scale.

ii. Background:

   The background of the observed patterns is fitted by a separate mathematical function. A linear interpolation method between a set of fixed background points is commonly used for XRD and ND refinements using *FullProf* program.

iii. Peak-shape Function

   A Pseudo-Voigt function was chosen to reproduce the line shape of the peaks in a powder pattern. The Pseudo-Voigt approximation has been widely used for X-Ray and constant-wavelength ND data [12], and is a linear combination of Lorentzian and Gaussian functions, Equations 2.9–2.10

$$\text{Lorentzian function: FWHM} = X \tan\theta + Y/\cos\theta \quad (2.9)$$

$$\text{Gaussian function: FWHM}^2 = U \tan^2\theta + V \tan\theta + W \quad (2.10)$$

where *X*, *Y*, *U*, *V*, and *W* are the refined parameters.

The Pseudo-Voigt function gives a better description of a symmetrical X-ray diffraction peak and in addition, it appears to describe the asymmetric peak shape resulting from beam divergence at low angle [13].

iv. Lattice Parameters

These values must be refined to reach the global minimum if the peak positions are slightly displaced between the observed and calculated patterns.

v. Atomic Positions

The atomic coordinates (x, y, z) of each atom in the model are refined to obtain accurate positions. In general, it is advisable to start the refinement of the positions with heavy atoms and then to refine those of the lighter ones. If the latter converges, all atomic positions in the model would then be refined simultaneously.

vi. Thermal Parameters

Thermal parameters, U_{iso} (Å^2), are essentially a measure of atomic vibration and/or displacement on a particular site. The U_{iso} of a site can be influenced by the atoms occupying that site and the size of the site. Negative U_{iso} values but those within one or two standard deivation from zero may be accepted since they are not statistically distinguishable from small positive values.

vii. Site Occupancies

The fractional occupancy at each site can be changed to clarify whether the site is fully or partially occupied in the structural model. Note that it is compulsory to apply constraints to a site occupied by two different atoms and the thermal parameters and atomic coordinates must be fixed to be the same. The sum of the fractional occupancies should correspond to the total site occupancy.

2.5 Scanning Electron Microscopy (SEM)

The particle size and morphology of the sintered pellets were examined by scanning electron microscopy (SEM) JEOL JSM-6400 (JEOL Ltd., Japan) operated at 20 kV with a working distance of 15 mm. The chemical composition and elemental distribution of the powders were measured using an Oxford Link ISIS (Oxford Instruments Ltd., UK) X-ray energy dispersive spectroscopy (EDS) instrument installed in the SEM with an *INCA* software package attached. The poorly conductive or nonconductive specimens were carbon-coated with an Edwards Carbon Coating Unit for ~1 min in vacuum to prevent surface-charging during SEM observation.

2.6 Mössbauer Spectroscopy

Mössbauer spectroscopy has been widely used for Fe-containing substances. Room temperature ^{57}Fe Mössbauer spectra were collected relative to α-Fe by a WissEl spectrometer (Wissenschaftliche Elektronik GmbH, Germany) over the velocity range using a constant acceleration spectrometer with a ^{57}Co/Rh source. A data acquisition module CMCA-550, was used to run the analyses for 42 hours. The spectra were analysed using the *RECOIL* analysis software package [14] and satisfactorily fitted with two broadened Lorentzian paramagnetic doublets. Mössbauer measurements and data analysis were performed by Dr Paul A. Bingham.

2.7 Impedance Spectroscopy (IS)

2.7.1 Pellet Preparation

Impedance spectroscopy was utilized to measure electrical properties; pellets (~0.2 g) were sintered in N_2 or air at 600~700 °C for 12 hours with a heating/cooling rate of ±5.0 °C/min. Prior to sintering, samples were pressed into pellets, vacuumed in a plastic glove, and then placed in a cold isostatic press (CIP) at ~200 MPa to increase the green density of the pellets. All samples were platinum- and/or gold-sputtered on opposite parallel faces for 4 min with 2 cycles to form electrodes using a sputter coater (Emitech K575XD, UK) at 30 mA. Different metals, Au, Pt, Ag and InGa, were deposited on opposite

parallel faces to form electrodes, as summarised in **Table 2-4**.

Table 2-4 Preparation of metal electrodes.

Electrodes	Firing Temp. (°C)	Firing Time (h)	Heating Rate (°C/min)
Sputtered Au	25	…..	……
Sputtered Pt	25	……	……
Au paste	800	2	10
Pt paste	900	1	10
Ag paste	600	2	10
InGa alloy	25	……	……

2.7.2 Impedance Measurement

Room- and high-temperature impedance spectroscopy of the sputtered-coated pellets, chapter VI, was conducted using a HP4192A (Hewlett Packard, USA) impedance analyser. The voltage amplitude and frequency range were set at 100 mV and 50–10^7 Hz, respectively. A small ac voltage was applied across a sample connected to Pt wires supported in a compression jig via Au electrodes, as shown in **Fig. 2-4**.

For chapter III-V, high temperature impedance testing was carried out to investigate the electronic, ionic, and/or mixed conductivities. A pellet was connected to an atmosphere jig via two Pt wires in different atmospheres, e.g. N_2 and compressed air. In addition, the flow rate of input gas was monitored through an output gas bubbles observed in a pyrex gas-wash bottle with water, see **Fig. 2-5**. The atmosphere was equilibrated by purging gas for at least 30 minutes before measurements. Low frequency impedance response was measured using a Solartron SI 1260 (Solartron Analytical, UK) impedance analyser with voltage amplitude and frequency range set at 100 mV and 10^{-2}–10^7 Hz, respectively. A small *dc* bias of 1–3 V was also applied to get insight into the nature of materials. Collected IS data were presented using the *ZVIEW 3.3* software package [15].

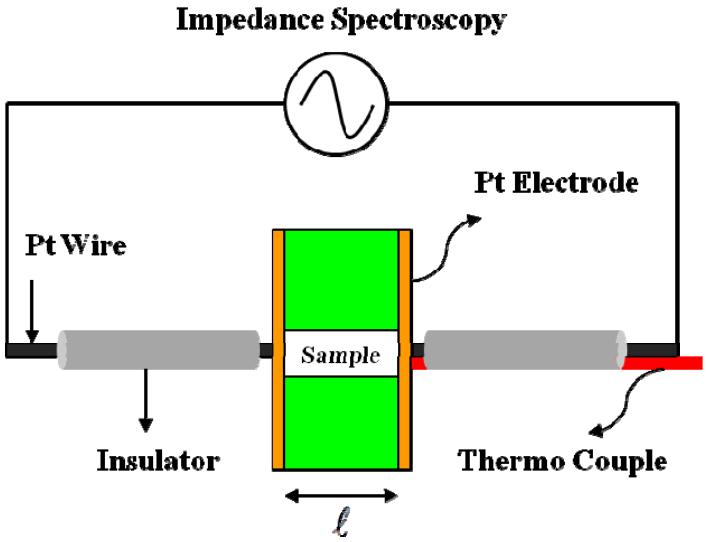

Figure 2-4 Schematic diagram of sample and compression-jig.

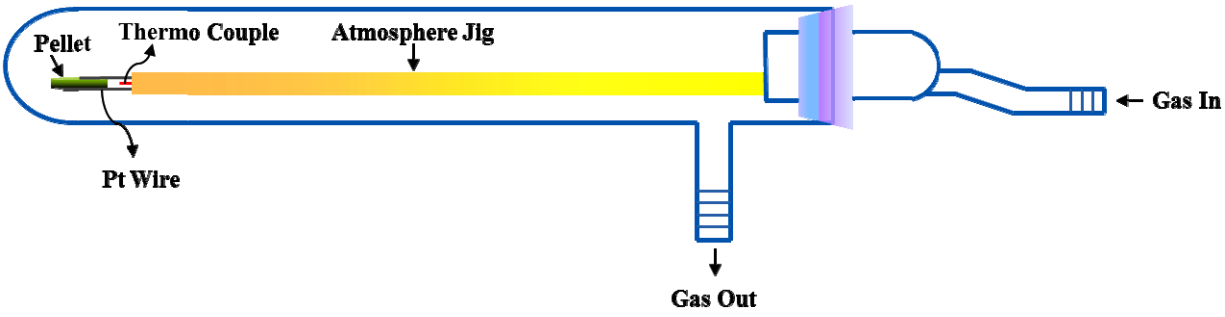

Figure 2-5 Schematic diagram of sample and atmosphere-jig.

2.8 Electrochemical Testing

2.8.1 Electrode and Coin-cell Preparation

In order to reduce the particle size of the active materials used for battery testing, samples were ball milled using zirconia beads as milling media with iso-propanol at a constant speed of 30 rpm for 24 hours. Experimental details are given in **Sec. 2.1**. Electrochemical tests were carried out using a CR2325-type coin cell assembled in an Ar-filled glove box, as shown in **Fig. 2-6 (a)**. The active material (84 wt.%), the Super C65 and

KS-6L (3.5:3.5, wt.%) as a conducting additive and the polyvinylidene fluoride (PVDF) binder (9 wt.%) were dissolved in N-methyl-2-pyrrolidone (NMP) solution for the preparation of the positive electrode. The black mixture was blended in an agate mortar for 30 minutes to form a uniform paste. The paste was then coated onto aluminum foil by a doctor blade and NMP was evaporated at 130°C in an oven to form the electrode. A disk, 13 mm in diameter, was punched from the electrode and dried in vacuum at 90°C for 4 hours, see **(b)**. The final test cell consisted of an electrode film (cathode) and a punched lithium metal of 0.2 mm thickness (anode), which were separated by porous polypropylene film, see **(c)**. The electrolyte solution was 1.0 M $LiPF_6$ in polycarbonate (PC) or a mixture of ethylene carbonate (EC) and dimethyl carbonate (DMC) with a weight ratio of 1:1.

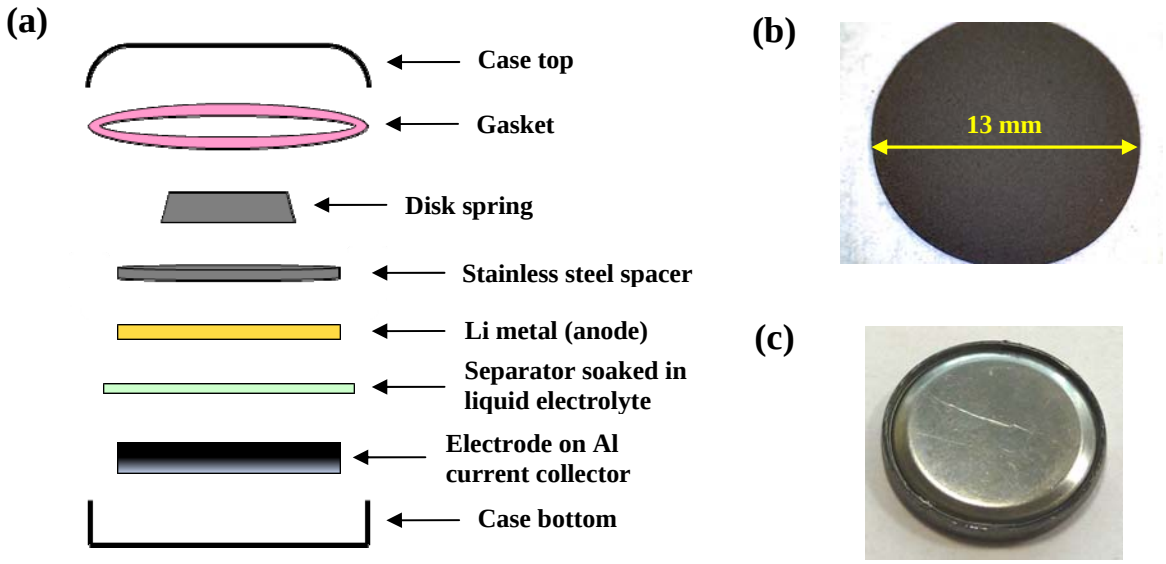

Figure 2-6 (a) Coin-cell construction, (b) punched electrode film ($Li_2FeP_2O_7$), and (c) final coin-cell configuration.

2.8.2 Battery Testing

Electrochemical measurements were carried out using a versatile multichannel potentiostat (VMP) system (Perkin-Elmer, UK) connected to 16 channels (made in-house) and to a computer with the *EC-Lab V10.19* software.

(a) Galvanostatic Cycling with Potentiostatic Limitation (GCPL)

Battery performances were examined using the GCPL technique that applied a constant current across the cell while the variation in cell potential was recorded during both charge and discharge. To know the current rate required for the cell to be (dis)charged, firstly, it is necessary to calculate the theoretical capacity (Q) for the cell, Equation 2.11

$$Q(mAh/g) = \left[\left(F \times n_{Li}\right)/\left(M \times 3600\right)\right] \times 1000 \quad (2.11)$$

where, F = Faraday's constant (96485.33 C/mol)

n_{Li} = Number of Li per formula unit of the active material

M = Molecular weight of the active material (g/mol)

It is noted that 3.6 Coulomb =1mAh, hence the correction factor in Eq. 2.11. The maximum theoretical capacity (assuming that all lithium ions which can be deintercalated) has units of mAh·g^{-1}.

For example, the theoretical capacity of $Li_2FeP_2O_7$ cathode is calculated if two Li ions can be electrochemically extracted, Equation 2.12, and therefore Q=220 mAh/g is obtained as follows.

$$Cathode: Li_2FeP_2O_7 \rightarrow 2Li^+ + 2e^- + FeP_2O_7 \quad (2.12)$$

$$Q_{Li_2FeP_2O_7} = \frac{96485.33 \times 2}{243.67 \times 3600} \times 1000 = 220 \ (mAh/g)$$

When a constant current, I, is applied for a fixed time t, the amount of charge, Q_T, passed across the cell can be described by Equation 2.13

$$Q_T = I \times t \quad (2.13)$$

where I is the current (mA) and t is time (h).

Charge/discharge current is often expressed as a *C-rate* in order to normalise against battery capacity. The C-rate is a measure of the rate at which a battery is (dis)charged

relative to its maximum capacity. A *1C* rate is designated as the rate required to (de)intercalate one Li ion in 1 hour. For t=20, the current rate is denoted by *C/20*.

(b) Cyclic Voltammetry (CV)

Cyclic voltammetry (CV) is widely used to acquire qualitative information about electrochemical reactions in Li-ion battery research. It gives information on redox processes, heterogeneous electron-transfer reactions and adsorption processes. A rapid determination of the redox potential can be obtained for the electroactive species. **Fig. 2-7** shows the potential change as a function of time within a chosen potential 'window' at a constant scan rate. Note that the scan rate (v) can be calculated from $\left|dE/dt\right|$. A number of sequential cycled sweeps are performed in CV via a linearly triangular potential waveform to study the reversibility of the working electrode. During the potential sweep, the current resulting from electrochemical reactions can be observed.

In this thesis, CV measurements were performed at a scanning rate of 0.02 mV/s between 2 V and 4.5~5.0 V. Cycle tests were performed at various charge and discharge rates with constant cut-off voltages at room temperature (25°C).

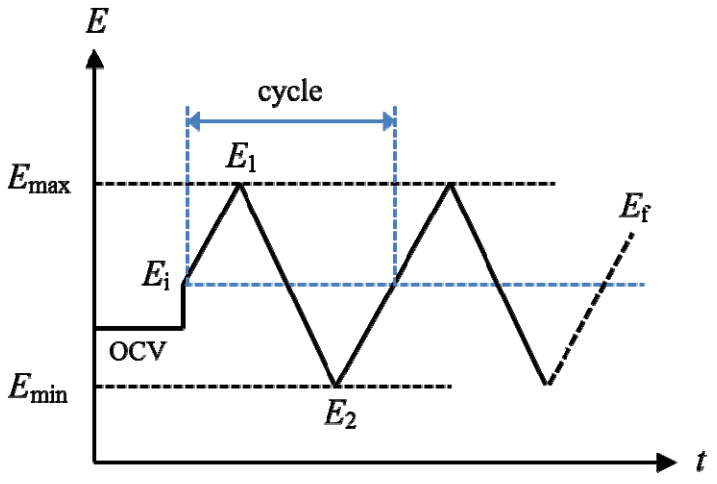

Figure 2-7 Schematic diagram of the variation of applied potential with time. E_{max} and E_{min}: the upper and lower limits of the potential 'window'; E_i and E_f: the initial and final potential; OCV: Open-Circuit-Voltage.

2.9 References

1. N. Reeves-McLaren, *In Focus: Transmission Geometry*, X-ray Diffraction Laboratory, Dept. Materials Science & Engineering, University of Sheffield.

2. N. Reeves-McLaren, *Basic instructions for WinX^{POW}*, Internal Training Note, Dec. **2004**.

3. A.R. West, *Basic Solid State Chemistry*, 2nd Edition, Wiley, New York, **2000**, pp. 14.

4. (a) B. D. Cullity, *Elements of X-ray Diffraction*, 2nd Edition, Addison-Wesley Publishing Company, Inc, **1978**, pp. 102. (b) H.F. Lin, S.C. Liao and S.W. Hung, "The dc thermal plasma synthesis of ZnO nanoparticlesfor visible-light photocatalyst", *J. Photochem. Photobiol.* **2005**, *174*, pp. 82–87.

5. A.R. West, *Solid State Chemistry and its Application*, 2nd Edition, Student Edition, Wiley, New York, **2014**, pp. 266–267.

6. V.F. Sears, "Neutron scattering lengths and cross sections", *Neutron News* **1992**, *3*, pp. 26–37.

7. H. M. Rietveld, "A Profile Refinement Method for Nuclear and Magnetic Structures", *J. Appl. Cryst.* **1969**, *2*, pp. 65–71.

8. http://pd.chem.ucl.ac.uk/pdnn/inst3/diff1.htm

9. R.A. Young, *The Rietveld Method*, Oxford University Press, **1993**, pp. 1–38.

10. J. Rodriguez-Carvajal, "FULLPROF: A Program for Rietveld Refinement and Pattern Matching Analysis", *Abstracts of the Satellite Meeting on Powder Diffraction of the XV Congress of the IUCr*, p. 127, Toulouse, France (**1990**).

11. L. B. McCusker, R. B. Von Dreele, D. E. Cox, D. Louër and P. Scardi, "Rietveld refinement guidelines", *J. Appl. Cryst.* **1999**, *32*, pp. 36–50.

12. P. Thompson, D. E. Cox and J. B. Hastings, "Rietveld refinement of Debye-Scherrer synchrotron X-ray data from Al_2O_3", *J. Appl. Cryst.* **1987**, *20*, pp. 79–83.

13. L. W. Finger, D. E. Cox and A. P. Jephcoat, "A correction for powder diffraction peak asymmetry due to axial divergence", *J. Appl. Cryst.* **1994**, *27*, pp. 892–900.

14. K. Lagarec and D. G. Rancourt, Recoil: Mössbauer spectral analysis software for windows, http://www.isapps.ca/recoil/ (**1998**).

15. http://www.scribner.com/

CHAPTER III

Synthesis, Characterisation, Electrical and Electrochemical Properties of $Li_2MP_2O_7$ (M=Fe, Mn, Co)

3.1 Introduction

In recent years, various abundant and different insulating Li-based compounds such as silicates (Li_2MSiO_4), borates ($LiMBO_3$), fluorophosphates ($Li_{2-x}MPO_4F$), and fluorosulphates ($LiMSO_4F$) are attracting wide attention specifically for the increase of electrode redox potential [1-4]. As reported by Goodenough *et al.* [5], substitution of polyanionic phosphates $(PO_4)^{3-}$ by sulfates $(SO_4)^{2-}$ in isostructural NASICON $[Li_xTM_2(XO_4)_3]$ can increase the open circuit voltage by 0.8 V. Therefore, sulfate polyanionic-based electrodes can present better performance than their phosphate counterparts. In addition, fluoride-based electrodes display greater potential because of the larger ionicity of M–F bonds as compared to M–O bonds. For instance, Tarascon *et al.* have reported two novel Fe-based polyanionic materials, 3.6 V $LiFeSO_4F$ [4] and 3.9 V $Li(Fe_{1-\delta}Mn_\delta)SO_4F$ [6], with theoretical capacities of 151 mAh/g and 125 mAh/g, respectively. To store more energy density with novel cathode systems, new PO_4-based polyanionic compounds are needed in which the redox reaction exceeds one electron per transition metal.

Novel lithium transition metal pyrophosphates ($Li_2MP_2O_7$) have been recently reported as polyanionic cathode material for lithium-ion batteries. In 2008, the structure of $Li_2MnP_2O_7$ was first reported by Adam *et al.* with no electrochemical data [7]. Subsequently, a new lithium iron pyrophosphate, $Li_2FeP_2O_7$, as 3.5 V cathode with one electron theoretical capacity of 110 mAh/g was demonstrated by Nishimura *et al.* in 2010 [8], followed with $Li_2Mn_{1-y}Fe_yP_2O_7$ solid solution by Zhou *et al.* [9] and $Li_{2-x}MP_2O_7$ (M = Fe, Co) by Kim *et al.* [10] in 2011. In comparison to $LiFePO_4$, $Li_2FeP_2O_7$ possesses many positive characteristics such as electrochemical activity without the need for nanosizing or carbon coating, a quasi-two dimensional pathway for Li ion diffusion, and the possibility of a two-electron redox reaction (theoretical capacity: 220 mAh/g). Electrical properties, however, were not reported in ref. 7-10.

In order to increase the operating voltage for the development of high-energy density for Li-ion batteries, it may be possible to substitute Fe by other isovalent metal elements, e.g. Mn, Co, to form $Li_2[Fe_{1-x}M_x]P_2O_7$ compounds [9]. The chemical potential of the Mn^{2+}/Mn^{3+} couple is located at ~4.5 V and of Co^{2+}/Co^{3+} at ~4.9 V, which is higher than that of the Fe^{2+}/Fe^{3+} couple at 3.8 V [9-10]. In other words, it may be practical to increase the redox potential of pure $Li_2FeP_2O_7$ (3.5 V) by replacing the Fe^{2+}. The higher voltage profile of $Li_2[Fe_{1-x}M_x]P_2O_7$ could be attractive to increase the energy density to 200 mAh/g.

AC impedance is an invaluable technique to characterise lithium ion conductivity of new materials for possible lithium battery applications. Herein, we present a systematic investigation of the structure, composition, electrical properties, and electrochemical performance of $Li_2Fe_{1-x}M_xP_2O_7$ (M=Mn and/or Co) solid solution cathodes synthesised by conventional solid state method, with compositions shown in **Fig. 3-1**. Most importantly, the focus of this chapter is to determine whether the isostructural compounds are lithium ion conductors, electronic conductors or mixed conductors using the impedance spectroscopy technique.

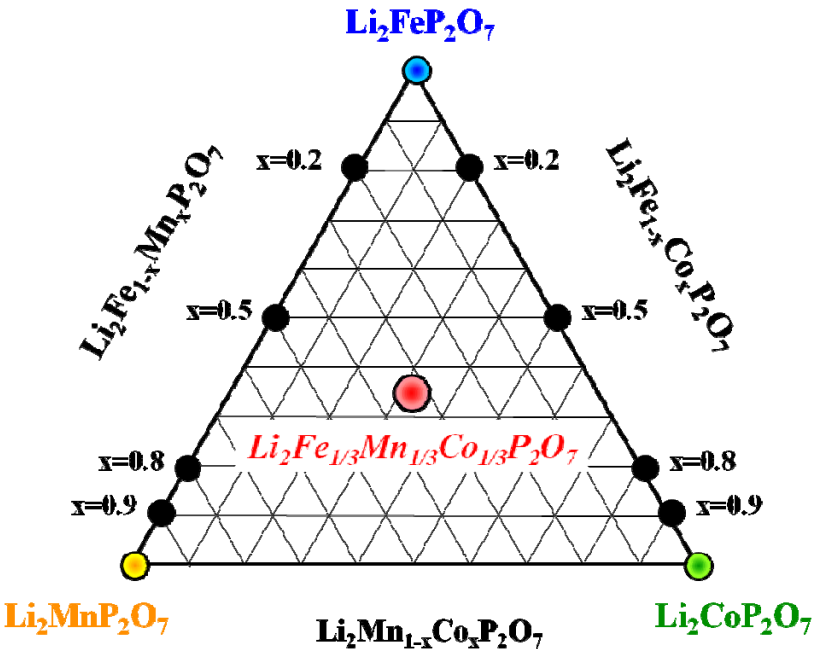

Figure 3-1 Composition triangle of the $Li_2MP_2O_7$ (M=Fe, Mn, Co) solid solution systems. The compositions synthesised are marked by closed circles.

3.2 Synthesis

The materials with formula $Li_2Fe_{1-x}Mn_xP_2O_7$ (x=0–1), $Li_2Fe_{1-y}Co_yP_2O_7$ (y=0–1), and $Li_2Fe_{1-x-y}Mn_xCo_yP_2O_7$ (x=y=1/3) were synthesised from stoichiometric amounts of Li_2CO_3 (Aldrich, 99%), $FeC_2O_4{\cdot}2H_2O$ (Aldrich, 99%); $MnCO_3$ (Aldrich, ≥ 99.9%); CoO (Aldrich, 99%), and $(NH_4)H_2PO_4$ (Fluka, ≥ 99%) by conventional solid-state reaction. The mixtures were ground for ~40 min in an agate mortar with acetone, pressed into pellets and heated at 350°C for 6 h and 600~800 °C for 12 h under nitrogen atmosphere. The furnace tube containing samples was sealed and then purged by nitrogen for several hours to ensure an oxygen-free atmosphere before the heat treatment. A schematic experimental flow chart for the synthesis is shown in **Fig. 3-2**.

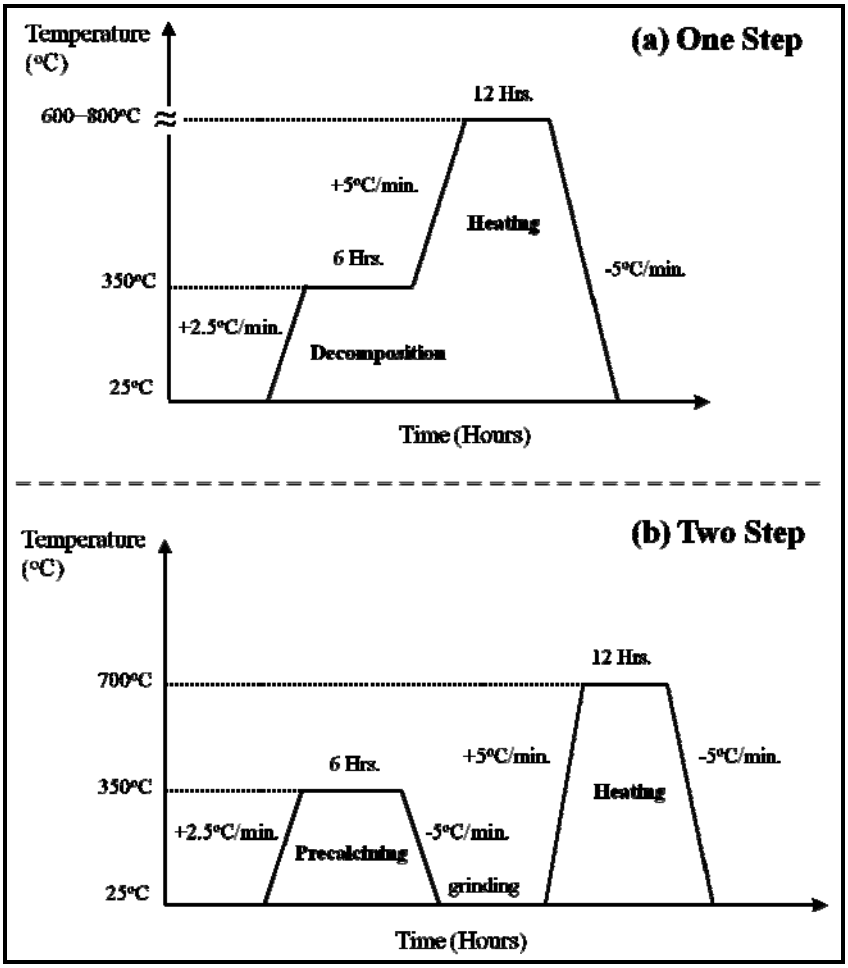

Figure 3-2 (a) One- and (b) two-step processes for heat treatment in N_2.

3.3 Results

3.3.1 XRD Patterns and Crystallinity

(i) $Li_2MP_2O_7$ (M=Fe, Mn, Co, $Fe_{1/3}Mn_{1/3}Co_{1/3}$)

Lithium pyrophosphate $Li_2MP_2O_7$ (M=Fe, Mn, Co) compounds were synthesised according to the following Equations 3.1–3.3:

$Li_2FeP_2O_7$: $Li_2CO_3 + FeC_2O_4{\cdot}2H_2O + 2(NH_4)H_2PO_4 \rightarrow Li_2FeP_2O_7 + CO + CO_2 + H_2O$ (3.1)

$Li_2MnP_2O_7$: $Li_2CO_3 + MnCO_3 + 2(NH_4)H_2PO_4 \rightarrow Li_2MnP_2O_7 + CO + CO_2 + H_2O$ (3.2)

$Li_2CoP_2O_7$: $Li_2CO_3 + CoO + 2(NH_4)H_2PO_4 \rightarrow Li_2CoP_2O_7 + CO + CO_2 + H_2O$ (3.3)

Table 3-1 summarizes XRD results of stoichiometric $Li_2MP_2O_7$ (M=Fe) prepared by one-step solid state reaction, **Fig. 3-2(a)**, at different temperatures in N_2. Phase-pure material was produced in the sample synthesised at 700°C, however, $LiFePO_4$, $Li_4P_2O_7$, and $LiFeP_2O_7$ impurities were detected in the final product of samples synthesised at 600°C and 800°C, respectively. The simulated and measured X-ray power diffraction patterns (Co radiation) of $Li_2FeP_2O_7$ heated at 700°C are presented in **Fig. 3-3**. Note that the theoretical XRD pattern is drawn using published lattice parameters and atomic coordinates [8]. In general, the intensity distribution is similar without any impurities. The Li_2O-FeO-P_2O_5 composition triangle is presented in **Fig. 3-4**, which shows different stable binary and ternary compounds.

The key point to obtain pure $Li_2FeP_2O_7$ is the synthesis conditions; the ground powders need to be purged with enough N_2 gas in the tube furnace, and subsequently the precalcined samples must be reground well before high-temperature heating, following the two-step solid state reaction in **Fig. 3-2(b)**. Based on the successful synthesis of $Li_2FeP_2O_7$, the experimental approach and temperature of 700°C was adopted to synthesise other isostructural analogues, e.g. M=Mn, Co, and $Fe_{1/3}Mn_{1/3}Co_{1/3}$.

Table 3-1 Results of $Li_2FeP_2O_7$ composition reacted at different temperatures.

Process	Synthesis Temperature	Phases Present
One-step	600°C	$Li_2FeP_2O_7$, $LiFePO_4$, $Li_4P_2O_7$, $LiFeP_2O_7$
One-step	700°C	$Li_2FeP_2O_7$, $LiFePO_4$ (<1%)
Two-step	**700°C**	**Phase Pure**
One-step	800°C	$Li_2FeP_2O_7$, $LiFePO_4$, $Li_4P_2O_7$, $Fe_2P_2O_7$, $LiFeP_2O_7$, $LiPO_3$, Li_3PO_4

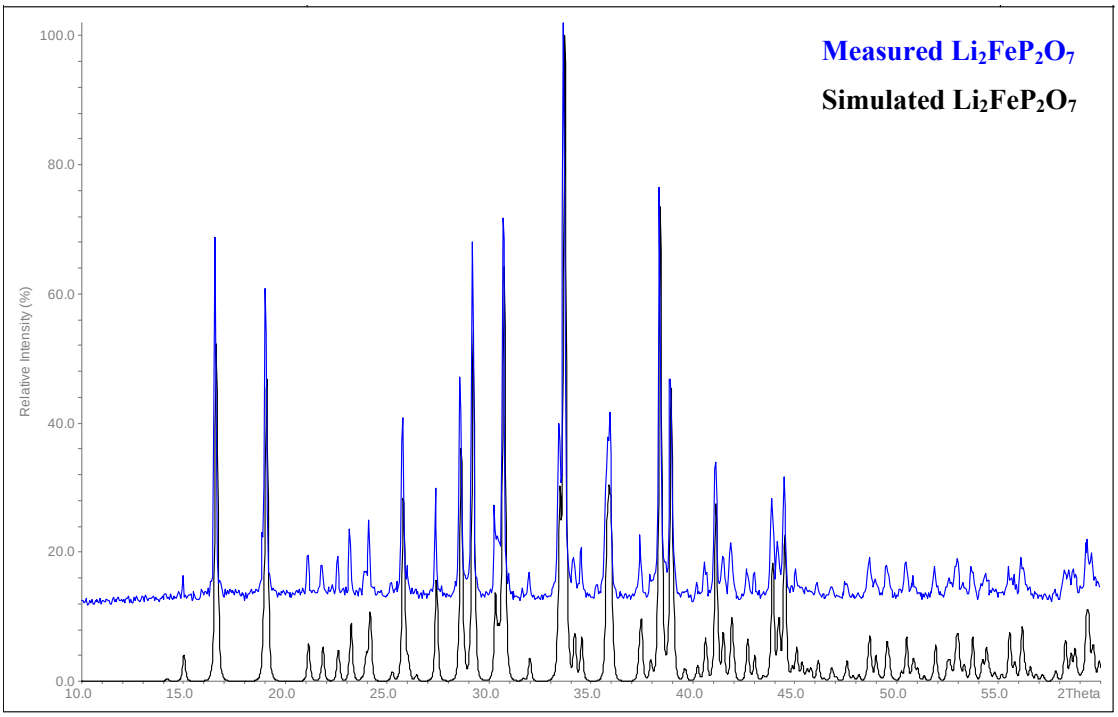

Figure 3-3 Simulated (black) and synthesised (blue) XRD patterns (Co radiation) of $Li_2FeP_2O_7$ synthesised at 700°C following a two-step process.

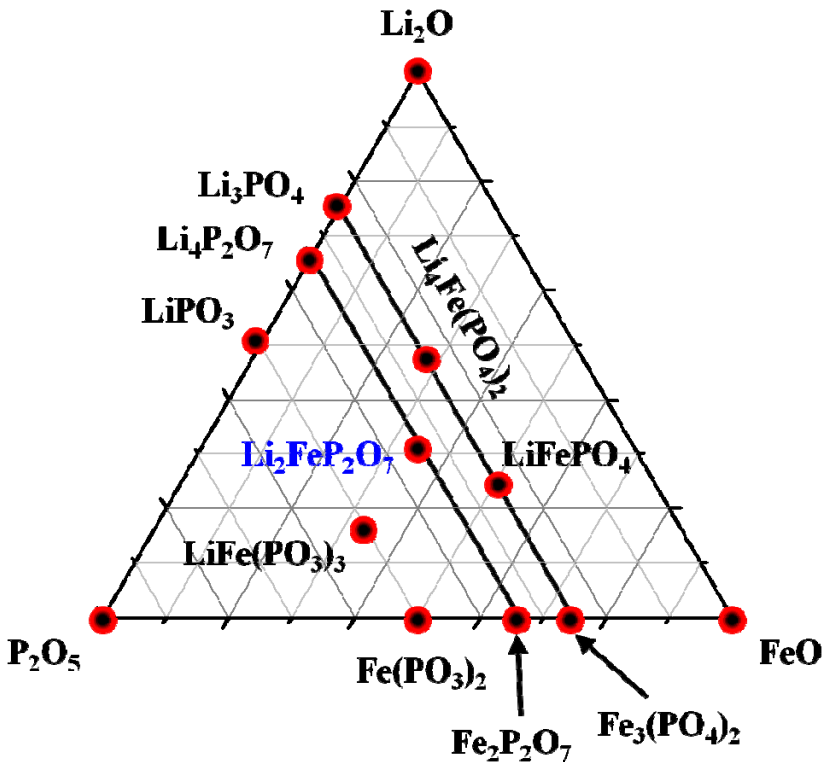

Figure 3-4 The Li_2O-FeO-P_2O_5 composition triangle.

The XRD patterns of $Li_2MnP_2O_7$ and $Li_2CoP_2O_7$ compounds synthesised at 700°C for 12 h in N_2 atmosphere are similar, consistent with the retention of the $Li_2FeP_2O_7$ structure, as shown in **Fig. 3-5(a)**. The intensities of some diffraction peaks, however, were different which was attributed to a different cation distribution in the two structures [8]. All samples are single phase with monoclinic symmetry and were indexed on space group $P2_1/c$. In general, all peaks present a shift toward lower 2θ values in the sequence: Co; Fe; Mn; the magnified positions of the $(\bar{1}11)$ and (200) reflections are highlighted in **Fig. 3-5(b)**. The lattice parameters and unit cell volume of $Li_2MnP_2O_7$ are a = 11.169(5) Å, b = 9.821(4) Å, c = 9.897(5) Å, β = 102.49(4)°, V = 1059.9(6) Å^3, of $Li_2FeP_2O_7$ are a = 11.019(5) Å, b = 9.746(6) Å, c = 9.791(8) Å, β = 101.49(5)°, V = 1059.9(6) Å^3, and of $Li_2CoP_2O_7$ are a = 10.974(4) Å, b = 9.684(5) Å, c = 9.766(6) Å, β = 101.87(4)°, V = 1015.7(6) Å^3.

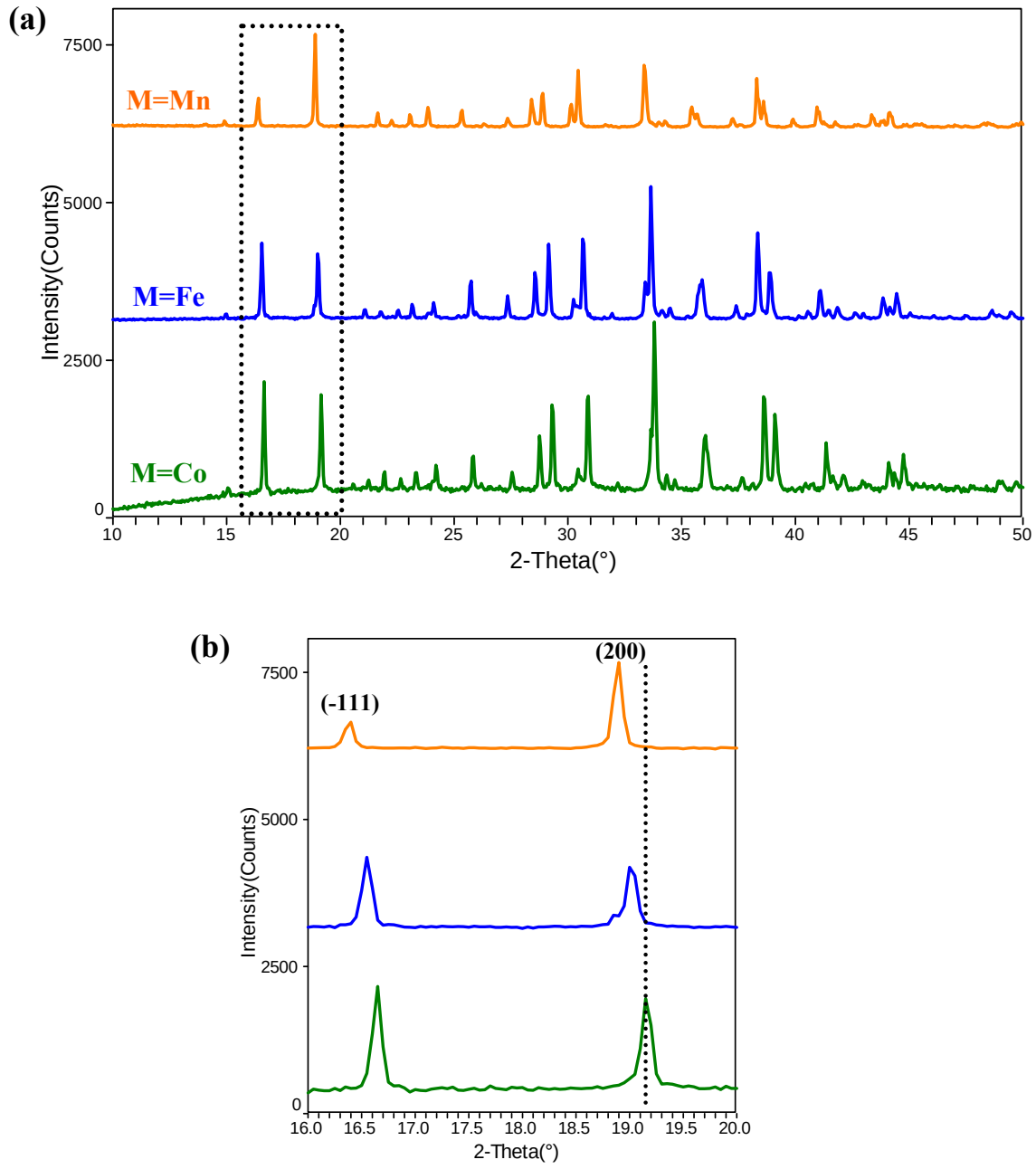

Figure 3-5 (a) XRD patterns of $Li_2MP_2O_7$ (M=Fe, Mn, Co); (b) Magnified shift of (-111) and (200) peaks in (a).

The structural difference, **Fig. 3-6**, between $Li_2FeP_2O_7$ and $Li_2MnP_2O_7$ cause different intensities of the XRD data. $Li_2MnP_2O_7$ has a 3D framework built of fully-occupied MnO_6 octahedra sharing edges with MnO_5 trigonal bipyramids to form Mn_2O_9 units **(a)**. $Li_2MnP_2O_7$ was regarded as an ordered pyrophosphate and the Li atoms occupy four distinct sites (Li1, Li2, Li3 and Li4) with full occupancy. Its structure possesses two-dimensional lithium migration channels, e.g. two Li ions in the tunnels along the *a*-axis **(b)** and one along the *b*-axis **(c)**. However, for $Li_2FeP_2O_7$, the fully-occupied FeO_6 octahedra share edges with the mixed-occupied FeO_5/LiO_5 trigonal bipyramids **(a)**. The occupancy ratio of Fe and Li in FeO_5 polyhedra, labelled by Fe2:Li4, is ~ 2:1 and in LiO_5, Fe3:Li5, ~ 1:2 [11]. The Li–Fe anti-site mixing is highlighted. 2-D channels for Li diffusion are observed along the *b*-axis **(d)** and *c*-axis **(e)**. Further structural details are described in Chapter I (1.3.2).

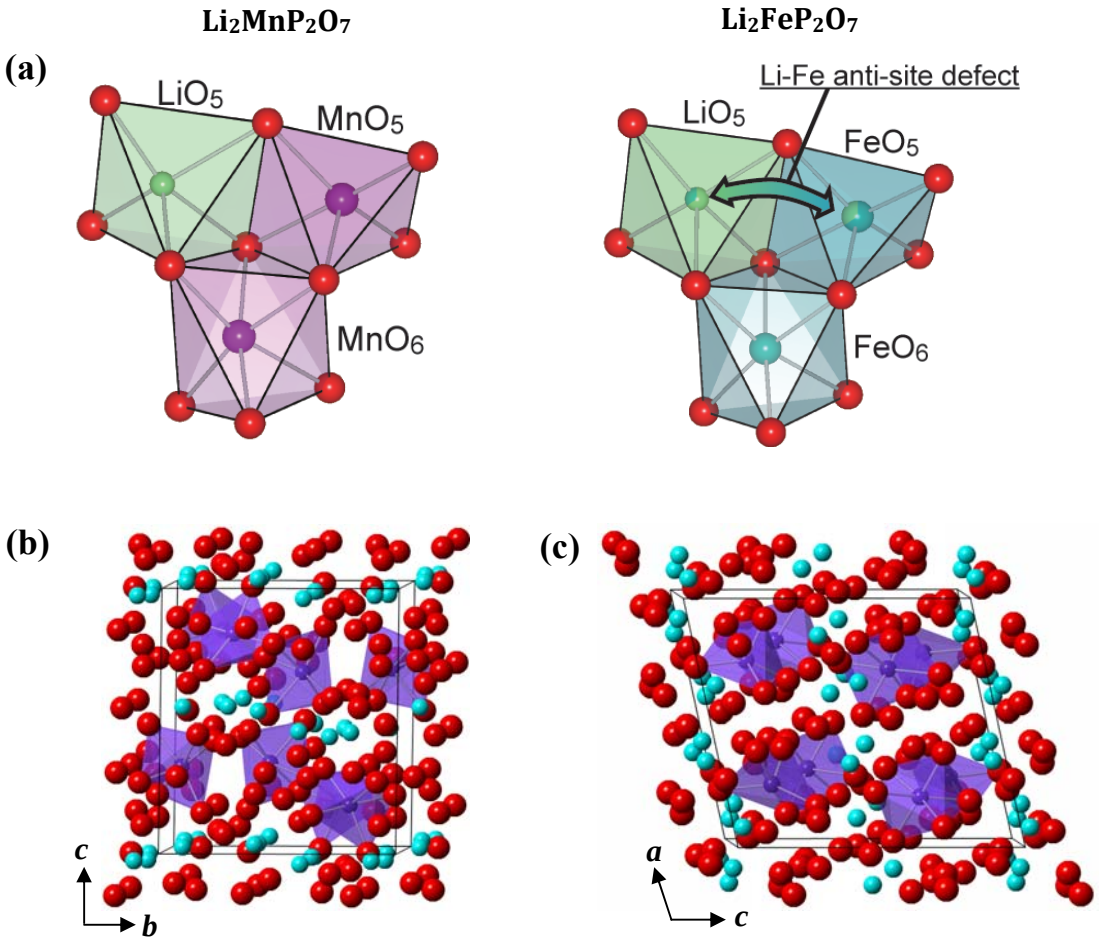

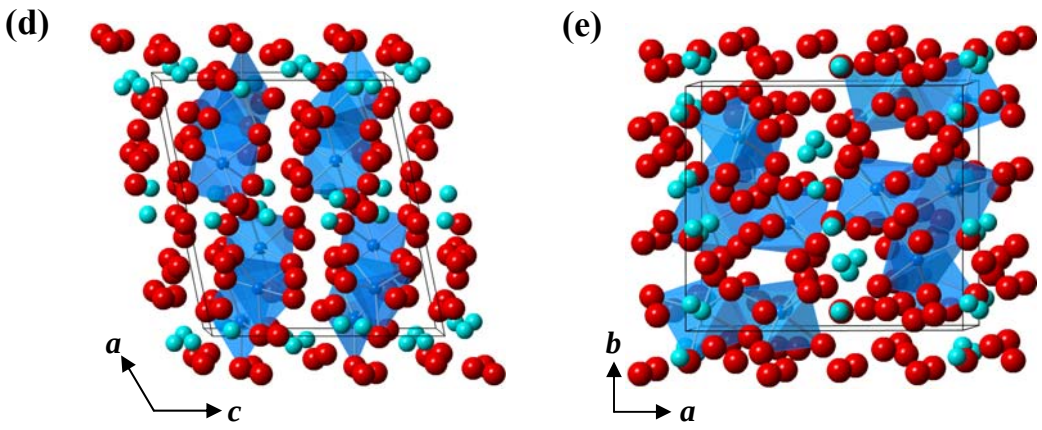

Figure 3-6 Local crystal structure of $Li_2MP_2O_7$ (M=Mn and Fe) in *ac* plane (a); M=Mn: projected along the (b) *a*-axis, (c) *b*-axis, and M=Fe: along the (d) *b*-axis and (e) *c*-axis. Purple polyhedra are edge-sharing Mn_2O_9 units, blue ones are edge-sharing FeO_6 + FeO_5/LiO_5 units; Blue and red spheres indicate Li and O atoms.

Lithium multi-transition pyrophosphate, i.e. $Li_2Fe_{1/3}Mn_{1/3}Co_{1/3}P_2O_7$, was prepared by solid-state reaction at 700°C for 12 h in N_2 gas. The XRD pattern was similar to that of simulated $Li_2FeP_2O_7$ with a = 11.041(6) Å, b = 9.757(4) Å, c = 9.818(6) Å, β = 102.05(4)°, V = 1034.3(6) Å^3, as shown in **Fig. 3-7**. The lattice parameters are comparable to the average values of $Li_2FeP_2O_7$, $Li_2MnP_2O_7$, and $Li_2CoP_2O_7$, indicating all three components are likely present homogeneously, with no phase segregation. Lattice parameters and unit cell volumes of $Li_2MP_2O_7$ (M=Fe, Mn, Co, $Fe_{1/3}Mn_{1/3}Co_{1/3}$) are illustrated in **Fig. 3-8**. The reported lattice parameters for different $Li_2MP_2O_7$ compounds are summarised in **Table 3-2**. Indexed summaries of the $Li_2MP_2O_7$ (M=Fe, Mn, Co) XRD reflections together with their corresponding powder patterns are given in **Tables A3-1~3-3** and **Figs. A3-1~3-2**. The M=Mg, Cu unit cells, however, are different from that of M=Fe, Mn, Co. This is because $Li_2MgP_2O_7$ and $Li_2CuP_2O_7$ phase have quite different X-ray powder diffraction patterns; probably they have a different structure. The patterns of $Li_2MgP_2O_7$ and $Li_2CuP_2O_7$ were indexed in a monoclinic unit cell with space group $P2_1/n$ (13) and $C2/c$ (14), respectively.

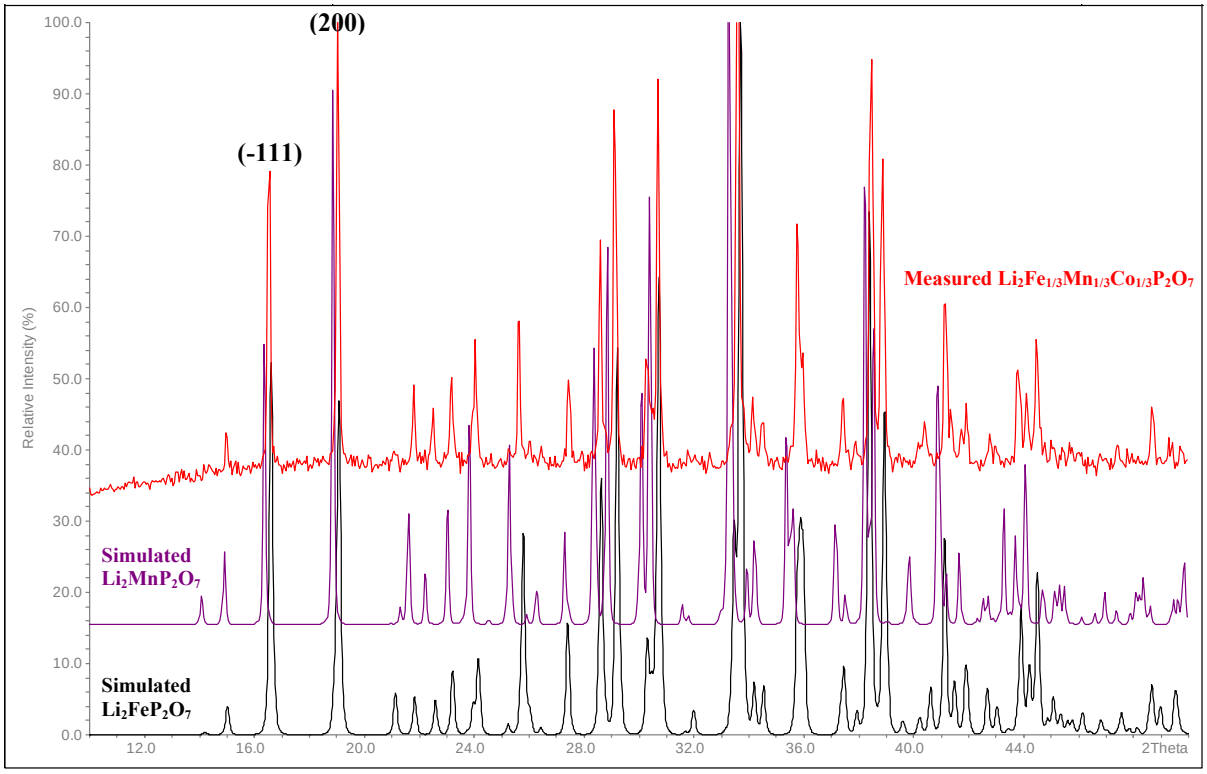

Figure 3-7 XRD patterns (Co radiation) of measured $Li_2Fe_{1/3}Mn_{1/3}Co_{1/3}P_2O_7$ (red) and simulated $Li_2MnP_2O_7$ (purple) drawn from ref. [7] and $Li_2FeP_2O_7$ (black).

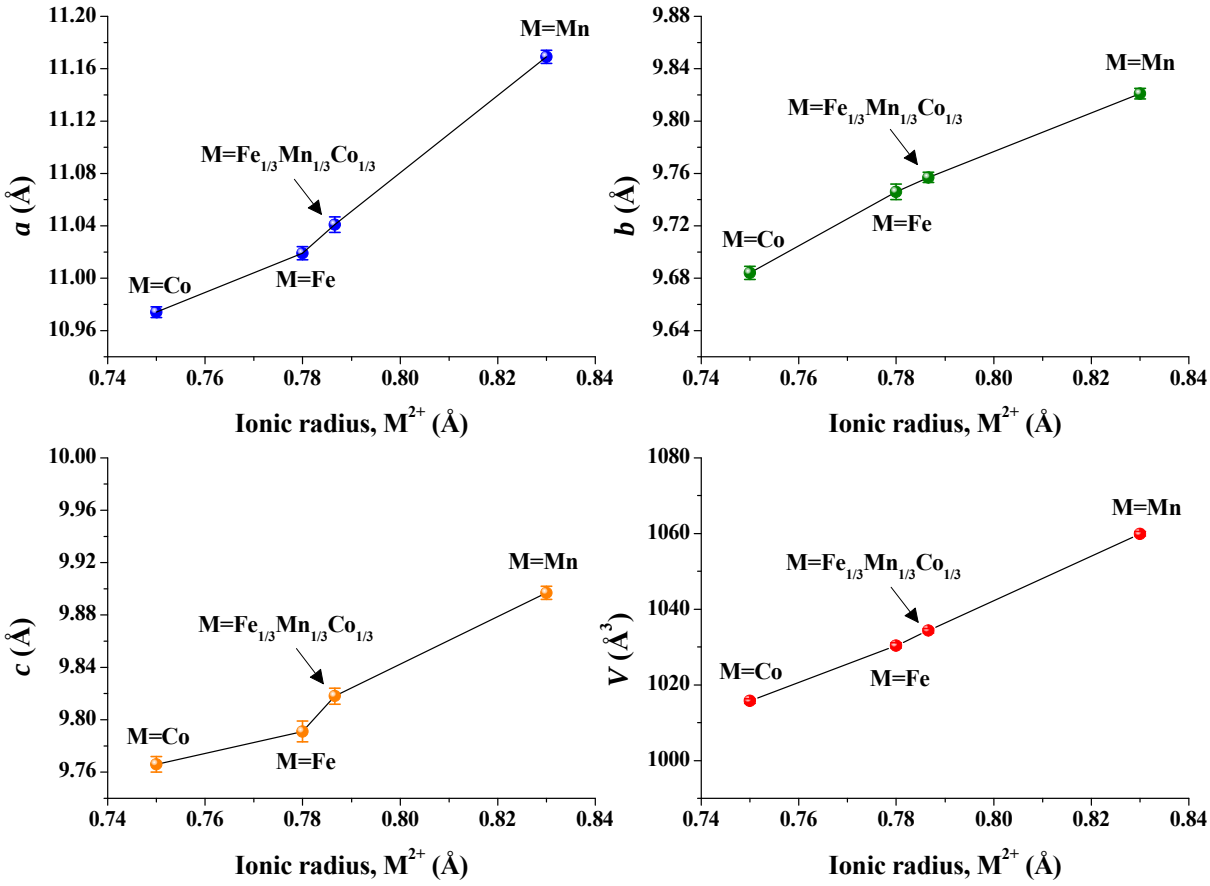

Figure 3-8 Unit cell parameters of $Li_2MP_2O_7$ (M=Fe, Mn, Co, $Fe_{1/3}Mn_{1/3}Co_{1/3}$) against the standard octahedral ionic radiṅ of the divalent M cations [12].

Table 3-2 Reported lattice parameters for lithium pyrophosphate $Li_2MP_2O_7$ compounds with monoclinic symmetry.

References	Chemical formula	*a* parameter (Å)	*b* parameter (Å)	*c* parameter (Å)	*β* (deg)	*Volume* (Å^3)
PDF card 00-048-0573 [13]	$Li_2MgP_2O_7$	12.410	6.270	9.690	104.75	729.14
PDF card 04-016-0327 [14]	$Li_2CuP_2O_7$	15.3360(14)	4.8733(13)	8.6259(16)	114.795(10)	585.24
Laure Adam *et al* [7]	$Li_2MnP_2O_7$	9.9158(6)	9.8289(6)	11.1800(4)	102.466(5)	1063.9(1)
Shin-ichi Nishimura *et al* [8]	$Li_2FeP_2O_7$	11.01847(4)	9.75536(3)	9.80517(3)	101.5416(2)	1033.01
Hui Zhou *et al* [9]	$Li_2FeP_2O_7$ $Li_2MnP_2O_7$ $Li_2Mn_{0.8}Fe_{0.2}P_2O_7$ $Li_2Mn_{0.5}Fe_{0.5}P_2O_7$ $Li_2Mn_{0.2}Fe_{0.8}P_2O_7$ $Li_2Mn_{0.1}Fe_{0.9}P_2O_7$	9.7997(5) 9.8941(6) 9.8879(4) 9.8768(2) 9.8712(7) 9.8267(5)	9.7488(8) 9.8111(1) 9.8129(4) 9.8085(1) 9.8124(6) 9.7693(5)	11.0123(6) 11.1597(8) 11.1368(2) 11.1038(0) 11.0898(2) 11.0389(3)	101.516 102.482 102.348 102.111 101.799 101.681	1030.907 1057.705 1055.608 1051.759 1051.480 1037.801
Hyungsub Kim *et al* [10]	$Li_{2-x}FeP_2O_7$ $Li_{2-x}CoP_2O_7$	11.0224(4) 10.9603(3)	9.7541(3) 9.6957(2)	9.8080(3) 9.7641(2)	101.564(2) 101.784(1)	1033.083 1015.740
Naoya Furuta *et al* [15]	$Li_2FeP_2O_7$ $Li_2(Fe_{0.75}Mn_{0.25})P_2O_7$ $Li_2(Fe_{0.50}Mn_{0.50})P_2O_7$ $Li_2(Fe_{0.25}Mn_{0.75})P_2O_7$ $Li_2MnP_2O_7$	11.0262(3) 11.0528(2) 11.0849(3) 11.1232(2) 11.1584(2)	9.7558(2) 9.7739(2) 9.7879(2) 9.8034(2) 9.8116(1)	9.8128(2) 9.8361(2) 9.8586(2) 9.8798(1) 9.8948(1)	101.5666(13) 101.8770(15) 102.1290(17) 102.3383(15) 102.4802(13)	1034.12(4) 1039.84(4) 1045.76(4) 1052.47(4) 1057.71(3)
This Study	$Li_2MnP_2O_7$ $Li_2FeP_2O_7$ $Li_2CoP_2O_7$	11.169(5) 11.019(5) 10.974(4)	9.821(4) 9.746(6) 9.684(5)	9.897(5) 9.791(8) 9.766(6)	102.49(4) 101.49(5) 101.87(4)	1059.9(6) 1030.4(7) 1015.7(6)

(ii) $Li_2Fe_{1-x}Mn_xP_2O_7$: $0 \le x \le 1$

The XRD patterns of $Li_2Fe_{1-x}Mn_xP_2O_7$ synthesised at 700°C for 12 h in N_2 gas are presented in **Fig. 3-9(a)**. In general, the similar intensity distribution of XRD patterns indicates the probable existence of a complete solid solution between $Li_2FeP_2O_7$ and $Li_2MnP_2O_7$. All samples are single phase with monoclinic symmetry and were indexed on space group $P2_1/c$. The enlarged peaks present a shift toward lower 2θ values in the positions of the (-111) and (200) reflections, indicating increases of lattice parameters and unit cell volume, **Fig. 3-9(b)**. Moreover, there is a clearer splitting of the (222) and $(13\bar{2})$ peaks as x goes from 1 to 0, caused by the difference in unit cell parameters. Since Fe^{2+} and Mn^{2+} are almost isoelectronic, the intensities of some diffraction peaks from x=0 to x=1 (arrowed) varied which must be due to a different cation distribution in the two structures [8]. In particular, the intensity of (-111) peak decreased significantly with increasing x. **Fig. 3-10** compares the relative intensity ratio, I(-111)/I(200), in $Li_2Fe_{1-x}Mn_xP_2O_7$; it decreased linearly from 1.158 to 0.317 as x increased from 0 to 1.

The variations of lattice parameters and unit cell volume as a function of x are illustrated in **Fig. 3-11(a)**; the data look like a solid solution for all x, and *a*, *b* and *c* increase from x=0 to x=1. Zhou *et al.*'s data, however, indicate partial solid solutions only form, showing a minimal change in lattice parameter "*b*" but sharp change in all other parameters with increasing Fe content from 80 to 100 %, see black circles [9]. The lattice parameters and unit cell volumes of $Li_2Fe_{1-x}Mn_xP_2O_7$ synthesised by solid-state method are summarised in **Table A3-4**, and these values are identical to those of previous reports from the Yamada group [15].

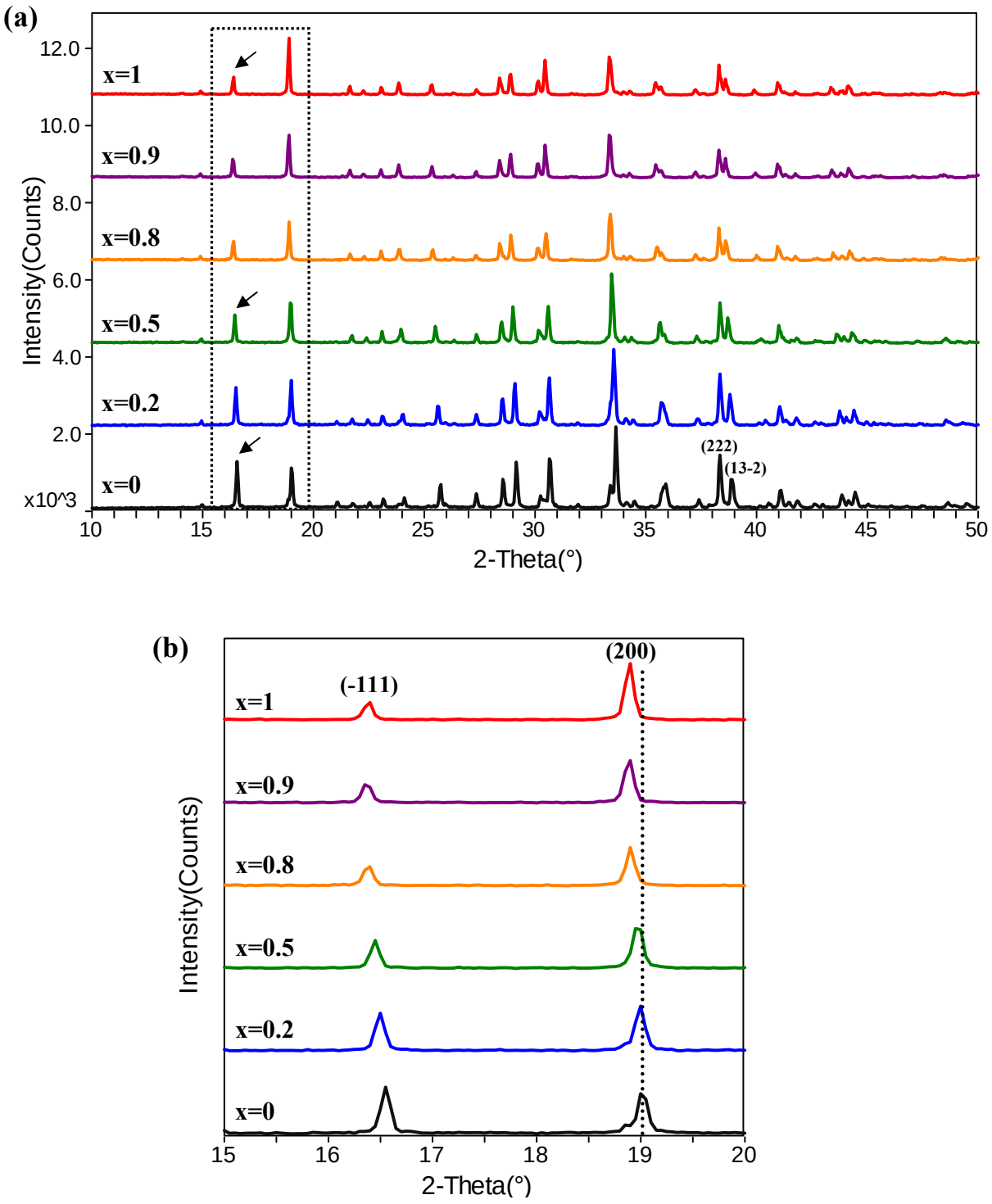

Figure 3-9 XRD patterns of $Li_2Fe_{1-x}Mn_xP_2O_7$ solid solution with continuous 2θ shift to low angle.

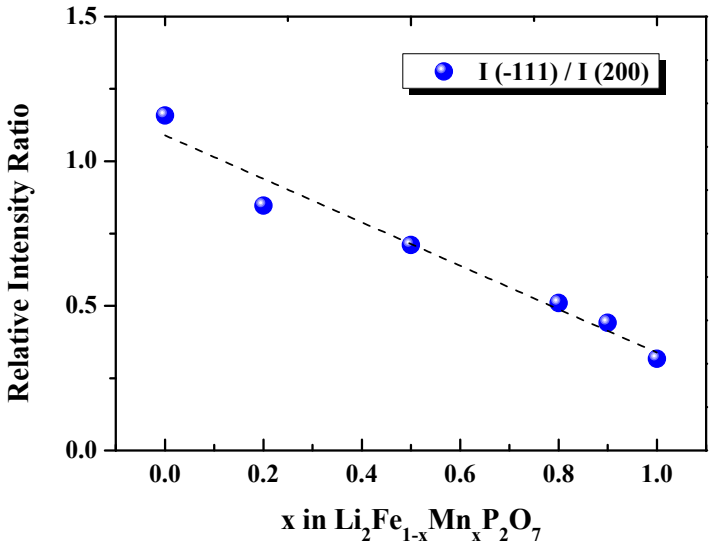

Figure 3-10 Relative intensity ratio, I(-111)/I(200), in $Li_2Fe_{1-x}Mn_xP_2O_7$ (x=0−1).

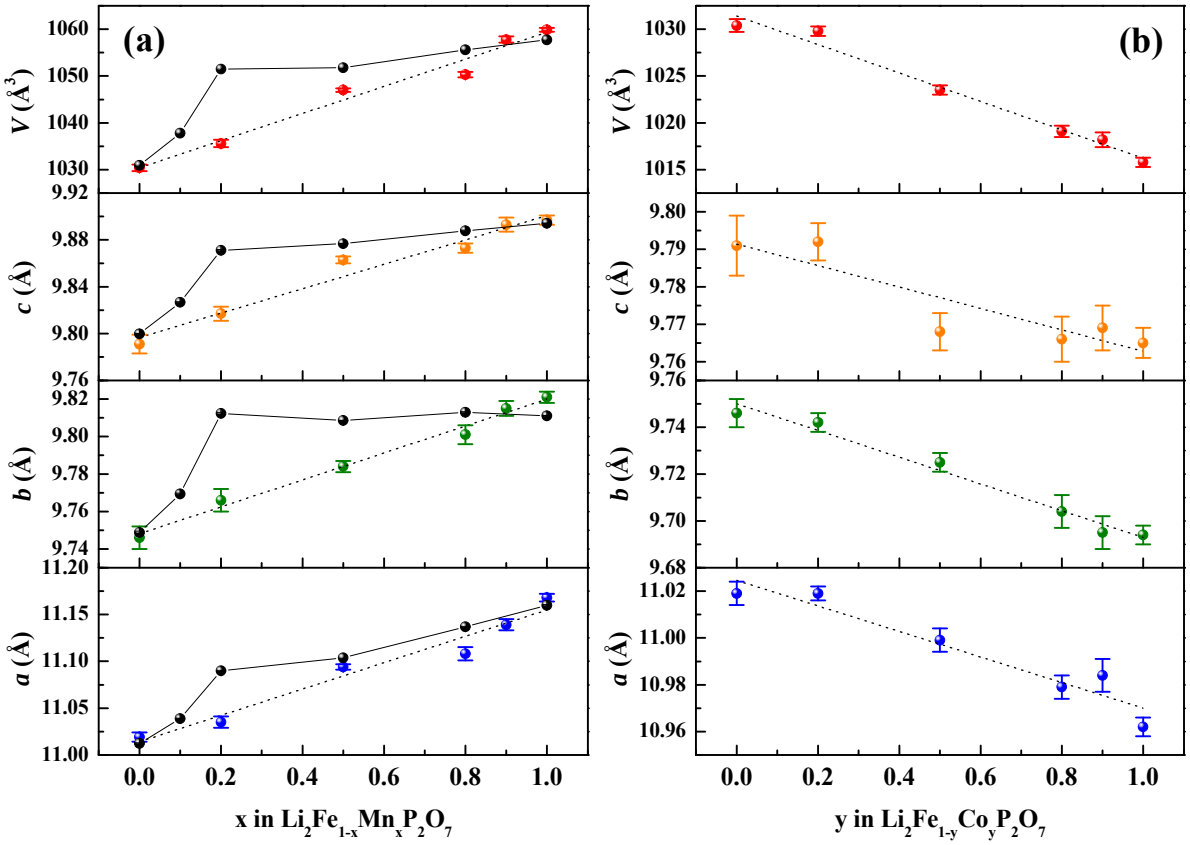

Figure 3-11 Lattice parameters of $Li_2Fe_{1-x}Mn_xP_2O_7$ (a) and $Li_2Fe_{1-y}Co_yP_2O_7$ (b) as a function of Mn and Co content x and y. Black data points in (a) are taken from Ref. 9.

(iii) $Li_2Fe_{1-y}Co_yP_2O_7$: $0 \le y \le 1$

XRD patterns show the $Li_2Fe_{1-y}Co_yP_2O_7$ compositions synthesised at 700°C for 12 h in N_2 are a complete solid solution with assumed monoclinic symmetry and space group $P2_1/c$ between two end members, $Li_2FeP_2O_7$ and $Li_2CoP_2O_7$, see **Fig. 3-12**. The relative intensity ratio I(-111)/I(200) in $Li_2Fe_{1-y}Co_yP_2O_7$ was similar, but different from that of $Li_2Fe_{1-x}Mn_xP_2O_7$, **Fig. 3-13**. The Fe- and Co-based lithium pyrophosphates have a partial exchange between the MO_5 and LiO_5 (M=Fe/Co) pyramid sites by ~ 30% [10]. The degree of site exchange can be evaluated by the intensity ratio between the (-111) and (200) XRD peaks at around 15° (Co Kα); the higher the intensity ratio of I(-111)/I(200), the higher the degree of site exchange [10]. $Li_2CoP_2O_7$ has lattice parameters close to those reported for $Li_{2-x}CoP_2O_7$ with a = 10.9603(3) Å, b = 9.6957(2) Å, c = 9.7641(2) Å, β = 101.784(1)°, V = 1015.740 Å^3 [10]. **Fig. 3-11(b)** shows variation of the lattice parameters of $Li_2Fe_{1-y}Co_yP_2O_7$ with y; the data look like a solid solution for all y. The unit cell parameters and V decrease gradually with y, attributable to the smaller ionic size of Co.

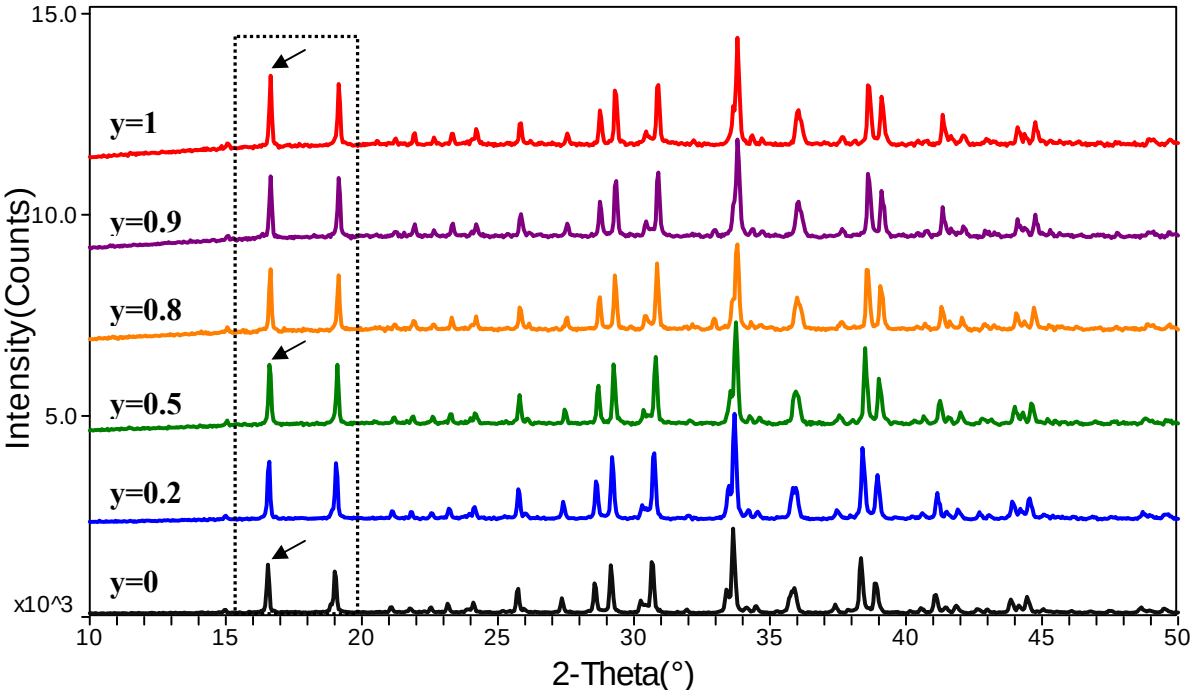

Figure 3-12 XRD patterns of $Li_2Fe_{1-y}Co_yP_2O_7$ solid solution showing continuous 2θ shift to high angle.

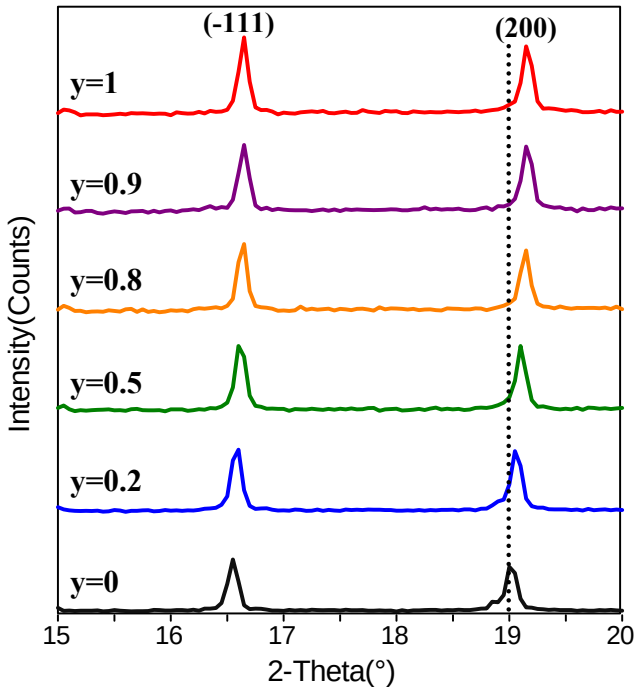

Figure 3-12 (Continued)

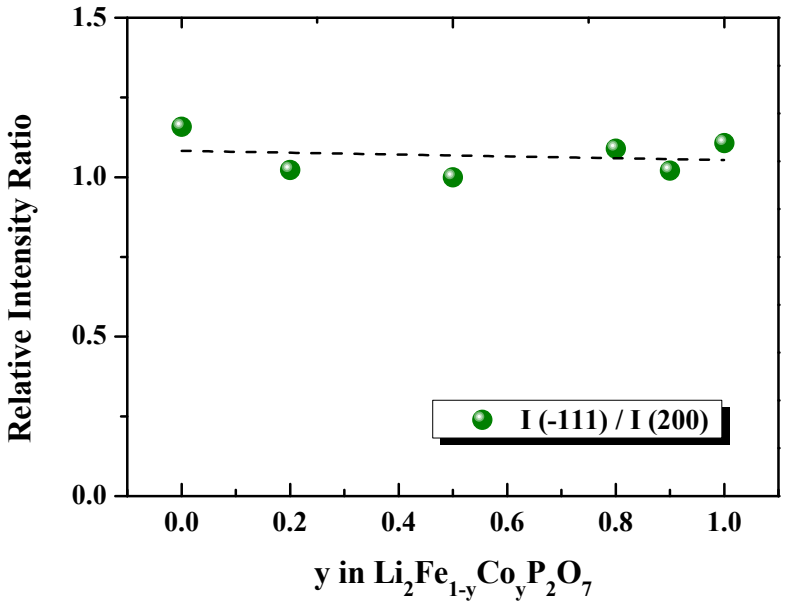

Figure 3-13 Relative intensity ratio, I(-111)/I(200), in $Li_2Fe_{1-y}Co_yP_2O_7$ (y=0−1).

3.3.2 Morphology

SEM was used to evaluate the morphology and densification of the sintered samples. **Fig. 3-14** shows the cross-section SEM images of the $Li_2MP_2O_7$ (M=Fe, Mn, Co, $Fe_{1/3}Mn_{1/3}Co_{1/3}$) pellets sintered at 700°C for 12 h under N_2 atmosphere. Most of the particles have shapes of aggregated spheres and an average particle size of less than 10 μm for M=Fe and $Fe_{1/3}Mn_{1/3}Co_{1/3}$, and of larger than 10 μm for M=Mn and Co. SEM shows all four samples have a porous microstructure, and the measured density of $Li_2FeP_2O_7$, $Li_2MnP_2O_7$, $Li_2CoP_2O_7$ and $Li_2Fe_{1/3}Mn_{1/3}Co_{1/3}P_2O_7$ is 2.629 g/cm^3, 2.646 g/cm^3, 2.866 g/cm^3, and 2.724 g/cm^3, respectively, consistent with a final density ~ 84%, 87%, 89%, and 87% of the theoretical X-ray value, see **Table 3-3**.

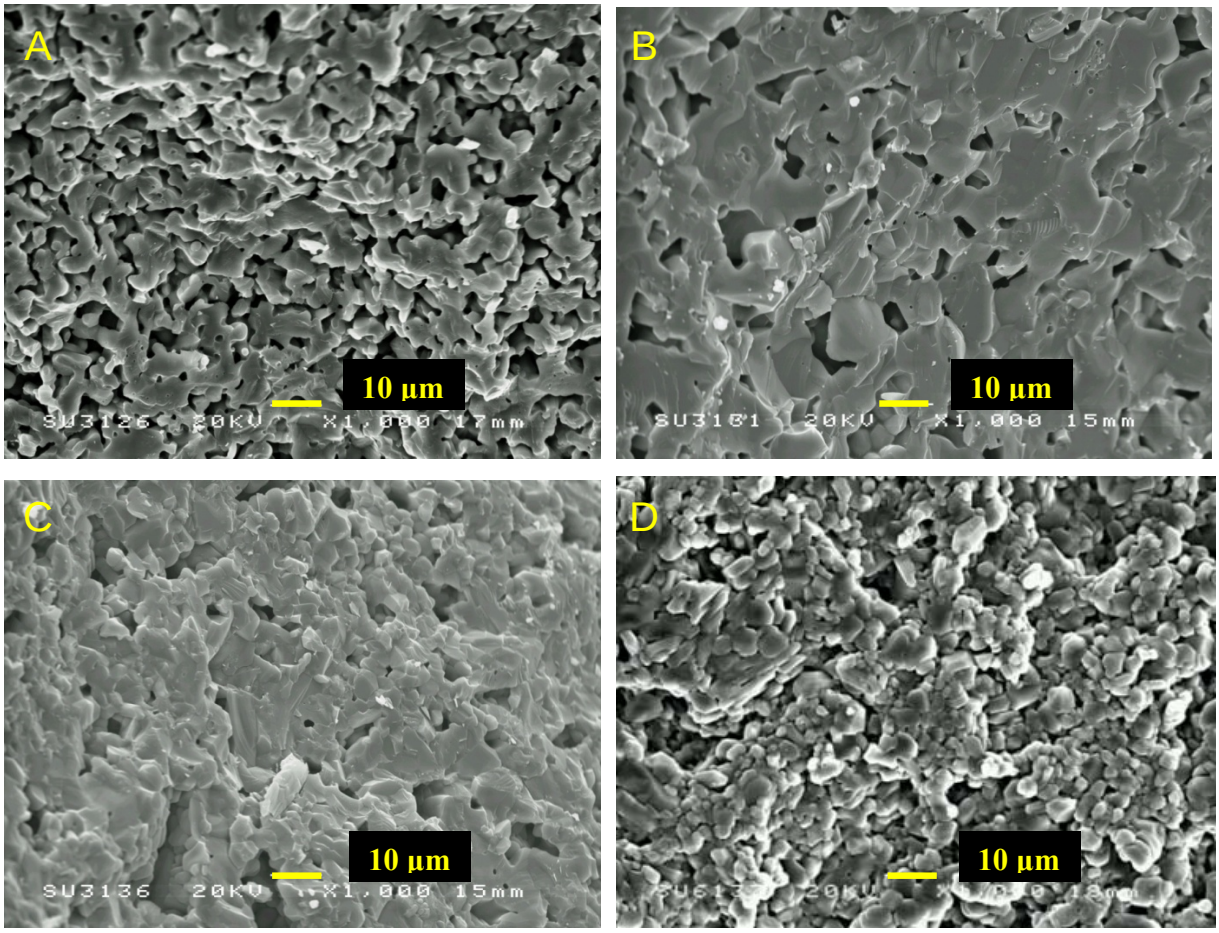

Figure 3-14 SEM pictures of cross section of the sintered (a) $Li_2FeP_2O_7$, (b) $Li_2MnP_2O_7$, (c) $Li_2CoP_2O_7$ and (d) $Li_2Fe_{1/3}Mn_{1/3}Co_{1/3}P_2O_7$ pellets.

Table 3-3 Theoretical, measured and relative density of $Li_2MP_2O_7$ (M=Fe, Mn, Co, $Fe_{1/3}Mn_{1/3}Co_{1/3}$) pellets.

Materials	X-ray Density (g/cm^3)	Measured Density (g/cm^3)	Relative Density (%)
$Li_2FeP_2O_7$	3.141	2.629	83.7
$Li_2MnP_2O_7$	3.042	2.646	86.9
$Li_2CoP_2O_7$	3.226	2.866	88.8
$Li_2Fe_{1/3}Mn_{1/3}Co_{1/3}P_2O_7$	3.138	2.724	86.8

3.3.3 Chemical Composition

The chemical compositions of the as-produced $Li_2Fe_{1/3}Mn_{1/3}Co_{1/3}P_2O_7$ powders were determined by elemental analysis from energy dispersive X-ray spectra (EDS), as illustrated in **Fig. 3-15(a)**. Inset shows the average calculated atomic percentage of each element. The EDS spectra reveal that the stoichiometric ratio of ($Fe_{1/3}Mn_{1/3}Co_{1/3}$):P analysed from the average of 10 distinct points in **(b)** is 0.48(4):1, which is close to the expected value of 0.5:1 within errors. This may indicate homogeneous mixing of the three transition metals. Note that the value of oxygen is not measured directly but could be calculated by element differences. It is not possible to analyse Li because of the limited detection capability for Li element with lower energy X-rays.

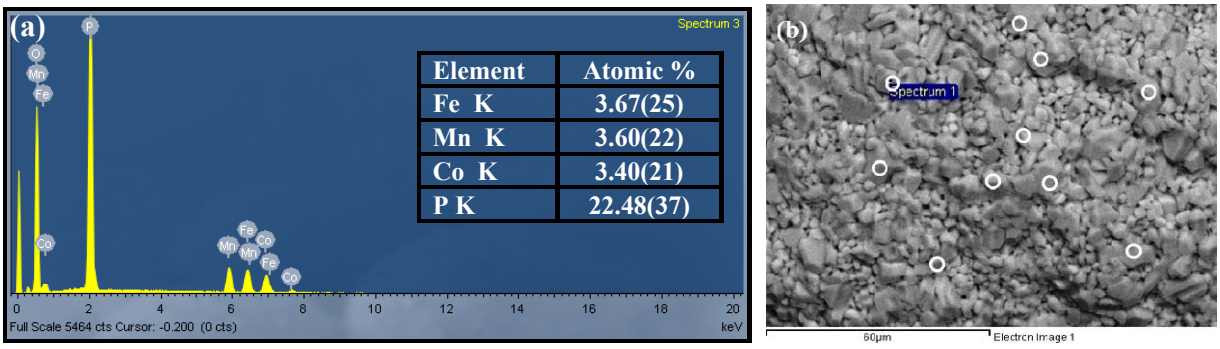

Figure 3-15 EDS spectra (a) and EBSD image (b) of $Li_2Fe_{1/3}Mn_{1/3}Co_{1/3}P_2O_7$ powders.

3.3.4 Electrical Properties

(i) $Li_2FeP_2O_7$

Impedance complex plane, Z* plots, **Fig. 3-16**, show the total resistivity of pure-phase $Li_2FeP_2O_7$ pellet with sputtered-Pt electrodes at different measuring temperatures. Specifically, at T=200°C **(b)**, a nearly ideal semicircle is found with associated capacitance of C_1 ~4.5 $pFcm^{-1}$ and of C_2 ~1.0 μFcm^{-1}, calculated from $\omega RC=1$ at the first and second semicircle maximum, respectively. Low frequency data at all temperatures show a well-resolved second arc but no evidence for a Warburg impedance or inclined spike that could result from the (partial) blockage of ionic species at the sample-electrode interface **(d, e, f)**. Further discussion of the possible origins of R_2 will be described in the next section.

The parallel capacitance (C_p) of the bulk response as a function of frequency over the temperature range 150°C to 400°C can be observed from **Fig. 3-17(a)**, in which a capacitance plateau at higher frequency is ~5.0 $pFcm^{-1}$ (arrowed). As the temperature increases, the data show a very broad dispersion, probably following a power law at intermediate frequencies, and in addition, the capacitance at lower frequencies increases up to an approximate value of ~10^{-5} Fcm^{-1} and is therefore associated with the sample-electrode interfacial response.

Conductivity, Y', data as a function of frequency are shown in **Fig. 3-17(b)** for the same temperature range as in **Fig. 3-17(a)**. The Y' data show a dispersion at high frequencies and present a nearly frequency-independent *dc* conductivity plateau at intermediate frequencies. At T > 300°C, Y' spectra present a frequency-independent *dc* conductivity plateau.

Combined Z''/M'' spectra at 250°C in N_2 show Z'' and M'' peaks at similar frequency, **Fig. 3-18**. The peak maxima coincide, which indicates the sample is electrically homogeneous. The full width at half maximum (FWHM) of the Z'' peak is ~1.16 decades, which is close to the ideal value of 1.14 decades. A broad low-frequency arc in the Z'' peak, which is also seen in the Z* plots, may be associated with an electrode effect.

The conductivity data for $Li_2FeP_2O_7$ pellet are presented in **Fig. 3-19**. The activation energy was calculated using the Arrhenius Equation 3.4:

$$\sigma = A \exp(-E_a / RT) \quad (3.4)$$

, where conductivity, σ=1/R, was obtained from impedance data, E_a is the activation energy, A is the pre-exponential factor, and R is the gas constant [16]. Note that an Arrhenius plot, ln σ (i.e. ln 1/R) against 1000/T (in Kelvin), can be constructed to give a straight line of slope $-E_a/R$ and therefore, the activation energy value of E_a was obtained from Eqn. 3.4. The data for R_1^{-1} and R_2^{-1} show a linear response with activation energy 0.63±0.02 and 0.68±0.03 eV, respectively.

Fig. 3-20(a) compares the complex impedance spectra of sputtered-Au $Li_2FeP_2O_7$ measured at various temperatures so as to gain an insight into the effect of electrode material on the second semicircle at low frequencies. An obvious low frequency depressed semicircle is still observed similar to those results obtained using Pt electrodes. Specifically, no spike attributed to ionic conduction behavior, i.e. Li^+, was observed as the temperature increased to 350°C. The high frequency arc is related to the electronic and/or ionic migration in the bulk of the ceramics with a capacitance of $\sim 5\times10^{-12}$ Fcm^{-1}, **Fig. 3-20(b)**. The calculated bulk activation energy of $Li_2FeP_2O_7$ is 0.613±0.008 eV (not shown) for sputtered Au, which is consistent with previous value in **Fig. 3-19** within errors.

The effect of *dc* bias with 1 V potential on the impedance results at 400°C in N_2 using Pt electrodes is shown in **Fig. 3-21**. The resistance of the high frequency arc, R_1, slightly decreased **(a)** but its capacitance **(b)** and admittance **(c)** did not change with the applied *dc* bias. In addition, the response of low frequency arc stayed unchanged with *dc* bias. On removal of the *dc* bias, however, the resistance of R_1 continued decreasing to a lower value.

The effect of atmosphere at measuring temperature of 400°C without a *dc* bias is shown in **Fig. 3-22**. The value of R_1 **(a)** in air, after 6 h, is slightly lower than that in N_2, probably due to the sample's partial oxidation (Fe^{2+}/Fe^{3+}) or decomposition. Further studies are necessary to clarify this point. Moreover, the capacitance **(b)** does not show big difference, but a small increased conductivity **(c)** is observed in air.

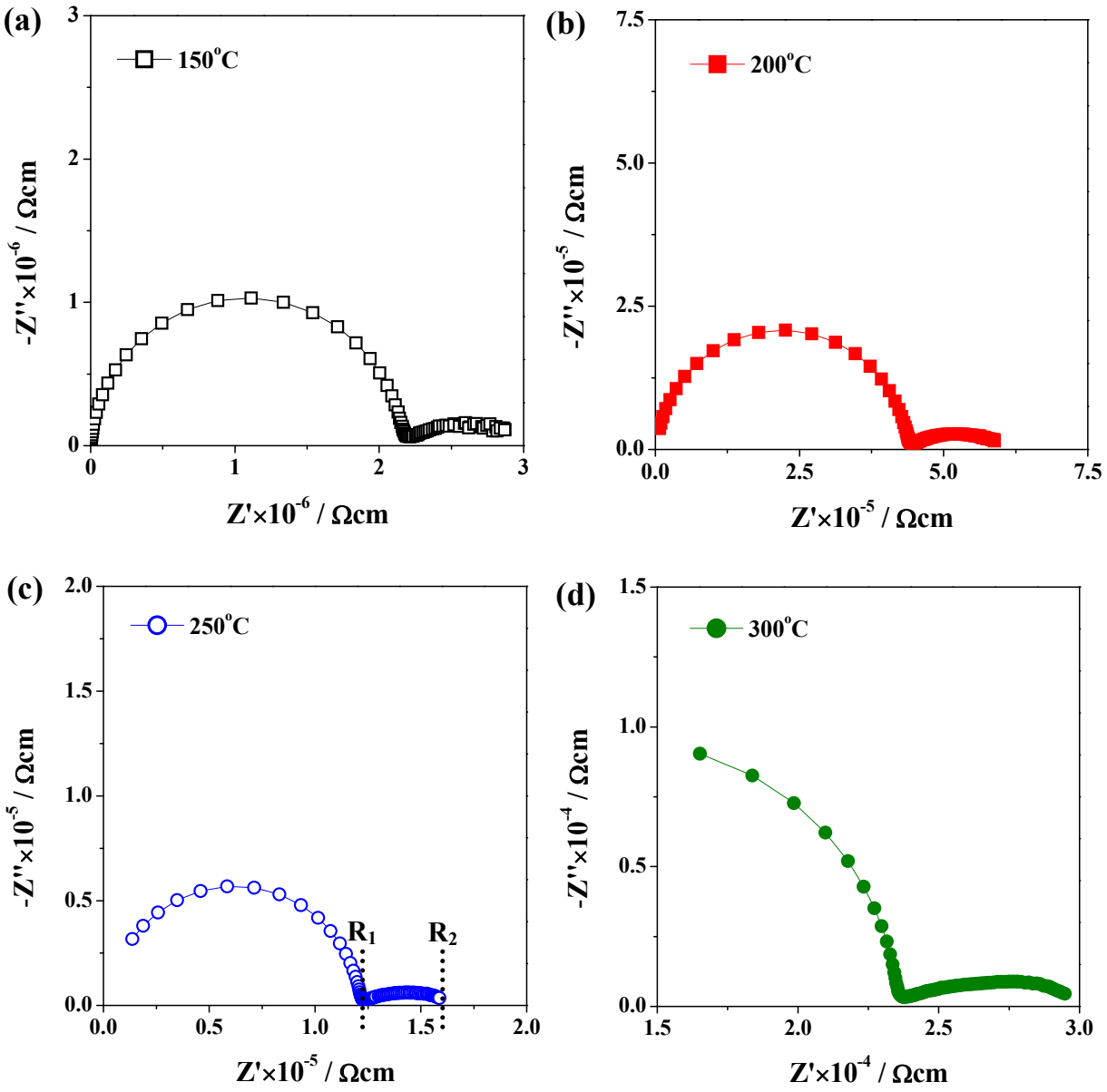

Figure 3-16 $Li_2FeP_2O_7$: Impedance complex plane plots, Z*, at (a) 150°C to (f) 400°C in N_2.

(continued on next page)

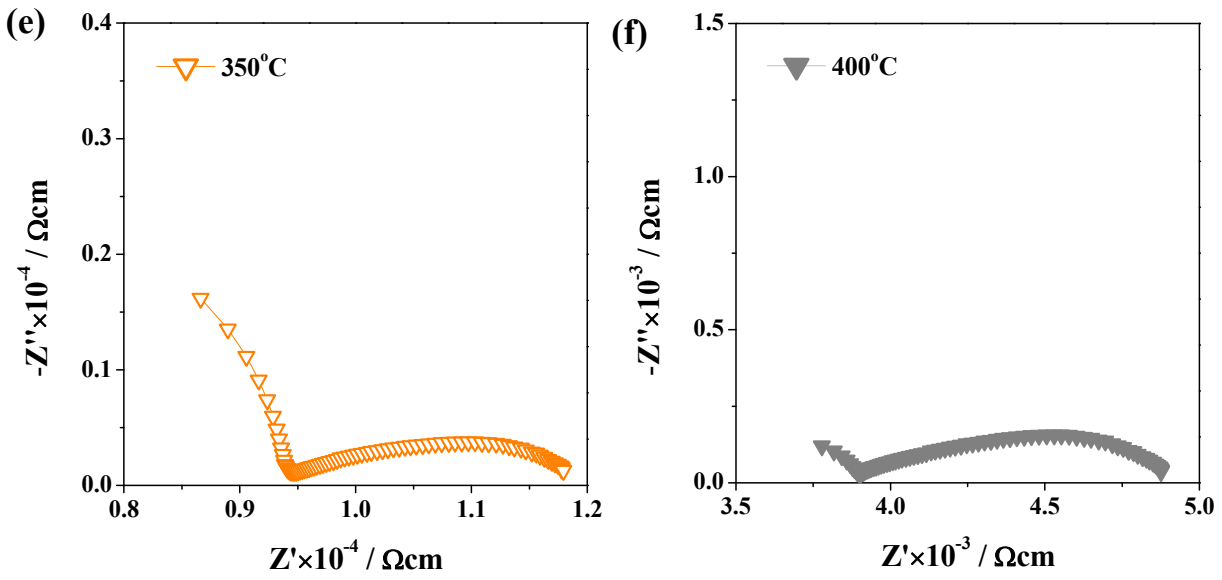

Figure 3-16 (continued)

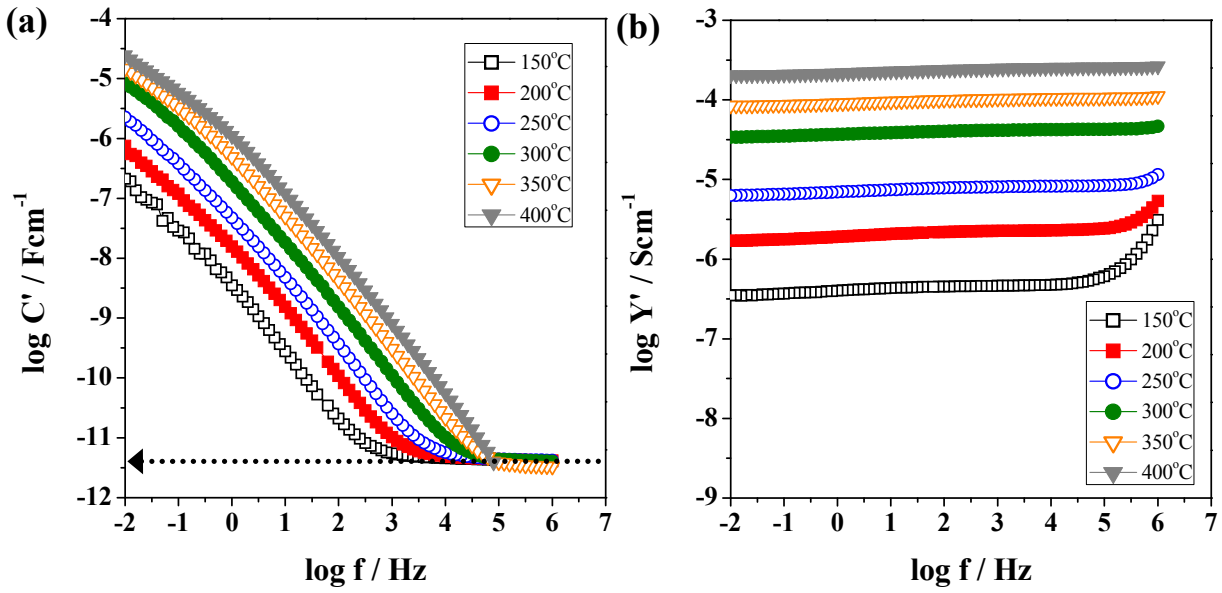

Figure 3-17 $Li_2FeP_2O_7$: spectroscopic plots of (a) capacitance, C' and (b) admittance, Y', at temperatures of 150°C to 400°C.

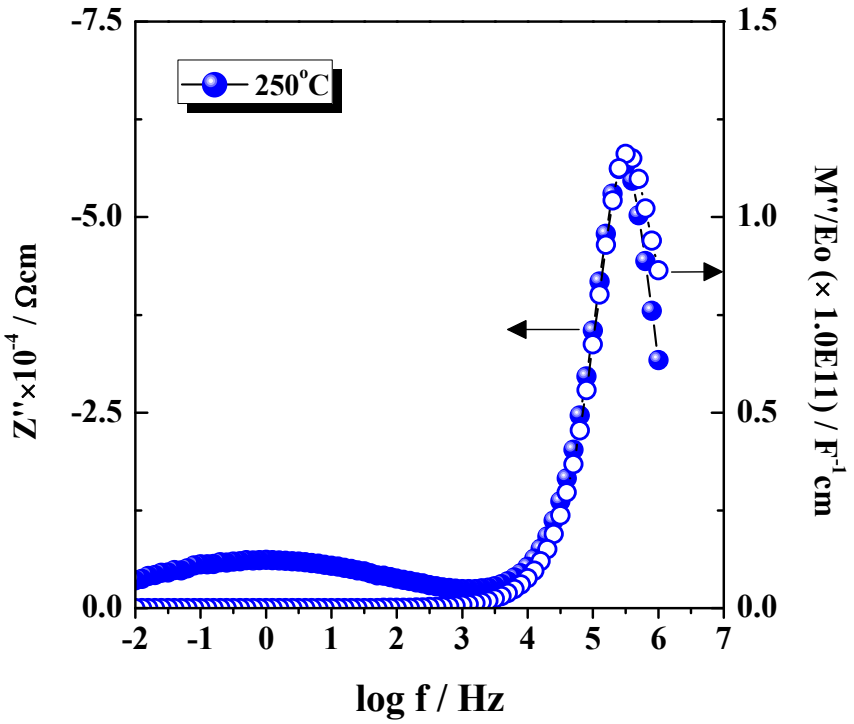

Figure 3-18 Z''/M'' spectroscopic plots for $Li_2FeP_2O_7$ at 250°C in N_2.

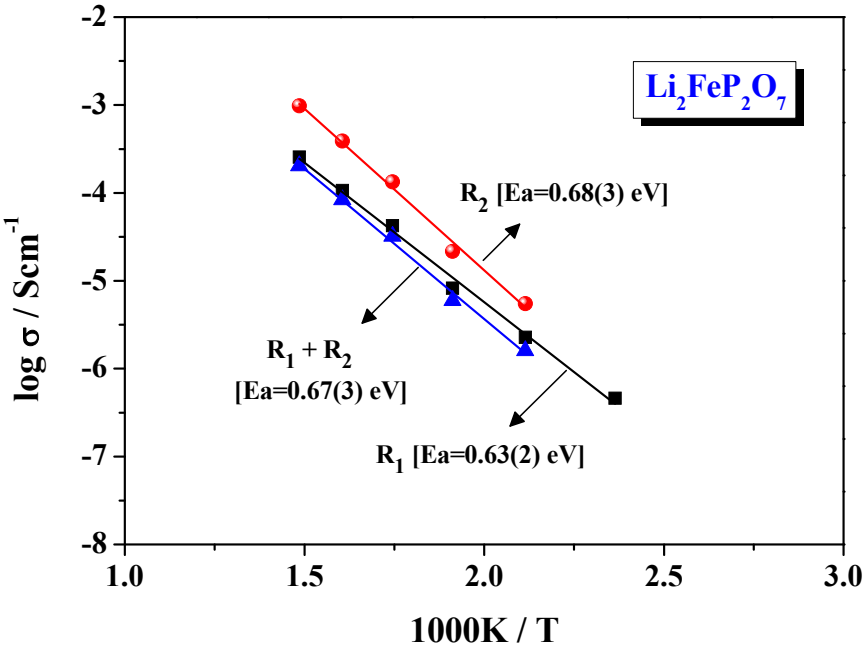

Figure 3-19 Arrhenius plots of R_1^{-1}, R_2^{-1}, and total conductivity in N_2 for $Li_2FeP_2O_7$ with sputtered-Pt electrodes.

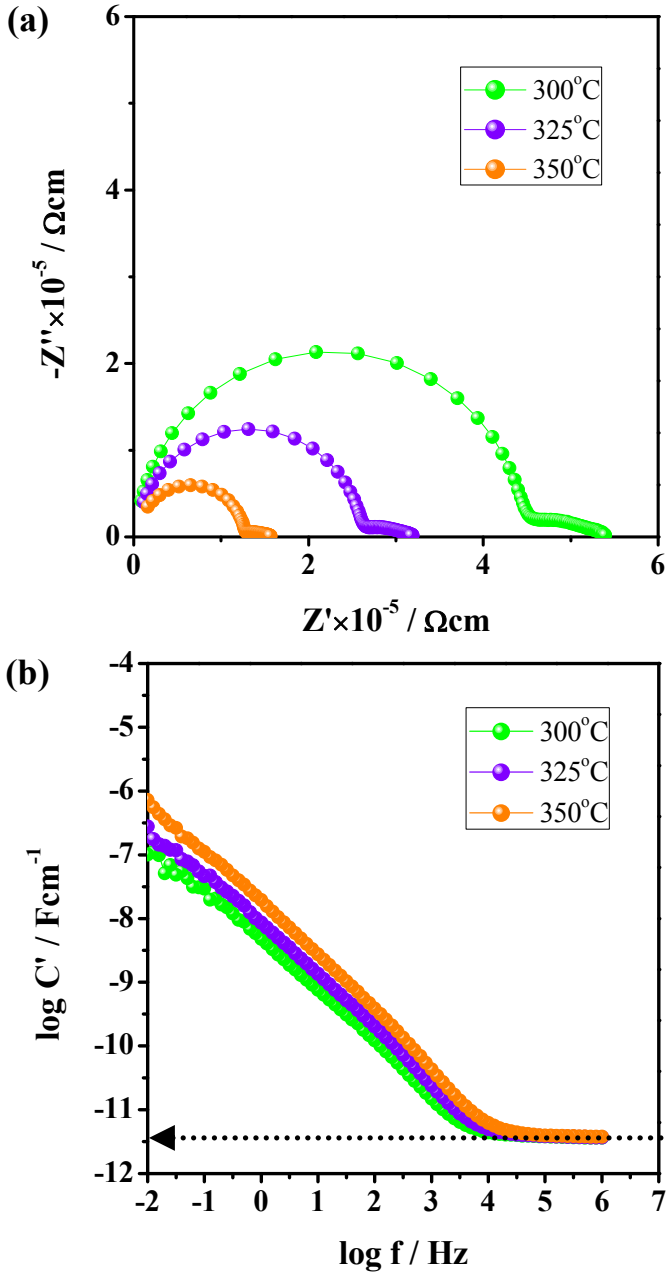

Figure 3-20 (a) Complex resistivity plots, Z*, and (b) capacitance plots, C', measured at 300~350 °C in N_2 for $Li_2FeP_2O_7$ pellet with sputtered-Au electrodes.

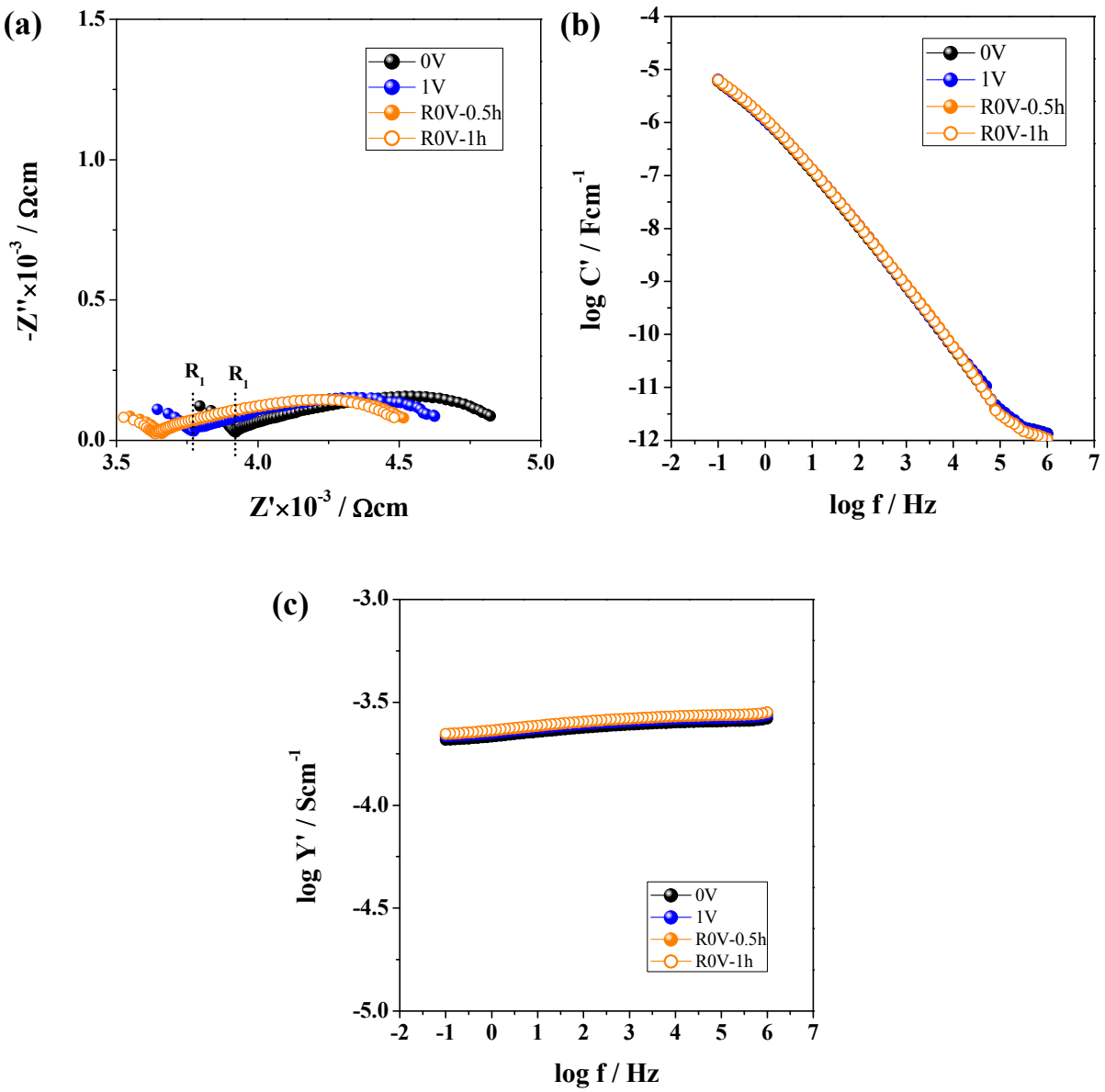

Figure 3-21 (a) Impedance complex plane plots, Z*; (b) spectroscopic plots of capacitance, C'; (c) spectroscopic plots of admittance, Y', at a measuring temperature of 400°C with different *dc* bias of 0 and 1 V in N_2.

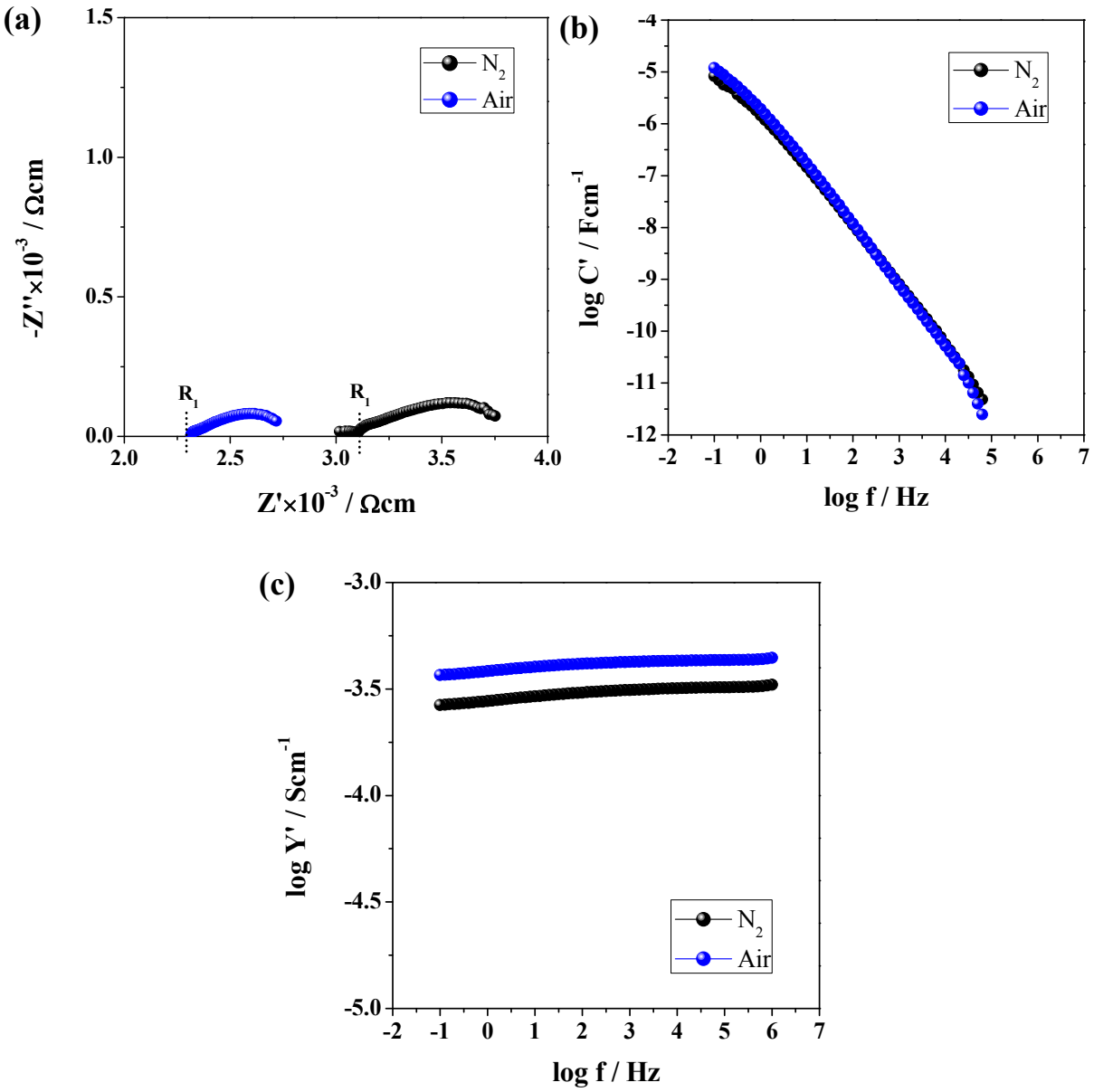

Figure 3-22 (a) Impedance complex plane plot, Z*; (b) spectroscopic plots of capacitance, C'; (c) spectroscopic plots of admittance, Y', for $Li_2FeP_2O_7$ in various atmospheres at 400°C without *dc* bias.

(ii) $Li_2MnP_2O_7$

Impedance complex plane, Z* plots, are shown in **Fig. 3-23**, for $Li_2MnP_2O_7$ with sputtered Pt electrodes at different temperatures from 150°C to 400°C in N_2. There are two distorted semicircles and low frequency dispersions at low temperatures, as shown in **(a, b)**. At higher temperature of 250°C, the Z* plot shows a high-frequency arc of resistance (R_1), an intermediate-frequency arc of resistance (R_2), and a large low-frequency electrode spike, see **(c)**. At temperatures above ~ 300°C, the length of electrode spike at lower frequencies increases, but the slope, at ~ 60° **(d, e)**, becomes a Warburg, at 45° at the highest measuring temperature of 400°C, **(f)**.

The capacitance, C', data as a function of frequency at different temperatures can be observed from **Fig. 3-24(a)**. A plateau at high frequency is attributed to the bulk capacitance, ~5 $pFcm^{-1}$ (arrowed), and a dispersion at lower frequency is observed at 150°C. The capacitance C_2 associated with the R_2 response at lower frequency is partially resolved at temperatures above 250°C with a value in the range 10^{-8} to 10^{-9} Fcm^{-1}. Higher temperature IS measurement up to 400°C was carried out to show an approximately constant capacitance at low frequencies of ~ 10^{-5}–10^{-4} Fcm^{-1} which could be attributed to the sample-electrode interface and a double layer effect.

Conductivity, Y', data as a function of frequency are shown in **Fig. 3-24(b)**. At 150°C, the Y' plot presents two approximately frequency independent plateaus, first one below ~ 1 Hz and second one between ~ 10^3 and 10^4 Hz, and a high frequency dispersion, above ~ 10^5 Hz. As the temperature increases, the data at lower frequencies show a curvature to lower conductivity values attributed to the ionic blocking character consistent with the electrical double layer effect. In addition, the second low-frequency plateau shifts forward to higher frequencies, and the high-frequency dispersion out of the frequency window.

Fig. 3-25 shows the Arrhenius response with activation energy of R_2, 0.75(3) eV, which is higher than that of bulk (R_1), 0.64(1) eV, for $Li_2MnP_2O_7$. The total conductivity is limited by large R_2 resistances.

Typical impedance results at 400°C in N_2 with different *dc*-bias of 0, 1, 2, 3 V are shown in **Fig. 3-26**. A decreased slope of Warburg spike **(a)** and slightly increased

electrode capacitance **(b)** at low frequencies are observed applying *dc*-bias from 0 to 3 V. The responses of C' and Y' of bulk and grain boundary do not change with the applied *dc*-bias, **(c)**, however, an increase in conductivity at low frequencies is observed with *dc*-bias of above 1 V, and is fully reversible on removing the *dc*-bias, see orange line.

Lithium is able to form well-defined intermetallic phases (Li_xM) with various metals M (M=Pt, Ag, Au, etc.) at room temperature if the metal is polarized to a sufficiently negative potential (17). The so-called 'lithium alloys' are formed according to Equation 3.5:

$$xLi^+ + xe^- + M \underset{discharge}{\overset{charge}{\rightleftharpoons}} Li_xM \qquad (3.5)$$

The voltage probably can induce the Li ions to diffuse toward the electrode-sample interface, and therefore, an intermetallic phase may form, e.g. Li_xPt;

$$Li^+ \text{ conductor } (Li_2MnP_2O_7) \mid Li_xPt \mid \text{Metal electrode (Pt)}$$

The movement of lithium ions, however, is reversible at the sample-electrode interface after removing a *dc*-bias, following an electrochemical reaction, Equation 3.6:

$$xLi^+ + xe^- + Pt \underset{removing}{\overset{applying}{\rightleftharpoons}} Li_xPt \qquad (3.6)$$

Similar impedance results with different metal electrodes, e.g. Au, are illustrated in appendices, **Figs. A3-1~A3-3**. Micrographs of the surface of sputtered platinum electrodes after applying *dc*-bias at 400°C in N_2 are shown in **Fig. 3-27**. The color of both sides, positive (+) and negative (−), did not show any difference after *dc* bias. Note that Li ions can move toward the negative side while applying bias similar to the charging process in a battery.

Higher temperature impedance testing with different atmospheres was carried out to understand the conduction mechanism for pure $Li_2MnP_2O_7$, as shown in **Fig. 3-28**. The bulk, grain boundary and electrode response without a *dc*-bias is independent of atmosphere.

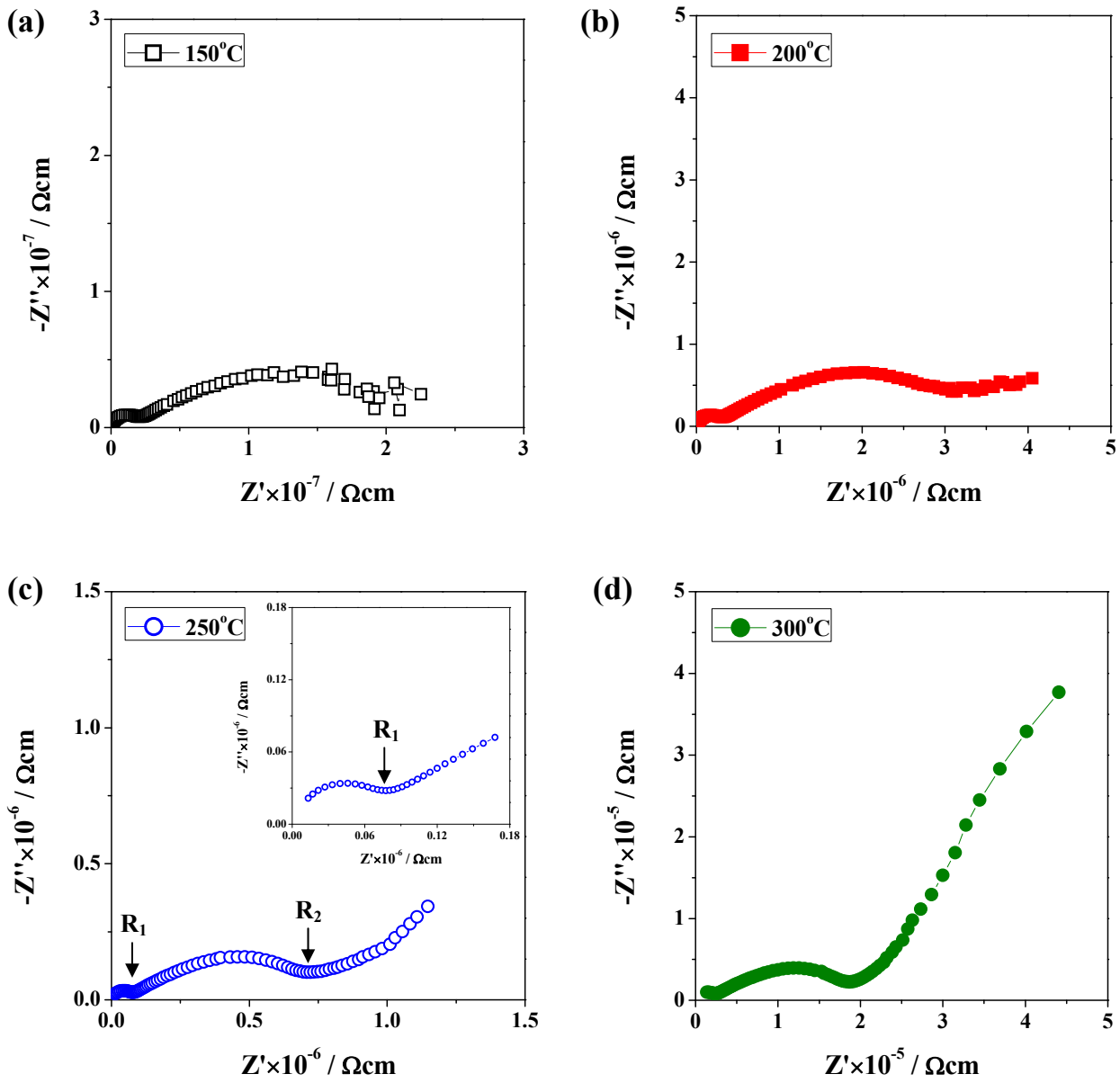

Figure 3-23 $Li_2MnP_2O_7$: Impedance complex plane plots, Z*, at (a) 150°C to (f) 400°C in N_2.

(continued on next page)

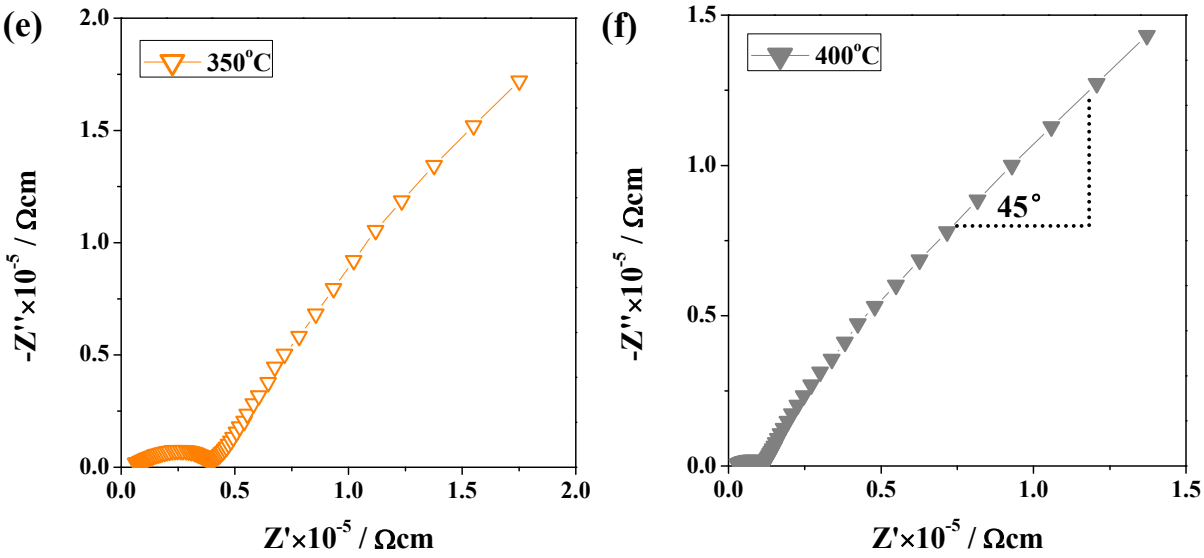

Figure 3-23 *(continued)*

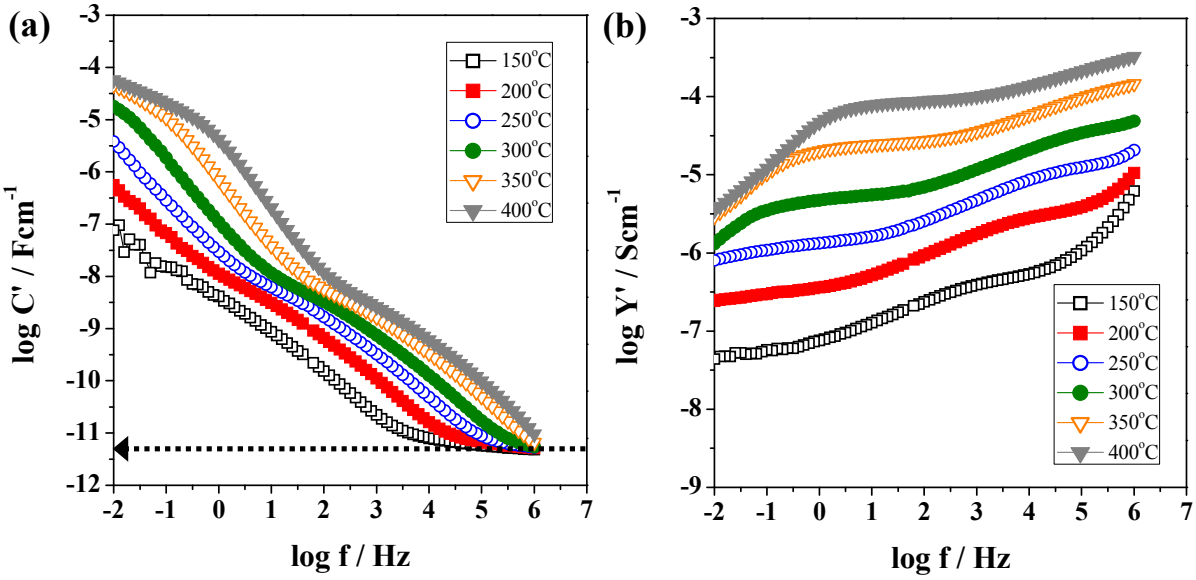

Figure 3-24 $Li_2MnP_2O_7$: (a) spectroscopic plots of capacitance, C', (b) spectroscopic plots of admittance, Y', at different temperatures of 150°C to 400°C.

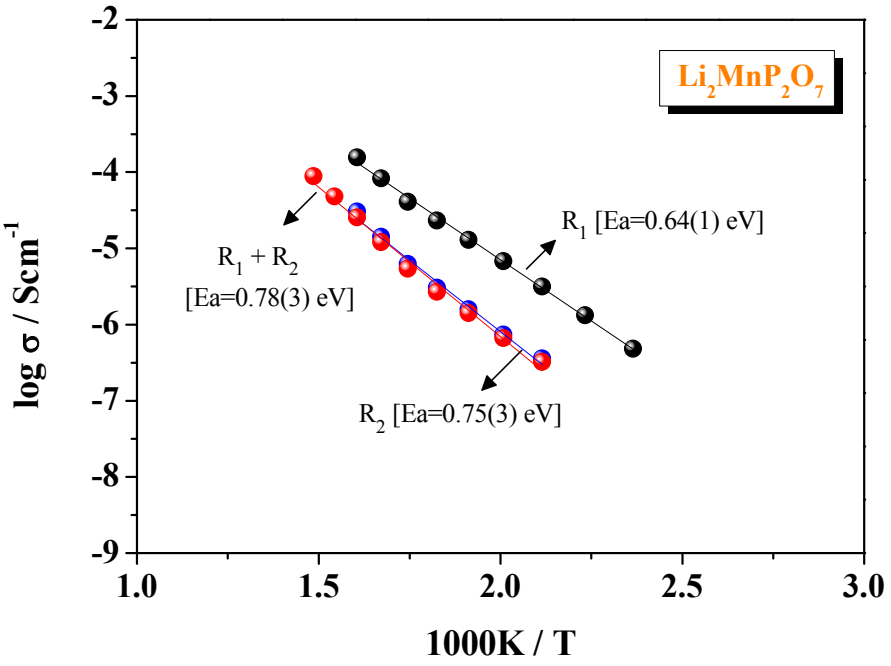

Figure 3-25 Arrhenius plots of the R_1^{-1}, R_2^{-1}, and total conductivity ($R_1^{-1} + R_2^{-1}$) in N_2 for $Li_2MnP_2O_7$ with sputtered-Pt electrodes.

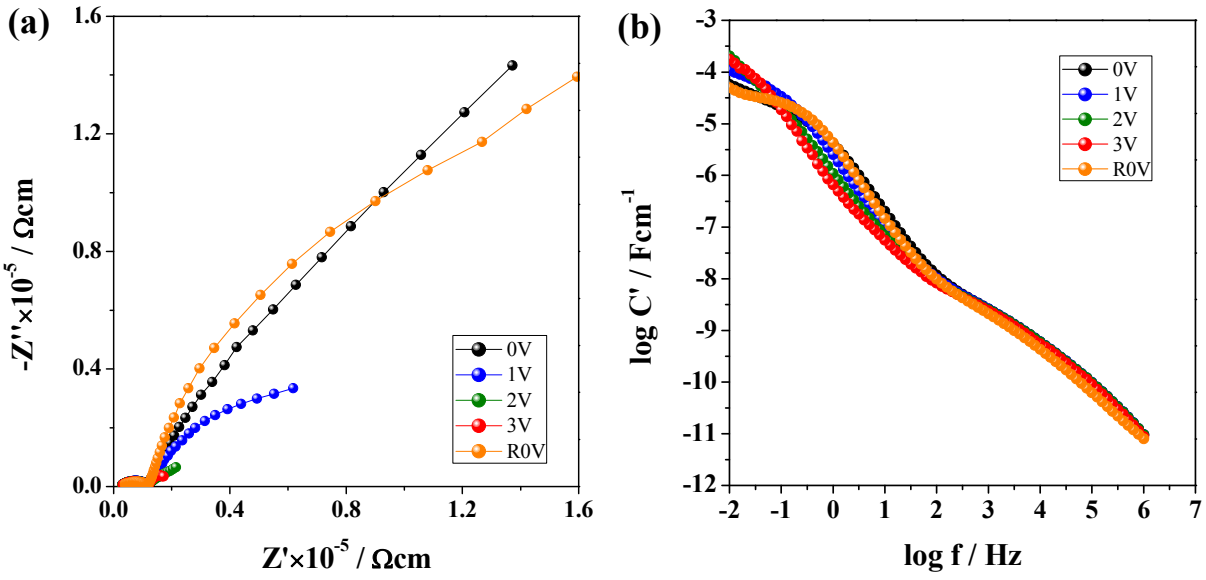

Figure 3-26 (a) Impedance complex plane plots, Z*; (b) spectroscopic plots of capacitance, C'; (c) spectroscopic plots of admittance, Y', at a measuring temperature of 400°C with different *dc*-bias of 0–3 V in N_2.

(continued on next page)

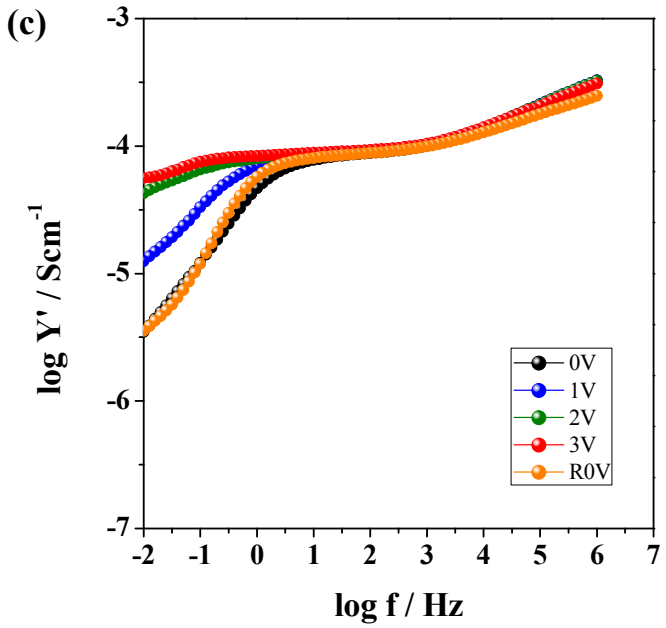

Figure 3-26 *(continued)*

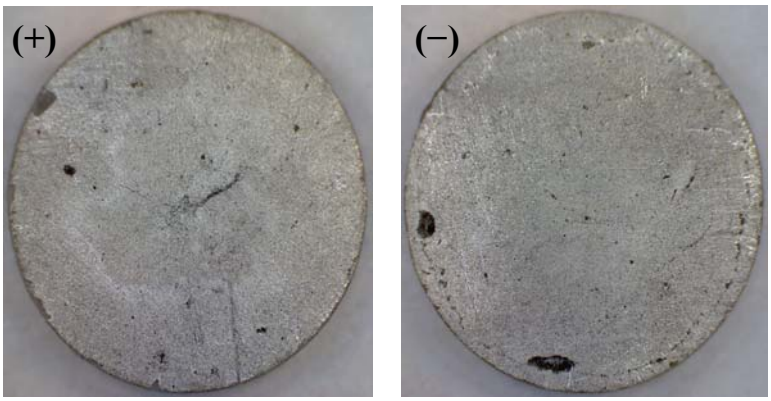

Figure 3-27 Positive (+) and negative (−) side micrographs of sputtered-Pt $Li_2MnP_2O_7$ pellet after applying 3 V *dc*-bias.

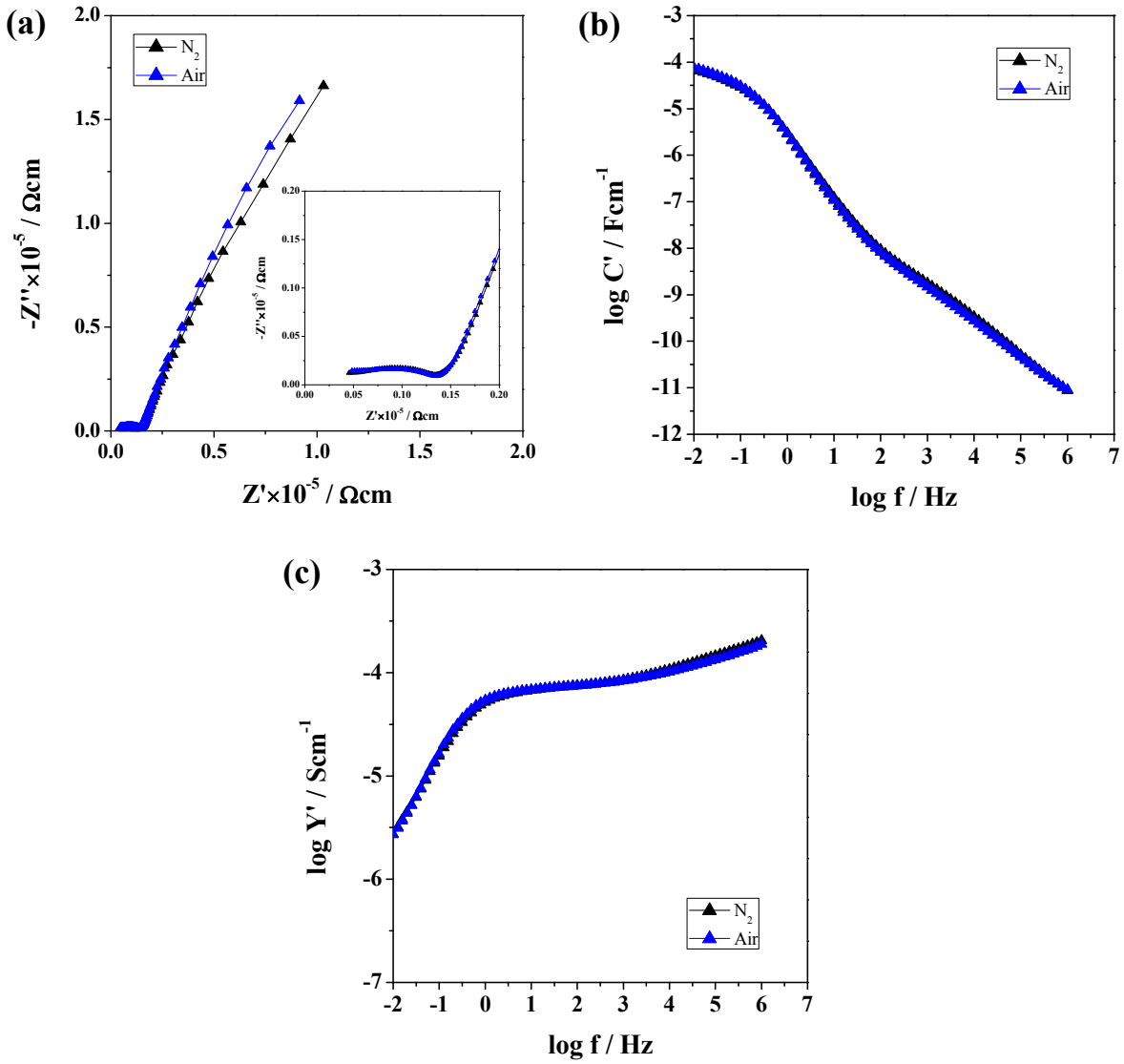

Figure 3-28 (a) Impedance complex plane plot, Z*; (b) spectroscopic plots of capacitance, C'; (c) spectroscopic plots of admittance, Y', for $Li_2MnP_2O_7$ in various atmospheres at 400°C without *dc*-bias.

(iii) $Li_2MP_2O_7$ (M=Co and $Fe_{1/3}Mn_{1/3}Co_{1/3}$)

Z* plots of $Li_2CoP_2O_7$ and $Li_2Fe_{1/3}Mn_{1/3}Co_{1/3}P_2O_7$ with sputtered Pt electrodes at different temperatures in N_2 are given in **Fig. 3-29**. At T ≳ 200°C, these two compounds show a high-frequency arc of resistance (R_b), an intermediate-frequency arc of resistance (R_{gb}), and a large low-frequency spike representing charge carrier blocking at the electrode-sample interface. At temperatures above ~ 300°C, only the resistance R_{gb} can be identified and the low frequency effect gives a combination of a curve at low frequency and a linear response at higher frequency.

C' plots as a function of frequency at 300°C in N_2 can be observed from **Fig. 3-30(a)**; both show three poorly-resolved plateaus. The first plateau at high frequencies is attributed to the bulk capacitance of ~5 $pFcm^{-1}$, C_1. A second one at intermediate frequencies is partially resolved, and is assigned to capacitance C_2 with ~10 $nFcm^{-1}$. A third capacitance C_3, with a capacitance value ~3×10^{-5} Fcm^{-1} is attributable to the double layer interface.

Y' data as a function of frequency are presented in **Fig. 3-30(b)**. The data at lower frequencies show a curvature to lower conductivity values. Two poorly-resolved plateaus are seen at intermediate frequencies, and the high-frequency dispersion lies outside the frequency window.

Based on the previous study of the effect of *dc* bias on $Li_2MnP_2O_7$, the applied voltage can induce the Li ions to diffuse towards the electrode-sample interface. An increased conductivity at low frequencies is obtained by applying a *dc*-bias of ≥ 1V, **Fig. 3-31**. The movement of lithium ions, however, is not fully reversible after removing the *dc* bias (see orange line). **Fig. 3-32** shows an increased electrode capacitance at low frequencies on increasing the *dc*-bias from 0 to 2 V, but with a slightly decrease between 2 to 3 V bias. The high-frequency responses of capacitance are not obviously changed with the applied *dc*-bias. On removal of the *dc* bias, the values of capacitance at high frequencies are similar to the original ones, however, an increased response for C' are found at lower frequencies.

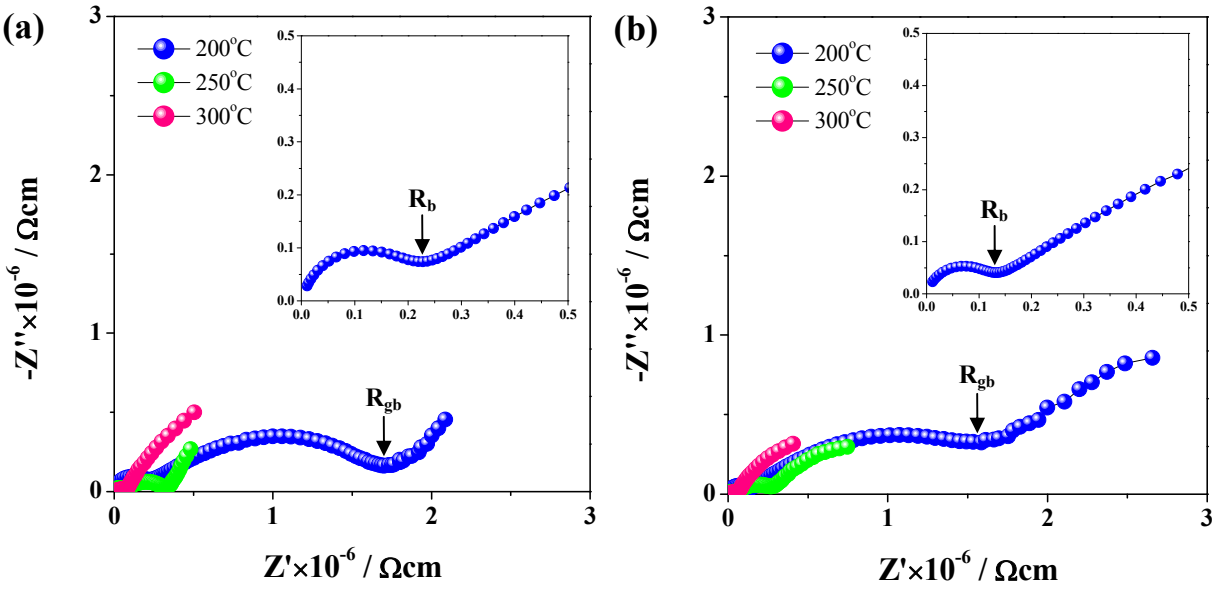

Figure 3-29 Complex resistivity plots, Z*, at 200~300 °C in N_2 for (a) $Li_2CoP_2O_7$ and (b) $Li_2Fe_{1/3}Mn_{1/3}Co_{1/3}P_2O_7$, with sputtered Pt electrodes.

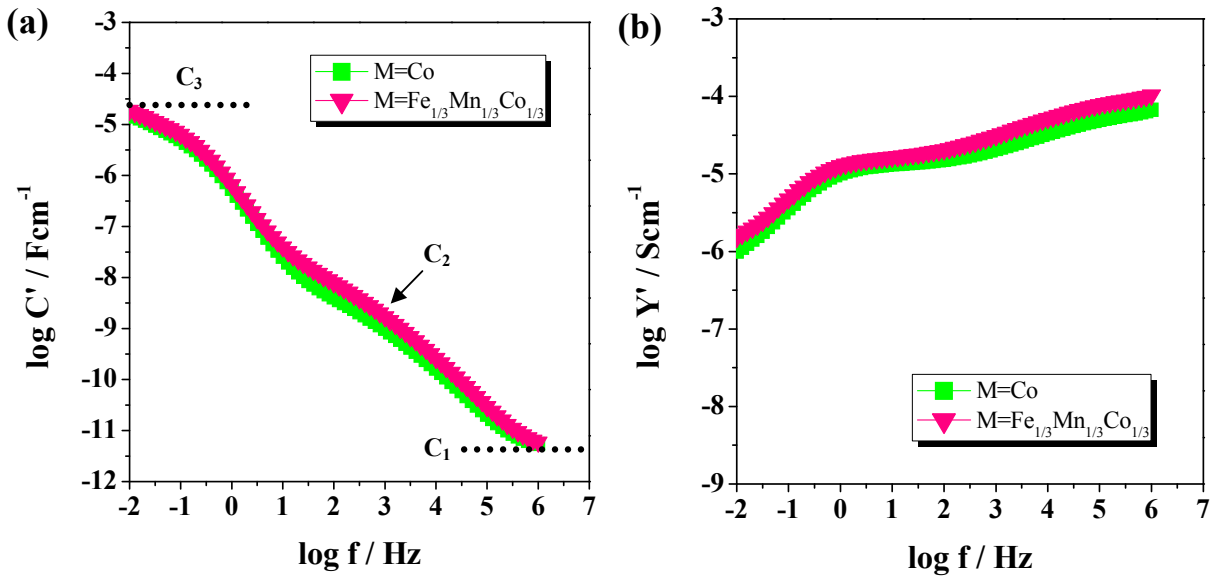

Figure 3-30 Capacitance plots, C', (a) and admittance plots, Y', (b), measured at 300°C in N_2 for M=Co and $Fe_{1/3}Mn_{1/3}Co_{1/3}$, with sputtered Pt electrodes.

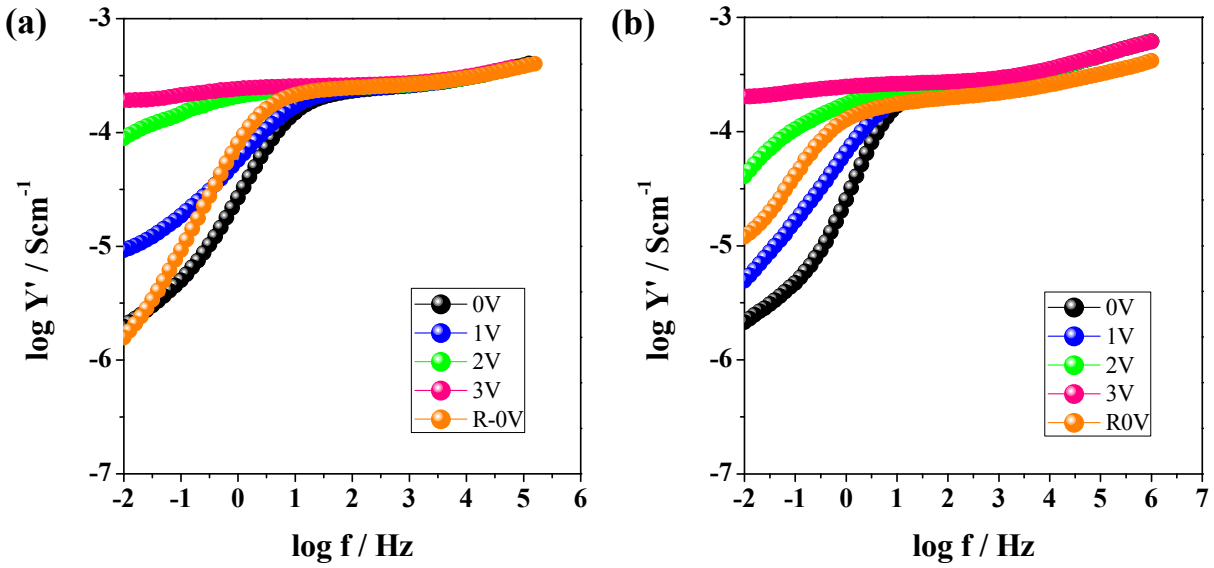

Figure 3-31 Admittance, Y', at a measuring temperature of 400°C with different *dc* bias of 0–3 V in N_2 for (a) $Li_2CoP_2O_7$ and (b) $Li_2Fe_{1/3}Mn_{1/3}Co_{1/3}P_2O_7$.

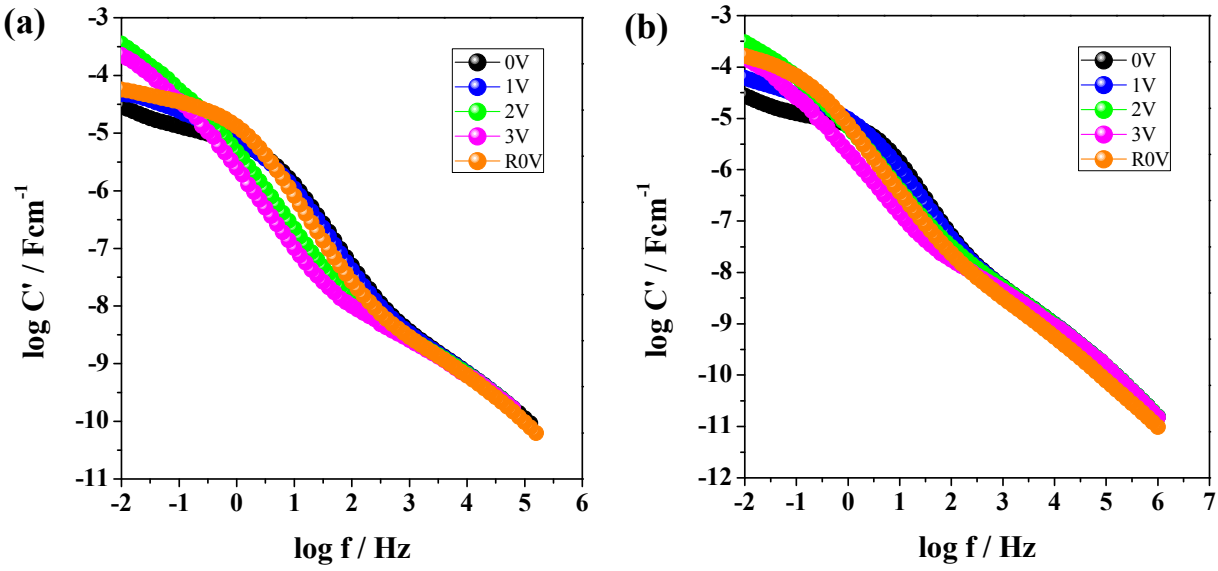

Figure 3-32 Capacitance, C', at a measuring temperature of 400°C with different *dc* bias of 0–3 V in N_2 for (a) $Li_2CoP_2O_7$ and (b) $Li_2Fe_{1/3}Mn_{1/3}Co_{1/3}P_2O_7$.

The effect of atmosphere, **Fig. 3-33**, shows that the responses of bulk, grain boundary and electrode effect at 400°C have no big difference. Further impedance data of $Li_2CoP_2O_7$ and $Li_2Fe_{1/3}Mn_{1/3}Co_{1/3}P_2O_7$ as a function of temperature, *dc*-bias, and atmosphere are summarised in the appendices.

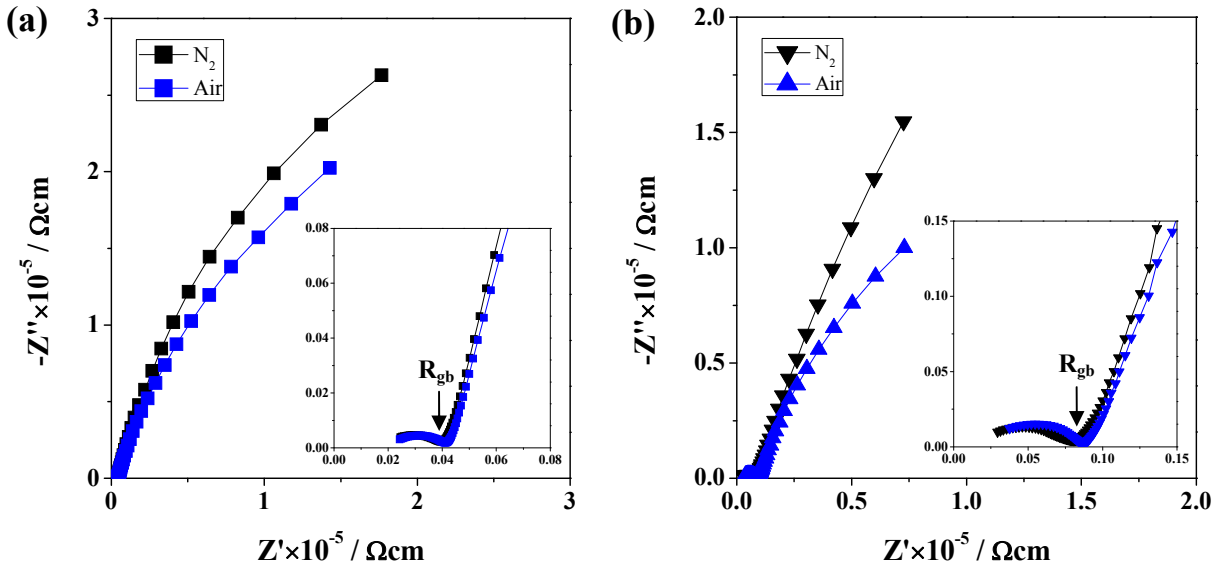

Figure 3-33 Impedance complex plane plot, Z*, in various atmospheres at 400°C without a *dc* bias for (a) $Li_2CoP_2O_7$ and (b) $Li_2Fe_{1/3}Mn_{1/3}Co_{1/3}P_2O_7$.

3.3.5 Electrochemical Properties: $Li_2MP_2O_7$ (M=Fe, Co, $Fe_{1/3}Mn_{1/3}Co_{1/3}$)

Fig. 3-34 shows the charge and discharge curves of $Li_2FeP_2O_7$ electrode material tested at a constant rate of $C/20$ at 25°C for five cycles. The cut-off voltage was set between 2.0 V and 4.5 V. The average working voltage is observed at ~3.6 V. The first discharge capacity at $C/20$ rate is > 70 mAh/g and decreases slightly with cycle number. A distinct voltage drop of ~0.1 V is found between the first and second charging curves, highlighted in **Fig. 3-35**. A similar phenomenon is reported in Li_2FeSiO_4 cathode, **Fig. 3-36**; the charging voltage drops ~0.3 V from the first (3.1 V) to second (2.8 V) cycle due to an irreversible phase transition and structural ordering on Li/Fe sites [18]. **Fig. 3-37** shows the discharge curves of the $Li_2FeP_2O_7$ electrode material tested at a constant charge rate of $0.05C$ and the discharge rate varied from $C/20$ to $2C$ at 25°C. The cut-off voltage was set

between 2.0 V and 4.5 V. It can be seen that the discharge capacity at $C/5$ rate is ~47 mAh/g and decreases with the discharge rate.

Fig. 3-38 shows the 1st charge and discharge curves of $Li_2FeP_2O_7$ and $Li_2Fe_{1/3}Mn_{1/3}Co_{1/3}P_2O_7$ at constant charge/discharge rate of $C/20$ at 25°C, with constant voltage relaxation down to $C/400$ applied at 4.5 V for 2 hours. The discharge plateau of $Li_2FeP_2O_7$ appears at ~3.3 V, and the first discharge capacity is ~70 mAh/g. $Li_2Fe_{1/3}Mn_{1/3}Co_{1/3}P_2O_7$ has low capacity of ~12 mAh/g, high polarization, and no voltage plateau at the first charge-discharge. Cyclic voltammetry (CV) was investigated to verify the electrochemical reactions during charge and discharge, **Fig. 3-39**. The oxidation peak of $Li_2FeP_2O_7$ is observed at ~3.8 V, which may correspond to the Fe^{2+}/Fe^{3+} redox couple. No peak is seen for $Li_2Fe_{1/3}Mn_{1/3}Co_{1/3}P_2O_7$.

Fig. 3-40 shows the high-rate discharge capacity for the $Li_2FeP_2O_7$ and $Li_2Fe_{1/3}Mn_{1/3}Co_{1/3}P_2O_7$ powders without carbon additives. $Li_2FeP_2O_7$ had a discharge capacity of ca. 70 mAh/g, 48 mAh/g, 30 mAh/g, and 15 mAh/g at discharging rates $C/20$, $C/5$, $C/2$, and $1C$, respectively, using constant charge rate of $C/20$. $Li_2Fe_{1/3}Mn_{1/3}Co_{1/3}P_2O_7$ had a low discharge capacity of ~5 mAh/g at $C/20$ discharge rate and ~3 mAh/g at $C/5$ discharge rate after 5 cycles. The high-rate discharge capacity of $Li_2FeP_2O_7$ is much higher than that of $Li_2Fe_{1/3}Mn_{1/3}Co_{1/3}P_2O_7$. After being subjected to the high-rate charge/discharge cycles, $Li_2FeP_2O_7$ still demonstrates a good capacity retention of ~68 mAh/g at $C/20$ charge/discharge rate after 30 cycle numbers, **Fig. 3-41**.

Fig. 3-42 shows the charge and discharge curves of the $Li_2CoP_2O_7$ electrode material tested at a constant current rate of $C/20$ at 25°C. The cut-off voltage was set between 2.0 V and 5.2 V. An average charge voltage was estimated close to 5.0 V versus Li^+/Li. This active material has a theoretically capacity of ~108 mAh/g, for 1 Li/formula; however, the first discharge capacity at $C/20$ rate is only ~20 mAh/g in our results. A representative SEM image shows large micron-sized particles with aggregated morphology. Further discussion will be addressed in next section.

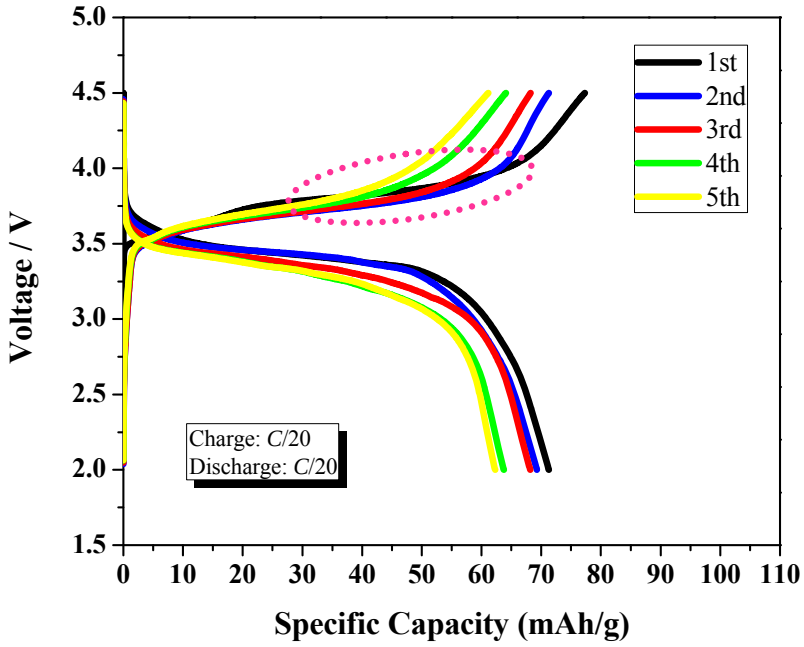

Figure 3-34 Charge-discharge curves of $Li_2FeP_2O_7$ at a constant charge/discharge rate of $C/20$ at 25°C (Cut-off voltage: 2.0–4.5 V).

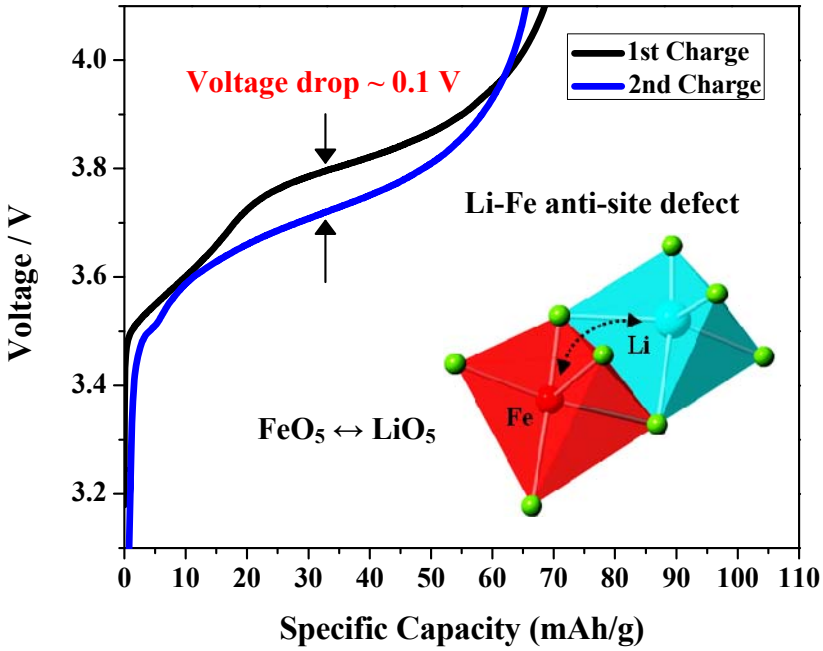

Figure 3-35 Voltage drop magnification in Fig. 3-34 between first and second charge.

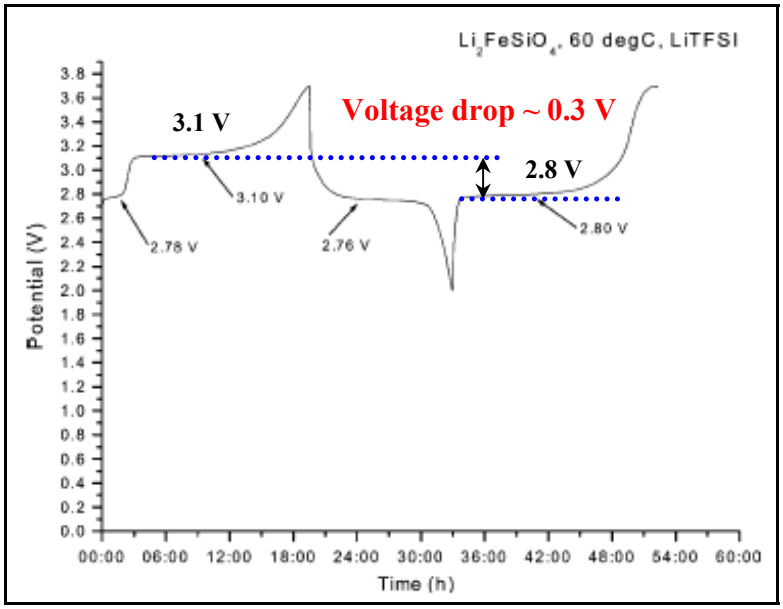

Figure 3-36 A voltage profile of Li_2FeSiO_4 cycled at 60°C at a $C/16$ rate on the first and second charging cycle [18].

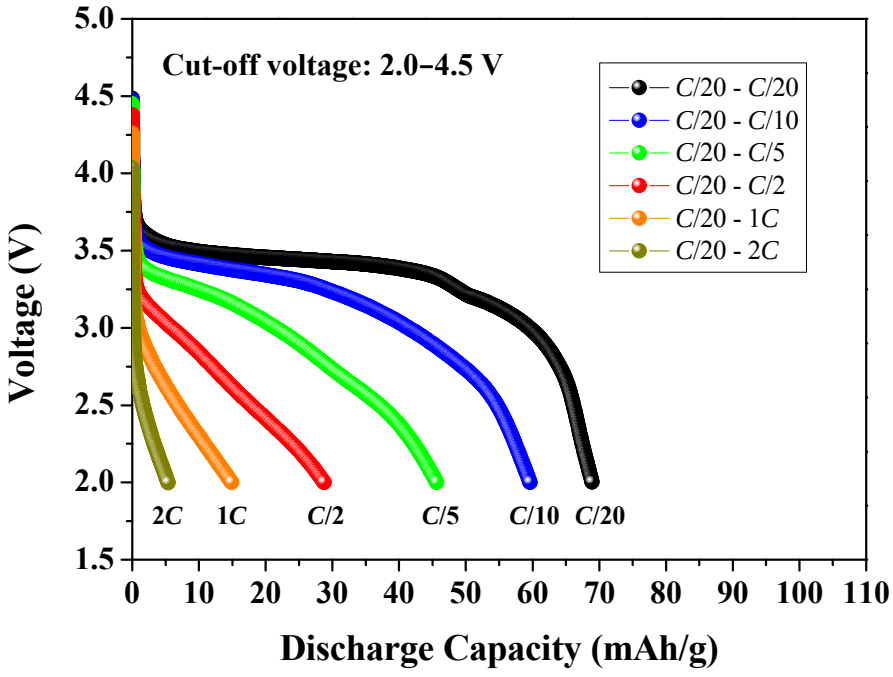

Figure 3-37 Discharge curves of the $Li_2FeP_2O_7$ cell tested at a constant charge rate of $C/20$ and various discharge rates at 25°C.

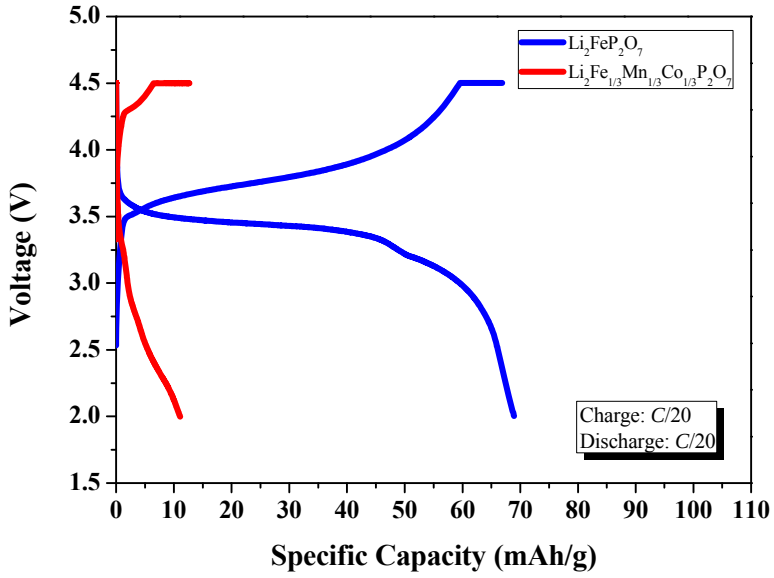

Figure 3-38 Charge–discharge curves of the $Li_2FeP_2O_7$ and $Li_2Fe_{1/3}Mn_{1/3}Co_{1/3}P_2O_7$ cells tested at a constant charge rate of $C/20$ at 25°C for the 1st cycle.

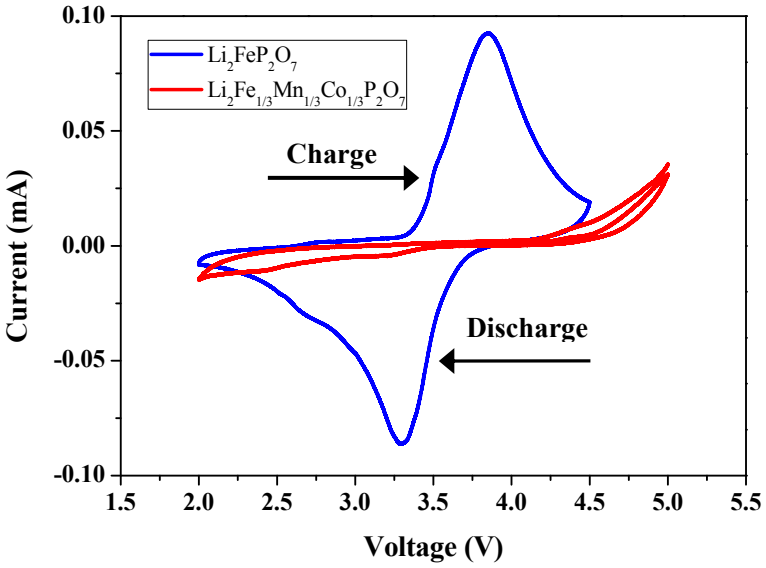

Figure 3-39 Cyclic voltammetry of $Li_2FeP_2O_7$ and $Li_2Fe_{1/3}Mn_{1/3}Co_{1/3}P_2O_7$ samples at a scanning rate of 0.02 mV/s between 2V and 4.5~5.0 V.

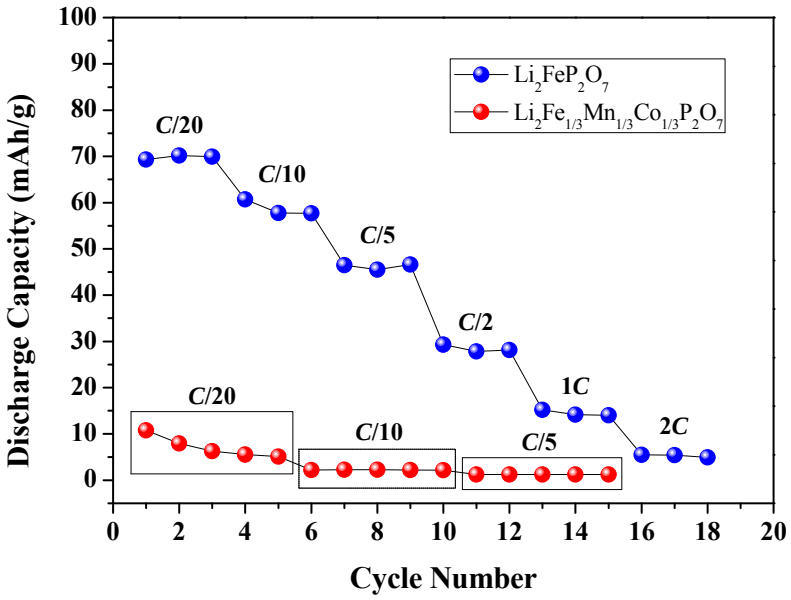

Figure 3-40 Discharge capacity of $Li_2FeP_2O_7$ and $Li_2Fe_{1/3}Mn_{1/3}Co_{1/3}P_2O_7$ as a function of discharge rate at a constant charge rate of $C/20$ (cut-off voltages: 2.0–4.5 V).

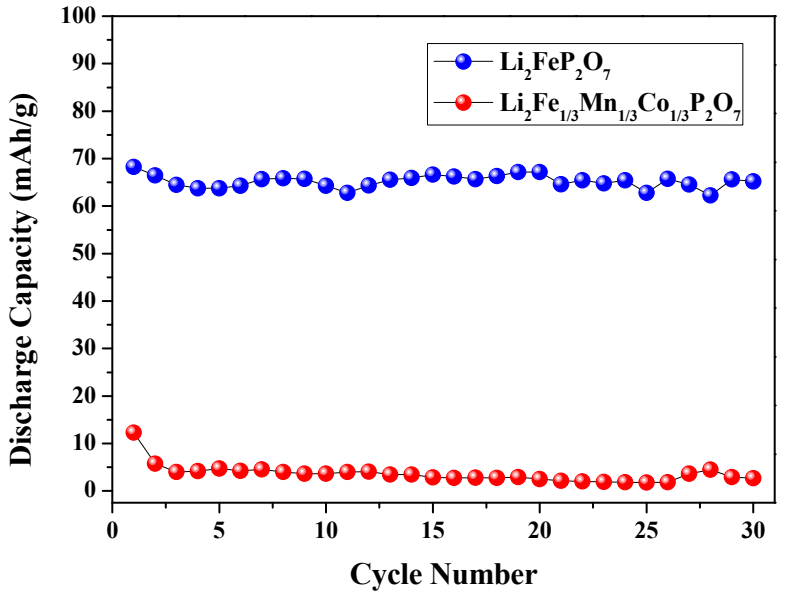

Figure 3-41 Cycling performance of $Li_2FeP_2O_7$ and $Li_2Fe_{1/3}Mn_{1/3}Co_{1/3}P_2O_7$ at $C/20$ discharge capacity with a constant charge rate of $C/20$ (cut-off voltages: 2.0–4.5 V).

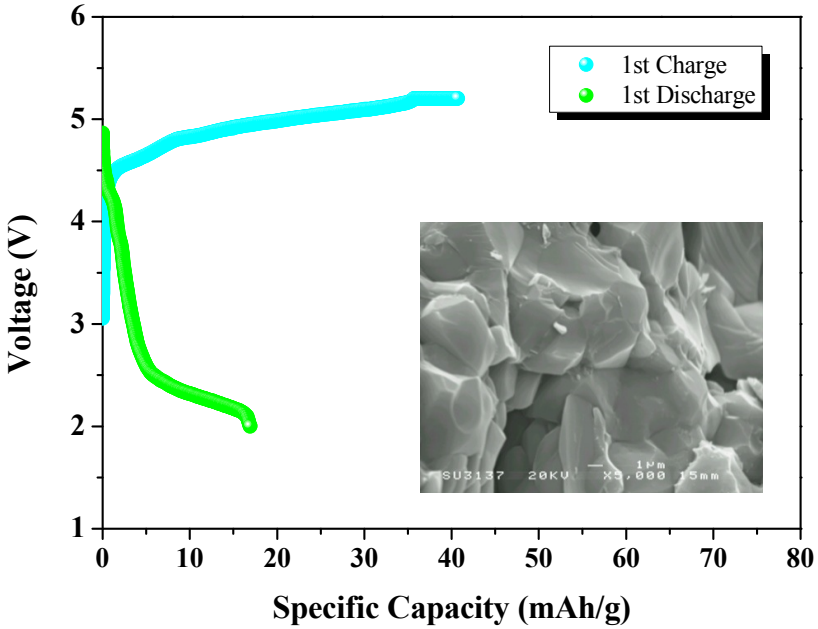

Figure 3-42 First charge–discharge curves of the $Li_2CoP_2O_7$ cell tested at a constant charge rate of $C/20$ at 25°C (cut-off voltages: 2.0–5.2 V). The insert SEM image shows the size and morphology of the $Li_2CoP_2O_7$ particles.

3.4 Discussion

3.4.1 XRD Patterns and Crystallinity

Lithium mixed-metal pyrophosphates, $Li_2Fe_{1-x}Mn_xP_2O_7$ ($0 \le x \le 1$), $Li_2Fe_{1-y}Co_yP_2O_7$ ($0 \le y \le 1$), and $Li_2Fe_{1/3}Mn_{1/3}Co_{1/3}P_2O_7$ have been successfully made though a solid-state method. In the preparation of phase-pure compounds, a two-step synthesis route is preferred to achieve complete reaction and to get rid of impurities in the final products. XRD patterns show the Mn- or Co- substituted $Li_2FeP_2O_7$ synthesized at 700°C for 12 h in N_2 form a complete solid solution with monoclinic symmetry and space group $P2_1/c$. The unit cell parameters in $Li_2Fe_{1-x}Mn_xP_2O_7$ ($0 \le x \le 1$) decrease linearly with Fe content as a result of the smaller ionic radius of Fe^{2+} (0.78 Å) than Mn^{2+} (0.83 Å), and which typically follows Vegard's law even if small deviations are observed. Zhou *et al.*'s results [9], however, show an obviously positive deviation from Vegard's law, specifically, a sharp change in all parameters at x=0.2 composition referred to in **Fig. 3-11(a)**. This cause could be usually ascribed to the occurrence of incipient immiscibility in an apparently homogenous solid solution [19], or to incomplete reaction though a wet method followed by a heat treatment at lower temperatures ranging from 400°C to 700°C [9].

For the $Li_2Fe_{1-y}Co_yP_2O_7$ ($0 \le y \le 1$) compositions, the unit cell volume shows nearly linear decrease with increasing Co substitution y. This phenomenon was reasonable given the smaller ionic radius of Co^{2+} (0.75 Å) than Fe^{2+} (0.78 Å). The reason, however, why the c-axis increased and reduced deviation from Vegard's law at y=0.2 and 0.5, respectively, is still unclear and further experiments are necessary to check whether this is a real effect, e.g. comparison of rapidly quenched and slowly cooling samples.

The multi-transition metal pyrophosphate $Li_2Fe_{1/3}Mn_{1/3}Co_{1/3}P_2O_7$ has a lower degree of site exchange, ~0.7, calculated from I(-111)/I(200) in **Fig. 3-7**, in comparison to those of the $Li_2FeP_2O_7$ and $Li_2CoP_2O_7$ compounds with ~1.2 (**Fig. 3-10**) and ~1.1 (**Fig. 3-13**), respectively. This result indicates the site exchange between TM and Li in multi-component compound can be less significant than that of single-component, Fe or Co counterparts.

3.4.2 Electrical Properties

(i) $Li_2FeP_2O_7$

Z* plots of Pt- and Au-sputtered $Li_2FeP_2O_7$ pellets show a high frequency arc with an associated capacitance value ~5 $pFcm^{-1}$, which is confirmed to be the bulk response. The capacitance at intermediate frequencies did not show a clear plateau close to ~10^{-11} Fcm^{-1}, which make it difficult to resolve the grain boundary response for all temperatures. In addition, both samples have a second distorted semicircle at low frequency with a capacitance of ~1 μFcm^{-1}, probably due to an electrode effect. At high temperatures, no blocking spike attributed to ionic conduction was present at low frequencies in these samples. The Pt or Au electrode used is reversible for electronic charge carriers but it blocks the Li ions, indicating that electronic conduction mechanism is predominant.

However, some Li ion conduction is perhaps present due to the corresponding capacitance of ~10^{-6} Fcm^{-1} obtained from the second semicircle, R_2, at low frequencies. At T < 300°C, the resistivity just slightly increases as the measuring frequencies changed to 10^{-2} Hz, **Fig. 3-17(b)**. This fact perhaps shows a non-ideal blocking electrode effect caused from the poorly-sintered $Li_2FeP_2O_7$ ceramics with a pellet density ~84 %. Sputtered Pt and/or Au electrodes, without hardening treatment, probably have discrete contacts with sample and therefore, the air gap may exist along the electrode-sample interface. Similar phenomena were observed in doped-lanthanum gallate ceramics, $La_{0.8}Sr_{0.2}Ga_{0.83}Mg_{0.17}O_{2.815}$ (LSGM), reported by Abram *et al.* [20]; an additional semicircle with associated capacitance 1 $nFcm^{-1}$ was obtained at a measuring temperature of ~328 °C using gold paste electrodes hardened at 500~850 °C. This additional resistance is due to partially-sintered Au particles in the paste, resulting in discrete contacts with the samples [20]. The measured bulk activation energy of $Li_2FeP_2O_7$ for electronic conduction is ~0.6 eV similar to data for polycrystalline and single crystal $LiFePO_4$ from *ac* impedance using blocking electrodes, Au and Ti, respectively [21-22].

The *dc*-bias has no distinct influence on the electrical properties of $Li_2FeP_2O_7$ at the highest measuring temperature of 400°C although a slight increase in bulk conductivity is observed with a *dc* bias of 1 V. This could be due to a tiny degree of oxidation from Fe^{2+} to

Fe^{3+} during measurement. Applying a *dc*-bias also can be carried out to verify the effect of sample-electrode interface (non-Ohmic contact) to get insight into this material [23]. For example, a Schottky barrier can form as a result of charge transfer across the metal-semiconductor interface. Generally, the Schottky barrier height is created by the space charge and is voltage dependent. Herein, in order to clearly indicate the *dc*-bias effect on the second arc at low frequencies, the bulk conductivities R_1 at 1 V and 3 V are shifted forward to the same value as 0 V, and therefore, the assumed oxidation factor in sample could be ignored, as shown in **Fig. 3-43**. Specifically, the resistance of low frequency arc decreases slightly with applying a higher *dc*-bias of 3 V, which perhaps means the height of a Schottky barrier could be decreased for electron to transfer across the interface.

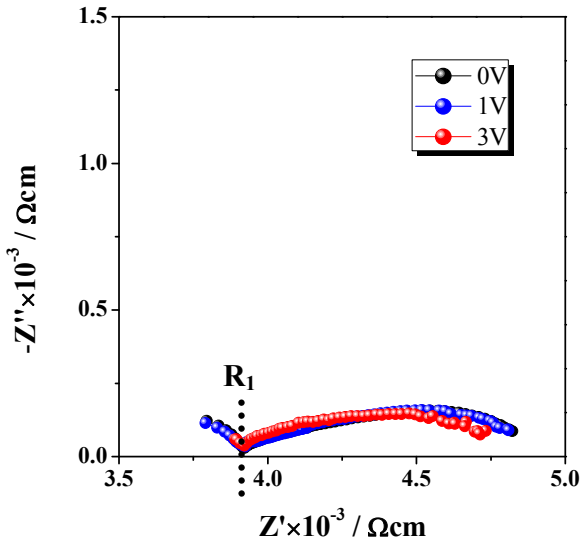

Figure 3-43 Effect of *dc* voltage effect on low frequency response, with constant R_1 at 400°C applying different *dc*-bias of 1 and 3 V in N_2.

In general, if the conductivity increases with the oxygen partial pressure (P_{O_2}), the conduction mechanism should be *p*-type due to a change in electronic carrier concentration, i.e. $O_2 + 2V_O^{\bullet\bullet} \rightarrow 2O_O^{\times} + 4h^{\bullet}$. Herein, the bulk conductivity of $Li_2FeP_2O_7$ at higher frequency in air is slightly higher than that in N_2, indicating the conduction is now probably *p*-type. However, as the atmosphere changed from Air to N_2 once again for 6 hours, the

conductivity does not decrease reversibly to its original value, suggesting a partial oxidation of Fe^{2+} to Fe^{3+} occurred in sample at 400°C. This could be in agreement with the following reaction proposed by Whittingham *et al.* [9], Equation 3.7:

$$12\ Li_2FeP_2O_7 + 3\ O_2 \rightarrow 8\ LiFeP_2O_7 + 4\ Li_4P_2O_7 + 2\ Fe_2O_3 \qquad (3.7)$$

(ii) $Li_2MnP_2O_7$

Z* plots of Pt-sputtered $Li_2MnP_2O_7$ pellet show a high frequency semicircle with an associated capacitance value ~5 $pFcm^{-1}$ attributed to the bulk resistance. At temperatures above 200°C, a second semicircle can be clearly distinguished with an associated higher capacitance close to 10 $nFcm^{-1}$; this value can be due to a Schottky barrier and either different electrode material or thick/thin pellet. In order to clarify this point, a different electrode, Au, was utilized and compared to the results in **Figs. 3-23** and **3-24**. A large second semicircle, however, is still observed with a similar capacitance of ~50 $nFcm^{-1}$, see **Figs. A3-3** and **A3-4**. On the other hand, a Schottky barrier usually occurs in electronic conductors, but not in ionic conductors. As a result, this second semicircle can correspond to large grain boundary resistances (R_{gb}) or to a surface layer.

Typically, partial blocking behavior of metal electrodes identifies ionic conduction within a sample [24]. High temperature IS measurements for $Li_2MnP_2O_7$ were carried out to provide detailed insight into conduction mechanisms; a low frequency Warburg spike ~ 45^o above 350°C, **Fig. 3-23(f)**, is exhibited and attributed to ionic diffusion between the electrode/sample interface. In addition, a blocking double layer associated with a low frequency capacitance of ~10^{-5} Fcm^{-1} above 300°C is obtained and the R_T of cell + electrodes cannot be measured. *DC*-bias effect on $Li_2MnP_2O_7$ shows the Li ion diffusion is fully reversible across the electrode-sample interface after applying *dc*-bias. However, there is no difference in bulk and grain boundary responses. These results are similar using platinum or gold electrodes, which indicate less decomposition in electrodes is obtained after *dc*-bias. A schematic model of bias-dependence is given in **Fig. 3-44**; since the height of a Schottky barrier could be decreased by applying a *dc*-bias and therefore a decreased resistance and increased capacitance appear for charge transfer across the sample-electrode interface (**Fig. 3-26**).

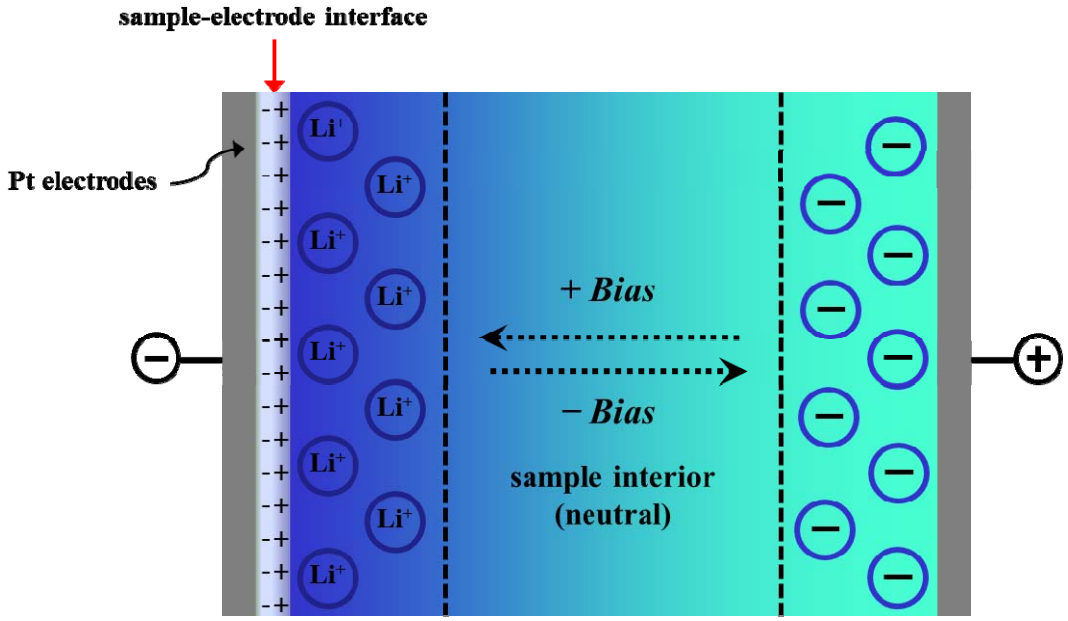

Figure 3-44 Schematic model of the Li^+ movement with applied and removed *dc* bias.

The responses of bulk, grain boundary and electrode effect without a *dc*-bias do not show a big difference at high temperature, 400°C, in different atmospheres, which means the manganese is stable and hard to oxidize from Mn^{2+} to Mn^{3+}. This is expected from the relative oxidation state stability at 600°C: $Mn^{2+} > Mn^{3+}$ [25], and confirmed by a TGA study of $Li_2Mn_{1-y}Fe_yP_2O_7$ from Whittingham *et al.* [9]. $Li_2MnP_2O_7$, therefore, cannot be clarified as either *p*- or *n*-type material, and its conducting species is almost primarily dominated by ionic conduction instead of electronic conduction.

(iii) $Li_2CoP_2O_7$

The results of Nyquist plots of $Li_2CoP_2O_7$ were similar to those of $Li_2MnP_2O_7$; a high frequency bulk semicircle and a second depressed semicircle with a higher capacitance ~50 $nFcm^{-1}$, which is attributed to a grain boundary resistances or a surface layer. A similar phenomenon was observed using Au electrodes, **Fig. A3-21(a)**. At T > 300°C, an inclined spike at lower frequencies is displayed due to a blocking interfacial effect. Specifically, a low frequency Warburg spike ~45° is present at 350°C and 400°C because of ionic diffusion across the electrode/sample interface.

The Li ion diffusion in $Li_2CoP_2O_7$, however, is not fully reversible across the electrode-sample interface after applying *dc*-bias, which may be due to decomposition on the surface of Pt electrode, as shown by a dark colour on the pellet surface. In contrast, with sputtered Au electrodes, the Li ions are more reversible due to less electrode cracking, **Fig. A3-22**. A high measuring temperature above 300°C and applied voltage may influence electrode stability. The electrical responses of $Li_2CoP_2O_7$ are almost independent of different atmospheres, indicating the cobalt is quite stable and is not easy to oxidize from Co^{2+} to Co^{3+}. This suggests the electrical behaviour of $Li_2CoP_2O_7$ is predominately ionic conduction with much lower electronic conduction.

(iv) $Li_2Fe_{1/3}Mn_{1/3}Co_{1/3}P_2O_7$

Z* plots at different temperatures from 200°C to 300°C in N_2 show two distorted semicircles and a low frequency inclined spike which may be attributed to a partially blocked electrode interface with an associated capacitance of ~10^{-5} Fcm^{-1}. The capacitance shows a typical plateau at high frequency of ~5 $pFcm^{-1}$, which is associated with the first R_1 resistance, and therefore, attributed to the bulk response. Similar to the second disordered semicircles in Z* plots of $Li_2MnP_2O_7$ and $Li_2CoP_2O_7$, R_2, in $Li_2Fe_{1/3}Mn_{1/3}Co_{1/3}P_2O_7$ can be also attributed to a grain boundary resistance. Comparable results using Au electrodes were demonstrated in **Figs. A3-23~A3-24**. As the temperature increased to 350°C and 400°C, a low frequency Warburg spike ~45^o is exhibited, and the total resistance of cell + electrodes cannot be evaluated.

DC-bias results show the movement of lithium ions, however, is not fully reversible at the sample-electrode interface after applying *dc*-bias of 3 V at 400°C in N_2. One possible explanation is the decomposition of the surface of Pt electrode with time. Nevertheless, the lithium ions are full reversible using a sputtered Au electrode at 300°C in N_2, indicating less decomposition on the pellet surface is more probable at lower measuring temperature, as shown in **Fig. A3-25**. Atmosphere studies find that the responses of bulk, grain boundary and electrode effect without a *dc*-bias at 400°C do not show big difference in various atmospheres. This means the valence (M^{2+}) of manganese and cobalt species are still quite stable in multi-component $Li_2Fe_{1/3}Mn_{1/3}Co_{1/3}P_2O_7$, and in addition, probably the Fe

oxidation could be inhibited. $Li_2Fe_{1/3}Mn_{1/3}Co_{1/3}P_2O_7$, therefore, seems to be primarily an ionic conductor with perhaps some electronic conduction.

The comparative bulk (R_b) conductivity data measured in N_2 of Pt-sputtered $Li_2MP_2O_7$ (M=Fe, Mn, Co, $Fe_{1/3}Mn_{1/3}Co_{1/3}$) analogues are summarized in **Fig. 3-45**. The bulk activation energy *Ea* of $Li_2Fe_{1/3}Mn_{1/3}Co_{1/3}P_2O_7$ (0.60 eV) is slightly lower than that of $Li_2CoP_2O_7$ (0.62 eV), $Li_2FeP_2O_7$ (0.63 eV) and $Li_2MnP_2O_7$ (0.64 eV). The *E*a values of M=Mn and Co are compared to previous results in lithium orthophosphates, e.g. 0.65 eV of $LiMnPO_4$ and 0.62 eV of $LiCoPO_4$, by *ac* conductivity measurements reported by Rissouli *et al*. [26]. Moreover, their results showed that the activation energy decreases slightly with a decrease of the unit cell volume as a result of a shrinking lattice effect. That is, the increasing repulsion between Li^+ and M^{2+} cations may diminish the strength of Li–O bonding in smaller lattice, and therefore, result in lower activation energy and higher conductivity [26]. A similar phenomenon was observed in our results of $Li_2MnP_2O_7$ and $Li_2CoP_2O_7$ pyrophosphates. More detailed structure refinement, however, should be carried out to get insight into this explanation.

The specific grain boundary (R_{gb}) conductivities and activation energies of $Li_2MP_2O_7$ are seen in **Fig. 3-46**. The *Ea* value of R_{gb} is 0.75±0.02 eV for M=Mn, 0.79±0.02 eV for M=Co, 0.84±0.03 eV for M=$Fe_{1/3}Mn_{1/3}Co_{1/3}$. The reason, however, why the resistance of R_{gb} of $Li_2MnP_2O_7$ is much higher with a slightly lower *Ea*, is still unclear and further studies are necessary for clarification. The total conductivity of M=Mn is lower than that of the other three samples due to its high grain boundary resistance, as shown in **Fig. 3-47**. This implies the grain boundary resistance should be the limiting factor for room temperature Li ion transport in $Li_2MnP_2O_7$, and therefore, can be one explanation for its very poor electrochemical behavior, i.e. discharge capacity of ≈ 0 mAh/g, is observed [9, 15]. Recently, Yamada *et al.* reported the low conductivity and sluggish kinetics of $Li_2MnP_2O_7$ could be improved through moderate thermal activation [27]. For example, $Li_2MnP_2O_7$ cathode could observe a reversible (de)lithiation reaction involving a redox plateau of ~4.5 V with a first discharge capacity close to 60 mAh/g obtained while subjecting to galvanostatic cycling at 40°C using a slower rate of *C*/50 [27].

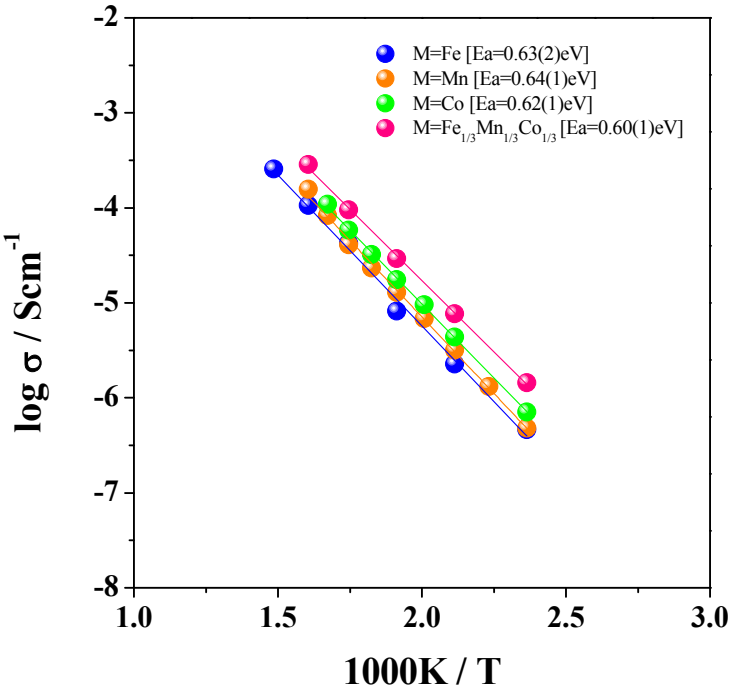

Figure 3-45 Arrhenius plots of bulk conductivities (R_b^{-1}) for $Li_2FeP_2O_7$, $Li_2MnP_2O_7$, $Li_2CoP_2O_7$ and $Li_2Fe_{1/3}Mn_{1/3}Co_{1/3}P_2O_7$ ceramics.

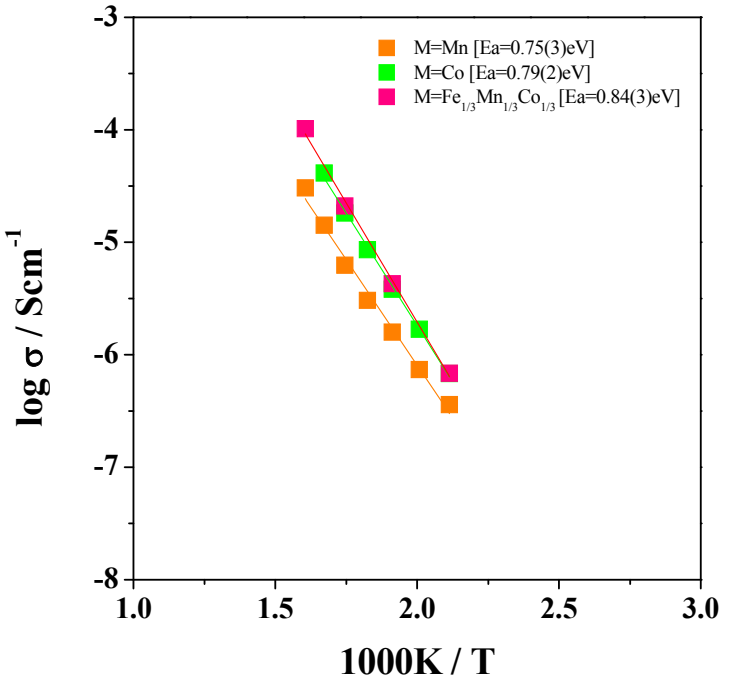

Figure 3-46 Arrhenius plots of grain boundary conductivities (R_{gb}^{-1}) for $Li_2MnP_2O_7$, $Li_2CoP_2O_7$ and $Li_2Fe_{1/3}Mn_{1/3}Co_{1/3}P_2O_7$ ceramics.

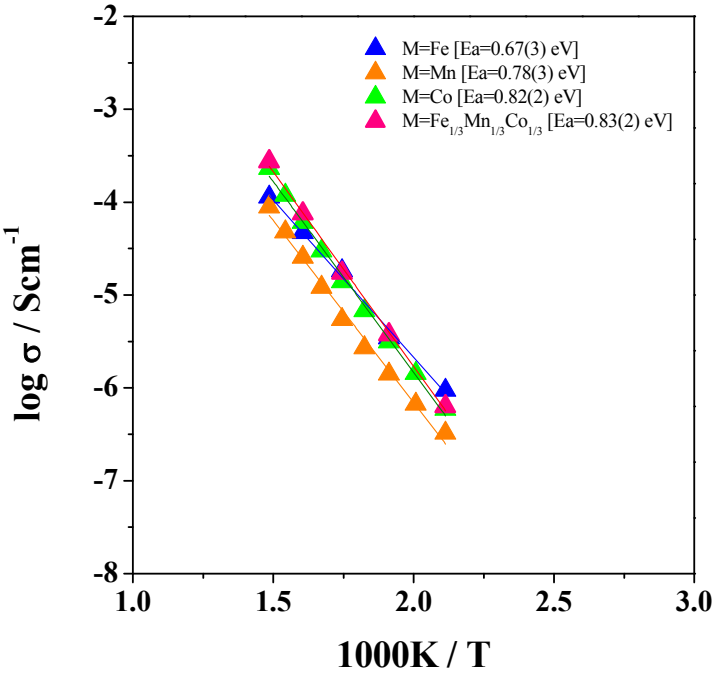

Figure 3-47 Arrhenius plots of total conductivities (R_T^{-1}) for $Li_2FeP_2O_7$, $Li_2MnP_2O_7$, $Li_2CoP_2O_7$ and $Li_2Fe_{1/3}Mn_{1/3}Co_{1/3}P_2O_7$ ceramics.

3.4.3 Electrochemical Testing

$Li_2FeP_2O_7$ demonstrates an average working voltage of ~3.6 V, which is higher than that of 3.45 V for $LiFePO_4$, 3.22 V for $LiFe_{1.5}P_2O_7$, and 2.9 V for $LiFeP_2O_7$ [28], and the first reversible discharge capacity is ~72 mAh/g, indicating 65% of the capacity of one-electron theoretical value of 110 mAg/g. Although this value is relatively lower than those reported in references [8-10], the reason is that no conductive additives are added into our active materials before electrode fabrication. As a result, a lower electronic conductivity of ~10^{-9} Scm^{-1} at room temperature and larger particle size of 5~10 μm could limit the discharge capacity performance at low and high rates, **Fig. 3-37**. Nanosizing and/or carbon coating may overcome this drawback, and further improve the capacity. Recently, Saito *et al.* showed that the carbon coating on the surface of $Li_2FeP_2O_7$ particles was effective to inhibit the fast capacity degradation at high rates, providing a high discharge capacity of ~80 mAh/g at 1*C* rate due to the significantly increased electronic conductivity [29].

The voltage drop (~0.1 V) between the first and second charging could be due to formation of Li-Fe anti-site defects, wherein the occupancy of LiO_5 and FeO_5 pyramidal sites may rearrange, resulting in an irreversible structural change. A similar phenomenon, a voltage drop of ~0.07 V, was obtained in Shimizu *et al.*'s results, and the detailed electrochemical redox mechanism was elucidated by *Ex-situ* X-ray diffraction [30]. Although *ab* initio calculations indicated the 2nd redox reaction (Fe^{3+}/Fe^{4+}) can be active at a higher voltage of ~5.2 V, so far, it has been difficult to extract two lithium ions out of $Li_2FeP_2O_7$ until a stable high-voltage electrolyte is developed and electronic conductivity is increased [9]. $Li_2FeP_2O_7$ demonstrates excellent capacity retention of ~98 % at $C/20$ charge/discharge rate, after 30 cycles, which is attributed to its stable 3-D structure.

The electrochemical properties of $Li_2Fe_{1/3}Mn_{1/3}Co_{1/3}P_2O_7$ as cathode were not anticipated to be better without carbon-coating; it has high polarization and a lower discharge capacity of ~12 mAh/g at $C/20$; in addition, no clear voltage plateau is exhibited during the first charge and discharge. The possible reasons are the inactive Mn species in $Li_2Fe_{1/3}Mn_{1/3}Co_{1/3}P_2O_7$, and poor conductivity of $\sim 10^{-10}$ Scm^{-1} at RT in N_2 as a result of the large grain boundary resistance.

$Li_2CoP_2O_7$ is electrochemically active with a Co^{2+}/Co^{3+} redox centre close to 5 V consistent with the value, ~4.9 V, from Kim *et al.*'s results [10]. The first discharge capacity obtained here is ~18 mAh/g at $C/20$, which is much smaller than that ~85 mAh/g reported in reference [10]. Unlike the powders mixed with Super P (15%) in [10], no conductive additives were added to our active materials before electrode fabrication; as a result, a low conductivity of $\sim 5\times10^{-12}$ Scm^{-1} at 298 K in N_2 was extracted by fitting the Arrhenius plot of total conductivity in **Fig. A3-8**. The second reason is a particle size > 10 μm (inserted in **Fig. 3-42**) which may increase the Li^+ diffusion path in $Li_2CoP_2O_7$. In addition, the electrolyte may partially decompose while charging to 5.2 V. Further development of a stable, high voltage electrolyte, carbon coating, and reducing particle size should be helpful to improve the performance of $Li_2CoP_2O_7$.

3.5 Conclusions

$Li_2Fe_{1-x}Mn_xP_2O_7$ ($0 \le x \le 1$), $Li_2Fe_{1-y}Co_yP_2O_7$ ($0 \le y \le 1$) and $Li_2Fe_{1/3}Mn_{1/3}Co_{1/3}P_2O_7$ have been successfully synthesized by conventional solid-state reaction following a two-step process. The reaction temperature cannot be over a wide range to obtain phase-pure $Li_2FeP_2O_7$ and its isostructural analogues; specifically, reaction at 700°C in N_2 is feasible. The Mn- and Co- substituted $Li_2FeP_2O_7$ synthesized at 700°C for 12 h in N_2 form a complete solid solution with monoclinic symmetry and space group $P2_1/c$. Lattice parameters increase and decrease with Mn and Co content, respectively. $Li_2Fe_{1/3}Mn_{1/3}Co_{1/3}P_2O_7$ formed a homogenous phase in agreement with the accurate stoichiometric ratio confirmed by EDS.

A detailed investigation by ac impedance measurements of $Li_2MP_2O_7$ (M=Fe, Mn, Co) as a function of temperature was carried out to determine their conductivity and activation energy, and most importantly, to determine whether the conduction species are electronic, ionic, or mixed. Of the three phases, first, as the Pt and/or Au electrodes are reversible for electronic exchange but blocking for Li ions, which indicates the species responsible for conduction in $Li_2FeP_2O_7$ is predominantly electrons. No electrode and Warburg spike are observed at low frequencies over a wide range of temperatures from 150°C to 400°C. The second resistance (R_2) may result from the poorly-sintered $Li_2FeP_2O_7$ pellet with discrete contacts between sample and electrode interface. The bulk activation energy of $Li_2FeP_2O_7$ for electronic conduction is 0.63 eV similar to the value of 0.6 eV for $LiFePO_4$.

Second, for $Li_2MnP_2O_7$, the total conductivity is limited by large grain boundary resistances, and the activation energy of grain boundary (R_{gb}), 0.75(3) eV, is higher than that of bulk (R_b), 0.64(1) eV. A decreased electrode resistance and slightly increased electrode capacitance at low frequencies are observed applying *dc*-bias from 0 to 3 V, and in addition, the movement of lithium ions is fully reversible at the sample-electrode interface after removing the *dc*-bias. The effect of atmosphere without a *dc*-bias had no effect on bulk, grain boundary and electrode response, which indicates that the conduction in $Li_2MnP_2O_7$ is primarily ionic.

Third, for $Li_2CoP_2O_7$, the total conductivity is limited by large grain boundary resistances, and the activation energy of grain boundary (R_{gb}), 0.79(2) eV, is higher than

that of bulk (R_b), 0.62(1) eV. The transport of lithium ions, using Pt as electrode, is not fully reversible at the sample-electrode interface after removing a *dc*-bias due to a partial decomposition on electrode at high temperature of 400°C. A blocking double layer associated with a low frequency capacitance of $\sim 10^{-5}$ Fcm^{-1} above 300°C is observed and R_T of cell + electrodes cannot be measured, indicating that ionic conduction in $Li_2CoP_2O_7$ is more probable instead of electronic conduction.

Multi-component $Li_2Fe_{1/3}Mn_{1/3}Co_{1/3}P_2O_7$ shows similar electrical behavior to $Li_2CoP_2O_7$; the room-temperature lithium transport is limited by large grain boundary resistances with a slightly higher activation of 0.84 eV than those in Mn- and Co-base. Electrochemical properties of $Li_2MP_2O_7$ (M=Fe, Co, $Fe_{1/3}Mn_{1/3}Co_{1/3}$), e.g. working voltage, rate performance, and cycle life, were evaluated through a coin-cell configuration. The Fe phase demonstrates better discharge capacity rather than Mn [9], Co and multi-component counterparts, probably because it is the only material in this group which has electronic conductivity. The irreversible capacity of M=$Fe_{1/3}Mn_{1/3}Co_{1/3}$ or Co electrode may be reduced through improved fast ion diffusion and high electron conductivity in materials. $Li_2CoP_2O_7$ could be used as a new high-voltage cathode of ~5.0 V, however, increased conductivity and stable high-voltage electrolytes need to be developed before its practical application.

3.6 References

1. A. Nyten, A. Abouimrane, M. Armand, T. Gustafsson and J.O. Thomas, "Electrochemical performance of Li_2FeSiO_4 as a new Li-battery cathode material", *Electrochem. Commun.* **2005**, *7*, pp. 156–160.

2. A. Yamada, I. Iwane, Y. Harada, S. Nishimura, Y. Koyama and I. Tanaka, "Lithium Iron Borates as High-Capacity Battery Electrodes", *Adv. Mater.* **2010**, *22*, pp. 3583–3587.

3. T. N. Ramesh, K.T. Lee, B. L. Ellis and L.F. Nazar, "Tavorite Lithium Iron Fluorophosphate Cathode Materials: Phase Transition and Electrochemistry of $LiFePO_4F$–Li_2FePO_4F", *Electrochem. Solid-State Lett*. **2010**, *13*, pp. A43–A47.

4. N. Recham, J. N. Chotard, L. Dupont, C. Delacourt, W. Walker, M. Armand and J. M. Tarascon, "A 3.6 V lithium-based fluorosulphate insertion positive electrode for lithium-ion batteries", *Nat. Mater.* **2010**, *9*, pp. 68–74.

5. A. K. Padhi, V. Manivannan and J. B. Goodenough, "Tuning the Position of the Redox Couples in Materials with NASICON Structure by Anionic Substitution", *J. Electrochem. Soc.* **1998**, *145* (5), pp. 1518–1520.

6. P. Barpanda, M. Ati, B. C. Melot, G. Rousse, J-N. Chotard, M-L. Doublet, M. T. Sougrati, S. A. Corr, J-C. Jumas and J-M. Tarascon, "A 3.90 V iron-based fluorosulphate material for lithium-ion batteries crystallizing in the triplite structure", *Nat. Mater.* **2011**, *10*, pp. 772–779.

7. Laure Adam, Anne Guesdon and Bernard Raveau, "A new lithium manganese phosphate with an original tunnel structure in the $A_2MP_2O_7$ family ", *J. Solid State Chem.* **2008**, *181* (11), pp. 3110–3115.

8. Shin-ichi Nishimura, Megumi Nakamura, Ryuichi Natsui and Atsuo Yamada, "New Lithium Iron Pyrophosphate as 3.5 V Class Cathode Material for Lithium Ion Battery", *J. Am. Chem. Soc.* **2010**, *132*, pp. 13596–13597.

9. Hui Zhou, Shailesh Upreti, Natasha A. Chernova, Geoffroy Hautier, Gerbrand Ceder and M. Stanley Whittingham, "Iron and Manganese Pyrophosphates as Cathodes for Lithium-Ion Batteries", *Chem. Mater.* **2011**, *23* (2), pp. 293–300.

10. Hyungsub Kim, Seongsu Lee, Young-Uk Park, Haegyeom Kim, Jongsoon Kim, Seokwoo Jeon and Kisuk Kang, "Neutron and X-ray Diffraction Study of Pyrophosphate-Based $Li_{2-x}MP_2O_7$ (M = Fe, Co) for Lithium Rechargeable Battery Electrodes", *Chem. Mater.* **2011**, *23* (17), pp. 3930–3937.

11. John M. Clark, Shin-ichi Nishimura, Atsuo Yamada and M. Saiful Islam, "High Voltage Pyrophosphate Cathode: Insights into Local Structure and Lithium Diffusion Pathways", *Angew. Chem.* **2012**, *51*, pp. 13149–13153.

12. R.D. Shannon, "Revised effective ionic radii and systematic studies of interatomic distances in halides and chalcogenides", *Acta Cryst.* **1976**, *A32*, pp. 751–767.

13. Lyutsko and P. Frenkel`, *Russ. J. Inorg. Chem. (Engl. Transl.)* **1991**, *36*, pp. 930.

14. G.S. Gopalakrishna, M.J. Mahesh, K.G. Ashamanjari and Prasad J. Shashidhara, "Structure, thermal and magnetic characterization of hydrothermal synthesized $Li_2CuP_2O_7$ crystals", *Mater. Res. Bull.* **2008**, *43*, pp. 1171–1178.

15. Naoya Furuta, Shin-ichi Nishimura, Prabeer Barpanda and Atsuo Yamada, "Fe^{3+}/Fe^{2+} Redox Couple Approaching 4 V in $Li_{2-x}(Fe_{1-y}Mn_y)P_2O_7$ Pyrophosphate Cathodes", *Chem. Mater.* **2012**, *24* (6), pp. 1055–1061.

16. Anthony R. West, *Basic Solid State Chemistry*, 2nd Edition, Wiley, New York, **2000**, pp. 323.

17. Martin Winter and Jürgen O. Besenhard, "Electrochemical lithiation of tin and tin-based intermetallics and composites", *Electrochimica Acta*, **1999**, *45*, pp. 31–50.

18. Anton Nytén, Ali Abouimrane, Michel Armand, Torbjörn Gustafsson and John O. Thomas, "Electrochemical performance of Li_2FeSiO_4 as a new Li-battery cathode material", *Electrochem. Commun.* **2005**, *7*, pp. 156–160.

19. Anthony R. West, *SOLID STATE CHEMISTRY AND ITS APPLICATIONS*, 1st Edition, Wiley, New York, **1984**, pp. 51.

20. E.J. Abram, D.C. Sinclair and A.R. West, "Electrode-Contact Spreading Resistance Phenomena in Doped-Lanthanum Gallate Ceramics", *J. Electroceramics* **2001**, *7*, pp. 179–188.

21. C. Delacourt, L. Laffont, R. Bouchet, C. Wurm, J.B. Leriche, M. Morcrette, J.M. Tarascon and C. Masquelier, "Toward Understanding of Electrical Limitations (Electronic, Ionic) in $LiMPO_4$ (M = Fe, Mn) Electrode Materials", *J. Electrochem. Soc.* **2005**, *152* (5), pp. A913–A921.

22. Ruhul Amin, Palani Balaya and Joachim Maier, "Anisotropy of Electronic and Ionic Transport in $LiFePO_4$ Single Crystals", *Electrochem. Solid-State Lett*. **2007**, *10* (1), pp. A13–A16.

23. M. Li, A. Feteira and D.C. Sinclair, "Relaxor ferroelectric-like high effective permittivity in leaky dielectrics/oxide semiconductors induced by electrode effects: A case study of CuO ceramics", *J. Appl. Phys.* **2009**, *105*, pp. 114109.

24. D.C. Sinclair, "Characterization of Electro-materials using as Impedance Spectroscopy", *Bol. Soc. Esp. Cerám. Vidrio* **1995**, *34* [2], pp. 55–65.

25. M. Stanley Whittingham, Yanning Song, Samuel Lutta, Peter Y. Zavalij and Natasha A. Chernova, "Some transition metal (oxy)phosphates and vanadium oxides for lithium batteries", *J. Mater. Chem.* **2005**, *15*, pp. 3362–3379.

26. K. Rissouli, K. Benkhouja, J.R. Ramos-Barrado and C. Julien, "Electrical conductivity in lithium orthophosphates", *Mater. Sci. Eng. B* **2003**, *98*, pp. 185–189.

27. Mao Tamaru, Prabeer Barpanda, Yuki Yamada, Shin-ichi Nishimura and Atsuo Yamada, "Observation of the highest Mn^{3+}/Mn^{2+} redox potential of 4.45 V in a $Li_2MnP_2O_7$ pyrophosphate ", *J. Mater. Chem.* **2012**, *22*, pp. 24526–24529.

28. Prabeer Barpanda, Shih-ichi Nishimura and Atsuo Yamada, "High-Voltage Pyrophosphate Cathodes", *Adv. Energy Mater.* **2012**, *2*, pp. 841–859.

29. Morihiro Saito, Sosuke Yano, Akimasa Tasaka and Minoru Inaba, "Synthesis and Electrochemical Properties of Carbon-coated $Li_2FeP_2O_7$ for Li-ion Batteries", *Abstr. 896 – The Electrochem. Soc.* (**2012**).

30. Daisuke Shimizu, Shin-ichi Nishimura, Prabeer Barpanda and Atsuo Yamada, "Electrochemical Redox Mechanism in 3.5 V $Li_{2-x}FeP_2O_7$ ($0 \leq x \leq 1$) Pyrophosphate Cathode", *Chem. Mater.* **2012**, *24* (13), pp. 2598–2603.

CHAPTER IV

Aliovalent Doping in Lithium Iron Pyrophosphate ($Li_2FeP_2O_7$)

4.1 Introduction

The enhancement of efficient electron and ion transport is a critical issue to further improve lithium transition metal phosphate olivines as cathodes for lithium-ion batteries [1]. To date, lithium iron phosphate ($LiFePO_4$) is a leading contender due to its low cost, good cycle life, safety, and low toxicity. However, in comparison with other cathode materials, e.g. $LiCoO_2$ and $LiMn_2O_4$, the main inherent shortcomings of $LiFePO_4$ are its low electronic conductivity ($\sigma \sim 10^{-9}$ Scm^{-1}) and low Li ion diffusivity ($D_{Li} \sim 10^{-14}$ cm^2s^{-1}), which result in low working voltage and poor capacity at high rate discharge [2].

It is important for electrical and ionic conductivities to be optimized in cathode materials as they can dictate the overall cell properties, such as capacity and cycle life [3-4]. Assuming that diffusion influences charge-discharge rates, however, greater emphasis usually falls on ionic conductivity rather than electronic conductivity, because high ionic conductivity will allow the rapid diffusion of Li-ions into the cathode material. To date, many different approaches have been used to improve electronic and ionic conductivity of $LiFePO_4$, e.g. cation doping [5-6], carbon coating [7] and reducing particle size [8]. Nevertheless, efforts to improve the electrical conductivity of $LiFePO_4$ via aliovalent doping have not yet been unambiguously successful [9].

In 2002, Y.M. Chiang *et al.* showed that the electronic conductivity of $LiFePO_4$ can be drastically increased to $\sim 10^{-2}$ Scm^{-1} at room temperature, by a factor of more than 10^8 relative to the pure endmember, through selective doping with supervalent cations [5]. Subsequently, M. Armand et al. stated that the results seen by Chiang *et al.* are attributable to the presence of carbon for low-temperature samples, and to low-valence iron derivatives exhibiting semimetallic conductivity in samples fired above 750°C, instead of the desired intrinsic doping effect [10].

In 2004, L.F. Nazar *et al.* reported that $Li_{1-x}Zr_yMPO_4$ (M=Fe, Ni) compositions prepared under appropriate conditions have an enhanced conductivity of $\sim 10^{-3}$ and 10^{-5}

Scm^{-1} at 25°C for M=Fe and Ni due to a percolating nano-network of metal-rich phosphides within grain boundary regions [1]. In 2006, Delacourt *et al.* reported an unsuccessful attempt at doping $LiFePO_4$ with Nb to produced $Li_{1-x}Nb_xFePO_4$; instead, crystalline *β*–$NbOPO_4$ and/or an amorphous (Nb, Fe, C, O, P) coating around $LiFePO_4$ particles was formed [11]. In addition, the pure $LiFePO_4$ and $LiFePO_4$/*β*–$NbOPO_4$ composites have a similar total conductivity of ~10^{-9} Scm^{-1} at 25°C with an activation energy of ~0.65 eV [11]. However, M. Wagemaker *et al.* studied the incorporation of supervalent-cation dopants (Zr, Nb, Cr) in $LiFePO_4$ by neutron and X-ray diffraction in 2008 and showed that low levels of dopants are feasible in olivine structure up to the extent of 3 mol % for bulk materials [12].

In 2011, M.S. Whittingham *et al.* demonstrated that V^{3+} can be substituted into the iron site of $LiFePO_4$ at 550°C to form a $LiFe_{1-3y/2}V_yPO_4$ solid solution up to at least 10 mol%, which was confirmed by the linear change in lattice parameters with vanadium substitution. The excess positive charge of V^{3+} is compensated by vacancies on the Fe site. In addition, the doping of vanadium enhances the electrochemical properties of materials especially the high-rate discharge capacity [13].

The objective of this chapter is to attempt modification of the electrical properties of $Li_2FeP_2O_7$ by aliovalent doping, in particular with a view to increasing the level of lithium ion conductivity. Herein, we use Kröger–Vink notation [14] to indicate the charge compensation of supervalent doping by cation vacancies. Compositions shown in **Table 4.1** were prepared to study the ionic defect compensation Mechanism I-V; each case represents the dopant substituted on either the M1 or M2 sites and is charge-balanced by vacancies formed on the M1 or M2 sites. Note that the low-valent cation (Li) locates on the M1 site, and higher charged cation (Fe) on the M2 site. Al^{3+}, Zr^{4+}, and Nb^{5+}, are used as dopants, each of which has slightly smaller ionic radius than that of Li^+ (0.76 Å) and Fe^{2+} (0.78 Å). The phase content, lattice parameters, doping levels, and electrical properties are characterized in this research.

Table 4.1 Defect compensation mechanisms with M^{n+} substituted on M1 and/or M2 sites in $Li_2FeP_2O_7$. M^{n+} represents Al^{3+}, Zr^{4+}, or Nb^{5+} ions.

#	Composition Formula	Defect Compensation Mechanism [M=Nb]	Kröger-Vink Notation [M=Nb]
I	$Li_2Fe_{1-ny/2}M_y^{n+}P_2O_7$	$5\ Fe^{2+} \rightarrow 2\ Nb^{5+}$ Fe-substitution & Fe-vacancy	$5Fe_{Fe}^{\times} \rightarrow 2Nb_{Fe}^{\bullet\bullet\bullet} + 3V_{Fe}^{''}$
II	$Li_{2-(n-2)y}M_y^{n+}Fe_{1-y}P_2O_7$	$Fe^{2+} + 3\ Li^{+} \rightarrow Nb^{5+}$ Fe-substitution & Li-vacancy	$Fe_{Fe}^{\times} + 3Li_{Li}^{\times} \rightarrow Nb_{Fe}^{\bullet\bullet\bullet} + 3V_{Li}^{'}$
III	$Li_{2-ny}M_y^{n+}FeP_2O_7$	$5\ Li^{+} \rightarrow Nb^{5+}$ Li-substitution & Li-vacancy	$5Li_{Li}^{\times} \rightarrow Nb_{Li}^{\bullet\bullet\bullet\bullet} + 4V_{Li}^{'}$
IV	$Li_{2-y}M_y^{n+}Fe_{1-(n-1)y/2}P_2O_7$	$2\ Fe^{2+} + Li^{+} \rightarrow Nb^{5+}$ Li-substitution & Fe-vacancy	$2Fe_{Fe}^{\times} + Li_{Li}^{\times} \rightarrow Nb_{Li}^{\bullet\bullet\bullet\bullet} + 2V_{Fe}^{''}$
V	$Li_{2+(n-2)y}Fe_{1-(n-1)y}M_y^{n+}P_2O_7$	$4\ Fe^{2+} \rightarrow Nb^{5+} + 3\ Li^{+}$ Stoichiometric	$4Fe_{Fe}^{\times} \rightarrow Nb_{Fe}^{\bullet\bullet\bullet} + 3Li_{Fe}^{'}$

4.2 Synthesis

Samples were synthesized from stoichiometric amounts of Li_2CO_3, $FeC_2O_4 \cdot 2H_2O$, and $(NH_4)H_2PO_4$ by conventional solid-state reaction; the dopants Al, Zr, and Nb were added using $Al(OC_2H_5)_3$ (Aldrich, 97%), ZrO_2 (Aldrich, 99%), and Nb_2O_5 (Aldrich, 99.9%), respectively. The mixtures were ground for ~40 min in an agate mortar with acetone, pressed into pellets and decomposed at 350°C for 6 h and then heated 700°C for 12 h with a heating rate of 5 °C/min under nitrogen atmosphere. The phase content of the produced materials was determined using X-ray diffraction operated at 40 kV and 30 mA with Co $K_{\alpha 1}$ (1.78896 Å) radiation.

Impedance spectroscopy was utilized to measure the electrical properties; samples (0.2 g) were sintered in N_2 at 600°C for 12 hours with a heating rate of 5.0 °C/min. Gold or platinum electrodes were applied using an Emscope SC500 gold sputter-coater on each side of the pellet for 4 minutes with a current of 30 mA. High-temperature testing of the

Au-sputtered pellets in air was conducted using a Hewlett Packard 4192A impedance analyzer. Low frequency impedance response in N_2 was measured using a Solartron SI 1260 impedance analyzer with voltage amplitude and frequency range set at 0.1 V and 10^{-2}–10^{6} Hz, respectively.

4.3 Results

4.3.1 XRD Patterns and Crystallinity

Table 4.2 summarizes results of solid-state reaction following Mechanism I to V using different ionic radii of M^{n+} ions as dopants (Al^{3+}=0.54 Å; Zr^{4+}=0.72 Å; Nb^{5+}=0.64 Å), with a nominal atomic doping level of 5.0 %. Solid solution (S.S.) product was obtained in Nb-doped samples synthesized at 700°C for 12 hours in N_2 following II and IV; however, phase mixtures were present in all other samples. The intensity distribution of XRD patterns of Nb-doped $Li_2FeP_2O_7$ is similar to that of undoped $Li_2FeP_2O_7$, and assumed to be a monoclinic solid solution with space group $P2_1/c$, as shown in **Fig. 4-1(a)**. However, in particular, there is no clear shift toward higher or lower 2θ values in the positions of (-111) and (200) reflections, **Fig. 4-1(b)**, indicating probably no change in lattice parameters and unit cell volume.

Fig. 4-2 compares the relative intensity ratio, I(-111)/I(200), in two Nb-doped $Li_2FeP_2O_7$ samples; the value for $Li_{1.85}Nb_{0.05}Fe_{0.95}P_2O_7$ is similar to that of undoped one, but it slightly decreased for $Li_{1.95}Nb_{0.05}Fe_{0.9}P_2O_7$. The lattice parameter and unit cell volume of $Li_{1.85}Nb_{0.05}Fe_{0.95}P_2O_7$ and $Li_{1.95}Nb_{0.05}Fe_{0.9}P_2O_7$ are summarized in **Table 4-3**; in particular, the values of *a*, *b*, *c*, and *V* are similar within one *esd* in comparison to those in undoped $Li_2FeP_2O_7$.

Table 4.2 Phase results of the samples synthesized from Mechanism I to V with different M^{n+} ions.

M^{n+} / #	Al^{3+}	Zr^{4+}	Nb^{5+}
I	$Li_2FeP_2O_7$, $LiFeP_2O_7$, and $Li_9Al_3P_8O_{29}$	$Li_2FeP_2O_7$, $LiFeP_2O_7$, ZrP_2O_7, and $Li_9Fe_3P_8O_{29}$,	$Li_2FeP_2O_7$ and $NbPO_5$
II	$Li_2FeP_2O_7$ and $Li_9Al_3P_8O_{29}$	$Li_2FeP_2O_7$ and ZrP_2O_7	**$Li_{1.85}Nb_{0.05}Fe_{0.95}P_2O_7$ (II-N5)**
III	$Li_2FeP_2O_7$, $Fe_2P_2O_7$ and $Li_9Al_3P_8O_{29}$	$Li_2FeP_2O_7$, ZrP_2O_7, and $Fe_2P_2O_7$	$Li_2FeP_2O_7$, $Fe_2P_2O_7$ and Nb_2O_5
IV	$Li_2FeP_2O_7$ and $Li_9Al_3P_8O_{29}$	$Li_2FeP_2O_7$, $LiFeP_2O_7$, ZrP_2O_7, and $Li_9Fe_3P_8O_{29}$	**$Li_{1.95}Nb_{0.05}Fe_{0.9}P_2O_7$ (IV-N5)**
V	$Li_9Fe_3P_8O_{29}$, $Li_2FeP_2O_7$, $LiFeP_2O_7$, $Li_3Fe(PO_4)_3$, Al_2O_3	$Li_9Fe_3P_8O_{29}$, $Li_2FeP_2O_7$, ZrP_2O_7	$Li_9Fe_3P_8O_{29}$, $Li_2FeP_2O_7$, $NbPO_5$, and $LiFePO_4$
Ionic radius: Li^+=0.76 Å, Fe^{2+}=0.78 Å, Al^{3+}=0.54 Å, Zr^{4+}=0.72 Å, Nb^{5+}=0.64 Å			

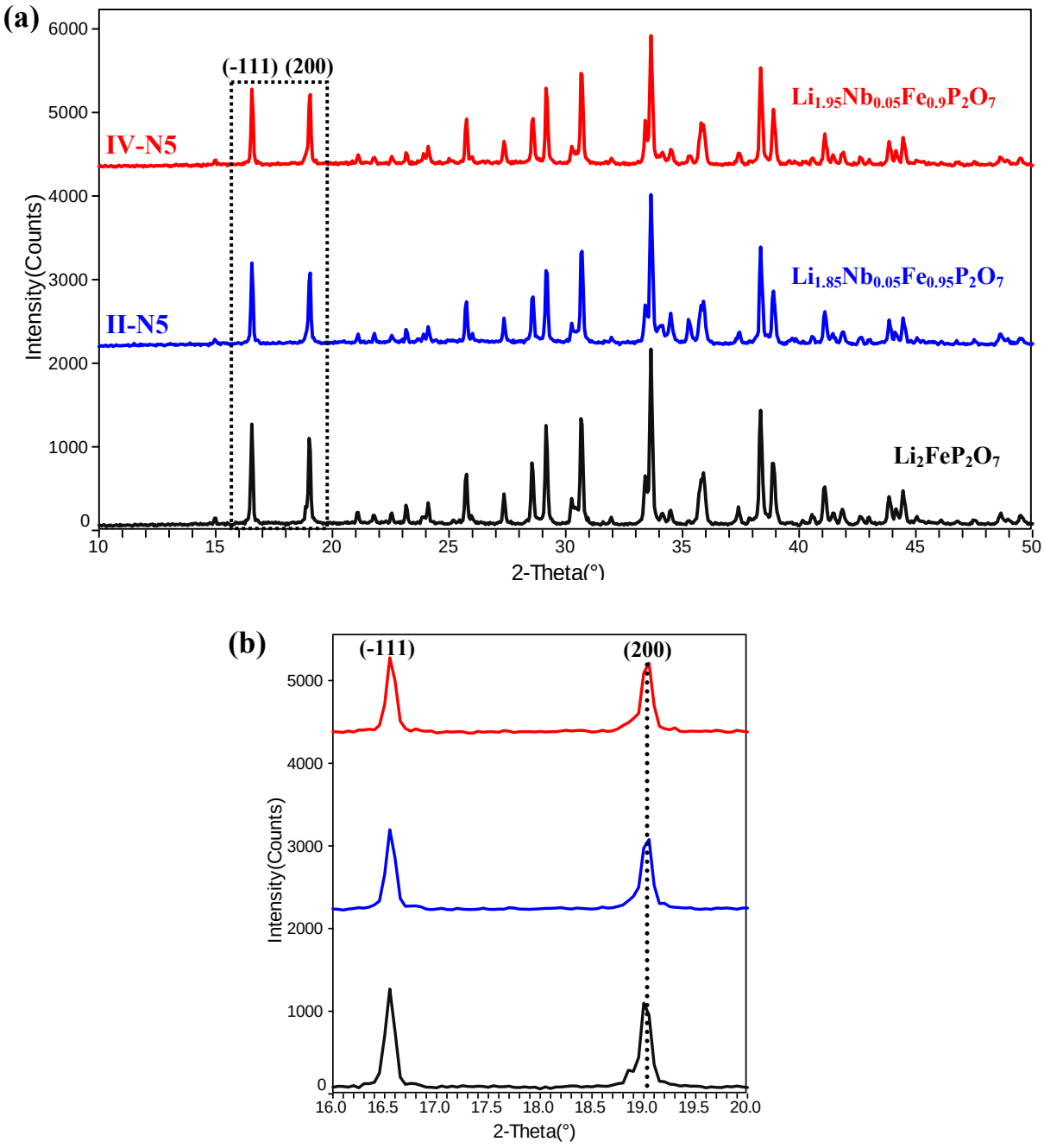

Figure 4-1 (a) XRD patterns of undoped and Nb-doped $Li_2FeP_2O_7$ according to Mechanisms II and IV; (b) magnified positions of (-111) and (200) peaks.

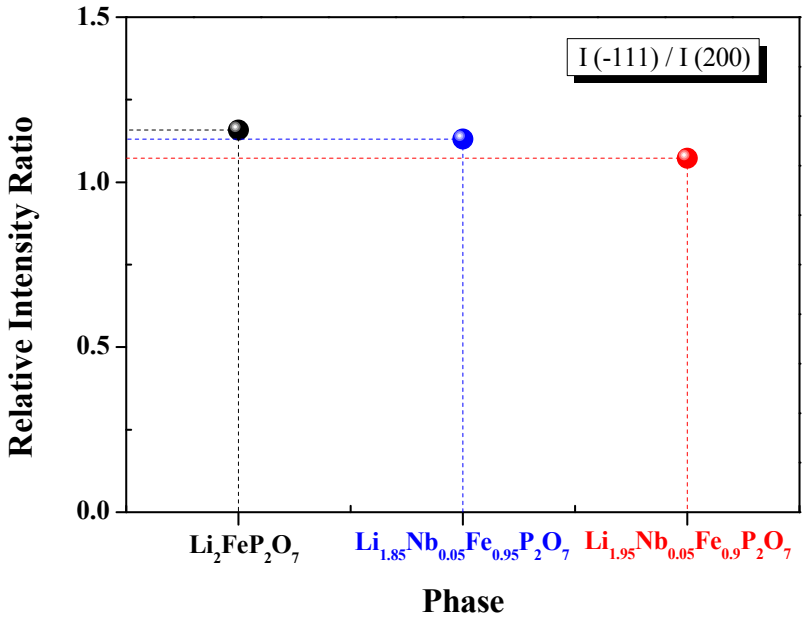

Figure 4-2 Relative intensity ratio, I(-111)/I(200), of XRD spectrum of pure and Nb-doped $Li_2FeP_2O_7$.

Table 4-3 Lattice parameters for undoped and Nb-doped $Li_2FeP_2O_7$ compounds with monoclinic symmetry.

Chemical formula	*a* (Å)	*b* (Å)	*c* (Å)	*β* (deg)	*V* (Å^3)
$Li_2FeP_2O_7$	11.019(3)	9.746(6)	9.791(8)	101.49(5)	1030.4(7)
$Li_{1.85}Nb_{0.05}Fe_{0.95}P_2O_7$	11.020(7)	9.751(7)	9.793(11)	102.51(7)	1031.3(11)
$Li_{1.95}Nb_{0.05}Fe_{0.9}P_2O_7$	11.012(4)	9.749(5)	9.804(3)	101.56(3)	1031.2(4)

4.3.2 Morphology and Chemical Composition

SEM/EDS were used to evaluate the morphology and densification as well as composition of the Nb-doped $Li_2FeP_2O_7$ pellets sintered at 600°C for 12 h in N_2, i.e. $Li_{1.85}Nb_{0.05}Fe_{0.95}P_2O_7$ (II-N5) and $Li_{1.95}Nb_{0.05}Fe_{0.9}P_2O_7$ (IV-N5). The EDS spectra of the molar ratio of Fe and P in samples are given in **Table 4-4**. The average observed values of Fe/P ratio are of 0.472 for II-N5, and of 0.446 for IV-N5, which are close to their individual theoretical value of 0.475 and 0.45, respectively.

Table 4-4 Molar ratio of expected and EDS results of Nb-doped $Li_2FeP_2O_7$.

Stoiciometry	Theoretical value of Fe/P molar ratio	Average value of EDS results of Fe/P molar ratio
$Li_{1.85}Nb_{0.05}Fe_{0.95}P_2O_7$	0.475	0.472
$Li_{1.95}Nb_{0.05}Fe_{0.9}P_2O_7$	0.450	0.446

The presence of Nb was visualized by electron back scatter diffraction (EBSD) mapping analysis. **Fig. 4-3 (a)** shows the SEM picture of the II-N5 pellet sintered at 600°C for 12 h in N_2; aggregated particles with size of ~10 μm are observed, however, other area of smaller than 5 μm are specified by inserted circle. The EDS spectra **(c)** indicate that the lighter regions of EBSD image in **(b)** are the evidence of Nb in II-N5, in which the darker ones correspond to Nb-free particles, **(d)**. Elemental mapping shows a homogenous distribution of both phosphorus and iron, **Fig. 4-4 (b)** and **(c)**. Nb map, specifically, was observed at the brighter green dot in **(d)**.

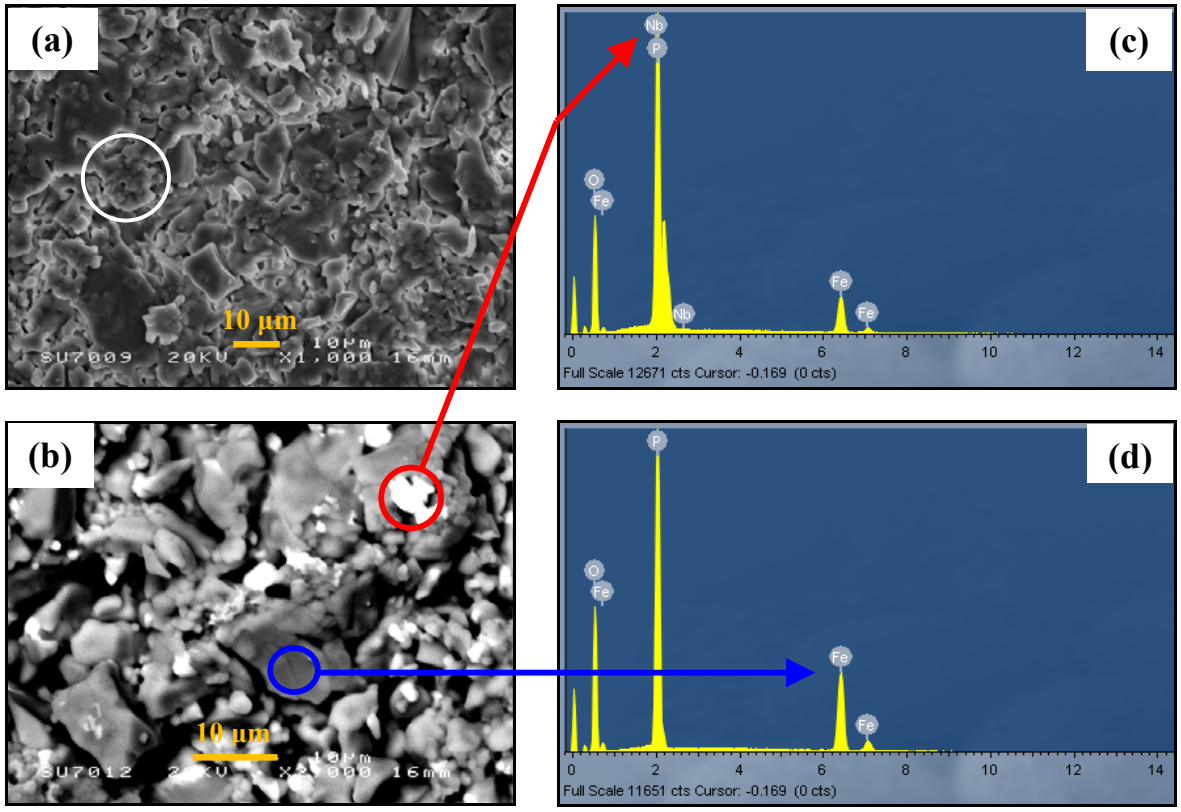

Figure 4-3 (a) SEM and (b) EBSD micrographs of $Li_{1.85}Nb_{0.05}Fe_{0.95}P_2O_7$; (c) and (d) EDS analyses for the particles.

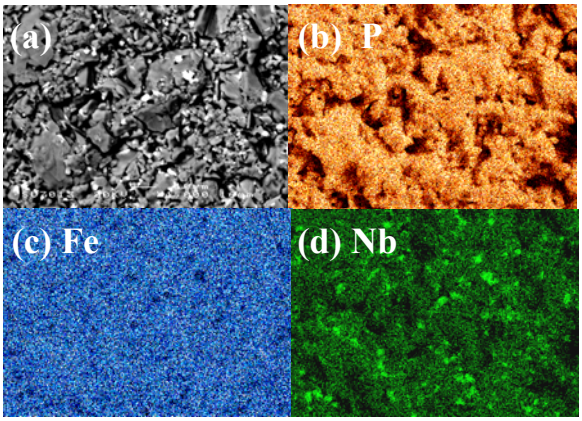

Figure 4-4 (a) EBSD image of $Li_{1.85}Nb_{0.05}Fe_{0.95}P_2O_7$ and its elemental mapping referred to (b) P, (c) Fe, and (d) Nb distribution in sample.

Fig. 4-5 (a) shows the surface image of the IV-N5 pellet sintered at 600°C for 12 h in N_2 atmosphere. Most of the particles have shapes of aggregated spheres and two average particle size of smaller 10 μm in solid-circled area, and of larger than 10 μm in dash-circled area. The EDS spectra **(c)** confirm that the bright regions of EBSD image in **(b)** indicate the presence of Nb in IV-N5 whereas the darker ones corresponding to Nb-free particles, **(d)**. Elemental maps of P and Fe distribution are well-spread, **Fig. 4-6 (b)** and **(c)**, and the Nb dopants are clearly mapped in the brighter area, **(d)**.

SEM shows both samples have a poorly sintered microstructure, and the measured density of II-N5 and IV-N5 is 2.3925 g/cm^3 and 2.3833 g/cm^3, respectively, consistent with a final density ~ 76% and 76.4% of each theoretical X-ray value. In short, the results of EDS mapping probably shown that the Nb dopants are not present unifomily in $Li_{1.85}Nb_{0.05}Fe_{0.95}P_2O_7$ and $Li_{1.95}Nb_{0.05}Fe_{0.9}P_2O_7$, respectively, and therefore, do not form a complete solid solution, which is different from the observation by XRD patterns.

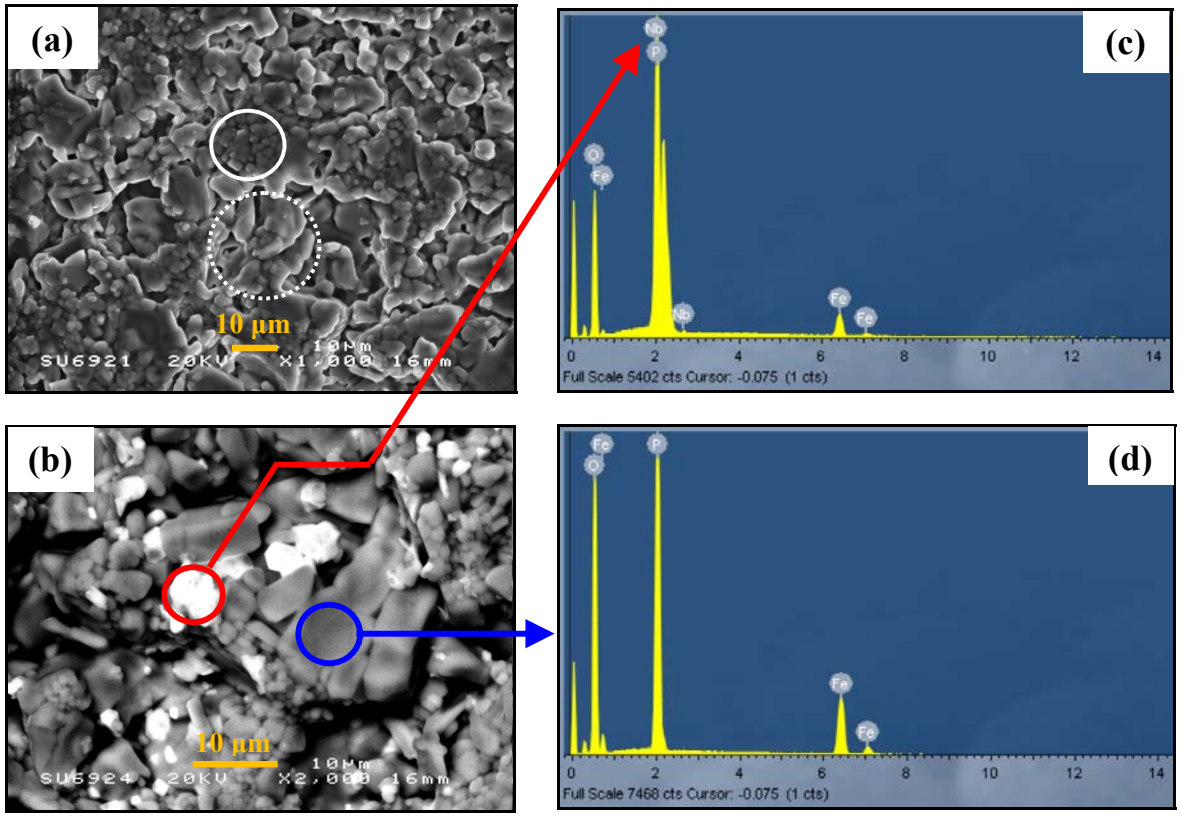

Figure 4-5 (a) SEM and (b) EBSD micrographs of $Li_{1.95}Nb_{0.05}Fe_{0.9}P_2O_7$; (c) and (d) EDS analyses for the particles.

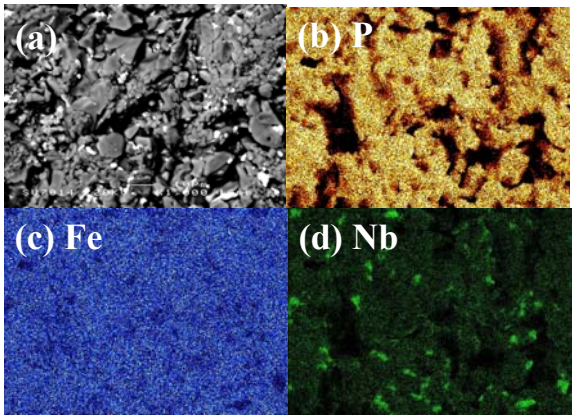

Figure 4-6 (a) EBSD image of $Li_{1.95}Nb_{0.05}Fe_{0.9}P_2O_7$ and its elemental mapping referred to (b) P, (c) Fe, and (d) Nb distribution in sample.

4.3.3 Electrical Properties

Z* plots at 200°C of $Li_2FeP_2O_7$ and two Nb-doped samples in air using sputtered-Au electrodes are presented in **Fig. 4-7(a)**. They show a high-frequency non-ideal semicircle of resistance R_1 (dash-arrowed) and a low frequency flat tail and inclined spike for II-N5 and IV-N5, respectively (solid-arrowed). Specifically, the resistivity of IV-N5, R ~0.23 MΩcm, is lower than that of others. Capacitance, C', data as a function of frequency are observed in **(b)**, which show one well-resolved plateau. A capacitance plateau at higher frequency has value close to 1.0 $pFcm^{-1}$ for $Li_2FeP_2O_7$ and IV-N5, which are slightly lower than that of II-N5 without a frequency-independent plateau.

Conductivity, Y', data as a function of frequency are shown in **(c)**; a dispersion is observed at high frequencies and without a frequency-independent *dc* conductivity plateau for Nb-doped samples. A small decrease in conductivity at lower frequencies was found in IV-N5 perhaps due to an electrode or grain boundary effect (arrowed), nevertheless, a continuously decreasing conductivity without frequency-independence is observed in II-N5.

Combined Z'' and M'' spectroscopic plots show maxima of M'' and Z'' peaks which are not exactly coincident, but a long tail at low frequencies in the Z'' peak of Nb-doped $Li_2FeP_2O_7$ may be associated with an interfacial effect, as shown in **(d)**. In addition, the M'' peaks show a high frequency tail as a consequence of the non-ideal behaviour. More results of IS spectra of II-N5 and IV-N5 for a wide range of temperatures are given in the appendices, **Figs. A4-1~A4-2**.

The conductivity data of Nb-doped $Li_2FeP_2O_7$ pellets with Au electrodes are shown in **Fig. 4-8**; a set of parallel lines is observed with similar activation energies. Specifically, IV-N5 has Ea ~0.52 eV, which is slightly lower than that of $Li_2FeP_2O_7$ (0.57 eV) and II-N5 (0.58 eV). To verify the inclined spike in Z* plots, for II-N5 and IV-N5, low frequency impedance tests in the frequency range of 10^{-2} to 10^7 Hz were carried out to verify the temperature effect to get an insight into Nb-doped $Li_2FeP_2O_7$, as described in the next section.

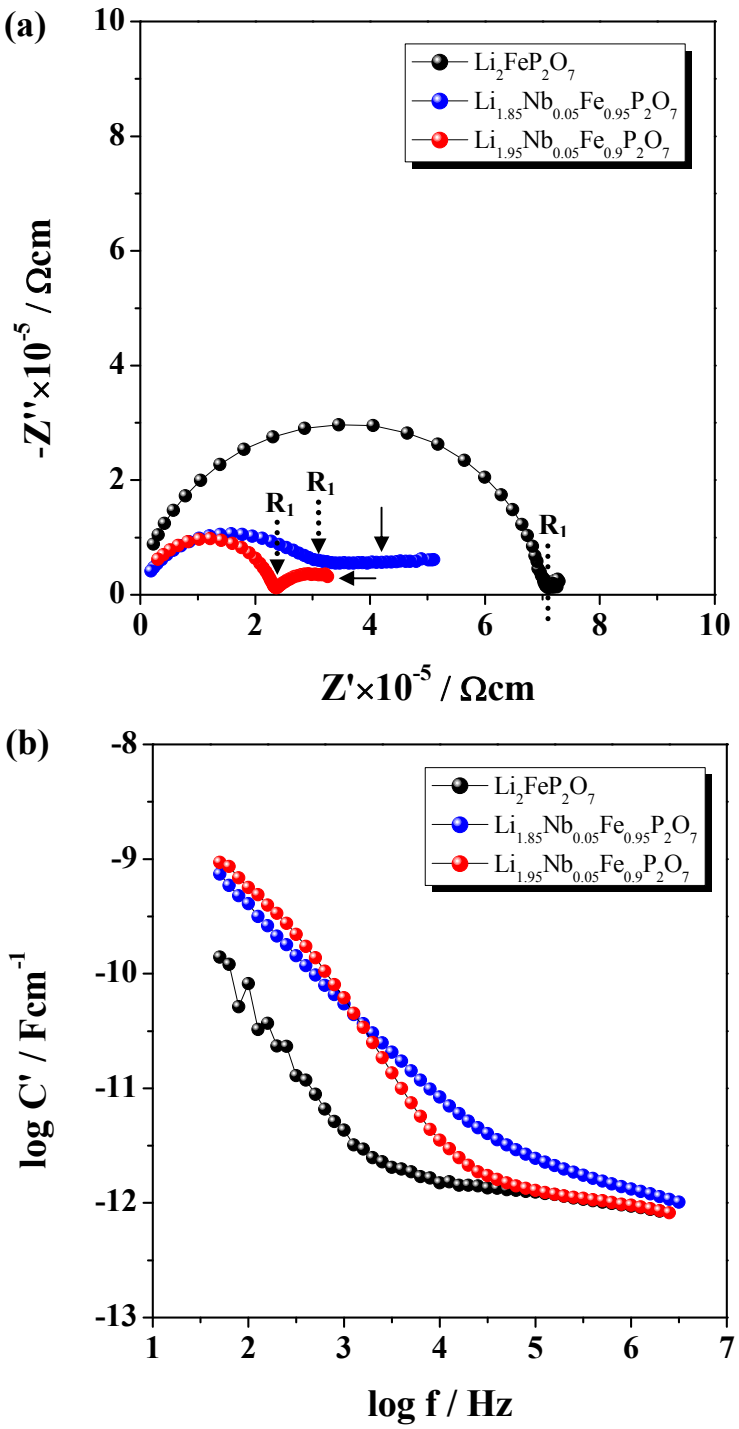

Figure 4-7 $Li_2FeP_2O_7$, $Li_{1.85}Nb_{0.05}Fe_{0.95}P_2O_7$ and $Li_{1.95}Nb_{0.05}Fe_{0.9}P_2O_7$: (a) Impedance complex plane plots, Z*, (b) spectroscopic plots of capacitance, C', (c) spectroscopic plots of admittance, Y', and (d) Z''/M'' spectroscopic plots at 200°C in air.

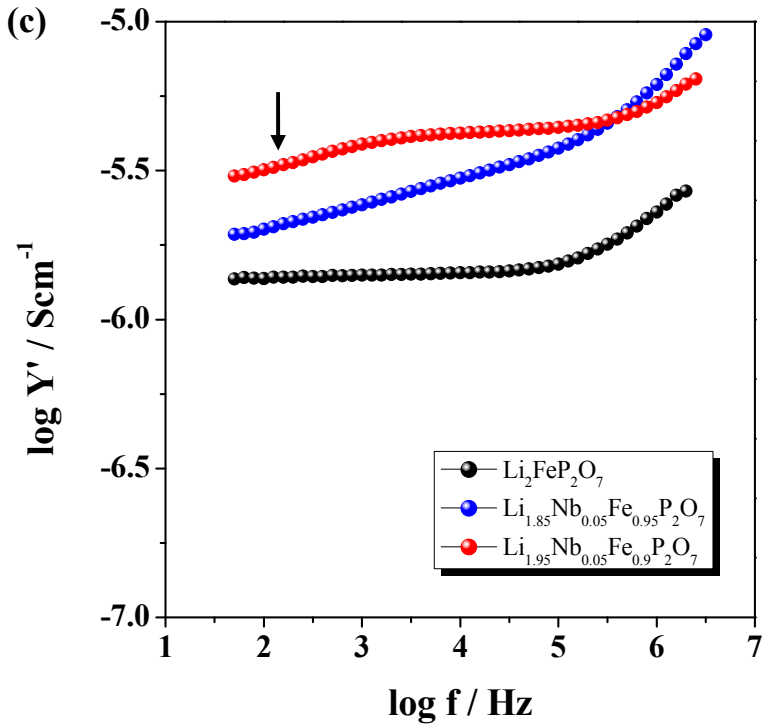

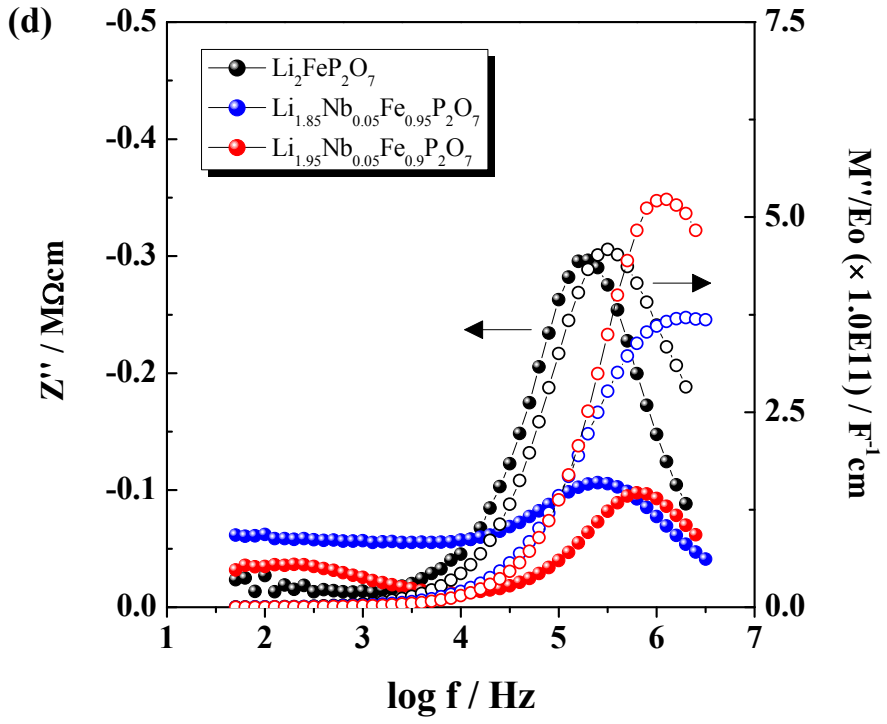

Figure 4-7 ***(continued)***

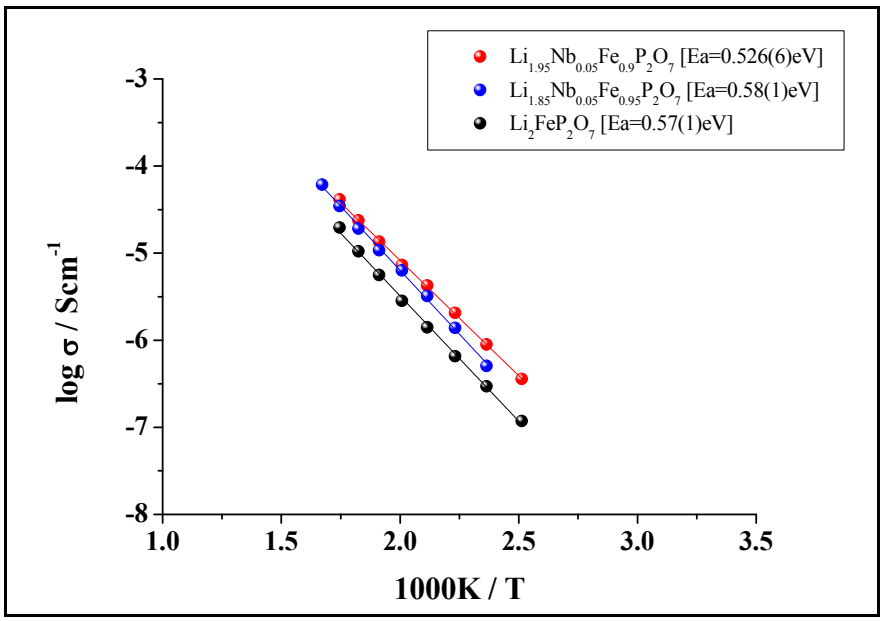

Figure 4-8 Bulk conductivity (R_b^{-1}) Arrhenius plots for $Li_2FeP_2O_7$, $Li_{1.85}Nb_{0.05}Fe_{0.95}P_2O_7$, and $Li_{1.95}Nb_{0.05}Fe_{0.9}P_2O_7$.

4.3.4 Low Frequency Measurement

(i) $Li_{1.85}Nb_{0.05}Fe_{0.95}P_2O_7$

Z* plots of $Li_{1.85}Nb_{0.05}Fe_{0.95}P_2O_7$ with Au-sputtered electrodes at various temperatures are given in **Fig. 4-9**. At low temperatures of 150°C and 200°C, they consist of a high-frequency non-ideal semicircle of resistance (R_1) and a low-frequency arc of resistance (R_2), **(a)** and **(b)**. At temperatures above ~ 250°C, the high frequency semicircle is increasingly displaced to frequencies outside the measurement range, and both R_1 and R_2 are still identified, **(c)** and **(d)**. The R_1 and R_2 values decrease as the temperature increases.

C' plots as a function of frequency over a wide temperature range can be observed from **Fig. 4-10(a)**, in which one well-resolved plateau at high frequencies, attributed to the bulk response with a capacitance value of ≈5 $pFcm^{-1}$, is seen. The capacitance at low frequencies increases up to ≈10^{-6} Fcm^{-1}, a typical double layer interface value, as the temperature increases above 250°C.

Conductivity, Y', data as a function of frequency are presented in **Fig. 4-10(b)**. At a lower temperature of 150°C, the Y' plot shows an approximately frequency independent plateau below ~10^4 Hz, and a high frequency dispersion, above ~10^5 Hz. As the temperature increases, the data at lower frequencies present an apparently frequency-independent *dc* conductivity plateau at higher temperatures above 250°C, and the high-frequency dispersion shifts out of the frequency window.

Fig. 4-11 shows a linear Arrhenius response with activation energy of R_2, 0.542(8) eV, which is slightly lower than that of bulk R_1, 0.554(5) eV, for $Li_{1.85}Nb_{0.05}Fe_{0.95}P_2O_7$ with Au electrode. The total conductivity, $R_1^{-1} + R_2^{-1}$, is thought to be limited by larger R_1 resistances.

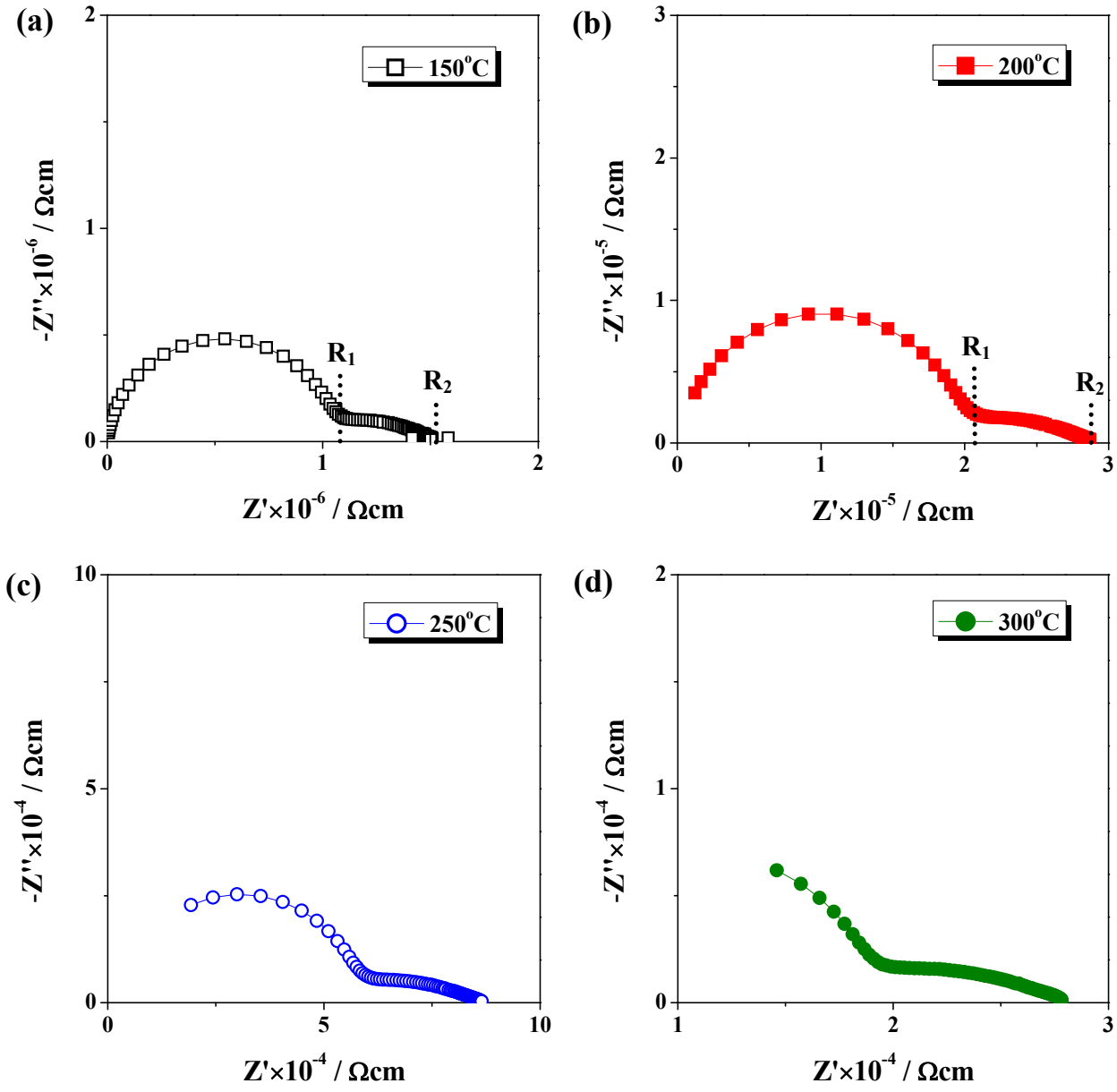

Figure 4-9 $Li_{1.85}Nb_{0.05}Fe_{0.95}P_2O_7$: Impedance complex plane plots, Z*, at (a) 150°C to (d) 300°C in N_2.

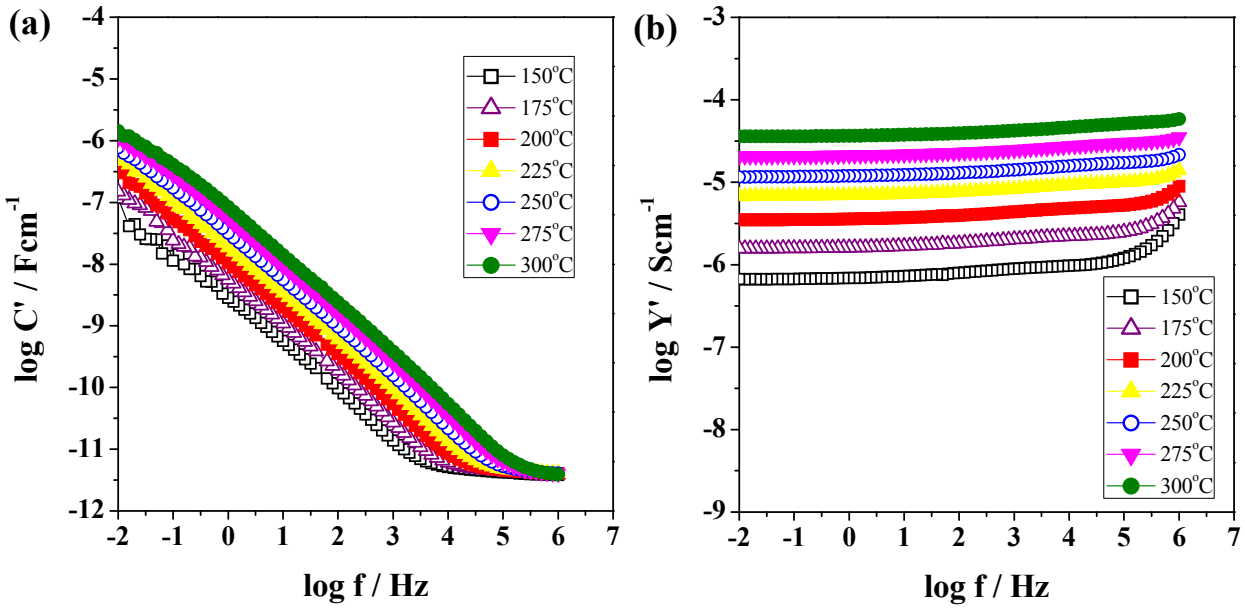

Figure 4-10 $Li_{1.85}Nb_{0.05}Fe_{0.95}P_2O_7$ (Au electrodes): (a) spectroscopic plots of capacitance, C', (b) spectroscopic plots of admittance, Y', at different temperatures of 150°C to 300°C in N_2.

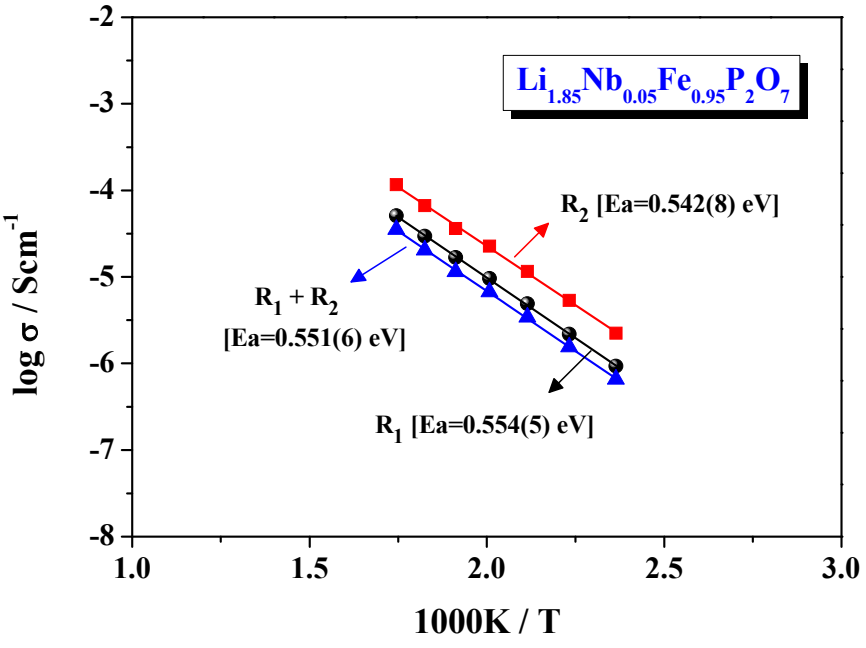

Figure 4-11 Arrhenius plots of R_1^{-1}, R_2^{-1}, and total conductivity R_T^{-1} for $Li_{1.85}Nb_{0.05}Fe_{0.95}P_2O_7$ pellet sintered at 600°C with Au electrodes.

(ii) $Li_{1.95}Nb_{0.05}Fe_{0.9}P_2O_7$

Impedance complex plane, Z* plots, **Fig. 4-12**, show the total resistivity of $Li_{1.95}Nb_{0.05}Fe_{0.9}P_2O_7$ pellet with Pt electrodes at different measuring temperatures in N_2. At lower temperatures of 150°C and 200°C, a nearly ideal first semicircle of resistance R_1 is found with associated capacitance of ~4 $pFcm^{-1}$ calculated from $\omega RC=1$ at the semicircle maximum, and, therefore, attributed to bulk contributions, see **(a)** and **(b)**. A well-resolved second arc of resistance R_2 at low frequencies over the temperature range 150~300 °C was observed but no evidence for a Warburg impedance or inclined spike which could result from the partial blockage of ionic species at the sample-electrode interface **(a-d)**.

The C' spectroscopic plots as a function of frequency over the temperature range 150°C to 300°C can be observed from **Fig. 4-13(a)**, where a high frequency plateau with a value of close to ~5.0 $pFcm^{-1}$ represents the bulk response in sample. As the temperature increases, the capacitance at lower frequencies increase up to approximately ~10^{-6} Fcm^{-1} and is associated with the sample-electrode interfacial response.

Conductivity, Y', data as a function of frequency are shown in **Fig. 4-13(b)** for the same temperature range as in **Fig. 4-13(a)**. The Y' data show a dispersion at high frequencies and present a nearly frequency-independent *dc* conductivity plateau at lower frequencies. At T > 250°C, Y' spectra present a frequency-independent *dc* conductivity plateau.

Fig. 4-14 shows a linear Arrhenius response with activation energy of R_2, 0.574(7) eV, which is nearly identical to the bulk R_1 of 0.575(3) eV, and to total R_T of 0.575(4) eV, for $Li_{1.95}Nb_{0.05}Fe_{0.9}P_2O_7$ with Pt-sputtered electrode. The total conductivity of $R_1^{-1} + R_2^{-1}$ is dominated by large R_1 resistances.

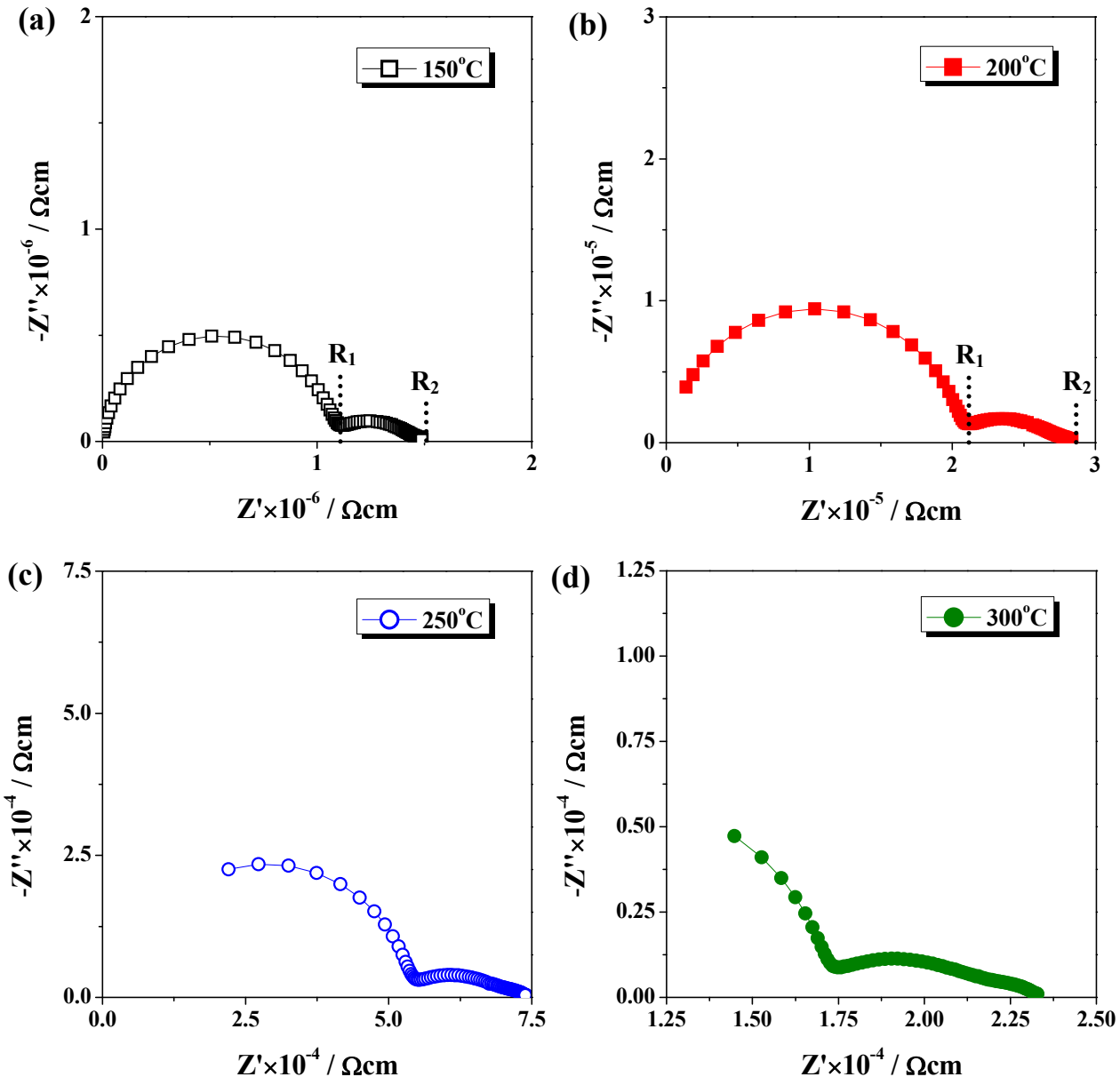

Figure 4-12 $Li_{1.95}Nb_{0.05}Fe_{0.9}P_2O_7$: Impedance complex plane plots, Z*, at (a) 150°C to (d) 300°C in N_2.

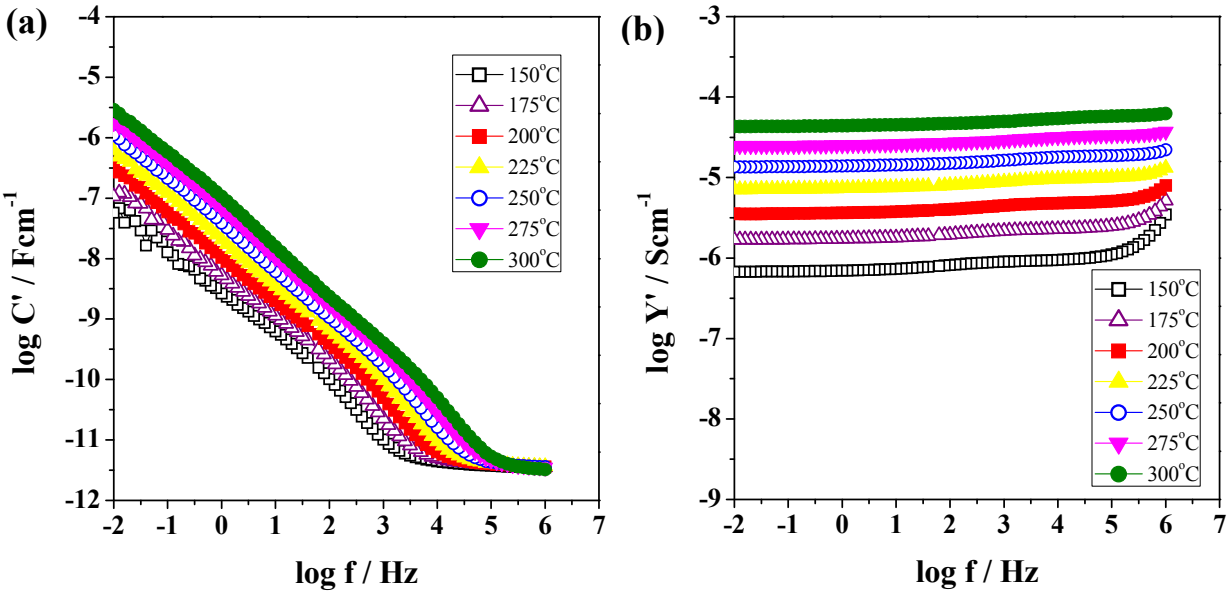

Figure 4-13 $Li_{1.95}Nb_{0.05}Fe_{0.9}P_2O_7$ (Pt electrodes): (a) spectroscopic plots of capacitance, C', (b) spectroscopic plots of admittance, Y', at different temperatures of 150°C to 300°C in N_2.

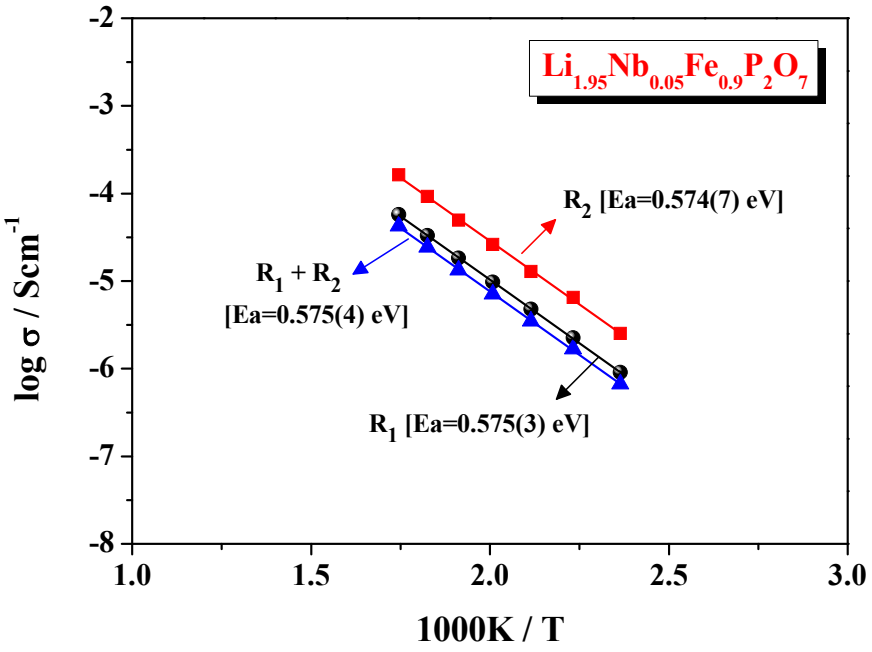

Figure 4-14 Arrhenius plots of R_1^{-1}, R_2^{-1}, and total conductivity R_T^{-1} for $Li_{1.95}Nb_{0.05}Fe_{0.9}P_2O_7$ pellet sintered at 600°C with Pt electrodes.

4.4 Discussion

4.4.1 XRD Patterns and Crystallinity

XRD results appear to show that supervalent dopant, Nb^{5+}, can be substituted into M1 or M2 sites of $Li_2FeP_2O_7$ synthesized at 700°C in N_2 to form $Li_{1.85}Nb_{0.05}Fe_{0.95}P_2O_7$ and $Li_{1.95}Nb_{0.05}Fe_{0.9}P_2O_7$ solid solutions following mechanism II and IV, respectively. The doping concentration of Nb, however, is limited by a small amount of 5% to form a solid solution. Mainly secondary phases containing $Li_4P_2O_7$, $Fe_2P_2O_7$ and $NbO(PO_4)$ are characterized as the Nb concentration increased up to 10% in both samples. Lattice parameters and unit cell volume of Nb dopant at 5% in $Li_2FeP_2O_7$ stay unchanged within errors as compared to the undoped one. Similar results have been found in Nb-doped $LiFePO_4$ using the same charge compensation mechanism as II and IV from Chiang's group [15]. Nevertheless, Zhang's results show a slightly decreased cell volume in $Li_{1.99}Nb_{0.01}FePO_4$ compound because the ionic radius of Nb^{5+} (0.64 Å) is less than that of Li^+ (0.76 Å) [16].

The value of I(-111)/I(200) ratio of undoped $Li_2FeP_2O_7$ (1.158) is slightly higher than that of Nb-doped one, which reduced from 1.131 to 1.073 as Nb occupancy changed from Fe to Li site. Kim's simulated results showed that the relative intensity ratio of I(-111)/I(200) in $Li_{2-x}FeP_2O_7$ strongly depended on the partial occupancy of Fe and Li sites [17]. Herein, it is thought whether the Nb doping could inhibit formation of the antisite defect of between LiO_5 and FeO_5 in $Li_2FeP_2O_7$, i.e. Fe partial occupancy in Li sites and vise versa. To confirm Nb-doping, further studies are required, e.g. site occupancies need to be determined. The defect can be described by Kröger-Vink notation, Equation 4.1:

$$Li_{Li}^{\times} + Fe_{Fe}^{\times} \rightarrow Li_{Fe}^{'} + Fe_{Li}^{\bullet} \qquad (4.1)$$

Modeling work from Islam's group claimed that supervalent doping by, e.g. V^{5+} and Nb^{5+}, appears unfavorable on both Li^+ and Fe^{2+} sites by calculating dopant solution energies as elucidated in **Fig. 4-15**; in general, the higher energy of more than 2 eV, the less favorable is doping [18]. Isovalent doping, e.g. Mn^{2+}, Co^{2+}, and Cu^{2+} (red-circled) on the Fe^{2+} sites appears favorable due to their lower energies and without the need for charge

compensation. This is consistent with results of the $Li_2Fe_{1-x}Mn_xP_2O_7$ and $Li_2Fe_{1-y}Co_yP_2O_7$ solid solutions presented in chapter III.

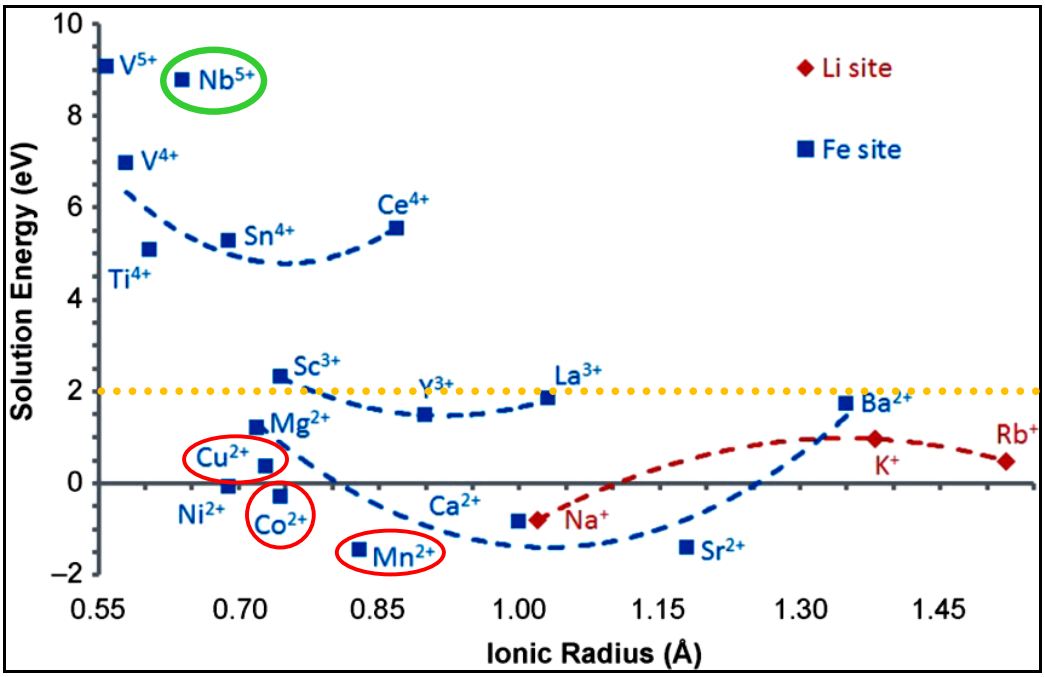

Figure 4-15 Calculated dopant solution energies as a function of ionic radius for $Li_2FeP_2O_7$ [18].

In **Fig. 4-15**, it is suggested these ions are likely to be doped below very low concentration of less 3 %. However, our experimental results from XRD indicated that 5 % Nb doping in $Li_2FeP_2O_7$ is probably feasible with compensation mechanisms of Li^+ and Fe^{2+} vacancies on substitution of Fe and Li sites, respectively. Examples can be represented using Kröger-Vink notation, Equations 4.2–4.2:

Fe site – Li^+ vacancy: $$\frac{1}{2}Nb_2O_5 + Li_{Li}^{\times} + 2Fe_{Fe}^{\times} \rightarrow Nb_{Fe}^{\bullet\bullet\bullet} + 3V_{Li}^{'} + \frac{1}{2}Li_2O + 2FeO \qquad (4.2)$$

Li site – Fe^{2+} vacancy: $$\frac{1}{2}Nb_2O_5 + 2Li_{Li}^{\times} + \frac{3}{2}Fe_{Fe}^{\times} \rightarrow Nb_{Li}^{\bullet\bullet\bullet\bullet} + 2V_{Fe}^{''} + Li_2O + \frac{3}{2}FeO \qquad (4.3)$$

A ternary pyrophosphate composition triangle of the $Li_4P_2O_7$–$Fe_2P_2O_7$–$Nb_{4/5}P_2O_7$ system is given in **Fig. 4-16**. All 5 mechanisms in **Table 4-1** can be represented on this triangle, as follows. Herein, it is considered to check whether there is a solid solution between II and IV, i.e. 4Li + 3Fe → 2Nb (see yellow region).

(I) $Li_2Fe_{1-\frac{5x}{2}}Nb_xP_2O_7$: $x = \frac{2}{5} \rightarrow Li_2Nb_{\frac{2}{5}}P_2O_7$

(II) $Li_{2-3x}Nb_xFe_{1-x}P_2O_7$: $x = \frac{2}{3} \rightarrow Fe_{\frac{1}{3}}Nb_{\frac{2}{3}}P_2O_7$

(III) $Li_{2-5x}FeNb_xP_2O_7$: $x = \frac{2}{5} \rightarrow FeNb_{\frac{2}{5}}P_2O_7$

(IV) $Li_{2-x}Fe_{1-2x}Nb_xP_2O_7$: $x = \frac{1}{2} \rightarrow Li_{\frac{3}{2}}Nb_{\frac{1}{2}}P_2O_7$

(V) $Li_{2+3x}Fe_{1-4x}Nb_xP_2O_7$: $x = \frac{1}{4} \rightarrow Li_{\frac{11}{4}}Nb_{\frac{1}{4}}P_2O_7$

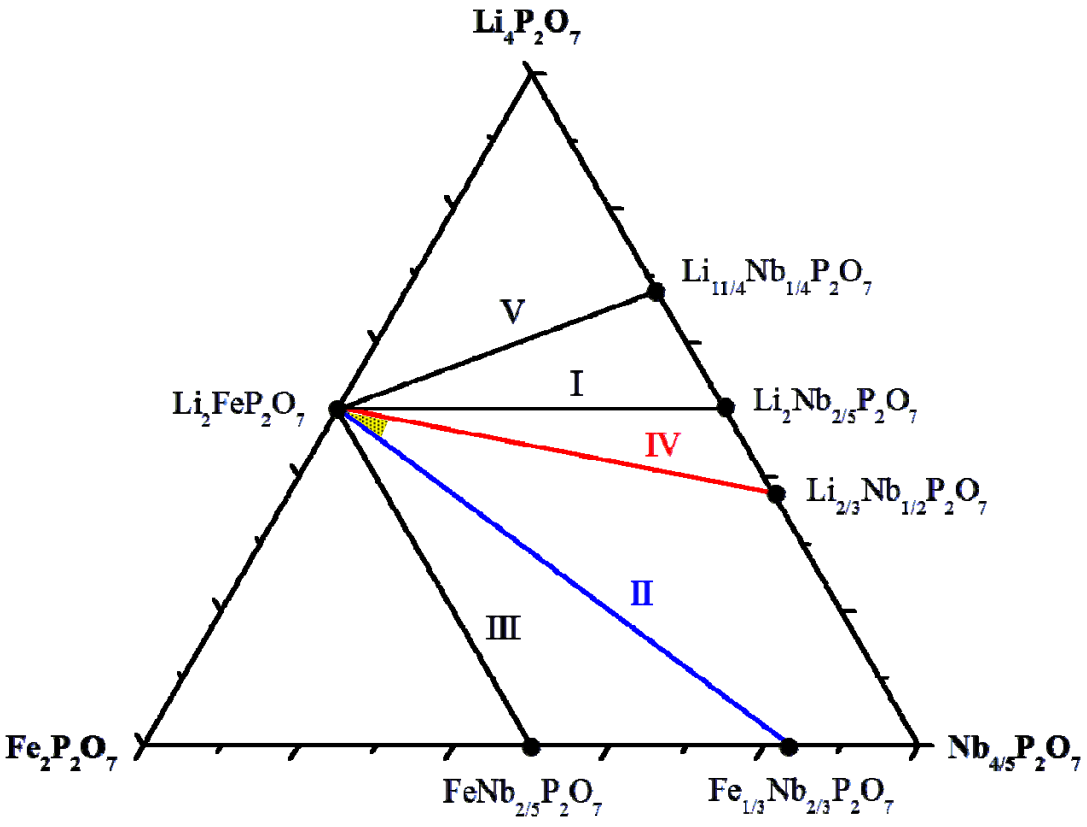

Figure 4-16 The ternary pyrophosphate composition triangle: $Li_4P_2O_7$–$Fe_2P_2O_7$–$Nb_{4/5}P_2O_7$.

4.4.2 Element Analysis and Morphology

The EDS results of $Li_{1.85}Nb_{0.05}Fe_{0.95}P_2O_7$ and $Li_{1.95}Nb_{0.05}Fe_{0.9}P_2O_7$ samples confirm Nb doped in $Li_2FeP_2O_7$ is feasible and with each good satisfactory molar ratios of Fe/P, 0.472 and 0.446, consistent with the expected theoretical values. However, the elemental mapping exhibit that the Nb dopants are not distributed homogeneously in both samples with 5% Nb. Therefore, it is suggested that the Nb doping concentration in $Li_2FeP_2O_7$ should be less than 5%, and the extra impurity phases could not be detected due to the XRD sensitivity of ca. 3% limitation.

The SEM images show porous and inhomogeneous grain size microstructure in both Nb-doped $Li_2FeP_2O_7$ pellets with lower relative density close to ~76 %. Higher sintering temperature of 700°C for densification, however, is not suggested due to the thermal expansion in Nb-doped samples, resulting in a spherical-shaped and hollow pellet.

4.4.3 Electrical Properties

Conductivity data measured in air show that the doping of niobium merely enhances the conductivity of $Li_2FeP_2O_7$ by a factor of ~2, according to the charge-compensation mechanism in II and IV without altering the Fe^{2+} valence state and hence is unlikely to enhance electronic conductivity [18]. However, the reasons for slightly increased conductivity in both of $Li_{1.85}Nb_{0.05}Fe_{0.95}P_2O_7$ and $Li_{1.95}Nb_{0.05}Fe_{0.9}P_2O_7$, **Fig. 4-8**, are still difficult to confirm. Modeling calculations from Islam's group reported the lowest energy pathways for Li diffusion are parallel to the *b*- and *c*- axes with energy barriers of 0.4 eV, but a higher value of 0.73 eV along *a*-axis [18], as shown in **Fig. 4-17**.

Low frequency impedance data measured in N_2, Z* plots of $Li_{1.85}Nb_{0.05}Fe_{0.95}P_2O_7$ and $Li_{1.95}Nb_{0.05}Fe_{0.9}P_2O_7$, show a high frequency arc of R_1 with an associated capacitance value ~5 $pFcm^{-1}$, which is confirmed to be bulk contributions for both samples. In addition, a second disordered semicircle of R_2 at low frequency with a capacitance of ~1 μFcm^{-1} is obtained, probably due to an electrode effect. At high temperatures, no blocking or Warburg spike attributed to ionic conduction behavior at low frequencies was observed,

indicating that the conduction mechanism is primarily electronic instead of ionic. The capacitance of the grain boundary response, 10^{-8}~10^{-11} $pFcm^{-1}$, in these two samples, **Fig. 4-10(a)** and **4-13(a)** is not well-resolved at intermediate frequencies over the temperature range 150~300 °C. The resistance of the secondary low frequency arc slightly decreases with applying a higher *dc* bias of 3 V (not shown), which means the height of a Schottky barrier could be decreased for electron transfer across the interface.

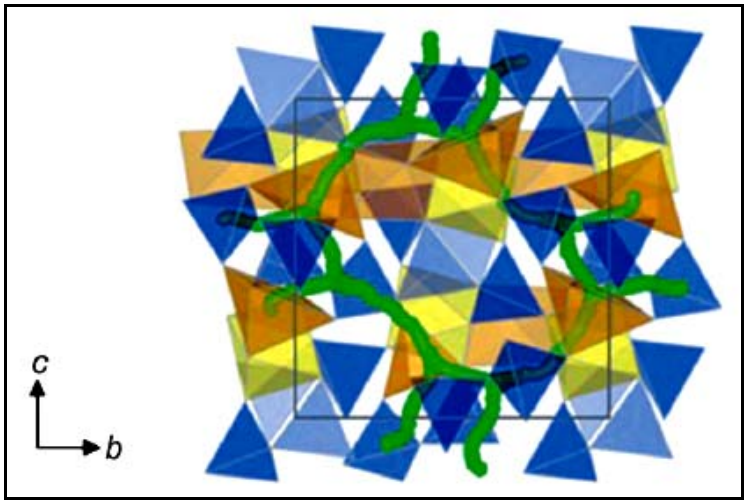

Figure 4-17 Calculated paths for long-range Li^+ migration along the *b*- and *c*-axis directions; simulations indicate quasi-2D transport and nonlinear pathways [18].

4.5 Conclusions

The effect of aliovalent dopants (Al^{3+}, Zr^{4+}, Nb^{5+}) on phase composition and/or electrical properties were studied and compared with that of undoped $Li_2FeP_2O_7$ via a conventional solid-state method. Our results showed Al and Zr are not feasible to substitute into $Li_2FeP_2O_7$ structure, following different doping mechanism of I to V. Only ≤ 5% Nb^{5+} can be substituted into $Li_2FeP_2O_7$ synthesized at 700°C in N_2 to form homogenous sold solutions, $Li_{1.85}Nb_{0.05}Fe_{0.95}P_2O_7$ and $Li_{1.95}Nb_{0.05}Fe_{0.9}P_2O_7$, following II and IV, respectively. In general, lattice parameters and unit volume are not changed in Nb-doped compounds and the distribution of Nb dopants in samples is confirmed by EDS spectra and elemental mapping.

Impedance spectroscopy (IS) results show the doping of niobium enhances the bulk conductivity of material by a factor of 2~3, instead of indicating enhanced electronic conductivity due to the mixed $Fe^{2+/3+}$ valence created by Nb dopant. Low frequency IS results, however, do not provide evidence for Li^+ diffusion and mobility, which means that electronic conduction is more probable instead of ionic conduction in Nb-doped samples.

4.6 References

1. P. Subramanya Herle, B. Ellis, N. Coombs and L. F. Nazar, "Nano-network electronic conduction in iron and nickel olivine phosphates", *Nat. Mater.* **2004**, *3*, pp. 147–152.

2. Myounggu Park, Xiangchun Zhang, Myoungdo Chung, Gregory B. Less and Ann Marie Sastry, "A review of conduction phenomena in Li-ion batteries" *J. of Power Sources* **2010**, *195*, pp. 7904–7929.

3. C. Wang and J. Hong, "Ionic/Electronic Conducting Characteristics of $LiFePO_4$ Cathode Materials: The Determining Factors for High Rate Performance Batteries and Energy Storage", *Electrochem. Solid-State Lett.* **2007**, *10(3)*, pp. A65–A69.

4. J. Ma, C. Wang and S. Wroblewski, "Kinetic characteristics of mixed conductive electrodes for lithium ion batteries", *J. of Power Sources* **2007**, *164*, pp. 849–856.

5. S.Y. Chung, J.T. Bloking and Y.M. Chiang, "Electronically conductive phosphor-olivines as lithium storage electrodes", *Nat. Mater.* **2002**, *1*, pp. 123–128.

6. A. Yamada, Y. Takei, H. Koizumi, N. Sonoyama, R. Kanno, K. Itoh, M. Yonemura and T. Kamiyama, "Electrochemical, Magnetic, and Structural Investigation of the $Li_x(Mn_yFe_{1-y})PO_4$ Olivine Phases", *Chem. Mater.* **2006**, *18*, pp. 804–813.

7. Sung Woo Oh, Seung-Taek Myung, Seung-Min Oh, Kyu Hwan Oh, Khalil Amine, Bruno Scrosati and Yang-Kook Sun, "Double Carbon Coating of $LiFePO_4$ as High Rate Electrode for Rechargeable Lithium Batteries", *Adv. Mater.* **2010**, *22*, pp. 4842–4845.

8. A. Yamada, S.C. Chung and K. Hinokuma, "Optimized $LiFePO_4$ for Lithium Battery Cathodes", *J. Electrochem. Soc.* **2001**, *148*, pp. A224–A229.

9. Sathiyaraj Kandhasamy, Kalaiselvi Nallathamby and Manickam Minakshi, "Role of structure defects in olivine cathodes", *Progress in Solid State Chemistry* **2012**, *40*, pp. 1–5.

10. N. Ravet, A. Abouimrane and M. Armand, *Nat. Mater.* **2003**, *2*, pp. 702.

11. C. Delacourt, C. Wurm, L. Laffont, J.-B. Leriche and C. Masquelier, "Electrochemical and electrical properties of Nb- and/or C-containing $LiFePO_4$ composites", *Solid State Ionics* **2006**, *177*, pp. 333–341.

12. M. Wagemaker, B. L. Ellis, D. Lutzenkirchen-Hecht, F. M. Mulder and L. F. Nazar, "Proof of Supervalent Doping in Olivine $LiFePO_4$, *Chem. Mater.* **2008**, *20*, pp. 6313–6315.

13. Fredrick Omenya, Natasha A. Chernova, Shailesh Upreti, Peter Y. Zavalij, Kyung-Wan Nam, Xiao-Qing Yang and M. Stanley Whittingham, "Can Vanadium Be Substituted into $LiFePO_4$?", *Chem. Mater.* **2011**, *23*, pp. 4733–4740.

14. Anthony R. West, *Basic Solid State Chemistry*, 2nd Edition, Wiley, New York, **2000**, pp. 215.

15. Nonglak Meethong, Yu-Hua Kao, Scott A. Speakman and Yet-Ming Chiang, "Aliovalent Substitutions in Olivine Lithium Iron Phosphate and Impact on Structure and Properties", *Adv. Funct. Mater.* **2009**, *19*, pp. 1060–1070.

16. Peixin Zhang,z Yanyi Wang, Muchong Lin, Dongyun Zhang, Xiangzhong Ren and Qiuhua Yuan, "Doping Effect of Nb^{5+} on the Microstructure and Defects of $LiFePO_4$", *J. Electrochem. Soc.* **2012**, *159*, pp. A402–A409.

17. Hyungsub Kim, Seongsu Lee, Young-Uk Park, Haegyeom Kim, Jongsoon Kim, Seokwoo Jeon and Kisuk Kang, "Neutron and X-ray Diffraction Study of Pyrophosphate-Based $Li_{2-x}MP_2O_7$ (M = Fe, Co) for Lithium Rechargeable Battery Electrodes", *Chem. Mater.* **2011**, 23 (17), pp. 3930–3937.

18. John M. Clark, Shin-ichi Nishimura, Atsuo Yamada and M. Saiful Islam, "High Voltage Pyrophosphate Cathode: Insights into Local Structure and Lithium Diffusion Pathways", *Angew. Chem.* **2012**, *51*, pp. 13149–13153.

CHAPTER V

Investigation of N-doped $Li_2FeP_2O_7$ Cathode Material

5.1 Introduction

Lithium iron pyrophosphate, $Li_2FeP_2O_7$, has received considerable attention as a cathode material for lithium-ion batteries due to its high theoretical capacity 220 mAh/g and working voltage ~3.6 V which compare favourably with 170 mAh/g and ~3.4 V for $LiFePO_4$. To date, $Li_2FeP_2O_7$ can reversibly extract and insert only one lithium ion per iron atom (one electron theoretical capacity: 110 mAh/g), at about 3.5 V vs. Li^+/Li [1]. Besides, in comparison with other cathode materials, $Li_2FeP_2O_7$ also suffers from the problem of low working voltage and poor capacity at high rate mainly because of its low electronic conductivity (~10^{-9} Scm^{-1}, in air) and Li ion diffusivity [2]. These shortcomings need to be overcome before its realization for practical uses.

In 1992, J.B. Bates *et al.* discovered a new thin-film amorphous lithium phosphorous oxynitride (LiPON), $Li_{3.3}PO_{3.9}N_{0.17}$, prepared by sputtering Li_3PO_4 in pure N_2; it has conductivity at 25°C of 2.4×10^{-6} Scm^{-1}, which is higher than that of 6.6×10^{-8} Scm^{-1} for $Li_{2.7}PO_{3.9}$ [3]. One possible reason for the enhanced conductivity and stability of the oxynitride films is attributed to the formation of a cross-linked structure causing an increase in Li^+ mobility [4]. In 1995, B. Wang *et al.* reported a polycrystalline lithium phosphorous oxynitride of $Li_{2.88}PO_{3.73}N_{0.14}$ synthesized by solid state method using Li_3N and $LiPO_3$ as reagents under a flowing N_2 atmosphere [5]. The $Li_{2.88}PO_{3.73}N_{0.14}$ has higher ionic conductivity of 1.4×10^{-13} Scm^{-1} at 25°C than that of γ-Li_3PO_4 (4.2×10^{-18} Scm^{-1}) due to its relatively low activation energy as a result of the Li and anion site vacancies as well as expanded cell dimensions.

In 2008, Liu *et al.* first investigated the effect of N doping in $LiFePO_4$ and studied its crystal structure, charge distribution and transport by using first-principle calculations [6]. They predicted the valence of the Fe nearest to N to be Fe^{3+} to maintain charge balance, and claimed that the coexistence of Fe^{2+} and Fe^{3+} ions will benefit the electronic conductivity. Moreover, N doping will probably extend the Li_xFePO_4 solid solution range. The activation

energy for Li diffusion in N-doped $LiFePO_4$, of *Ea* ~0.48 eV, is predicted to be slightly lower than that of undoped $LiFePO_4$, of *Ea* ~0.5 eV. The chemical diffusion coefficient of Li ions, D_{Li} ~10^{-11} cm^2s^{-1}, is expected to be enhanced as a result of the increased mobility of electrons. In 2011, M. Armand *et al.* investigated the effect of N substituted for O on the electrochemical properties of Li_2FeSiO_4 using first principles calculations [7]. The results show the average working voltage associated with the Fe^{3+}/Fe^{4+} redox couple decreased with N substitution in $Li_2FeSiO_{4-y}N_y$. In addition, the theoretical capacity of Li_2FeSiO_4 (330 mAh/g) could be maintained in $Li_2FeSiO_{4-y}N_y$ as a result of the oxidation of N^{3-} anions.

In spite of numerous studies on the LiPON thin films and powders prepared by RF magnetron sputtering and solid-state method, respectively, the effect of N-doping of $Li_2FeP_2O_7$ on the electrochemical properties has not been delineated and discussed. In this chapter, we have fabricated lithium iron pyrophosphate oxynitrides ($Li_{2+x}FeP_2O_{7-x}N_x$ and $Li_2FeP_2O_{7-y}N_y$) with different N-doping (x, y) in an attempt to investigate the phase composition, doping levels and electrical properties with or without N-doping. Herein, we use Kröger–Vink notation [8] to indicate the charge compensation of N doping by cation interstitial sites and/or electronic charge. Compositions shown in **Table 5-1** were prepared to study the defect compensation Mechanism I and II; each case represents the dopant substituted on O site and is charge-balanced by either lithium interstitials or electronic charge on the M2 sites. Note that the low-valent cation (Li) locates on the M1 site, and higher charged cation (Fe) on the M2 site.

Table 5-1 Defect compensation mechanisms by N^{3-} substituted on O sites in $Li_2FeP_2O_7$.

#	Composition Formula	Defect Compensation Mechanism	Kröger-Vink Notation
I	$Li_{2+x}FeP_2O_{7-x}N_x^{3-}$	$O^{2-} \rightarrow N^{3-} + Li^{+}$ O-substitution & Li-interstitial	$O_O^{\times} \rightarrow N_O' + Li_{Li}^{\bullet}$
II	$Li_2Fe^{(II)}_{1-y}Fe^{(III)}_yP_2O_{7-y}N_y^{3-}$	$O^{2-} \rightarrow N^{3-} + Fe_{Fe}^{\bullet}$ O-substitution & Fe-charge +1	$O_O^{\times} \rightarrow N_O' + Fe_{Fe}^{\bullet}$

5.2 Synthesis and Characterisation

$Li_{2+x}FeP_2O_{7-x}N_x$ and $Li_2FeP_2O_{7-y}N_y$ (x, y = 0–0.1) compositions were synthesized from stoichiometric amounts of Li_2CO_3, $FeC_2O_4{\cdot}2H_2O$, $(NH_4)H_2PO_4$, and Li_3N (Aldrich, 99.9%) by conventional solid-state reaction. In order to reduce any possibility of Li_3N decomposition, the initial weighing of Li_3N was done in an Ar-filled glove box and then it was quickly immersed in acetone with other reagents. All mixtures were immediately ground for 30 min using an agate mortar in air, and then calcined at 350°C with a heating rate of 2.5 ^oC/min in an alumina-tube furnace under flowing N_2 atmosphere for 6 hours. The calcined precursors were subsequently heated at 700°C for 12 hours in N_2 to obtain final products. A detailed schematic experimental flow chart for the synthesis and characterisation is summarised in **Fig. 5-1(a)**.

A new improved method to synthesize $Li_2FeP_2O_{7-y}N_y$ was developed for y=0.05, noted as "I-LFPN005". Small amounts of reagents, Li_2CO_3, $FeC_2O_4{\cdot}2H_2O$, $(NH_4)H_2PO_4$, were ground with acetone in air (~1.5 g) and transferred to an Ar-filled glove box. Inside the glove box, Li_3N was weighed, mixed dry with precursors in an agate mortar and pestle and the mixtures transferred to Mo foil boats and placed inside a silica glass tube. Samples were decomposed and then heated using the same condition as mentioned in **(a)**, see **Fig. 5-1(b)**.

The phase composition of these materials was determined using X-ray diffraction (XRD). Room temperature ^{57}Fe Mössbauer spectra were collected for the undoped and N-doped $Li_2FeP_2O_7$. Nitrogen analysis was done by *LSM Analytical Services* (Leco instrument: TC-436) using the inert gas combustion method, typically based on a furnace with water-cooled copper electrodes. The principle was to fuse the sample in a high purity graphite crucible in the furnace by taking it to very high temperature of 3000°C in Helium. The nitrogen was evolved into a helium carrier gas and detected by a thermal conductivity cell. Impedance spectroscopy (IS) was used to measure the electrical properties. Electrochemical testing was evaluated in a coin-cell configuration.

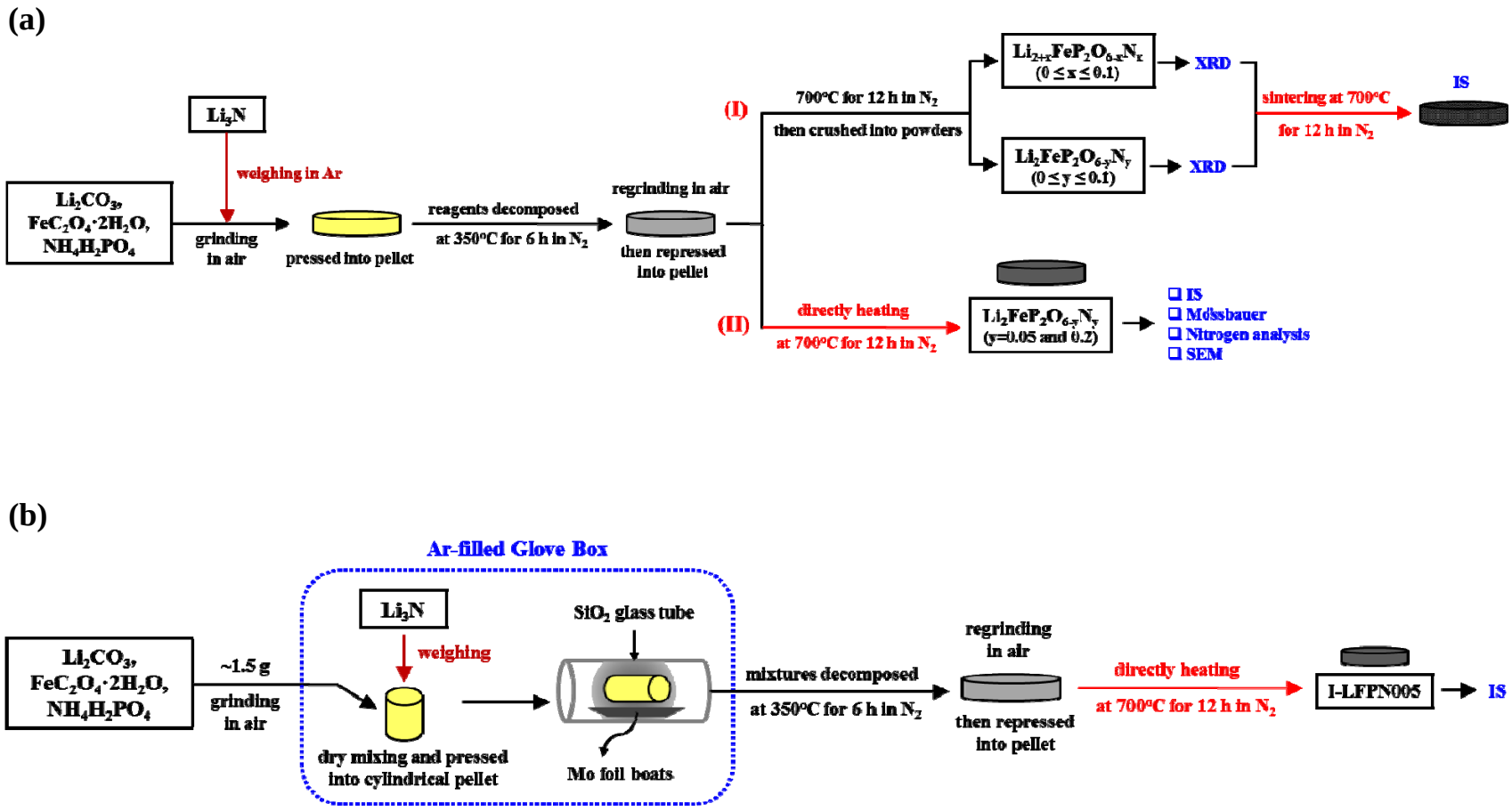

Figure 5-1 The experimental flow chart for N-doped $Li_2FeP_2O_7$ using different synthesis methods.

5.3 Results

5.3.1 XRD Patterns and Crystallinity

(i) $Li_{2+x}FeP_2O_{7-x}N_x$

Fig. 5-2(a) shows the XRD patterns of N-doping for oxygen, $Li_{2+x}FeP_2O_{7-x}N_x$, synthesized at 700°C for 12 hours in N_2 following two different stoichiometries, in which x are 0.05 and 0.1, respectively. In general, the intensity distribution of XRD patterns is identical to that of pure $Li_2FeP_2O_7$, and characterized as a solid solution which assumed a monoclinic symmetry and space group $P2_1/c$. Lattice parameters and unit cell volumes of the $Li_{2+x}FeP_2O_{7-x}N_x$ obtained by Rietveld refinement of X-ray data (Mo PSD) are illustrated in **Table 5-2**. With increasing dopant concentration of N from x=0 to x=0.05 in $Li_{2+x}FeP_2O_{7-x}N_x$, there is a decrease in *a*, *b*, *c* and *V* by -0.15%, -0.29%, -0.17%, and -0.55%, respectively but for x=0.1, all values are identical to the undoped sample within errors.

(ii) $Li_2FeP_2O_{7-y}N_y$

The XRD patterns of $Li_2FeP_2O_{7-y}N_y$ powders with N doping contents from y=0 to y=0.1 are shown in **Fig. 5-3(a)**. The intensity distribution of XRD patterns for y=0.025, 0.05, and 0.075 is similar to that of pure $Li_2FeP_2O_7$. A minor-phase $Li_3Fe_2(PO_4)_3$, however, was observed when y varies from 0.075 to 0.1, see arrowed. As a result, the amount of oxygen content replaced by nitrogen appears to be limited. No obvious peak shift was observed with increasing y from y=0 to y=0.075, see **Fig. 5-3(b)**. Lattice parameters and unit cell volumes are illustrated in **Table 5-3**. It is found that the unit cell constant *a* shows a small, systematic decrease with y; within errors *b*, *c* and β do not change. Therefore, *V* also shows a small decrease with y. Again, however, results for y=0.1, which is beyond the solid solution limit, appear to be anomalous.

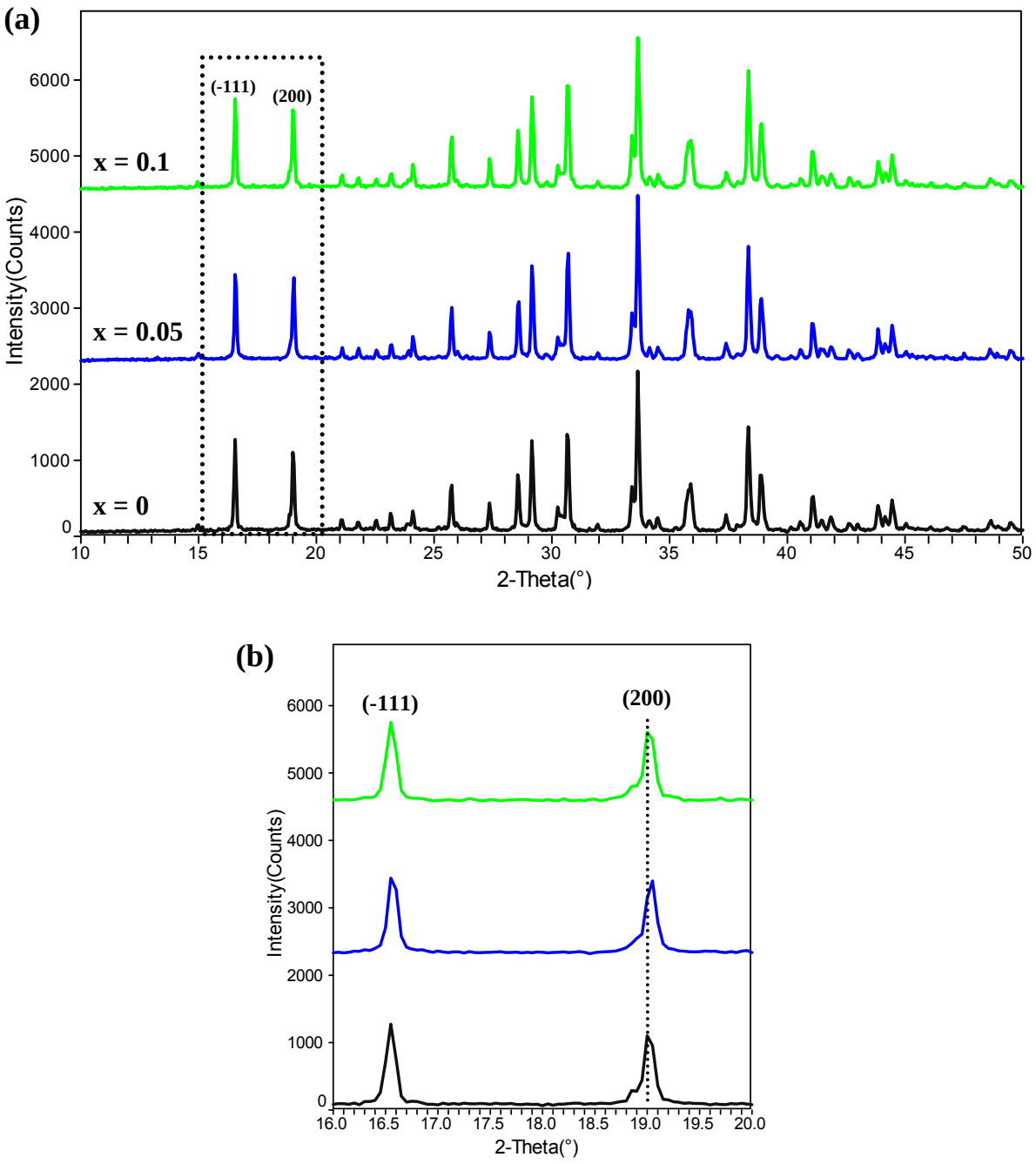

Figure 5-1 (continued)

Figure 5-2 (a) XRD patterns of the different level of N doping for $Li_{2+x}FeP_2O_{7-x}N_x$ ($0 \le x \le 0.1$); (b) magnified shift of (-111) and (200) peaks.

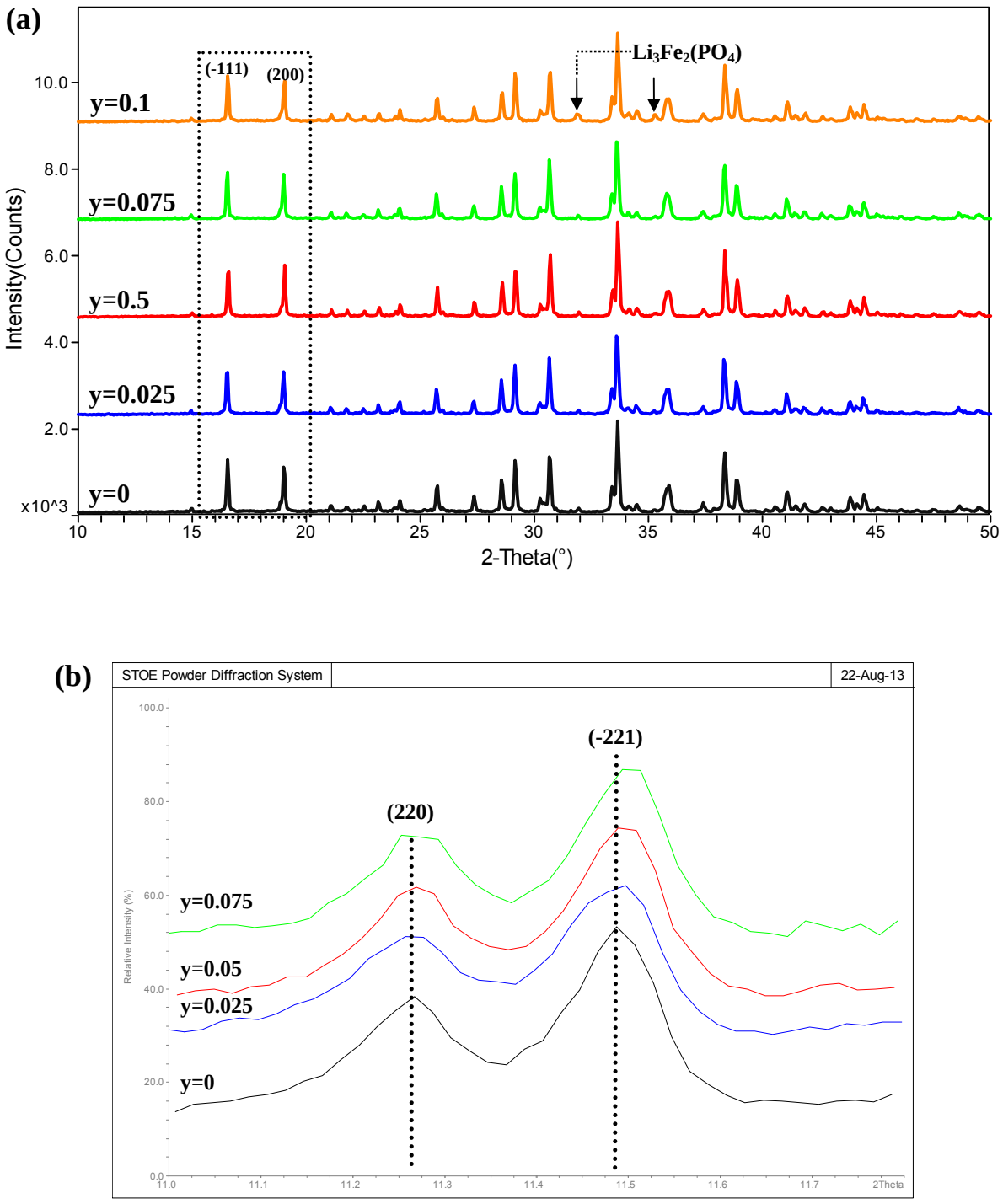

Figure 5-3 (a) XRD patterns of the different level of N doping for $Li_2FeP_2O_{7-y}N_y$ ($0 \le y \le 0.1$); (b) magnified position of (220) and (-221) peaks by Mo PSD.

Table 5-2 Lattice parameters for $Li_{2+x}FeP_2O_{7-x}N_x$ compounds with monoclinic symmetry.

Chemical formula	*a* (Å)	*b* (Å)	*c* (Å)	*β* (deg)	*V* (Å^3)
$Li_2FeP_2O_7$ (x=0)	11.019(3)	9.746(6)	9.791(8)	101.49(5)	1030.4(7)
$Li_{2.05}FeP_2O_{6.95}N_{0.05}$ (x=0.05)	11.003(5)	9.718(5)	9.774(5)	101.33(4)	1024.7(6)
$Li_{2.1}FeP_2O_{6.9}N_{0.1}$ (x=0.1)	11.011(3)	9.747(4)	9.806(4)	101.61(3)	1030.8(4)

Table 5-3 Lattice parameters for $Li_2FeP_2O_{7-y}N_y$ compounds with monoclinic symmetry.

Chemical formula	*a* (Å)	*b* (Å)	*c* (Å)	*β* (deg)	*V* (Å^3)
$Li_2FeP_2O_7$ (y=0)	11.019(3)	9.746(6)	9.791(8)	101.49(5)	1030.4(7)
$Li_2FeP_2O_{6.975}N_{0.025}$ (y=0.025)	11.004(4)	9.749(4)	9.797(4)	101.55(3)	1029.8(4)
$Li_2FeP_2O_{6.95}N_{0.05}$ (y=0.05)	10.996(7)	9.735(7)	9.796(7)	101.51(6)	1027.5(9)
$Li_2FeP_2O_{6.925}N_{0.075}$ (y=0.075)	10.987(8)	9.742(7)	9.790(7)	101.55(5)	1026.6(8)
$Li_2FeP_2O_{6.9}N_{0.1}$ (y=0.1)	11.030(9)	9.753(8)	9.796(10)	101.55(8)	1032.5(9)

5.3.2 Mössbauer Spectroscopy

The Fe sites occupied in $Li_2FeP_2O_{7-y}N_y$ heated at 700°C for 12 hours in N_2 were investigated using ^{57}Fe Mössbauer spectroscopy, as shown in **Fig. 5-4**; the blue line indicates the calculated spectrum and pink ones represent the fitting data. All spectra were fitted satisfactorily with two and three Lorentzian doublets for y=0 and 0.05, respectively. Refined parameters of center shift (δ), quadrupole splitting (Δ), and line width (Γ) are summarized in **Table 5-4**. The first outer fitted doublet in $Li_2FeP_2O_7$ **(a)** has a center shift of ~1.2 mm s^{-1}, a quadrupole splitting of ~2.5 mm s^{-1}, and a fitted area of ~ 49% and is consistent with Fe^{2+} (site 1) corresponding to the FeO_6 octahedral site. The second inner doublet has a center shift of ~1.2 mm s^{-1}, a lower quadrupole splitting of ~2.1 mm s^{-1}, and a fitted area of ~ 51% and is consistent with Fe^{2+} (site 2) assigned to FeO_5 and/or FeO_5/LiO_5 sites [9]. Attempts to add a third Fe^{3+} doublet with $Li_2FeP_2O_7$ were not successful. However, for $Li_2FeP_2O_{6.95}N_{0.05}$ **(b)**, the Mössbauer spectra show the presence of a third doublet, indicating the presence of Fe^{3+} in the N-doped sample with a low center shift of ca. 0.2 mm s^{-1}, a low quadrupole splitting of ca. 0.8 mm s^{-1}, and a fitted area of ~ 1%. The color of sample y=0 is grey, but it becomes lighter brown for y=0.05.

Table 5-4 Fitted Mössbauer spectrum parameters of $Li_2FeP_2O_{7-y}N_y$ materials.

y in $Li_2FeP_2O_{7-y}N_y$	site	center shift, δ/±0.02 mm s^{-1}	quadrupole splitting, Δ/±0.02 mm s^{-1}	line width, Γ/±0.02 mm s^{-1}	fraction, % /±1.0
0	Fe^{2+} (1)	1.23	2.53	0.16	49.1
	Fe^{2+} (2)	1.21	2.12	0.18	50.9
0.05	Fe^{2+} (1)	1.24	2.51	0.16	47.3
	Fe^{2+} (2)	1.21	2.11	0.18	51.5
	Fe^{3+} (3)	0.23	0.85	0.10	1.2

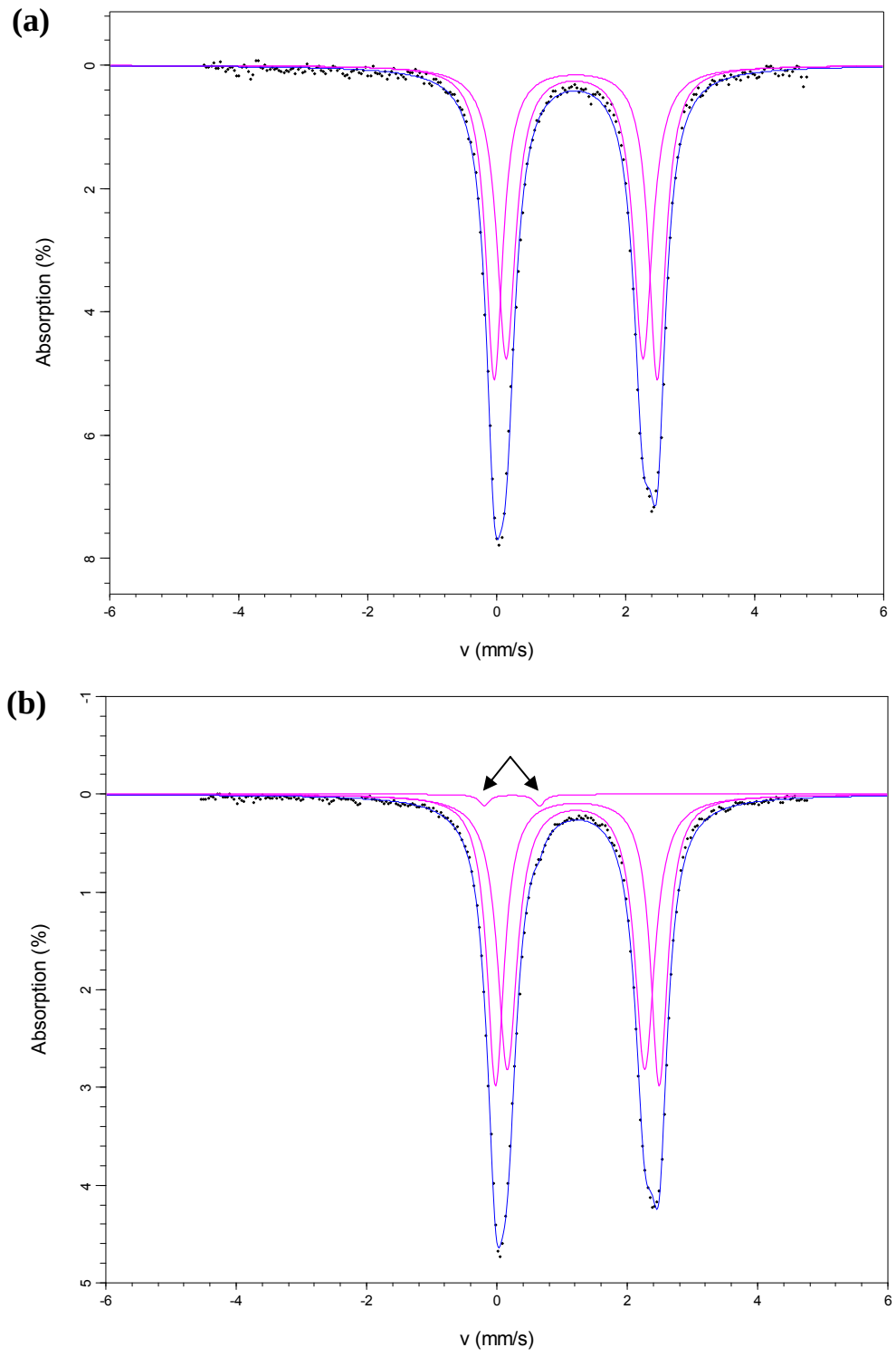

Figure 5-4 Mössbauer spectra of (a) $Li_2FeP_2O_7$ and (b) $Li_2FeP_2O_{6.95}N_{0.05}$ measured at room temperature.

5.3.3 Nitrogen Analysis

A thermal conductivity cell measured the nitrogen content in weight % in the $Li_2FeP_2O_{6.95}N_{0.05}$ sample as 0.097 %, i.e. **$N_{(Exp.)}$ = 0.00097 g**.

In $Li_2FeP_2O_{7-y}N_y$ (e.g. y=0.05),

$$y = \frac{\text{moles N}}{\text{moles sample}} = \frac{\frac{\text{wt N measured}}{14}}{\frac{\text{wt sample}}{\text{Fwt sample}}} = \frac{\text{wt N measured} \times 243.573}{14 \times \text{wt sample}} = \frac{0.00097 \times 243.573}{14 \times 1} = 0.016876$$

Therefore, the nitrogen loss (%) in $Li_2FeP_2O_{6.95}N_{0.05}$ can be calculated using Equation 5.1:

$$\frac{N_{(loss)}}{N_{(theoretical)}} = \frac{N_{(theoretical)} - N_{(real)}}{N_{(theoretical)}} = \left[\frac{0.05 - 0.016876}{0.05}\right] \times 100 = 66.25\ \% \qquad (5.1)$$

(Note: assume Fwt sample is independent of y)

This result indicates that some reaction of Li_3N with air/decomposition took place during mixing in air and/or heating in N_2. Results of nitrogen analysis are summarised in **Table 5-5**.

Table 5-5 Summarised results of nitrogen analysis for $Li_2FeP_2O_{7-y}N_y$.

Sample	N(g) in 1(g) sample (Calc.)	N(g) in 1(g) sample (Exp.)	mol N (Calc.)	mol N (Exp.)
$Li_2FeP_2O_{6.95}N_{0.05}$	0.00288	0.00097	0.05	0.01688
$Li_2FeP_2O_{6.8}N_{0.2}$	0.01152	0.00083	0.20	0.01444

5.3.4 Electrical Characterisation

(i) $Li_{2+x}FeP_2O_{7-x}N_x$

Z* plots of the pure-phase $Li_2FeP_2O_7$ and $Li_{2+x}FeP_2O_{7-x}N_x$ (x=0.05 and 0.1) pellets with Au electrodes measured at 200°C in air show a nearly ideal semicircle with associated capacitance of ~1.1, ~2.1 and ~0.9 $pFcm^{-1}$ calculated from $\omega RC=1$ at the semicircle maximum, and, therefore, attributed to bulk regions of the samples. The total resistivity of $Li_{2.05}FeP_2O_{6.95}N_{0.05}$, R ~0.45 MΩcm, is slightly lower than that of $Li_2FeP_2O_7$, R ~0.7 MΩcm, **Fig. 5-5(a)**. The resistance of $Li_{2.1}FeP_2O_{6.9}N_{0.1}$, R ~1.0 MΩcm, however, increases with the N doping level of x from 0.05 to 0.1.

Capacitance, C', of the bulk response as a function of frequency at 200°C with different N doping level can be observed from **(b)**. A capacitance plateau at higher frequency has value close to 1 $pFcm^{-1}$. Conductivity, Y', data as a function of frequency at 200°C are shown in **(c)**. The Y' data show a power law response at higher frequencies and a frequency-independent *dc* conductivity plateau at lower frequencies. $Li_{2.05}FeP_2O_{6.95}N_{0.05}$ has a total conductivity of ~2.1×10^{-6} Scm^{-1}, which is slightly higher than ~1.4×10^{-6} Scm^{-1} and ~1.0×10^{-6} Scm^{-1} for $Li_2FeP_2O_7$ and $Li_{2.1}FeP_2O_{6.9}N_{0.1}$, respectively.

Combined Z'' and M'' spectroscopic plots show all maxima of M'' and Z'' peaks are not exactly coincident as in ideal "Debye" theory prediction; a low frequency tail in the Z'' peak of $Li_2FeP_2O_7$ **(d)** may be associated with an interfacial effect.

Impedance measurements at higher temperature were carried out. No spike was observed in the impedance Z* plots of x= 0.1 on increasing the temperature to 275°C, **Fig. 5-6**, indicating that electronic conduction is more probable than ionic conduction.

Conductivity data of $Li_{2+x}FeP_2O_{7-x}N_x$ are presented in **Fig. 5-7**; a set of parallel lines is observed with activation energies: 0.57 eV for x=0, 0.58 eV for x=0.05, 0.62 eV for x=0.1. The activation energy in N-doped $Li_2FeP_2O_7$ is slightly higher than that of pure $Li_2FeP_2O_7$, and increases with increasing N-doping concentration.

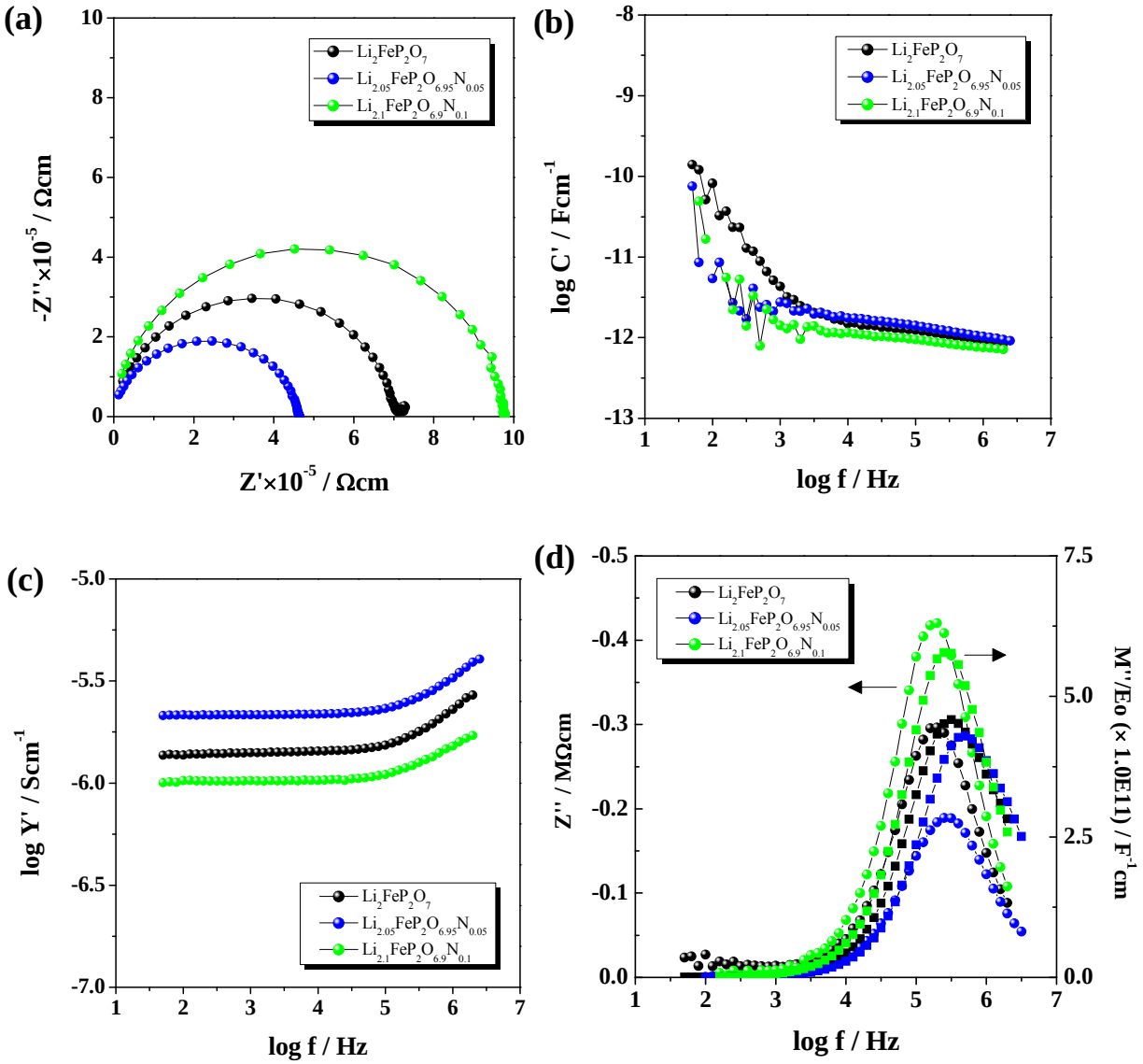

Figure 5-5 $Li_{2+x}FeP_2O_{7-x}N_x$ (x=0, 0.05 and 0.1): (a) Impedance complex plane plots, Z*, (b) spectroscopic plots of capacitance, C', (c) spectroscopic plots of admittance, Y', and (d) Z''/M'' spectroscopic plots at 200°C in air.

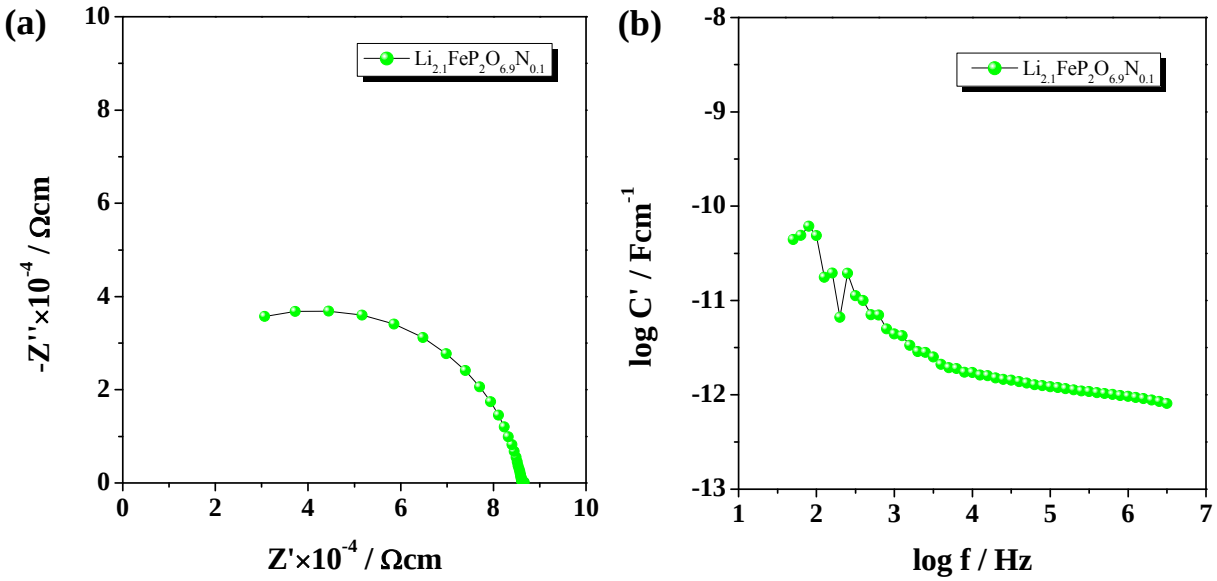

Figure 5-6 $Li_{2.1}FeP_2O_{6.9}N_{0.1}$: (a) Complex plane plot, Z*, (b) capacitance plot, C' at 275°C in air.

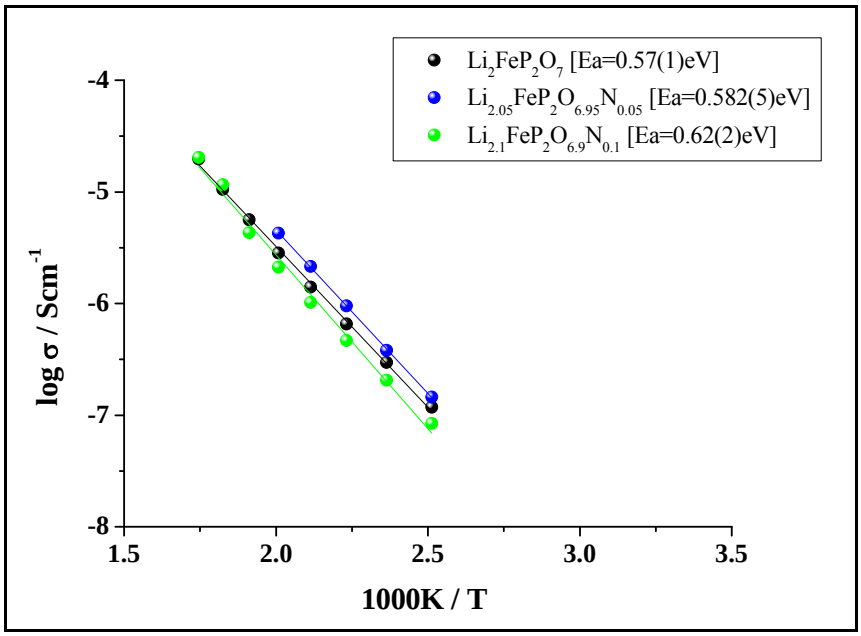

Figure 5-7 Arrhenius plots of the bulk conductivity (R_b^{-1}) for $Li_{2+x}FeP_2O_{7-x}N_x$ (x=0, 0.05 and 0.1) pellets with Au electrodes in air.

(ii) $Li_2FeP_2O_{7-y}N_y$

Low frequency impedance measurements in N_2 atmosphere were conducted at different temperatures. The samples of $Li_2FeP_2O_{6.95}N_{0.05}$ (y=0.05) and $Li_2FeP_2O_{6.8}N_{0.2}$ (y=0.2) were prepared following a one-step process, **(II)** in **Fig. 5-1(a)**; the decomposed mixtures were pelleted directly and heated at 700°C for 12 h in N_2. The phase compositions of, y=0.05 and y=0.2, were checked by XRD and were identical to undoped $Li_2FeP_2O_7$.

Impedance complex plane, Z* plots, **Fig. 5-8**, show the total resistivity of $Li_2FeP_2O_{6.95}N_{0.05}$ pellet with sputtered Au electrodes at various measuring temperatures in N_2. At 100°C and 150°C, a nearly ideal first semicircle of resistance R_1 with associated capacitance of ~4 $pFcm^{-1}$ is attributed to sample bulk, see **(a)** and **(b)**. A well-resolved second arc of resistance R_2 at low frequencies over the temperature range 150~300 °C was observed without any evidence for a Warburg or inclined spike.

The C' spectroscopic plots as a function of frequency over the temperature range 100°C to 350°C are shown in **Fig. 5-9(a)**, in which a high frequency plateau with a capacitance value close to ~5.0 $pFcm^{-1}$ represents the bulk response in sample and a low frequency dispersion was observed at temperatures below 150°C. As the temperature increases, the data show a very broad dispersion, probably following a power law at intermediate frequencies from about 10^3 to 1 Hz, and the capacitance value at lower frequencies increases up to ~10^{-6} Fcm^{-1}.

Conductivity plots, Y', as a function of frequency, **Fig. 5-9(b)**, show a dispersion at high frequencies and a nearly frequency-independent *dc* conductivity plateau at lower frequencies. At T > 300°C, Y' spectra present a frequency-independent *dc* conductivity plateau. Combined Z''/M'' spectra at 150°C in N_2 show Z'' and M'' peaks at similar frequency, **Fig. 5-10**. The peak maxima coincide, which indicates the sample is electrically homogeneous. The FWHM of the Z'' peak is ~1.2 decades, which is close to the ideal value of 1.14 decades. A broad low-frequency arc in the Z'' peak, which is also seen in the Z* plots, may be associated with an electrode effect.

Fig. 5-11 shows a linear Arrhenius response with activation energy of R_2, ~0.29 eV, which is slightly lower than that of bulk R_1, ~0.34 eV, and of total R_T, ~0.36 eV, for $Li_2FeP_2O_{6.95}N_{0.05}$ with Au-sputtered electrode. The total conductivity R_T^{-1}, i.e. $(R_1 + R_2)^{-1}$, is dominated by large R_1 resistances.

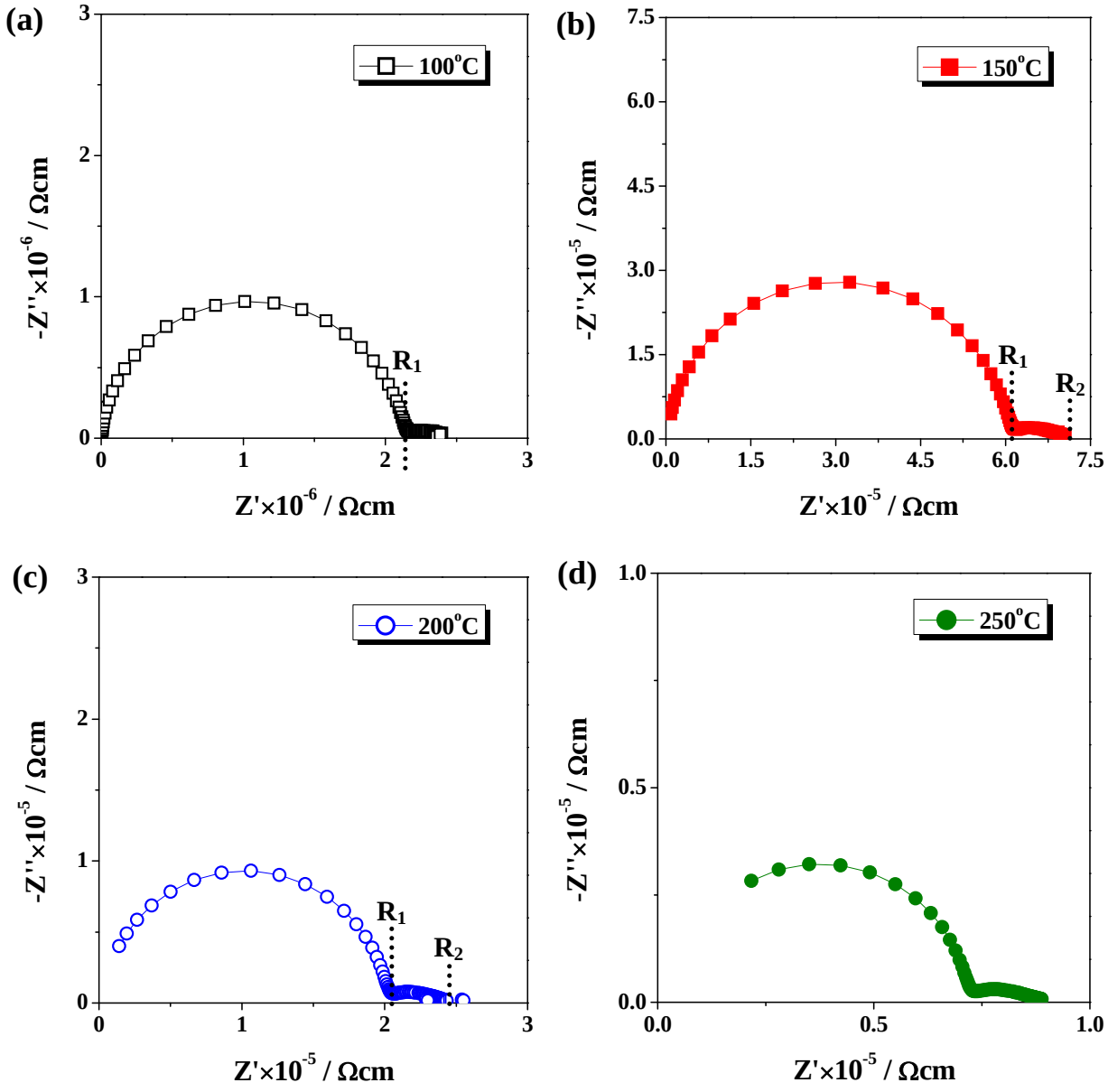

Figure 5-8 $Li_2FeP_2O_{6.95}N_{0.05}$: Impedance complex plane plots, Z*, at (a) 100°C to (f) 350°C in N_2.

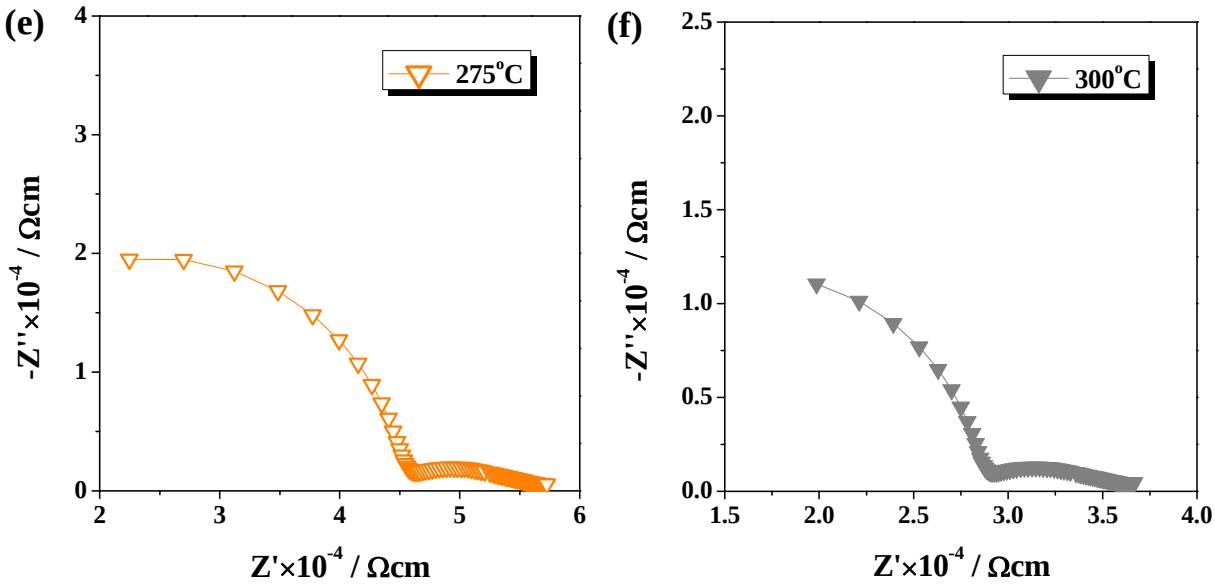

Figure 5-8 (continued)

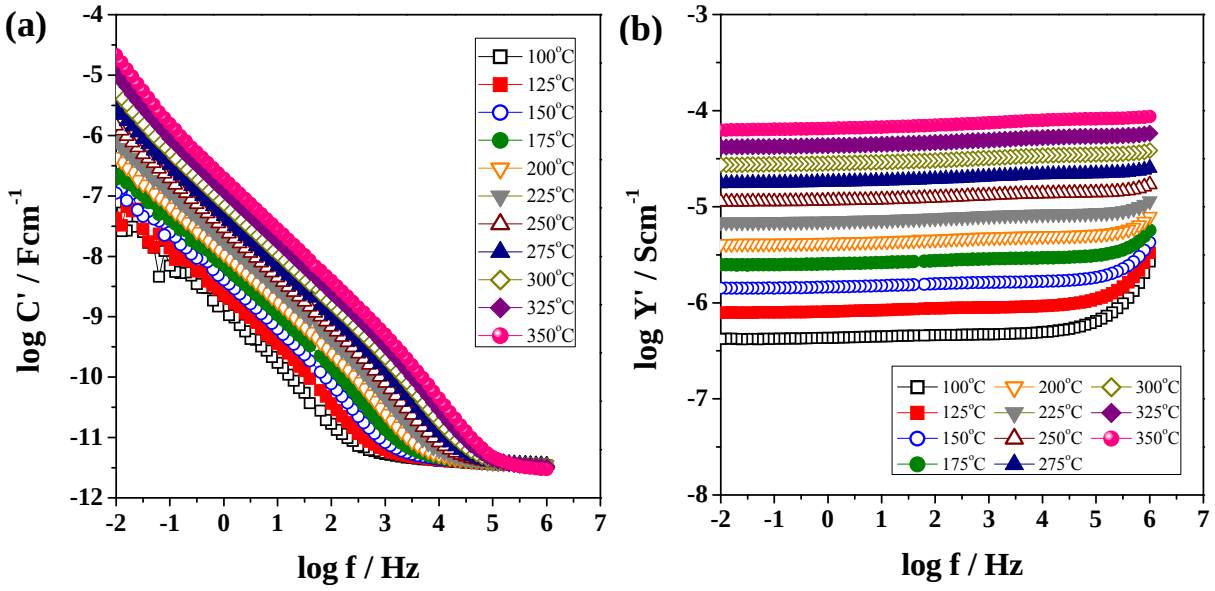

Figure 5-9 $Li_2FeP_2O_{6.95}N_{0.05}$ (Au electrode): (a) spectroscopic plots of capacitance, C', (b) spectroscopic plots of admittance, Y', at various temperatures, 100~350 °C in N_2.

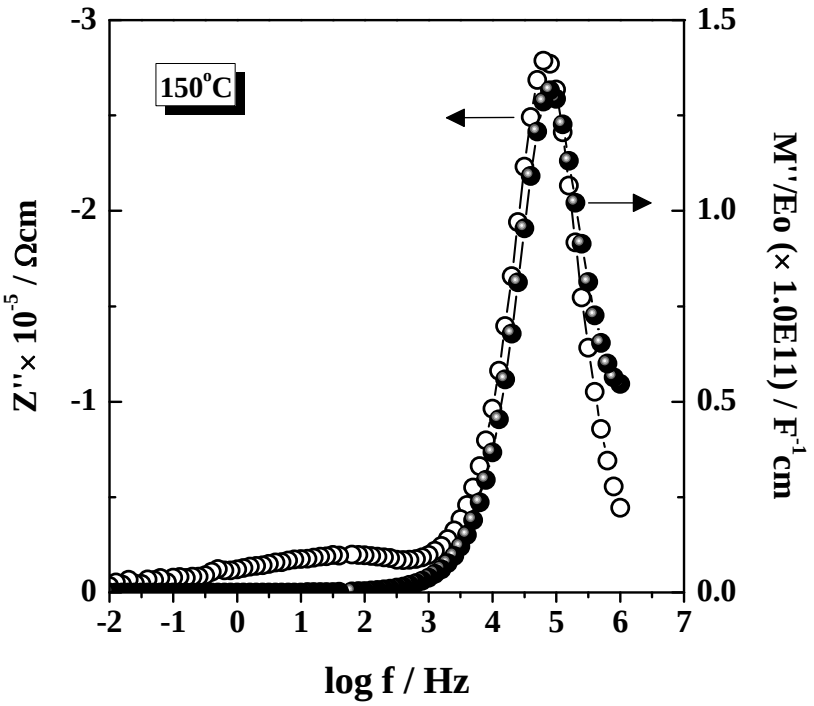

Figure 5-10 Z"/M" spectroscopic plots at 150°C in N_2 for $Li_2FeP_2O_{6.95}N_{0.05}$.

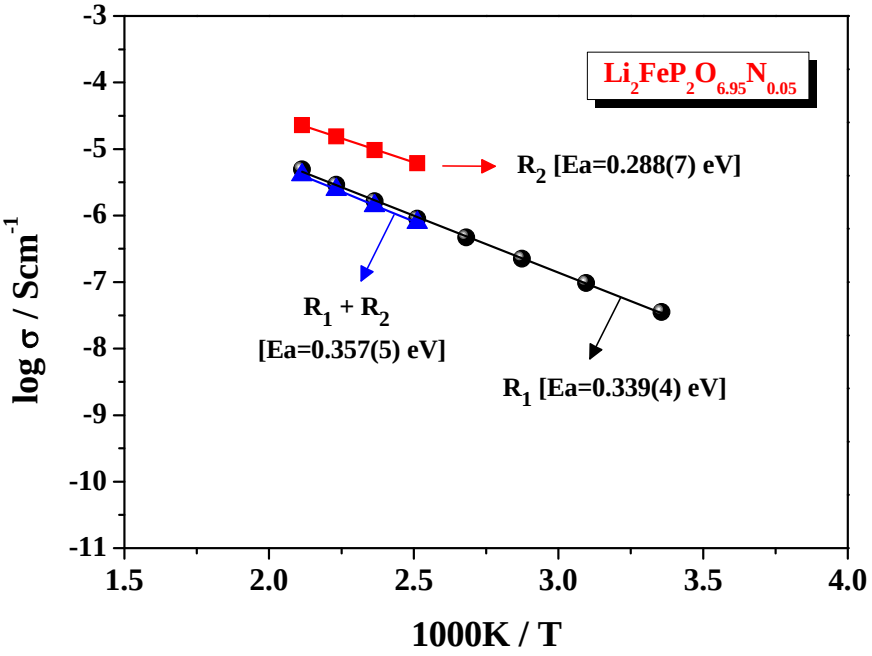

Figure 5-11 Arrhenius plots of R_1^{-1}, R_2^{-1}, and total conductivity R_T^{-1} for $Li_2FeP_2O_{6.95}N_{0.05}$ pellet heated at 700°C with sputtered Au electrodes.

The conductivities of $Li_2FeP_2O_7$ and $Li_2FeP_2O_{7-y}N_y$ ceramics are represented as Arrhenius plots in **Fig. 5-12**. For y=0.05 and 0.2, both had a conductivity of ~5×10^{-8} Scm^{-1} at room temperature in N_2, which is approximately 3 orders of magnitude greater than that of y=0 (~5×10^{-11} Scm^{-1}). The bulk activation energies at low temperature, ~0.33 eV and ~0.31 eV, are much lower than that of pure $Li_2FeP_2O_7$ of ~0.61 eV and the high temperature data rather similar to that of sample y=0. A second pellet of y=0.05 was measured with similar results and the conductivity values are reversible from heating to cooling in N_2, see **Fig. 5-13**.

Fig. 5-14 shows the Arrhenius plots of bulk conductivity (R_b^{-1}) $Li_2FeP_2O_7$ heated in N_2 and slow cooled in air. The initial data point on cooling was collected after the sample was heated to 350°C in N_2, subsequently changed to air and maintained at 350°C for 6 hours. The conductivity in air is ~10^{-9} Scm^{-1} at room temperature, which is ~1.5 orders of magnitude greater than that heated in N_2 and with a lower activation energy of ~0.55 eV.

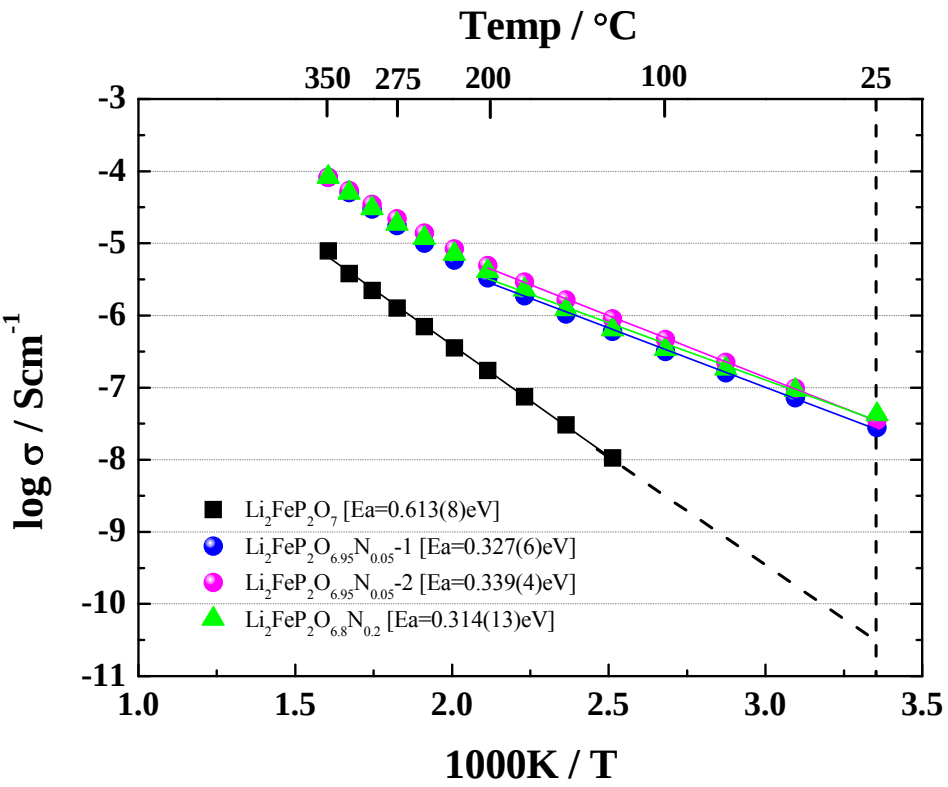

Figure 5-12 Arrhenius plots of the bulk conductivity of $Li_2FeP_2O_7$, $Li_2FeP_2O_{6.95}N_{0.05}$ and $Li_2FeP_2O_{6.8}N_{0.2}$ pellets with sputtered Au electrodes in N_2.

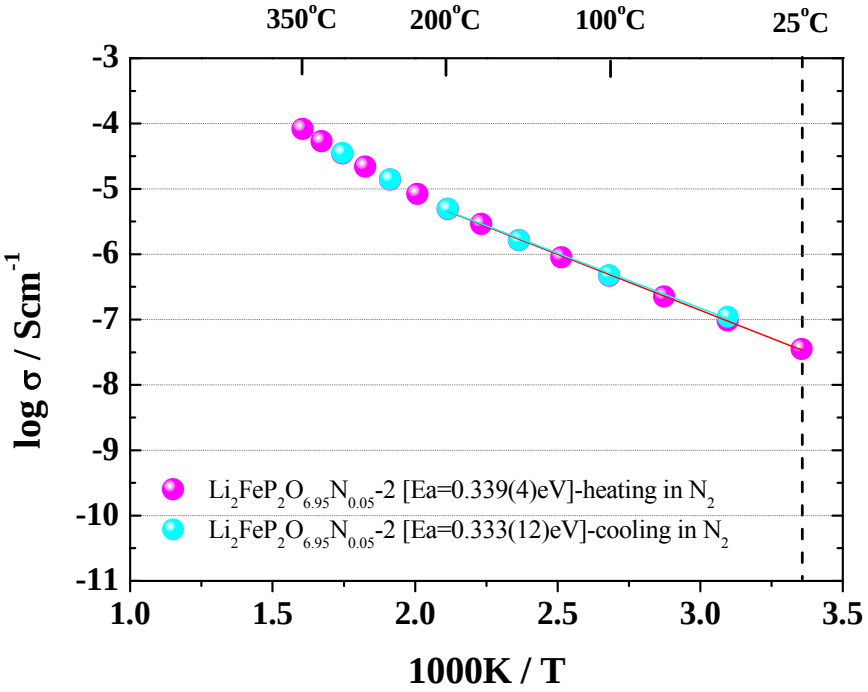

Figure 5-13 Arrhenius plots of the bulk conductivity of $Li_2FeP_2O_{6.95}N_{0.05}$ heated and cooled in N_2.

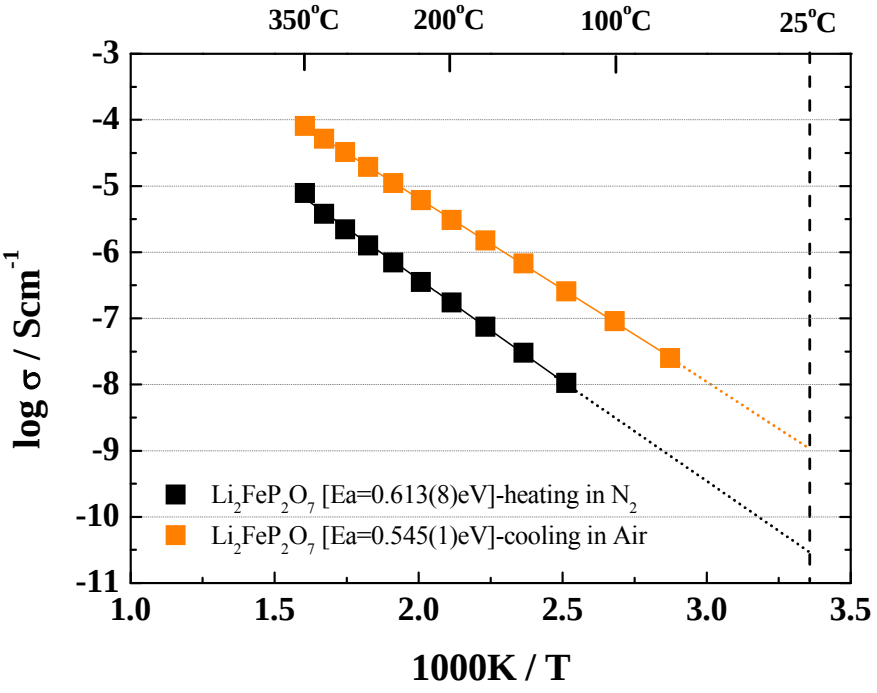

Figure 5-14 Arrhenius plots of the bulk conductivity of $Li_2FeP_2O_7$ heated in N_2 and slow cooled in air.

5.3.5 Morphology

Fig. 5-15(a) and **(b)** show SEM pictures of the two kinds of $Li_2FeP_2O_{6.95}N_{0.05}$ powders sintered at 700°C in N_2; one was prepared by solid-state (SS) method using mortar and pestle grinding for 30 minutes in acetone; the other used a planetary ball-milling (BM) with acetone for 2 hours (400 rpm) in air. The BM-$Li_2FeP_2O_{6.95}N_{0.05}$ particles **(b)** have irregular spheres with an average particle size < 10 μm, which is smaller than that of SS-sample **(a)**.

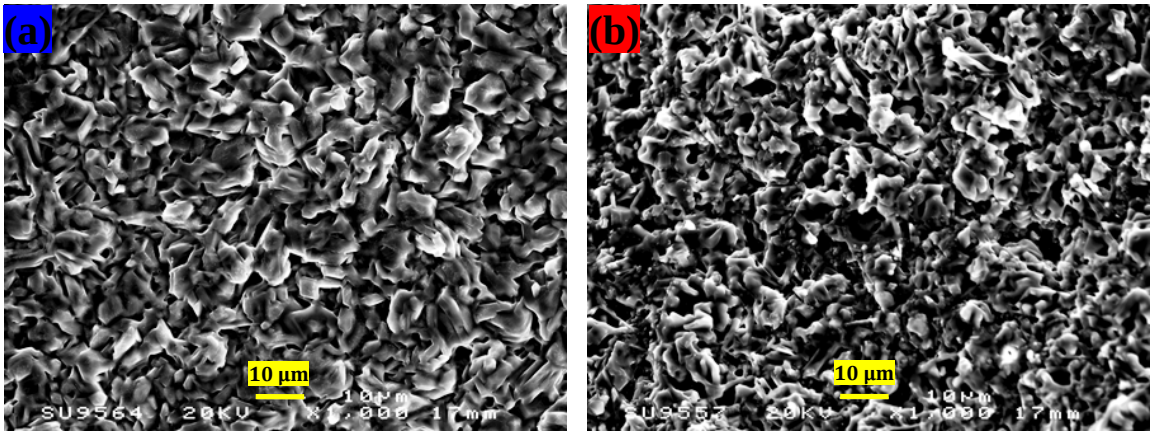

Figure 5-15 SEM pictures of surface section of sintered (a) SS-$Li_2FeP_2O_{6.95}N_{0.05}$ and (b) BM-$Li_2FeP_2O_{6.95}N_{0.05}$ pellets.

5.3.6 Electrochemical Properties: $Li_2FeP_2O_{6.95}N_{0.05}$

Fig. 5-16 shows the 1st charge and discharge curves of SS and BM $Li_2FeP_2O_{6.95}N_{0.05}$ electrodes at constant charge/discharge rate of $C/20$ at 25°C, with constant voltage relaxation down to $C/400$ applied at 4.5 V for 2 hours. The discharge plateau of BM appears at ~3.75 V, and the first discharge capacity is ~50 mAh/g. SS has a lower discharge capacity of ~10 mAh/g, a high polarization, and no voltage plateau on the first cycle. **Fig. 5-17** shows the high-rate discharge capacity for SS and BM electrodes without carbon additives. BM had a discharge capacity of ca. 50 mAh/g, 30 mAh/g, 17 mAh/g, and 9 mAh/g at discharging rates $C/20$, $C/5$, $C/2$, and $1C$, using constant charge rate of $C/20$. SS had discharge capacity of ~10 mAh/g at $C/20$ rate, and ~5 mAh/g at $C/5$ rate for the first cycle. Thus, the high-rate capacity of BM is much higher than that of SS.

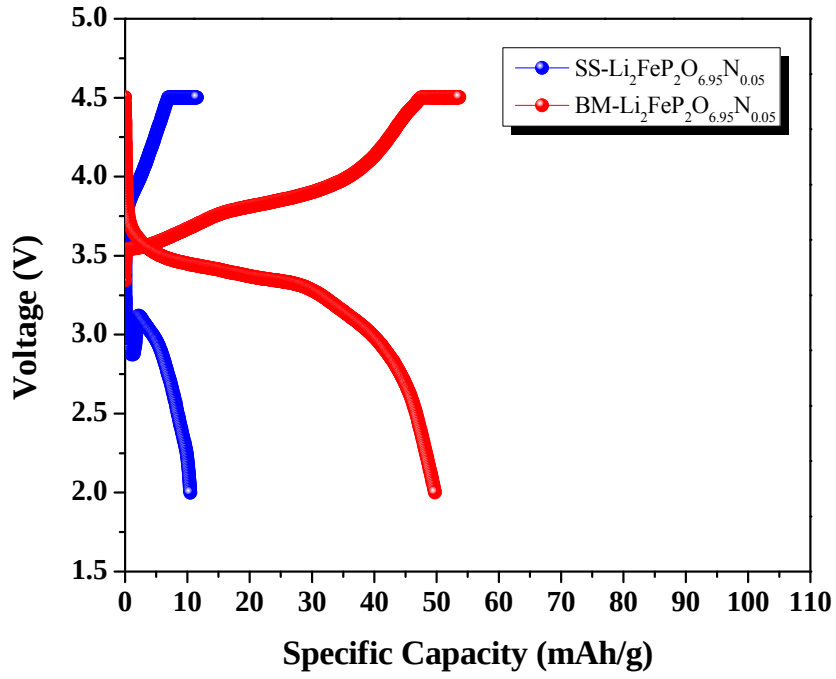

Figure 5-16 Charge–discharge curves of the SS- and BM-$Li_2FeP_2O_{6.95}N_{0.05}$ cells tested at a constant charge rate of *C*/20 at 25°C for the 1st cycle.

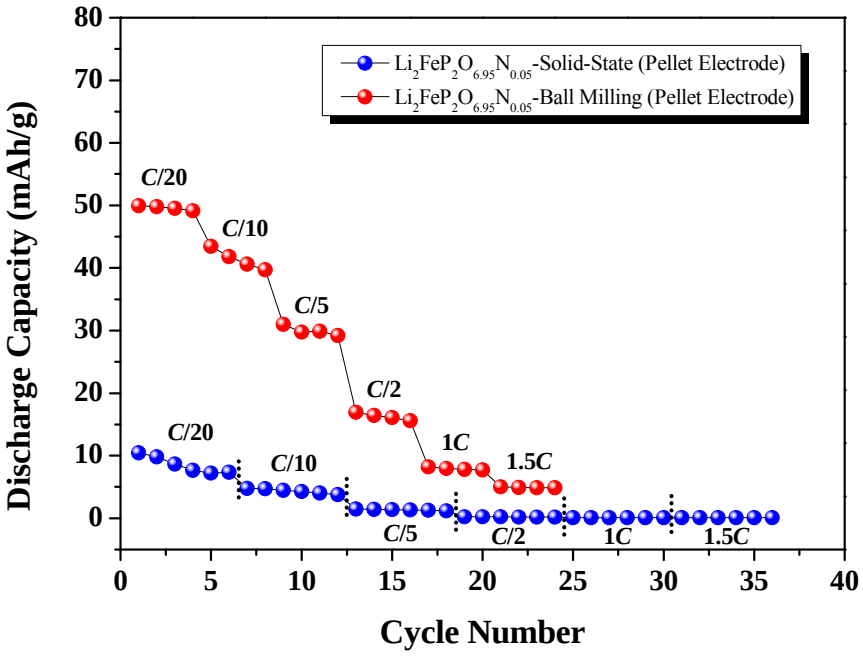

Figure 5-17 Discharge capacity of SS- and BM-$Li_2FeP_2O_{6.95}N_{0.05}$ as a function of discharge rate at a constant charge rate of *C*/20 (cut-off voltages: 2.0–4.5 V).

Fig. 5-18 shows the initial charge and discharge curves of BM-$Li_2FeP_2O_{6.95}N_{0.05}$ and, for comparison, BM-$Li_2FeP_2O_7$ at $C/20$ at room temperature; the discharge capacity of the N-doped sample, however, is ~50 mAh/g, which is lower than that of undoped $Li_2FeP_2O_7$ ~70 mAh/g. A distinct voltage increase of ~0.1 V in BM-$Li_2FeP_2O_{6.95}N_{0.05}$ is observed during the first charge stage, highlighted in insert.

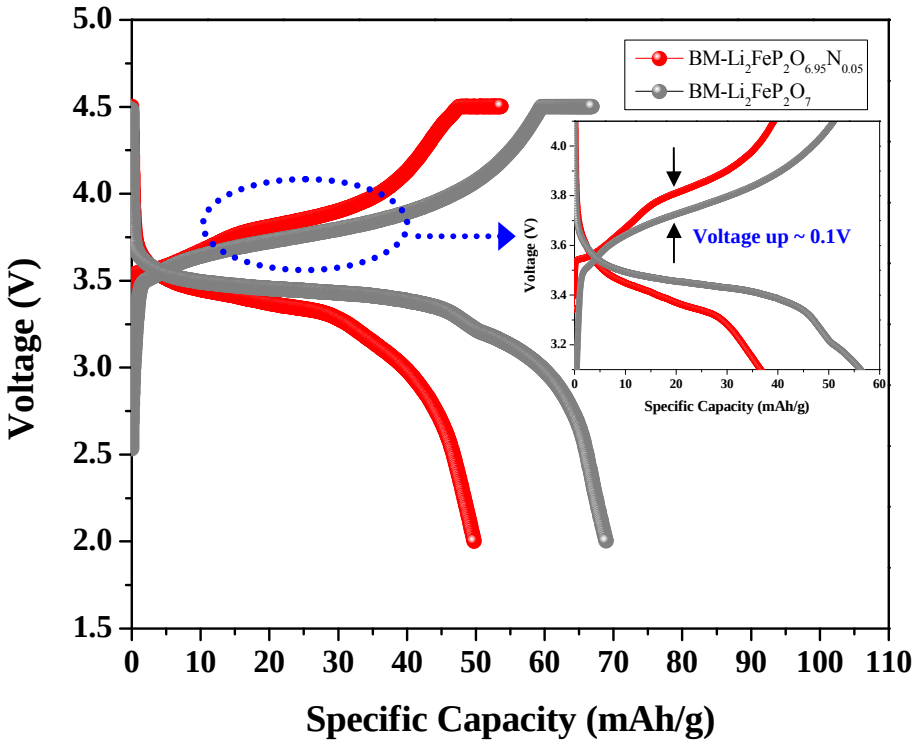

Figure 5-18 Charge–discharge curves of BM-$Li_2FeP_2O_{6.95}N_{0.05}$ and BM-$Li_2FeP_2O_7$ at constant charge rate of $C/20$ at 25°C for the 1st cycle. The insert shows the voltage increase on expanded scale in the first charge stage.

5.3.7 Improved-$Li_2FeP_2O_{6.95}N_{0.05}$ (I-LFPN005)

$Li_2FeP_2O_{6.95}N_{0.05}$ was synthesised via a new approach as described in **Fig. 5-1(b)**. The phase composition and pellet density of I-LFPN005 were similar to those of $Li_2FeP_2O_7$. Conductivity data of I-LFPN005 with sputtered-Au electrodes as a function of temperature in N_2 are presented in **Fig. 5-19**. A single, high frequency semicircle R_1 is seen with associated capacitance of ~7 $pFcm^{-1}$ using $\omega RC=1$ at the semicircle maximum and therefore attributed to bulk response, see **(a)**. No inclined spike characteristic of either a double layer capacitance or a Warburg impedance are observed at low frequencies, indicating I-LFPN005 is predominantly an electronic conductor. Y' plots, as a function of frequency over the range 25–100 °C, show a dispersion at high frequencies and a frequency-independent *dc* conductivity plateau at low frequencies, see **(b)**.

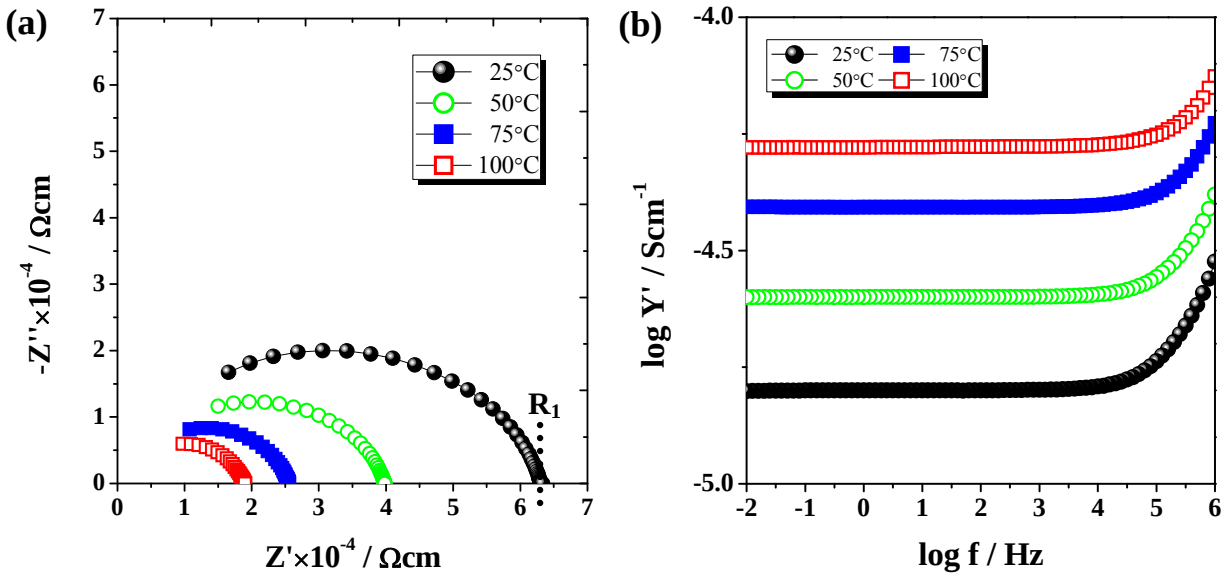

Figure 5-19 (a) Z* and (b) Y' plots, for I-LFPN005, at 25–100 °C in N_2 with sputtered-Au electrodes.

Bulk conductivities were extracted and are shown in Arrhenius plots in **Fig 5-20**; I-LFPN005 has the highest conductivity ~10^{-5} Scm^{-1} at room temperature in N_2. Its conductivity shows a linear response over the range 25–200 °C with the lowest activation energy ~0.16 eV and a high temperature value with a change of slope at ~200 °C which is similar to that of other samples.

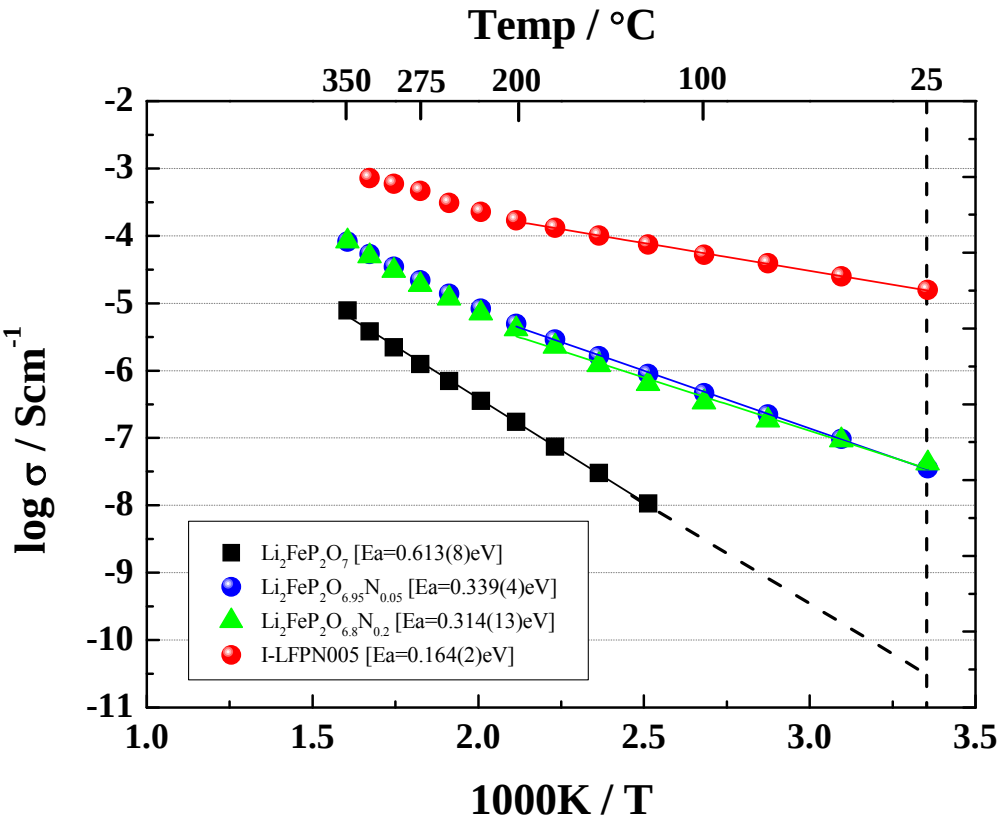

Figure 5-20 Arrhenius plots of the bulk conductivity of $Li_2FeP_2O_{7-y}N_y$ (y=0.05 and 0.2) with different synthesis methods in Fig. 5-1.

5.4 Discussion

5.4.1 XRD Patterns and Crystallinity

N-doped $Li_2FeP_2O_7$ has been synthesized by solid-state method. A quick synthesis route, section 5.2 is preferred for the final products. XRD patterns of the reacted samples, in which x and y varied from 0 and 0.05, synthesized at 700°C for 12 hours in N_2 are similar to that of undoped $Li_2FeP_2O_7$. However, a very small amount of secondary phase, $Li_3Fe_2(PO_4)_3$, is characterized for $y > 0.075$. The differences in XRD peak positions for compositions $0 \lesssim y \lesssim 0.075$ are very small. Thus, differences in lattice parameters are small. XRD is not sensitive to detect small amounts of secondary phases and therefore, the XRD results were inconclusive as to the possibility of N-doping and solid solution formation.

5.4.2 Electrical Properties

(i) $Li_{2+x}FeP_2O_{7-x}N_x$

Impedance data show that the conductivity of x=0.05 and x=0.1 has no real difference within errors, using porous pellets, in comparison to that of $Li_2FeP_2O_7$. This is consistent with the charge-compensation mechanism ($O^{2-} \leftrightarrow Li^+ + N^{3-}$) which does not alter the Fe^{2+} valence state and hence is unlikely to enhance electronic conductivity. In general, a good interconnect and a high sintered density in samples are favourable for the electron transfer and therefore, resulting higher electrical conductivity [10]. The sample, x=0.1, has a slightly decreased conductivity probably due to its lower pellet density of ~75 % in comparison to that of ~84% for both x=0 and 0.05.

(ii) $Li_2FeP_2O_{7-y}N_y$

Low frequency impedance measurements over the temperature range 100~350 °C were conducted in N_2 atmosphere to reduce any oxidation effect in samples, and to get further insight into the $Li_2FeP_2O_{7-y}N_y$ (y=0.05 and 0.2) compound. The specimen was pelleted following a one-step heating reaction without secondary sintering to decrease nitrogen evolution from sample, see **(II)** in **Fig. 5-1(a)**. For example, the conductivity data of y=0.05 pellets through a two-step sintering **(I)** are not reproducible.

Z* data of $Li_2FeP_2O_{6.95}N_{0.05}$ measured in N_2 show a high frequency arc of R_1 with an associated capacitance value ~5 $pFcm^{-1}$, which is contributed to bulk responses. In addition, a second disordered semicircle of R_2 at low frequency with a capacitance of 10^{-5}~10^{-6} Fcm^{-1} is obtained above 250°C, probably due to an electrode effect. Similar phenomenon was observed on $Li_2FeP_2O_7$ and discussed in chapter III. At high temperatures, no blocking or Warburg spike attributed to ionic conduction behavior at low frequencies was observed, indicating that the conduction mechanism is thought to be primarily electronic.

The resistivity and activation energy (~0.3 eV) in $Li_2FeP_2O_{6.95}N_{0.05}$ are much lower than that of undoped $Li_2FeP_2O_7$ (~0.6 eV) due to the coexistence of Fe^{2+} and Fe^{3+} ions benefitting the electron conductivity and increased mobility of electrons, which has been confirmed by Mössbauer spectrum with a mixed oxidation state of $Fe^{2+/3+}$, **Fig. 5-4(b)**. Modeling work from Huang *et al.* reported the coexistence of Fe^{2+} and Fe^{3+} ions may benefit the electron conductivity of $LiFePO_4$ by N doping [6]. Doped compositions of y=0.05 and y=0.2 gave similar conductivity over the temperature range 25–350 °C attributed to the approximate nitrogen content measured in samples, **Table 5-5**.

The slowly air-cooled $Li_2FeP_2O_7$ has a higher conductivity and a slightly lower activation energy of ~0.5 eV than that heated in N_2, probably attributed to a gradual oxidation of ferrous ions to ferric ions with time through the pellet surface to form an oxidized shell with Fe^{3+}, as shown schematically in **Fig. 5-21(a)**. The iron valence in the core area is envisaged to be Fe^{2+} without enough oxygen concentration and/or limited diffusion time to reach the sample interior. In contrast, data for $Li_2FeP_2O_{6.95}N_{0.05}$ heated or slow cooled in N_2 have a much higher conductivity and the lowest activation energy resulting from the well-distributed coexistence of Fe^{2+}/Fe^{3+} in samples attributed to N doping, **(b)**.

5.4.3 Electrochemical Testing

The much higher capacity of the $Li_2FeP_2O_{6.95}N_{0.05}$ prepared by ball-milling at low or high charge/discharge rates was attributed to the shorter transport path of Li ions in samples as a result of its smaller particle size and higher surface area compared with those of $Li_2FeP_2O_{6.95}N_{0.05}$ synthesized by solid-state method. The first discharge capacity at $C/20$

of BM-$Li_2FeP_2O_{6.95}N_{0.05}$ is lower than that of pristine BM-$Li_2FeP_2O_7$. One reason is probably that the increased conductivity of 3 orders, ~5×10^{-8} Scm^{-1} at room temperature, by N doping method is still not high enough to improve the electronic conductivity for cathodes in comparison to other strategies, such as nanosizing and carbon coating. Another reason is the $Fe^{2+/3+}$ redox activity in $Li_2FeP_2O_{6.95}N_{0.05}$ may be slightly inhibited owing to ferric ions of Fe^{3+} in samples observed from Mössbauer results, which influence the capacity.

Although the $Li_2FeP_2O_{6.95}N_{0.05}$ has a decreased discharge capacity, its working voltage is increased up to ~3.75 V about 0.1–0.15 V higher than that of undoped $Li_2FeP_2O_7$, and therefore, may compensate for the loss of energy density. Similar phenomenon, voltage increase ~0.13 V (Fe^{2+}/Fe^{3+}), was obtained from 3.12 V of the pristine Li_2FeSiO_4 to 3.25 V of the $Li_2FeSiO_{3.5}N_{0.5}$, which was predicted by Dompablo *et al.*'s calculations with first principles method [11]. Also, it was indicated that the 2nd redox reaction (Fe^{3+}/Fe^{4+}) could be decreased at a voltage of ~4.75 V in $Li_2FeSiO_{3.5}N_{0.5}$ lower than that of ~4.85 V for undoped Li_2FeSiO_4. In short, substitution of N for O may affect the electrode characteristics of $Li_2FeP_2O_7$ and Li_2FeSiO_4 based on experimental and modelling study, respectively.

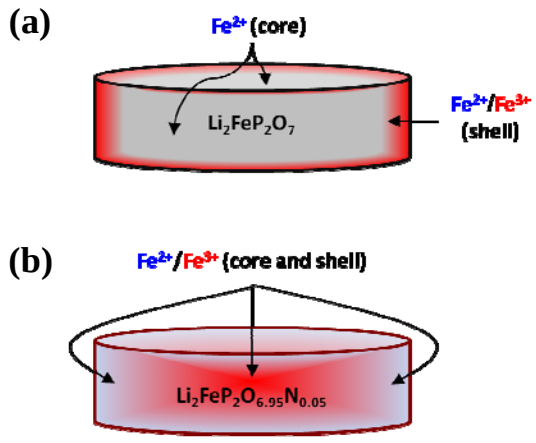

Figure 5-21 Schematic plot of a core-shell structure for (a) y=0, cooling in air; (b) y=0.05, heating in N_2.

5.5 Conclusions

N-doped $Li_2FeP_2O_7$ compositions, i.e. $Li_{2+x}FeP_2O_{7-x}N_x$ and $Li_2FeP_2O_{7-y}N_y$, have been synthesized via solid-state reaction but the N_2 evolution during sample preparation is a general concern. The effect of N doping on phase composition, electrical, and electrochemical properties were studied in comparison with that of pure-phase $Li_2FeP_2O_7$. Lattice parameters of the $Li_2FeP_2O_{7-y}N_y$ samples alter and its unit cell volume slightly decreases with increasing N doping concentration below the saturation of y=0.1. Nitrogen composition in $Li_2FeP_2O_{6.95}N_{0.05}$ was confirmed using inert gas fusion method; an estimated nitrogen loss of ~67 % may occur during sample preparation and synthesis.

Impedance spectroscopy (IS) results show there is no real difference in the total conductivity and bulk activation energy of x=0.05 and 0.1 compared with those of x=0. As a result, for $Li_{2+x}FeP_2O_{7-x}N_x$, N doping has little effect within errors.

The resistivity and activation energy in $Li_2FeP_2O_{7-y}N_y$ (y=0.05) are lower than that of undoped $Li_2FeP_2O_7$ due to the coexistence of Fe^{2+} and Fe^{3+} ions benefitting the electronic conductivity and increased mobility of electrons. Mössbauer results confirmed different oxidation state of Fe which leads to increased electronic conductivity in N-doped $Li_2FeP_2O_7$. So far, attempts to prepare a solid solution up to y=0.1 have failed probably because of a limited N-substitution as shown by the presence of a minor-phase from the oxidation of Fe^{2+} to Fe^{3+}, and therefore, results in lower conductivity. Specifically, I-LFPN005 sample has the highest conductivity ~10^{-5} Scm^{-1} at room temperature with the lowest activation energy, ~0.16 eV, than other N-doped compositions.

Electrochemical properties of $Li_2FeP_2O_{6.95}N_{0.05}$, e.g. effect of particle size, working voltage, and rate performance, were evaluated through a coin-cell. Although the N-doped $Li_2FeP_2O_7$ did not demonstrate better battery performance rather than undoped one.

5.6 References

1. Shin-ichi Nishimura, Megumi Nakamura, Ryuichi Natsui and Atsuo Yamada, "New Lithium Iron Pyrophosphate as 3.5 V Class Cathode Material for Lithium Ion Battery", *J. Am. Chem. Soc.* **2010**, *132*, pp. 13596–13597.

2. K.C. Hsiao and A.R. West, "Synthesis, characterization and electrical properties of $Li_2MP_2O_7$ (M=Fe, Mn, Co) cathode materials for lithium-ion batteries," Tenth International Conference on Materials Chemistry (MC10), Manchester, UK, 4-7 July **2011**.

3. J.B. Bates, N.J. Dudney, G.R. Gruzalski, R.A. Zuhr, A. Choudhury and C.F. Luck, "Electrical properties of amorphous lithium electrolyte thin films", *Solid State Ionics* **1992**, *53-56*, pp. 647–654.

4. D.E. Day, "Structural role of nitrogen in phosphate glasses", *J. Non-Cryst. Solids* **1989**, *112*, pp. 7–14.

5. B. Wang, B.C. Chakoumakos, B.C. Sales, B.S. Kwak and J.B. Bates, "Synthesis, Crystal Structure, and Ionic Conductivity of a Polycrystalline Lithium Phosphorus Oxynitride with the γ-Li_3PO_4 Structure", *J. Solid State Chem*. **1995**, *115*, pp. 313–323.

6. Zhaojun Liu, Xuejie Huang and Dingsheng Wang, "First-principle investigations of N doping in $LiFePO_4$" *Solid State Commun*. **2008**, *147*, pp. 505–509.

7. M. Armand and M.E. Arroyo-de Dompablo, "Benefits of N for O substitution in polyoxoanionic electrode materials: a first principles investigation of the electrochemical properties of $Li_2FeSiO_{4-y}N_y$ (y=0, 0.5, 1)", *J. Mater. Chem.* **2011**, *21*, pp. 10026–10034.

8. Anthony R. West, *Basic Solid State Chemistry*, 2nd Edition, Wiley, New York, **2000**, pp. 215.

9. Naoya Furuta, Shin-ichi Nishimura, Prabeer Barpanda and Atsuo Yamada, "Fe^{3+}/Fe^{2+} Redox Couple Approaching 4 V in $Li_{2-x}(Fe_{1-y}Mn_y)P_2O_7$ Pyrophosphate Cathodes", *Chem. Mater.* **2012**, *24* (6), pp. 1055–1061.

10. Randall M. German, *Sintering Theory and Practice*, J. Wiley & Sons, **1996**, pp. 465.

11. M. Armand, J.-M. Tarascon and M.E. Arroyo-de Dompablo, "Comparative computational investigation of N and F substituted polyoxoanionic compounds", *Electrochem. Commun.* **2011**, *13*, pp. 1047–1050.

CHAPTER VI

Synthesis, Characterisation and Ionic Conductivity of Lithium Zinc Pyrophosphate Phases

6.1 Introduction

The reported lithium zinc phosphate phases in the ternary ZnO-Li_2O-P_2O_5 diagram are shown in **Fig. 6-1**. In early 1986, the binary $Zn_3(PO_4)_2$–Li_3PO_4 system, was first investigated by Torres-Trevino and West, through solid-state reaction and thermal analysis [1]. Three new phases, α-, β-$Li_4Zn(PO_4)_2$, and α-$LiZnPO_4$ were reported and the monoclinic unit cell of α-$LiZnPO_4$ determined. For the $Zn_2P_2O_7$–$Li_4P_2O_7$ system, in 1995, Mikirticheva *et al.* studied the composition $Li_2ZnP_2O_7$ as a mixture of two new phases, solid solution $Li_{4x}Zn_{2-2x}P_2O_7$ ($0.15 \leq x \leq 0.28$) and $Li_{2.4}Zn_{0.8}P_2O_7$, illustrated in **Fig. 6-2** [2-3]. In 2009, Ma *et al*. proposed a new phase, $LiZn_{1.5}P_2O_7$, which was indexed as orthorhombic (S.G. P*bcm*) [4]. Subsequently, Liang *et al.* reported the phase relations of the ternary system ZnO–Li_2O–P_2O_5, and specifically, a new ternary compound, $Li_3Zn_{0.5}P_2O_7$, was reported [5]. Its low-temperature phase (< 365°C) was indexed as monoclinic with probable S.G. C2/*m*, C2 or C*m*, and the high-temperature phase (365–766 °C) with probable S.G. C*c* or C2/*c*.

In 2010, Lapshin *et al.* investigated the crystal structure of low-temperature $Li_{2.4}Zn_{0.8}P_2O_7$ with monoclinic crystal symmetry; it has a 3-D framework structure wherein the zinc and lithium atoms partially occupy the same sites [6]. In addition, a change in the intensities of diffraction patterns and an abrupt change in the thermal expansion coefficient were observed as the sample was heated above 300°C, which indicates that the Li^+ ions are probably mobile in $Li_{2.4}Zn_{0.8}P_2O_7$ at higher temperature [7].

In this chapter, the pseudobinary phase diagram $Zn_2P_2O_7$–$Li_4P_2O_7$ was chosen for study and the aim is to a) attempt synthesis and confirm the complex series of reported phases and/or solid solutions based on the $Li_{4x}Zn_{2-2x}P_2O_7$ (0 < x < 1) formula, b) study the crystal structure of $Li_{2.4}Zn_{0.8}P_2O_7$ (x=0.6) by neutron diffraction, and c) measure the electrical properties using impedance spectroscopy. Based on these results, a fundamental understanding of structure-composition-property relations may be developed.

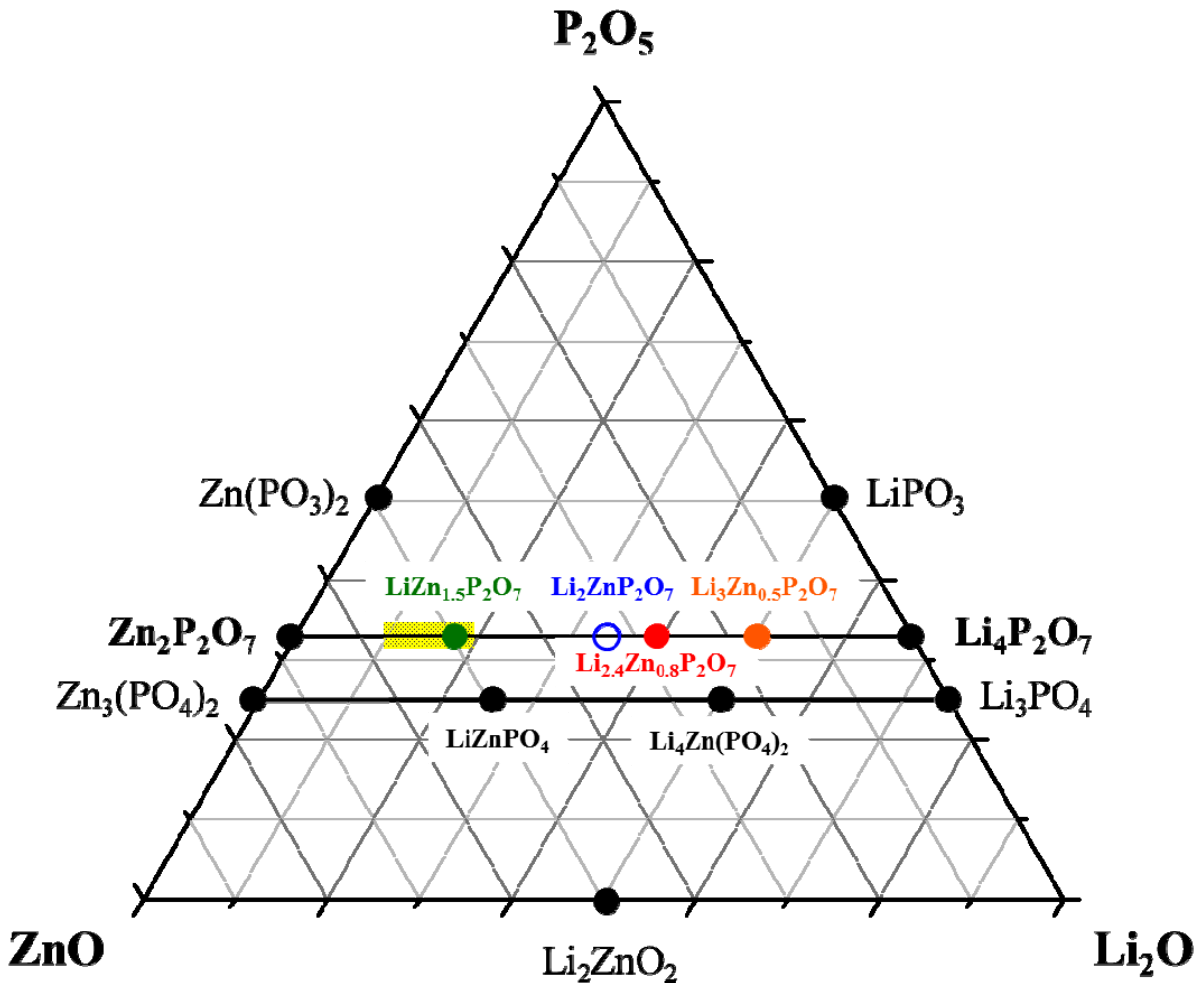

Figure 6-1 Composition triangle of the ZnO-Li_2O-P_2O_5 system. Solid solution $Li_{4x}Zn_{2-2x}P_2O_7$ ($0.15 \leq x \leq 0.28$) reported in Ref. 2 is represented with the yellow bar.

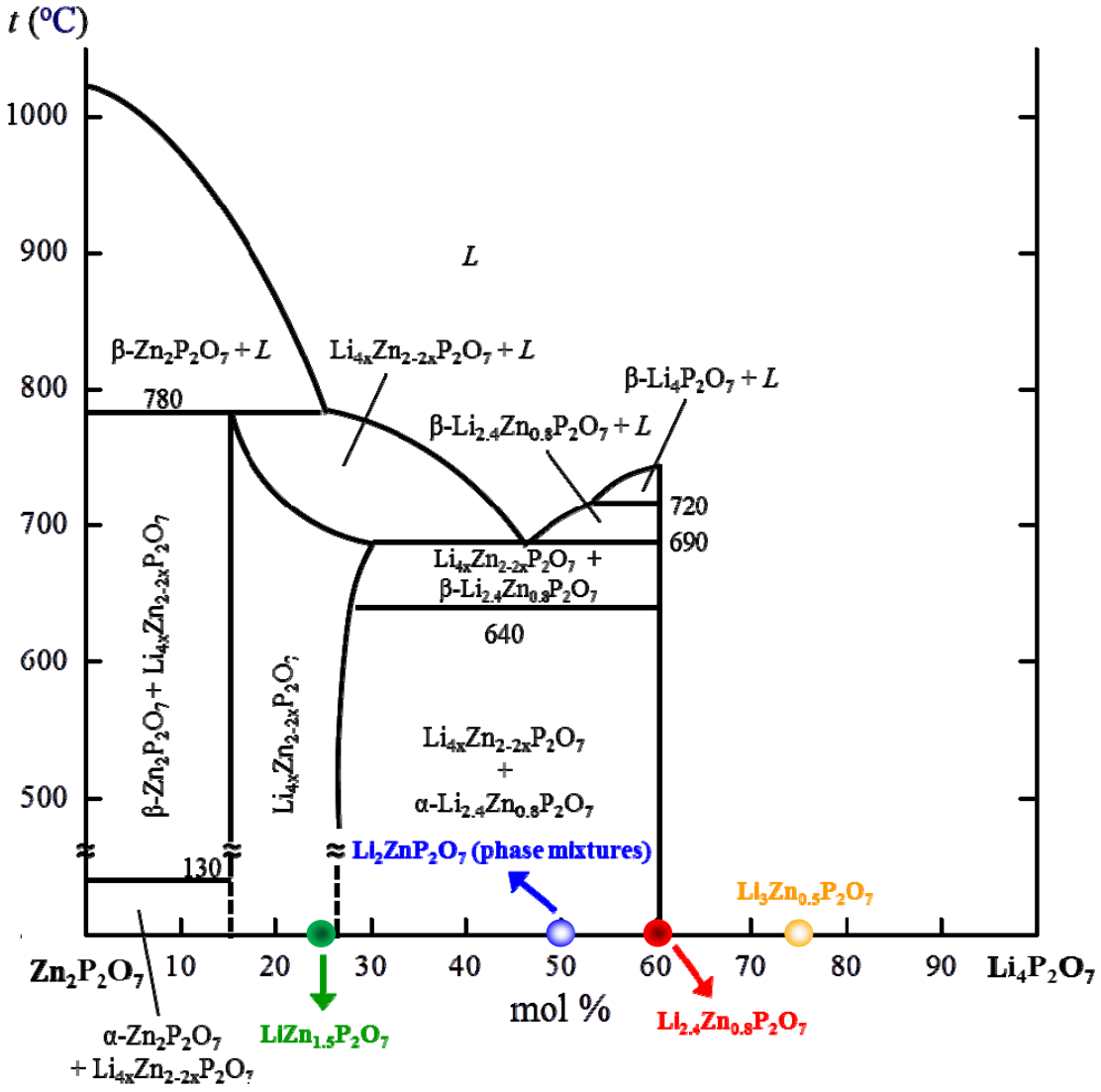

Figure 6-2 Partial phase diagram of the binary system $Zn_2P_2O_7$–$Li_4P_2O_7$ modified from Ref. 3. Compositions synthesised here were expressed with the general formula, $Li_{4x}Zn_{2-2x}P_2O_7$ (0 < x <1), for which mole % $Li_4P_2O_7$ = 100 x.

6.2 Synthesis

Samples were synthesised from stoichiometric amounts of Li_2CO_3, $(NH_4)H_2PO_4$, ZnO (Sigma-Aldrich, 99.9%) by conventional solid-state reaction. The mixtures were ground for ~40 min in an agate mortar with acetone, pressed into pellets, decomposed at 350°C for 6 h and then heated at 600°C for 24 h with a heating rate of 5°C/min under air atmosphere, **Fig. 6-3**. The phase content of the produced materials was determined using X-ray diffraction operated at 40 kV and 30 mA with Co $K_{\alpha1}$ (1.78896 Å) radiation. Lattice parameters were calculated using a Cu PSD operated at 40 kV and 35 mA with Cu $K_{\alpha1}$ (1.5406 Å) radiation for samples reheated at 625°C for 24 h. The scanning step size and counting time were set at 0.2° and 100 seconds in the 2θ range 5–80°. Rietveld refinement of the powder ND patterns of $Li_{2.4}Zn_{0.8}P_2O_7$ collected from D2B diffractometer (λ=1.59432 Å) was performed using *FullProf* software.

Impedance spectroscopy was utilized to measure the electrical properties; samples (0.2 g) were sintered in air at 600°C for 12 hours with a heating rate of 5.0 °C/min. Gold electrodes were applied using an Emscope SC500 gold sputter-coater on each side of the pellet for 4 minutes with 2 cycles using a current of 30 mA. High-temperature testing of the Au-sputtered pellets in air was conducted using a Hewlett Packard 4192A impedance analyzer.

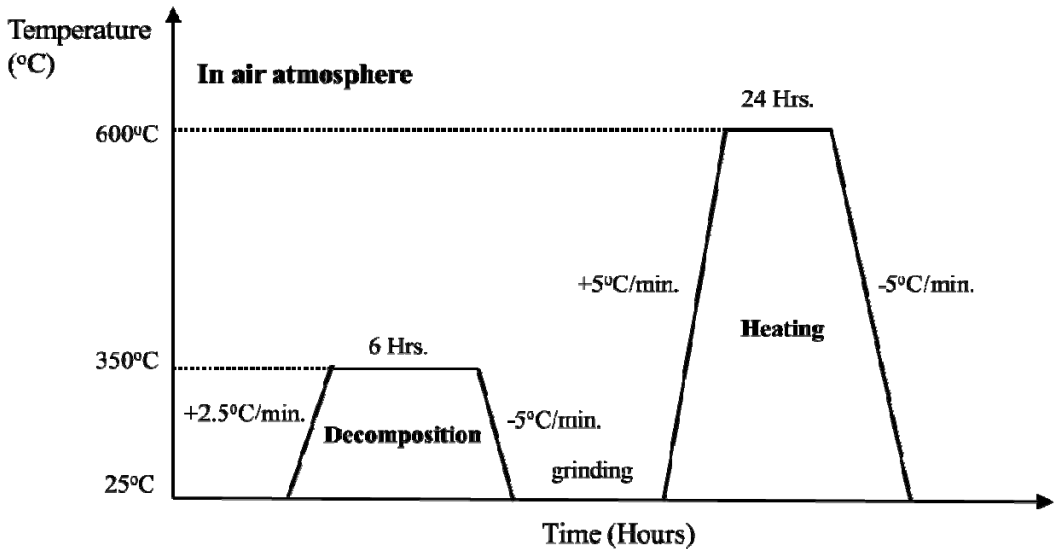

Figure 6-3 Two-step process for heat treatment in air.

6.3 Results

6.3.1 Binary Phase Diagram of the $Zn_2P_2O_7$–$Li_4P_2O_7$ System

Lithium zinc pyrophosphates $Li_{4x}Zn_{2-2x}P_2O_7$ (0 < x < 1) were synthesized according to the following reaction 6.1:

$$(2x)\ Li_2CO_3 + (2\text{-}2x)\ ZnO + 2(NH_4)H_2PO_4 \rightarrow Li_{4x}Zn_{2-2x}P_2O_7 + 2NH_3 + (2x)\ CO_2 + 3H_2O \quad (6.1)$$

Table 6-1 summarises the XRD results for 19 compositions where x varied from 0.20 to 0.75. Compositions of x in the ranges of 0 to 0.20 and 0.75 to 1 were not studied because the structure and electrical properties of x=0 ($Zn_2P_2O_7$) and x=1 ($Li_4P_2O_7$) are reported [8-9]. Phase-pure materials were produced in samples at x=0.20, 0.25, 0.33, 0.40, 0.575, 0.6 and 0.625. The simulated and measured X-ray powder diffraction patterns (Co radiation) of x=0.25, $LiZn_{1.5}P_2O_7$, heated at 600°C for 24 h in air are presented in **Fig. 6-4**. The theoretical XRD pattern is calculated using published lattice parameters and atomic coordinates [4]. In general, the intensity distribution of synthesized $LiZn_{1.5}P_2O_7$ is identical to that of the theoretical pattern without any impurities, and the phase is therefore assumed to have orthorhombic symmetry with space group P*bcm*. The indexed powder pattern is listed in **Table A6-1** and the refined lattice parameters and unit cell volume are similar to those reported in PDF card 04-017-1973. **Fig. A6-1** shows a solid solution formation of $Li_{4x}Zn_{2-2x}P_2O_7$ heated at 625°C in the x range between x=0.2~0.25 which is in agreement with previous studies in Ref. 2.

Table 6-1 XRD results of heating compositions in the $Zn_2P_2O_7$–$Li_4P_2O_7$ system with formula $Li_{4x}Zn_{2-2x}P_2O_7$ (0.2 ≤ x ≤ 0.75).

Composition (x)	Molar ratio of Li_2O : ZnO : P_2O_5	Formula	Temp. (°C)	Time (h)	Phase present
0.20	0.14 : 0.53 : 0.33	$Li_{0.8}Zn_{1.6}P_2O_7$	600~625	24~48	**S.S. $LiZn_{1.5}P_2O_7$**
0.25	0.17 : 0.50 : 0.33	$LiZn_{1.5}P_2O_7$			**$LiZn_{1.5}P_2O_7$**
0.28	0.19 : 0.48 : 0.33	$Li_{1.12}Zn_{1.44}P_2O_7$	600~625	24~48	$LiZn_{1.5}P_2O_7$, $Li_{1.33}Zn_{1.33}P_2O_7$
0.30	0.20 : 0.47 : 0.33	$Li_{1.2}Zn_{1.4}P_2O_7$			
0.33	0.22 : 0.44 : 0.33	$Li_{1.33}Zn_{1.33}P_2O_7$	600~625	24~48	**$Li_{1.33}Zn_{1.33}P_2O_7$**
0.40	0.26 : 0.40 : 0.33	$Li_{1.6}Zn_{1.2}P_2O_7$			**S.S. $Li_{1.33}Zn_{1.33}P_2O_7$**
0.425	0.28 : 0.38 : 0.33	$Li_{1.7}Zn_{1.15}P_2O_7$	600~625	24~48	$Li_{1.33}Zn_{1.33}P_2O_7$, $Li_{2.4}Zn_{0.8}P_2O_7$
0.45	0.30 : 0.37 : 0.33	$Li_{1.8}Zn_{1.1}P_2O_7$			
0.475	0.32 : 0.35 : 0.33	$Li_{1.9}Zn_{1.05}P_2O_7$			
0.50	0.33 : 0.33 : 0.33	$Li_2ZnP_2O_7$			
0.55	0.37 : 0.30 : 0.33	$Li_{2.2}Zn_{0.9}P_2O_7$	600~625	24~48	$Li_{1.33}Zn_{1.33}P_2O_7$, $Li_{2.4}Zn_{0.8}P_2O_7$
0.575	0.38 : 0.28 : 0.33	$Li_{2.3}Zn_{0.85}P_2O_7$	600~625	24~48	**S.S. $Li_{2.4}Zn_{0.8}P_2O_7$**
0.60	0.40 : 0.27 : 0.33	$Li_{2.4}Zn_{0.8}P_2O_7$	600~625	24~48	**$Li_{2.4}Zn_{0.8}P_2O_7$**
0.625	0.42 : 0.25 : 0.33	$Li_{2.5}Zn_{0.75}P_2O_7$	600~625	24~48	**S.S. $Li_{2.4}Zn_{0.8}P_2O_7$**
0.65	0.43 : 0.23 : 0.33	$Li_{2.6}Zn_{0.7}P_2O_7$	600~625	24~48	$Li_{2.4}Zn_{0.8}P_2O_7$, $Li_3Zn_{0.5}P_2O_7$, $Li_4P_2O_7$
0.675	0.45 : 0.22 : 0.33	$Li_{2.7}Zn_{0.65}P_2O_7$	600~625	24~48	$Li_{2.4}Zn_{0.8}P_2O_7$, $Li_3Zn_{0.5}P_2O_7$, $Li_4P_2O_7$
0.70	0.47 : 0.20 : 0.33	$Li_{2.8}Zn_{0.6}P_2O_7$	600~625	24~48	$Li_3Zn_{0.5}P_2O_7$, $Li_4Zn(PO_4)_2$, $Li_4P_2O_7$
0.725	0.48 : 0.19 : 0.33	$Li_{2.9}Zn_{0.55}P_2O_7$	600~625	24~48	$Li_3Zn_{0.5}P_2O_7$, $Li_4Zn(PO_4)_2$, $Li_4P_2O_7$, $Li_3PO_4/LiPO_3$
0.75	0.50 : 0.17 : 0.33	$Li_3Zn_{0.5}P_2O_7$	600~850	24~48	

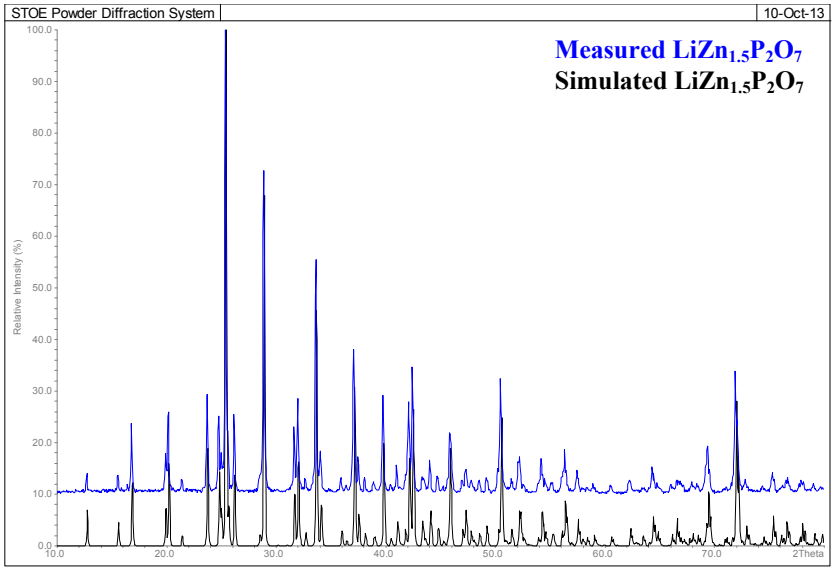

Figure 6-4 Simulated (blak) and synthesised (blue) XRD patterns (Co radiation) of $LiZn_{1.5}P_2O_7$ (x=0.25) synthesised at 600°C following a two-step process.

In order to increase the reactivity and/or crystallinity in materials, all samples were ground again and reheated at 625°C for 24 h in air. The XRD patterns of $Li_{4x}Zn_{2-2x}P_2O_7$ powders with increasing Li content from stoichiometry 1 (x=0.25) to 1.33 (x=0.33) are shown in **Fig. 6-5**; several peaks were observed to be similar in the same 2θ positions (see arrowed). The intensities of some diffraction peaks decreased significantly and disappeared when *x* increased to 0.33, see positions marked by red line (|). As a result, the composition x=0.33 is suggested to be a new phase, $Li_{1.33}Zn_{1.33}P_2O_7$; it was indexed on a monoclinic system by *WinX^{POW} 3.05* program with F(30)=9.0. The probable space group is $P2_1/a$ with lattice parameters a = 15.502(7) Å; b = 5.297(2) Å; c = 18.767(9) Å; β = 92.36(4)° and unit cell volume V = 1540.0(8) Å^3. The indexing results are listed in **Table 6-2**, which could be used as a standard for phase identification. A phase mixture may be present between x=0.25 and x=0.33.

As *x* varied from 0.33 → 0.4 → 0.5, **Fig. 6-6**, there are some overlapping lines but some new lines start to appear and their intensities increase greatly with x, see arrowed. There may be a solid solution of $Li_{1.33}Zn_{1.33}P_2O_7$ from x=0.33 up to ~0.4 as indicated by big line shifts at high 2θ angle (see dashed region); the calculated lattice parameters and unit cell volume for x=0.4 are a = 15.536(14) Å, b = 5.307(6) Å, c = 18.695(22) Å, β = 91.97(9)°,

V = 1540.4(22) Å^3. Attempts to synthesise a single-phase $Li_2ZnP_2O_7$ were not successful, but a phase mixture of x=0.33 + x=0.6 obtained, **Fig. 6-7**. At x ranged from 0.425 to 0.475, these phases are similar to that of x=0.5.

Fig. 6-8 shows the XRD patterns with three different compositions, in which x varied from 0.5 to 0.6. Although the pattern for x=0.6, i.e. $Li_{2.4}Zn_{0.8}P_2O_7$, at room temperature is slightly poor quality, it appears to be a pure phase and was indexed as monoclinic, space group $P2_1/n$, **Fig. 6-9**. The refined lattice parameters and unit cell volume are similar to those reported in PDF card 00-055-0703, **Table A6-2**. A possible solid solution covering the range x=0.575 to 0.6 was observed in **Fig. 6-8** and compared with the XRD patterns for those samples quenched from 625°C in air, see **Fig. 6-10**. The extra shoulder peaks appear in x=0.575 (see arrowed). The XRD patterns of x between 0.6 and 0.675 are shown in **Fig. 6-11**; x ranging from 0.6 to 0.625 appears to be a solid solution of low-temperature $Li_{2.4}Zn_{0.8}P_2O_7$. However, the XRD pattern of x=0.625 quenched from 625°C consists of a multi-phase mixture, giving rise to the difficulty to determine its high-temperature form, **Fig. 6-10**.

$Li_{2.4}Zn_{0.8}P_2O_7$ was reported to have a phase transition in the temperature range of 300~350 °C [7]. **Fig. 6-12** shows the XRD diffraction patterns of $Li_{2.4}Zn_{0.8}P_2O_7$ followed by cooling at slower rate to 25°C and then rapid quenched from 200, 300, 400 and 625°C under air atmosphere. In both quenched samples at 400°C and 625°C, the intensities of some peaks are redistributed and there is a clearer splitting of certain peaks. However, the sample quenched from 300°C has a complex peak distribution and probably, it shows an intermediate phase between 200°C and 400°C. The thermal-phase stability of $Li_{2.4}Zn_{0.8}P_2O_7$ was further analysed using DSC, **Fig. 6-13**; apparently three endothermic reactions were observed at ~320 °C, ~575 °C and ~645 °C on heating, which indicate there may be three phase transformations in this compound. Lapshin *et al.* reported the XRD pattern at 650°C could not be indexed due to the multiphase composition in sample [7]. Further study should be carried out to investigate the phase variation in x=0.6 at different temperatures. The high-temperature form at 625°C was indexed as orthorhombic with a = 5.140(2) Å, b = 8.217(4) Å, c = 13.421(5) Å and V = 566.9(3) Å^3 consistent with previous studies in Ref. 7.

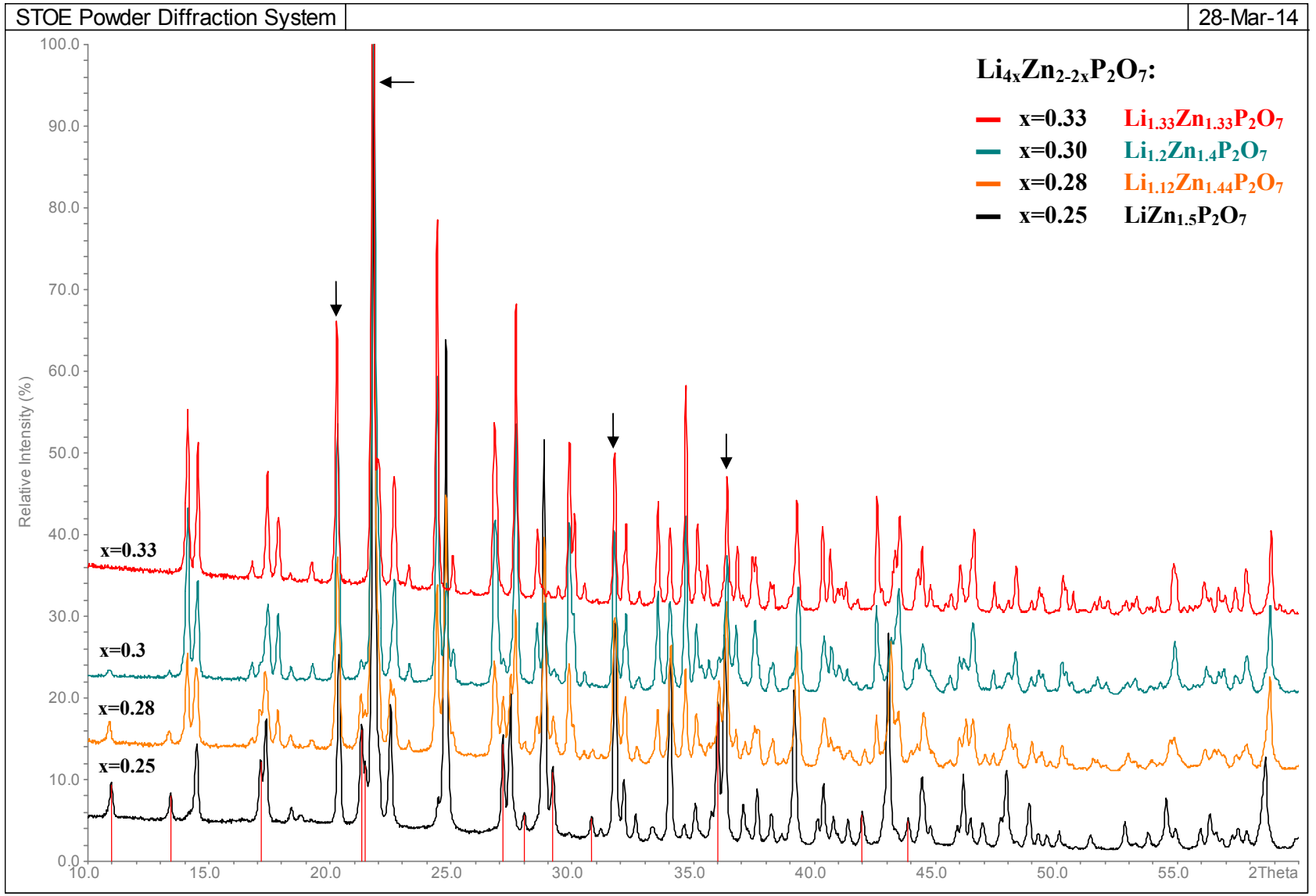

Figure 6-5 XRD patterns (Cu PSD) of $Li_{4x}Zn_{2-2x}P_2O_7$ ($0.25 \leq x \leq 0.33$).

Table 6-2 The indexed results of $Li_{1.33}Zn_{1.33}P_2O_7$ reheated at 625°C by XRD (Cu PSD) with Si as external standard for *d*-space measurement.

2θ [obs] (°)	H K L	2θ [calc] (°)	△2θ (°)	Int.	d [obs] (Å)	d [calc] (Å)
14.112	0 0 3	14.158	-0.0459	22.8	6.2707	6.2505
14.542	-2 0 2	14.521	0.0210	20.0	6.0864	6.0952
16.794	--- not indexed ---			3.1	5.2748	
17.395	0 1 1	17.381	0.0144	14.2	5.0940	5.0982
17.865	-2 0 3	17.852	0.0130	11.7	4.9611	4.9647
19.223	0 1 2	19.228	-0.0046	3.5	4.6134	4.6123
20.264	2 1 0	20.293	-0.0287	38.2	4.3787	4.3725
21.761	-2 0 4	21.736	0.0250	100.0	4.0808	4.0854
22.639	2 1 2	22.618	0.0201	17.5	3.9246	3.9280
23.242	-4 0 1	23.245	-0.0029	3.7	3.8240	3.8235
24.409	-3 1 1	24.380	0.0289	50.3	3.6438	3.6481
25.072	2 1 3	25.104	-0.0324	5.7	3.5490	3.5445
26.788	2 0 5	26.814	-0.0259	30.5	3.3254	3.3222
27.660	-3 1 3	27.644	0.0157	50.2	3.2224	3.2242
28.556	0 0 6	28.538	0.0176	11.2	3.1233	3.1252
29.881	1 1 5	29.921	-0.0399	30.1	2.9878	2.9839
30.494	4 0 4	30.517	-0.0232	2.9	2.9291	2.9270
31.748	2 1 5	31.767	-0.0189	24.7	2.8162	2.8146
32.202	--- not indexed ---			9.1	2.7776	
33.528	-3 1 5	33.503	0.0251	16.5	2.6707	2.6726
34.027	5 1 1	34.004	0.0225	9.5	2.6327	2.6344
34.683	1 2 1	34.694	-0.0103	30.7	2.5843	2.5836
35.164	0 2 2	35.178	-0.0143	12.5	2.5501	2.5491
35.562	-1 2 2	35.601	-0.0394	6.6	2.5225	2.5198
36.383	6 0 2	36.448	-0.0654	19.9	2.4674	2.4631
36.808	0 2 3	36.823	-0.0147	9.5	2.4398	2.4389
37.426	1 2 3	37.389	0.0375	7.2	2.4010	2.4033
37.569	0 1 7	37.595	-0.0268	10.5	2.3922	2.3905
38.170	3 2 0	38.155	0.0156	4.0	2.3559	2.3568
38.305	1 1 7	38.276	0.0299	3.7	2.3479	2.3496
39.268	6 1 1	39.263	0.0050	16.6	2.2925	2.2928
40.327	6 1 2	40.349	-0.0221	11.7	2.2347	2.2335
40.655	2 0 8	40.638	0.0163	8.1	2.2174	2.2183
41.296	4 2 0	41.260	0.0360	3.8	2.1845	2.1863
42.596	-3 2 4	42.576	-0.0192	18.2	2.1208	2.1217

Final 2θ window: 0.08, Symmetry: monoclinic ($P2_1/a$), a = 15.502(7) Å; b = 5.297(2) Å; c = 18.767(9) Å; V = 1540.0(8) Å^3.

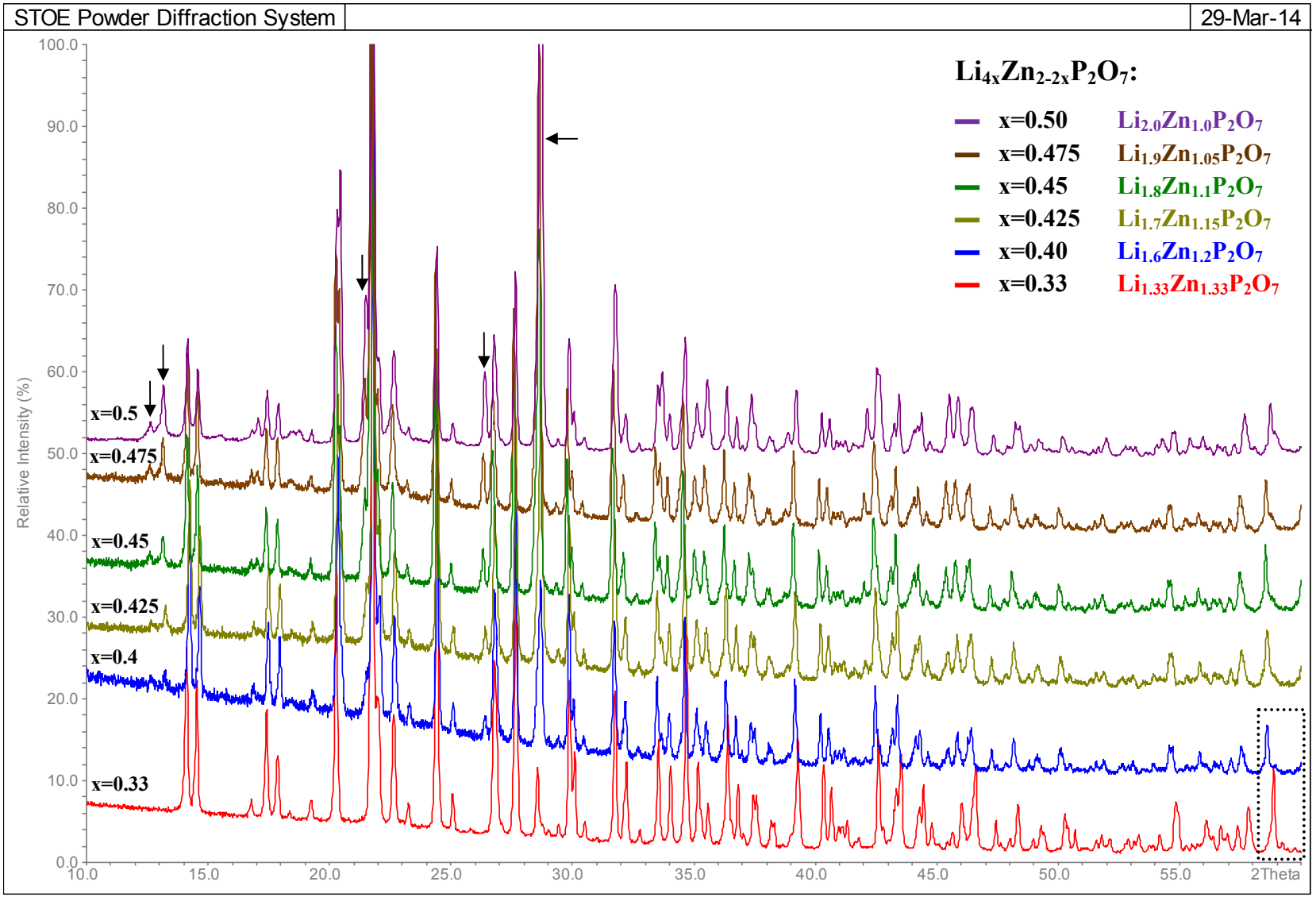

Figure 6-6 XRD patterns (Cu PSD) of $Li_{4x}Zn_{2-2x}P_2O_7$ ($0.33 \leq x \leq 0.5$).

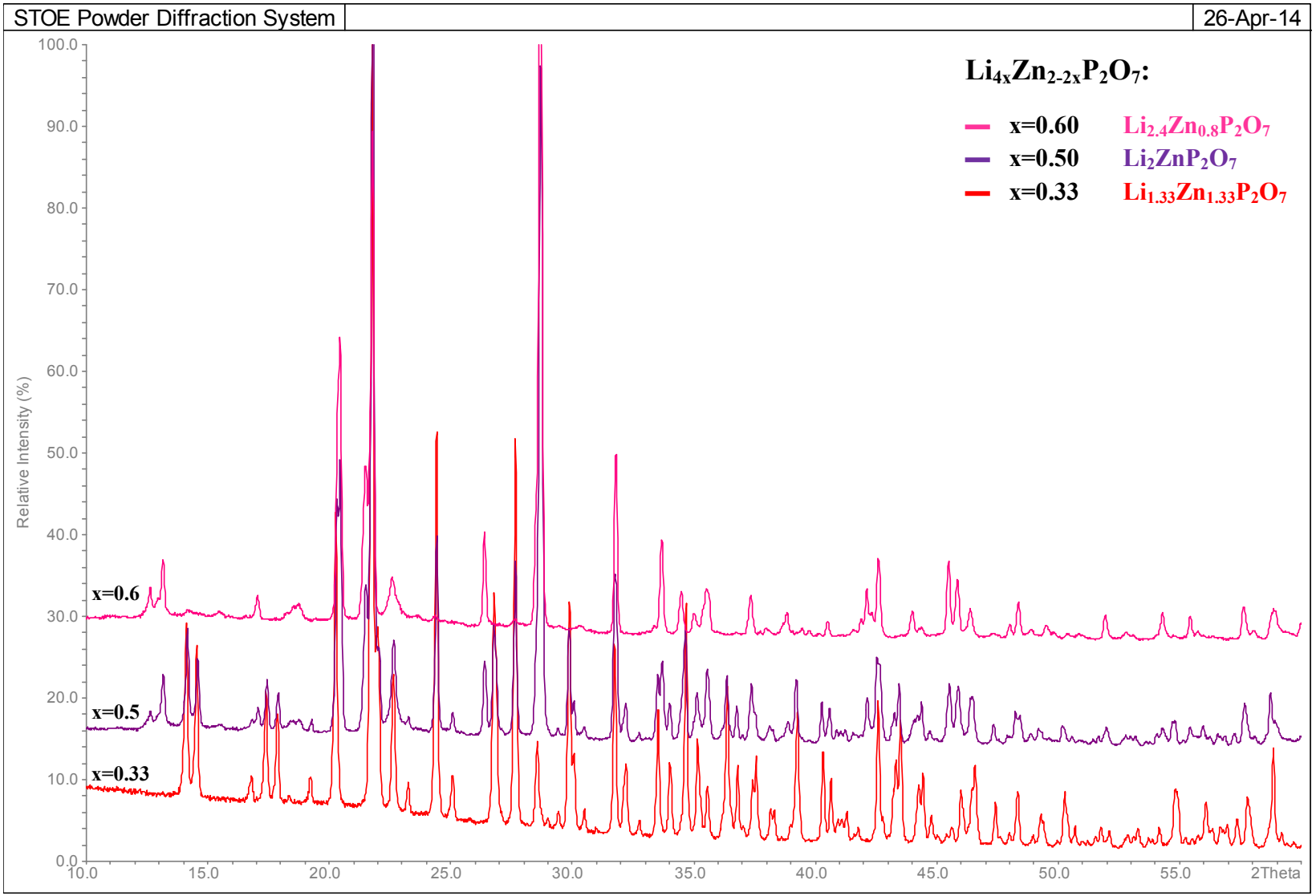

Figure 6-7 XRD patterns (Cu PSD) of $Li_{4x}Zn_{2-2x}P_2O_7$ (x=0.33, 0.5 and 0.6).

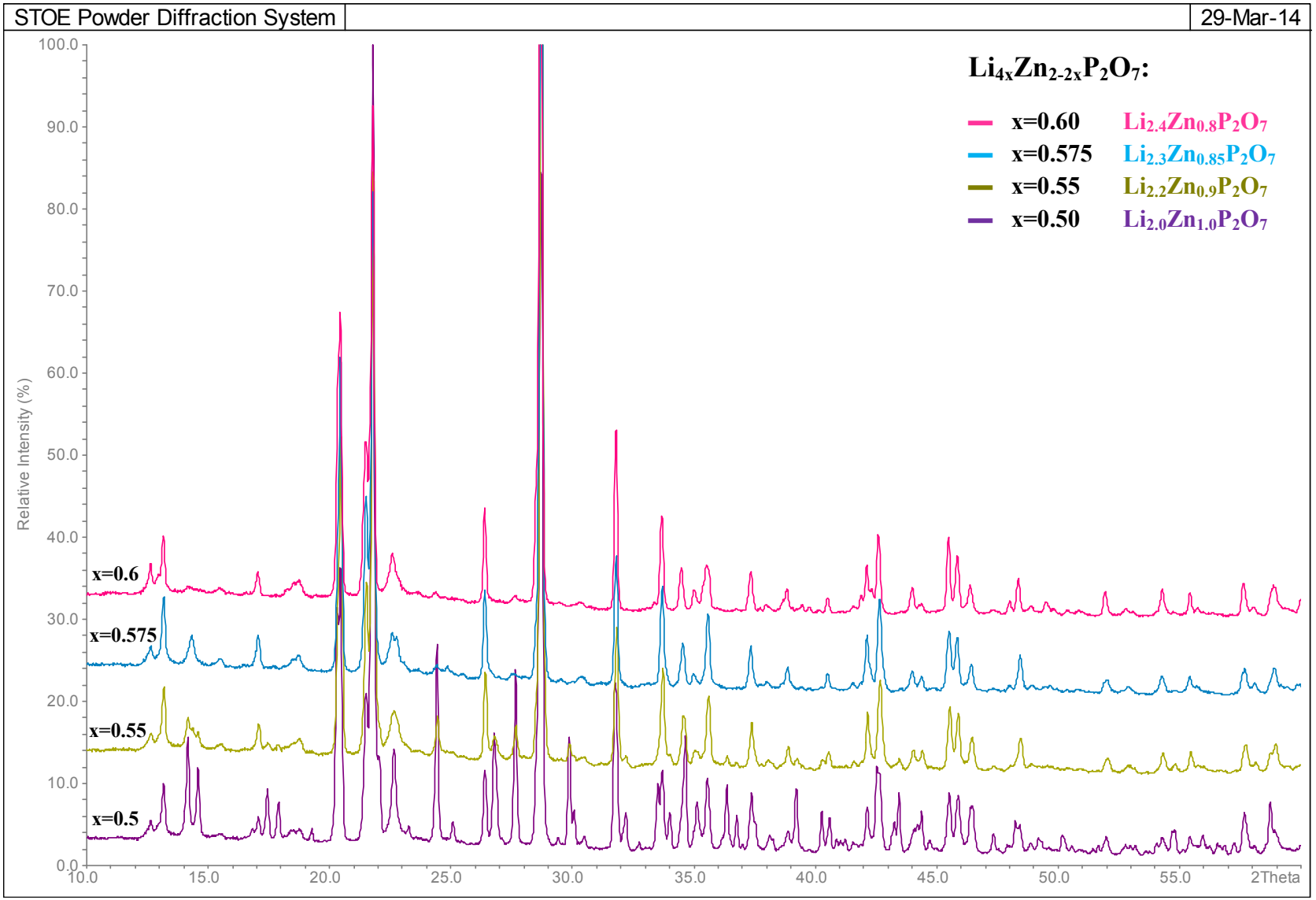

Figure 6-8 XRD patterns (Cu PSD) of $Li_{4x}Zn_{2-2x}P_2O_7$ ($0.5 \leq x \leq 0.6$).

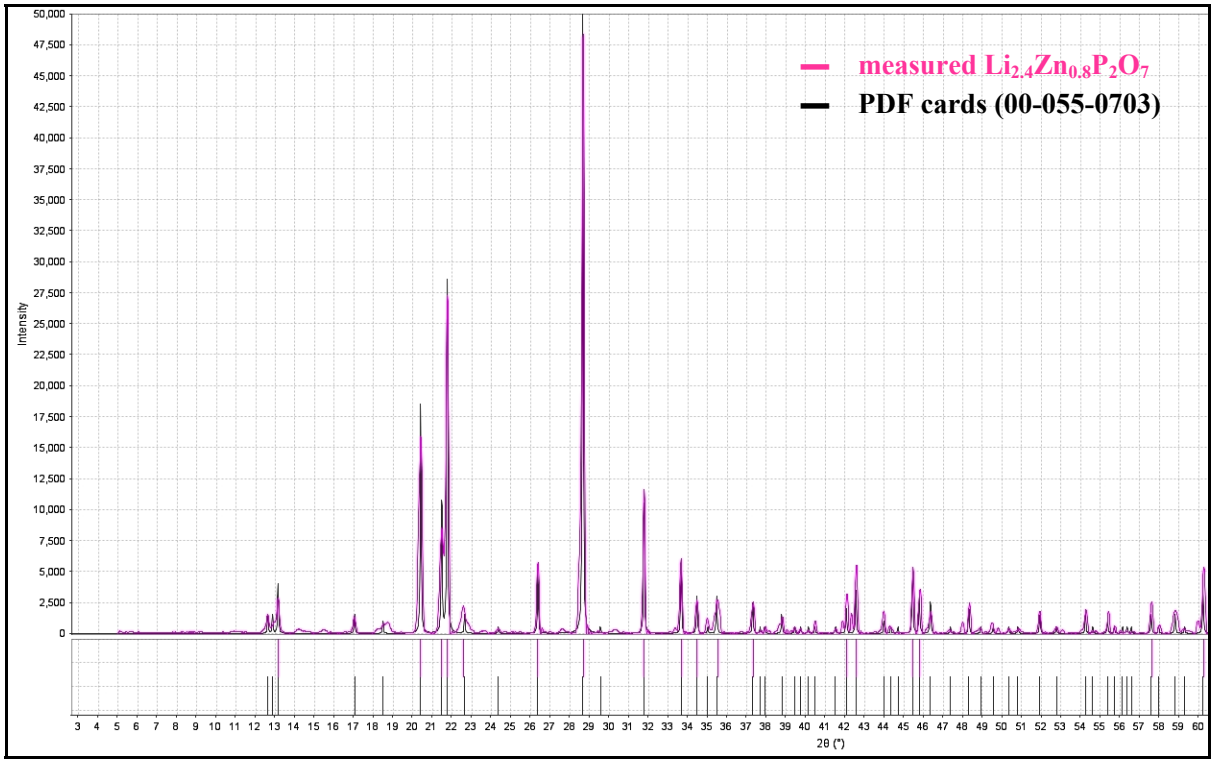

Figure 6-9 PDF cards (00-055-0703) of the low-temperature (≤ 300°C) $Li_{2.4}Zn_{0.8}P_2O_7$ phase with monoclinic form (black); XRD profiles of $Li_{2.4}Zn_{0.8}P_2O_7$ (red) synthesised at 625°C.

Fig. 6-14 shows the XRD pattern of $Li_3Zn_{0.5}P_2O_7$ (x=0.75) powder synthesised at 600°C for 24 hours in air together with indexed patterns (|) from Ref. 5. $Li_3Zn_{0.5}P_2O_7$ was found to be a mixture, containing $Li_4P_2O_7$, Li_3PO_4 and/or $LiPO_3$ and $Li_4Zn(PO_4)_2$. The 2θ positions of Li_3PO_4 and $LiPO_3$ peaks are, however, very close, giving rise to the difficulty to determine the exact secondary phase. In addition, the intensities of secondary phases, e.g. $Li_4Zn(PO_4)_2$ and $Li_4P_2O_7$, at x=0.725, are decreased in comparison to those at x=0.75. Composition $Li_3Zn_{0.5}P_2O_7$ was reheated at 625, 700, 750 and 850°C in air for 24 h, but with similar results, see **Fig. 6-15**. At x from 0.65 to 0.675, a mixture of three phases, $Li_{2.4}Zn_{0.8}P_2O_7$, $Li_3Zn_{0.5}P_2O_7$ and $Li_4P_2O_7$ was obtained, **Fig. 6-16**.

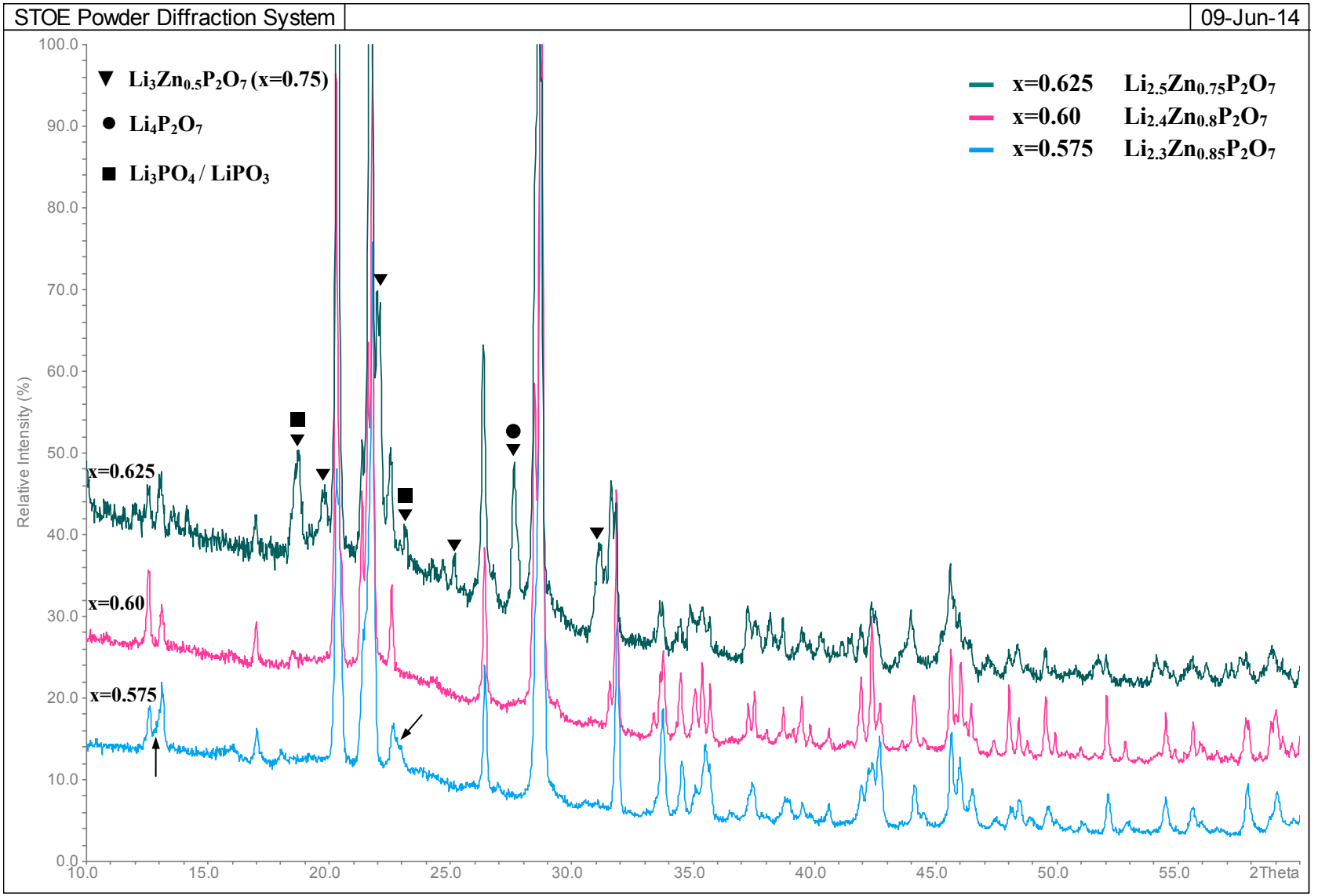

Figure 6-10 XRD patterns (Cu PSD) of the samples for x=0.575, 0.60 and 0.625 rapidly quenched from 625°C in air.

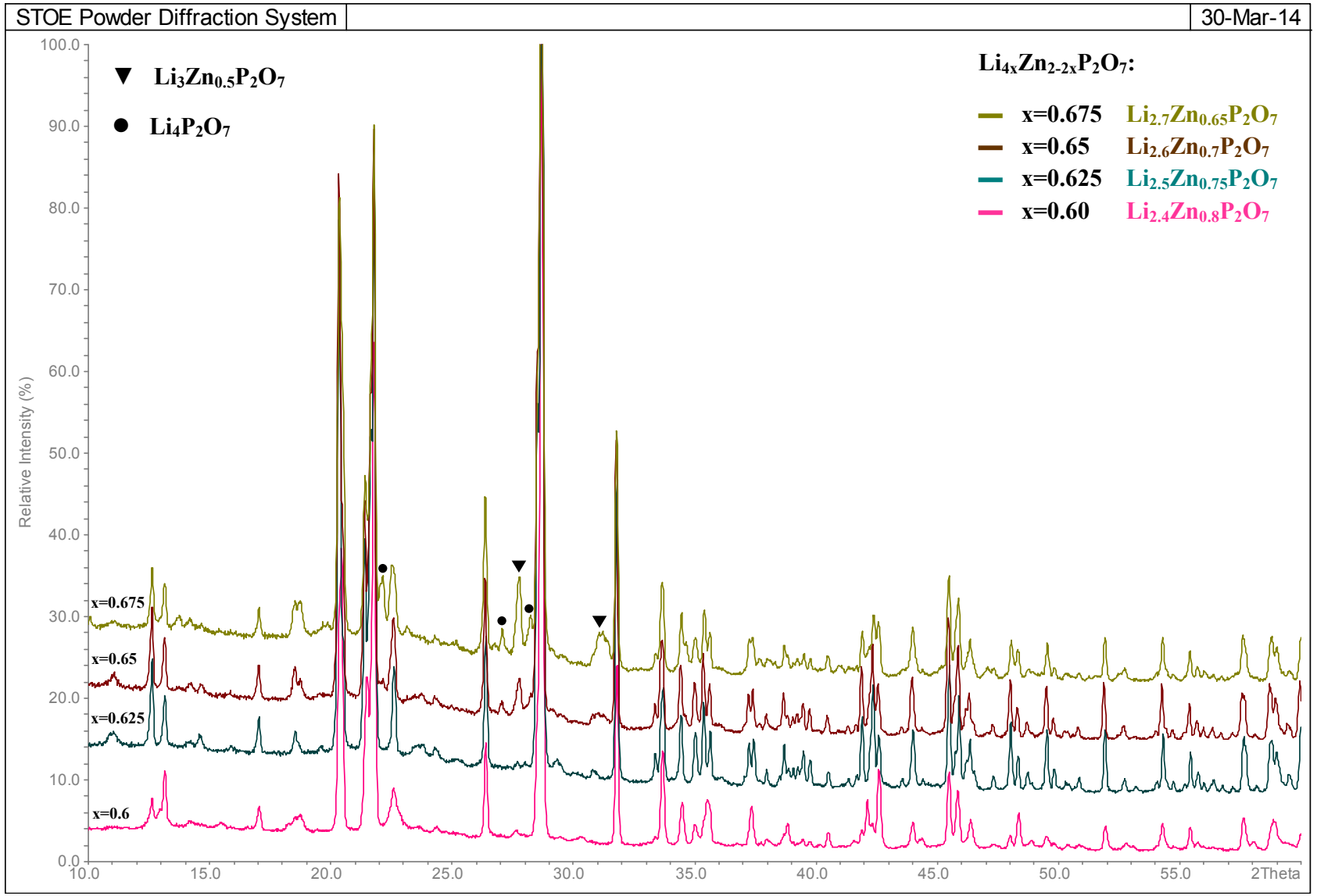

Figure 6-11 XRD patterns (Cu PSD) of $Li_{4x}Zn_{2-2x}P_2O_7$ (x=0.6 to 0.675).

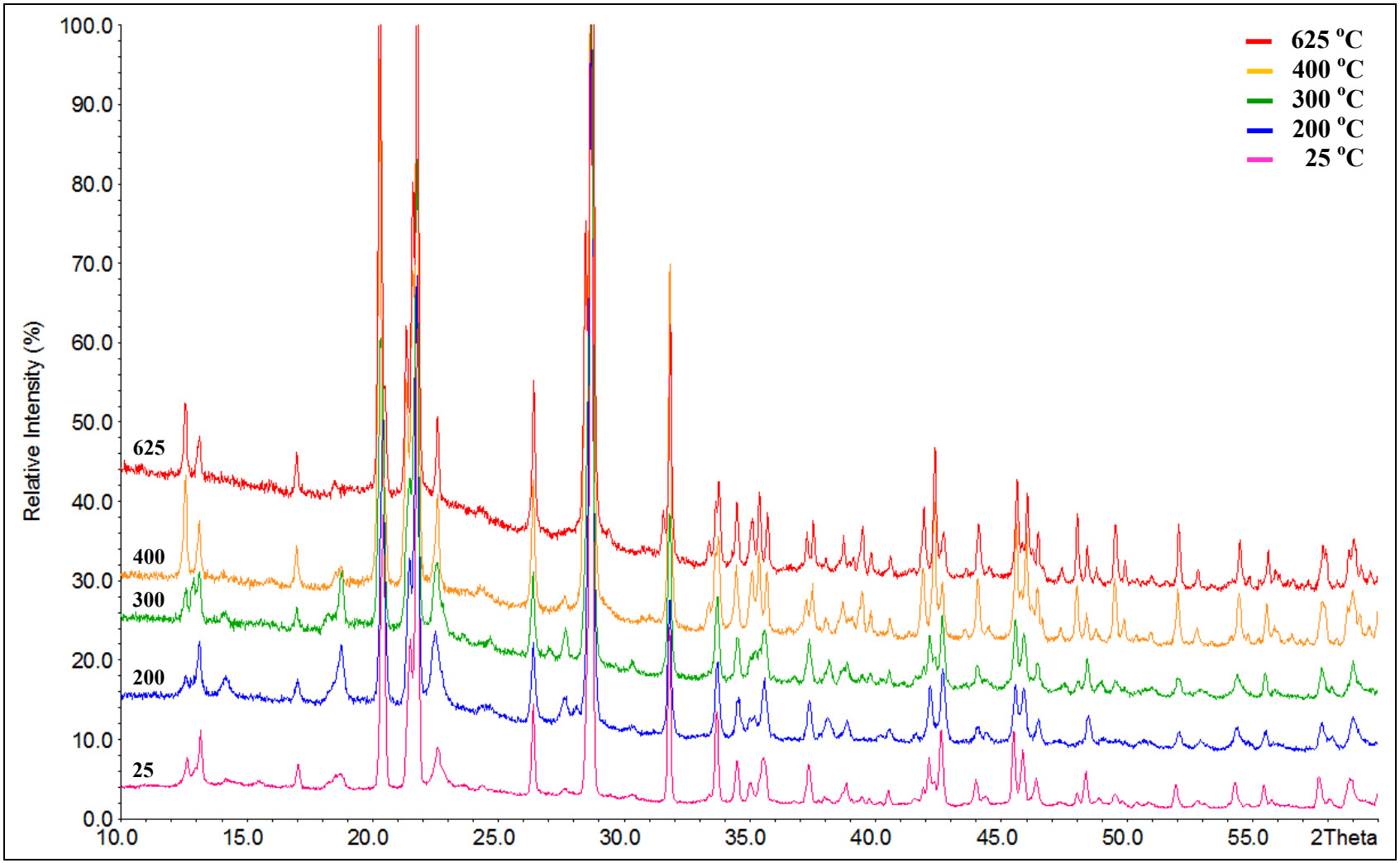

Figure 6-12 XRD patterns (Cu PSD) of the $Li_{2.4}Zn_{0.8}P_2O_7$ (x=0.6) at temperatures of 25, 200, 300, 400 and 625°C in air.

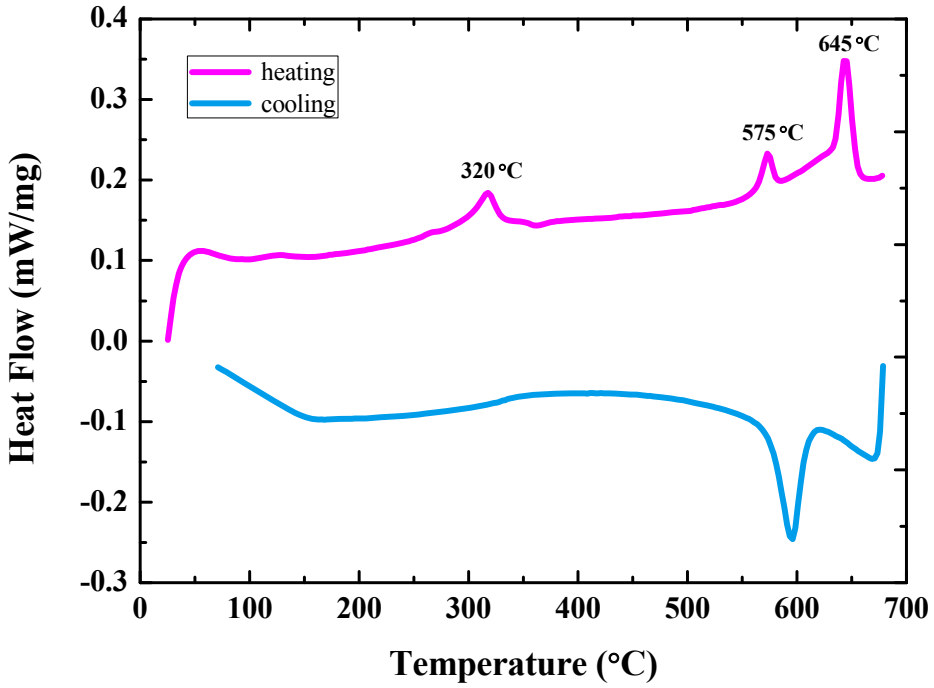

Figure 6-13 DSC analysis of $Li_{2.4}Zn_{0.8}P_2O_7$ over the temperature range 20–680 °C in air, using a heating/cooling rate of 10 °C/min.

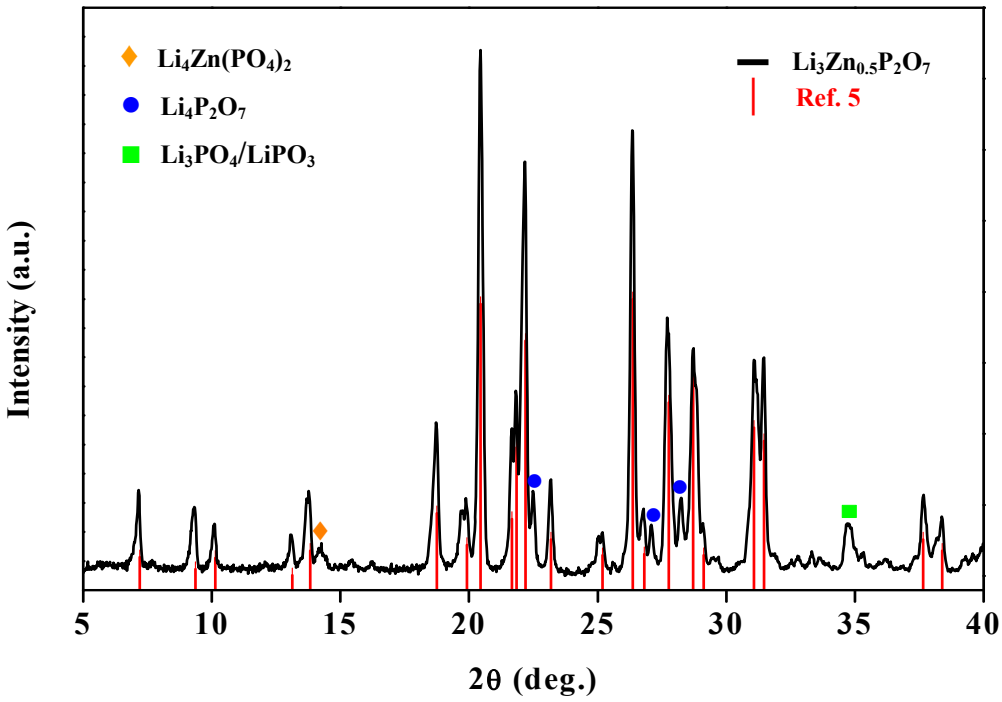

Figure 6-14 XRD patterns (Cu radiation) of the $Li_3Zn_{0.5}P_2O_7$ powder.

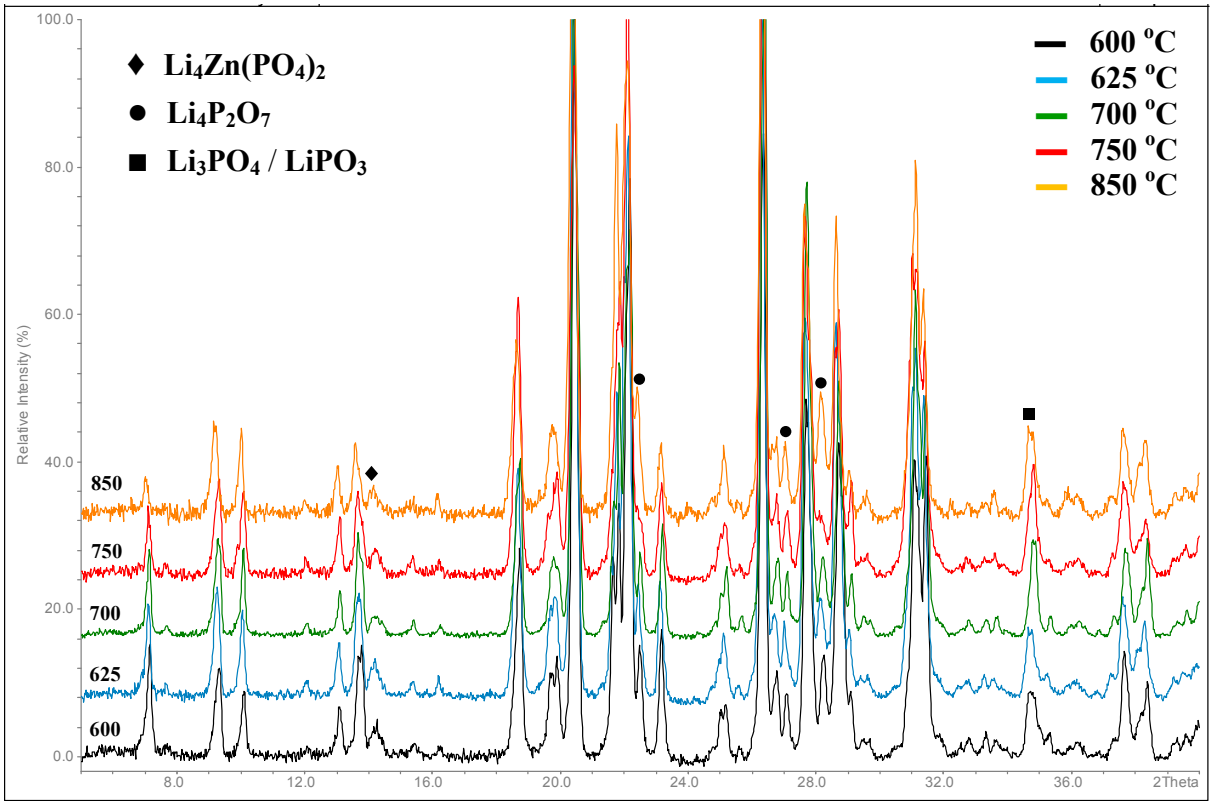

Figure 6-15 XRD patterns (Cu PSD) of the $Li_3Zn_{0.5}P_2O_7$ powders reheated at 600, 625, 700, 750 and 850°C for 24 h in air.

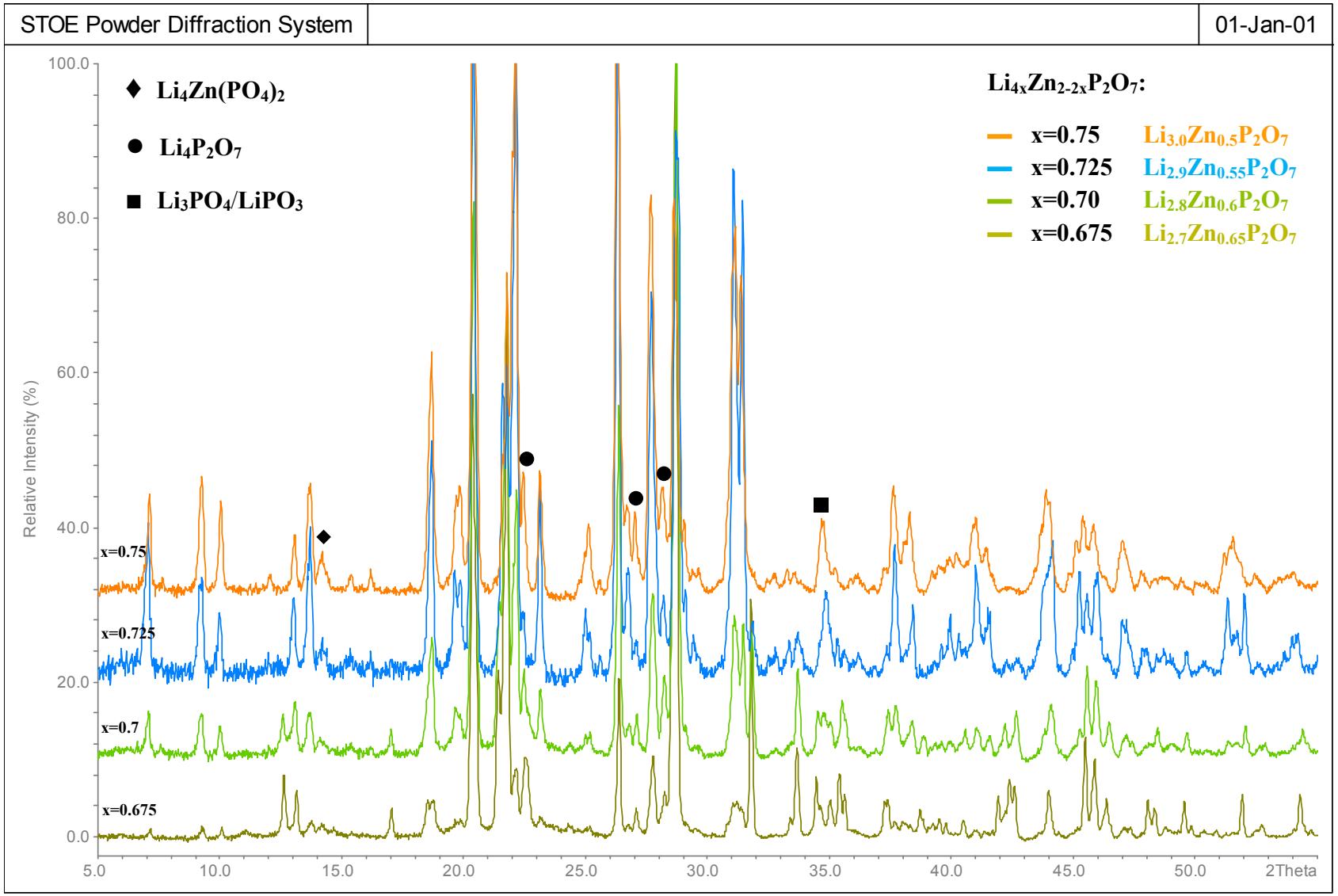

Figure 6-16 XRD patterns (Cu PSD) of $Li_{4x}Zn_{2-2x}P_2O_7$ (x=0.675 to 0.75).

6.3.2 Structural Characterisation of $Li_{2.4}Zn_{0.8}P_2O_7$

Literature work

The structure reported in Ref. 6 using XRD data has disorder of Li1 and M1 sites, together with a large U_{iso} for Li1. From *Lapshin*'s model, the condition of charge balance was not imposed in the refinement. The initial results showed that the occupancy ratio on M1 position was 0.7(3) Li and 0.24(1) Zn and M2 position 0.3(2) Li and 0.56(1) Zn. It was assumed that both M1 and M2 positions were fully occupied and therefore; the occupancies were specified to be 0.76 Li and 0.24 Zn for M1 site, with fixed 0.44 Li and 0.56 Zn for M2 site. In this case, the value of the divergence factor, R_{Bragg}, just slightly increased from 0.035 to 0.036, which suggested the Li occupancies varied on M1 and M2 sites were reasonable within errors [6]. As a result, it was claimed that the obtained chemical composition of the unit cell $4[Li_{2.2}Zn_{0.8}P_2O_7]$ within the error limits corresponds to $Li_{2.4}Zn_{0.8}P_2O_7$. The coordinates and isotropic thermal parameters of *Lapshin*'s model are listed in **Table A6-3**.

This work

Lapshin's model was used as a starting model to analyse room-temperature ND data. Rietveld refinements were conducted following five typical steps in the order: background, scale factors, FWHM and cell parameters, and atomic coordinates. Finally, thermal parameters were refined with constraints applied to those atoms on shared sites. However, a satisfactory refinement was not obtained; the U_{iso} value for M1 [occupied by the Li and Zn atoms] was large and negative, and that for O7 was zero within one *esd*, see **Table 6-3**. It was considered that there may be different Li and Zn occupancies on the M1 site because *Lapshin*'s model, based on XRD data, was not feasible to determine occupancies accurately.

In order to obtain different occupancies for M1 and M2 sites, atomic coordinates were refined and fixed followed an initially fixed default U_{iso} value of 0.01; the occupancy ratio on the M1 site with applying constraints was changed to 0.82 Li and 0.18 Zn and the M2 site was fixed with 0.38 Li and 0.62 Zn. The refinement of this revised model converged and gave reasonable fits to the data, **Table 6-4**; selected bond lengths are listed in **Table 6-5**. Although the values of U_{iso} for Li1 and M2 for the revised model are slightly increased, the U_{iso} value for M1 is significantly improved. The values of average P-O and Li-O distances

are reasonable in the PO_4 and LiO_4 tetrahedra. However, many of the bond lengths, e.g. P2-O6 and M1-O2 are too short ~1.4 Å, which are much less than a typical P-O (1.57 Å), Li-O (1.99 Å) and/or Zn-O (2.00 Å) bond length [10]; the structure is therefore not correct in all its details. The refinement profile of $Li_{2.4}Zn_{0.8}P_2O_7$ using ND data at room temperature is presented in **Fig. 6-17**; the unit cell volume of ~564.6 $Å^3$ is slightly smaller than that, ~566.3 $Å^3$, reported using XRD data, **Table 6-6**.

Table 6-3 Refinement results of atomic coordinates and occupancies and isotropic displacement parameters of $Li_{2.4}Zn_{0.8}P_2O_7$ by ND data, using the structural model reported by XRD from Lapshin *et al.* [6].

Atom	Site	*x*	*y*	*z*	U_{iso} (Å²)	Occ.
P1	4a	0.1877(2)	0.6895(1)	0.2233(2)	0.0093(2)	1
P2	4a	0.1254(2)	0.4749(1)	0.2349(2)	0.0033(2)	1
Li1	4a	0.2239(8)	0.7992(3)	0.5055(4)	0.0235(10)	1
M1 (Li2, Zn2)	4a	0.081(2)	0.032(6)	0.555(10)	-0.1166(18)	(0.76, 0.24)
M2 (Li3, Zn3)	4a	0.1206(5)	0.0983(3)	0.9174(4)	0.0144(6)	(0.44, 0.56)
O1	4a	0.4714(2)	0.7385(1)	0.6991(1)	0.0069(3)	1
O2	4a	-0.3377(3)	0.3166(1)	0.9260(2)	0.0203(3)	1
O3	4a	0.3313(3)	0.6906(1)	0.3827(2)	0.0024(3)	1
O4	4a	0.0221(2)	0.5836(1)	0.2407(2)	0.0076(2)	1
O5	4a	0.1194(2)	0.5860(1)	0.7418(2)	0.0101(2)	1
O6	4a	0.2311(3)	0.9521(1)	0.3876(2)	0.0261(4)	1
O7	4a	0.1945(3)	0.9691(1)	0.0856(2)	-0.0002(3)	1
χ^2 =2.15; R_{wp}=6.65%; R_p=5.20%; R_{exp}=4.54% **a(Å) = 5.12323(19); b(Å) = 13.4608(4); c(Å) = 8.1890(3); β(deg) = 90.195(3);** ***Volume*(Å³) = 564.728(33)**						

Table 6-4 Refinement results of atomic coordinates, occupancies and isotropic displacement parameters for $Li_{2.4}Zn_{0.8}P_2O_7$ using ND data with revised occupancy of Zn and Li.

Atom	Site	*x*	*y*	*z*	U_{iso} (Å^2)	Occ.
P1	4a	0.1853(3)	0.6889(1)	0.2225(2)	0.0093(3)	1
P2	4a	0.1258(2)	0.4746(1)	0.2334(2)	0.0047(2)	1
Li1	4a	0.1832(7)	0.8275(3)	0.5282(5)	0.0285(10)	1
M1 (Li2, Zn2)	4a	0.1190(30)	0.1362(11)	0.5782(16)	0.0235(36)	**(0.82, 0.18)**
M2 (Li3, Zn3)	4a	0.1170(5)	0.1022(2)	0.9037(3)	0.0251(6)	**(0.38, 0.62)**
O1	4a	0.4668(2)	0.7404(1)	0.6969(2)	0.0043(2)	1
O2	4a	-0.3424(3)	0.3215(1)	0.9241(2)	0.0173(3)	1
O3	4a	0.3285(3)	0.6969(1)	0.3815(2)	0.0079(3)	1
O4	4a	0.0250(2)	0.5832(1)	0.2382(2)	0.0044(2)	1
O5	4a	0.1178(2)	0.5870(1)	0.7328(2)	0.0108(2)	1
O6	4a	0.2167(3)	0.9548(1)	0.3950(2)	0.0130(4)	1
O7	4a	0.2115(3)	0.9676(1)	0.0829(2)	0.0055(3)	1
χ^2 =2.36; R_{wp}=6.97%; R_p=5.51%; R_{exp}=4.53% **a(Å) = 5.1215(2); b(Å) = 13.4617(5); c(Å) = 8.1894(4); β(deg) = 90.172(4);** ***Volume*(Å^3) = 564.606(42)**						

Table 6-5 Selected bond lengths (Å) for $Li_{2.4}Zn_{0.8}P_2O_7$.

Bonds	*Distance*, Å	Bonds	*Distance*, Å
P1-O1	1.483(4)	M1-O1	2.357(8)
P1-O2	1.453(9)	M1-O2	1.39(9)
P1-O3	1.496(6)	M1-O5	2.153(8)
P1-O4	1.648(5)	M1-O6	2.12(3)
P1–O	**1.520(6)**	**M1–O**	**2.008(4)**
P2-O4	1.550(7)	M2-O1	2.078(9)
P2-O5	1.523(7)	M2-O3	2.189(9)
P2-O6	1.353(5)	M2-O5	1.773(9)
P2-O7	1.720(6)	M2-O7	1.930(3)
P2–O	**1.537(1)**	M2-O7*	2.380(7)
Li1-O1	2.319(5)	**M2–O**	**2.070(7)**
Li1-O2	1.791(5)	Note: 1) The asterisk (*) marks the atoms with coordinates transformed by symmetry matrices. 2) Average distances are in bold type.	
Li1-O3	2.256(7)		
Li1-O6	2.038(8)		
Li1–O	**2.101(6)**		

Table 6-6 Refined lattice parameters of $Li_{2.4}Zn_{0.8}P_2O_7$ by XRD and ND data.

Formula	Data	*a* (Å)	*b* (Å)	*c* (Å)	*β* (°)	*V* (Å^3)
$Li_{2.4}Zn_{0.8}P_2O_7$	X-ray	5.131(2)	13.451(4)	8.209(3)	90.45(4)	566.6(3)
	ND	5.1215(2)	13.4617(5)	8.1894(4)	90.172(4)	564.606(42)
	Ref. 6	5.130(1)	13.454(1)	8.205(1)	90.36(1)	566.305(48)

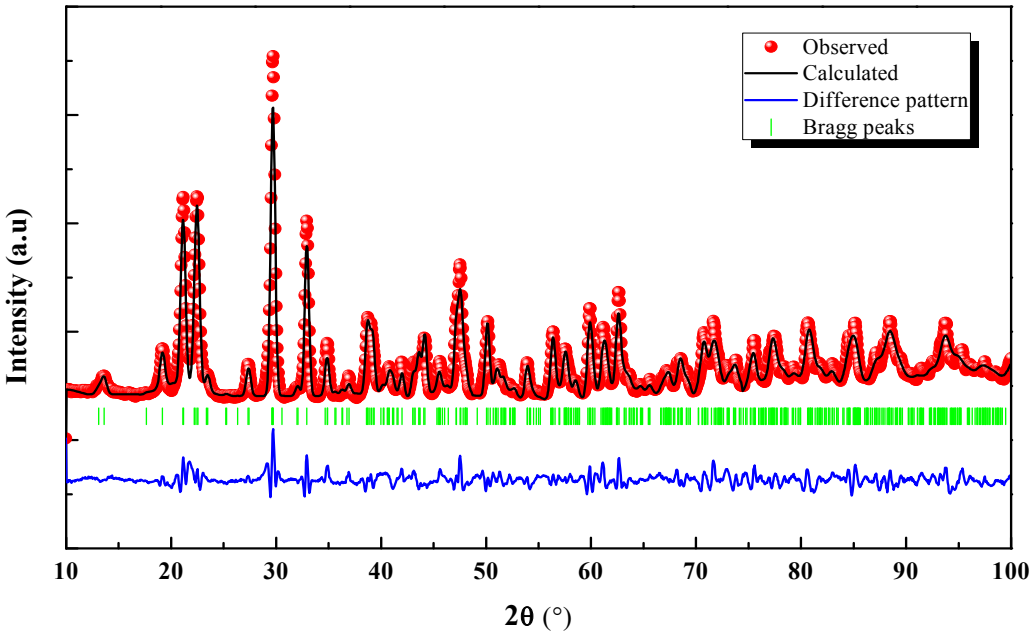

Figure 6-17 Observed, calculated, and difference profiles from ND data of monoclinic $Li_{2.4}Zn_{0.8}P_2O_7$ at room temperature. The vertical green tick marks indicate the peak position of all possible Bragg reflections.

Fig. 6-18(a) shows the polyhedral structure of $Li_{2.4}Zn_{0.8}P_2O_7$ projected along the *a*-axis; purple trigonal pyramid is shown for [$M2O_5$] and grey, yellow, and blue tetrahedra for [$M1O_4$], [PO_4], [$Li1O_4$], respectively. The diphosphate groups (P_2O_7) form a layer parallel to *b*-axis, and each P_2O_7 layer was separated by the distance of ½ *c* in a unit cell. The cation polyhedra, [$M2O_5$], [$M1O_4$], and [$Li1O_4$], are located between the P_2O_7 layers. The tetrahedral size of PO_4 in the P_2O_7 is smaller than that of the Li1 tetrahedra. $M2O_5$ trigonal pyramid shares an edge with $M1O_4$ tetrahedra, **(b)**; both of them are interconnected through P_2O_7 groups, **(c)**, and therefore, a 3D framework is built up.

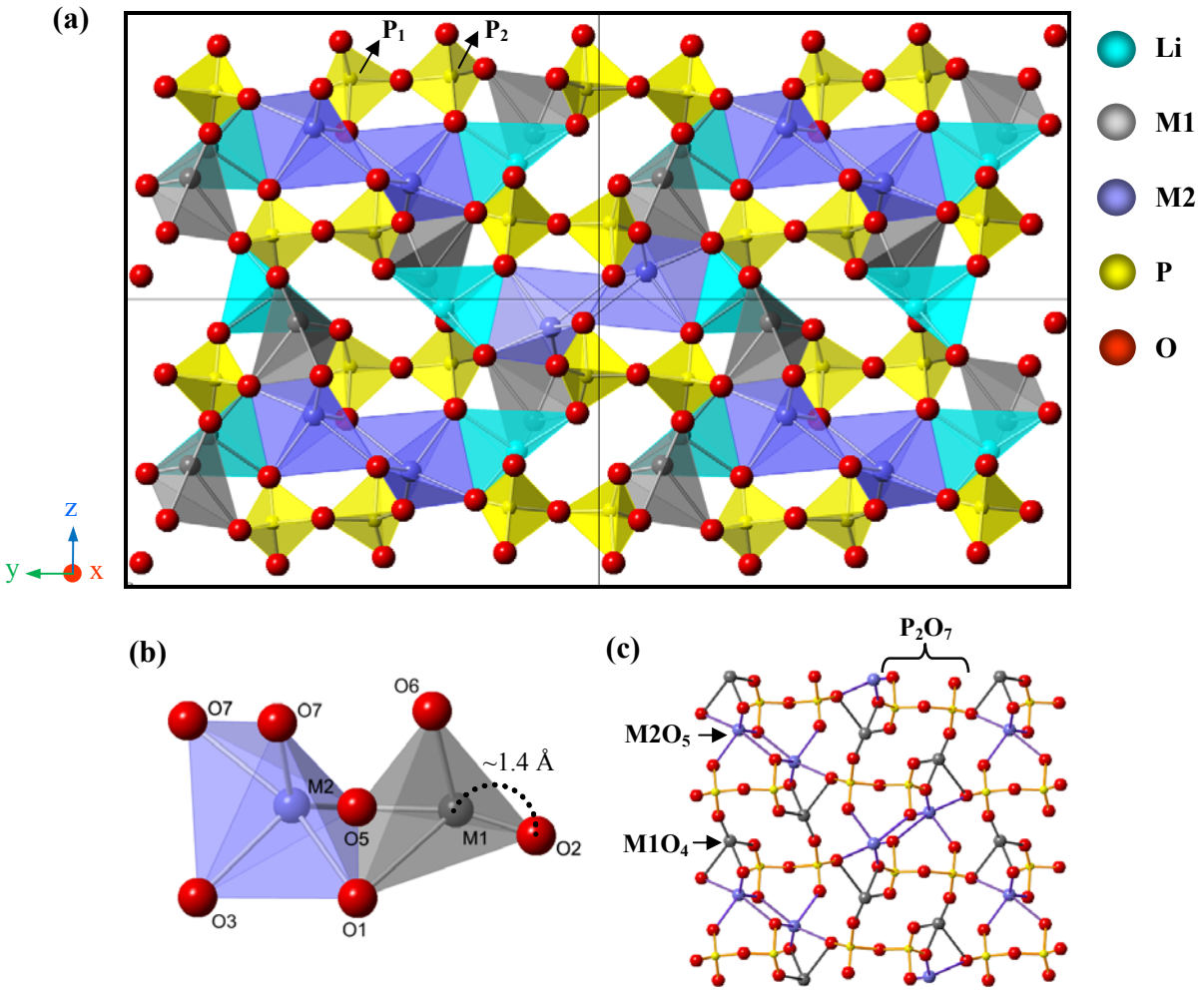

Figure 6-18 (a) 3D crystal structure of $Li_{2.4}Zn_{0.8}P_2O_7$ along the *a*-axis, (b) local atomic coordination shared by $M1O_4$ and $M2O_5$, and (c) connection between M1 and M2 cations interconnected with P_2O_7 groups in the *bc* plane.

6.3.3 Morphology and Chemical Composition

SEM and EDS were used to evaluate the morphology and pellet density as well as composition of the $Li_{4x}Zn_{2-2x}P_2O_7$ pellets sintered at 600°C for 12 h in air, where x is 0.25, 0.5, and 0.6. The EDS spectra of the molar ratio of Zn/P are given in **Table 6-7**. The average value of Zn/P ratio analyzed from 10 distinct points is 0.75(1) for x=0.25, and 0.39(2) for x=0.6. These are close to the expected values 0.75 and 0.40. For $Li_2ZnP_2O_7$ phase mixture, two different Zn/P values of 0.64(2) and 0.40(1) were detected from 4 distinct points and within errors, in agreement with the theoretical molar ratio of Zn/P of 0.665 and 0.40 respectively for $Li_{1.33}Zn_{1.33}P_2O_7$ (x=0.33) and $Li_{2.4}Zn_{0.8}P_2O_7$ (x=0.6), which next would be confirmed by EBSD image.

Table 6-7 Molar ratio of expected and EDS results of $Li_{4x}Zn_{2-2x}P_2O_7$ pellets.

Stoichiometry	Theoretical value of Zn/P molar ratio	Average value of EDS results of Zn/P molar ratio
$LiZn_{1.5}P_2O_7$ (x=0.25)	**0.75**	**0.75(1)**
$Li_2ZnP_2O_7$ (x=0.5)	**0.50**	**…….**
→ $Li_{1.33}Zn_{1.33}P_2O_7$ (x=0.33)	0.665	0.64(2)
→ $Li_{2.4}Zn_{0.8}P_2O_7$ (x=0.6)	0.40	0.40(1)
$Li_{2.4}Zn_{0.8}P_2O_7$ (x=0.6)	**0.40**	**0.39(2)**

Fig. 6-19 (a) shows the surface image of the $LiZn_{1.5}P_2O_7$ pellet sintered at 600°C for 12 h in air atmosphere. Most of the particles have aggregate pentagon shapes, with two average particle sizes of 5 μm marked by solid-circle, and of ~10 μm by dash-circle, **(b)**. The EDS spectra **(d)** confirm that the selected regions of EBSD image in **(c)** indicate the presence of Zn and P elements.

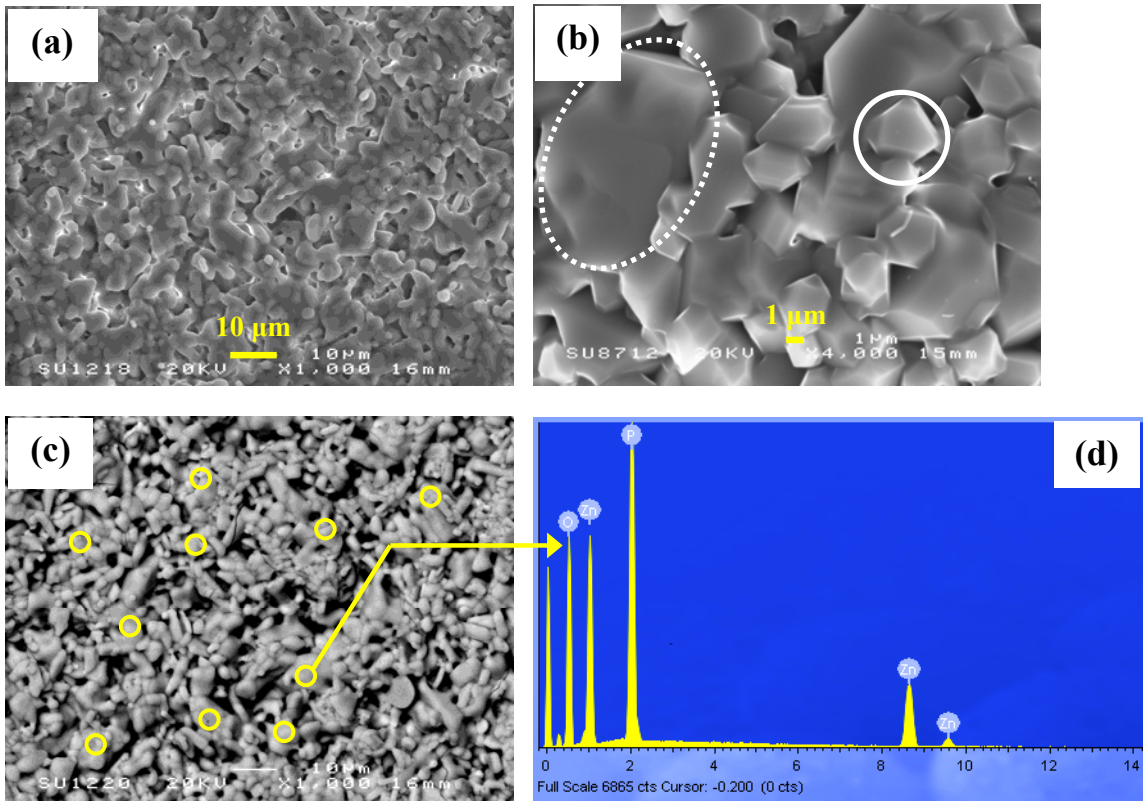

Figure 6-19 (a) SEM image for the surface of pellet $LiZn_{1.5}P_2O_7$ and (b) close-up image; (c) EBSD micrograph, and (d) corresponding EDS analyses for the particles.

Fig. 6-20 (a) shows the SEM picture of the $Li_2ZnP_2O_7$ pellet sintered at 600°C for 12 h in air; aggregated particles with size ~10 μm are observed, **(b)**. The EDS spectra **(d)** show that the darker regions of EBSD image, yellow-marked in **(c)**, indicate the expected Zn and P compositions in $Li_{2.4}Zn_{0.8}P_2O_7$, whereas the lighter blue ones closely correspond to $Li_{1.33}Zn_{1.33}P_2O_7$.

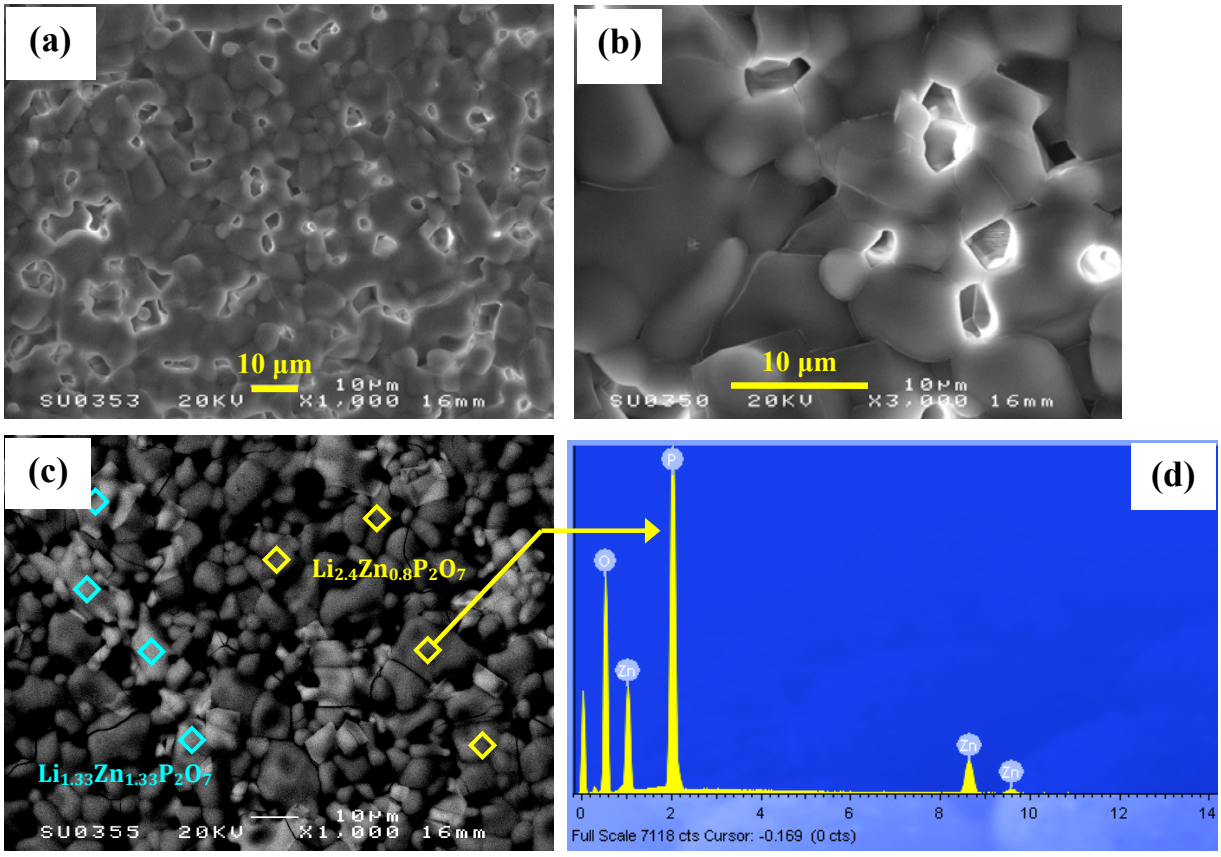

Figure 6-20 (a) SEM image for the surface of pellet $Li_2ZnP_2O_7$ and (b) close-up image; (c) EBSD micrograph, and (d) corresponding EDS analyses for the particles.

The presence of Zn and P were visualized by electron back scatter diffraction (EBSD) mapping analysis. **Fig. 6-21 (a)** shows the SEM picture of the $Li_{2.4}Zn_{0.8}P_2O_7$ pellet sintered at 600°C for 12 h in N_2; uniform particle size of ca. 10 μm is observed with similar-polygonal shape, **(b)**. The EDS spectra **(d)** confirm that all regions of EBSD image in **(c)** have the elements of Zn and P in $Li_{2.4}Zn_{0.8}P_2O_7$. Elemental mapping shows a homogenous distribution of both zinc and phosphorus, **Fig. 6-22 (b)** and **(c)**.

SEM shows all samples have a poorly sintered microstructure, and the measured density of x=0.25 and 0.6 is ~ 2.364 and 2.082 g/cm^3, respectively, consistent with a final density ~ 70% and 73% of each theoretical X-ray value, **Table 6-8**. The relative densities of x=0.5 and 0.75 were not determined due to the phase mixture in $Li_2ZnP_2O_7$ and impurity in $Li_3Zn_{0.5}P_2O_7$, making it difficulty to calculate their theoretical density.

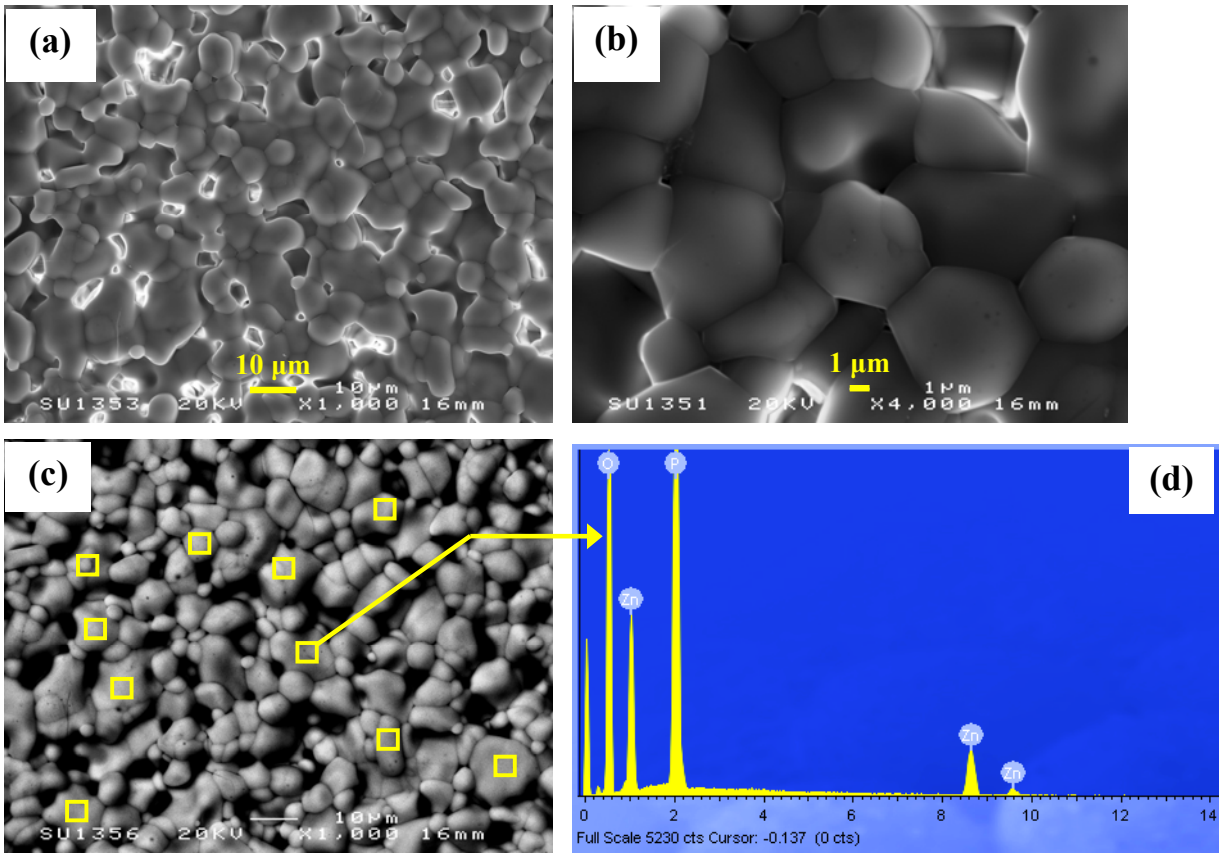

Figure 6-21 (a) SEM image for the surface of pellet $Li_{2.4}Zn_{0.8}P_2O_7$ and (b) close-up image; (c) EBSD micrograph, and (d) corresponding EDS analyses for the particles.

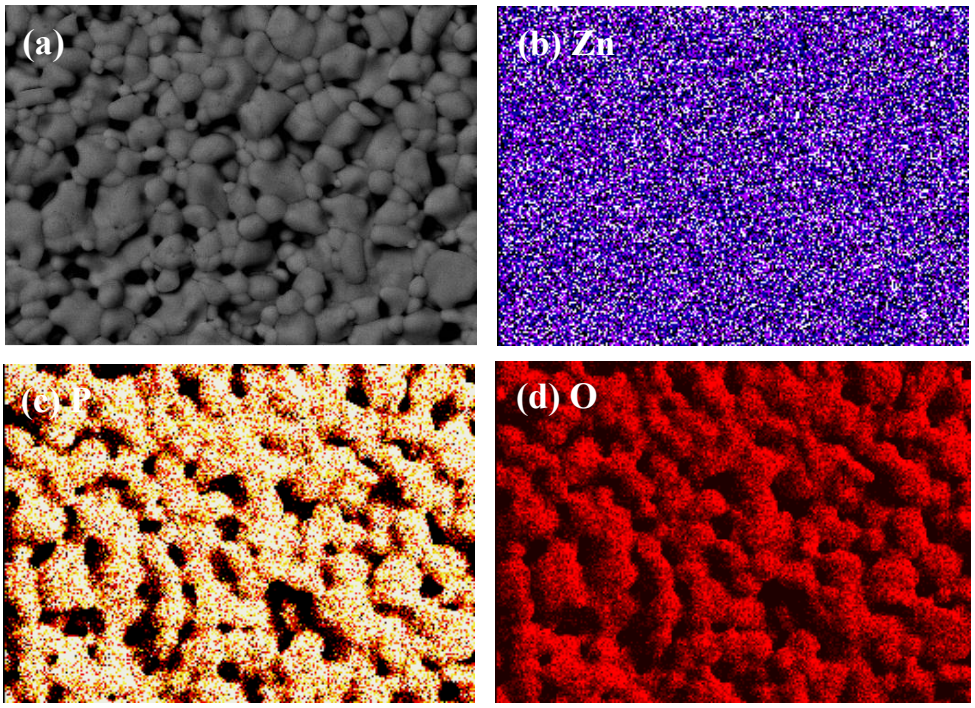

Figure 6-22 (a) EBSD image of $Li_{2.4}Zn_{0.8}P_2O_7$ and its elemental mapping for (b) Zn, (c) P and (d) O.

Table 6-8 Theoretical, measured, and relative density of $Li_{4x}Zn_{2-2x}P_2O_7$ pellets with various composition x.

Materials	X-ray Density (g/cm^3)	Measured Density (g/cm^3)	Relative Density (%)
$LiZn_{1.5}P_2O_7$	3.373	2.364	70.10
$Li_2ZnP_2O_7$	.....	1.951	.....
$Li_{2.4}Zn_{0.8}P_2O_7$	2.854	2.082	72.94
$Li_3Zn_{0.5}P_2O_7$	.....	1.820	.....

6.3.4 Electrical Properties

(i) $LiZn_{1.5}P_2O_7$ (x=0.25)

Impedance complex plane, Z* plots, **Fig. 6-23**, show the total resistivity of pristine $LiZn_{1.5}P_2O_7$ pellet with Au electrodes at different measuring temperatures in air. A poorly resolved arc or two arcs overlapped is observed at 250°C, **(a)**. As temperature increased to 300°C, two overlapped semicircles, R_1 and R_2, are seen with the associated capacitances of ~0.6×10^{-12} and ~3×10^{-11} Fcm^{-1}, calculated from $\omega RC=1$ at their individual semicircle maximum, and, therefore, attributed to bulk and grain boundary regions of the sample, **(b)**. At 400~425 °C, the high frequency semicircle, R_1, is increasingly displaced to frequencies outside the measurement range, but R_2 is still identified. In addition, a short low-frequency electrode spike with a slope of ~70° is observed, probably resulting from the (partial) blockage of ionic species at the sample-electrode interface, **Fig. 6-24**.

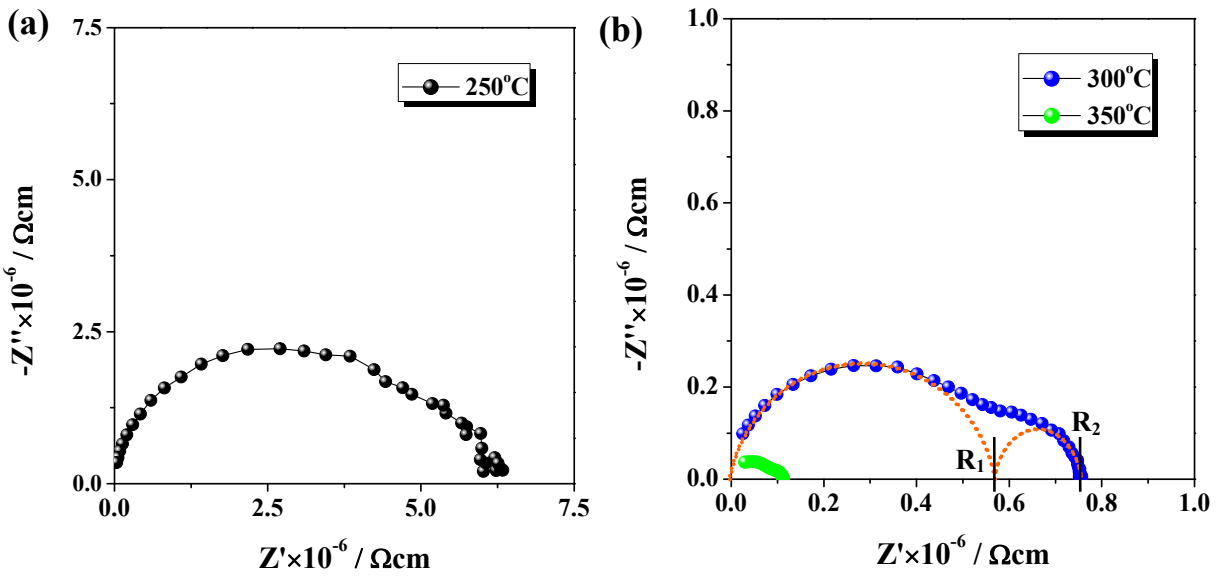

Figure 6-23 Z* plots of $LiZn_{1.5}P_2O_7$ (sputtered Au) measured at (a) 250°C and (b) 300~350 °C in air.

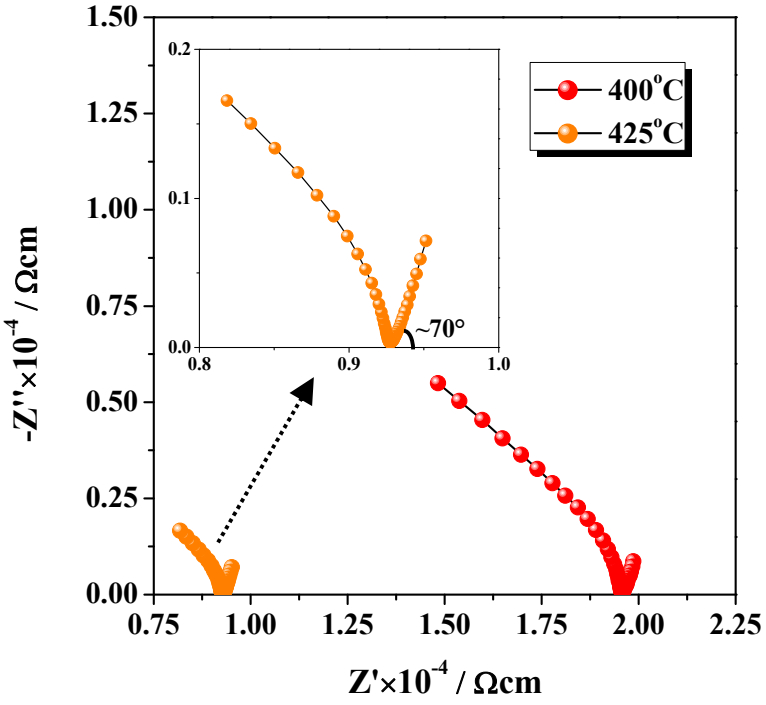

Figure 6-24 Z* plots of $LiZn_{1.5}P_2O_7$ measured at 400°C and 425°C in air.

The capacitance, C', data as a function of frequency at different temperatures are shown in **Fig. 6-25(a)**; a plateau at high frequency is attributed to the bulk capacitance, ~0.7 $pFcm^{-1}$ (arrowed), and a dispersion at lower frequency is observed below 350°C. As the temperature increases, a second capacitance plateau associated with the R_2 response at intermediate frequency is nicely resolved at temperatures above 300°C with a value ~3.5 $pFcm^{-1}$. An increased capacitance at low frequencies of ~ 10^{-8}–10^{-7} Fcm^{-1} is found at the highest temperature up to 425°C, which could be attributed to the effect on the sample-electrode interface.

Conductivity, Y', data as a function of frequency are shown in **Fig. 6-25(b)** for the same temperature range as in **(a)**. The Y' data show a dispersion at high frequencies and present a nearly frequency-independent *dc* conductivity plateau at frequencies below ~10^4 Hz. As the temperature increases, the data at lower frequencies do not show a clear curvature to lower conductivity values and the high-frequency dispersion shifts out of the frequency window. Above 400°C, Y' spectra present a frequency-independent *dc* conductivity plateau.

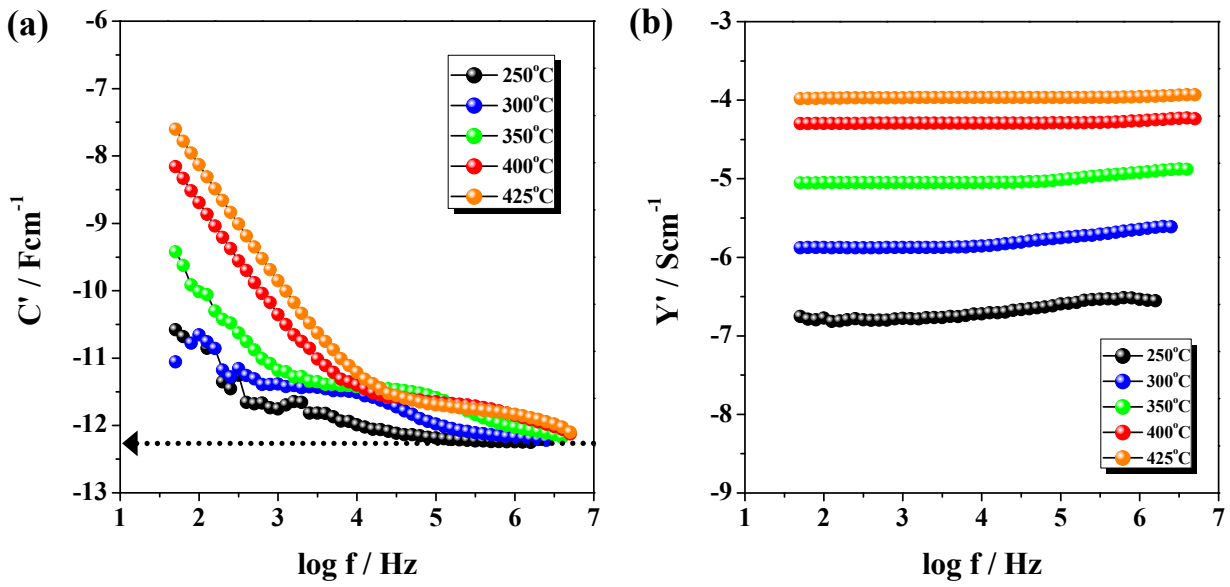

Figure 6-25 $LiZn_{1.5}P_2O_7$: (a) spectroscopic plots of capacitance, C', (b) spectroscopic plots of admittance, Y', at different temperatures of 250°C to 425°C.

Combined Z'' and M'' spectroscopic plots at 300°C for $LiZn_{1.5}P_2O_7$ are shown in **Fig. 6-26**. R_b and C_b values of ~0.35 MΩcm and ~0.8 $pFcm^{-1}$ were estimated from the high frequency M'' Debye peak using the relationships $R_b=2M''_{max}/(\omega_{max})$ and $C_b=1/(2M''_{max})$ and are assigned to a bulk component. The frequency maxima of M'' peak and Z'' peak do not coincide exactly as an ideal "Debye" theory prediction. The conductivity data of $LiZn_{1.5}P_2O_7$ pellet are presented in **Fig. 6-27**; two parallel lines are observed with similar activation energies: 1.11 eV for bulk conductivity, R_b, extracted from M'' peak, 1.18 eV for total conductivity, R_T^{-1}. The bulk conductivity data are slightly higher than total conductivity values. R_b data above 325°C are not obtained because the M''_{max} peak at high frequency is increasingly displaced to frequencies outside the measurements, **Fig. 6-28**.

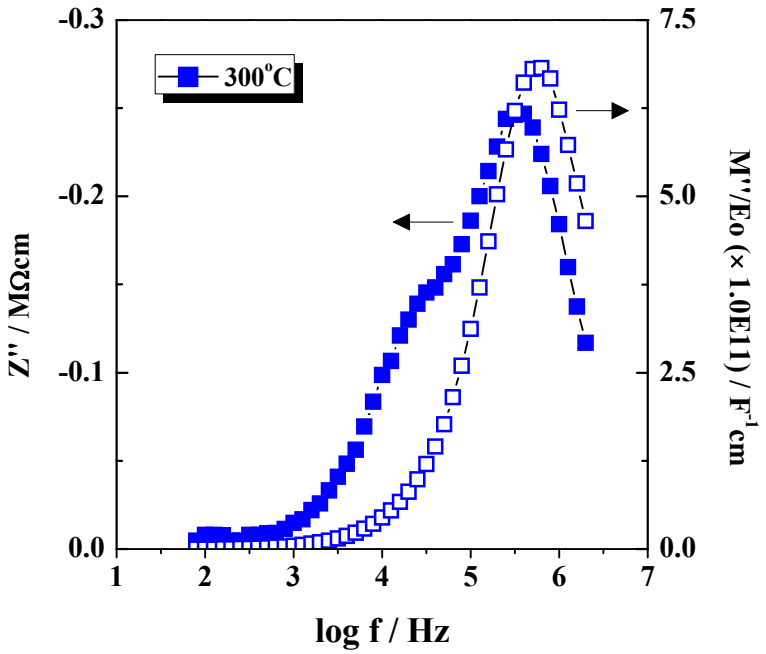

Figure 6-26 Z''/M'' spectroscopic plots for $LiZn_{1.5}P_2O_7$ at 300°C in air.

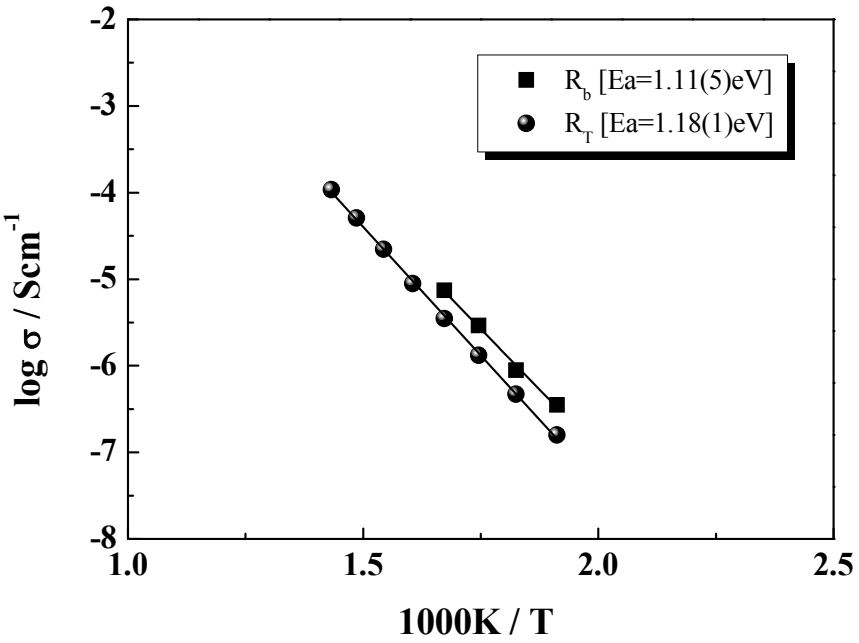

Figure 6-27 Arrhenius plots of bulk conductivity (R_b^{-1}) extracted from M'' plots and total conductivity (R_T^{-1}) for $LiZn_{1.5}P_2O_7$.

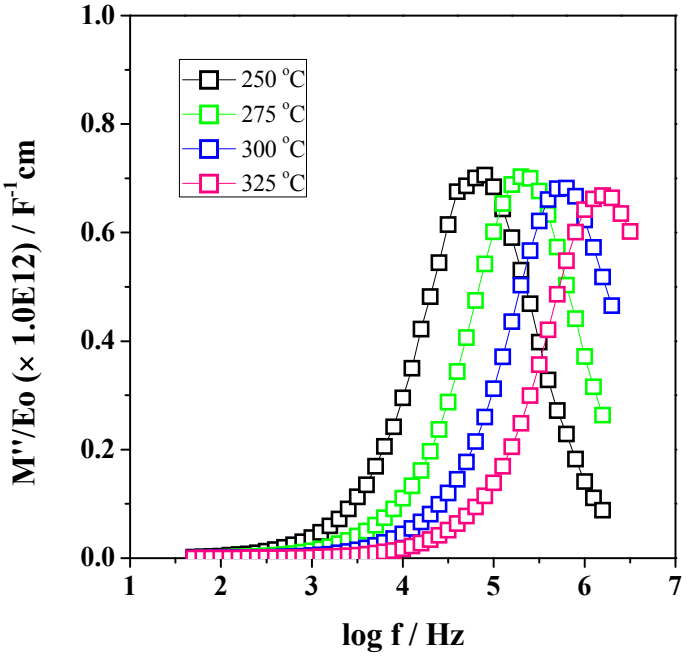

Figure 6-28 M'' spectroscopic plots of $LiZn_{1.5}P_2O_7$ at different temperatures.

(ii) $Li_2ZnP_2O_7$ (x=0.5)

Z* plots of $Li_2ZnP_2O_7$ with Au-sputtered electrodes at different temperatures in air are given in **Fig. 6-29**. At 200°C, they consist of a smaller high-frequency poorly-resolved semicircle of resistance (R_1) and a larger intermediate-frequency arc of resistance (R_2), see **(a)**. As temperature increased to 300°C, the high frequency semicircle R_1 is increasingly displaced to frequencies outside the measurement range, but the R_2 is still identified, **(b)** and **(c)**. At higher temperature up to 350°C, an obvious low-frequency spike with slope ~73° is observed to represent charge build-up at the blocking metal electrodes, see **(d)**.

The C' spectroscopic plots as a function of frequency over the temperature range 200°C to 325°C can be observed from **Fig. 6-30(a)**; a tiny dispersion at lower frequency is observed below 225°C. The high- and intermediate-frequency plateaus with values ~0.7×10^{-12} Fcm^{-1} and ~0.8×10^{-11} Fcm^{-1}, respectively, identify the bulk and grain boundary response in sample (arrowed). As the temperature increases, the capacitance at lower frequencies increases to ~0.5×10^{-6} Fcm^{-1} and is associated with the sample-electrode interfacial response.

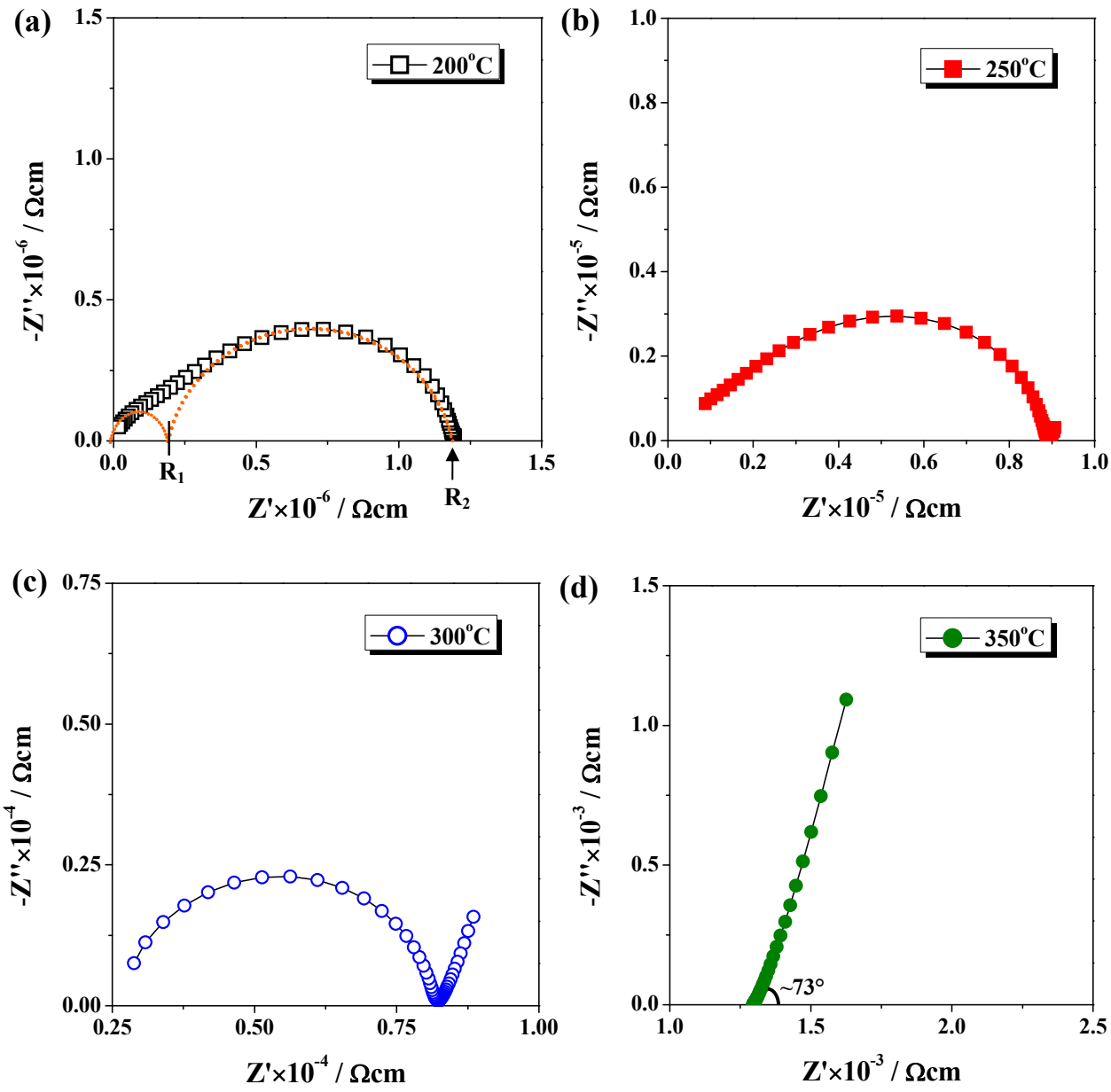

Figure 6-29 $Li_2ZnP_2O_7$: Impedance complex plane plots, Z*, at (a) 200°C to (d) 350°C in air.

Conductivity, Y', data as a function of frequency are shown in **Fig. 6-30(b)**. The Y' data show a dispersion at high frequencies and present a nearly frequency-independent *dc* conductivity plateau at intermediate frequencies. At T > 300°C, the data at lower frequencies show a tiny curvature to lower conductivity values (arrowed).

Combined Z'' and M'' spectroscopic plots at 200°C show one Z'' peak at low frequency and a non-ideal M'' peak at high frequency, **Fig. 6-31**. The peak maxima of M'' peak and Z'' peak do not coincide exactly as an ideal "Debye" theory prediction and a tiny low-frequency tail in the Z'' peak may be associated with an interfacial effect. The full width at half maximum (FWHM) of the Z'' peak is ~1.65 decades, which is higher than expected value of 1.14 decades. The total conductivity data as a function of temperature for $Li_2ZnP_2O_7$ pellet is presented in **Fig. 6-32**; the calculated activation energy is ~1.14 eV.

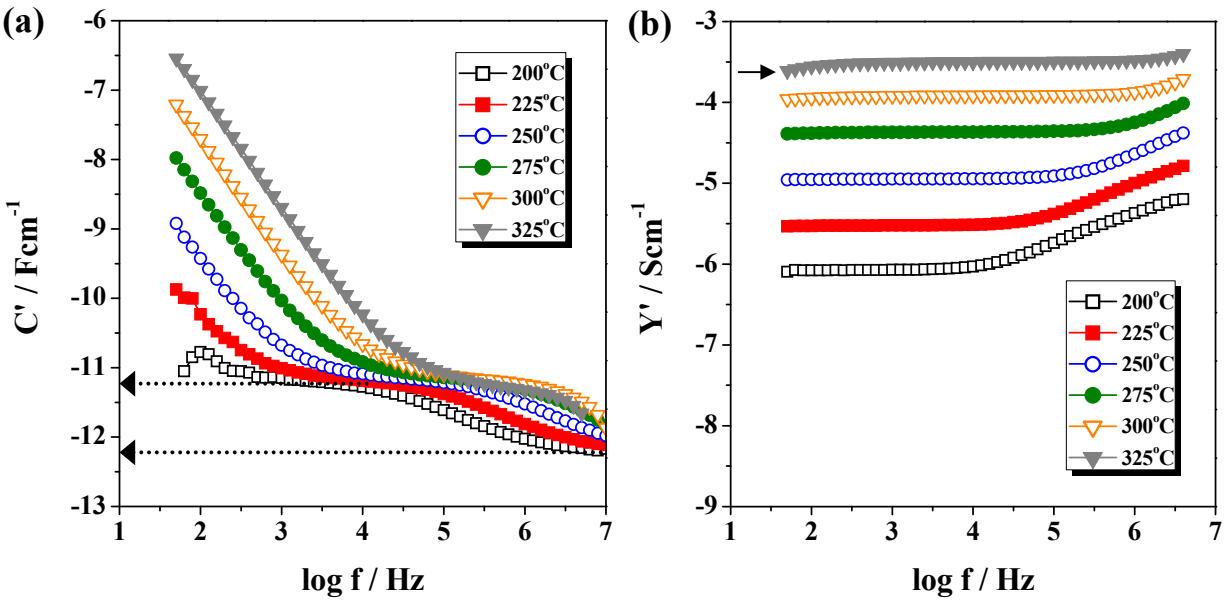

Figure 6-30 $Li_2ZnP_2O_7$ (Au electrode): (a) spectroscopic plots of capacitance, C', (b) spectroscopic plots of admittance, Y', at different temperatures of 150~300 °C in air.

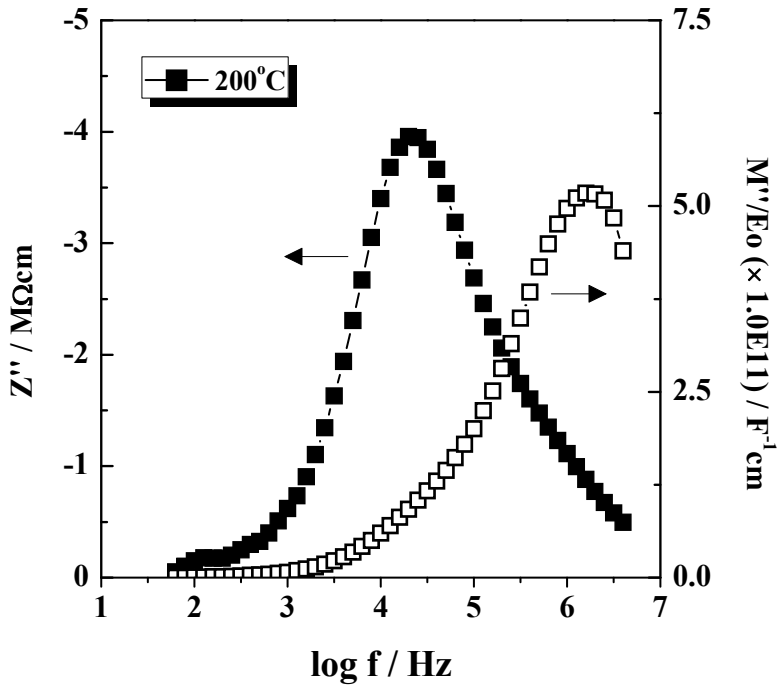

Figure 6-31 Z''/M'' spectroscopic plots for $Li_2ZnP_2O_7$ at 200°C in air.

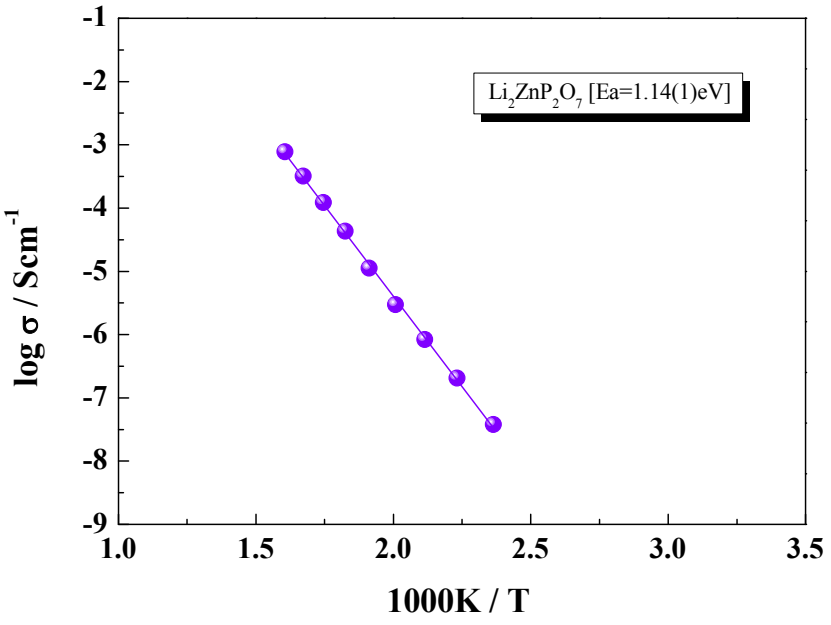

Figure 6-32 Arrhenius plots of total conductivity (R_T^{-1}) for $Li_2ZnP_2O_7$.

(iii) $Li_{2.4}Zn_{0.8}P_2O_7$ (x=0.6)

Z* plots of $Li_{2.4}Zn_{0.8}P_2O_7$ at various temperatures in air are given in **Fig. 6-33**. One slightly distorted semicircle at 150°C is observed with associated capacitance of ~1 $pFcm^{-1}$ attributed to the bulk response (R_b), **(a)**. At 200°C, the high frequency semicircle R_b is increasingly displaced to frequencies outside the measurement range, and a tiny tail at low frequency is seen, **(b)**. Above 250°C, a low-frequency spike with slope ~74° is clearly identified, and the length of the spike increases with temperature, **(c)** and **(d)**.

C' and Y' plots as a function of frequency are shown in **Fig. 6-34**; both of them have similar results to those of $Li_2ZnP_2O_7$. One resolved plateau at high frequencies is attributed to the bulk capacitance, **(a)**. Its value is ≈ 1 $pFcm^{-1}$ at 150°C (arrowed). As the temperature increases, specifically at 300°C, the Y' data at lower frequencies show an obvious curvature to lower conductivity values and the high-frequency dispersion shifts out of the frequency window, **(b)**. Z''/M'' spectra at 150°C show the Z'' and M'' peaks appear over a similar frequency range, and a non-ideal Debye peak is observed, **Fig. 6-35**.

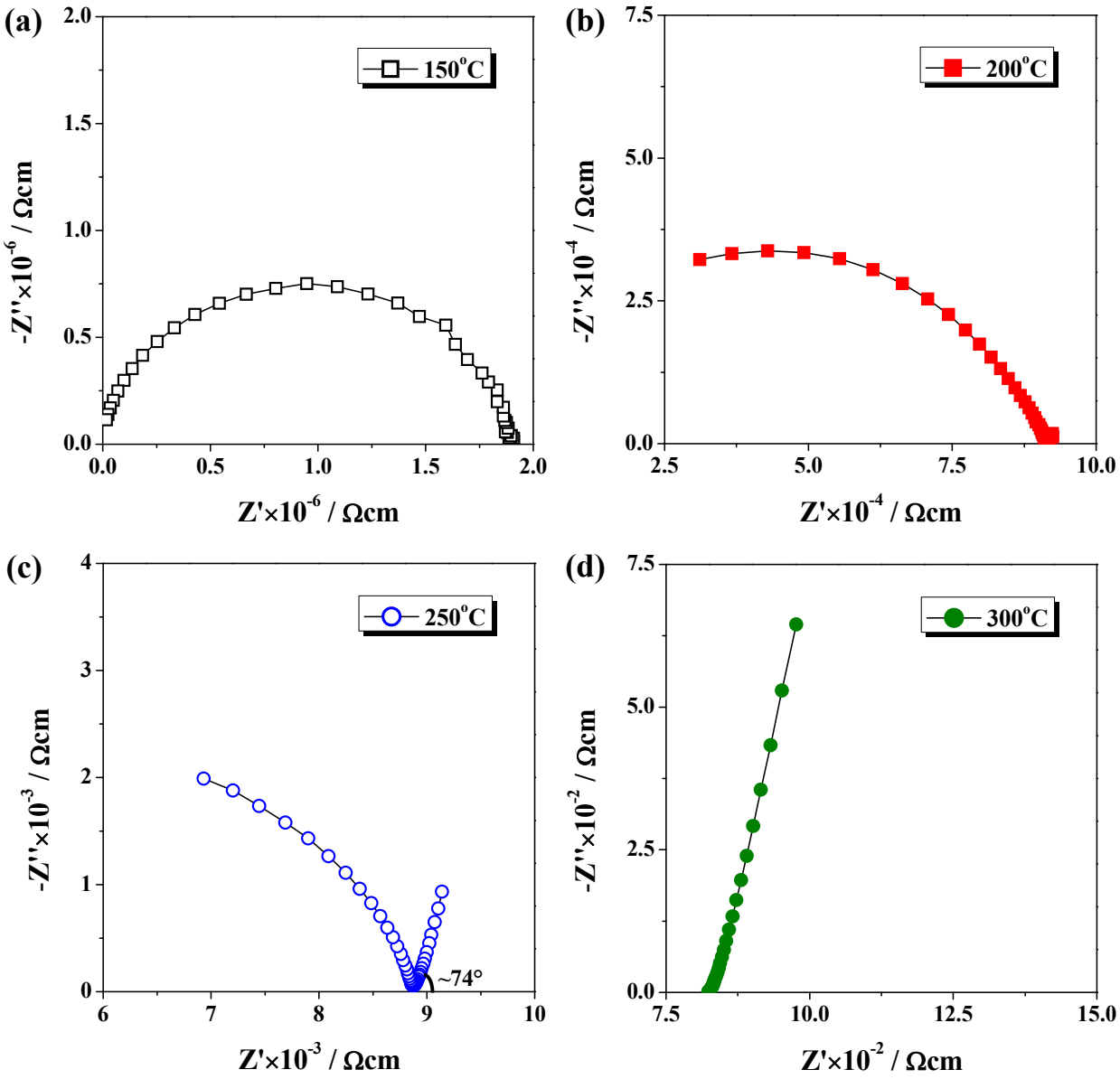

Figure 6-33 $Li_{2.4}Zn_{0.8}P_2O_7$ (Au electrode): Impedance complex plane plots, Z*, at (a) 200°C to (d) 300°C in air.

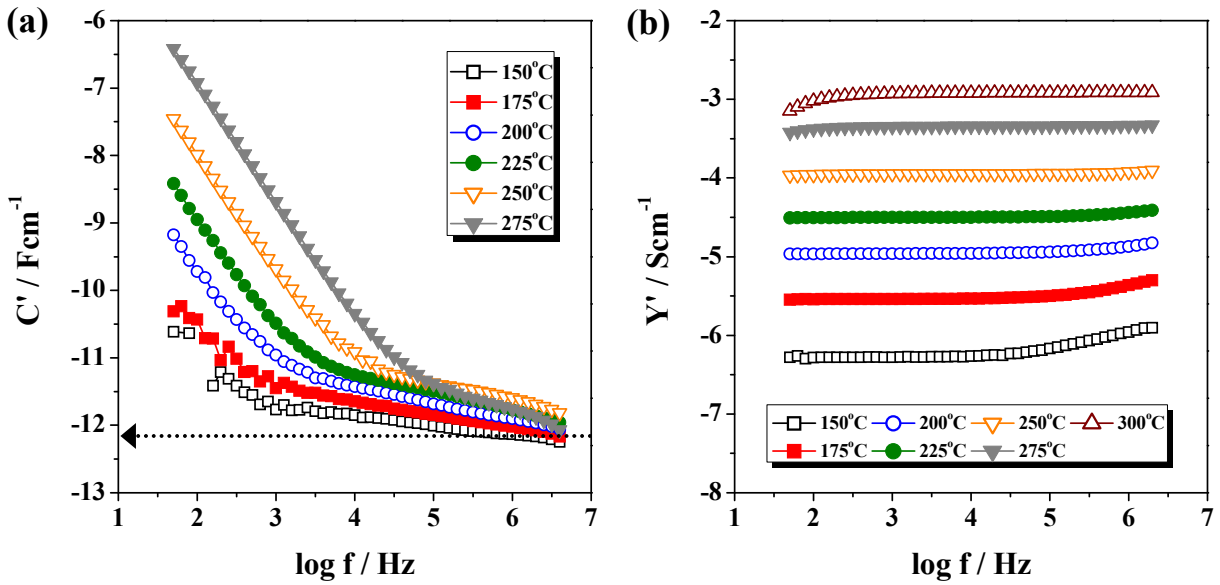

Figure 6-34 $Li_{2.4}Zn_{0.8}P_2O_7$ (Au electrode): (a) spectroscopic plots of capacitance, C', (b) spectroscopic plots of admittance, Y', at 150~300 °C in air.

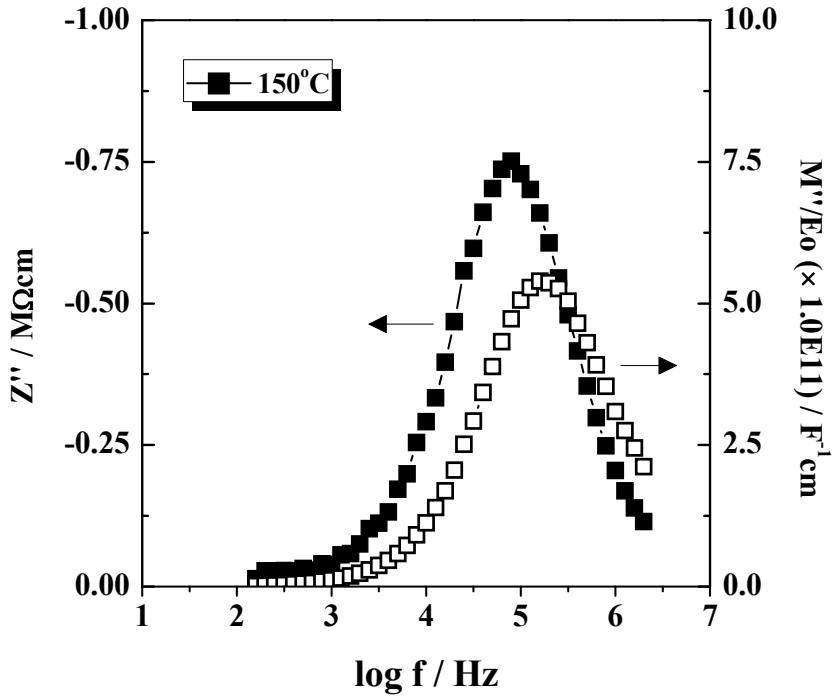

Figure 6-35 Z''/M'' spectroscopic plots for $Li_{2.4}Zn_{0.8}P_2O_7$ at 150°C in air.

(iv) Analysis of Arrhenius Conductivity

The total conductivity data plotted in the form log σ versus T^{-1} are shown in **Fig. 6-36**; for six different compositions in which x increases from 0.2 to 0.75, a set of parallel lines is observed with activation energies, *Ea*, between ~ 0.9–1.3 eV. In general, the conductivity linearly increases with temperature for all compositions except for x=0.75, and specifically, at x=0.2, S.S. $LiZn_{1.5}P_2O_7$ has a lower conductivity. The conductivity at three temperatures as a function of composition *x* is further shown in **Fig. 6-37**; it can be seen that the conductivity of the $Li_{4x}Zn_{2-2x}P_2O_7$ increases with increasing Li content until x=0.65 but does not attain the highest value observed with the right end-member, $Li_4P_2O_7$ [8]. In contrast, the left one, $Zn_2P_2O_7$, has the lowest conductivity [9], and our results show the conductivity maximum occurs in the $Li_{2.4}Zn_{0.8}P_2O_7$ at 350°C. The *Ea* for conduction in $Li_{4x}Zn_{2-2x}P_2O_7$ is given in **Fig. 6-38**; a small variation with composition is observed except x=0 and 1, in which shows the highest and lowest values, ~2 eV [9] and ~0.17 eV [8], respectively, for the high temperature regions. In addition, the values of *Ea* slightly decrease as x increases from 0.4 to 0.65.

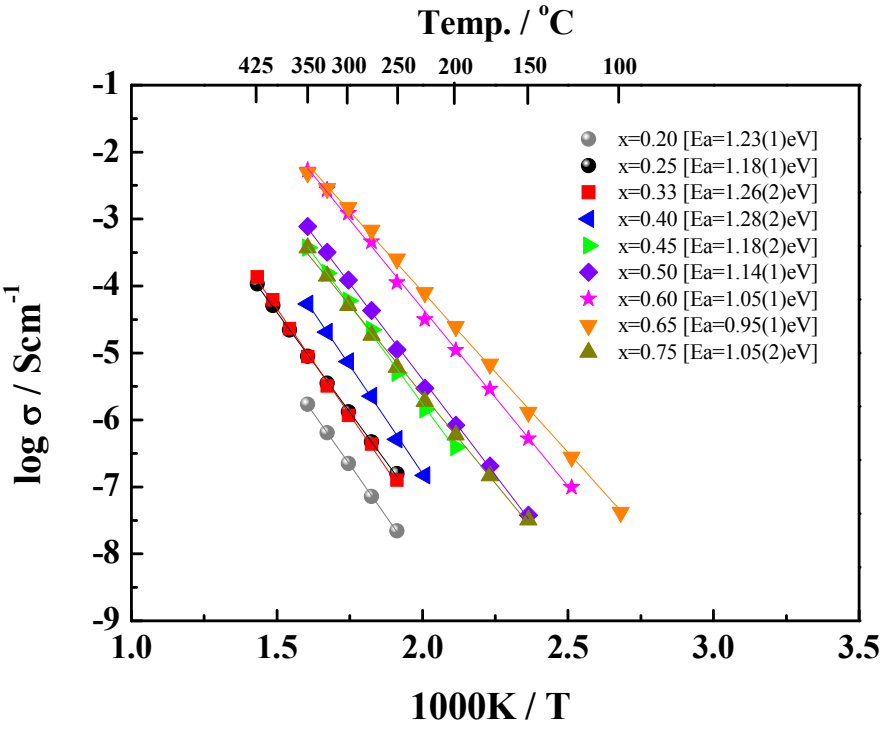

Figure 6-36 Arrhenius plots of measured total conductivity for $Li_{4x}Zn_{2-2x}P_2O_7$ with x varied from 0.2 to 0.75.

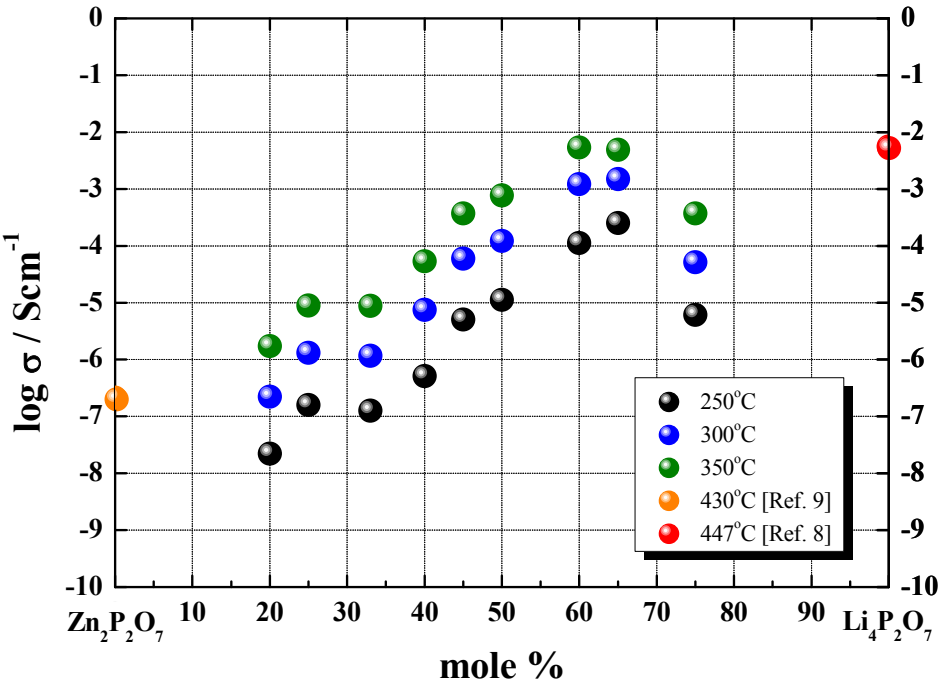

Figure 6-37 Conductivity at three temperatures as a function of composition. Data at 430°C and 447°C are compared for $Zn_2P_2O_7$ (x=0) and $Li_4P_2O_7$ (x=1), respectively.

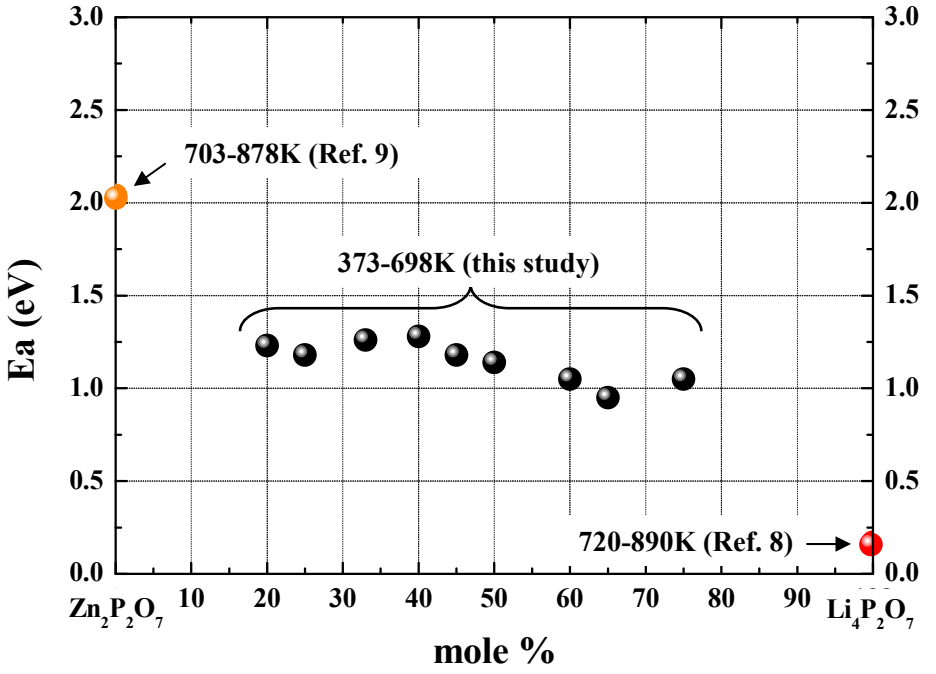

Figure 6-38 Variation of activation energy, *Ea*, with composition.

6.4 Discussion

6.4.1 ZnO-Li_2O-P_2O_5 System

Nineteen ternary compositions based on $Li_{4x}Zn_{2-2x}P_2O_7$ formula were studied in this work and with x in the range 0.2 to 0.75. In preparation of phase-pure compounds, a two-step synthesis route is adapted to reach a complete reaction and to get rid of impurities in the final products.

First, for x=0.25, single-phase $LiZn_{1.5}P_2O_7$ was successfully synthesized at 600°C in air for 24 h and indexed on an orthorhombic unit cell. Lattice parameters are in good agreement with the single-crystal $LiZn_{1.5}P_2O_7$ data reported using $Zn_2P_2O_7$ and $Li_4P_2O_7$ mixed in a molar ratio of 3:1 and reacted at 920°C for 0.5 h followed by a specific cooling and quenching step [4]. A formation of a solid solution is found in the range of x=0.2 to 0.25. Although the phase and structure of stoichiometric $LiZn_{1.5}P_2O_7$ were not solved in Malshikov's work, this composition was involved in the limited solid solution $Li_{4x}Zn_{2-2x}P_2O_7$ (0.15 < x < 0.28) on the phase diagram of the binary system $Zn_2P_2O_7$–$Li_4P_2O_7$ [3]. As x increased up to < 0.33, XRD patterns show that there are some overlapping lines and generally two phase mixture of x=0.25 and 0.33 in these compositions is obtained. At x=0.33, the x=0.25 pattern is absent from the others and a new phase $Li_{1.33}Zn_{1.33}P_2O_7$ is discovered. For *x* in the range 0.33 to 0.5, a solid solution of $Li_{1.33}Zn_{1.33}P_2O_7$ extends from x=0.33 to 0.4 but between x=0.4 and x=0.5, the mixture of two phases may consist of $Li_{1.33}Zn_{1.33}P_2O_7$ and $Li_{2.4}Zn_{0.8}P_2O_7$, which were not found in Liang's work on phase relations of the ZnO-Li_2O-P_2O_5 system.

Second, for x=0.5, attempts to synthesise a single phase composition of $Li_2ZnP_2O_7$ were not successful, but a phase mixture of $Li_{1.33}Zn_{1.33}P_2O_7$ and $Li_{2.4}Zn_{0.8}P_2O_7$ was obtained at 625°C for 24 h in air, **Fig. 6-7**. Although the result is similar to a previous study of $Zn_2P_2O_7$–$Li_4P_2O_7$ with a molar ratio of 1:1 at 600°C [2-3], this study has identified the phases present in composition $Li_2ZnP_2O_7$. Trying higher reaction temperature of > 700°C to explore any phase differences for $Li_2ZnP_2O_7$ is not feasible because of the eutectic point close to 690°C for this composition, **Fig. 6-2**.

Third, for x=0.6, XRD patterns show that $Li_{2.4}Zn_{0.8}P_2O_7$ reacted at 600~625 °C for 24 h in air forms a pure phase with monoclinic symmetry (S.G. $P2_1/n$), and corresponds to Lapshin's results prepared using $Zn_2P_2O_7$ and $Li_4P_2O_7$ (2:3) at 600°C for 20 h [6]. The unit cell parameters are quite close to those of $Li_{2.4}Zn_{0.8}P_2O_7$ in Ref. 6, and of $Li_4P_2O_7$ [11]. Similar work from Liang's group, claimed that pure $Li_{2.4}Zn_{0.8}P_2O_7$ was not obtained, but gave a mixtures of two phases, i.e. $10Li_{2.4}Zn_{0.8}P_2O_7 = 3LiZn_{1.5}P_2O_7 + 7Li_3Zn_{0.5}P_2O_7$, by reacting ZnO, Li_2CO_3 and P_2O_5 at different temperatures between 600°C and 900°C [5]. Detailed synthesis conditions were not provided, making it difficult to clarify this point. A two phase region may exist for compositions of *x* from 0.25 to 0.33 and 0.4 to 0.575. From data x=0.5 to 0.65, a solid solution may exist between x=0.575 and x=0.625.

Fourth, for x=0.75, synthesis of pure-phase $Li_3Zn_{0.5}P_2O_7$ was not successful due to the existence of secondary phases. In order to increase reactivity, higher annealing temperatures were used but the phases obtained appeared to be independent of temperature over the range 600°C to 850°C. The intensities of these secondary phases are decreased for x=0.725, suggesting the single phase sample may be nearer to 0.725 than 0.75. The experimental XRD pattern of $Li_3Zn_{0.5}P_2O_7$ was not shown in the previous work from Liang *et al.*, making it difficult to confirm this reported phase [7]. More studies are needed to get insight into this compound.

6.4.2 Crystal Structure of $Li_{2.4}Zn_{0.8}P_2O_7$

Structural analysis of $Li_{2.4}Zn_{0.8}P_2O_7$ by powder neutron diffraction is preferable to locate the light Li atoms and to investigate the occupancy of Li and Zn in the crystal structure. An initial refinement of ND data at room temperature was done using the structural mode refined by XRD reported from Lapshin *et al.* but unsatisfactory thermal displacement parameters were obtained, specifically, on M1 site with the occupancy of Li2:Zn2 of 0.76:0.24. A revised model with occupancy of M1 site by 0.82 Li and 0.18 Zn, and of M2 site by 0.38 Li and 0.62 Zn was introduced; the results show a good fit and satisfactory parameters at room temperature, **Table 6-4**. The values of U_{iso} for Li1, M1, M2, and O2 by ND data are still relatively large, which suggests residual disorder or site

displacements. The average distance of the P-O bond in P_2O_7 groups is equal to ~1.53 Å, in agreement with the typical tetrahedral bond lengths of ~1.57 Å.

The mean bond lengths for $Li1O_4$ and $M1O_4$ tetrahedra, and $M2O_5$ trigonal pyramid are similar to those reported by Lapshin *et al.*, however, the individual ones within them are different probably due to the varied lithium and zinc occupancies on M1 and M2 site. The distances of Li1-O2 and M1-O2 are relatively short which indicate the $Li1O_4$ and $M1O_4$ tetrahedra are distorted. In addition, the $M2O_5$ trigonal pyramid is also distorted owing to the short bond length between M2 and O5 atoms, **Fig. 6-18(b)**, making a structural difference to $Li_4P_2O_7$, whereas all cations have the distorted tetrahedral coordination reported by Voronin *et al.* [8] and Daidouh *et al.* [12].

Fig. 6-39 shows the Li-diffusion channels considered in the $Li_{2.4}Zn_{0.8}P_2O_7$ crystal structure extracted from refined ND data along three different axes. The lithium ions may migrate along the *b*- and *c*-axis, probably showing that the lowest energy pathways to involve Li diffusion are in the *bc*-plane, see **(a)**. A higher activation energy barrier for migration, however, could be expected parallel to the *a*-axis, which involves a path that is significantly obstructed by P_2O_7 polyhedra, see **(b)**. As a result, $Li_{2.4}Zn_{0.8}P_2O_7$ may have two-dimensional (2D) Li chains in the *bc*-plane, and a good ionic conductivity can be expected in this compound.

6.4.3 Element Analysis and Morphology

The EDS results of $LiZn_{1.5}P_2O_7$ and $Li_{2.4}Zn_{0.8}P_2O_7$ samples confirm each molar ratio of Zn/P has a satisfactory value of ~0.75 and ~0.39, consistent with the expected theoretical values within errors. However, the EBSD image of $Li_2ZnP_2O_7$ reveals that its composition is not homogenous but is a mixture of two phases with Zn/P molar ratios of ~0.64 and ~0.4 closely corresponding to x=0.33 and 0.6, illustrated in lighter and darker areas, **Fig. 6-20(c)**. This result corresponds to XRD patterns showing two phases determined in $Li_2ZnP_2O_7$. Elemental mapping shows that Zn and P are uniformly distributed in $Li_{2.4}Zn_{0.8}P_2O_7$.

The SEM images show porous and inhomogeneous grain size in both $LiZn_{1.5}P_2O_7$ and $Li_2ZnP_2O_7$ pellets but $Li_{2.4}Zn_{0.8}P_2O_7$ has more regular grain morphology. $LiZn_{1.5}P_2O_7$ and

$Li_{2.4}Zn_{0.8}P_2O_7$ pellets had relative density ~ 70%. Higher sintering temperature of > 600°C for densification is not suggested due to the lower eutectic temperature ~ 690°C for these compositions.

6.4.4 Electrical Properties

Conductivity data of $Li_{4x}Zn_{2-2x}P_2O_7$ for solid solutions over the x ranges of 0.2 < x < 0.25 and 0.33 < x < 0.4 measured in air show that the ionic conductivity increases with x, according to the aliovalent substitution, $Zn \rightleftharpoons 2Li^+$, which may lead to the creation of Li^+ interstitials. The defect compensation mechanism can be described using Kröger-Vink notation:

$$Zn_{Zn}^{\times} \rightarrow Li_{Zn}^{'} + Li_i^{\bullet}$$

The conductivity of $Li_{2.4}Zn_{0.8}P_2O_7$ increases up to ~10^{-3} Scm^{-1}, which is ~3 orders magnitude greater than that of $LiZn_{1.5}P_2O_7$ and with a relatively lower activation energy of 1.05(1) eV. One reason is due to the structural differences between them. In addition, the conductivity data at x=0.6 are non-linear which would be due to the phase transition at high temperature. There are two-dimensional channels in $Li_{2.4}Zn_{0.8}P_2O_7$, which can provide a mobile channel for Li^+ ion diffusion, and therefore, attributed to higher ionic conductivity. Nevertheless, as shown in **Fig. 6-40**, no feasible channels for Li^+ ion migration can be apparently observed along the *b*-, *c*- **(a)**, and *a*-axis **(b)** in the crystal structure of $LiZn_{1.5}P_2O_7$. This could be one of the reasons to explain its low ionic conductivity ~10^{-7} Scm^{-1} at 250°C and a short electrode spike at low frequency merely occurred at higher temperatures of 400~425 °C.

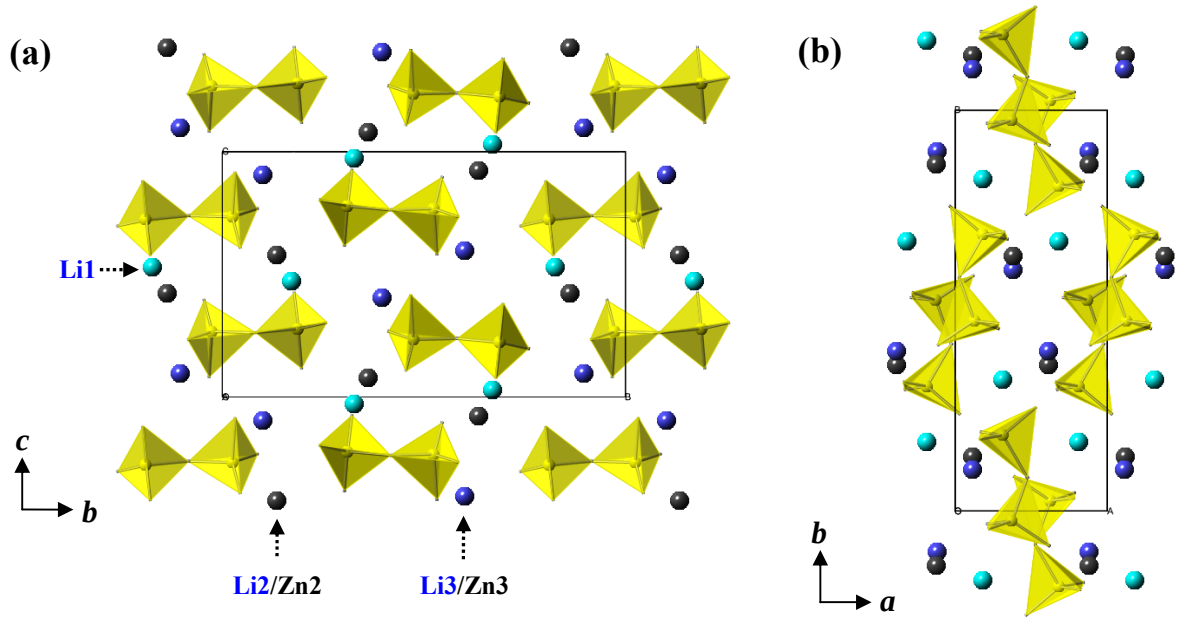

Figure 6-39 Li^+ migration in $Li_{2.4}Zn_{0.8}P_2O_7$ showing the possible migration channels. Li–Li connections parallel to the (a) *bc*-plane and (b) *ab*-plane.

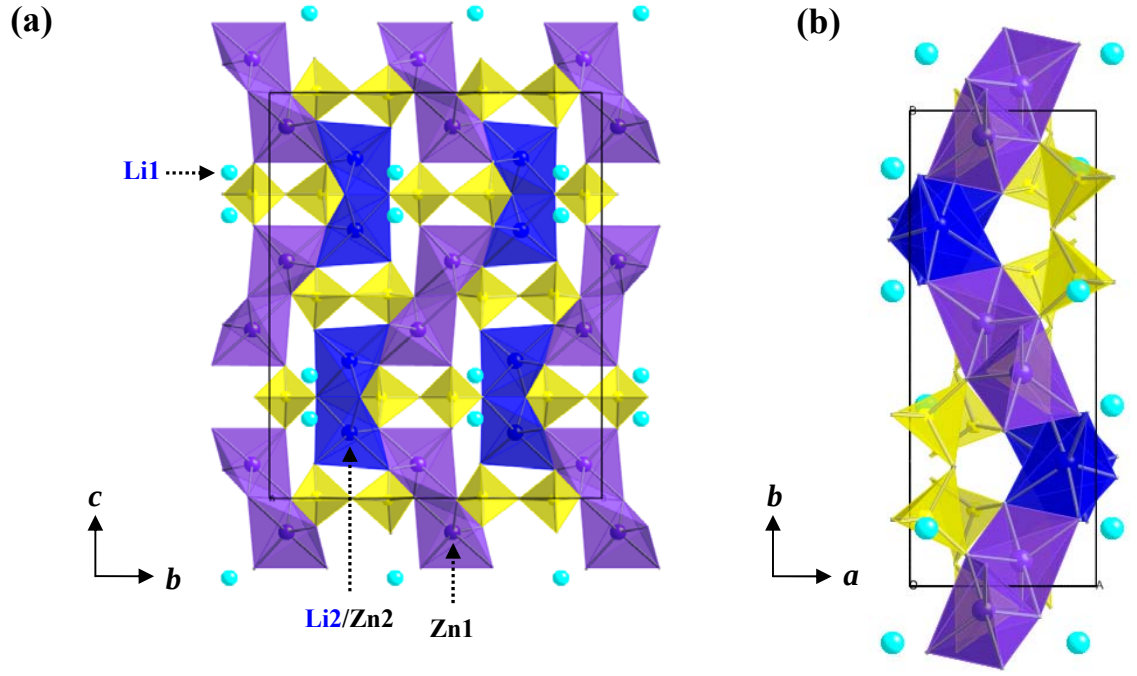

Figure 6-40 Crystal structure of $LiZn_{1.5}P_2O_7$ projected to the (a) *a*-axis and (b) *c*-axis.

Fig. 6-41 shows an Arrhenius plot of ionic conductivity of the $Li_{2.4}Zn_{0.8}P_2O_7$ in comparison to those of other polycrystalline LISICONs with their highest ionic conductivity reported. It is found that LISICONs have higher conductivity over a wide of temperature range. However, the $Li_{2.4}Zn_{0.8}P_2O_7$ exhibits an ionic conductivity of ~10^{-2} Scm^{-1} at 350°C, close to those of previously discovered $Li_{3.4}P_{0.6}Si_{0.4}O_4$ and $Li_{2.4}Zn_{0.8}SiO_4$, but shows a high activation energy, ~1.05 eV, probably due to a longer pathway for Li^+ migration in the structure. The $Li_{3.5}Zn_{0.25}GeO_4$ possesses a conductivity of > 10^{-1} Scm^{-1} at 350°C, which is one of the highest Li-ion conductivity at this temperature.

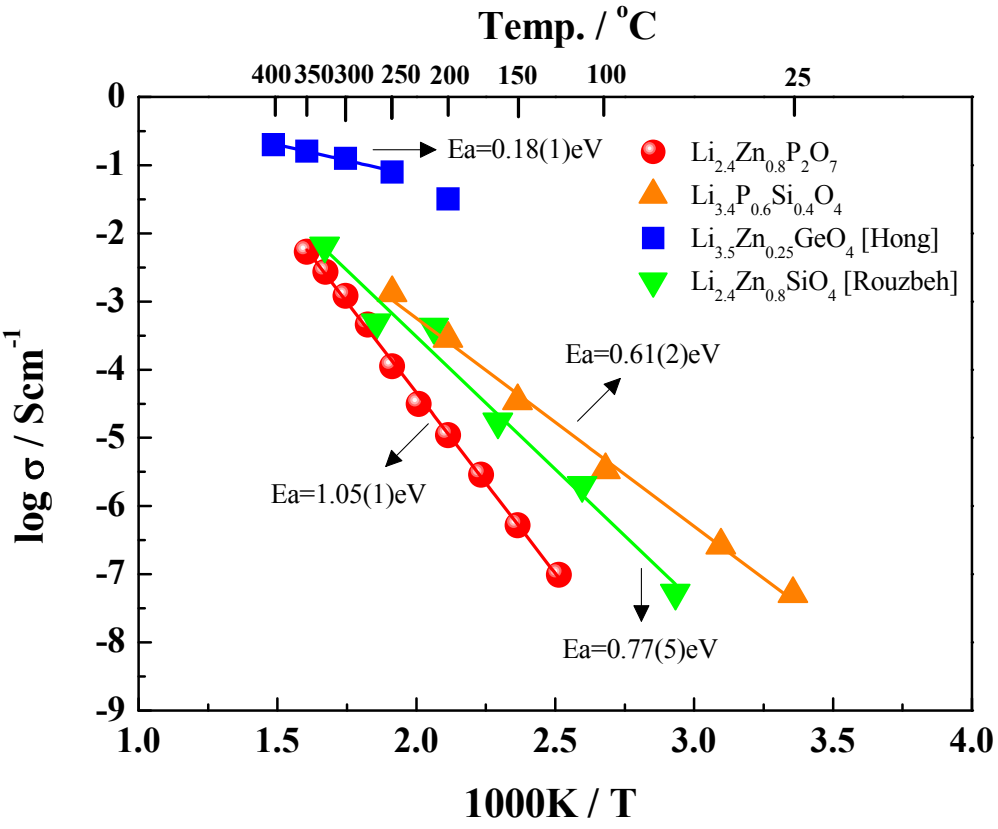

Figure 6-41 Arrhenius plots of ionic conductivity of the $Li_{2.4}Zn_{0.8}P_2O_7$ and poly-crystalline LISICONs, e.g. $Li_{3.4}P_{0.6}Si_{0.4}O_4$, $Li_{3.5}Zn_{0.25}GeO_4$ [13] and $Li_{2.4}Zn_{0.8}SiO_4$ [14].

6.5 Conclusions

Lithium zinc pyrophosphates, $Li_{4x}Zn_{2-2x}P_2O_7$ (0 < x < 1), have been synthesized via a conventional solid-state method. The phase composition was studied by X-ray diffraction and compared with that of previously reported results. XRD patterns show two phases, at x=0.25 ($LiZn_{1.5}P_2O_7$) and x=0.6 ($Li_{2.4}Zn_{0.8}P_2O_7$), synthesized at 600°C for 24 h in air, are single phase with orthorhombic (P*bcm*) and monoclinic ($P2_1/n$) symmetry, corresponding to a previous study. A new phase with composition around x=0.33, $Li_{1.33}Zn_{1.33}P_2O_7$, is discovered in this study and its XRD patterns are indexed as monoclinic with S.G. $P2_1/a$. Three solid solutions are found for compositions over the *x* ranges of 0.2 < x < 0.25, 0.33 < x < 0.4 and 0.575 < x < 0.625. Two-phase mixtures of $Li_{1.33}Zn_{1.33}P_2O_7$ and $Li_{2.4}Zn_{0.8}P_2O_7$ are observed in $Li_2ZnP_2O_7$ (x=0.5) by XRD and confirmed using EDS spectra showing different chemical stoichiometry. Attempts to reproduce pure-phase $Li_3Zn_{0.5}P_2O_7$ (x=0.75) were not successful under our experimental conditions. Elemental mapping shows the distribution of Zn and P atoms in $Li_{2.4}Zn_{0.8}P_2O_7$ is homogeneous.

The crystal structure of $Li_{2.4}Zn_{0.8}P_2O_7$ is closely related to that reported previously by XRD data but contains different Li/Zn site occupancies in the distorted tetrahedra and trigonal-pyramid sites using ND data at room temperature. Two dimensional channels for lithium transport are also observed in the *bc*-plane.

Electrical properties of $Li_{4x}Zn_{2-2x}P_2O_7$, with *x* from 0.2 to 0.75, were carried out systematically by impedance spectroscopy (IS). In general, the ionic conductivity increases with increasing the level of mobile Li ions to x=0.65. Specifically, at x=0.6, the conductivity reaches a maximum of 10^{-2} Scm^{-1} at 350°C, similar to those of reported LISICONs, such as $Li_{3.4}P_{0.6}Si_{0.4}O_4$ and $Li_{2.4}Zn_{0.8}SiO_4$. Compared with the crystal structure of $LiZn_{1.5}P_2O_7$, $Li_{2.4}Zn_{0.8}P_2O_7$ has a 2D Li channels and this helps in increasing Li^+ diffusion and mobility contributed to higher Li^+ ion conductivity. Based on above data characterizations, a basic understanding of structure-composition-property relations for $Li_{4x}Zn_{2-2x}P_2O_7$ (0 < x < 1) has been further studied in this chapter.

6.6 References

1. G. Torres-Trevino and A.R. West, "Compound Formation, Crystal Chemistry, and Phase Equilibria in the System Li_3PO_4-$Zn_3(PO_4)_2$", *J. Solid State Chem.* **1986**, *61*, pp. 56–66.

2. G.A. Mikirticheva, V.I. Shitova, M.A. Petrova, V.F. Popova and A.E. Malshikov, "Phase Diagram of the $Zn_2P_2O_7$–$M_2ZnP_2O_7$ System", *Zh. Prikl. Khim.* (St. Petersburg) **1995**, *68*, pp. 462–467.

3. M.A. Petrova, G.A. Mikirticheva and R.G. Grebenshchikov, "Phase Equilibria in the $Zn_2P_2O_7$–$M_2ZnP_2O_7$ and $M'_2ZnP_2O_7$ – $M''_2ZnP_2O_7$ (M, M',M''=Li, Na, K)", Glass-Forming Systems, *Inorg. Mater.* **2007**, *43*, pp. 1024–1031.

4. L.N. Ji, H.W. Ma and J.K. Liang, "Lithium zincopyrophosphate, $Li_2Zn_3(P_2O_7)_2$", *Acta Crystallogr.* **2009**, *C65*, pp. i30–i32.

5. L.N. Ji, J.B. Li, Y.Q. Chen, J. Luo, J.K. Liang and G.H. Rao, "Subsolidus phase relations of the ZnO–Li_2O–P_2O_5 system", *J. Alloys Compd.* **2009**, *486*, pp. 352–356.

6. A. E. Lapshin and M. A. Petrova, "Synthesis and Crystal Structure of the Low-Temperature Modification of $Li_{12}Zn_4(P_2O_7)_5$", *Glass Phys. Chem.* **2010**, *36*, pp. 75–79.

7. A. E. Lapshin, M. A. Petrova, Yu. N. Osipova, A. S. Novikova and Yu. F. Shepelev, "Thermal Behavior of Alkali Zinc Phosphates", *Glass Phys. Chem.* **2005**, *31*, pp. 684–689.

8. V.I. Voronin, E.A. Sherstobitova, V.A. Blatov, G. Sh.Shekhtman, "Lithium-cation conductivity and crystal structure of lithium diphosphate", *J. Solid State Chem.* **2014**, *211*, pp. 170–175.

9. A. Jarboui, A. Ben Rhaeim, F. Hlel, K. Guidara and M. Gargouri, "NMR study and electrical properties investigation of $Zn_2P_2O_7$", *Ionics* **2010**, *16*, pp. 67–73.

10. A.R. West, *Basic Solid State Chemistry*, 2nd Edition, Wiley, New York, **2000**, pp. 457–458.

11. O.V. Yakubovich and O.K. Mel'nikov, "Crystal Structure of the $Li_4P_2O_7$ Compound", *Crystallogr. Rep.* **1994**, *39*, pp. 737–742.

12. A. Daidouh, M.L. Veiga, C. Pico and M. Martinez-Ripoll, "A new Polymorph of $Li_4P_2O_7$", *Acta Cryst.* **1997**, *C53*, pp. 167–169.

13. H.Y-P. Hong, "Crystal structure and ionic conductivity of $Li_{14}Zn(GeO_4)_4$ and other new Li^+ superionic conductors", *Mat. Res. Bul.* **1978**. *13*, pp. 117–124.

14. R. Jarkaneh and A.R. West, unpublished results.

CHAPTER VII

Conclusions and Future Work

7.1 Conclusions

- Impedance spectroscopy (IS) measurement of $Li_2MP_2O_7$ (M=Fe, Mn, Co, $Fe_{1/3}Mn_{1/3}Co_{1/3}$) cathodes as a function of temperature, *dc*-bias and atmosphere were carried out to investigate their electrical properties and to further determine their conduction mechanisms, i.e. electronic, ionic or mixed, with results summarised in **Fig. 7-1**.

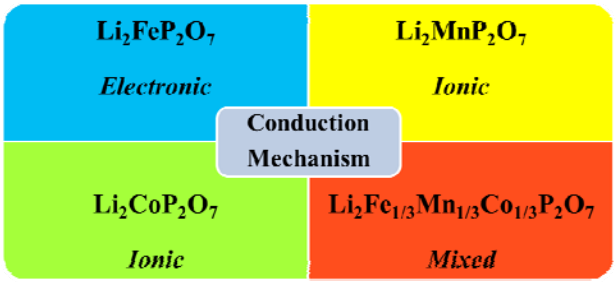

Figure 7-1 Summarised conduction mechanisms of $Li_2MP_2O_7$ cathodes.

- The effect of aliovalent dopants (Al^{3+}, Zr^{4+}, Nb^{5+}) in $Li_2FeP_2O_7$ on phase composition and electrical properties was studied; only ≤ 5% Nb^{5+} can be substituted into $Li_2FeP_2O_7$ synthesized at 700°C in N_2 to form a solid solution, i.e. $Li_{1.85}Nb_{0.05}Fe_{0.95}P_2O_7$ and $Li_{1.95}Nb_{0.05}Fe_{0.9}P_2O_7$ and the doping of niobium enhances the bulk conductivity by a factor of 2~3 in air.
- N-doped $Li_2FeP_2O_7$ compositions were synthesized for the first time via a solid-state reaction and $Li_2FeP_2O_{6.95}N_{0.05}$ has an increased electronic conductivity ~0.5×10^{-7} Scm^{-1} (*Ea* = ~0.3 eV) at 25°C in N_2 due to the coexistence of $Fe^{2+/3+}$. Sample I-LFPN005 prepared by a modified synthesis method has a much higher conductivity, ~10^{-5} Scm^{-1}, with low *Ea* ~0.16 eV and is an electronic conductor.
- The structure-composition-property relations of $Li_{4x}Zn_{2-2x}P_2O_7$ based on the $Zn_2P_2O_7$–$Li_4P_2O_7$ system were studied; a new phase $Li_{1.33}Zn_{1.33}P_2O_7$ was found and indexed as monoclinic with probable space group $P2_1/a$. Solid solutions in the x ranges of 0.2 to 0.25, 0.33 to 0.4 and 0.575 to 0.625 were found and two phases present confirmed for

x=0.5. At x=0.6, the value of ionic conductivity reaches a maximum ~10^{-2} Scm^{-1} at 350°C in air. Details are as follows:

7.1.1 $Li_2MP_2O_7$ (M=Fe, Mn, Co)

Lithium mixed-metal pyrophosphates, $Li_2Fe_{1-x}Mn_xP_2O_7$ ($0 \le x \le 1$), $Li_2Fe_{1-y}Co_yP_2O_7$ ($0 \le y \le 1$), and $Li_2Fe_{1/3}Mn_{1/3}Co_{1/3}P_2O_7$ have been successfully synthesised by a conventional solid-state method. Pure phase $Li_2FeP_2O_7$ was obtained, at 700°C, following a two-step process. XRD patterns show the Mn- and Co- substituted $Li_2FeP_2O_7$ synthesised at 700°C for 12 h in N_2 form a complete solid solution with monoclinic symmetry and space group $P2_1/c$. Lattice parameters increase and decrease with Mn and Co content, respectively. Electrical properties are as follows:

- For $Li_2FeP_2O_7$, no electrode or Warburg spike is observed at low frequencies over a wide range of temperatures but a second semicircle with an associated capacitance of ~10^{-6} Fcm^{-1} was obtained due to an electrode effect, attributed to point contacts with the sample using Pt- and/or Au-sputtered electrodes. The conductivity increased when the atmosphere changed from N_2 to air which suggests a *p*-type conduction mechanism consistent also with *dc*-bias results. These results indicate that the $Li_2FeP_2O_7$ is predominantly an electronic conductor with perhaps some lithium ion conduction as well.
- The effect of temperature, *dc*-bias and atmosphere elucidated that the conduction of $Li_2MnP_2O_7$ or $Li_2CoP_2O_7$ is primarily ionic, as evidenced by:
  1) a low frequency Warburg spike at ~45° in the impedance complex plane plot above 300°C and a blocking double layer capacitance of ~10^{-5} Fcm^{-1}.
  2) fully reversible charge transfer towards the electrode-sample interface by applying/removing *dc*-bias, e.g. Mn case.
  3) the stable valence of Mn and Co at high temperature of 400°C in air, i.e. it is hard to oxidize from $Mn^{2+} \rightarrow Mn^{3+}$ or $Co^{2+} \rightarrow Co^{3+}$.

- $Li_2Fe_{1/3}Mn_{1/3}Co_{1/3}P_2O_7$ shows similar electrical behavior to $Li_2CoP_2O_7$; the total conductivity is limited by large grain boundary resistances (R_{gb}) with a slightly higher activation energy of 0.84 eV than those in Mn- and Co-based materials. A low frequency electrode spike above 250°C is observed. Li ion transfer across the electrode-sample interface is not fully reversible after applying 3V *dc*-bias, probably due to the deposition of lithium on Pt electrodes as shown by the formation of a black coating. A tiny increase in conductivity at lower frequencies is found in air, probably due to partial oxidation ($Fe^{2+/3+}$) of the sample, suggesting the conduction mechanism of $Li_2Fe_{1/3}Mn_{1/3}Co_{1/3}P_2O_7$ is mixed.

Electrochemical results indicate that the Fe phase is a much better cathode than the others owing to its stable voltage plateau, higher discharge capacity, high rate performance and good cycle stability. This is probably because $Li_2FeP_2O_7$ has smaller grain size and is the only material in this group which possesses a high electronic conductivity. $Li_2CoP_2O_7$ can be a potential ~5 V cathode.

7.1.2 Aliovalent doping of $Li_2FeP_2O_7$

The effect of aliovalent doping by Al^{3+}, Zr^{4+} and Nb^{5+}, of $Li_2FeP_2O_7$ on phase composition and electrical properties was studied and compared with undoped $Li_2FeP_2O_7$. Al and Zr dopants do not substitute into the $Li_2FeP_2O_7$ structure. Only ≤ 5% Nb can be substituted at 700°C in N_2 to form solid solutions, i.e. $Li_{1.85}Nb_{0.05}Fe_{0.95}P_2O_7$ and $Li_{1.95}Nb_{0.05}Fe_{0.9}P_2O_7$, using a solid-state reaction. Vacancies are introduced in both cases. In general, lattice parameters and unit volume are not changed in Nb-doped compounds. EDS mapping indicated that the Nb dopants are not present uniformly in $Li_{1.85}Nb_{0.05}Fe_{0.95}P_2O_7$ and $Li_{1.95}Nb_{0.05}Fe_{0.9}P_2O_7$; therefore, they do not form homogeneous solid solutions.

IS results show the doping of Nb enhances the bulk conductivity by a factor of 2~3, perhaps due to a slightly increased lithium ion conductivity. The charge-compensation mechanism found for Nb doping does not alter the Fe^{2+} valence state and hence is unlikely to enhance electronic conductivity. Although the results of aliovalent doping in $Li_2FeP_2O_7$ do not improve its electronic and/or ionic conductivity dramatically, consideration of these five possible doping mechanisms proposed in this study may be useful for the other

isostructural pyrophosphate compounds which show ionic conduction, e.g. $Li_2MnP_2O_7$ and $Li_2CoP_2O_7$, to improve their electrical and electrochemical properties.

7.1.3 N-doped $Li_2FeP_2O_7$

N-doped $Li_2FeP_2O_7$ materials, e.g. $Li_{2+x}FeP_2O_{7-x}N_x$ and $Li_2FeP_2O_{7-y}N_y$, have been synthesised by the solid-state method. However, nitrogen loss during preparation and reaction of samples was perhaps inevitable and confirmed by gas combustion analysis. The effect of N doping on their phase compositions and electrical properties was studied. XRD patterns of the reacted samples were very similar to that of $Li_2FeP_2O_7$ for compositions $0 \lesssim x \lesssim 0.1$ and $0 \lesssim y \lesssim 0.075$. No obvious change in XRD peak positions was observed and therefore, unit cell parameters have no big differences. For $y \gtrsim 0.075$, a small amount of $Li_3Fe_2(PO_4)_3$ was detected.

IS results show the bulk conductivity and activation energy of x=0.05 and 0.1 have no real difference within errors compared with those for x=0, and therefore do not alter the Fe^{2+} oxidation state. For $Li_2FeP_2O_{7-y}N_y$, the increased conductivity with lower activation energy of both y=0.05 and 0.2 is attributed to the coexistence of Fe^{2+} and Fe^{3+} ions which benefits the electron conductivity and increased mobility of electrons in comparison to those of y=0. For y=0.05, the mixture of 2^+ and 3^+ oxidation states of Fe was further confirmed by Mössbauer spectroscopy which indicated the presence of ~ 1% Fe^{3+} ions in agreement with the nitrogen content of y=0.0167 obtained for the targeted composition y=0.05.

Attempts to increase the ionic conductivity of $Li_2FeP_2O_7$ by aliovalent and nitrogen doping, with a view to increasing lithium ion conductivity have been unsuccessful. However, the electronic conductivity of $Li_2FeP_2O_{6.95}N_{0.05}$ and $Li_2FeP_2O_{6.8}N_{0.2}$ measured at room temperature in N_2 is increased by ~3 orders and specifically, of I-LFPN005, which is ~6 orders higher than that of undoped $Li_2FeP_2O_7$. This new strategy of anionic doing may provide a suggestive data base for the other novel polyoxoanionic compounds to improve their electrical and electrochemical properties.

7.1.4 $Li_{4x}Zn_{2-2x}P_2O_7$ ($0.2 \leq x \leq 0.75$)

Lithium zinc pyrophosphates, $Li_{4x}Zn_{2-2x}P_2O_7$, based on the phase diagram $Zn_2P_2O_7$–$Li_4P_2O_7$ with variation of x have been systematically studied; the phases formed were studied by XRD to compare with reported results. Three single phase materials were synthesized at 600°C for 24 h in air. The first phase is at x=0.25 ($LiZn_{1.5}P_2O_7$) and second one, at x=0.6 ($Li_{2.4}Zn_{0.8}P_2O_7$); both correspond to previous results with orthorhombic (P*bcm*) and monoclinic ($P2_1/n$) symmetry, respectively. The third one, at x=0.33 ($Li_{1.33}Zn_{1.33}P_2O_7$), is a new phase and its diffraction pattern is indexed as monoclinic with space group $P2_1/a$. Three solid solutions are found over the x range from 0 to 1; one is verified between x=0.2 and 0.25 in agreement with the previous work from Petrova *et al.* and the others, x=0.33 to 0.4 and 0.575 to 0.625, are reported in this work.

For x=0.5 ($Li_2ZnP_2O_7$), two phases are present: $Li_{1.33}Zn_{1.33}P_2O_7$ and $Li_{2.4}Zn_{0.8}P_2O_7$, as observed by XRD and confirmed using EBSD image and EDS spectra. This result is different from that reported in the literature where it is claimed that the phase mixture of $Li_{4x}Zn_{2-2x}P_2O_7$ and α-$Li_{2.4}Zn_{0.8}P_2O_7$ forms for x=0.5. XRD patterns of $Li_{2.4}Zn_{0.8}P_2O_7$ quenched rapidly from different temperatures show that this composition has a complicated high-temperature polymorphism, probably consisting of three polymorphs by DSC measurement, and more work is needed. Attempts to prepare pure-phase $Li_3Zn_{0.5}P_2O_7$ (x=0.75), however, failed with impurities present over the heating range 600~850 °C in air.

The crystal structure of $Li_{2.4}Zn_{0.8}P_2O_7$ is similar to that reported using XRD data; however, in this study, different Li/Zn site occupancies of the distorted $M1O_4$ tetrahedra and $M2O_5$ trigonal-pyramids are determined with occupancy of the M1 site by 0.82 Li and 0.18 Zn, and of the M2 site by 0.38 Li and 0.62 Zn, using room-temperature ND data. There are two dimensional pathways along the *b*- and *c*-axes for the Li ion migration in $Li_{2.4}Zn_{0.8}P_2O_7$.SEM shows that the $Li_{2.4}Zn_{0.8}P_2O_7$ pellet sintered at 600°C for 12 h in air has uniform particle size of ~10 μm with similar-polygonal shape. EDS mapping shows the distribution of Zn and P atoms in $Li_{2.4}Zn_{0.8}P_2O_7$ is homogenous.

The electrical properties of $Li_{4x}Zn_{2-2x}P_2O_7$, with x from 0.20 to 0.75, were measured; generally, the ionic conductivity increases with increasing the Li content x to 0.65. Specifically, $Li_{2.4}Zn_{0.8}P_2O_7$ has an ionic conductivity of $\sim 10^{-4}$ Scm^{-1} at 250°C, which is three orders of magnitude higher than that of $LiZn_{1.5}P_2O_7$ ($\sim 10^{-7}$ Scm^{-1}), and is attributed to the

2D Li channels helping to increase Li^+ diffusion and mobility. The conductivity of $Li_{2.4}Zn_{0.8}P_2O_7$ reaches a maximum of $\sim 10^{-2}$ Scm^{-1} at 350°C, comparable to that of traditional *LISICON*s, e.g. $Li_{3.4}P_{0.6}Si_{0.4}O_4$ and $Li_{2.4}Zn_{0.8}SiO_4$. This present study may lead to a different family of polyanionic systems with a three-dimensional $(P_2O_7)^{-4}$-framework for solid-state electrolytes.

7.2 Future work

The following areas would be interesting to the author for future study.

- Electrical properties of $Li_2Fe_{0.5}Mn_{0.5}P_2O_7$ and $Li_2Fe_{0.5}Co_{0.5}P_2O_7$ to get insight into the electronic and/or ionic conductivity
- Equivalent circuit fitting to understand the methodology and interpretation of the IS data obtained by $Li_2MP_2O_7$ (M=Fe, Mn) cathodes
- Investigation of alternative doping mechanism in Nb-doped $Li_2FeP_2O_7$, e.g.
    1. $2Li^+ + Fe^{2+} \rightarrow 0.8\ Nb^{5+}$
    2. $Li^+ + Fe^{2+} \rightarrow 0.6\ Nb^{5+}$
    3. $4Li^+ + 3Fe^{2+} \rightarrow 2\ Nb^{5+}$ (a possible solid solution between mechanism II + IV)
- Synthesis and characterisation of the aliovalent doping of $Li_2MnP_2O_7$ using the five defect mechanisms which have been proposed in this study followed by electrical and electrochemical measurements, in particular with a view to increase the Li ion conductivity
- Optimization of synthesis conditions to reduce nitrogen loss in N-doped $Li_2FeP_2O_7$
- 1) Electrochemical testing of the high conductivity I-LFPN005 sample with reduced particle size and 2) TEM/EELS analysis to show whether N is substituted into the structure or coated on the surface of particles
- High temperature X-ray and neutron diffraction studies on the phase transformation and crystal structure for $Li_{2.4}Zn_{0.8}P_2O_7$ and new phase $Li_{1.33}Zn_{1.33}P_2O_7$

Table A3-1 Summary of the indexed XRD reflections of $Li_2FeP_2O_7$ using Mo radiation in the 2θ range of ~ 5–20°.

No.	2θ [obs] (°)	h k l	2θ [calc] (°)	△2θ (°)	Int.	Int. [calc]	d [obs] (Å)	d [calc] (Å)
1	5.964	0 1 1	5.947	0.0166	2.8	3.131	6.8177	6.8367
2	6.579	-1 1 1	6.574	0.0055	50.9	66.046	6.1806	6.1857
3	7.545	2 0 0	7.541	0.0041	30.5	40.771	5.3904	5.3933
4	8.363	0 2 0	8.348	0.0143	5.9	6.990	4.8639	4.8722
5	8.630	2 1 0	8.621	0.0090	5.7	8.976	4.7139	4.7188
6	8.940	-2 1 1	8.919	0.0214	4.6	4.036	4.5504	4.5613
7	9.167	1 2 0	9.162	0.0046	6.8	8.023	4.4381	4.4403
8	9.527	-1 1 2	9.531	-0.0039	8.0	8.853	4.2708	4.2691
9	10.166	-2 0 2	10.166	-0.0007	14.6	15.406	4.0030	4.0028
10	10.785	1 1 2	10.790	-0.0058	8.1	9.447	3.7739	3.7719
11	11.264	2 2 0	11.259	0.0051	27.3	25.630	3.6138	3.6154
12	11.488	-2 2 1	11.489	-0.0008	44.9	47.093	3.5434	3.5431
13	12.067	3 1 0	12.070	-0.0027	50.0	51.360	3.3740	3.3732
14	12.550	2 2 1	12.556	-0.0063	2.2	3.246	3.2447	3.2431
15	13.208	-1 1 3	13.219	-0.0112	100.0	100.000	3.0838	3.0929
16	13.507	-1 3 1	13.534	-0.0268	7.4	4.543	3.0158	3.0098
17	14.045	-3 2 1	14.041	0.0033	44.1	22.50	2.9009	2.9016
18	14.640	2 3 0	14.645	-0.0096	8.7	8.749	2.7843	2.7825
19	14.992	2 2 2	14.996	-0.0032	66.5	66.920	2.7184	2.7179
20	15.199	-1 3 2	15.203	-0.0042	50.2	49.313	2.6818	2.6810
21	15.452	-4 1 1	15.441	0.0107	3.5	2.694	2.6381	2.6399
22	15.831	-3 1 3	15.841	-0.0094	8.4	5.831	2.5753	2.5738
23	16.024	1 3 2	16.028	-0.0048	24.5	24.171	2.5445	2.5438
24	16.306	1 2 3	16.314	-0.0076	11.0	10.051	2.5007	2.4996
25	16.614	2 1 3	16.606	0.0078	6.6	8.471	2.4547	2.4558
26	17.067	-4 2 1	17.068	-0.0012	19.3	14.149	2.3901	2.3899
27	17.274	4 2 0	17.290	-0.0168	23.4	17.960	2.3617	2.3594
28	17.504	-1 4 1	17.506	-0.0012	5.2	5.033	2.3308	2.3306
29	17.886	-3 3 2	17.902	-0.0153	1.3	2.255	2.2814	2.2795
30	18.151	1 0 4	18.152	-0.0002	1.6	1.394	2.2483	2.2483
31	18.420	-2 3 3	18.426	-0.0059	2.0	2.730	2.2158	2.2151
32	18.824	1 3 3	18.828	-0.0038	7.6	3.298	2.1687	2.1682
33	19.128	-5 0 2	19.141	-0.0131	6.8	4.548	2.1346	2.1331
Final 2θ window: 0.04, Symmetry: monoclinic, $\boldsymbol{a}$ = 11.019(5) Å; $\boldsymbol{b}$ = 9.746(6) Å; $\boldsymbol{c}$ = 9.791(8) Å; $\boldsymbol{\beta}$ = 101.49(5)°; $\boldsymbol{V}$ = 1030.4(7) Å^3.								

Table A3-2 Summary of the indexed XRD reflections of $Li_2MnP_2O_7$ using Mo radiation in the 2θ range of ~ 5–20°.

No.	2θ [obs] (°)	h k l	2θ [calc] (°)	△2θ (°)	Int.	Int. [calc]	d [obs] (Å)	d [calc] (Å)
1	5.581	1 1 0	5.571	0.0104	3.2	5.786	7.2842	7.2978
2	5.909	0 1 1	5.903	0.0059	6.2	10.799	6.8809	6.8878
3	6.479	-1 1 1	6.478	0.0006	29.1	51.833	6.2761	6.2766
4	7.458	2 0 0	7.459	-0.0004	39.4	81.487	5.4528	5.4525
5	8.532	2 1 0	8.533	-0.0012	9.8	20.310	4.7677	4.7671
6	8.769	-2 1 1	8.773	-0.0035	5.7	8.890	4.6389	4.6371
7	9.093	1 2 0	9.086	0.0068	14.2	20.914	4.4742	4.4775
8	9.395	-1 1 2	9.403	-0.0074	21.9	27.357	4.3304	4.3270
9	9.964	-2 0 2	9.972	-0.0082	11.5	17.722	4.0837	4.0804
10	10.345	1 2 1	10.351	-0.0054	4.3	7.033	3.9336	3.9316
11	10.764	1 1 2	10.755	0.0089	6.3	9.703	3.7812	3.7843
12	11.167	2 2 0	11.155	0.0118	30.5	34.923	3.6451	3.6489
13	11.340	-2 2 1	11.340	-0.0003	40.6	58.831	3.5897	3.5896
14	11.839	0 2 2	11.821	0.0176	37.4	26.613	3.4388	3.4439
15	11.937	3 1 0	11.943	-0.0060	41.0	59.573	3.4107	3.4090
16	12.419	2 0 2	12.411	0.0078	2.0	3.463	3.2789	3.2809
17	13.062	-1 1 3	13.062	-0.0003	100.0	100.000	3.1181	3.1180
18	13.308	0 1 3	13.309	-0.0009	10.8	10.233	3.0606	3.0604
19	13.401	-1 3 1	13.406	-0.0056	11.9	13.344	3.0396	3.0384
20	13.864	-3 2 1	13.848	0.0153	34.5	28.985	2.9386	2.9418
21	14.534	1 1 3	14.550	-0.0161	12.0	9.407	2.8038	2.8007
22	14.949	2 2 2	14.939	0.0096	69.4	74.936	2.7263	2.7280
23	15.542	-3 1 3	15.550	-0.0076	12.3	9.715	2.6228	2.6215
24	15.943	1 3 2	15.936	0.0075	41.3	42.879	2.5573	2.5585
25	16.235	1 2 3	16.238	-0.0031	8.4	12.91	2.5116	2.5111
26	16.593	0 4 0	16.610	-0.0172	5.2	3.808	2.4578	2.4553
27	16.836	-4 2 1	16.832	0.0038	15.9	17.949	2.4226	2.4231
28	17.008	-1 1 4	17.002	0.0068	16.1	13.683	2.3982	2.3992
29	17.123	4 2 0	17.114	0.0096	24.3	19.757	2.3822	2.3835
30	17.364	-1 4 1	17.351	0.0129	5.6	4.488	2.3494	2.3512
31	17.570	-1 3 3	17.587	-0.0165	8.9	5.553	2.3221	2.3199
32	18.194	-2 3 3	18.193	0.0012	4.6	5.593	2.2431	2.2433
33	18.688	4 0 2	18.717	-0.0284	8.7	4.503	2.1543	2.1810
Final *2θ* window: 0.03, Symmetry: monoclinic, ***a*** = 11.169(5) Å; ***b*** = 9.821(4) Å; ***c*** = 9.897(5) Å; ***β*** = 102.49(4)°; ***V*** = 1059.9(6) Å^3.								

Table A3-3 Summary of the indexed XRD reflections of $Li_2CoP_2O_7$ using Mo radiation in the 2θ range of ~ 5–18°.

No.	2θ [obs] (°)	h k l	2θ [calc] (°)	△2θ (°)	Int.	d [obs] (Å)	d [calc] (Å)
1	5.975	0 1 1	5.977	-0.0023	4.0	6.8050	6.8023
2	6.590	-1 1 1	6.591	-0.0012	47.1	6.1704	6.1693
3	7.576	2 0 0	7.574	0.0027	34.6	5.3679	5.3698
4	8.401	0 2 0	8.401	0.0001	4.4	4.8419	4.8420
5	8.668	2 1 0	8.662	0.0063	8.7	4.6928	4.6962
6	8.938	-2 1 1	8.938	-0.0000	5.4	4.5513	4.5513
7	9.214	1 2 0	9.217	-0.0031	10.4	4.4156	4.4141
8	9.532	-1 1 2	9.552	-0.0198	10.4	4.2686	4.2597
9	10.182	-2 0 2	10.169	0.0135	11.3	3.9966	4.0018
10	10.852	1 1 2	10.856	-0.0034	4.8	3.7504	3.7492
11	11.323	2 2 0	11.320	0.0036	23.9	3.5948	3.5960
12	11.535	-2 2 1	11.533	0.0018	41.8	3.5291	3.5297
13	12.130	3 1 0	12.126	0.0044	46.1	3.3566	3.3578
14	12.635	2 2 1	12.637	-0.0021	2.1	3.2231	3.2225
15	13.244	-1 1 3	13.251	-0.0071	100.0	3.0754	3.0737
16	13.499	0 1 3	13.460	-0.0115	8.1	3.0288	3.0262
17	13.605	-1 3 1	13.607	-0.0019	4.5	2.9941	2.9937
18	14.108	-3 2 1	14.091	0.0173	44.3	2.8879	2.8915
19	14.722	2 3 0	14.730	-0.0083	6.8	2.7682	2.7666
20	15.094	2 2 2	15.094	-0.0007	64.6	2.7003	2.7002
21	15.266	-1 3 2	15.274	-0.0075	50.3	2.6699	2.6686
22	15.801	-4 0 2	15.814	-0.0129	6.4	2.5802	2.5781
23	15.880	-3 1 3	15.851	0.0295	6.3	2.5673	2.5721
24	16.121	1 3 2	16.128	-0.0066	28.8	2.5292	2.5282
25	16.393	1 2 3	16.407	-0.0144	11.5	2.4876	2.4855
26	16.718	2 1 3	16.713	0.0058	6.9	2.4395	2.4403
27	17.149	-4 2 1	17.127	0.0217	19.5	2.3787	2.3817
28	17.379	4 2 0	17.374	0.0047	23.2	2.3475	2.3481
29	17.605	-1 4 1	17.607	-0.0021	4.8	2.3176	2.3173
Final *2θ* window: 0.04, Symmetry: monoclinic, ***a*** = 10.974(4) Å; ***b*** = 9.684(5) Å; ***c*** = 9.766(6) Å; ***β*** = 101.87(4)°; ***V*** = 1015.7(6) $Å^3$.							

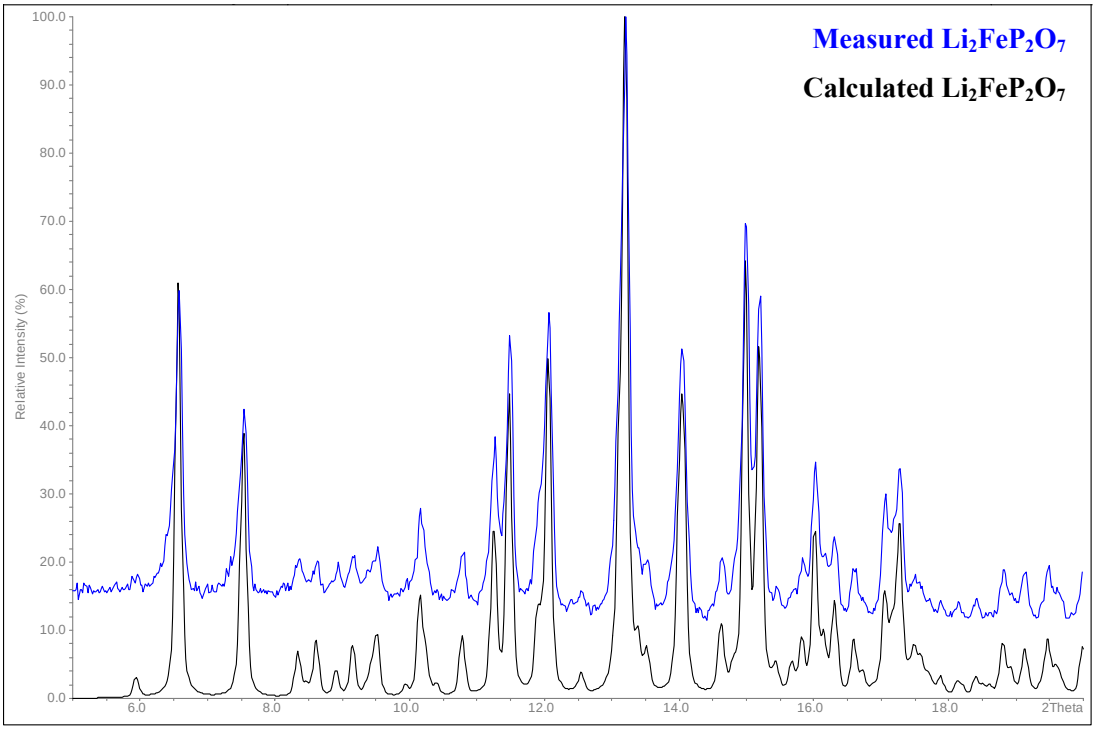

Figure A3-1 Measured and theoretical XRD patterns (Mo PSD) of $Li_2FeP_2O_7$.

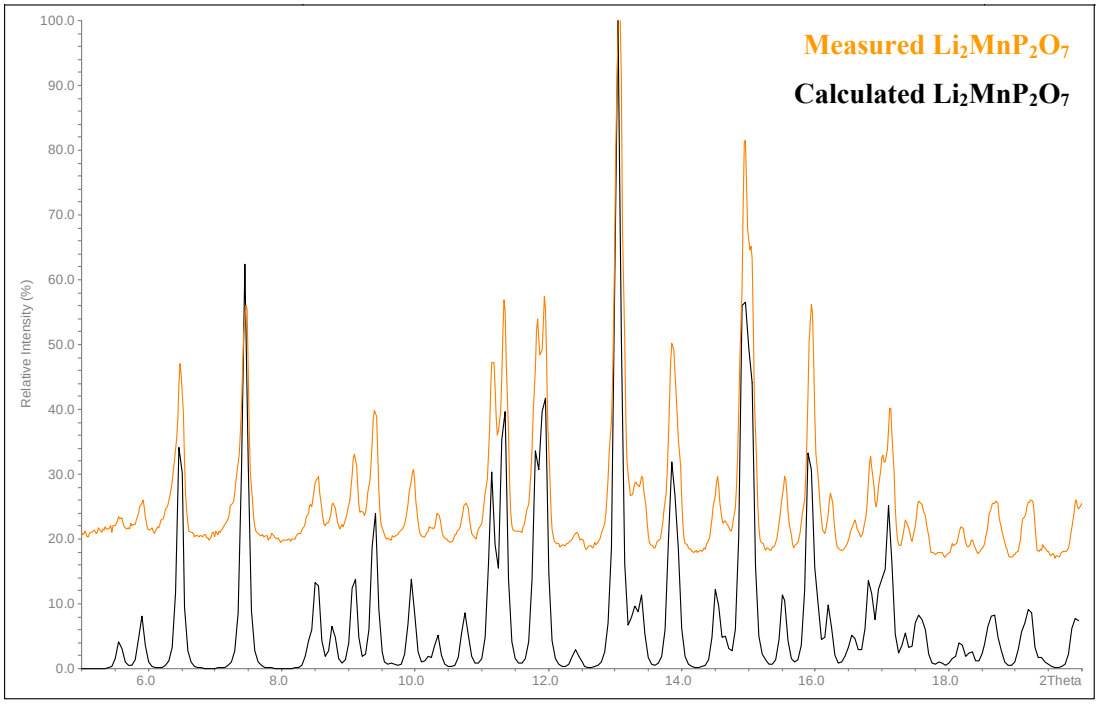

Figure A3-2 Measured and calculated XRD patterns (Mo PSD) of $Li_2MnP_2O_7$.

Table A3-4 Lattice parameters for $Li_2Fe_{1-x}Mn_xP_2O_7$, $Li_2Fe_{1-y}Co_yP_2O_7$ and $Li_2Fe_{1/3}Mn_{1/3}Co_{1/3}P_2O_7$ compounds with monoclinic symmetry.

Chemical formula	*a* (Å)	*b* (Å)	*c* (Å)	*β* (deg)	*V* (Å^3)
$Li_2MnP_2O_7$	11.169(5)	9.821(4)	9.897(5)	102.49(4)	1059.9(6)
$Li_2Fe_{0.1}Mn_{0.9}P_2O_7$	11.139(6)	9.815(7)	9.893(6)	102.42(4)	1057.8(7)
$Li_2Fe_{0.2}Mn_{0.8}P_2O_7$	11.108(7)	9.801(5)	9.873(4)	102.28(5)	1050.3(6)
$Li_2Fe_{0.5}Mn_{0.5}P_2O_7$	11.094(3)	9.784(3)	9.863(3)	102.05(3)	1047.0(4)
$Li_2Fe_{0.8}Mn_{0.2}P_2O_7$	11.035(6)	9.766(6)	9.817(6)	101.79(7)	1035.6(8)
$Li_2FeP_2O_7$	11.019(5)	9.746(6)	9.791(8)	101.49(5)	1030.4(7)
$Li_2Fe_{0.8}Co_{0.2}P_2O_7$	11.019(3)	9.742(4)	9.792(5)	101.56(4)	1029.8(5)
$Li_2Fe_{0.5}Co_{0.5}P_2O_7$	10.999(5)	9.725(4)	9.768(5)	101.61(5)	1023.5(5)
$Li_2Fe_{0.2}Co_{0.8}P_2O_7$	10.979(5)	9.704(7)	9.766(6)	101.65(6)	1019.1(6)
$Li_2Fe_{0.1}Co_{0.9}P_2O_7$	10.984(7)	9.695(7)	9.769(6)	101.82(6)	1018.2(8)
$Li_2CoP_2O_7$	10.974(4)	9.684(5)	9.766(6)	101.87(4)	1015.7(6)
$Li_2Fe_{1/3}Mn_{1/3}Co_{1/3}P_2O_7$	11.041(6)	9.757(4)	9.818(6)	102.05(4)	1034.3(6)

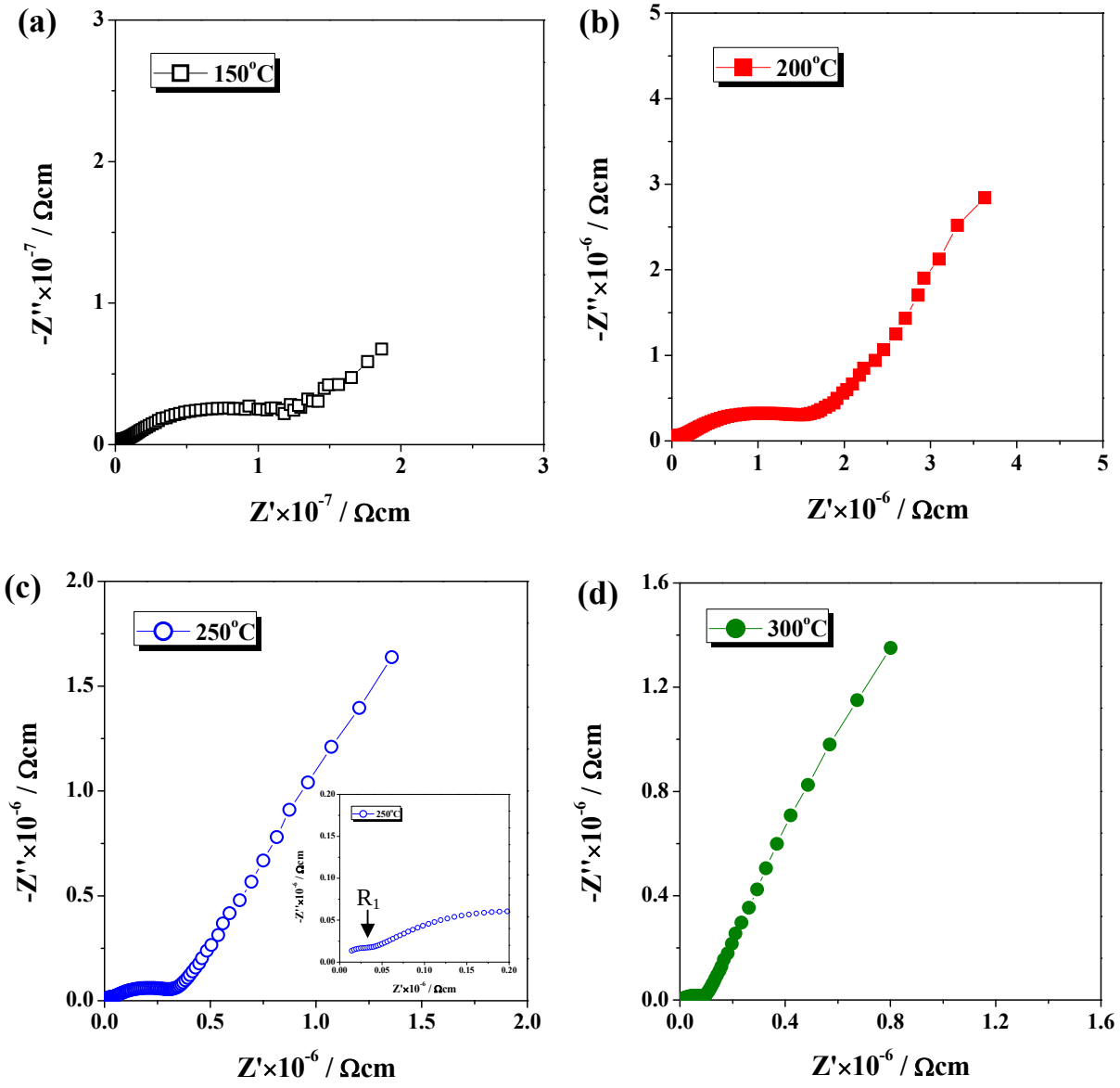

Figure A3-3 $Li_2MnP_2O_7$ (Au electrodes): Impedance complex plane plots, Z*, at 150°C to (d) 300°C in N_2.

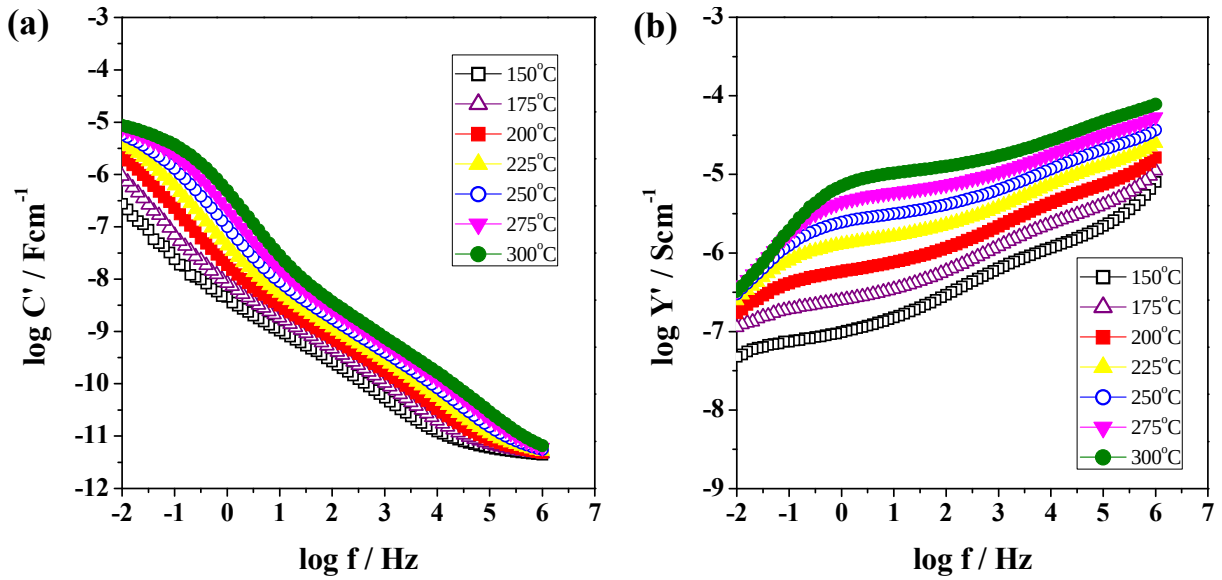

Figure A3-4 $Li_2MnP_2O_7$ (Au electrodes): (a) spectroscopic plots of capacitance, C', (b) spectroscopic plots of admittance, Y', at different temperatures of 150°C to 300°C.

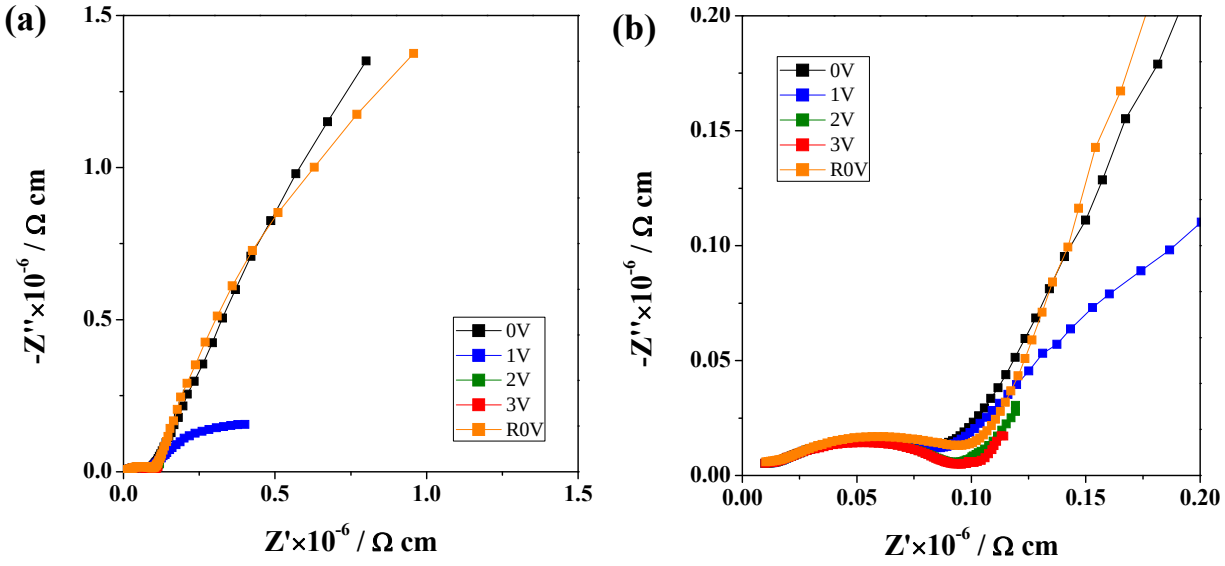

Figure A3-5 $Li_2MnP_2O_7$ (Au electrodes): (a, b) Impedance complex plane plots, Z*; (c) spectroscopic plots of capacitance, C'; (d) spectroscopic plots of admittance, Y', at a measuring temperature of 300°C with different *dc* bias of 0–3V in N_2.

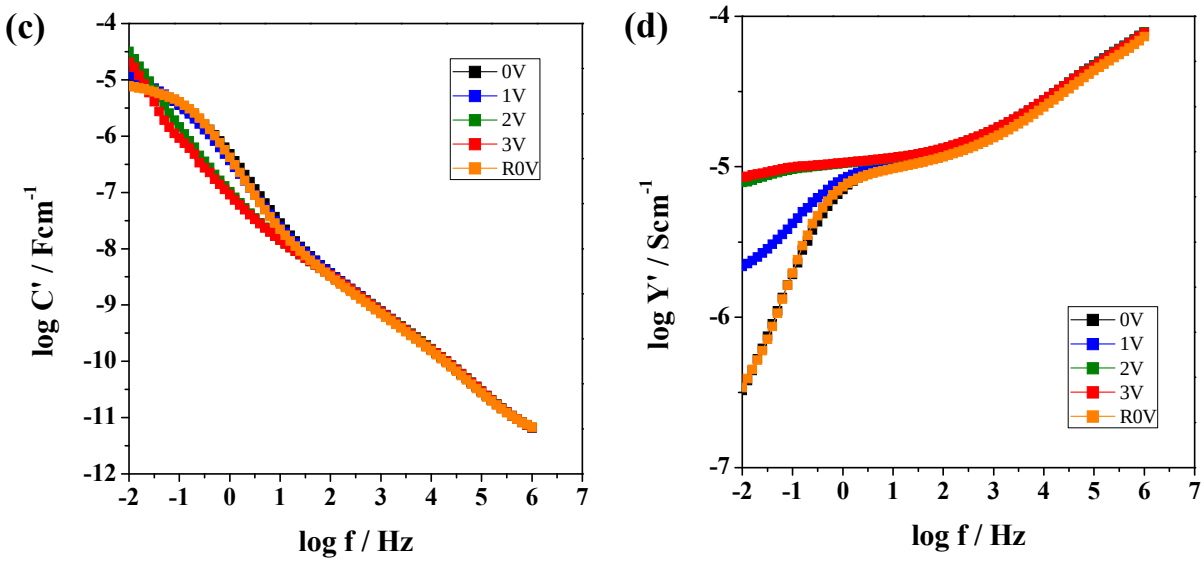

Figure A3-5 ***(continued)***

(III) $Li_2CoP_2O_7$

Z* plots of $Li_2CoP_2O_7$ with sputtered-Pt electrodes at various temperatures are given in **Fig. A3-6**. Two distorted semicircles at 150°C are observed, **(a)**. At higher temperatures of 200°C and 250°C, they consist of a high-frequency non-ideal semicircle of resistance (R_1), a larger intermediate-frequency arc of resistance (R_2), and a low-frequency arc or spike, **(b)** and **(c)**. At temperatures above ~250 °C, only the resistance R_2 can be identified, **(d)** and **(e)**. As the temperature increases, the low frequency effect is a combination of a curve at low frequency and a linear response at higher frequency, **(f)**.

C' plots as a function of frequency over a wide temperature range can be observed from **Fig. A3-7 (a)**, which shows three well-resolved plateaus. The first plateau at high frequencies is attributed to the bulk capacitance, C_1. Its value is ≈7 $pFcm^{-1}$ at 150°C (arrowed). A second one at intermediate-frequencies is nicely resolved at temperatures above 200°C, which is assigned to capacitance C_2 with ≈10 $nFcm^{-1}$. At the highest temperatures and lowest frequencies, the capacitance increases to ≈3×10^{-5} Fcm^{-1}, a third capacitance C_3, and is attributed to the typical double layer interface.

Conductivity, Y', data as a function of frequency are presented in **Fig. A3-7 (b)**. At 150°C, the Y' plot shows two approximately frequency independent plateaus, one below ~1 Hz and one between ~ 10^3 and 10^4 Hz, and a high frequency dispersion, above ~10^5 Hz. As the temperature increases, the data at lower frequencies show a curvature to lower conductivity values and the high-frequency dispersion shifts out of the frequency window.

Fig. A3-8 shows a linear Arrhenius response with activation energy of R_2, 0.79(2) eV, which is higher than that of bulk R_1, 0.62(1) eV, for $Li_2CoP_2O_7$ with Pt-sputtered electrode. The total conductivity, $(R_1 + R_2)^{-1}$, is limited by large R_2 resistances.

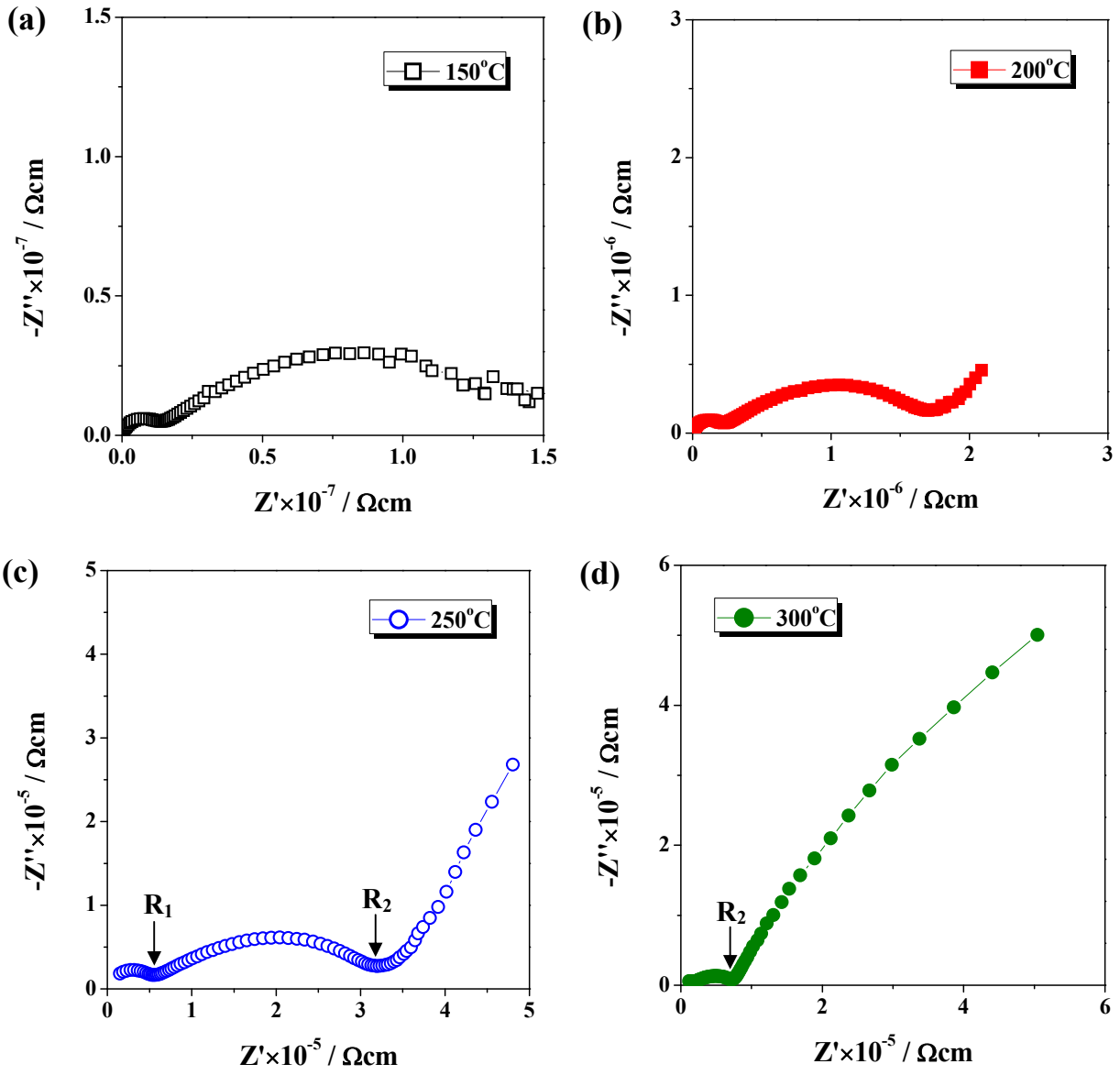

Figure A3-6 $Li_2CoP_2O_7$: Impedance complex plane plots, Z*, at (a) 150°C to (f) 400°C in N_2.

(continued on next page)

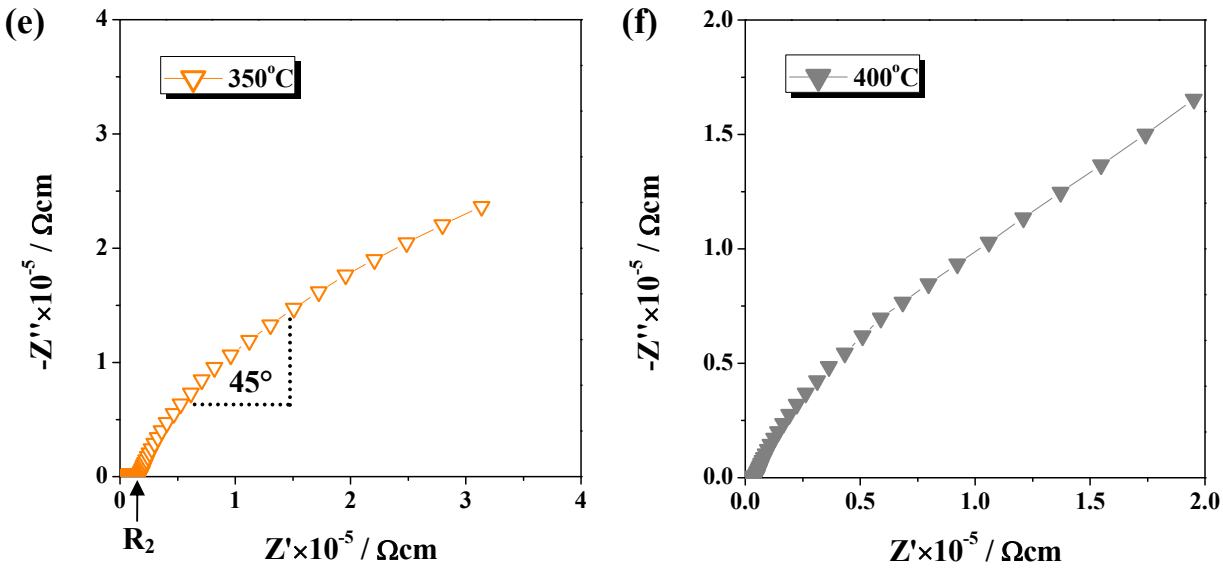

Figure A3-6 *(continued)*

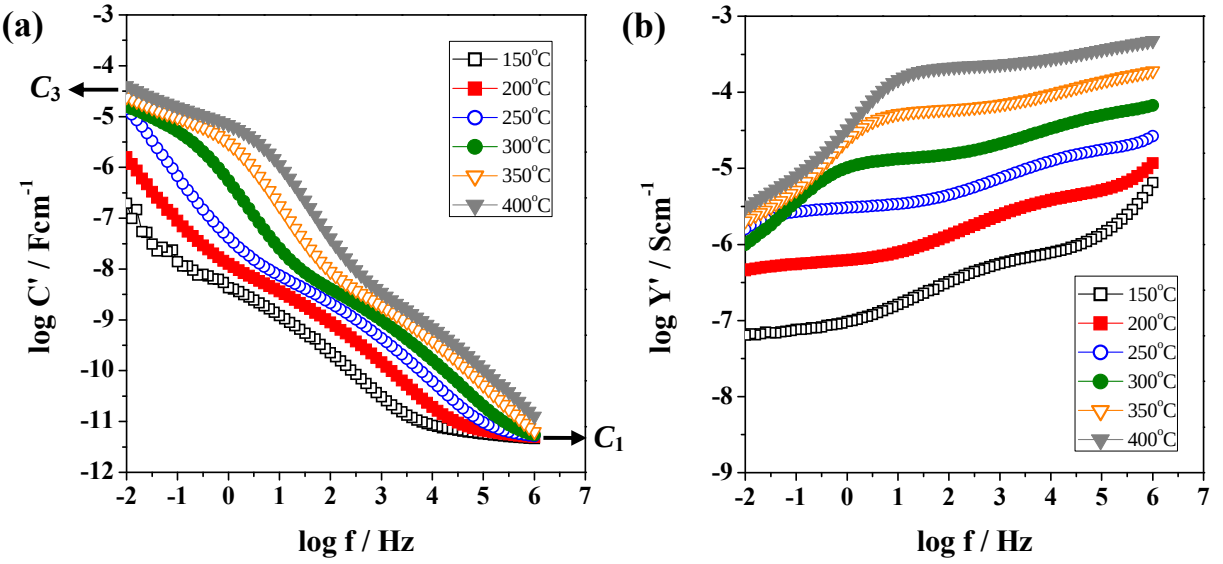

Figure A3-7 $Li_2CoP_2O_7$: (a) spectroscopic plots of capacitance, C', (b) spectroscopic plots of admittance, Y', at different temperatures of 150°C to 400°C.

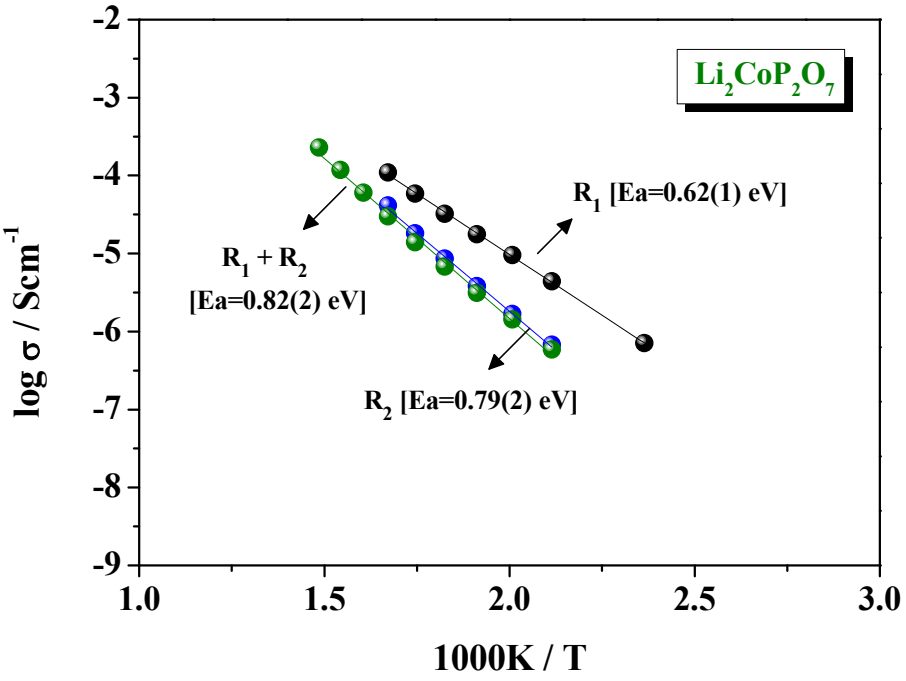

Figure A3-8 Arrhenius plots of R_1^{-1}, R_2^{-1} and total conductivity for $Li_2CoP_2O_7$.

Fig. A3-9 (a, b) shows the high temperature impedance data at 400°C in N_2 with various *dc*-bias of 0–3 V. As the bias was increased from 0V to 3V, R_1 and R_2 showed no difference, but the sloped tail at low-frequencies is getting much smaller. In addition, an increased electrode capacitance **(c)** at low frequencies is found on increasing the *dc*-bias from 0V to 2V, but with a slightly decrease between 2V to 3V bias. The high-frequency responses of capacitance **(c)** and admittance **(d)** do not change with the applied *dc*-bias, but an increased conductivity at low frequencies is obtained because of higher *dc*-bias of above 1V, see arrowed.

Fig. A3-10 shows the time-dependent impedance data after removal of 3V bias at 400°C in N_2. On removal of the *dc* bias, the angle of the low-frequency tail with the Z' axis increases with time and the resistance of R_2 has not changed, **(a)** and **(b)**. After 18 hours, the values of capacitance **(c)** and admittance **(d)** at high frequencies are still the same as the original ones. However, an increased response for C' and Y' are found at frequency less than 5 Hz.

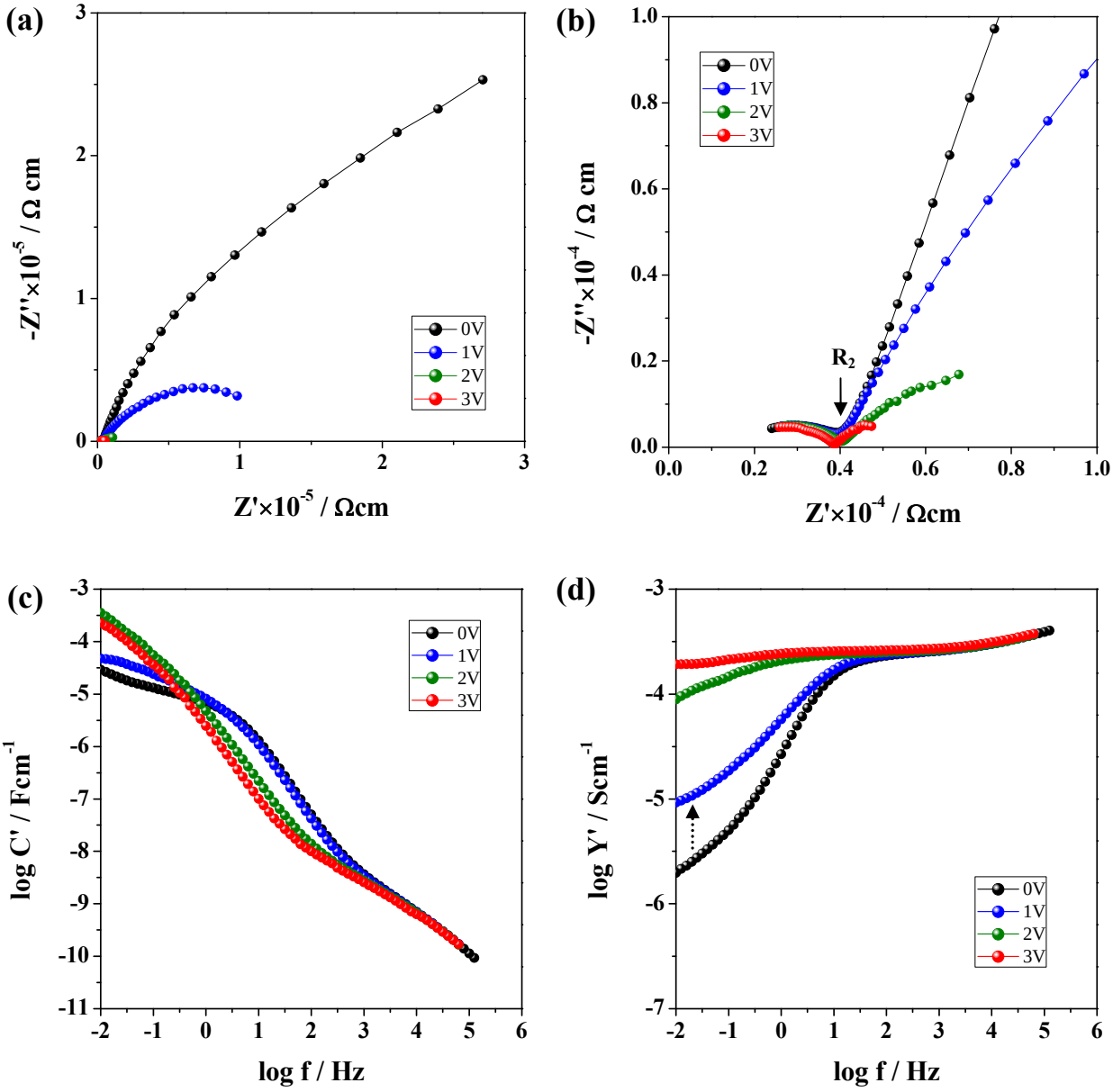

Figure A3-9 (a, b) Impedance complex plane plots, Z*; (c) spectroscopic plots of capacitance, C'; (d) spectroscopic plots of admittance, Y', at a measuring temperature of 400°C with different *dc* bias of 0–3V in N_2.

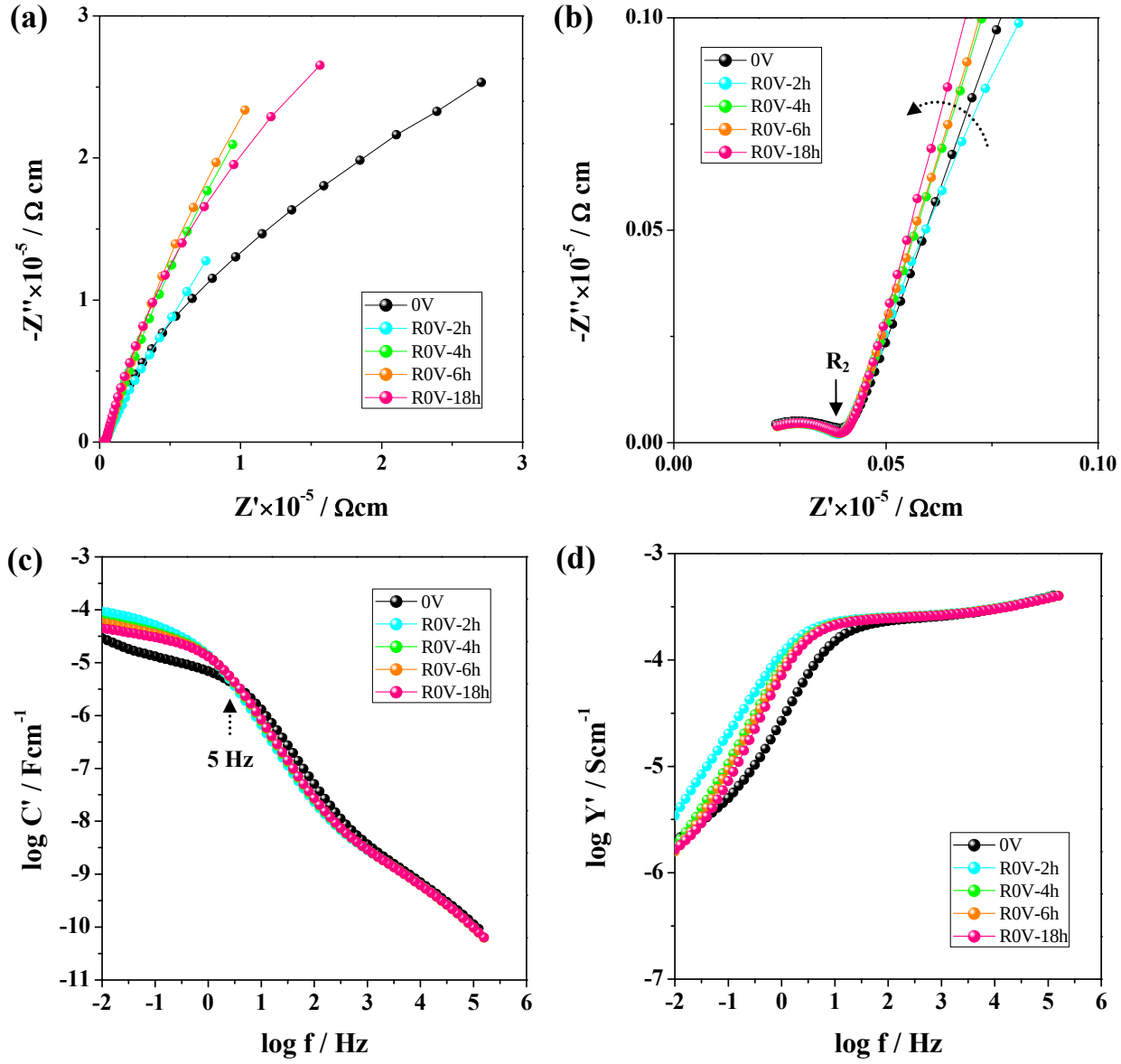

Figure A3-10 Impedance data with time after removal of 3V bias at 400°C in N_2.

Micrographs of the surface of Pt-sputtered $Li_2CoP_2O_7$, after applying 3V bias at 400°C in N_2, are shown in **Fig. A3-11**. The electrode color on the negative side became dark probably due to electrode decomposition as a result of voltage effect. Higher temperature impedance data in N_2 and Air, **Fig. A3-12**, show the R_1, R_2 and electrode responses without a *dc*-bias do not change a lot with different atmospheres. Only a tiny increased conductivity **(c)** is observed in air at low frequencies.

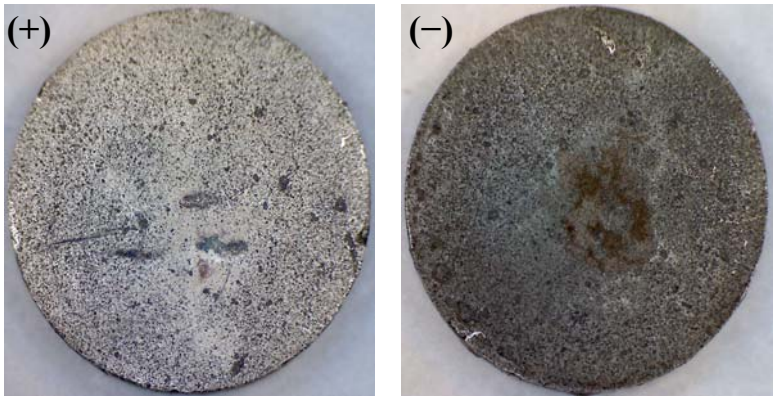

Figure A3-11 Positive (+) and negative (−) surface micrographs of Pt-sputtered $Li_2CoP_2O_7$ pellet after 3V *dc*-bias.

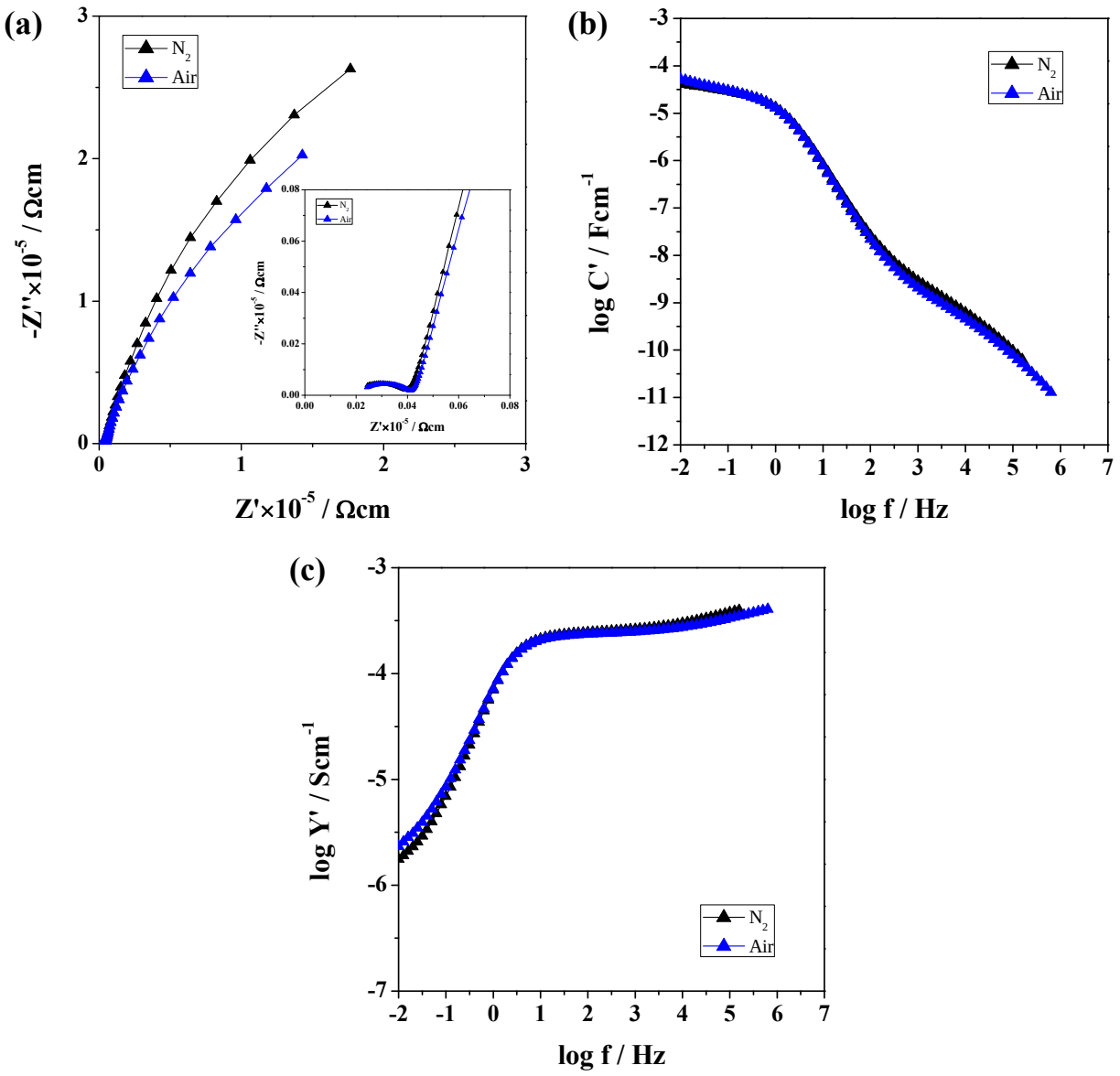

Figure A3-12 (a) Impedance complex plane plot, Z*; (b) spectroscopic plots of capacitance, C'; (c) spectroscopic plots of admittance, Y', for $Li_2CoP_2O_7$ in various atmospheres at 400°C without *dc*-bias.

(IV) $Li_2Fe_{1/3}Mn_{1/3}Co_{1/3}P_2O_7$

Impedance complex plane, Z* plots, for $Li_2Fe_{1/3}Mn_{1/3}Co_{1/3}P_2O_7$ with sputtered Pt electrodes at different temperatures from 150°C to 400°C in N_2 are shown in **Fig. A3-13**. Two distorted semicircles and low frequency dispersions at low temperature are observed, see **(a, b)**. At higher temperature of 250°C, Z* plot shows a high-frequency arc of bulk resistance (R_1), an intermediate-frequency arc of resistance (R_2), and a large low-frequency electrode spike, see **(c)**. At temperatures above ~300 °C, the length and slope of the electrode spike at lower frequencies increase, as shown in **(d, e, f)**.

The capacitance, C', data as a function of frequency at different temperatures, show an associated plateau at high frequency of ~7 $pFcm^{-1}$ (arrowed), see **Fig. A3-14 (a)**. A dispersion at lower frequency is found at 150°C. The capacitance of R_2 response at lower frequency can be resolved at temperatures of ≥ 250°C. Electrical double layer associated with a capacitance of ~5×10^{-5} Fcm^{-1} was verified at higher temperatures up to 300°C.

Conductivity, Y', data as a function of frequency are shown in **Fig. A3-14 (b)**. At the highest temperature, Y' spectra do not show a frequency-independent *dc* conductivity plateau but with increasing temperature above 300°C, the low frequency data show a rapid curvature to lower conductivity values. This is attributed to the ionic blocking character and the electrical double layer effect.

Fig. A3-15 shows a linear Arrhenius response with activation energy of R_2, 0.84(3) eV, which is higher than that of bulk R_1, 0.60(1) eV, for $Li_2Fe_{1/3}Mn_{1/3}Co_{1/3}P_2O_7$ with Pt-sputtered electrode. The total conductivity is limited by large R_2 resistances.

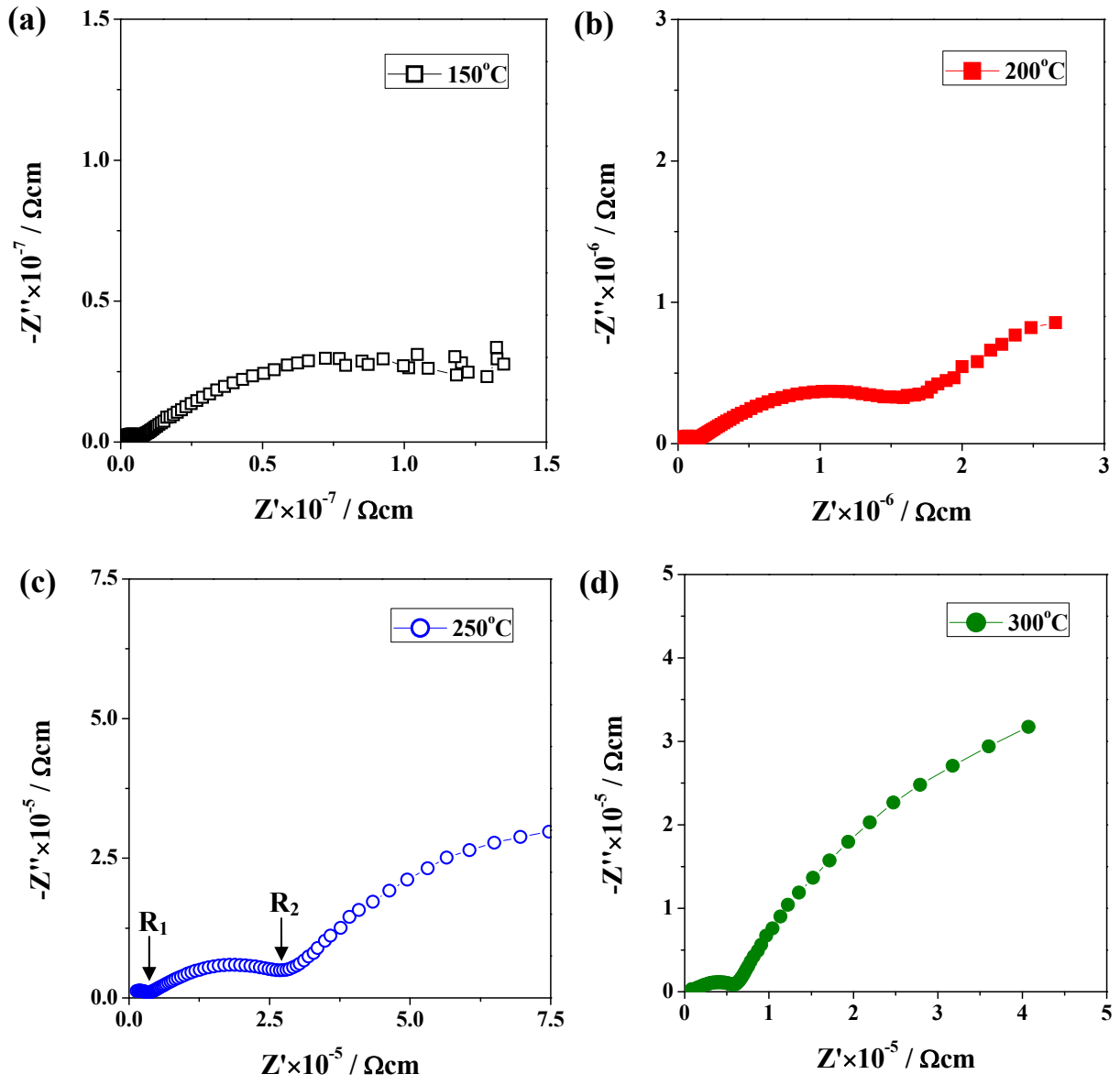

Figure A3-13 $Li_2Fe_{1/3}Mn_{1/3}Co_{1/3}P_2O_7$: Impedance complex plane plots, Z*, at (a) 150°C to (f) 400°C in N_2.

(continued on next page)

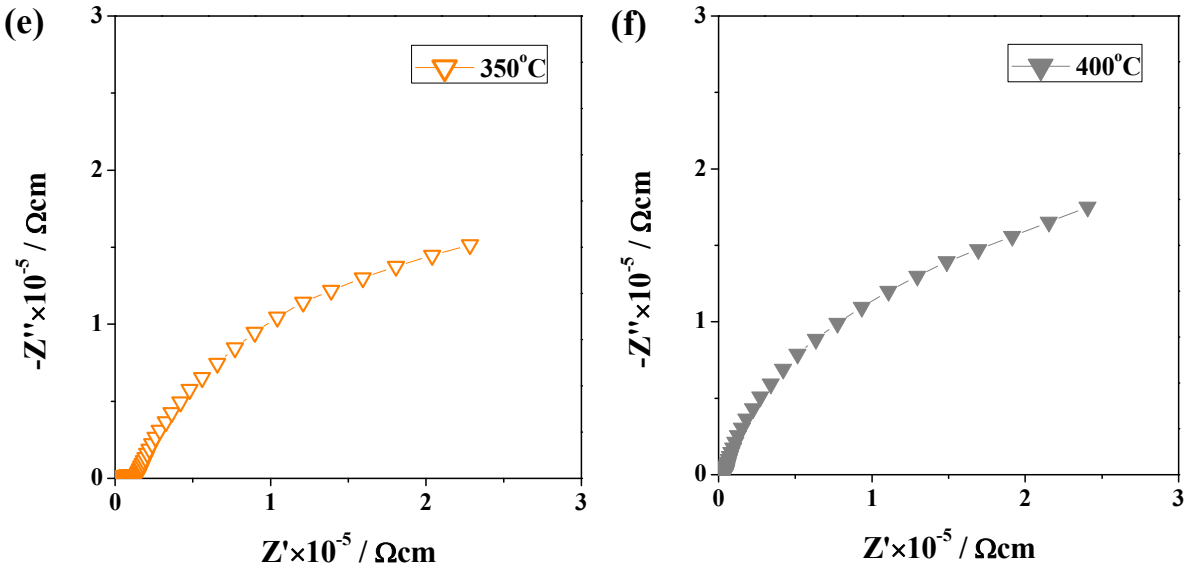

Figure A3-13 *(continued)*

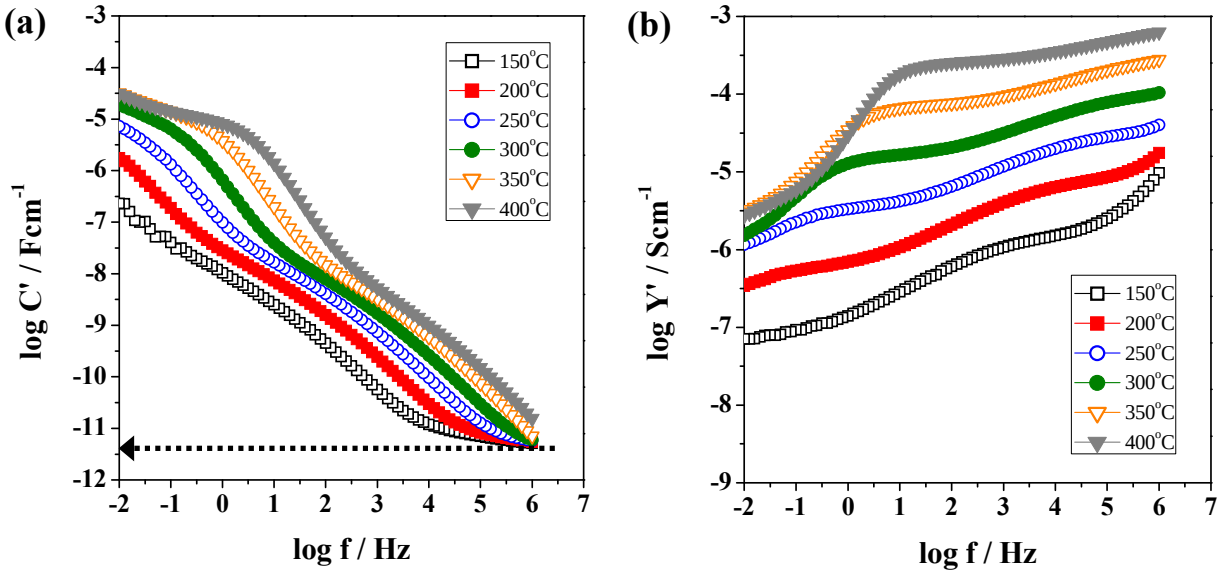

Figure A3-14 $Li_2Fe_{1/3}Mn_{1/3}Co_{1/3}P_2O_7$: (a) spectroscopic plots of capacitance, C', (b) spectroscopic plots of admittance, Y', at different temperatures of 150°C to 400°C.

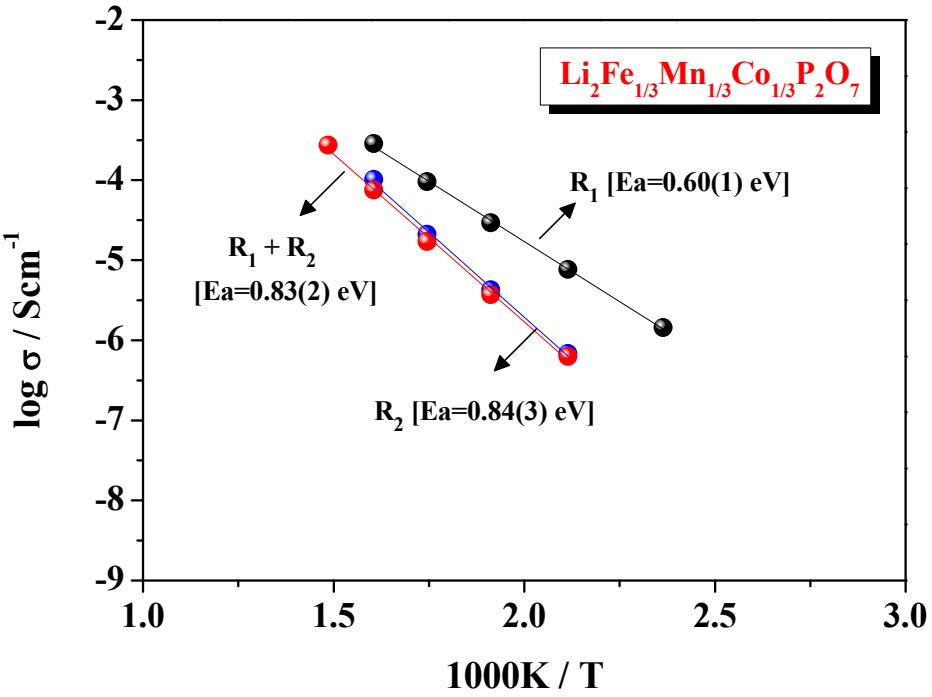

Figure A3-15 Arrhenius plots of the R_1^{-1}, R_2^{-1} and total conductivity for $Li_2Fe_{1/3}Mn_{1/3}Co_{1/3}P_2O_7$.

Fig. A3-16 (a) shows the impedance data at 400°C in N_2 with different *dc* bias of 0–3 V. The electrode slope decreased with applying *dc*-bias from 0V to 3V, and specifically, an inclined arc is observed at 3V **(b)**. An increased electrode capacitance **(c)** at low frequencies is found applying *dc*-bias from 0V to 2V, but slightly decreased from 2V to 3V. The responses of C' **(c)** and Y' **(d)** of bulk and grain boundary do not change with the applied *dc*-bias, however, an increase in conductivity is observed attributed to higher *dc*-bias of above 1V.

Fig. A3-17 (a) shows the time-dependent impedance data after removal of 3V bias at 400°C in N_2. On removal of the *dc* bias, after 10 hours, the resistance of R_2 **(b)** increased to higher value, and the responses of capacitance **(c)** and admittance **(d)** of R_1 + R_2 (arrowed) at high frequencies slightly decreased. In addition, increased values for C' and Y' at frequency less than 1 Hz are found.

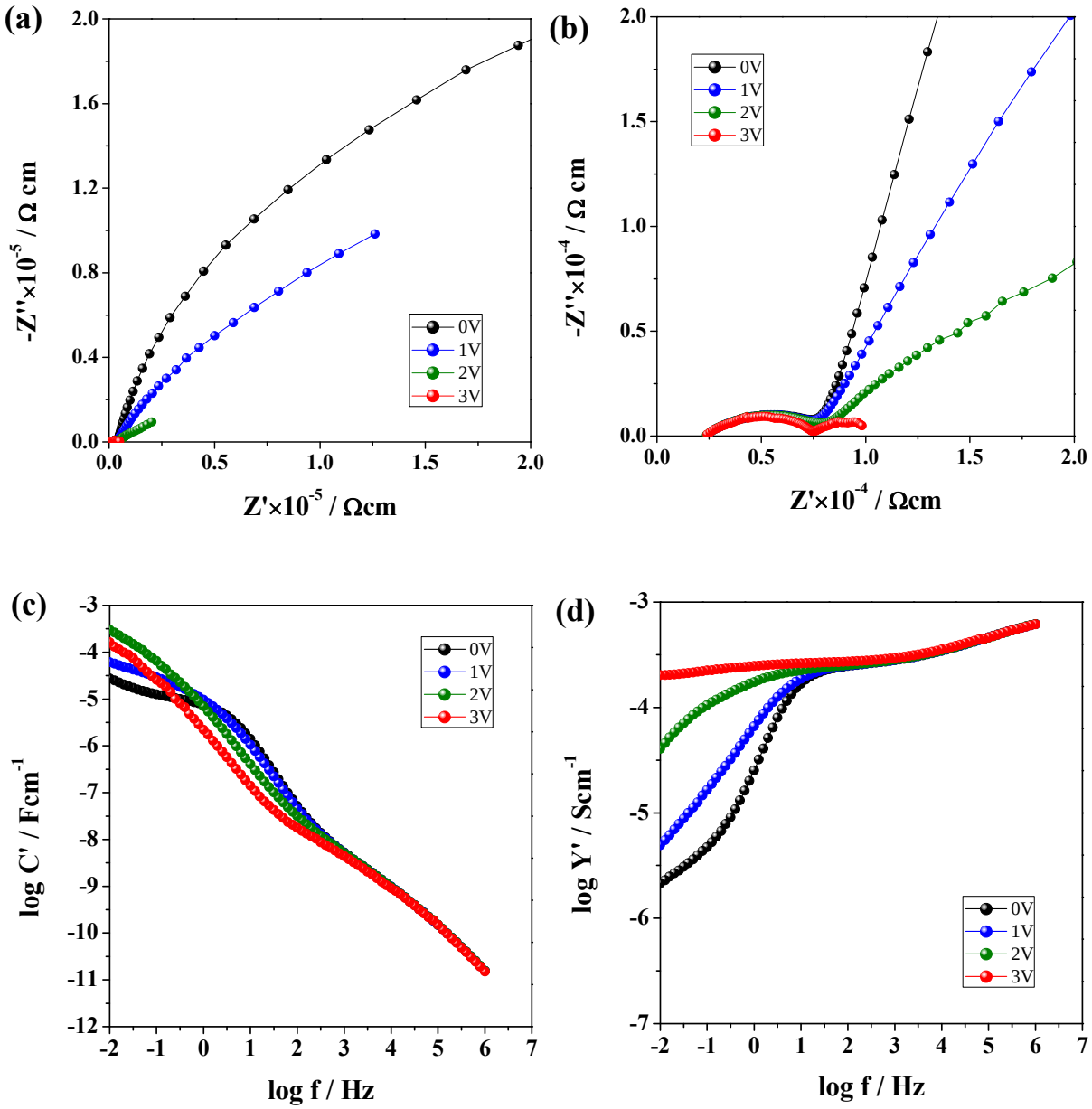

Figure A3-16 (a, b) Impedance complex plane plots, Z*; (c) spectroscopic plots of capacitance, C'; (d) spectroscopic plots of admittance, Y', at a measuring temperature of 400°C with different *dc* bias of 0–3V in N_2.

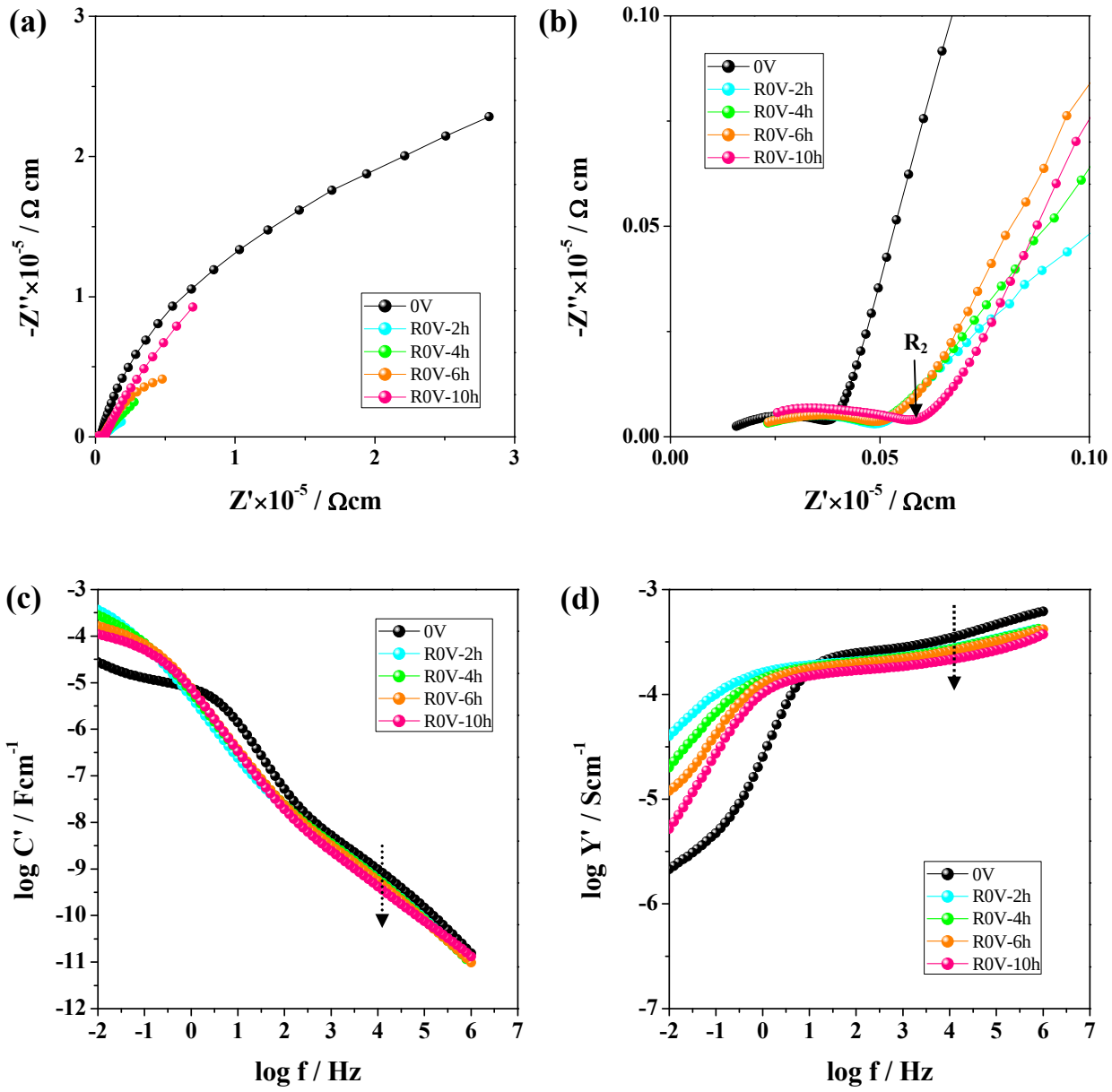

Figure A3-17 Impedance data with time after removal of 3V bias at 400°C in N_2.

Micrographs of surface of Pt-sputtered $Li_2Fe_{1/3}Mn_{1/3}Co_{1/3}P_2O_7$, after applying 3V bias at 400°C in N_2, are shown in **Fig. A3-18**. The electrode on negative side presents a dark color and a discrete contact on surface probably owing to electrode decomposition as a result of voltage applied. Higher temperature impedance data, at 400°C, in N_2 and Air, **Fig. A3-19 (a)**, show the bulk, grain boundary and electrode response without a *dc*-bias do not change a lot with different atmospheres. However, a slightly decreased capacitance **(b)** at intermediate frequencies is observed and a tiny decreased and increased conductivity **(c)** are found at higher and lower frequencies, respectively.

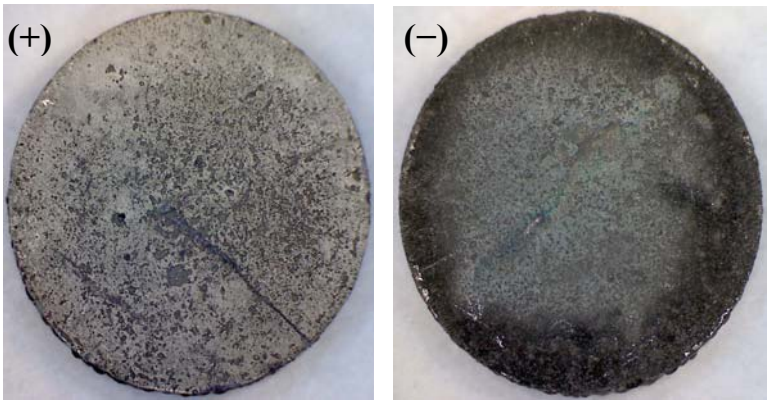

Figure A3-18 Positive (+) and negative (−) side micrographs of Pt-sputtered $Li_2Fe_{1/3}Mn_{1/3}Co_{1/3}P_2O_7$ after 3V *dc*-bias.

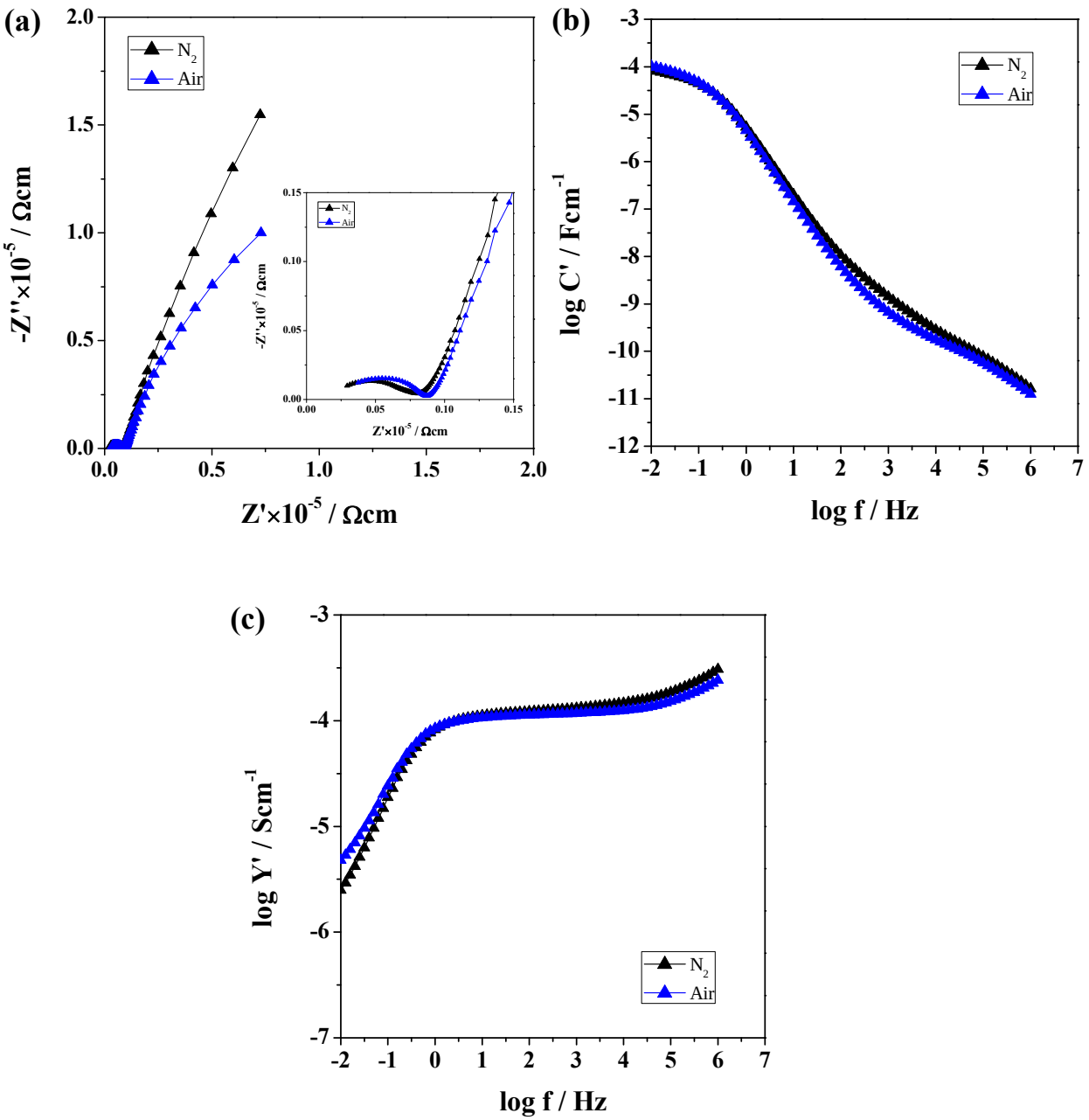

Figure A3-19 (a) Impedance complex plane plot, Z*; (b) spectroscopic plots of capacitance, C'; (c) spectroscopic plots of admittance, Y', for $Li_2Fe_{1/3}Mn_{1/3}Co_{1/3}P_2O_7$ in various atmospheres at 400°C without *dc*-bias.

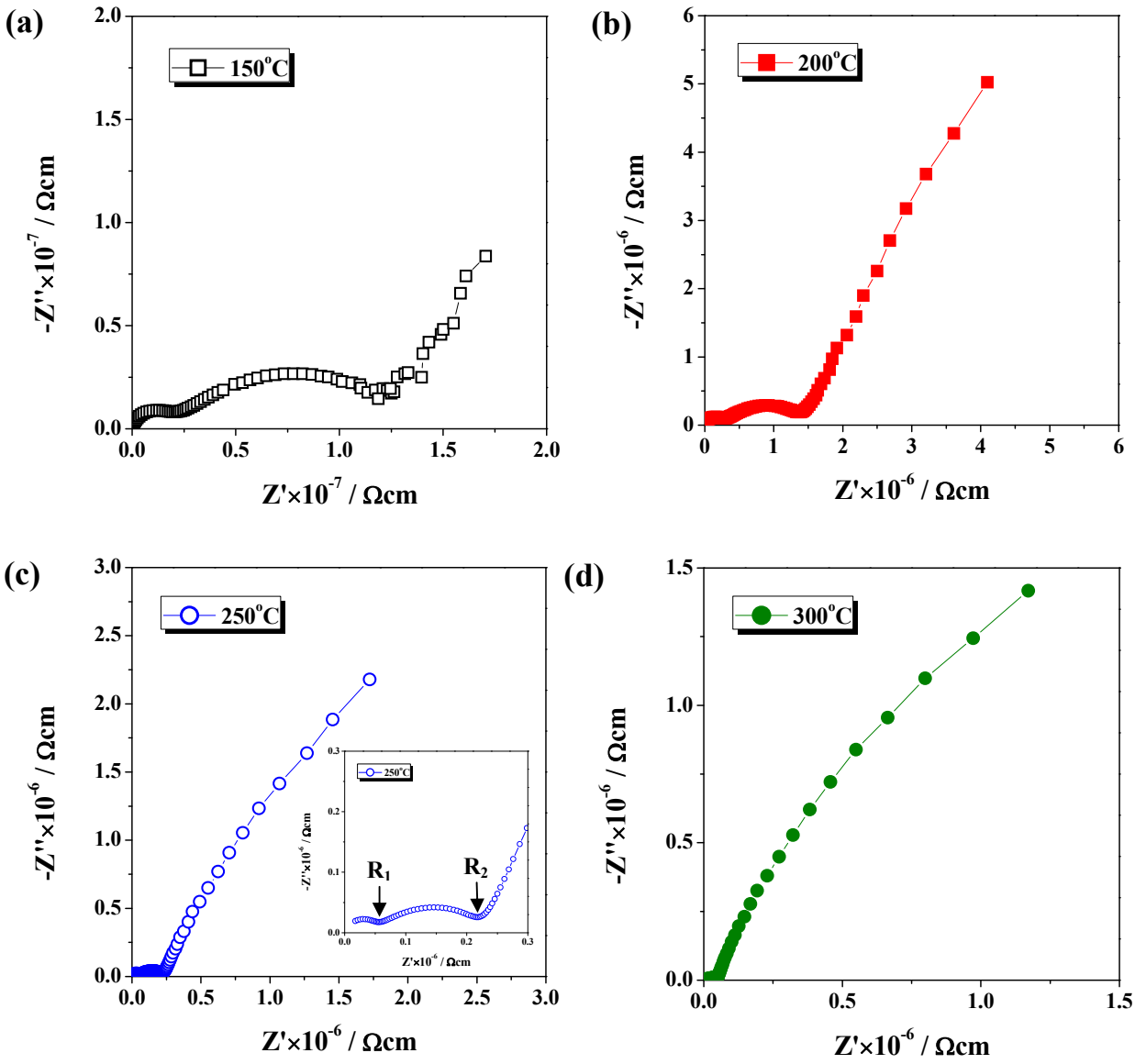

Figure A3-20 $Li_2CoP_2O_7$ (Au electrodes): Impedance complex plane plots, Z*, at (a) 150°C to (d) 300°C in N_2.

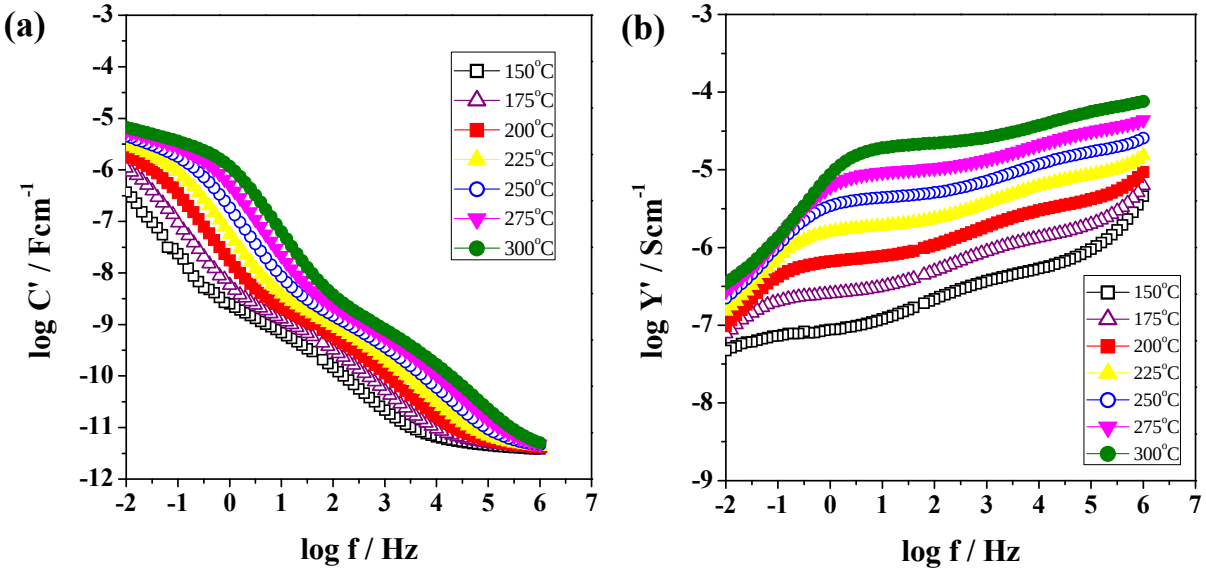

Figure A3-21 $Li_2CoP_2O_7$ (Au electrodes): (a) spectroscopic plots of capacitance, C', (b) spectroscopic plots of admittance, Y', at different temperatures of 150°C to 300°C.

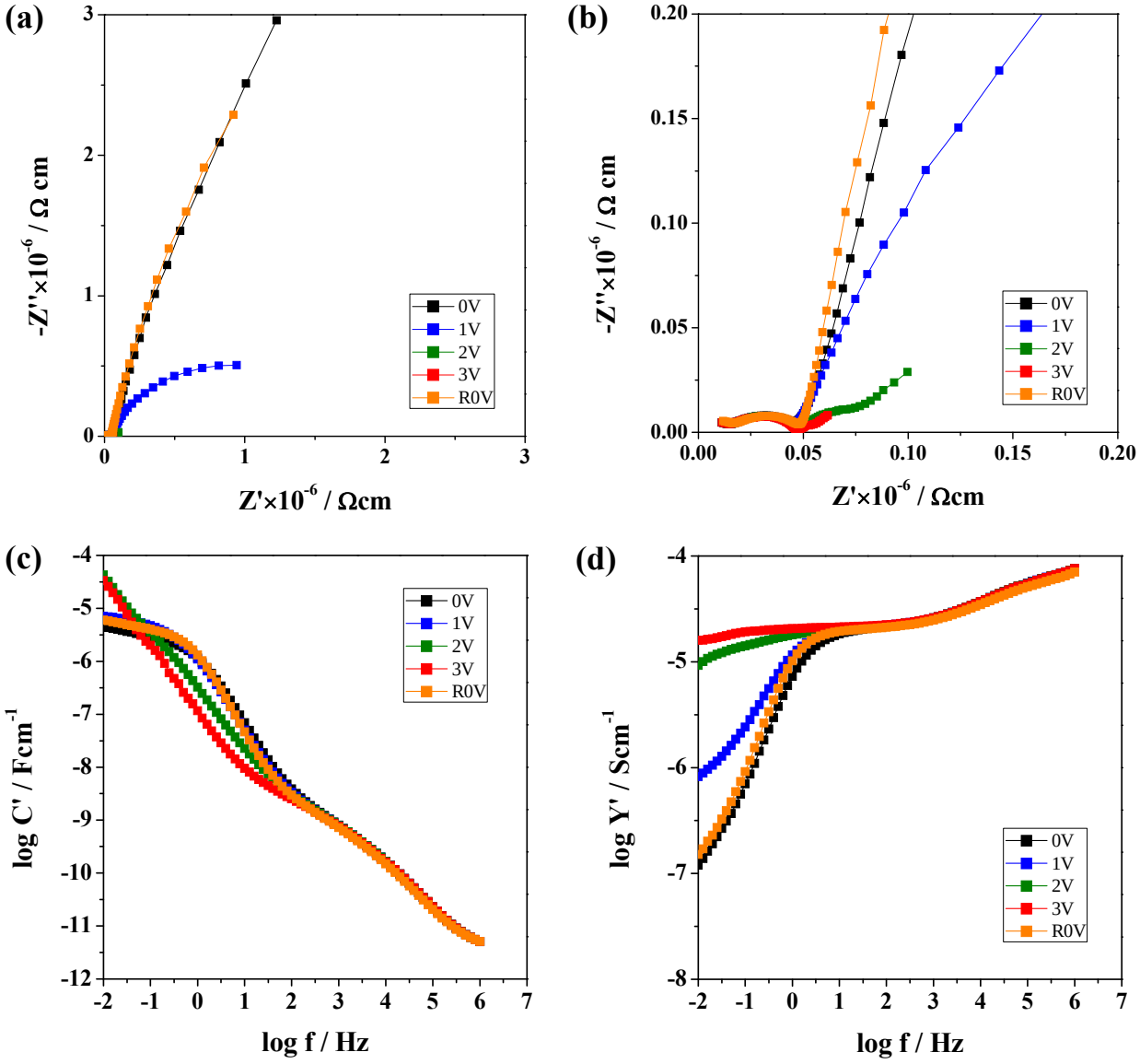

Figure A3-22 $Li_2CoP_2O_7$ (Au electrodes): (a, b) Impedance complex plane plots, Z*; (c) spectroscopic plots of capacitance, C'; (d) spectroscopic plots of admittance, Y', at a measuring temperature of 300°C with different *dc* bias of 0–3 V in N_2.

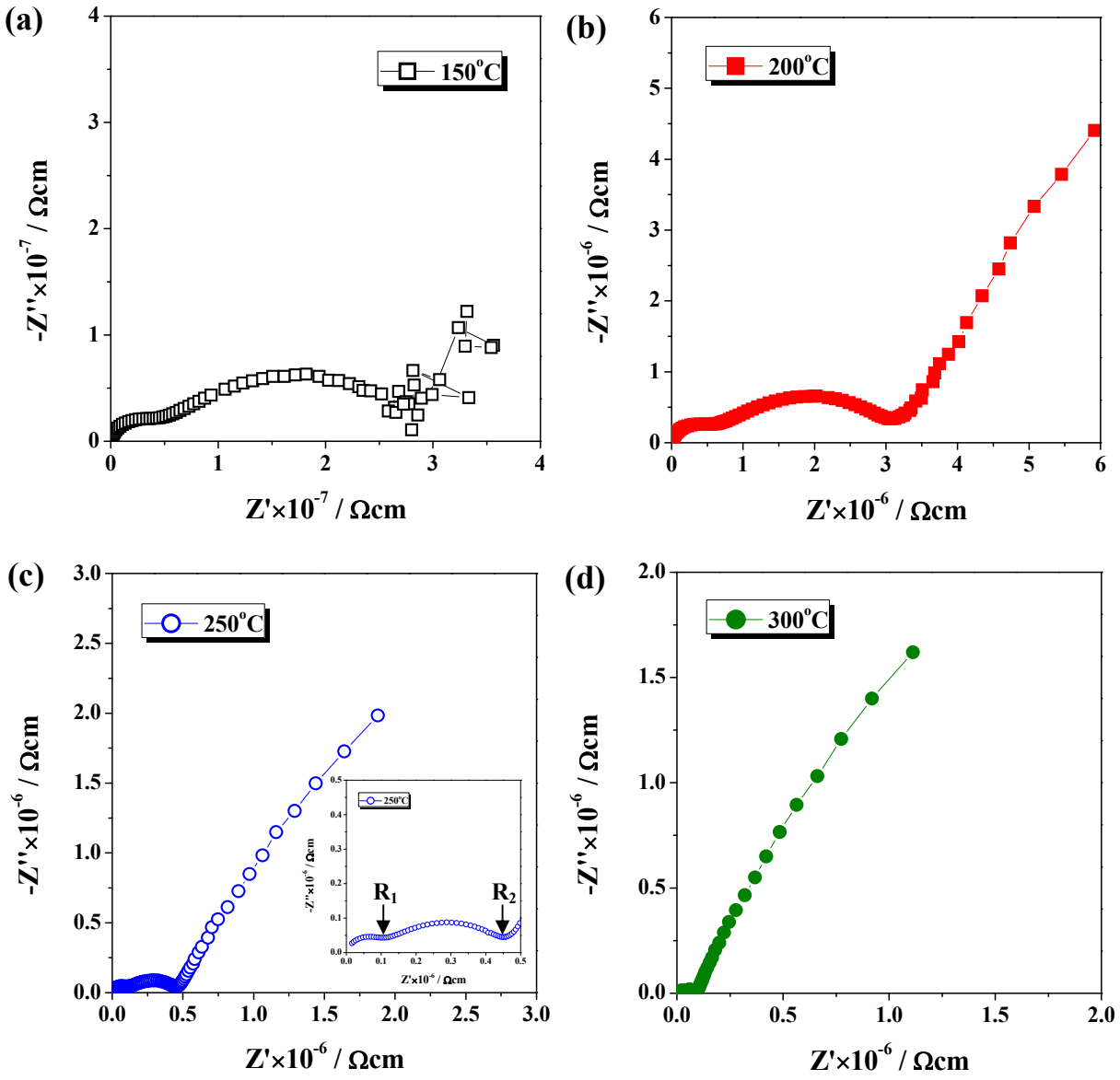

Figure A3-23 $Li_2Fe_{1/3}Mn_{1/3}Co_{1/3}P_2O_7$ (Au electrodes): Impedance complex plane plots Z*, at (a) 150°C to (d) 300°C in N_2.

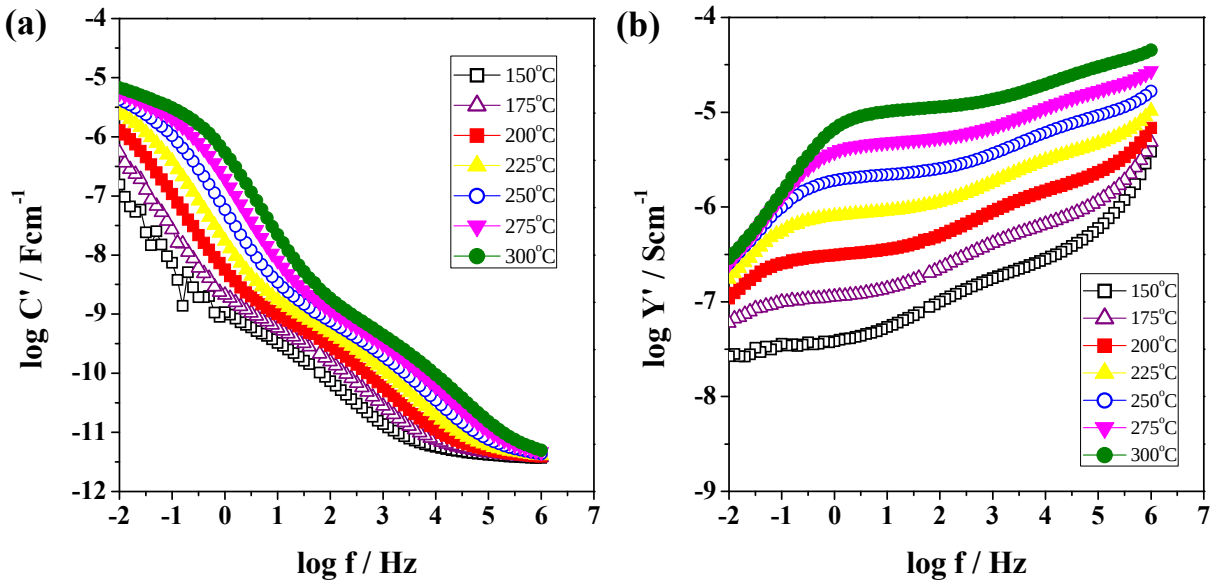

Figure A3-24 $Li_2Fe_{1/3}Mn_{1/3}Co_{1/3}P_2O_7$ (Au electrodes): (a) spectroscopic plots of capacitance, C', (b) spectroscopic plots of admittance, Y', at different temperatures of 150°C to 300°C.

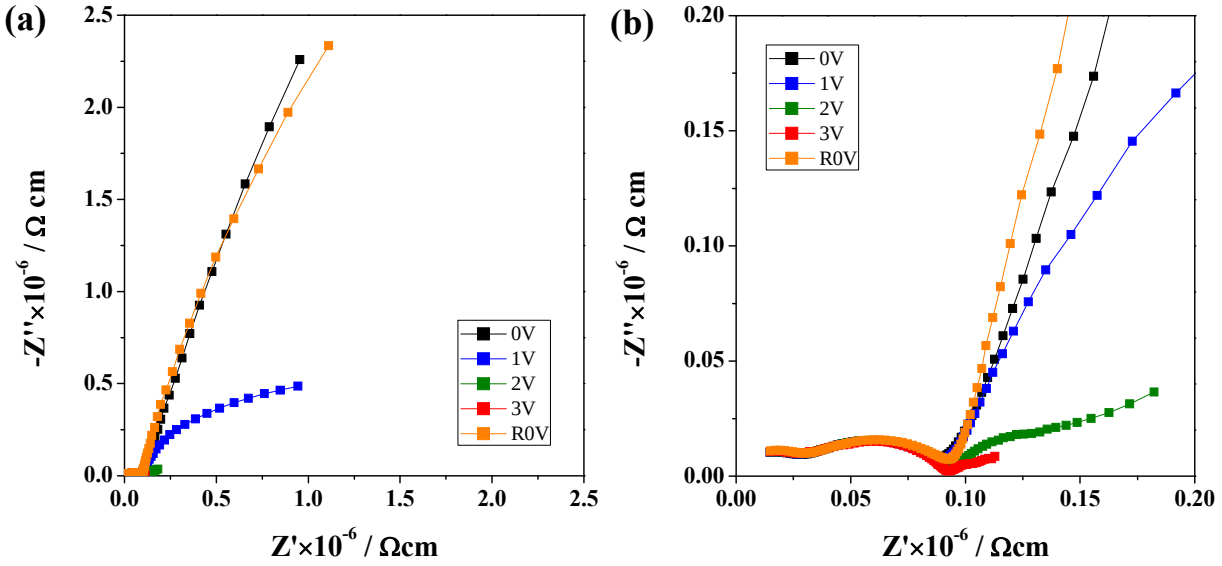

Figure A3-25 $Li_2Fe_{1/3}Mn_{1/3}Co_{1/3}P_2O_7$: (a, b) Impedance complex plane plots, Z*; (c) spectroscopic plots of capacitance, C'; (d) spectroscopic plots of admittance, Y', at a measuring temperature of 300°C with different *dc* bias of 0–3 V in N_2.

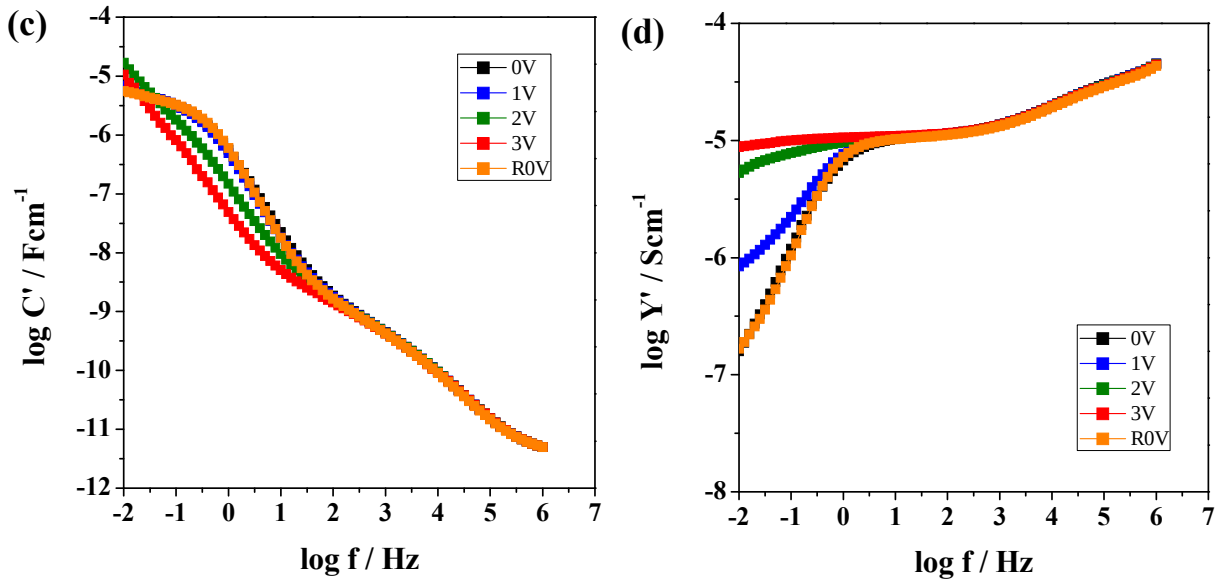

Figure A3-25 ***(continued)***

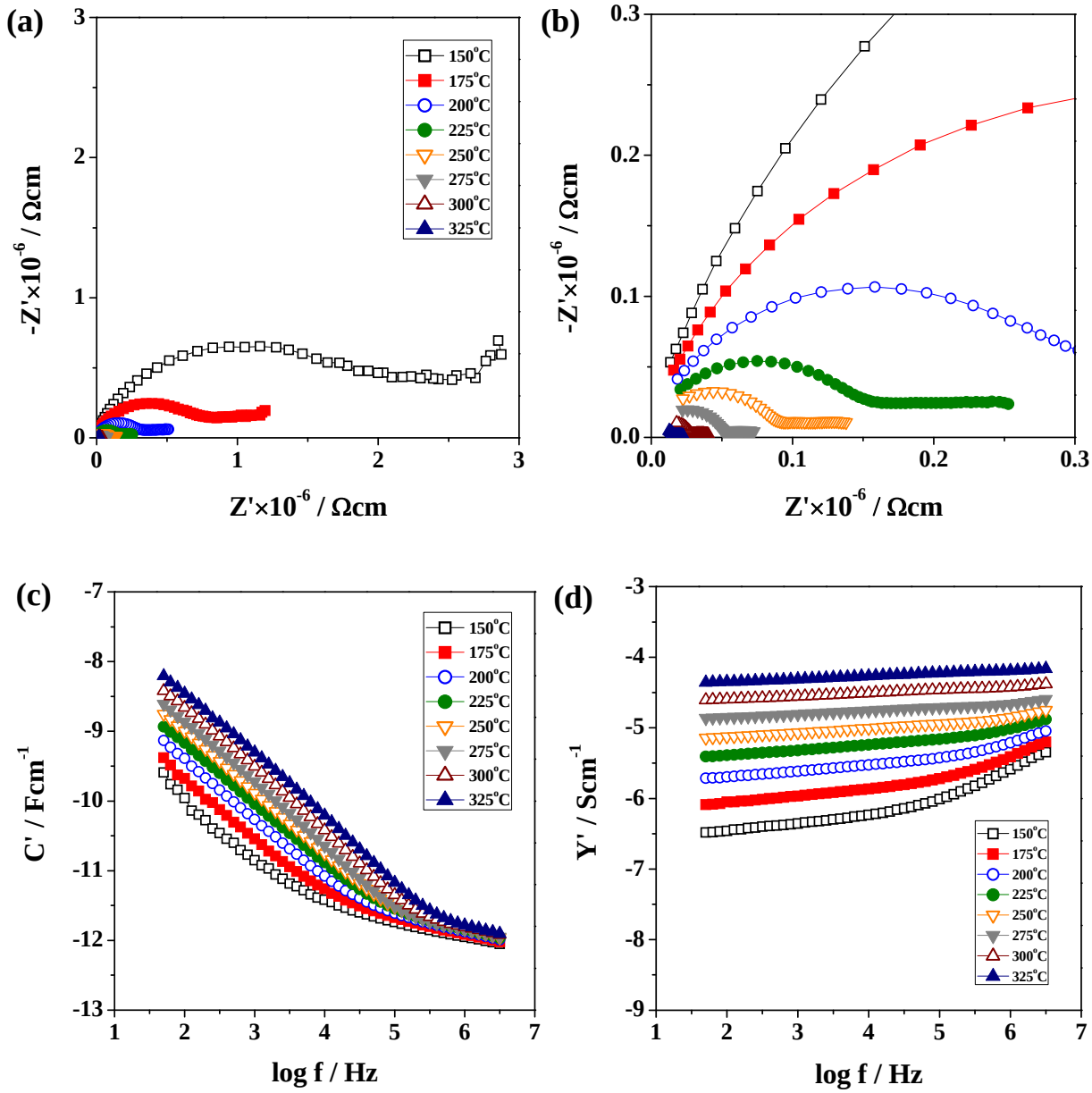

Figure A4-1 $Li_{1.85}Nb_{0.05}Fe_{0.95}P_2O_7$: Impedance complex plane plots, Z*, at (a) 150 to 325°C in air, (b) close-up image of (a); (c) spectroscopic plots of capacitance, C', and (d) spectroscopic plots of admittance, Y', in air.

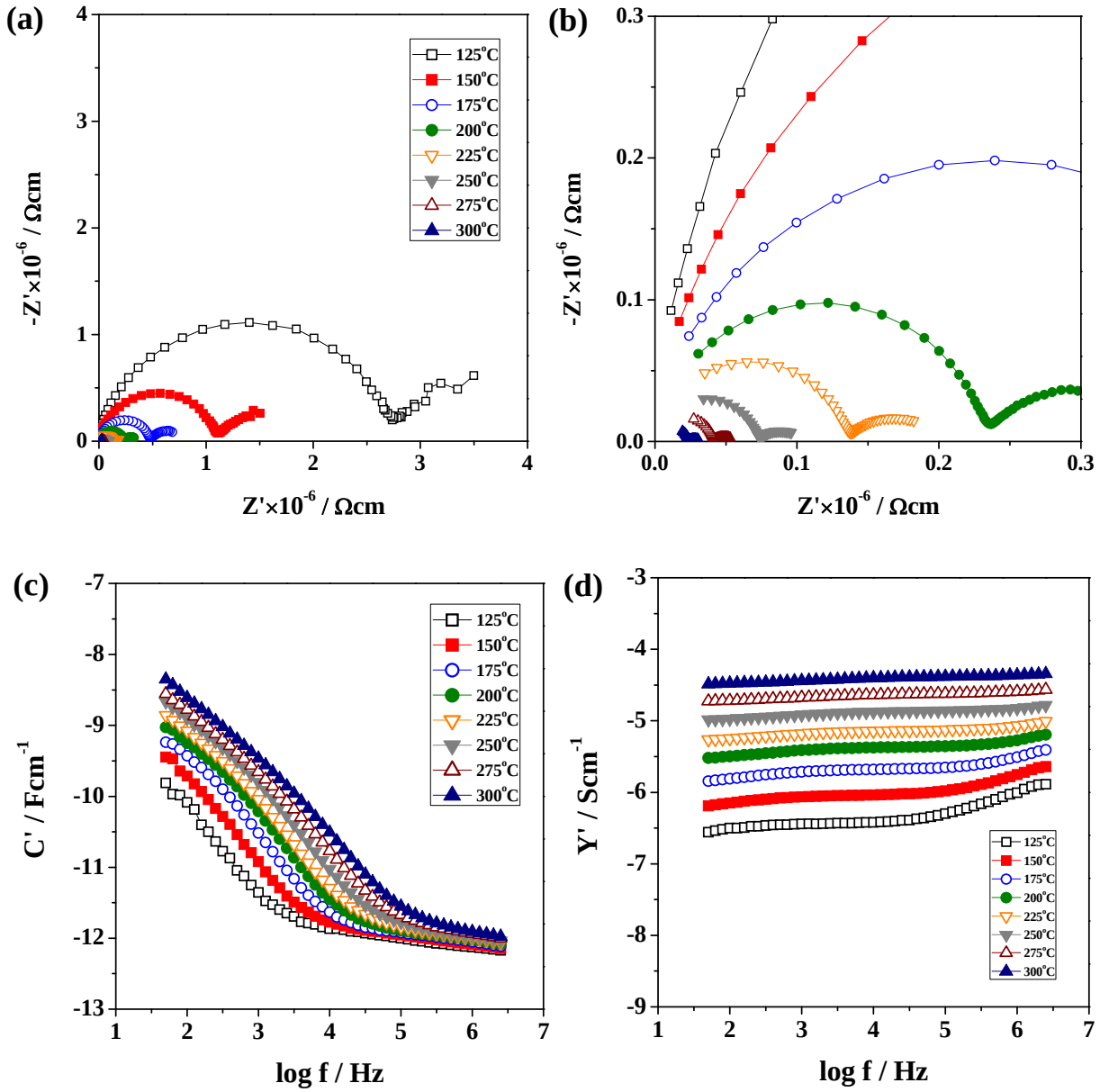

Figure A4-2 $Li_{1.95}Nb_{0.05}Fe_{0.9}P_2O_7$: Impedance complex plane plots, Z*, at (a) 125 to 300°C in air, (b) close-up image of (a); (c) spectroscopic plots of capacitance, C', and (d) spectroscopic plots of admittance, Y', in air.

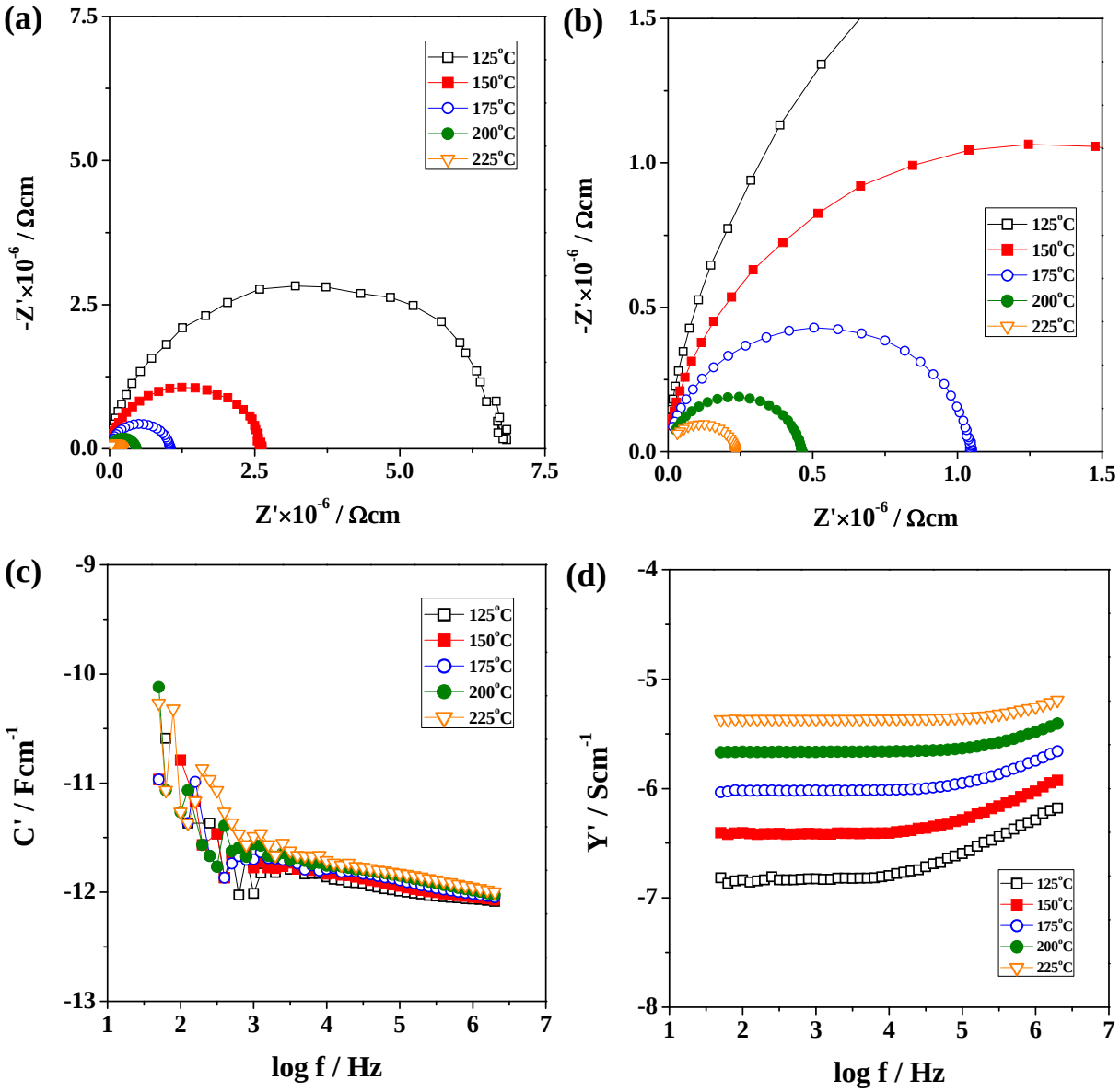

Figure A5-1 $Li_{2.05}FeP_2O_{6.95}N_{0.05}$: Impedance complex plane plots, Z*, at (a) 125 to 225°C in air, (b) close-up image of (a); (c) spectroscopic plots of capacitance, C', and (d) spectroscopic plots of admittance, Y'.

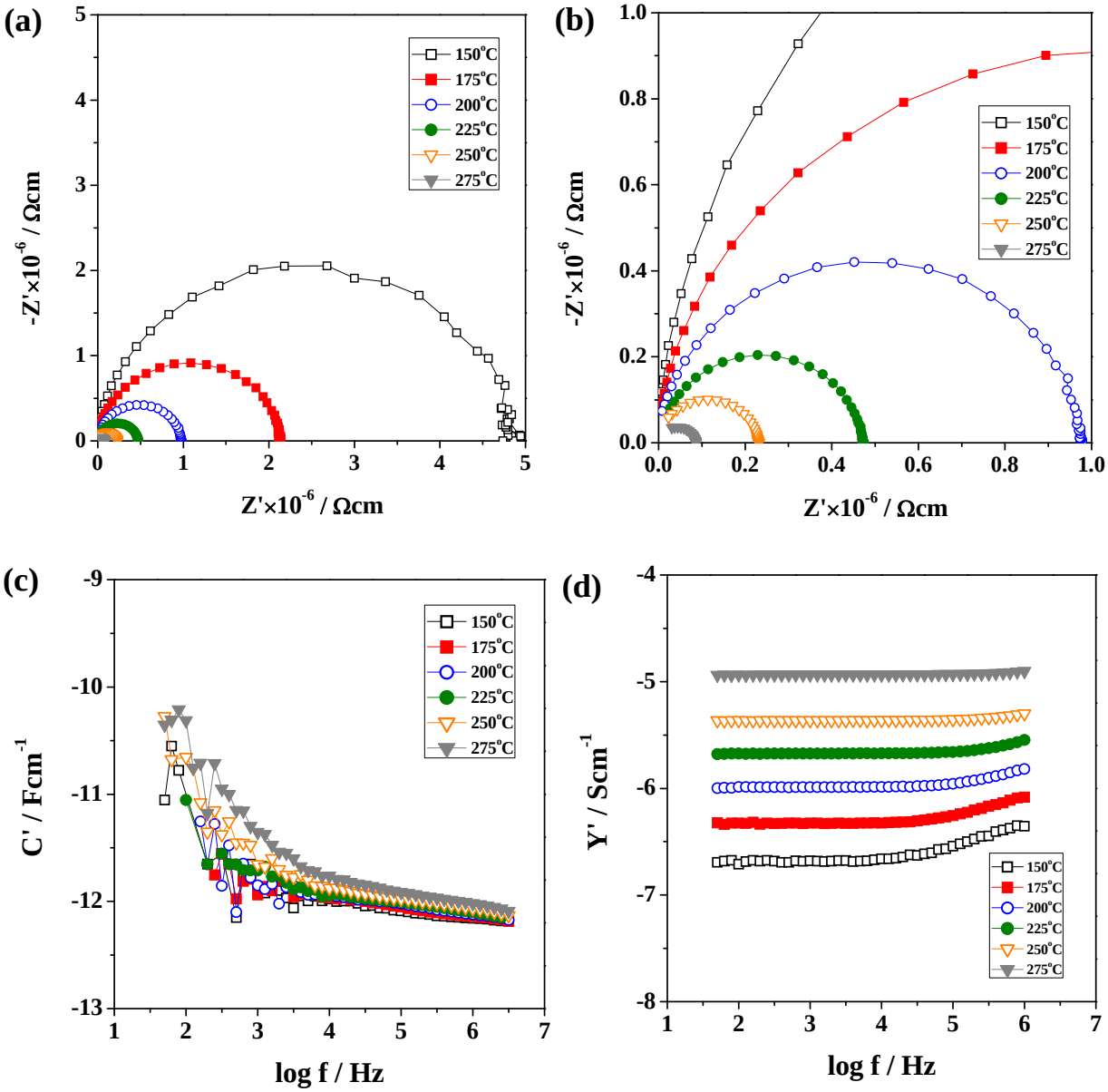

Figure A5-2 $Li_{2.1}FeP_2O_{6.9}N_{0.1}$: Impedance complex plane plots, Z*, at (a) 150 to 275°C in air, (b) close-up image of (a); (c) spectroscopic plots of capacitance, C', and (d) spectroscopic plots of admittance, Y'.

Table A6-1 Summary of the indexed XRD reflections of $LiZn_{1.5}P_2O_7$ using Cu radiation (PSD) in the 2θ range of ~ 10–40°.

No.	2θ [obs] (°)	H K L	2θ [calc] (°)	△2θ (°)	Int.	d [obs] (Å)	d [calc] (Å)	Int. [calc]
1	10.991	0 0 2	10.974	0.0176	5.0	8.0432	8.0561	5.944
2	13.434	0 2 0	13.422	0.0114	3.5	6.5859	6.5915	4.023
3	14.512	0 2 1	14.507	0.0040	9.4	6.0990	6.1007	12.287
4	17.151	1 0 0	17.126	0.0252	8.6	5.1659	5.1734	7.300
5	17.376	0 2 2	17.369	0.0073	13.6	5.0994	5.1015	14.820
6	18.419	1 1 0	18.408	0.0109	2.0	4.8130	4.8159	1.813
7	20.382	1 0 2	20.385	-0.0029	19.1	4.3537	4.3531	20.886
8	21.340	0 2 3	21.323	0.0173	13.7	4.1603	4.1636	14.994
9	21.826	1 2 0	21.821	0.0041	100.0	4.0689	4.0696	100.000
10	22.523	1 2 1	22.516	0.0071	15.1	3.9445	3.9457	14.754
11	24.495	1 2 2	24.486	0.0089	2.6	3.6312	3.6325	2.214
12	24.818	1 1 3	24.812	0.0060	65.2	3.5847	3.5855	70.842
13	26.591	1 3 0	26.594	-0.0028	0.2	3.3496	3.3492	0.250
14	27.174	1 3 1	27.173	0.0017	12.3	3.2789	3.2791	11.986
15	27.478	1 2 3	27.476	0.0025	20.9	3.2433	3.2436	19.112
16	28.054	1 0 4	28.052	0.0021	3.4	3.1780	3.1783	2.791
17	28.870	1 1 4	28.873	-0.0033	59.5	3.0901	3.0897	49.977
18	29.248	0 4 2	29.254	-0.0059	8.2	3.0510	3.0504	9.436
19	30.848	0 2 5	30.862	-0.0139	3.3	2.8963	2.8950	3.247
20	31.234	1 2 4	31.218	0.0166	1.2	2.8614	2.8629	1.236
21	31.825	0 4 3	31.831	-0.0062	30.9	2.8096	2.8090	34.863
22	32.176	1 4 0	32.177	-0.0009	7.5	2.7797	2.7796	7.078
23	32.662	1 4 1	32.666	-0.0040	3.1	2.7395	2.7392	3.216
24	33.374	0 0 6	33.339	0.0345	2.3	2.6827	2.6854	1.752
25	34.086	1 4 2	34.094	-0.0075	22.5	2.6282	2.6276	25.051
26	34.634	2 0 0	34.650	-0.0161	1.9	2.5879	2.5867	1.732
27	35.143	0 4 4	35.154	-0.0112	4.7	2.5515	2.5507	6.055
28	35.785	2 1 1	35.783	0.0022	3.9	2.5072	2.5074	3.680
29	36.083	0 2 6	36.087	-0.0044	18.0	2.4872	2.4869	21.793
30	36.362	1 4 3	36.364	-0.0020	27.8	2.4687	2.4686	31.105
31	37.106	2 1 2	37.105	0.0005	5.1	2.4210	2.4210	6.434
32	37.703	1 0 6	37.712	-0.0087	6.2	2.3839	2.3834	8.077
33	38.286	1 5 0	38.284	0.0024	3.3	2.3490	2.3491	4.068
34	38.715	1 5 1	38.705	0.0105	0.8	2.3239	2.3245	0.893
35	39.217	2 1 3	39.225	-0.0080	24.4	2.2954	2.2949	24.078
36	40.194	1 2 6	40.201	-0.0074	3.2	2.2418	2.2414	3.851

Final 2θ window: 0.04, Symmetry: orthorhombic, a = 5.1734(4) Å; b = 13.1830(8) Å; c = 16.1122(12) Å; V = 1098.87(10) Å^3; Z = 4.

PDF card 04-017-1973: a = 5.1733(3) Å; b = 13.1797(7) Å; c = 16.1108(9) Å; V = 1098.48 Å^3

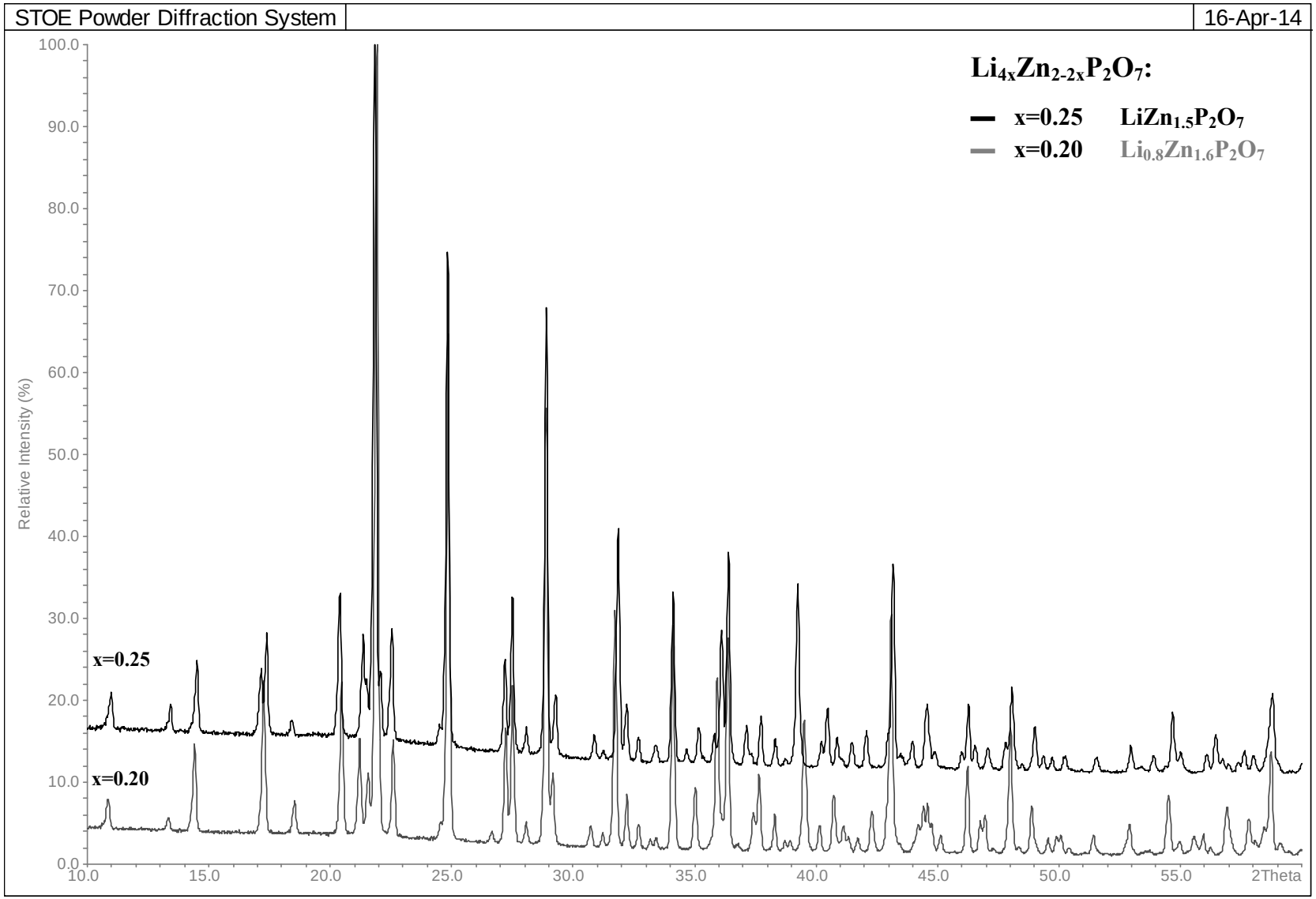

Figure A6-1 XRD patterns (Cu PSD) of $Li_{4x}Zn_{2-2x}P_2O_7$ (x=0.2 and 0.25).

Table A6-2 Summary of the indexed XRD reflections of room-temperature $Li_{2.4}Zn_{0.8}P_2O_7$ using Cu radiation (PSD) in the 2θ range of ~ 10–45°.

No.	2θ [obs] (°)	H K L	2θ [calc] (°)	△2θ (°)	Int.	d [obs] (Å)	d [calc] (Å)	Int. [calc]
1	12.617	0 1 1	12.623	-0.0058	3.8	7.0102	7.0070	10.61
2	13.148	0 2 0	13.153	-0.0059	7.2	6.7285	6.7255	13.41
3	17.040	0 2 1	17.030	0.0099	2.9	5.1994	5.2024	4.40
4	18.527	1 1 0	18.493	0.0348	1.7	4.7851	4.7940	0.30
5	20.415	1 0 1	20.467	-0.0520	34.4	4.3467	4.3357	20.02
6	21.497	1 1 1	21.516	-0.0191	19.4	4.1303	4.1267	13.81
7	21.779	1 2 0	21.769	0.0098	60.4	4.0776	4.0794	66.07
8	22.592	0 1 2	22.632	-0.0369	5.6	3.9325	3.9257	9.11
9	24.357	1 2 1	24.407	-0.0498	1.0	3.6515	3.6441	0.40
10	26.393	1 3 0	26.377	0.0168	11.8	3.3741	3.3762	13.61
11	28.692	0 4 1	28.664	0.0273	100	3.1089	3.1118	99.49
		1 1 2	28.713	-0.0212			3.1066	100.00
12	31.803	1 4 0	31.791	0.0122	22.3	2.8115	2.8125	25.13
13	33.690	1 4 1	33.703	-0.0128	11.5	2.6582	2.6572	10.31
14	34.498	0 4 2	34.451	0.0469	5.4	2.5978	2.6012	10.01
15	35.032	0 5 1	35.074	-0.0416	2.5	2.5594	2.5564	3.10
16	35.553	2 1 0	35.596	-0.0438	5.7	2.5231	2.5201	5.71
17	37.362	2 1 1	37.378	-0.0167	4.9	2.4050	2.4039	4.90
18	38.848	1 4 2	38.863	-0.0147	2.6	2.3163	2.3155	2.50
19	40.528	2 3 0	40.477	0.0512	1.8	2.2241	2.2267	1.80
20	41.912	-2 1 2	41.888	0.0247	2.2	2.1537	2.1550	7.41
21	42.138	2 1 2	42.189	-0.0519	5.9	2.1428	2.1403	5.81
22	42.622	1 3 3	42.602	0.0198	9.7	2.1195	2.1205	11.61
23	44.012	1 5 2	43.977	0.0349	3.3	2.0558	2.0573	3.30
		1 6 0	44.045	-0.0329			2.0543	3.90
24	44.378	2 4 0	44.377	0.0011	1.2	2.0396	2.0397	0.70
25	45.508	1 6 1	45.513	-0.0051	9.6	1.9916	1.9914	10.41

Final 2θ window: 0.07, Symmetry: monoclinic, a = 5.131(2) Å; b = 13.451(4) Å; c = 8.209(3) Å; β = 90.45(4); V = 566.6(3) Å^3; Z = 4.

PDF card 00-055-0703: a = 5.1294(8) Å; b = 13.4634(19) Å; c = 8.1865(19) Å; β = 90.060(24); V = 565.35 Å^3

Table A6-3 Coordinates, occupancies and isotropic thermal parameters of low-temperature $Li_{2.4}Zn_{0.8}P_2O_7$ by XRD data reported from Lapshin *et al.* [6].

Atom	Site	x	y	z	$100\times U_{iso}$ (Å^2)	Occ.
P1	4a	0.173(3)	0.688(7)	0.226(2)	1.47(2)	1
P2	4a	0.130(3)	0.4710(8)	0.248(2)	1.47(2)	1
Li1	4a	0.298(13)	0.793(5)	0.531(1)	3.57(3)	1
M1 (Li2, Zn2)	4a	0.113(4)	0.117(2)	0.589(3)	2.87(2)	(0.76, 0.24)
M2 (Li3, Zn3)	4a	0.118(2)	0.1027(6)	0.940(1)	1.94(2)	(0.44, 0.56)
O1	4a	0.467(4)	0.729(2)	0.704(3)	2.27(3)	1
O2	4a	−0.329(4)	0.322(2)	0.917(3)	2.27(3)	1
O3	4a	0.334(4)	0.701(2)	0.385(3)	2.27(3)	1
O4	4a	0.026(4)	0.583(2)	0.239(3)	2.27(2)	1
O5	4a	0.107(5)	0.578(2)	0.722(3)	2.27(2)	1
O6	4a	0.190(5)	0.956(2)	0.392(4)	2.27(4)	1
O7	4a	0.212(5)	0.961(2)	0.087(4)	2.27(3)	1
R_{Bragg} = 3.06 %; $R_{Rietveld}$ = 11.99 % **a(Å) = 5.130(1); b(Å) = 13.454(1); c(Å) = 8.205(1); β(deg) = 90.36(1);** ***Volume*(Å^3) = 566.305(48)**						